DOCTORAL RESEARCH THESIS

MODELLING OF DISTURBED FLOW REGIMES IN ASPIRATED PIPE SYSTEMS

by

MARTIN COLE, DipElecEng, ME(Monash), FAIM, FTSE, FIEAust, CPEng

Supervisors

Associate Professor PAULA BEEVER, PhD, FIEAust, CPEng
Associate Professor ÖZDEN TURAN, PhD

at the

CENTRE FOR ENVIRONMENTAL SAFETY AND RISK ENGINEERING

VICTORIA UNIVERSITY OF TECHNOLOGY

1999

SUMMARY

Aspirated systems such as those used for smoke detection are characterised by the use of long (e.g. $100m$), small-bore (e.g. $21mm$) pipes with sampling holes (e.g. $2mm$) drilled at regular intervals (e.g. $4m$). A low-power aspirator (e.g. 2W) draws a continuous sample of air from each hole throughout the monitored zone, via each pipe to a highly sensitive smoke detector. Critical objectives in the design of such systems are to achieve the highest possible "balance" (the distribution of hole flow rates and hence the effective smoke-sensitivity throughout the zone), commensurate with the lowest possible smoke "transport time" (from a hole to the detector). These two objectives are often in conflict.

Air flowing into the sampling hole constitutes an induction jet that disturbs the upstream flow regime. This disturbance, or that of a pipe bend, causes the established pipe velocity profile to reset to plug flow. The core velocity growth profile of the initially-disturbed, developing flow regime has been determined experimentally for a range of Reynolds numbers, having an effectivity length of up to 500 diameters. The range found relevant to aspirated pipe systems embraces the laminar, transitional and turbulent flow regions ($400 < \mathrm{Re} < 4000$). This family of growth profiles is used to determine the transport time for smoke entering a given hole, using a **Time Factor** algorithm. Dilution of the smoke due to mixing and due to the induction of fresh air from other holes is taken into account.

The disturbance also causes a local increase in the friction factor that affects the downstream pressure drop for at least 100 diameters. The friction factor for a range of disturbance levels and Reynolds numbers has been determined experimentally. The pressure drop in the vicinity of the hole is further increased as a result of the force required to accelerate the induction jet. Moreover, the hole flow rate is determined by the local pressure differential, the size of the hole and the size of the pipe, but this flow is enhanced by the upstream flow rate, in a phenomenon described as **Ultraflow**. External air flows typically caused by building ventilation and described as **crosswind**, cause a reduction in the hole flow rate in a phenomenon described as **Infraflow**. By superposition, these phenomena determine the net flow rate of each hole and therefore the flow rate in each pipe segment (between holes). This, coupled with the local friction factor determines the pressure distribution throughout the system. Since the local pressure differential determines the hole flow, all elements of the system are interactive and a computer program is required to obtain the system operating point by rapid iteration.

ACKNOWLEDGEMENTS

The supervision, advice and guidance provided throughout the project by Associate Professor Paula Beever at the Centre for Environmental Safety and Risk Engineering (CESARE) and by Associate Professor Özden Turan at the School of Built Environment (Mechanical Engineering), both at Victoria University of Technology (VUT), is greatly appreciated with thanks. Thanks also go to Professor Vaughan Beck, Pro Vice Chancellor (Research) at VUT for his support throughout the project, and to Vincent Rouillard of VUT for his assistance in providing equipment for temperature experiments.

Use of Laser Velocimetry (LV) apparatus was funded by VUT and made available by Melbourne University, at the G.K. Williams Cooperative Research Centre for Extractive Metallurgy. Thanks is extended to Dr Nicholas Lawson, Research Fellow in the Department of Chemical Engineering for his advice and guidance in the use of LV, and to Tim Berrigan for training and setup of the 3-axis LV traverse.

Thanks go to Mr Hans Verzijl who, through his company Vertech Pty Ltd provided facilities for experiments with dust filters, funded by IEI Pty Ltd.

Vision Systems Limited (VSL), in particular Dr James Fox and Peter Murphy, are thanked for continuing to support the project after the merger of IEI Pty Ltd with VSL, in the form of access to laboratory apparatus and the provision of time for research within the employment contract. The assistance of IEI / VSL technical sales staff and IEI / VSL clientele in the evaluation and testing of ASPIRE software, and the assistance of VSL R&D staff in the conversion of ASPIRE from a DOS to a Windows operating system, are also greatly appreciated.

Finally and most importantly, the tolerance and encouragement of family and friends has been an essential element in the ability to complete the project.

CONTENTS

CONTENTS

(continued)

TITLE PAGE

CONTENTS

(continued)

CONTENTS

(continued)

CONTENTS

(continued)

TITLE PAGE

LIST OF SYMBOLS

SYMBOL	UNIT	DESCRIPTION
A	m^2	cross-sectional area
A_{hole}	m^2	cross-sectional area of sampling hole
A_{Jet}	m^2	initial cross-sectional area of induction jet
A_{pipe}	m^2	cross-sectional area of pipe
B	m	boundary layer thickness
C_c	nil	loss coefficient in a component
C_h	nil	hole flow coefficient
C_I	$\%/m$	initial smoke concentration (undiluted)
C_S	$\%/m$	smoke concentration (diluted)
$C_{S\%}$	nil	smoke dilution factor
C_θ	nil	coefficient of flow at angular position
d	dia	pipe displacement in diameters
d_{250k}	dia	pipe displacement for $Re_e = 250{,}000$
d_{peak}	dia	pipe displacement for core velocity peak
e	nil	calculus constant (2.71828)
D	m	diameter
D_{hole}	m	diameter of a sampling hole
D_l	m	diameter of LV laser beam
D_{nozzle}	m	diameter of a sampling nozzle
D_{pipe}	m	internal diameter of pipe
E_u	$\%$	velocity measurement error (LV)
f	nil	friction factor
f_0	nil	friction factor at pipe entry
f_∞	nil	fully-developed friction factor
f_D	Hz	Doppler frequency (LV)
F_c	nil	Coil Friction Correction Factor
F_{2000}	nil	Time Factor at (e.g.) $Re = 2000$
F_{Re}	nil	Time Factor at any Reynolds number
F_T	nil	Time Factor
g	m/sec^2	acceleration due to gravity
H_{th}	Pa	aspirator net theoretical head
k	m^2/sec	kinematic viscosity (air: 0.000015 @ 20°C)
K_{asp}	nil	air density coefficient of aspirator pressure
K_{hole}	$m^{3.5}/kg^{1/2}$	hole flow coefficient ($f(D_{hole}, \rho)$)
K_{nozzle}	$m^{3.5}/kg^{1/2}$	nozzle flow coefficient ($f(D_{hole}, \rho)$)
K_{vent}	$m^{3.5}/kg^{1/2}$	vent flow coefficient ($f(D_{hole}, \rho)$)
$K(x)$	nil	friction factor correction term

LIST OF SYMBOLS

(continued)

SYMBOL	UNIT	DESCRIPTION
L_c	Pa	pressure loss in a component
L_d	%	level of flow disturbance
L_f	*dia*	friction factor development length
L_F	*m*	focal length of LV targeting lens
L_o	*m*	orifice thickness (length)
L_p	Pa	pressure drop in a pipe segment
L_h	*m*	head loss in a pipe segment
L_{pipe}	*m*	length of a pipe segment
L_{tube}	*m*	length of a capillary tube
n	*nil*	the value of an exponent
n_x	*nil*	the value of an exponent at displacement x
N_b	*nil*	number of additional bends in a pipe
N_p	*nil*	number of aspirators in parallel
N_s	*nil*	number of aspirators in series
O_{mV}	mV	Pressure gauge offset (millivolts)
P_{amb}	Pa	absolute ambient pressure
P_{asp}	Pa	aspirator operating pressure
P_{bend}	Pa	pressure drop of a single pipe bend
P_{bendN}	Pa	pressure drop of N additional bends
P_{max}	Pa	aspirator cutoff or maximum pressure
P_{gauge}	Pa	pressure gauge reading (Pascal)
$P_{max.c}$	Pa	corrected aspirator maximum pressure
P_0	Pa	absolute ambient pressure in the free stream
P_o	Pa	pressure drop of an orifice
P_{system}	Pa	system differential pressure
δP_{jet}	Pa	pressure drop due to acceleration of induction jet
ΔP	Pa	differential pressure
ΔP_{back}	Pa	pressure drop of a detector rear exhaust
ΔP_{bottom}	Pa	pressure drop of a detector bottom exhaust
ΔP_{chmb}	Pa	pressure drop of a detector chamber
ΔP_e	Pa	pressure drop of a filter element
ΔP_{filter}	Pa	pressure drop of a complete filter unit
ΔP_{hole}	Pa	pressure differential of a hole
ΔP_{man}	Pa	pressure drop of a detector manifold
ΔP_{mod}	Pa	pressure drop of a modified manifold
ΔP_{nozzle}	Pa	pressure differential of a nozzle

LIST OF SYMBOLS
(continued)

SYMBOL	UNIT	DESCRIPTION
ΔP_{side}	Pa	pressure drop of a detector side exhaust
ΔP_{stat}	Pa	static pressure differential
ΔP_{vent}	Pa	pressure differential of an end vent
Q	*litre/min*	volumetric flow rate (Figures show as l/min)
Q_{dn}	*litre/min*	pipe flow rate downstream of sampling hole
Q_{hole}	*litre/min*	flow rate through a sampling hole
Q_{hole}	*litre/min*	flow rate of hole induction jet into pipe
Q_{jet}	*litre/min*	flow rate through a sampling nozzle
Q_{pipe}	*litre/min*	flow rate through a pipe
Q_{stat}	*litre/min*	component of flow rate due to static pressure
Q_{system}	*litre/min*	system operating flow rate
Q_{tube}	*litre/min*	flow rate through a capillary tube
Q_{up}	*litre/min*	pipe flow rate upstream of sampling hole
ΔQ_{holeC}	*litre/min*	incremental hole flow rate due to Infraflow
r	*m*	radial dimension in a pipe or tube
r_{target}	*m*	effective radius of LV target
R	*m*	radius of pipe or tube
R^2	*nil*	least-squares approximation value
R_c	*m*	coiling radius of capillary tube
Re	*nil*	*pipe* Reynolds number
Re_e	*nil*	*entry* Reynolds number
Re_{eT}	*nil*	*entry* Reynolds number at flow transition
Re_{hole}	*nil*	nominal Reynolds number for a hole
Re_{holeU}	*nil*	hole Reynolds number with Ultraflow
$\mathrm{Re}\,n$	*nil*	normalised Reynolds number for a hole
$\mathrm{Re}\,n_A$	*nil*	normalised hole Re asymptote for Ultraflow
$\mathrm{Re}\,n_o$	*nil*	normalised hole Re with nil upstream flow
$\mathrm{Re}\,n_T$	*nil*	normalised Re Ultraflow transition component
$\mathrm{Re}\,n_U$	*nil*	normalised hole Re with Ultraflow
R_{mV}	*mV*	Pressure gauge reading (millivolts)
R_u	*nil*	ratio of core velocity to average velocity
R_{Umax}	*nil*	final value of core velocity ratio
R_{Ud}	*nil*	core velocity ratio at displacement d
S	*m*	displacement from pipe entrance
S_{asp}	RPM	tachometric speed of an aspirator
$Term1$	*nil*	linear coefficient in an equation
$Term2$	*nil*	second-order coefficient in an equation

LIST OF SYMBOLS
(continued)

SYMBOL	UNIT	DESCRIPTION
T_r	*sec*	smoke transport time at a radial position
$T_{r\%}$	*%*	increase in smoke transport time (penalty)
T_0	*sec*	smoke transport time at pipe core ($r = 0$)
T_T	*sec*	smoke transport time
T_x	*sec*	incremental smoke transport time
u	*m/sec*	average velocity
u_{avg}	*m/sec*	average velocity
u_{core}	*m/sec*	local velocity at pipe centreline
u_{hole}	*m/sec*	average velocity of air within a sampling hole
u_{max}	*m/sec*	maximum attainable velocity at pipe centreline
u_p	*m/sec*	velocity of particle in airstream (LV)
u_{pipe}	*m/sec*	average velocity of air within a pipe
u_r	*m/sec*	aspirator impeller radial air velocity
u_2	*m/sec*	aspirator impeller tangential air velocity
U_c	*m/sec*	crosswind velocity
α_i	*nil*	eigenvalue in friction factor equation
β	*nil*	momentum correction factor
β_2	*deg*	aspirator impeller blade outlet angle
ε	*m*	surface roughness of a pipe
ϕ	*deg*	angle between LV laser beams
λ	*m*	wavelength of light
μ	$N\ s/m^2$	viscosity (air: $1.80E$-05 @ 20°C)
π	*nil*	ratio of a diameter to circumference (3.1416)
ρ	kg/m^3	mass density (air: 1.204 @ 20°C)

LIST OF TABLES

LIST OF FIGURES

TITLE PAGE

LIST OF FIGURES
(continued)

TITLE PAGE

CHAPTER 3 - DUST FILTER CHARACTERISATION

LIST OF FIGURES
(continued)

TITLE PAGE

LIST OF FIGURES
(continued)

TITLE PAGE

LIST OF FIGURES
(continued)

TITLE PAGE

LIST OF FIGURES
(continued)

LIST OF FIGURES
(continued)

LIST OF FIGURES
(continued)

TITLE PAGE

LIST OF FIGURES
(continued)

LIST OF FIGURES
(continued)

TITLE PAGE

LIST OF FIGURES
(continued)

TITLE PAGE

LIST OF FIGURES
(continued)

TITLE PAGE

CHAPTER 1 - INTRODUCTION, LITERATURE REVIEW

1.0 INTRODUCTION

This project was prompted by an industrial development requirement but it very quickly became apparent that novel work would need to be undertaken, with the prospect of discovering new phenomena in fluid dynamics. The novelty in this thesis lies in describing the flow of fluids in pipes incorporating sampling holes that produce induction jets, which cause disturbances to developing flow conditions under laminar, transitional or turbulent regimes. From the outset, the objective was to develop a methodology to produce a working computer software model of such aspirated pipe systems, based upon the literature, as a means for scoping the critical factors. Then to comprehensively investigate all fundamental aspects of the fluid dynamics involved, thereby to revise and perfect the computer model by incorporating the new phenomena discovered, and investigating their consequences within any practical system. Such discoveries would be useful in a range of different applications.

This chapter deals with the historical development of conventional smoke detection technologies, the available levels of sensitivity to smoke, the more-recent development of nephelometric type smoke detection, the development of aspirated smoke detection technologies and the need for ongoing research in this area. The remainder of this chapter contains the literature survey which was conducted in two phases (fire industry search and fluid dynamics search) and a review thereof, the research requirements, initial concepts for the computer model, the research objectives and the thesis structure.

1.0.1 HISTORICAL DEVELOPMENT of FIRE DETECTION

Conventional smoke detectors were developed in the 1950's, initially by Cerberus of Switzerland. They were designed to be installed in a square grid pattern across a ceiling, in a manner similar to sprinkler heads or heat detectors. Over time, two kinds of smoke detector were developed - the ionisation and the optical.

The ionisation type uses a small radioactive pellet (originally Radium and more-recently the safer Americium) to generate an ionised pocket of air within a metal chamber. By application of voltage to the chamber in a high-impedance circuit, this ionisation allows a small electrical current to flow. If smoke enters the chamber, the current falls and at some predetermined level, the alarm is triggered.

Whereas all earlier technologies for automatic fire detection had relied upon heat activation, this new device heralded the era of "early warning" because smoke could be detected at an earlier stage of fire development, than heat could. The sensitivity of this technology is biased toward smoke from fast flaming fires, which reduces the prospect of early warning in the case of overheating or smoldering materials (being precursors to many flaming fires).

The advantage of this technology is its low cost, with battery-operated domestic versions being on sale for under $10 each (although the more-reliable hard-wired commercial units cost closer to $100). However the technology is prone to false alarms, particularly from draughts which cause the ionised pocket of air to be blown away, thereby reducing the chamber current and causing an alarm.

The optical smoke detector was developed later and fell into two categories - the beam type and the point type. The beam type uses a projector and a separate receiver typically located some tens of metres away. The projector is used to transmit a focused modulated light beam toward the receiver. The receiver is aligned to receive this modulated signal and monitor its intensity. Smoke crossing the path of the light beam would partially obscure the light, reducing the strength of the received signal. If this signal falls below a predetermined level, the alarm is triggered. Such a device has therefore become known as a light obscuration detector.

This concept was easily understood by users, because it related directly to human visual range (through smoke). Such a detector offered great promise for coverage of large open spaces with simple installation, however, problems of inadequate sensitivity, maintenance of good beam alignment (building movement), and dust buildup on lenses have severely limited its application.

The point type optical detector operates on a different principle from the beam detector. It is composed of a miniature projector and receiver within one small housing such that the receiver is shaded from the direct projector light. The presence of smoke within the detector chamber would cause some light to be scattered off the smoke particles towards the receiver. If the strength of this received signal exceeds a predetermined level, the alarm is triggered. Instead of detecting light obscuration therefore, point optical detectors operate on the principle of light scatter (which is the complement of light obscuration, given that light absorption is relatively insignificant). For ease of understanding however, both types of optical detector are calibrated in terms of their equivalent sensitivity to light obscuration by smoke.

Because of the relatively long wavelength generally used for the projector light (infra-red light-emitting diode or IR-LED), the sensitivity of this technology is biased toward smoldering fires. This reduces the prospect of early detection of fast flaming fires, particularly arson. Point optical smoke detectors do not suffer from the disadvantages of the ionisation or beam types mentioned above, but they are more costly than ionisation types and they are prone to false alarms caused by dust or lint.

1.0.2 AVAILABLE SENSITIVITY

The typical sensitivity of these point detectors has equated to about $15\%/m$ obscuration, with beam detectors more-likely to be set at 40% overall (40% obscuration of a $10m$ beam would equate to $4\%/m$, provided that this smoke was evenly spread across the entire $10m$ length). Some point detectors are now available with a sensitivity of $4\%/m$ while new. Over time with soiling there is a tendency to desensitise significantly. The available sensitivity has been constrained by the need for a product of small size and low cost, as well as the need to minimise false alarms.

There has been one very recent development in optical point detection technology utilising a semiconductor laser instead of an LED. This is claimed to provide sensitivity as high as $0.1\%/m$ but this has yet to be established. It relies upon a powerful computerised fire indicator panel to process the signals from each cluster of three detectors. This is done because an individual detector may not be able to provide such sensitivity, reliably. This system has not been installed in any significant quantity so its performance and reliability are uncertain, particularly with regard to a range of fuels (sensitivity), environments (false alarms) and air speeds (ventilation effects).

During the development of the ionisation detector several decades ago, the materials of risk as found in home or office environments were basically natural. Wood, cotton and similar cellulosic materials were used for all furniture and furnishings. These materials would burn with relatively low intensity and produce toxic fumes and gases at relatively slow rates. Accordingly it was reckoned that an occupant could have as much as 30 minutes to effect an escape following the onset of flame. Based upon this scenario, smoke detectors initially gained a good reputation for early warning.

Nowadays we see the widespread use of synthetic materials in furniture, furnishings and insulation, which burn more fiercely and produce a wider range of toxic fumes and gases at much faster rates than natural materials could. The fire protection industry now widely accepts that the vast majority of fire deaths occur due to "smoke" inhalation. Toxins such as Acrolein (CH_2CHCHO) produced in fat, oil, petroleum and plastics fires can be fatal in concentrations of one thousandth of one percent. Consequently it is widely recognised in the fire industry that following the onset of flame in a typical office or bedroom, an occupant would have only 3 minutes or even less to effect an escape. By this time it is likely that the toxic fumes would be untenable or the room would reach flashover.

By contrast, research under the leadership of Dr Caird Ramsay at CSIRO Division of Fire Technology (Victoria) during the 1980's has indicated that synthetic materials used in furniture can pyrolise or smolder for periods of typically 90 minutes before the likely onset of flame. Detection of this type of "smoke" at an early stage can provide a significant reduction in risk to the occupants, the equipment and the building.

Besides the threat to life and property, now emerging as one of the most important aspects of fire protection is consequential loss and the need to limit business (or service) interruption.

The Hinsdale (Illinois, USA) telephone exchange fire in 1988 was limited to a switcher unit occupying only a few square metres, but the fire cost an estimated US$100M. Moreover, some 100,000 people were unable to use their home telephone or a nearby public telephone even in an emergency to call the police, ambulance or fire brigade, for more than one month. Countless small businesses that relied upon the telephone (pizza delivery, florist etc) went out of business. O'hare airport, the world's busiest, was largely stalled for 10 days because telephone reservations could not be made. And this fire had occurred only 18 months after a telephone exchange fire of similar cost in The Bronx (New York, USA).

Society nowadays has become particularly dependent on the telephone network. Increasingly so with the advent of personal computers with modems, E-mail and the Internet. The network is largely taken for granted until it goes off-line. When it does, society is ill-equipped to cope. The same is true of other facilities such as transport in all its forms, and all the other essential services. Over the past two decades, authorities have become increasingly aware of the need to prevent any interruption to such services.

1.0.3 NEPHELOMETRIC SMOKE DETECTION

It was in the 1970's that the Australian Post Office (APO) as it was then known, engaged the Commonwealth Scientific & Industrial Research Organisation (CSIRO), to help investigate technologies that could prevent service interruption due to fire. APO provided a test site so that every available type of fire detection device could be installed, to discover the most appropriate technology for telephone exchanges, computer rooms and cable tunnels. The materials of risk were insulated cables in a wide range of sizes, which were overheated with electric current or hot plates.

Earlier, CSIRO had been undertaking research into forest fires, using a commercially-available laboratory nephelometer (optical air-pollution monitor). This had been installed in a light aircraft and flown through smoke plumes, principally during the 1970 bushfire outbreak in the Karri forests south of Perth (Western Australia). During these flights CSIRO had collected data to calibrate the nephelometer using absolute filters to weigh the mass of smoke monitored at each run. They were able to correlate these readings with visual range and light obscuration. The span of smoke concentration was some 20 to 240 $\mu g/m^3$ in a linear relationship. This corresponded to a visual range span of 40 to 4 km respectively in a hyperbolic relationship.

CSIRO suggested that this nephelometer should be used as the benchmark for the APO fire tests. This was installed to monitor smoke levels within the return-air ducts of the mechanical ventilation system, utilising a chart-recorder output display.

At the conclusion of several weeks of testing, it was discovered that there was not one commercially-available fire detection technology suitable for preventing major damage to telephone equipment. The currently-available detectors operated far too late, well into the fast flaming stage, when the fire had become almost uncontrollable.

The one technology that showed great promise was the nephelometer itself. Its available sensitivity was found equivalent to 0.1%/m obscuration full-scale, with useful indications down to one-tenth this value. Consequently its sensitivity could be hundreds of times greater than currently-available smoke detectors. With this it could detect the early overheating stage of a potential fire, allowing plenty if time for preventive action before the onset of flame.

As an installed, automatic fire detector, the nephelometer was unsuitable because of its high cost, long-term drift, lack of ruggedness and the lack of suitable alarm outputs (chart recorder only). At the APO workshops a prototype smoke detector was developed, which had adjustable detection thresholds to activate an alarm system, and comprised a dual-chamber design intended to compensate for drift in sensitivity as well as to compensate for externally-introduced pollution. They then sought industry's commercial development and manufacture of this nephelometric smoke detector.

At this time the broad concept for incipient fire detection was based upon the use of an ultra-sensitive smoke detector monitoring air from a ventilation duct. However, it remained to perfect the instrument for high reliability and low cost, and to develop efficient, reliable and economic alternative methods for gathering and conveying smoke to the detector, such that the high sensitivity could be properly utilised in a variety of built environments.

1.0.4 INITIAL DEVELOPMENT

It may be of passing interest at this juncture to briefly note the development history of the detector itself, because this can teach a valuable lesson in the research-development-commercialisation cycle involving government and industry.

In the mid-1970's APO approached Australia's then-largest electronics manufacturer, AWA to commercialise the detector. AWA undertook to investigate this and approached Australia's largest fire alarm company, Wormalds for advice. However Wormalds feared a high false alarm rate from such sensitive equipment and effectively discouraged AWA.

Some three years passed and APO became frustrated by a lack of progress. In 1977 they opened a tender for development of the technology, offering a $60,000 R&D grant, a blanket order for the first 60 products, and access to their patent rights relating to the dual-chamber version.

Of the five applicants, IEI Pty Ltd (then employing 50 people) was regarded as too small. Fire Fighting Enterprises had good fire industry knowledge and route to market, but lacked a credible R&D capacity. British Aerospace Australia had a good R&D capacity but lacked good fire industry knowledge. APO therefore encouraged FFE and BAA to present a joint venture submission, which was accepted.

However, various individuals at APO and CSIRO were dissatisfied, fearing that the AWA mistake would be repeated. They preferred a small, flexible company to take-on the challenge. While giving IEI moral encouragement, they could offer no financial support or blanket order, nor access to the dual-channel patent rights.

Two years later the FFE/BAA detector was launched at a price of $7000 each, and 60 units were delivered to APO. This unit was of high quality (aviation standard), but the first IEI model had been launched some six months earlier, at less than half the price.

Although APO/Telecom National Headquarters felt contractually bound not to purchase IEI units for five years, almost all of the original 60 FFE/BAA units were never installed and no further deliveries were made. It was primarily the support given to IEI by the State Electricity Commission of Victoria, who had originally planned to manufacture their own version of the detector, that gave IEI their initial market of any size. Apart from a few sites within the Victorian Region, widespread adoption of the system by Telecom came later. Now Telecom/Telstra is Australia's largest single user.

To provide the necessary reliability, features, miniaturisation and reduced cost for export markets, during 1982 the detector was completely re-designed from scratch at IEI, incorporating numerous patented inventions that were filed in Australia and throughout the developed world (Cole, 1983 a to g).

The world market for aspirated smoke detection was pioneered by IEI from 1983 onwards, to a very sceptical and conservative fire industry. Marketing persistence and improving technical performance maintained the company's market leadership and gained more than 50,000 sites for the system by mid 1998. From 1990 and again from 1993 this success had stimulated direct competitors (being former IEI UK distributors or employees), producing alternative brands of aspirated smoke detector and capturing a fairly static 20-25% total market share between them.

1.1 ASPIRATED SMOKE DETECTION

The new concept of aspirated smoke detection (as developed at IEI) involves the forced induction and transport of a continuous sample of air to a single detector. This air sample must faithfully represent the air quality throughout a designated fire zone, which may be as large as $2{,}000m^2$.

The detector is a form of nephelometer (air pollution monitor) which has an unusually high sensitivity, typically hundreds of times higher than conventional smoke detectors. A true nephelometer maintains this high sensitivity across the full spectrum of smoke particle sizes or types that are produced at any stage of fire development, possibly involving a wide range of combustible materials. Such high sensitivity is required for two purposes:

(a) to detect the earliest traces of airborne particles or aerosols released due to the overheating (decomposition or pyrolysis) of materials, and

(b) to overcome the dilution of this “smoke” caused by the predominantly “fresh” air within the zone.

A modern aspirated smoke detection system includes a number of small-bore pipes distributed across a ceiling (above or below). Sampling holes (pipe-wall orifices) are drilled into each pipe at suitable intervals. Air is continuously drawn into the pipework via all of the holes, towards the centrally located detector using an air suction pump (aspirator).

The location of the pipework and the holes is generally governed by local fire codes and standards such as Telecom Australia TPH1525 (1995) and Australian Standard AS 1603.8 (1996). Typically, the pipes and holes are laid out according to a square grid pattern that places each hole where a conventional point detector would otherwise be located. In the case of higher risk areas, the spacing of this grid pattern is reduced for denser coverage. Such a square grid is illustrated in Figure 1.1 (being a reflected ceiling plan).

A particular advantage of aspirated smoke detection is the high prospect of aggregation - that is, smoke from one source may enter several sampling holes at once, thereby increasing the smoke concentration (reducing the dilution) and causing an earlier warning. Aggregation cannot occur with conventional point detectors.

Sampling pipework is now being installed in a wide variety of configurations. If the pipework is at ceiling level, sometimes it is surface-mounted in full view. In areas where aesthetics dictate concealment of the system, the pipework is mounted above the ceiling, with flexible “capillary” tubes each coupling the pipe to a ceiling-mounted nozzle (which penetrates the ceiling). This nozzle is much smaller than a conventional point detector, and is often made invisible.

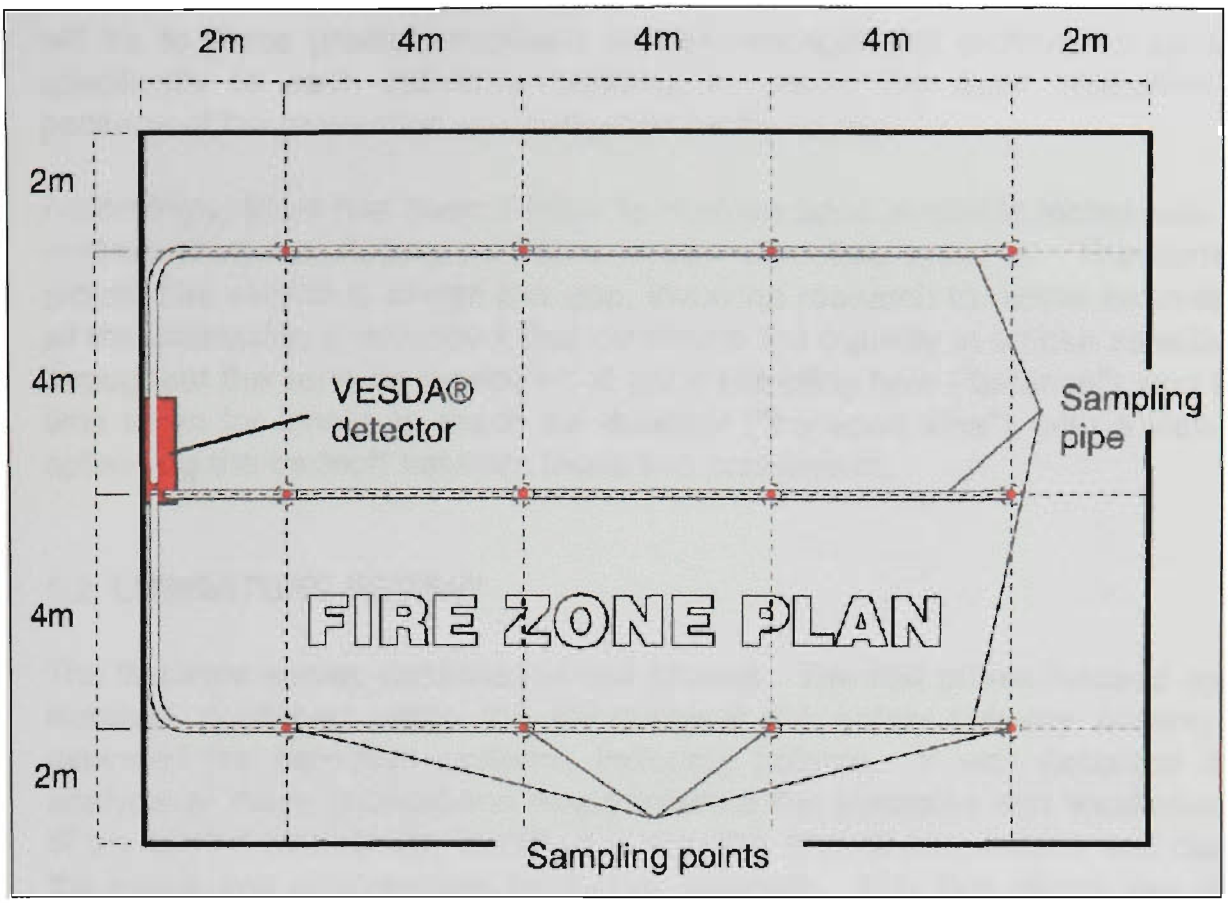

Figure 1.1 - A modern, grided pipe layout for a typical fire zone (IEI, 1991)

1.1.1 THE NEED FOR ONGOING RESEARCH

Until recent years, aspirated smoke detection system pipework was generally designed in close cooperation with the manufacturer. Nowadays, given the large annual volume of installations (with 50,000 systems installed by mid 1998), and a growing self-reliance within the fire industry, there is increasing concern to ensure that the growing number of system designers, installers and maintainers exercise sufficient competence to ensure system reliability. This is especially important because in most sites employing aspirated smoke detection, it is the only form of active fire protection provided.

In response to this concern, there is increasing pressure for the provision of approved system design tools (software). AS 1603.8 - 1996 calls for an assessment of the design tool as an essential part of new product approvals. Whereas Australia has led the world in developing such Standards, both Factory Mutual and Underwriters Laboratories in USA now have a similar requirement.

All of this should be understood within the context of Performance Based Building Codes which are emerging worldwide, as an alternative to prescriptive codes. This has the effect of placing increasing demands upon the competency with which building systems are designed. The end result will be to place greater emphasis on risk management techniques applied specifically to each individual building, to obtain the most cost-effective package of fire prevention and mitigation technologies.

Accordingly, there has been a need to improve upon available techniques for mathematically modelling aspirated smoke detection systems. The current project has served to bridge this gap, involving research to model accurately all the interacting phenomena that determine the equality in smoke sensitivity throughout the zone as measured at each sampling hole ("balance"), and the time taken for smoke to reach the detector ("transport time"), with a view to optimising the tradeoff between these two parameters.

1.2 LITERATURE REVIEW

The literature survey consisted of two phases. The first phase focused upon literature published within the international fire safety industry relating to aspirated fire detection systems, including patents. It was expected that analysis of these publications would indicate the strengths and weaknesses of the current technology, identify and size the system parameters, and clarify the needs and opportunities for further research. This first phase was also used to identify the specific areas of interest relating to orifice flow rates and pipe flow regimes requiring further study, thereby providing the basis for the second phase of the literature survey - the fluid dynamics literature.

1.2.1 PHASE 1 - ASPIRATED SMOKE DETECTION

1.2.1.1 THE DETECTOR

Ahlquist and Charlson (1967), Charlson (1968) and Charlson et al. (1969) describe a large nephelometer and its use in air pollution monitoring of urban environments, particularly for recording smog levels. Garland and Rae (1969) discuss the problems of its calibration. This very sensitive type of instrument formed a basis for the investigation and development of aspirated, ultra-high sensitivity smoke detection.

Claiming more stable and reliable operation, Packham and Gibson (1973) filed a patent describing a two-channel version of the nephelometer. Subsequently Cole (1983 f) found that this key feature is inappropriate.

Based upon airborne measurements of karri forest fire smoke plumes, Eccleston et al. (1974) calibrated the sensitivity of a nephelometer in terms of the light scattering coefficient and the smoke concentration relevant to this kind of smoke. The analysis was supported by a supplementary paper from Packham (1974). The scattering coefficient is obtained from:

$$\phi = 100\left(1 - e^{-bx}\right)$$

where ϕ ($\%/m$) is the scattering coefficient and b (m^{-1}) is the integrated scattering coefficient for a light wavelength of $550nm$. Correlation with the light scattering data obtained from testing clear gases - Helium, Air, Carbon Dioxide and Freon12 - yielded an equation to the line of best fit:

$$b_{scat550} = \left(2.385\, V_N - 1.702\right) * 10^{-4}$$

where V_N is the output voltage of the nephelometer used, and is readily converted to $0.1\%/m$ full-scale. Human visual range is reached when the light intensity received from a target by an observer differs from the background by less than 2%. By substitution of $\phi = (100 - 2)/100 = 0.98$, the visual range is:

$$R_v = \frac{3.9}{b_{scat550}}$$

where R_v is the visual range (m). The results of applying this set of equations are presented graphically in Figure 1.2, demonstrating that a nephelometer calibrated in the equivalent smoke obscuration span of 0.01 to 0.1 $\%/m$ has the resolution to detect smoke haze with a visual extinction range of 40 to 4 km, corresponding to an airborne smoke mass density range of 20 to 240 $\mu g/m^3$, respectively (as mentioned earlier).

This represents two to three orders of magnitude greater sensitivity than conventional smoke detectors, providing the capacity for detecting the pyrolysis ("overheating", or thermal decomposition) of most materials, as well as smoldering, or highly diluted smoke from distant flaming fires. Of importance to the next Section, note that all such "smoke" typically cools to ambient temperature before it is detected, and its low concentration has very little impact on the density of air flowing through pipes (~10^{-5}%).

Cole (1983 a to f, 1991 a, 1992 a & b, 1995 a & b) patented a series of inventions in Australia (extended worldwide), improving the nephelometer concept specifically for fire industry applications, affecting its reliability, miniaturisation, fluid kinematic loss, solid-state detection, signal processing, controls, displays, battery standby operation, ruggedness, cost reduction, and volume manufacture. This development resulted in the first practical, reliable and affordable instrument for aspirated smoke detection, suitable for export.

Although the nephelometer itself had originally been known as VESDA® (Very Early-warning Smoke Detection Apparatus), this term subsequently became understood to embrace the complete aspirated smoke detection system which includes the air-sampling pipework, pump, dust filter, associated hardware, and controls (not including the fire alarm indicator panel or the monitoring service).

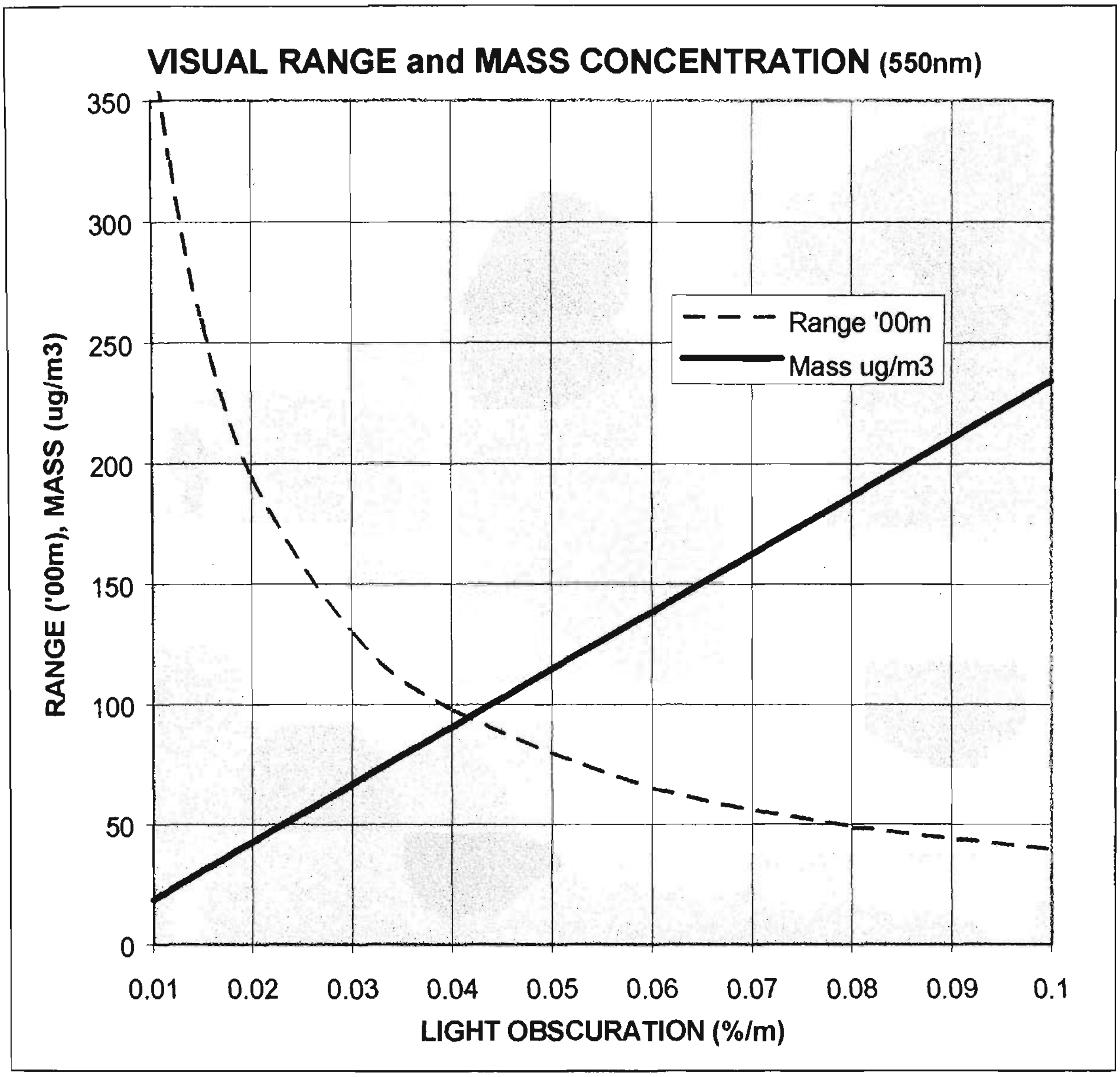

Figure 1.2 - Nephelometer sensitivity

1.2.1.2 ASPIRATION TECHNIQUES

The first known use of aspirated pipework for smoke detection systems is described by Marr (1928). This utilises a long pipe deployed around a ship's hold. Smoke is collected by a number of dome-shaped, downward-opening funnels connected to pipe inlets. This pipe carries smoke to an illuminated chamber with a visual (human) inspection window. There is no discussion of the design considerations for the pipe inlets, the pipe sizing or pump selection.

Packham et al. (1975) published the first known paper describing a method for conveying smoke from a room to a nephelometer. Shown in Figure 1.3, their method for smoke capture involves connecting a short pipe from the return air duct of a mechanical service, to the nephelometer and then to an air suction pump (100W, 240V AC centrifugal blower). No detail of the smoke pickup probe is provided, and the pump is used to overcome the negative relative pressures within the ducts. A supplementary "reference" detection channel is shown for reducing false alarms due to external smoke.

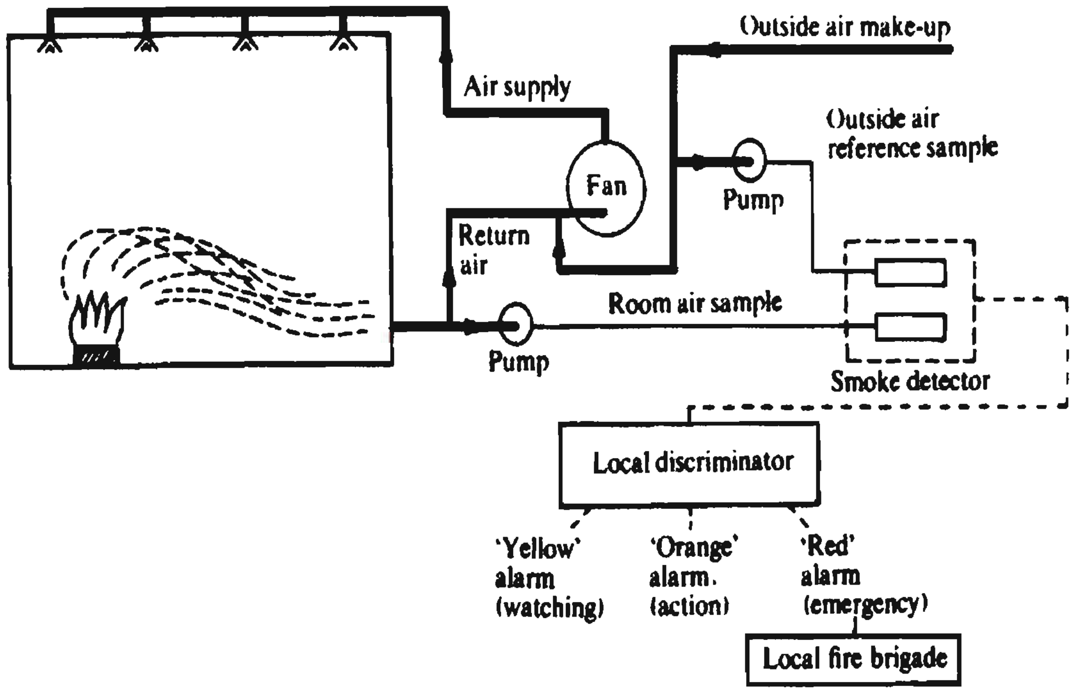

Figure 1.3 - Duct monitoring technique (Packham et al, 1975)

Petersen (1980) published concepts for the monitoring of several rooms within one zone by the use of branched, open-ended pipework as shown in Figure 1.4, and for area coverage using return ventilation duct detection as shown in Figure 1.5. It is notable that in both cases, a relatively high total airflow is indicated, with the detector positioned to draw only a sample of the total airflow (this would minimise time delay without affecting smoke density measurement).

To describe the various air sampling arrangements then envisaged, Cole (1982) directed the preparation of a series of illustrations. Figure 1.6 shows a computer room with suspended floor plenum, including a separate reference detector used to monitor incoming "fresh" air quality (its reading being subtracted from that of the other detector). Figure 1.7 shows three detectors in a return-air ventilation duct application, Figure 1.8 shows equipment racking (using holes in the pipe to draw-off samples of any rising smoke) and Figure 1.9 shows a method using small flexible tubes extended into hotel room air conditioners, used for sampling the air that recirculates throughout the room.

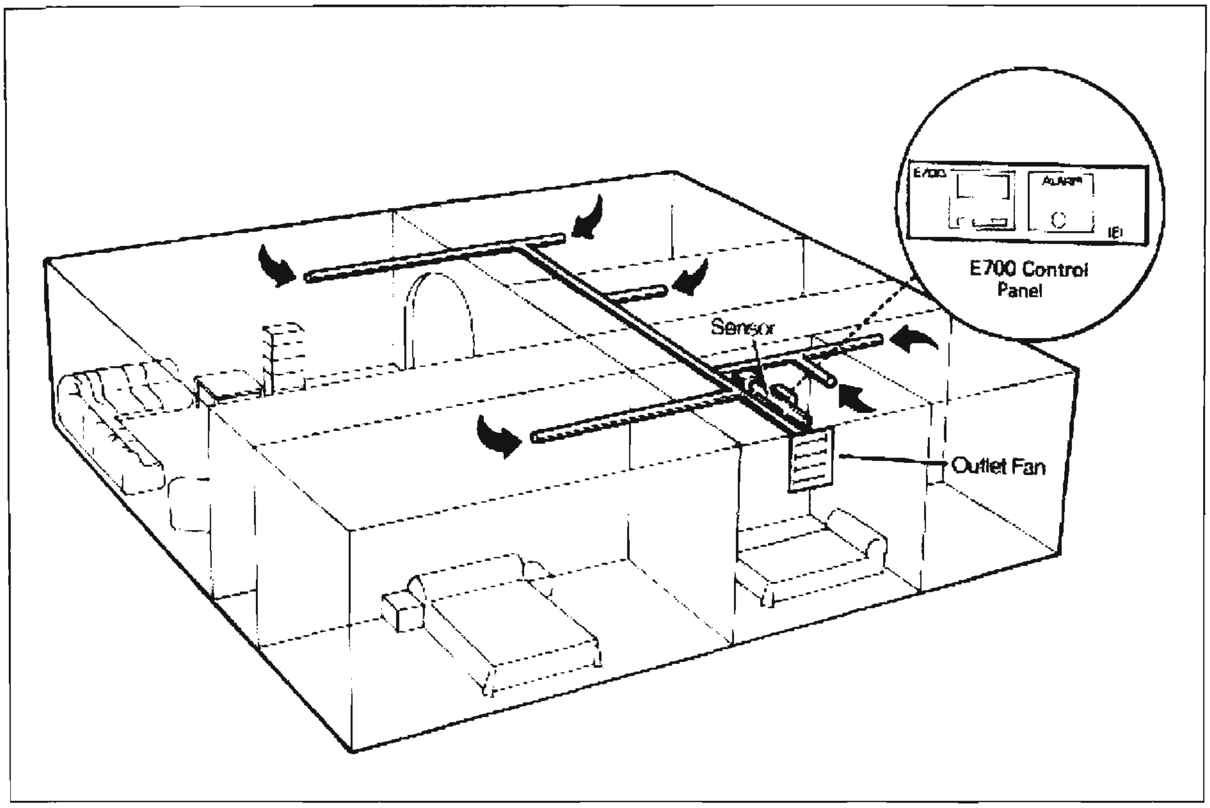

Figure 1.4 - Pipework smoke detection (Petersen, 1980)

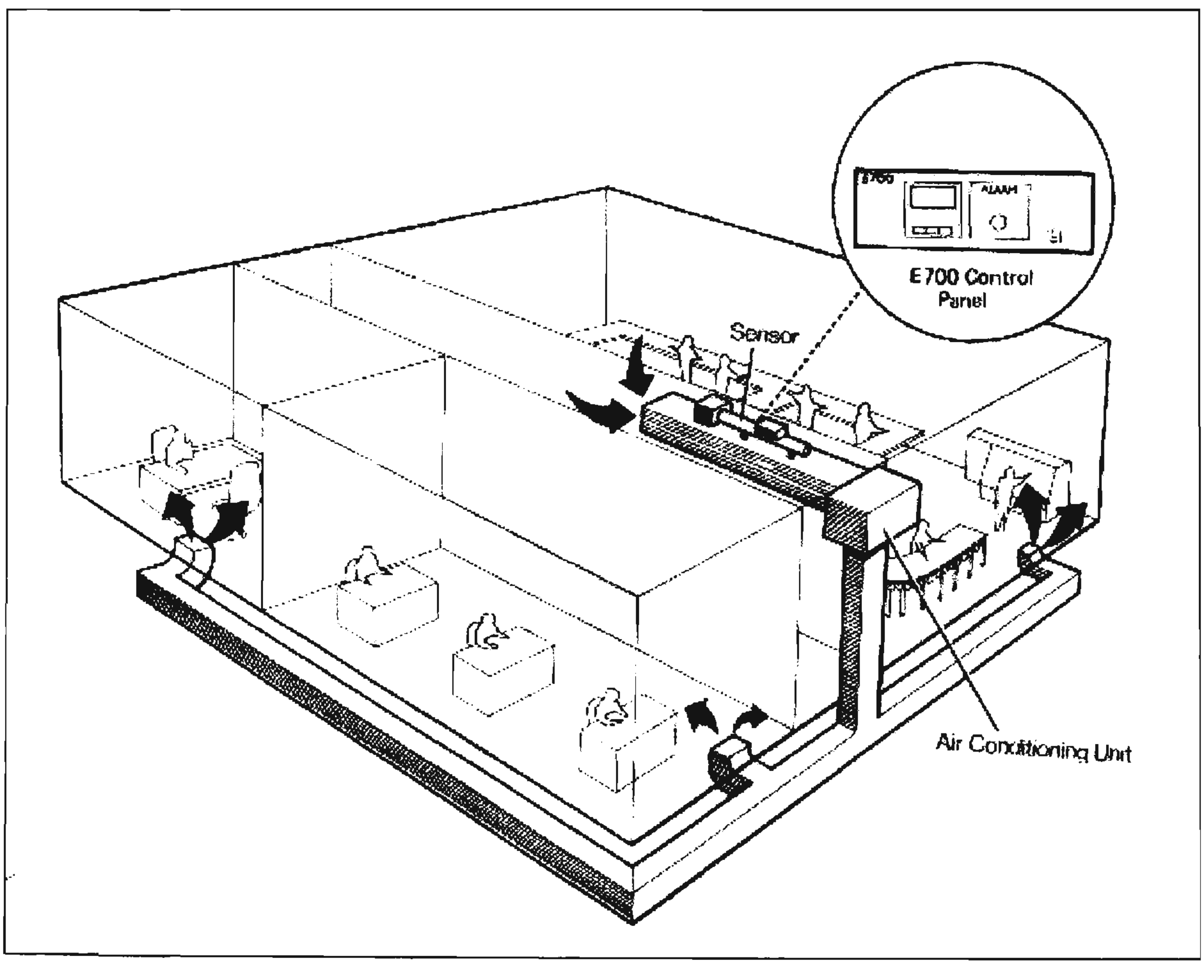

Figure 1.5 - Ductwork smoke detection (Petersen, 1980)

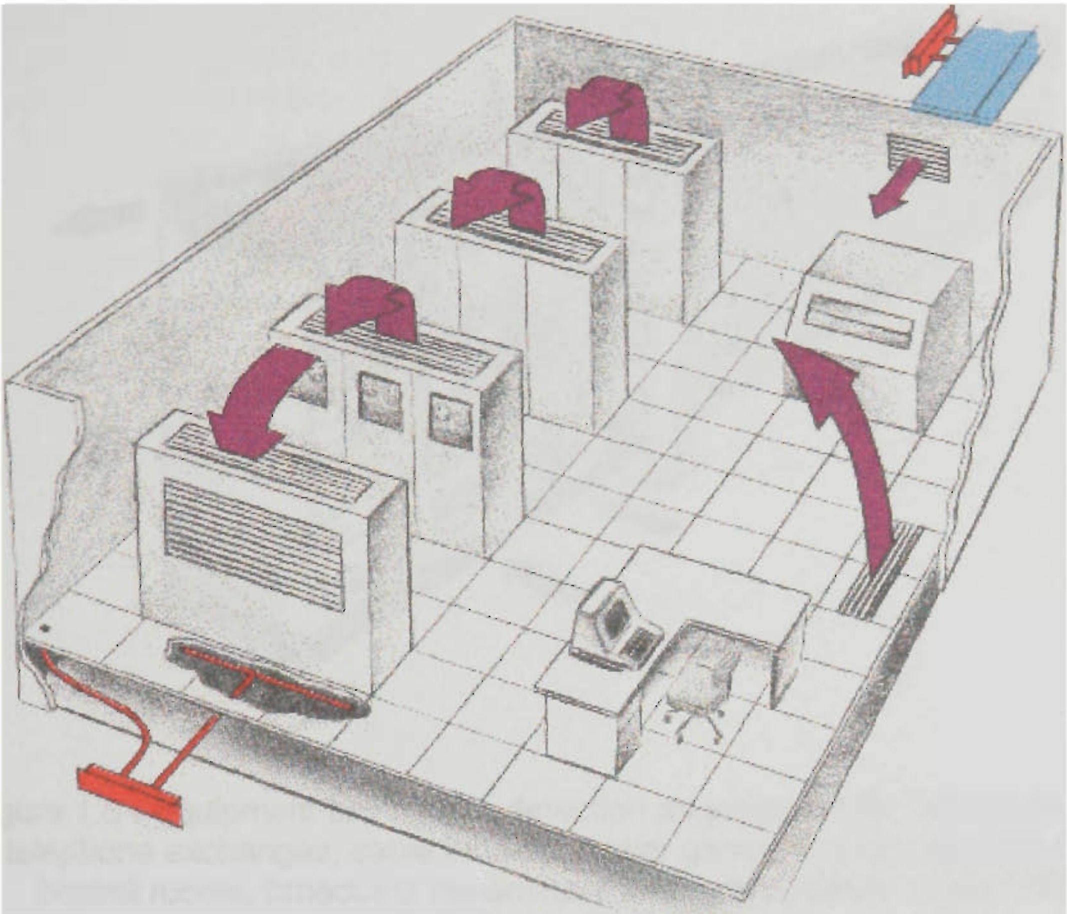

Figure 1.6 - Plenum smoke detection as proposed for "computer rooms, cleanrooms, control rooms, operating theatres and radio/tv studios using under-floor ventilation" (Cole, 1982)

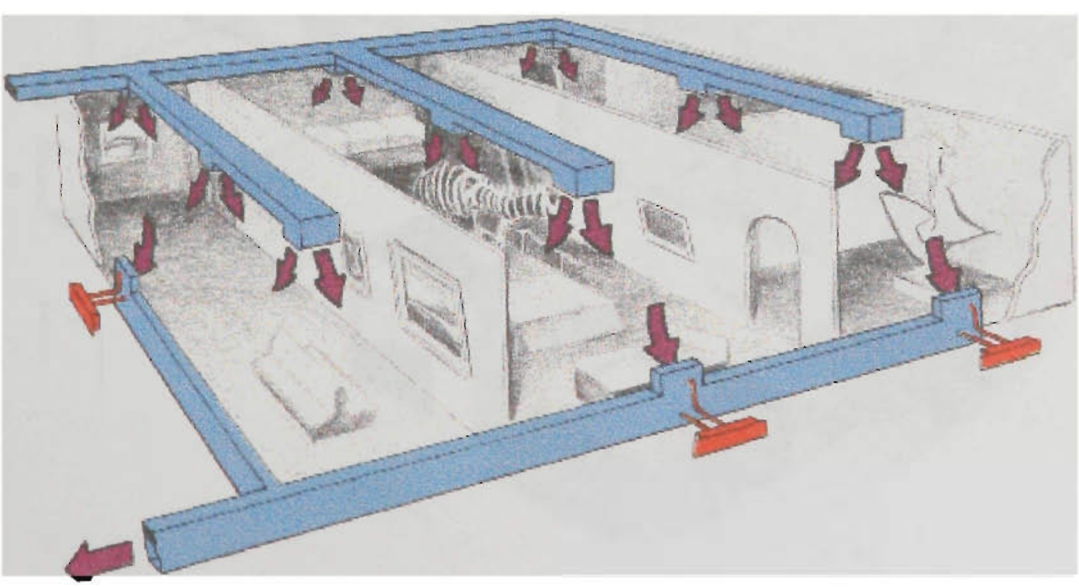

Figure 1.7 - Ductwork smoke detection as proposed for "laboratories, offices, supermarkets, hospitals, institutions, libraries, museums, art galleries, studios and theatres" (Cole, 1982)

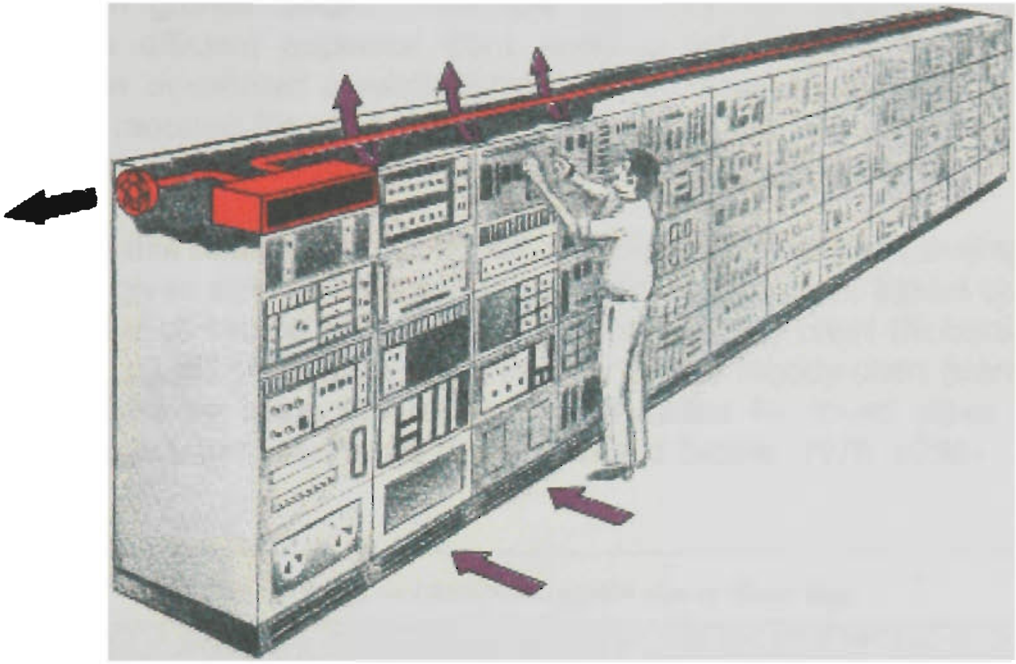

Figure 1.8 - Equipment bay smoke detection as proposed for "electronic racks, telephone exchanges, cable tunnels, power generators, transformer halls, control rooms, broadcast transmitters and switchboards" (Cole, 1982)

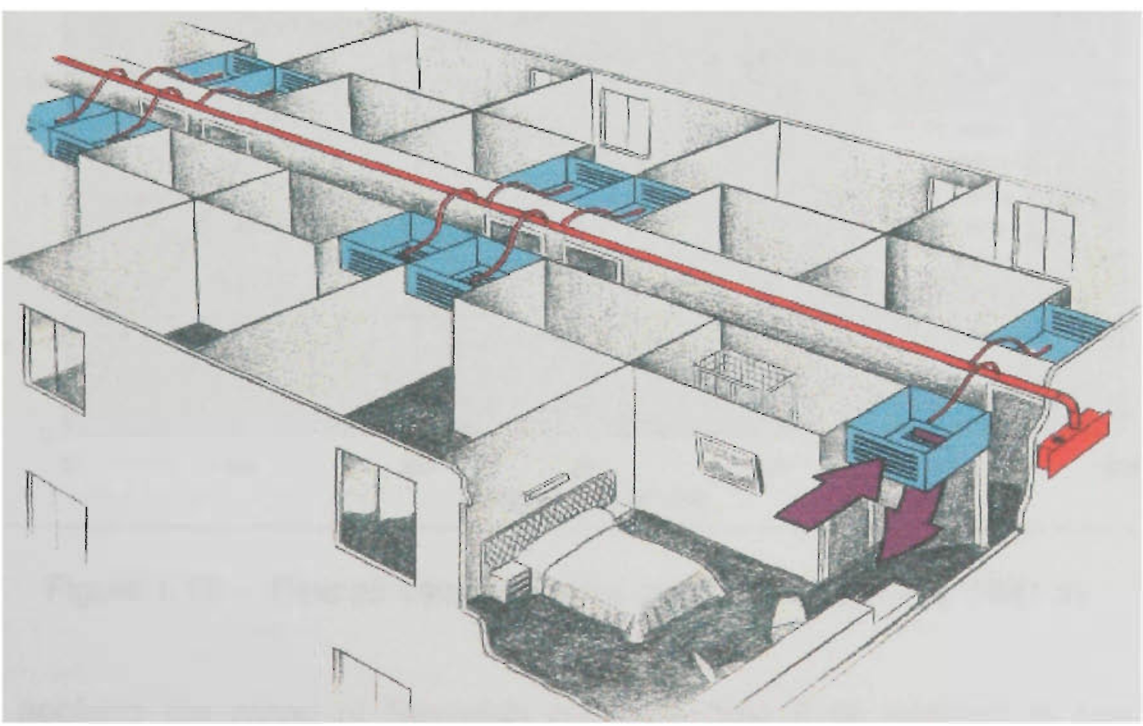

Figure 1.9 - Compartment or mechanical services smoke detection as proposed for "hotels, apartments, hospitals, barracks, prisons, dormitories, schools, trains and ships" (Cole, 1982)

Subsequently, Cole (1991 a) characterised a range of pipe systems (similar to Figure 1.1) in greater detail. This was done for the ultimate purpose of designing an efficient aspirator from scratch, optimised for early smoke detection. He developed a relationship between average velocity (providing the flow rate required for aspirator design) and core velocity (affecting smoke transport time) - a ratio of central importance to the current investigation.

In developing this relationship, Cole first calculates the expected average flow rate within a given pipe using the Darcy-Weisbach equation, based upon the usual estimates of friction factor obtained from a Moody chart (Roberson and Crowe, 1975, p298). The area of uncertainty on the Moody chart (transitional flow) is covered by using the results of Nikuradse for round pipes having smooth or rough internal surfaces (Roberson and Crowe, 1975, p296).

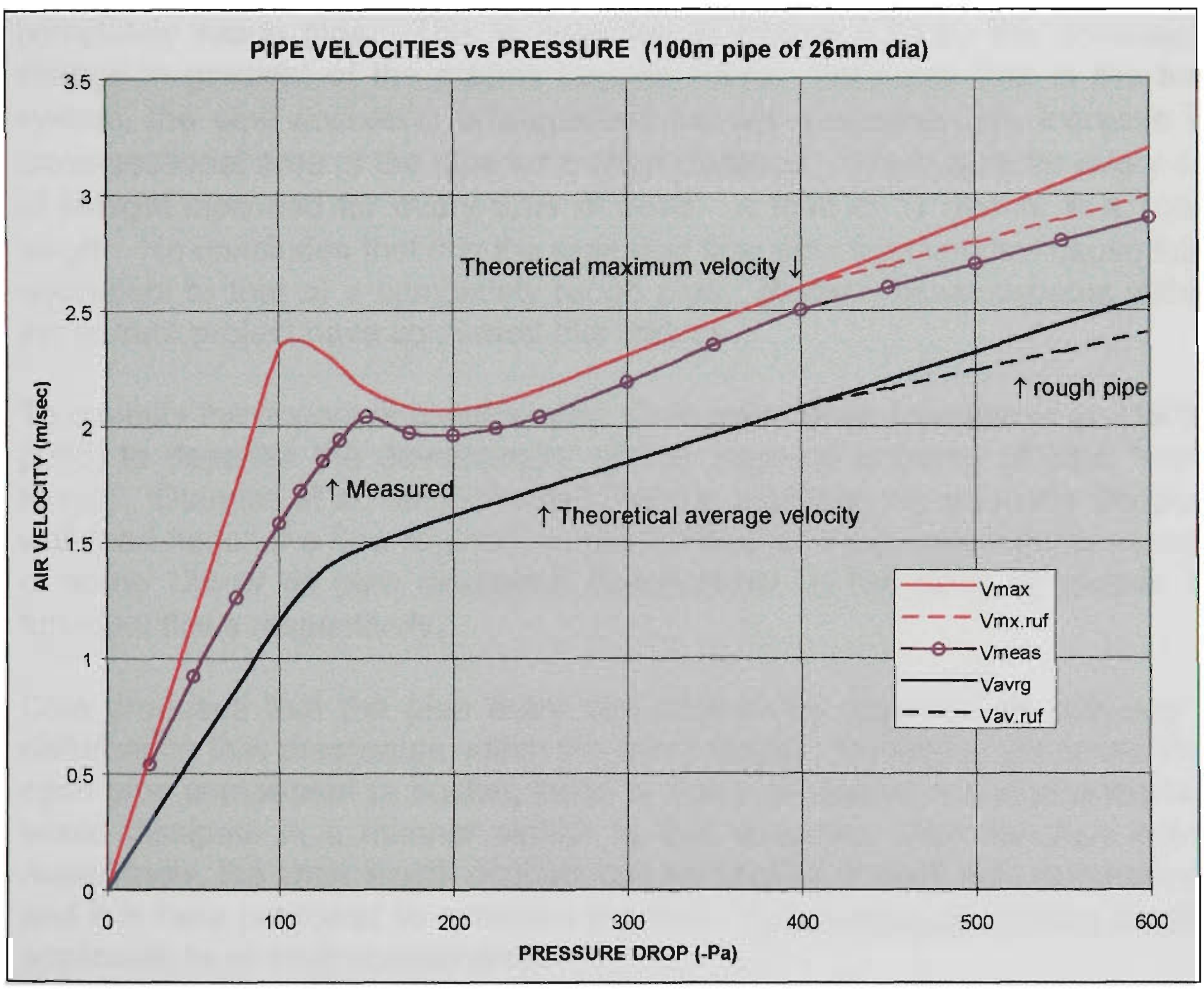

Figure 1.10 - Pipe air velocity versus pressure drop (Cole, 1991 a)

By applying the range of Reynolds numbers Cole finds relevant to typical aspirated pipe systems (*a few hundred* < Re < 4000), he calculates the range of average and maximum velocities, which he plots versus the calculated pressure drop. This plot provides an "envelope" defining the minimum and maximum possible velocities of smoke within the pipe at any pressure drop up to 600Pa (6Pa/m). Available data for the upper limit of this envelope are discontinuous between $\mathrm{Re} = 2000$ and $\mathrm{Re} = 3000$, so an estimation within this transition region is also presented and discussed. Here, Reynolds number is defined as $\mathrm{Re} = D\,u\,/\,k$ where D is the pipe internal diameter, u is the average air velocity in the pipe, and k is the fluid kinematic viscosity.

Cole finds that the experimental results all fit within this theoretically-derived envelope, as reproduced in Figure 1.10. This outcome provides validation of the experimental results, in addition to providing a conversion between the measured transport time and the average velocity (which could not be accurately measured directly).

In addition, Cole finds that despite the smoothness of the plastic pipework used, the data points are consistent with the Nikuradse friction factors for a completely rough pipe. This is indicated in Figure 1.10 by the consistent change in gradient of the graphs beyond 400Pa. He notes that in the test system, the pipe socketing arrangement causes a sudden 50% increase in cross-sectional area of the pipe for a short distance. This occurs for every 4m of straight pipe and for every 0.5m of bend - a total of 32 events in a 100m length. He concludes that it is the repeated flow disturbances that cause loss equivalent to that of a completely rough pipe. Recent measurements within the current project have confirmed this finding.

To quantify the impact of disturbances, Cole relies upon Douglas et al. (1979, p285) to describe the development of flow regimes in terms of pipe “entry length”. Douglas et al. had indicated that the boundary layer beside the pipe wall (and hence the flow regime), would not fully develop until a displacement of some 120 or 60 pipe diameters downstream (in the case of laminar or turbulent flows respectively).

Cole proposes that the pipe entry can instead be regarded as inducing a disturbance that **dissipates** within the entry length. He further proposes that each pipe component (a socket, bend or hole) will induce a disturbance that would dissipate in a manner similar to that occurring after the pipe entry. Accordingly, the entry length concept can be applied to each pipe component, and it is here proposed to establish the term “disturbance dissipation length” applicable to all such components.

Based upon this assumption, each pipe component will disturb the flow regime downstream for a displacement of up to 2.5m (in the case of laminar flow and a pipe internal diameter of 21mm). Given typical hole separations of 4m, interspersed with pipe sockets and bends, a significant proportion of the whole pipe will be affected by developing flow regimes. This would impact on smoke transport times.

Having discussed the results for pipes at the maximum practical length of 100m, Cole points out that two such pipes could be used either side of a centrally-mounted detector, to cover a $200m$ section of a tunnel. In other configurations, up to four pipe branches could be employed to cover a large roof space or floor void. Within the size of a statutory fire zone, the aggregate length of pipe attached to one detector would not exceed $200m$.

Taking into account all pipe configurations and worst cases, Cole concludes that the optimum aspirator performance specification requires a design flow rate of $1\,litre/sec$ at a design pressure of 300Pa. The resulting aspirator characteristic is a key input to the system modelling tool.

Cole's research resulted in the design and production of a new volute centrifugal air pump type of aspirator (used in VESDA Mk3) which has an efficiency 10 times that of the original muffin fan, exceeding expectations (based upon the literature) for such a pump of low specific speed (8.4). In practical terms, the transport time for smoke in a $100m$ pipe was reduced from five minutes down to one minute, while the electrical power input was reduced from 5W down to 2W. This was achieved by a purely theoretical design methodology without need for an empirical prototyping phase.

For the purposes of modelling an aspirated smoke detection system, Cole's thesis provides a useful introduction but its scope does not include a detailed analysis of system components and their impact upon the flow balance among sampling holes, nor the smoke transport time from each hole.

1.2.1.3 MATHEMATICAL MODELLING

Taylor (1984) is the first known researcher to mathematically model the air flows through a single sampling pipe within an aspirated smoke detection system. To characterise the flow through sampling holes, Taylor has derived the following equations as curves of best fit to experimental data for loss coefficients, where K_{inf} and K_{out} relate to the inflow and outflow respectively, and R_q is the ratio of the sample and main flows:

$$K_{\inf} = 2.053\,R_q - 2.473\,R_q^2 + 0.9796\,R_q^3$$

$$K_{out} = -0.07369\,R_q - 1.375\,R_q^2 + 5.319\,R_q^3 - 5.151\,R_q^4 + 0.646\,R_q^5$$

He states that these loss coefficients apply to turbulent flow and should be increased by a factor of about 1.3 with Reynolds numbers of less than 2000. Given that the friction loss of the sampling hole is negligible, the pressure drop across a sampling hole can be expressed as:

$$\Delta P = \frac{\rho}{2}\,u^2\,(1 + K_{\inf} + K_{out})$$

where u is the velocity of air in the hole. Taylor goes on to state that for the $2mm$ diameter sampling holes under consideration, $K_{inf} = 0.75$ and $K_{out} = 1.0$ but this claim appears to be in conflict with the above equations which are based upon the ratio of flow rates, which is expected to vary along the pipe.

Taylor wrote a computer program to determine the pressures and flow rates at all points along the pipe, based upon the VESDA Mk2 pump characteristics and using Bernoulli's equation with the Darcy-Weisbach representation of head loss. To calculate the transport time, Taylor assumes that smoke travels at the average air velocity and so the fluid transit time from the hole to the detector is taken to be the transport time. However, as indicated by Cole (1991 a), this assumption would provide conservative results because in practice, a significant proportion of smoke would be borne within the (faster) central core of air flow.

In order to gauge the relative smoke-sensitivity of each hole along the pipe, Taylor uses the volume flow rate through each hole as a proportion of the total system flow rate. This point is valid because smoke entering the pipe from one hole is diluted by the (possibly) fresh air entering all other holes, and mixes freely within the pipe prior to reaching the detector.

Taylor produces the results of seven different pipe arrangements. None of these is tested experimentally, which is the major weakness of his paper. In addition, pipework of $30mm$ internal diameter is modelled, which is large and inefficient by current standards. He finds that for a given pipe length, the transport time increases with the number of holes ($2mm$ diameter), stating that for a $100m$ pipe, the maximum transport time is $237sec$ with 11 sampling holes, and 40 minutes with 99 holes.

Such times would be unacceptable by today's standards whereby a maximum time of $90sec$ is usually required. Nevertheless it can be shown that for the then-current VESDA Mk2 detector, the more likely result for Taylor's pipe arrangement of a $100m$ pipe with 11 holes, would be a transport time of $69sec$ with a hole flow (un)balance of 50%.

The inaccuracy in Taylor's model is likely to reside in his calculation of hole flow rate. Nevertheless Taylor's approach can provide a useful starting point for computer modelling of aspirated smoke detection systems.

Notarianni (1988) uses a different approach to develop a mathematical model of a single-pipe system. She states that the flow through a sampling hole is proportional to the square root of the suction pressure inside the sampling pipe, and to the square of the hole diameter.

Because of pipe friction losses, the suction pressure behind each hole decreases in the direction away from the detector and aspirator. Notarianni points out that if equal sized holes are placed along the sampling pipe, these will not sample at equal rates and the overall performance of the system is unbalanced. The effective sensitivity, or alarm threshold, of each sampling hole would detect the fire at a different smoke density (fire size).

Notarianni cites as an extreme example, the case of a $90m$ open-ended pipe with $3mm$ diameter holes spaced $10m$ apart. For the given aspirator, she states that the (differential) pressure at the hole closest to the detector would be 73Pa, while the pressure at the hole furthest from the detector would be 1.5Pa. Given that the flow rate through a sampling hole varies proportionally with the square root of the pressure, she states that the hole closest to the detector will sample at a rate seven times greater than for the hole furthest away from the detector. In practice, it can be shown that the relevant pressures would be 83Pa and 5Pa respectively for that pipe configuration, producing an unbalance factor of four times, which is still very significant.

As distinct from minimising the transport time, the requirement for good balance becomes Notarianni's fundamental objective in system design. She states that to achieve balanced flows, the hole diameters must be increased along the pipe in the direction away from the detector, in accordance with the reduced local suction pressure.

Making the definitive assumption that the flows will be balanced, Notarianni states that the flow rate through each hole is equal to the total system flow rate divided by the total number of sampling holes. Notarianni then allocates the flow rate in each segment of pipe by counting the number of holes upstream. Based upon her further assumption of steady, fully-developed laminar, incompressible flow, she then calculates the friction loss (pressure drop) in each pipe segment using the Hagen-Poiseuille equation.

Notarianni includes the possibility of bends, of either a "standard" (short radius) or a "sweep" (long radius) type, which add to the loss within a given pipe segment. She also considers the aspirator performance characteristic, and the friction loss of the detector and dust filter combination.

This procedure allows Notarianni to obtain the internal pressure distribution along the sampling pipe. She then applies her "hole equation" to determine the hole diameter necessary, to achieve the pre-determined flow rate through each hole. This equation can be written as follows:

$$D_i = ((4\,Q_i)\,/\,(C\pi\,(2\,g\,(P_{amb} - P_i)\,/\rho\,)^{0.5})^{0.5}$$

where:

	D_i	is the cross-sectional area of the hole
	Q_i	is the volumetric flow rate of air through the hole
	C	is the hole coefficient, experimentally determined
	P_{amb}	is the ambient air pressure
	P_i	is the internal suction pressure at the hole

Notarianni wrote a computer program in accordance with the above procedure, to specify hole sizes and positions. The pipe internal diameter can be adjusted, and the procedure is readily adapted to multi-pipe systems.

Whereas Notarianni's overall approach is interesting, its fundamental weakness is the assumption that each sampling hole flow rate can be so controlled in a real installed environment. In practice, the hole diameter becomes critical because the flow rate varies proportionally with the fourth power of diameter, at a given pressure differential.

For example, a hole specified as $2mm$ could have an error in diameter (due to a blunt drill) of $0.2mm$ or 10%, resulting in a +46% error in flow. Despite such criticality, Notarianni's computer program specifies hole sizes in steps of 1/64" (which is 20% of 5/64"). This could result in greater than -50% or +100% error (a binary order of magnitude), defeating her objective to achieve perfectly balanced flow and significantly undermining the efficacy of her model.

Turning now to the computation of transport time, Notarianni states that this is governed by the length of each segment of pipe divided by the air velocity:

$$T_{resp} = \sum \Delta L / u_i$$

She correctly states that this equation would assume plug flow (a flat velocity profile) which, she says is unlikely for a flow regime that is assumed to be laminar. Although fully-developed laminar flow has a maximum core velocity that is twice the average velocity, she assumes that some dilution of the smoke would occur, delaying the operation of the detector in reaching its alarm threshold. Hence Notarianni states that a correction factor to the above equation should be determined experimentally. She does not publish this factor, which should lie somewhere between 1 and 2.

To establish the type of flow regime, Notarianni presents data on air velocity versus position across the 3/4" internal diameter pipe used. From these data, she states that the velocity profile is parabolic, concluding that the flow in the sampling pipe is laminar. However, her profile is distinctly that of turbulent flow, not laminar. Therefore, her conclusions are in doubt.

As to the remaining experimentally-derived data, Notarianni uses straight-line approximations to model the fan performance, the detector head and filter losses, as well as the standard and sweep elbow losses. It can be shown that in practice, each of these parameters would have a distinctly non-linear characteristic and losses are best represented by a quadratic equation.

1.2.1.4 DISCUSSION OF PHASE 1

Contrary to Notarianni (1988, 1992), Cole (1991 a) found that the flow in an aspirated system is neither steady, nor fully-developed laminar, although it can be regarded as incompressible.

Each sampling hole makes a contribution to the total flow rate, so the flow rate in each segment of pipe is different, increasing with each segment in the direction towards the detector. Consequently, the Reynolds number applicable to pipe segments close to the detector, would be much higher than for segments far from the detector (given that the same pipe internal diameter is used throughout). Cole stated that in typical pipe systems, Reynolds numbers range between *a few hundred* and 4000.

It has long been established (e.g. Mott 1990 p253 or Roberson and Crowe 1975 p289) that for round pipes of average roughness: (1) without special precautions, laminar flow cannot be sustained for Reynolds numbers in excess of about 2000, (2) turbulent flow can become established at Reynolds numbers in excess of about 3500, and (3) a state of transition exists for Reynolds numbers between these limits, wherein the friction factor can be somewhat indeterminate (see Figure 5.1).

Consequently, the flow regime will vary along the pipe according to the local Reynolds number. For the segments most distant from the detector, the flow may tend toward laminar. Within one particular segment closer to the detector, the transition (or "critical") region will be encountered. The next few segments may also contain transitional flow. Then, for the segments closest to the detector, the flow may tend toward complete turbulence. Use of the phrase "tend towards" is intentional, because a laminar or turbulent flow regime is not established immediately. According to Cole, these regimes are expected to become established over a significant displacement along a typical pipe (up to $2.5m$).

Notarianni found it most convenient to restrict her model to fully-developed laminar flow. To model a system that covers the complete range of flow regimes, would increase the complexity significantly. Given that the friction factor equation she uses ($f = 64 / \mathrm{Re}$) is applicable only to fully-developed laminar flow, then for turbulent flow it will be more appropriate to obtain friction factors from the Moody chart in conjunction with the Darcy-Weisbach equation, as was noted by Taylor (1984).

However, the friction factor is not well-defined throughout the transition region (also known as the critical region), so Cole has relied upon the results of Nikuradse. Nevertheless, it should be noted that all of the published values of friction factor apply to fully-developed flow regimes, whether laminar, transitional or turbulent. These values may not prove sufficiently accurate in the case of developing pipe flows, requiring experimental research.

1.2.2 PHASE 2 - FLUID DYNAMICS

The most significant shortfall in knowledge relates to the estimation of the smoke transport time. According to Cole (1991 a), this is determined by the core velocity at all positions along the pipe. This velocity is expected to be significantly affected by jet induction into the main airstream caused by the air entering a sampling hole. Therefore, it has been necessary to investigate the literature dealing with developing pipe flow regimes and the impact of disturbances, as well as experimental techniques for determining same.

Martinuzzi and Pollard (1989) evaluate six different turbulence models for use in CFD (computational fluid dynamics) analysis of developing turbulent pipe flow. Computations are performed at Reynolds numbers of 10,000, 38,000, 90,000 and 380,000 for a smooth round pipe of 82.5 pipe diameters length. The authors compare predictions of velocity, turbulence kinetic energy and Reynolds stress field with available experimental data (principally as published by Nikuradse and by Barbin and Jones). The algebraic stress model (ASM) is found applicable only to high Reynolds numbers. The best agreement with experimental data is found at comparatively low Reynolds numbers (10,000) using the κ-*epsilon* model. Here, κ is the turbulence kinetic energy and *epsilon* is the rate of dissipation.

At a Reynolds number of 10,000 and at 80 diameters from the pipe entry, the calculated ratio of core velocity to average velocity is 1.15, which is compared with the published Nikuradse data at 1.2. At a Reynolds number of 380,000 the velocity ratio at 5 diameters is 1.05, whereas at 80 diameters this ratio is 1.14. These results are in close agreement with the published data of Barbin and Jones, while the published Niukuradse data indicate a ratio of 1.24 at 80 diameters. Martinuzzi and Pollard's results are reproduced in Figure 1.11.

As seen in Figure 1.11, the core velocity grows steadily for the first 20 to 25 diameters. The rate of growth in core velocity then slows, and by 30 diameters it begins to decrease. The core velocity stabilises (at a ratio of 1.14) by 50 diameters. These results are given at a Reynolds number much higher than the range of current interest, namely, less than 4000.

The experimental setup used by Barbin and Jones (1963) consisted of an 8" (203*mm*) diameter pipe, 29ft (8.84*m*) in length, representing 43.5 diameters. The pipe entry is described as an adjustable 4:1 contraction providing a uniform core of fluid which was free of disturbances induced by the contraction. This contraction was constructed as a trumpet-shaped, smooth wooden cowling which slipped over the pipe entry. Its longitudinal position was adjusted for minimum flow disturbance.

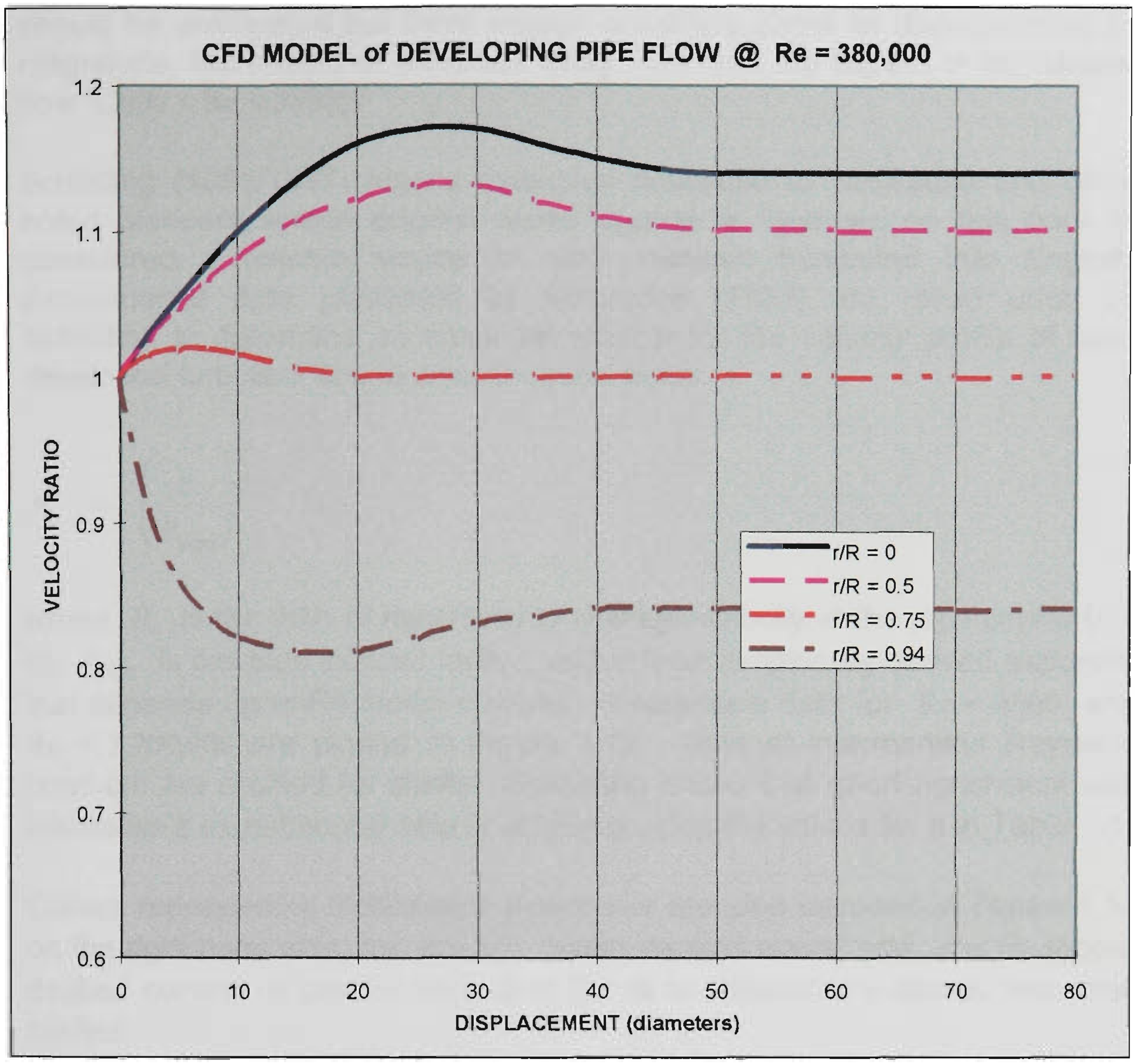

Figure 1.11 - Developing pipe flow (Martinuzzi and Pollard, 1989)

They published experimental data applicable to a Reynolds number of 388,000 where they found that the pipe length (43.5 diameters) was insufficient for the core velocity to reach its final value. They quote the velocity defect law of Schlicting (1951/1987, p643) to obtain approximate final values for the normalised velocities, being 1.22, 1.10, 1.00 and 0.87 at radius ratios (r/R) of 0, 0.499, 0.749 and 0.936 respectively. This velocity defect law is applicable in fully developed turbulent boundary layer flows and it governs the average velocity distribution beyond the buffer region where the logarithmic distribution exists.

The experimental data of Barbin and Jones are of similar form to the CFD results of Martinuzzi and Pollard shown in Figure 1.11. The most significant difference is that although these CFD results show the core velocity peaking between about 25 and 30 diameters, reducing thereafter to its final value at about 50 diameters, the experimental data indicate that the core velocity peaks between about 35 and 45 diameters. Accordingly, a peaking effect should be anticipated but there remain questions about its displacement, its magnitude, the impact of disturbed entry flow, and the impact of transitional flow $(2000 < \mathrm{Re} < 3500)$.

Schlicting (1951/1987) makes extensive reference to Nikuradse and other noted pioneers whose original works appear in German, so this book is considered a reliable source of such material translated into English. Experimental data published by Nikuradse (1932) are relied upon by Schlicting to determine an empirical relation for the velocity profile of fully-developed turbulent flow in smooth round pipes:

$$R_u = \left(\frac{r}{R_{pipe}}\right)^{\frac{1}{n}}$$

where R_u is the ratio of maximum to average velocity at the pipe centre (r = 0), R_{pipe} is the pipe internal radius, and n is an empirically-derived exponent that depends upon Reynolds number. Nikuradse's data for $\mathrm{Re} = 4000$ and $\mathrm{Re} = 3{,}200{,}000$ are plotted in Figure 1.12. Data at intermediate Reynolds numbers are omitted for clarity. Schlicting states that good agreement with Nikuradse's experimental data is achieved using the values for n in Table 1.1.

Curves representing Schlicting's power law are also included in Figure 1.12 on the right hand side, for $n = 6.0$ (lower dashed curve) and $n = 10$ (upper dashed curve). It can be seen that the fit to Nikuradse's data is less than perfect.

In seeking equations of better fit, alternative values of the exponent were tried. Included in Figure 1.12 on the left hand side are the curves for $n = 6.7$ (lower dashed curve) and $n = 12$ (upper dashed curve), providing a better overall fit. It will be shown by discussion of Figure 1.13 later that the resulting discrepancy reduces the ratio of maximum to average velocity by 2%.

Schlicting has derived the ratio of average to maximum velocity from the above equation, as:

$$R_u = \frac{2n^2}{(n+1)(2n+1)}$$

Re	4000	23000	110000	1100000	2000000	3200000
n	6.0	6.6	7.0	8.8	10	10

Table 1.1 - Velocity ratio exponent (Schlicting, 1954/1987)

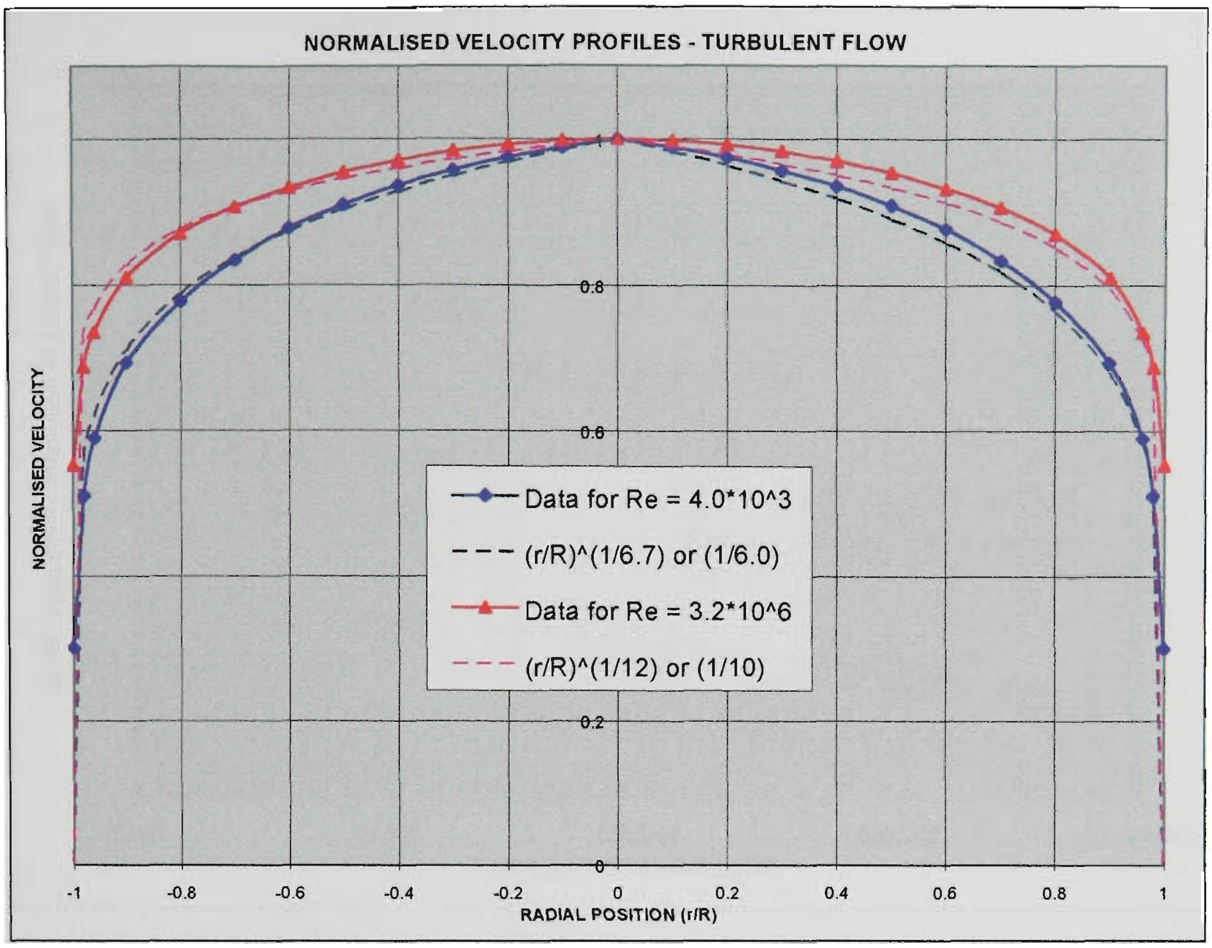

Figure 1.12 - Turbulent velocity profiles (Nikuradse, 1932)

This equation is now used with the values of Table 1.1 to produce the upper graph in Figure 1.13. This plot indicates the ratio of maximum to average velocity for fully-developed flows over a wide range of Reynolds numbers on a logarithmic scale. The known ratio for fully-developed laminar flow is included in Figure 1.13 for completeness, while the ratios applicable throughout the transition region (here approximated to $2000 < \mathrm{Re} < 4000$) are loosely represented by a straight interconnecting line.

This plot is next used to determine a proposed logarithmic curve of best fit to the points calculated from the Schlicting equation, as indicated by the upper dashed line, and resulting in a proposed equation of best fit:

$$R_u = 1.400 - 0.037\, Log(\mathrm{Re})$$

where R_u is the maximum to average velocity ratio as a function of Reynolds number in the fully-developed turbulent flow region. Alternatively, based upon the proposed curves of better fit to the Nikuradse data of Figure 1.12, the lower graph in Figure 1.13 has been obtained. The logarithmic curve of best fit to this lower graph is:

$$R_u = 1.373 - 0.037\, Log(\mathrm{Re})$$

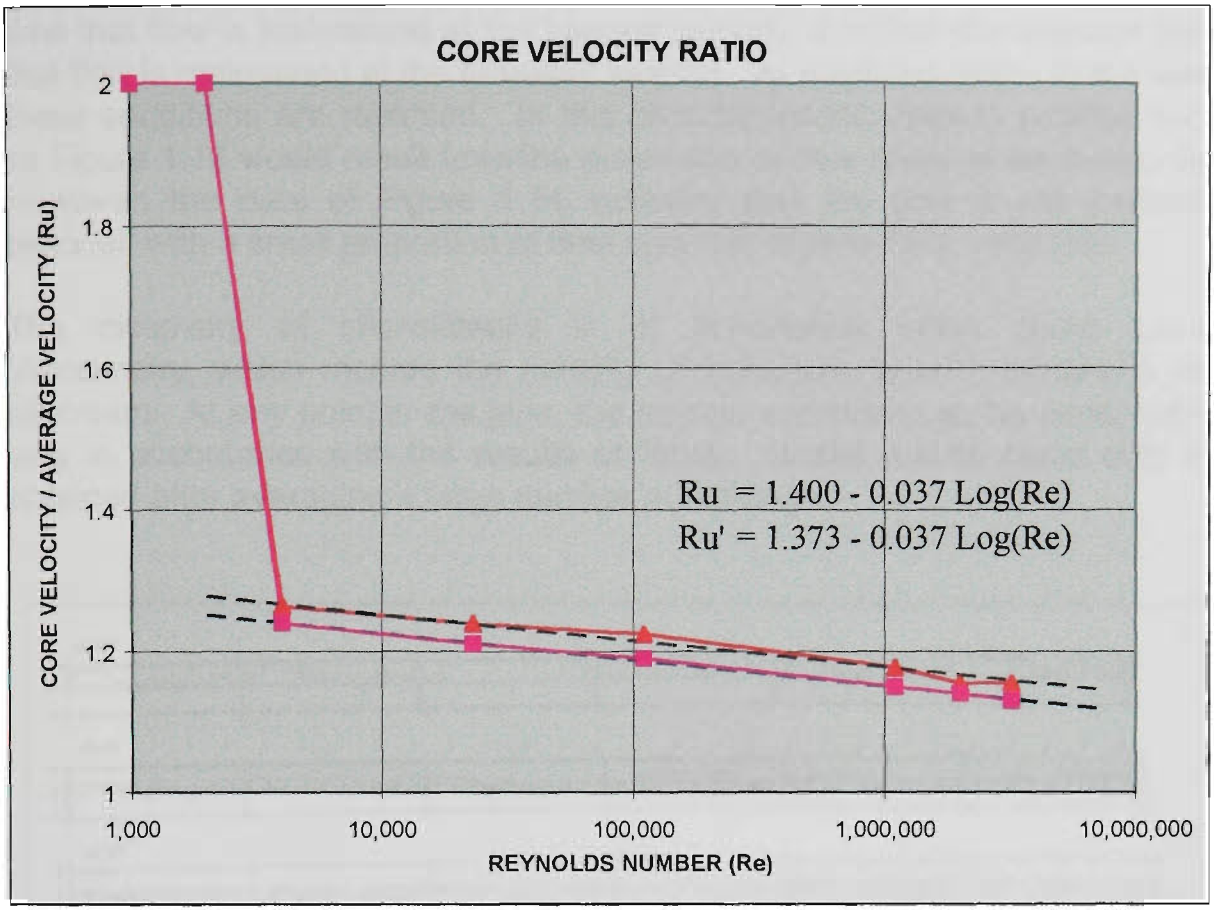

Figure 1.13 - Core velocity ratio versus Reynolds Number for fully-developed flow in round pipes

As previously mentioned, this new equation represents an overall 2% reduction in the ratio of maximum to average velocity. This equation of best fit will be useful within the proposed modelling software wherever it pertains to fully-developed turbulent flow regimes in smooth round pipes. Although this information takes no account of the developing phase of flow regimes, it does provide the end-points to which core velocity growth curves would be expected to asymptote.

It is important to note that the velocity profiles for turbulent flow as described in Figure 1.12 are not in fact smooth at any given instant in time, rather, these profiles represent the time-averaged velocity at each point. The deviation about this average is greatest for Reynolds numbers within the transition region of the flow regime. Schlicting states that in this region the flow at any point becomes “intermittent”, meaning that it alternates between the velocity of a fully-developed laminar flow distribution, and the velocity of fully-developed turbulent flow distribution. Measurements typical of this variation in flow velocity with time, at various radii from the pipe centre, are presented in Figure 1.14, attributed to Rotta (1956). These measurements were taken at a Reynolds number of 2550 using a hot wire anemometer.

Schlicting notes that the periods of laminar and turbulent flow follow each other in random sequence. At positions closer to the pipe centre, the average time that flow is maintained at the laminar velocity, exceeds the average time that flow is maintained at the laminar velocity, exceeds the average time that flow is maintained at the turbulent velocity. At positions closer to the wall, these conditions are reversed. In this bimodal model, velocity profiles such as Figure 1.12 would result from the proportion of time spent at each velocity. However, the data of Figure 1.14 indicates that the flow is not perfectly bimodal, with a small proportion of time spent at intermediate velocities.

The discovery of intermittency is of importance when using Laser Velocimetry, which records the velocity of individual "seed" particles in the airstream. At any point in the pipe, the particle velocities can be expected to vary in accordance with the results of Rotta. Useful results could only be obtained after averaging a large number of readings.

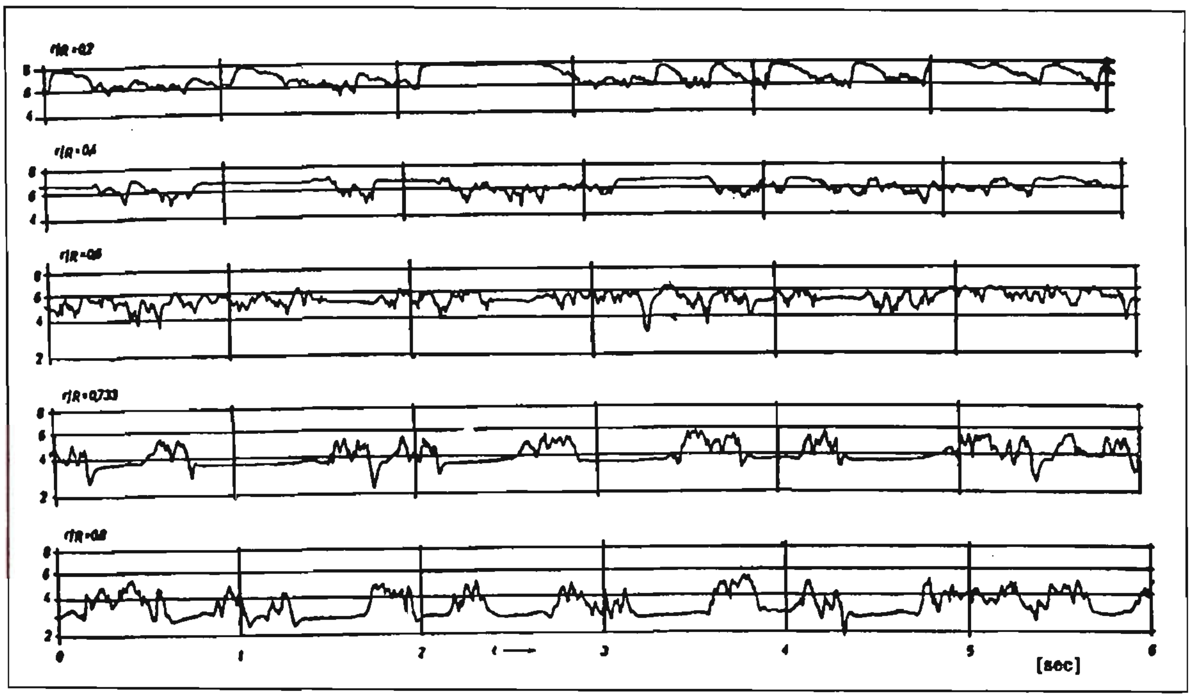

Figure 1.14 - Intermittency of velocity at various radii (Rotta, 1956)

Bernero and Munkutla (1995) also studied developing flow in round pipes. They published average flow and turbulence data applicable to Reynolds numbers in the range of 18,000 to 180,000. They claim that results at the lower end of this range had not previously been reported in the literature - which would explain the difficulties of the current investigation. They also publish results for developing turbulent kinetic energy in pipes. Contrary to other published results, they report that development of the flow regime occurs more quickly (i.e. within a shorter displacement) at lower Reynolds numbers. They also report that the Law of the Wall was found to be independent of Reynolds number during the flow development phase.

As previously noted, the value of the friction factor in a pipe is generally obtained from a Moody chart. Churchill and Chan (1994) recommend the following equation (which has been simplified here for clarity) as an improved, theoretically derived expression of friction factor (f) in fully turbulent flow (defined as $\mathrm{Re} > 3900$) in round pipes, both smooth and naturally rough:

$$\left(\frac{2}{f}\right)^{\frac{1}{2}} = 1.989 - \frac{161.2}{Rf} + \left(\frac{47.6}{Rf}\right)^2 + 2.5\, Ln\left\{\frac{1}{1/Rf + 0.301\,(r/R)}\right\}$$

where $Rf = \mathrm{Re}\sqrt{f/8}$ and (r/R) is the relative roughness of the surface. They state that since this expression is implicit in f, an iterative solution is necessary for specific values of Reynolds number and relative roughness, which they claim is rapidly convergent.

The works of Sparrow Lan and Lundgren (1964), Mohanty and Asthana (1978) and others are discussed in Chapters 6, 7 and 9.

1.2.3 OUTCOME OF LITERATURE REVIEW

After studying some 1200 synopses and papers, a limited coverage of undisturbed, developing pipe flow has been found. Much of this work applies either to idealised laminar flows or to Reynolds numbers well above the range applicable to aspirated pipe systems.

There is no coverage of disturbed, developing, transitional pipe flow, nor is there any reference to the impact of jet induction on developing or developed flow regimes. It is concluded that the literature does not describe the effects of jet induction upon the flow regime within a pipe, particularly in relation to its impact upon the core velocity.

No comprehensive and reliable theoretical study exists in the literature with experimentally verified results, that can model the real flow of smoke in aspirated pipes normally containing fresh air. Other authors interested in modelling aspirated smoke detection have made common assumptions about the friction factor and the effect of air velocity on smoke transport time, that are based upon fully-developed flow regimes within round pipes.

There is a significant uncertainty in determining the friction factor, in the region of transitional flow. This region is important, because it is relevant to a large proportion of the pipework in typical aspirated smoke detection systems.

Furthermore, it has <u>not</u> been established that the friction factor is unaffected by disturbances to the flow regime (whether that regime is nominally laminar, transitional or turbulent). The assumption that flow regimes can be regarded everywhere as fully-developed, may introduce significant error.

1.3 MODELLING METHODOLOGY

Based upon the literature review and an initial approach to theoretical computer-based modelling, the general parameters of a system model were developed along the following lines in order to determine the objectives and requirements for experimental research.

A sampling hole was expected to be a source of significant disturbance to the pipe flow regime. The low pressure inside the pipe (relative to atmosphere) would cause a jet of air to be projected inwardly from the hole, interfering with the main pipe flow and disrupting the flow regime (thereby increasing the transport time) to some extent. This disruption could also affect the friction factor in the pipe segment. The extent of these effects was not known.

It should be noted that unlike most pipe systems familiar to mechanical engineers, aspirated smoke detection systems involve pipes with induction sampling holes placed at frequent intervals along each pipe. Therefore, the flow regime is frequently disturbed. If the sampling holes are sufficiently close (say < $2m$ apart), the flow regime may never develop fully.

In modelling a pipe system, errors in friction factor would impact upon the pressure drop along each pipe segment and thereby affect the calculated pressure distribution throughout the pipe system. In turn, this would affect the calculated flow through each sampling hole, changing the system operating point and the balance among hole flows. Accordingly it was proposed that friction factor be investigated, particularly within a transitional flow regime. The impact on friction factor, caused by a disturbance within a laminar, transitional or turbulent flow regime, would also be investigated.

The apparent smoke transport time would be dominated by the core velocity (u_{core}) because a significant proportion of smoky air would be entrained within the central core of pipe flow. The ratio of core velocity to average velocity (u_{core}/u_{avg}) is initially $1{:}1$, but builds toward $2{:}1$ (assuming laminar flow) over a displacement of some metres in a typical pipe. The anticipated overall pipe velocity growth profile is illustrated three-dimensionally in Figure 1.15. For clarity, only one half of the pipe is shown (position 0 at the centre and 9 at the wall). This graph has been developed on the assumption of exponential core velocity growth, commencing with plug flow at the pipe entry. A parabolic velocity profile is shown as developed within 120 diameters.

At some further displacement along the pipe a sampling hole would be encountered, where the incoming jet of air would disturb the flow regime to some extent. The velocity ratio may be reset back to $1{:}1$ instantaneously, and the process of building towards $2{:}1$ would begin anew. Therefore, the velocity growth profile of Figure 1.15 may be repeated in the next pipe segment.

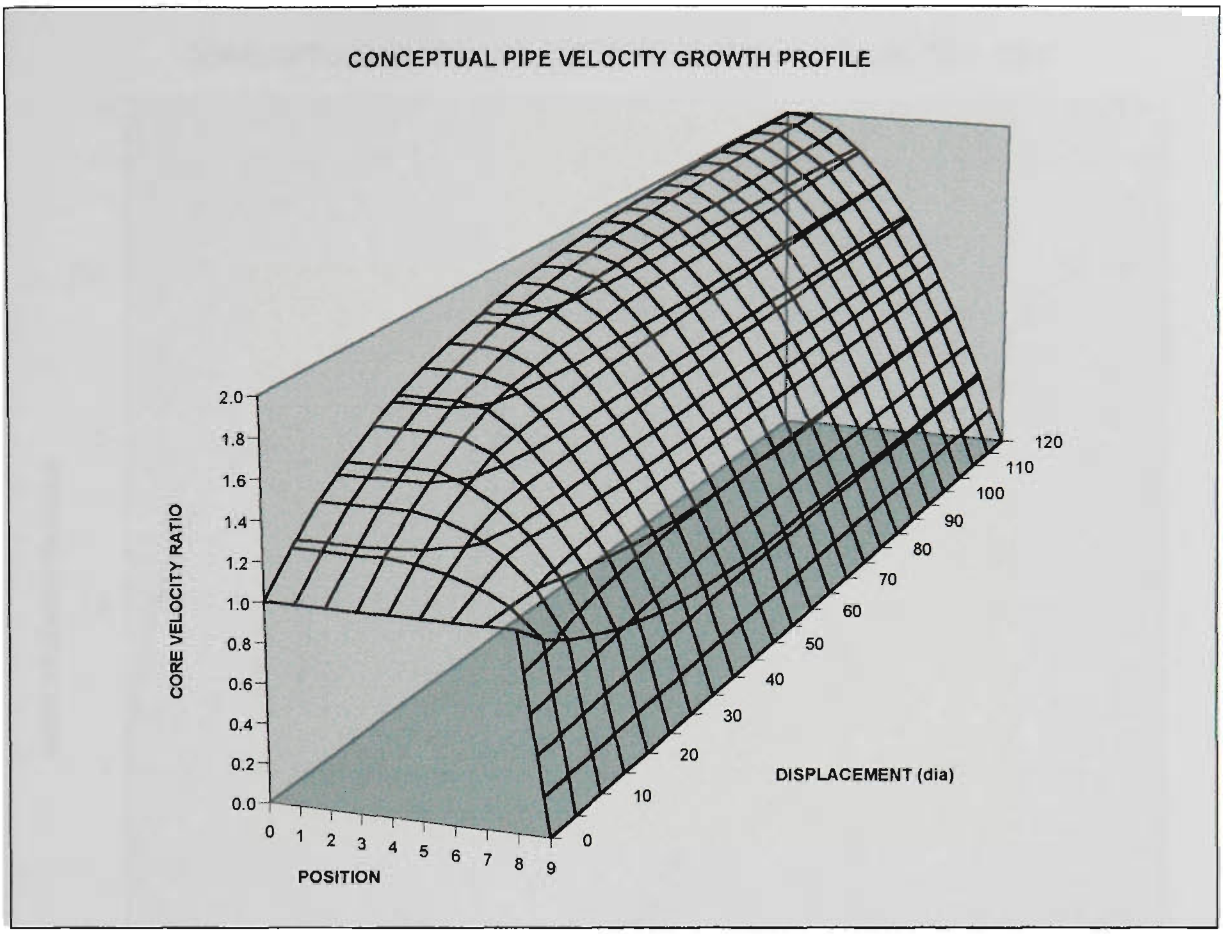

Figure 1.15 - Conceptual pipe velocity growth profile

Because of the contribution of flow from each hole, the flow rate for each pipe segment increases (in the direction towards the detector), so the Reynolds number increases (assuming a fixed pipe internal diameter). An initially laminar flow regime may become transitional further along the pipe and at greater displacements (with higher Reynolds numbers), a fully turbulent regime may exist. With turbulent flow the velocity ratio can only grow to about 1.25:1 instead of 2:1. What happens in the intervening transition region (between laminar and turbulent flow) is not clear, and requires investigation.

Accordingly, a graph of core velocity versus displacement along the entire pipe may appear like a climbing sawtooth pattern (with curved teeth), and the _core velocity (not the average velocity) would determine the transport time. This concept of core velocity growth, reset and regrowth is illustrated in Figure 1.16. For convenience, this graph represents a pipe with sampling holes placed at 100 diameters separation, with each hole contributing an additional 20% to the air flow in each subsequent pipe segment. For the first three pipe segments shown, the flow is assumed to be laminar so the core velocity grows asymptotically toward twice the average velocity. In subsequent segments, the flow is assumed to be transitional or turbulent. Here, because the core velocity grows at a more rapid rate, asymptotically toward a lower velocity ratio endpoint, these curves tend to plateau.

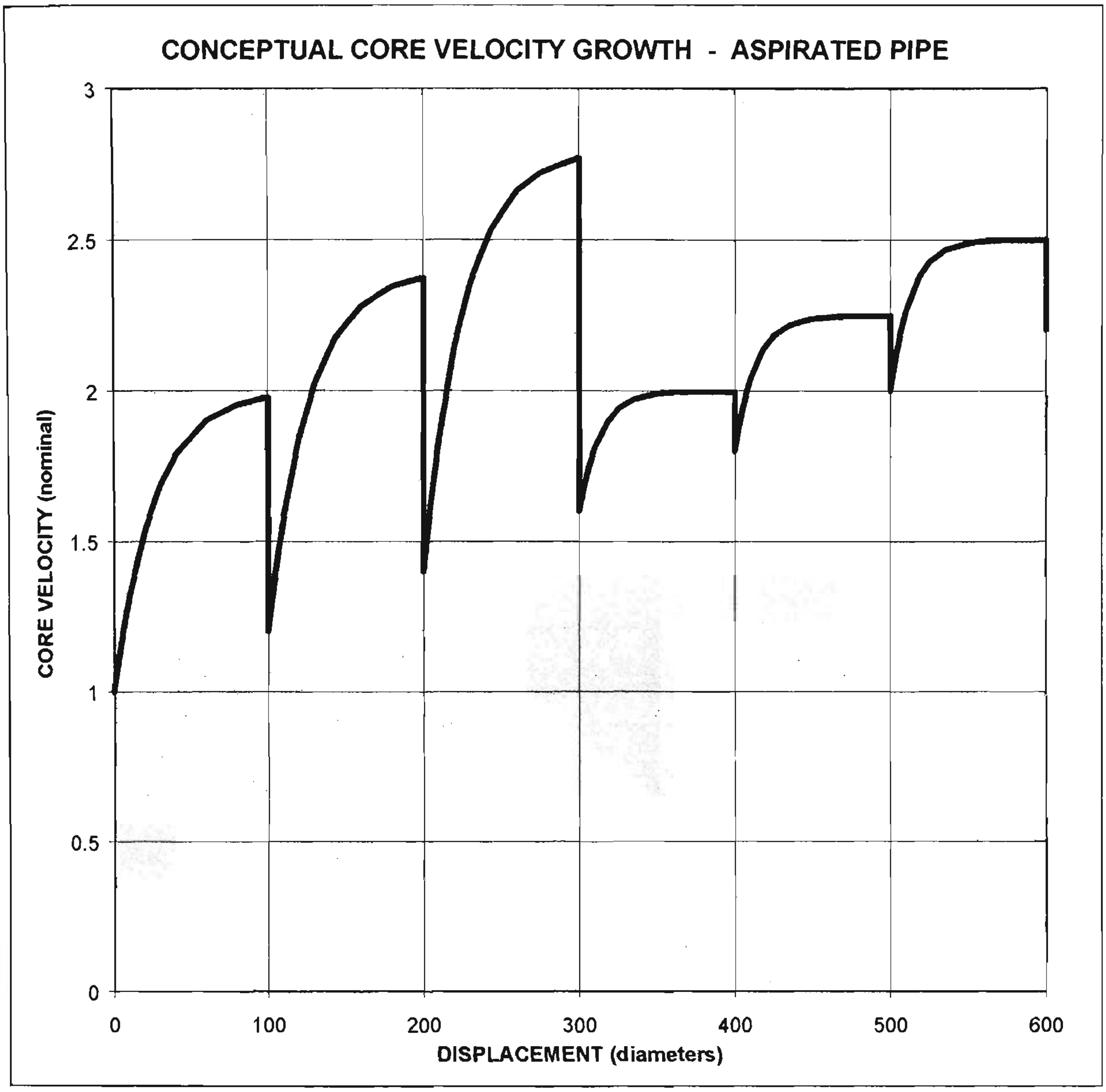

Figure 1.16 - Conceptual core velocity growth pattern for an aspirated pipe

Such a picture becomes even more irregular if some sampling holes are widely spaced, while others are placed close together such that the velocity ratio is reset well before it can reach its practical maximum. A quite varied hole spacing could be required (to suit a real zone layout), so it will be essential to mathematically model (a) the growth profile, and (b) the degree to which it is reset by an incoming jet of given strength. Neither of these parameters is known.

The strength of the incoming jet would vary along the pipe according to the local pressure and hole size. Therefore, the degree to which the pipe velocity growth curve is reset, could vary along the pipe. Furthermore, the growth curve could be reset, or partially reset by other types of flow disturbance caused by bends and sockets. Yet further complications could be introduced by step changes in pipe internal diameter or by the use of capillary tubes.

It is essential to understand the impact and interaction of all the phenomena associated with jet induction so that an accurate, or at least a probabilistic prediction of smoke transport time for any given hole can be made. Accordingly it was decided to observe the phenomena and determine the various parameters experimentally.

As a first step, the information available from the literature, together with the above approach to estimating the velocity growth profiles in each pipe segment, were used to develop a methodology for the computer software model. This methodology represented an adaptable platform onto which alternative equations and algorithms could be included as they were discovered, so that their impact on system performance could be immediately evaluated, and so that the emphasis of ongoing research could be adjusted. Once developed, the model methodology itself remained essentially unchanged and is described in Chapter 8, but the new discoveries that were incorporated over time served to improve the model reliability. Consequently this thesis will refer to the initial (or old) version, and the new version of the software model including its equations and algorithms.

1.4 EXPERIMENTAL PROGRAM AND SETUP

The experimental program within the project involved characterisation of the pressure-flow relationship of the various system components - aspirators, smoke detectors, dust filters, sockets, bends, sampling holes, nozzles, capillary tubes and pipes. In particular, the pipes were characterised in relation to disturbed, developing flow conditions within laminar, transitional and turbulent flow regimes. In each case a representative range of sizes, settings or brands was selected, to cover all system configurations anticipated in the field. In addition, extensive velocity profile measurements were made using Laser Velocimetry in association with a glass pipe. The final phase of the experimental program involved measurements of typical aspirated pipe systems as used in the field, for comparison with the computer model.

The component characteristics were measured with the most accurate available apparatus typically comprising a set of calibrated orifices, a digital pressure gauge, the test pipe, a digital flowmeter, and an aspirator bank, all coupled in that sequence (representing the direction of flow). The test pipe would typically contain a sampling hole, nozzle, filter, bend or other component being characterised.

The flowmeter (a Furness Controls, FC-096G laminar flow element with its FC-016 digital manometer) was used to monitor flow rates downstream of the test pipe in all experiments. It was also used to calibrate the set of stainless-steel "control orifices" in association with the digital pressure gauge (a Yokogawa UMO4). These calibrated orifices were fixed and sealed to the far end of the test pipe, adjacent to a 4-port pressure tap placed $150mm$ downstream. Initially, the rigid PVC test pipe was of $25mm$ outside, $21mm$

inside diameter, but other pipe diameters and various lengths were employed as required.

The outlet of the flowmeter was connected directly to the bank of four aspirators connected in series-parallel. This bank was necessary in order to obtain sufficient pumping capacity, principally to overcome the pressure drop caused by the flowmeter. Being a long, parallel-plate laminar-flow device, the flowmeter was expected to dampen any significant aspirator flow pre-rotation or induction pressure pulsation from transmitting upstream, and influencing the experimental results.

The pressure (being negative relative to atmosphere) developed by the aspirator bank could be adjusted by means of a 10-30V DC power supply, which thereby governed the flow rate for any given experiment.

A description of the various brands of aspirated smoke detector to be characterised is provided in Appendix 1, while further details of the experimental apparatus and data analysis are discussed in Appendix 2.

1.5 RESEARCH OBJECTIVES AND OUTCOMES

The overall objective of the current research program was to provide a better understanding of the physics of developing pipe flow regimes, as well as the impact of disturbances to flow regimes. In particular, the laminar, transitional and turbulent flow regimes, generally in the decade range $400 < Re < 4000$ were studied. This enables the friction factor and the core velocity to be predicted with greater accuracy than before.

The complex interaction of components was studied. In particular, the impact of disturbances to the flow regime caused by sockets, bends or sampling holes was investigated and equations or algorithms were determined, from which to model the friction factor in pipes and determine the pressure distribution throughout a system. It was found that the friction factor is significantly affected by the level of disturbance to the flow regime.

The flow through sampling holes was investigated and the new phenomena of "ultraflow" and "infraflow" were discovered. Ultraflow is the increase in hole flow, at a given pressure differential, caused by the upstream flow rate within the pipe. Infraflow is the reduction in hole flow, at a given pressure differential, caused by external air velocity ("crosswind"). Superposition of these two phenomena, together with the static hole flow characteristic can be used to determine the actual hole flow rate.

The core velocity growth profile for disturbed flow regimes in the laminar, transitional and turbulent region have been determined using Laser Velocimetry and the data have been interpolated and extrapolated to produce a complete model throughout the applicable range of Reynolds numbers. The "dissipation length" for a disturbance was also determined.

All of these results have been applied to a software-based modelling tool, initially developed from theoretical calculations based upon the literature review and subsequently improved by inclusion of the equations and algorithms discovered in this project. Any discrepancies between the model and various installed pipe systems have been applied to further refinement of the modelling tool until close correlation was obtained.

Such information has been applied to the modelling of aspirated pipe systems as found in fire detection or environmental monitoring. It would also be applicable to other pipe systems that contain a significant number components such as bends, sockets and valves, wherever the design of those components causes a significant disturbance to the flow regime.

Specifically, the current research program and thesis will improve the available techniques for mathematically modelling the performance of aspirated smoke detection systems, including accurate prediction of smoke transport times and the smoke sensitivity distribution throughout the system. This will ensure that systems are designed for optimal efficiency and reliability, increasing the likelihood of such systems being correctly installed and commissioned, and thereby reducing the risk to human life and property occasioned by fire.

1.6 STRUCTURE OF THE THESIS

The remainder of this thesis is structured as follows. In **Chapter 2** the main system components are characterised, including a complete range of aspirators and detectors. The impact of air density (ambient temperature and pressure i.e. altitude) is included. **Chapter 3** is devoted to a study of dust filters, being important components that have special implications for aspirated smoke detection systems, and the development of a new type of filter. **Chapter 4** deals with the characterisation of flow through sampling holes and the dependency of this flow upon hole size and geometry, pipe size, upstream flow rate and external wind velocity. End vents, capillary tubes and nozzles are also studied. **Chapter 5** considers in detail the friction factor applicable to pipes with initially disturbed, developing flow regimes, and studies the effects of pipe size, pipe bends and capillary tube coiling. **Chapter 6** is devoted to a study of core velocity development, by analysis of extensive data taken from Laser Velocimetry experiments. **Chapter 7** brings together the results of the previous chapters, to develop an integrated model for application to aspirated smoke detection systems. **Chapter 8** discusses the objectives, structure, presentation and implementation of a software model for such systems. **Chapter 9** is devoted to validation of the software model by comparison with real systems. **Chapter 10** summarises the conclusions of the project. **Appendix 1** describes several commercially-available aspirated smoke detectors (that are characterised in Chapter 2). Other **Appendices** have been extracted from many of the above chapters in order to improve readability and flow, but they remain important to the thesis.

CHAPTER 2 - CHARACTERISATION OF SYSTEM COMPONENTS

2.0 - INTRODUCTION

The physical components used within an aspirated smoke detection system need to be accurately characterised for inclusion in the model. Whereas numerous tables for pressure loss in various pipe system components are available from text books, such data is empirical in nature and therefore may be subject to the experimental conditions, which are rarely provided. Such data can be used only as a guide. In addition, the unique features of aspirated pipe flow require new characterisations not previously performed. Given that high accuracy is sought, this chapter will detail the study of each type of component, throughout its range of sizes or settings, to determine the equations suitable for use in the system model.

2.1 SQUARE LAW EVALUATED

Published tables of data relating to pipework components such as bends, elbows, tees, contractions, expansions and valves, indicate a head loss or pressure drop characteristic in the following forms:

$$L_h = C_c \frac{u^2}{2g} \qquad or \qquad L_p = \Delta P = C_c \, \rho \frac{u^2}{2}$$

where L_h (m) or L_p (Pa) is the loss of head or pressure respectively, C_c is an empirically-determined coefficient unique to the given component (or to a range of similar components), u is the average velocity of the fluid, g is the acceleration due to gravity, and ρ is the fluid density Here, the loss is entirely attributed to kinetic energy loss, and is therefore proportional to the square of velocity. This derives from the fact that kinetic energy loss equates to the acceleration and deceleration energies imparted to the airflow (where acceleration is the rate of change in velocity).

However, as became evident in the previous section, loss data does not follow a perfect, square-law parabolic curve. The typical example of Figure A2.2 (Appendix 2) indicated that one square-law curve could not fit the data both above and below the "discontinuity", and given that this discontinuity should be smoothed to remove the error, a curve of different shape is required to fit the data.

It can be shown that a curve of best fit to the data can be obtained in two alternative ways: (a) the velocity term is not squared, but is raised to a smaller power in the vicinity of 1.6 to 1.8 depending upon the component, or (b) the velocity term **is** squared, but there is an additional velocity term that is linear (becoming a quadratic curve). In either case the closeness of fit to the data can be very similar (within the bounds of experimental error).

To illustrate this point, during the testing of a dust filter it was found that the pressure drop *(ΔP)* as a function of flow rate *(Q)* could be characterised as:

$$\Delta P \approx 0.037\, Q^{1.6} \approx 0.0042\, Q^2 + 0.31\, Q$$

Whereas for the purposes of a mathematical model, either approach would be satisfactory, it was considered important to choose the approach that best reflected the normal conventions of fluid dynamics theory. This would boost confidence in results, particularly when interpolating or extrapolating to pipe components that could not be individually tested.

It was expected that the loss in any component, and a thick orifice plate in particular, could be broken down into three parts - an entry loss, an exit loss and a loss due to internal friction (which could equate to zero in some cases):

$$\textit{Total Loss} = \textit{Entry Loss} + \textit{Friction Loss} + \textit{Exit Loss}$$

To examine these terms individually, consider a very thick orifice. The entry and exit losses equate to a loss in kinetic energy. It is widely quoted that for an orifice which has square shoulders and that is small compared with the plate or pipe, the entry loss coefficient C_{ent} for this sudden pipe contraction is 0.5, while the exit loss coefficient C_{exit} for the sudden pipe expansion is 1.0. The value of these coefficients could be smaller depending upon the relative size of the orifice.

Because the orifice plate has thickness or length (L_o), the centre of this orifice may be thought of as a short round tube, to which the Darcy-Weisbach equation could be applied. The complete equation for loss in the component (L_c) then becomes:

$$L_c = C_{ent} \frac{\rho u^2}{2} + f \frac{L_o}{D_o} \frac{\rho u^2}{2} + C_{exit} \frac{\rho u^2}{2}$$

where f is the empirically-derived friction factor and D_o is the orifice diameter. Given that the purpose of this discussion is to determine the form of the equation rather than to derive exact coefficients at this stage, it is possible to make two simplifying assumptions: (a) the Reynolds number is low such that the flow tends toward a developed laminar regime within the orifice, thereby permitting the accepted equation for friction factor to be applied, and (b) that the effects of a vena contracta may be ignored (because in practice the orifice thickness would be small/short compared with the effective length of the vena contracta, so the degree of contraction within the orifice thickness would be minimal); then it may be appropriate to express the friction factor thus:

$$f = \frac{64}{\text{Re}} \quad \text{where the Reynolds number,} \quad \text{Re} = \frac{D\,u}{k} \quad \text{so,} \quad f = \frac{64\,k}{D\,u}$$

where k is the kinematic viscosity. Therefore we obtain for the complete equation:

$$L_c \;=\; C_{ent}\,\frac{\rho\,u^2}{2} \;+\; \frac{64\,k}{D_o\,u}\,\frac{L_o}{D_o}\,\frac{\rho\,u^2}{2} \;+\; C_{exit}\,\frac{\rho\,u^2}{2}$$

which by simplification, and by substitution of $u = Q/A$ where A is the cross-sectional area, becomes:

$$L_c \;=\; \frac{C_{ent} + C_{exit}}{2}\,\rho\,\frac{Q^2}{A^2} \;+\; \frac{64\,k}{2}\,\frac{L_o}{D_o^2}\,\rho\,\frac{Q}{A}$$

where for a given sized orifice and temperature, the loss can be expressed in terms of two (dimensioned) coefficients, C_2 and C_1 as:

$$L_c \;=\; C_2\,Q^2 + C_1\,Q$$

Thus in practice, to the extent that the assumptions are valid, we could expect to see a squared term together with a linear term, where the coefficients are derived experimentally. Only for a very thin orifice would we expect the linear coefficient to approach zero.

If alternatively, we do not assume laminar flow within the orifice (i.e. the Reynolds number is high), then it may be appropriate to obtain the friction factor from the Blasius equation of best fit to an established turbulent flow regime in smooth pipes (as often quoted on a Moody chart):

$$f \;=\; \frac{0.316}{\text{Re}^{0.25}}$$

which results in the following alternative equation for turbulent orifice loss:

$$L_c \;=\; C_2\,Q^2 + C_1\,Q^{1.75}$$

This reinforces the conclusion that we should not necessarily expect the loss to be described by a squared term alone. Moreover, an acceptable curve of best fit employing a single coefficient with an exponent less than 2 should be anticipated. However, the quadratic equation of best fit is preferred because it effectively separates the kinetic and friction components of loss.

In the case of other types of component, and especially for a dust filter which has a large friction loss, we would expect the linear coefficient to be relatively large. For each component, an inspection of the relative size of the two coefficients would provide an indication of the relative magnitude of kinetic energy loss compared with friction loss (at a given velocity or flow rate).

2.2 STANDARD ORIFICE PLATES

Apart from its calibration uncertainties, the difficulty with the Furness laminar plate flowmeter was its high restriction, developing some 180Pa pressure drop at full-scale. Since this would represent about half of the maximum available aspirator pressure (at zero flow), it was impossible to measure the maximum flow rate of an aspirator with this instrument connected to the inlet.

Therefore it was decided to use the instrument to calibrate a series of "standard" orifice plates in conjunction with the pressure gauge. This gauge could then be used in the dual role of measuring orifice pressure drop (converted to flow rate) as well as aspirator inlet pressure, because, with both readings referenced to atmosphere, and given only a short length of test pipe between the orifice and aspirator inlet, just the one pressure tapping in that pipe would provide the data for both flow rate and pressure.

In order to obtain consistent readings it proved necessary to use a standard pressure tapping method in the test pipe similar to that prescribed in the Australian Standard AS 2936-1987 - the SAA Fan Test Code. Page 12 of that document specifies that: "the mean static pressure of an airstream shall be measured in a parallel cylindrical duct by means of four wall tappings spaced 90 degrees apart around the circumference." It goes on to specify the tapping bore, removal of burrs and swarf, etc.

It was decided to fabricate a pressure tap of this general description for use with all measurements. A unique arrangement was devised, involving a collar that could be tightly fitted around a pipe in any desired location. The collar was provided with an internal, meridional gallery coupled to a tubing connector. At the required pipe location, a set of four $1.5mm$ tapping holes would be drilled, equi-spaced around the circumference of the pipe. The width of the gallery was made large enough ($10mm$ wide and $2mm$ deep) so that the positioning of the collar over the tapping holes would not be critical.
For the basic test pipe, a $225mm$ length of $21mm$ internal diameter PVC pipe was selected. The arrangement is illustrated in Figure 2.1. A difference in the order of 1 to 3 Pa was noted in relation to earlier experimental methods (involving a single side-wall tap of relatively large bore to suit the connector for the pressure gauge tubing).

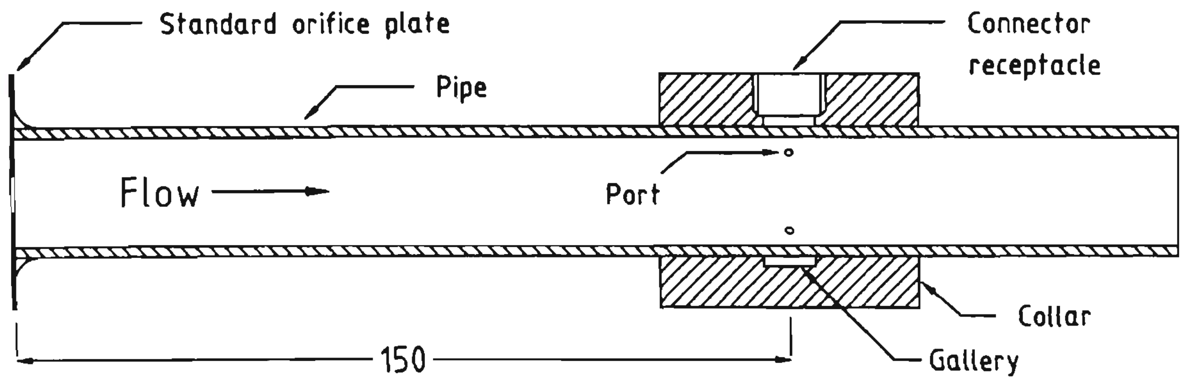

Figure 2.1 - Four-port pressure tap and orifice plate
used for upstream flow rate monitoring

Stainless-steel plates of 50*mm* diameter, punched with orifices in five different sizes were conveniently available (being optical irises used in the Xenon VESDA detector). These orifices measured 5.31, 7.37, 10.37, 12.9 and 16.36 *mm* diameter. The orifice plates were conveniently attached to the end of the test pipe, preventing leakage by using a "blue-tack" gasket-come-temporary-adhesive. To provide readings at cutoff (zero flow), a solid endcap (zero orifice) was attached to the test pipe. During experiments it proved desirable to obtain an intermediate reading between zero and 5.31*mm*, so an additional endcap was drilled with a 4.0*mm* diameter vent.

To take readings near to the maximum flow rate, a very small restriction would be required. For these readings the test pipe itself, when left open-ended, effectively provided a 21*mm* "orifice". Even this small restriction proved sufficient to generate a pressure drop in the region of 50Pa at 150 *litre/min*. In order to use the Furness instrument for calibration of orifices at such high flow rates, it proved necessary to use four aspirators in series-parallel to overcome the instrument's pressure drop.

Several considerations emerged in the process of perfecting the experimental technique, related to the instrumentation and data analysis, which are detailed in Appendix 2.

The final experimental results are provided in Figures 2.2 to 2.8 where the maximum practicable pressures and flow rates can be seen. The nominal Reynolds numbers are calculated for reference comparison among the orifices. The curves of best fit are included on each Figure, to indicate the quality of fit to the data. The calibration equations for the orifices were derived from the curves of best fit utilising Microsoft Excel, the results of which were examined and refined as discussed in Appendix 2:

$4.0mm \quad P_o = 1.309\,Q^2 + 4.61\,Q$

$5.31mm \quad P_o = 0.652\,Q^2 + 0.039\,Q$

$7.37mm \quad P_o = 0.186\,Q^2 + 0.142\,Q$

$10.36mm \quad P_o = 0.0404\,Q^2 + 0.0849\,Q$

$12.9mm \quad P_o = 0.0166\,Q^2 + 0.0583\,Q$

$16.37mm \quad P_o = 0.0052\,Q^2 + 0.0299\,Q$

$21mm \quad P_o = 0.002\,Q^2 + 0.0295\,Q$

The resulting intervals between these seven possible readings for an aspirator proved ideal for characterisation. Given that the calibration of the standard orifices, and the testing of system components, was undertaken using the same test pipe with its integral pressure tap, then any absolute errors caused by (say) the length of the test pipe and the location of the pressure tapping, were negated. Moreover, care was taken to ensure that the orifices were always used in the same orientation, to avoid any errors due to a possible lack of symmetry in the orifice geometry on opposing sides.

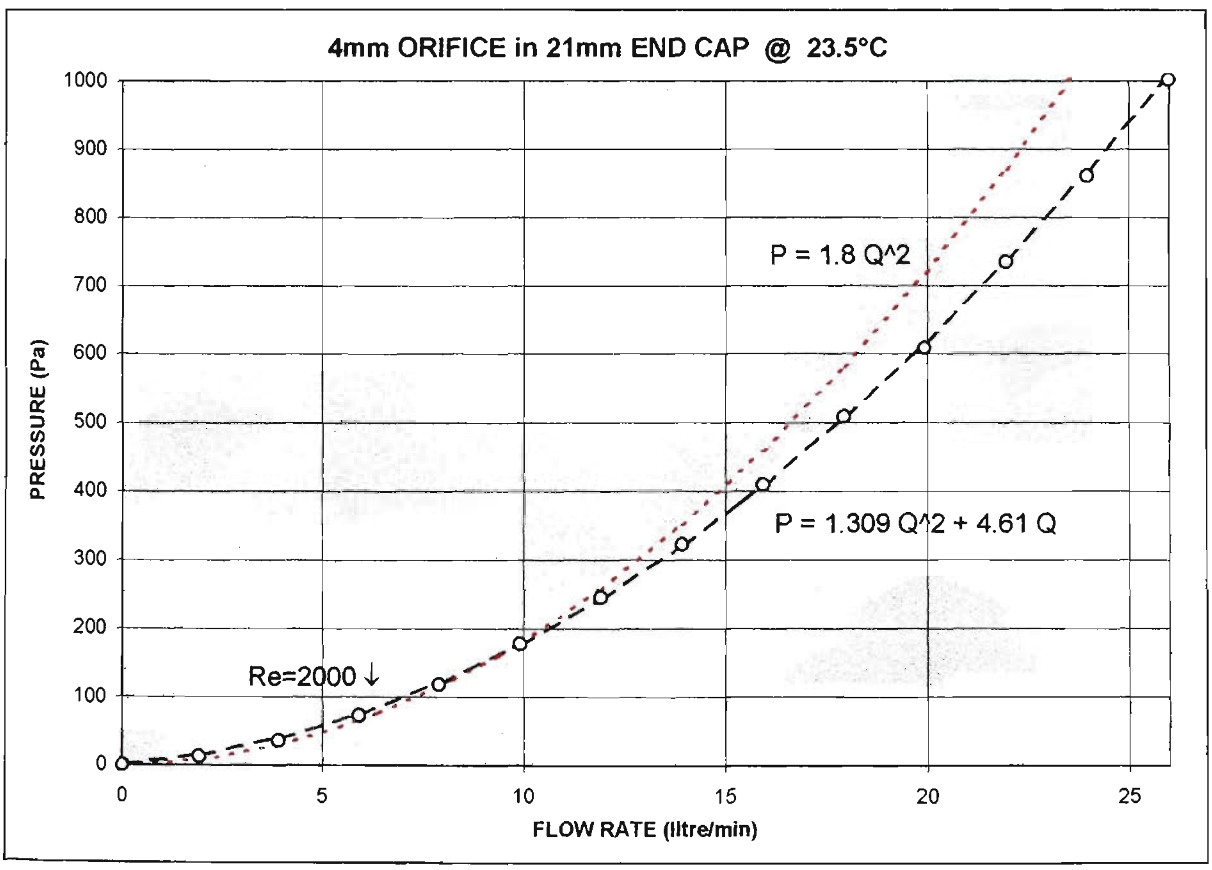

Figure 2.2 - Calibration of $4.0mm$ orifice

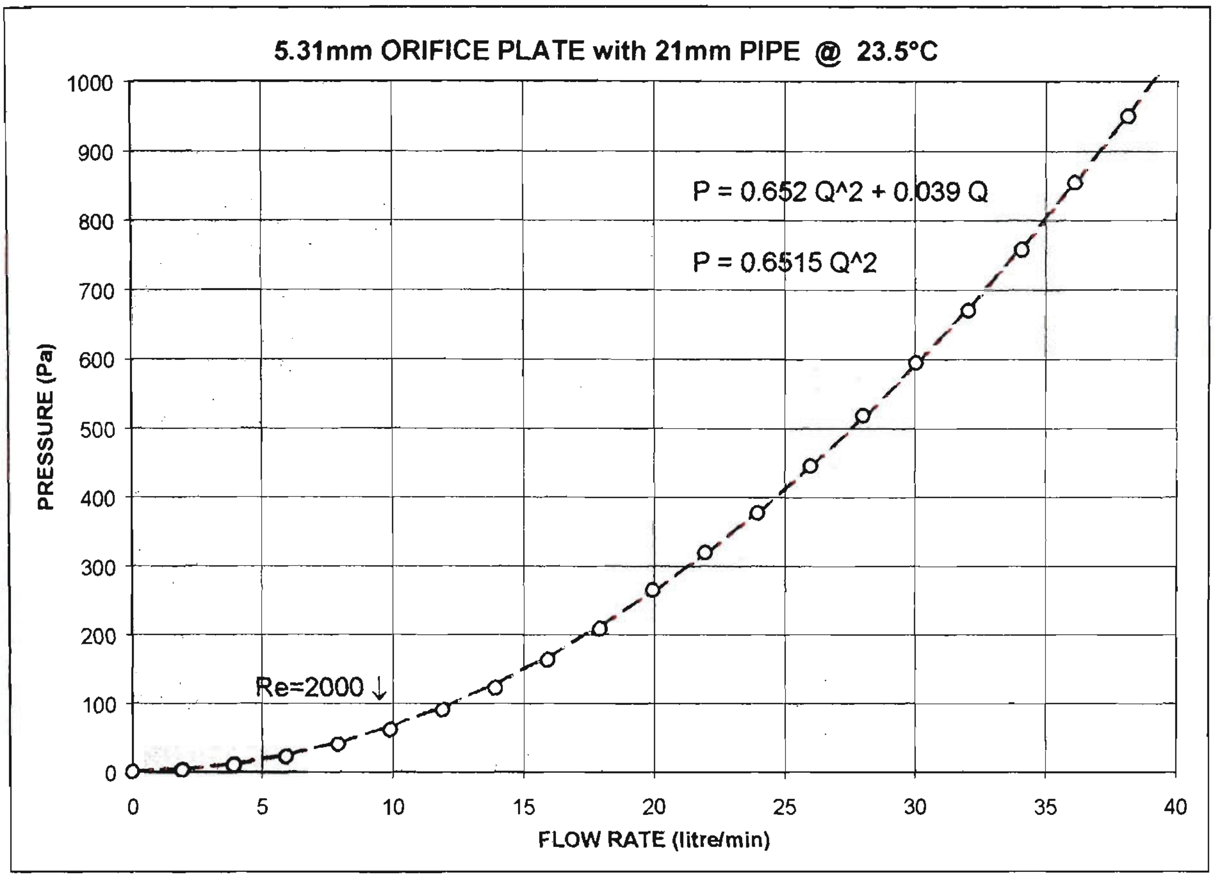

Figure 2.3 - Calibration of $5.31mm$ orifice

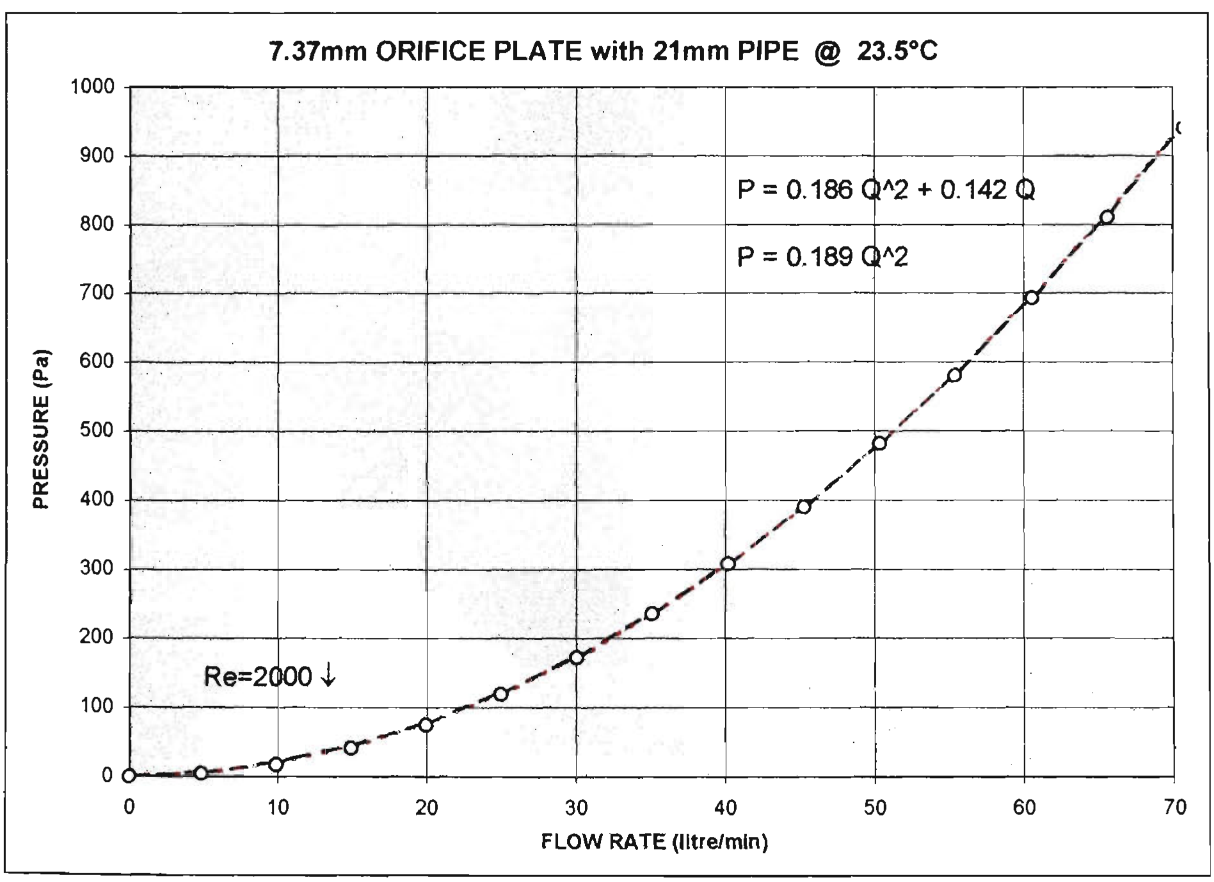

Figure 2.4 - Calibration of $7.37mm$ orifice

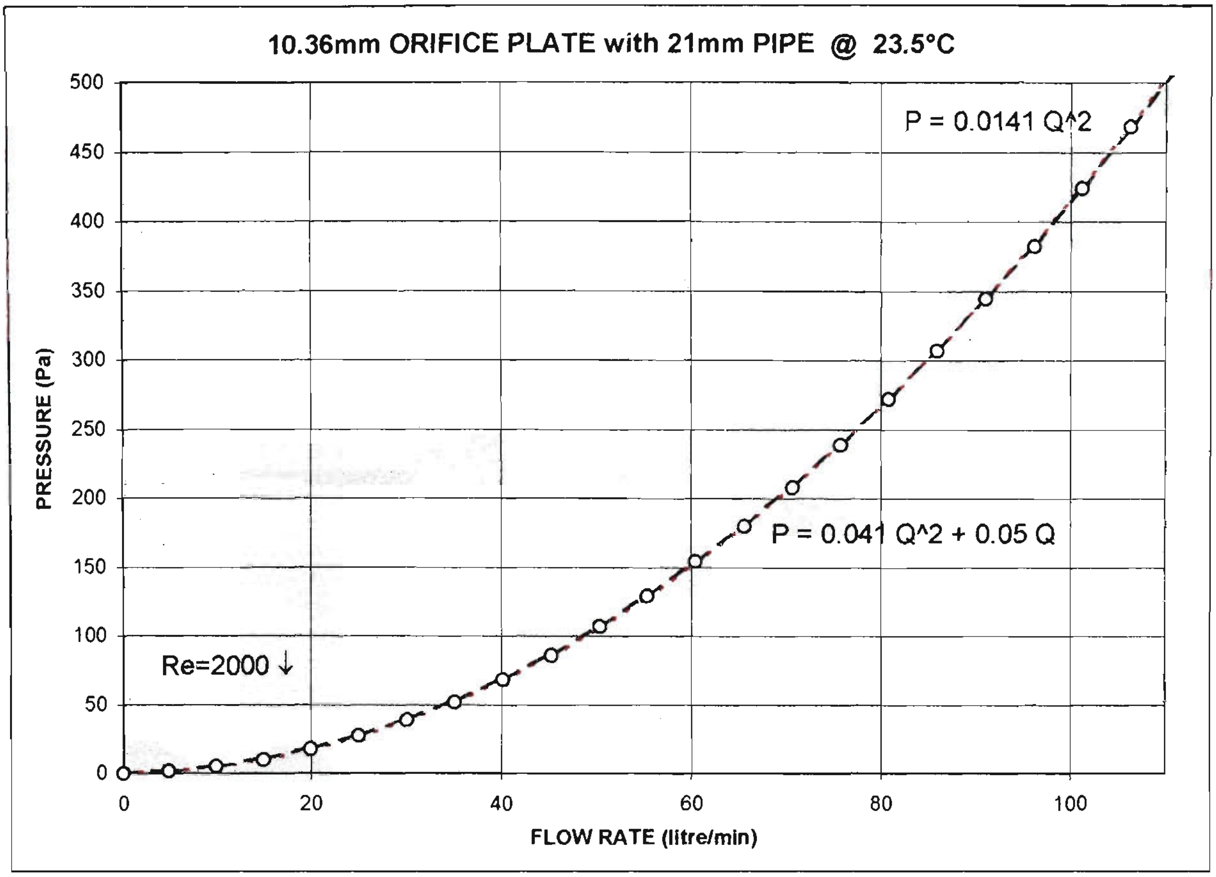

Figure 2.5 - Calibration of $10.36mm$ orifice

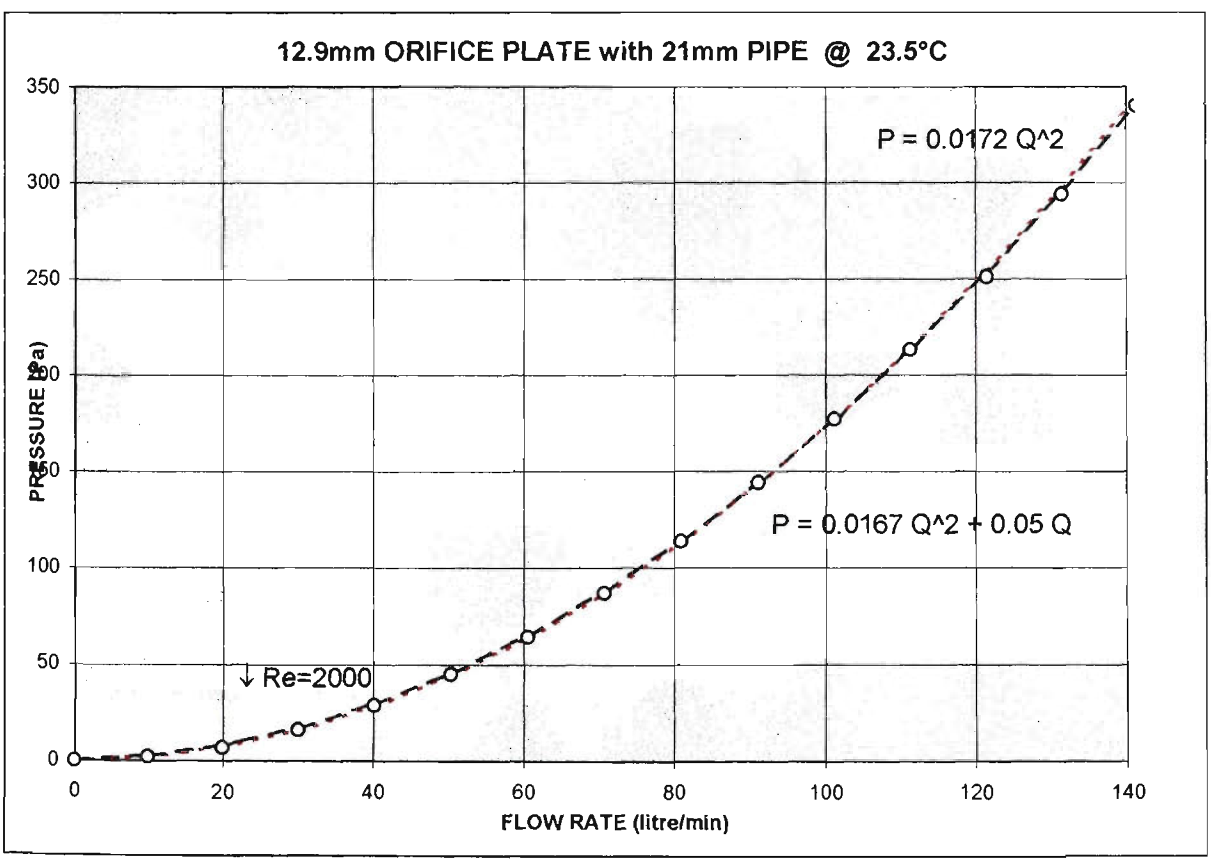

Figure 2.6 - Calibration of $12.9mm$ orifice

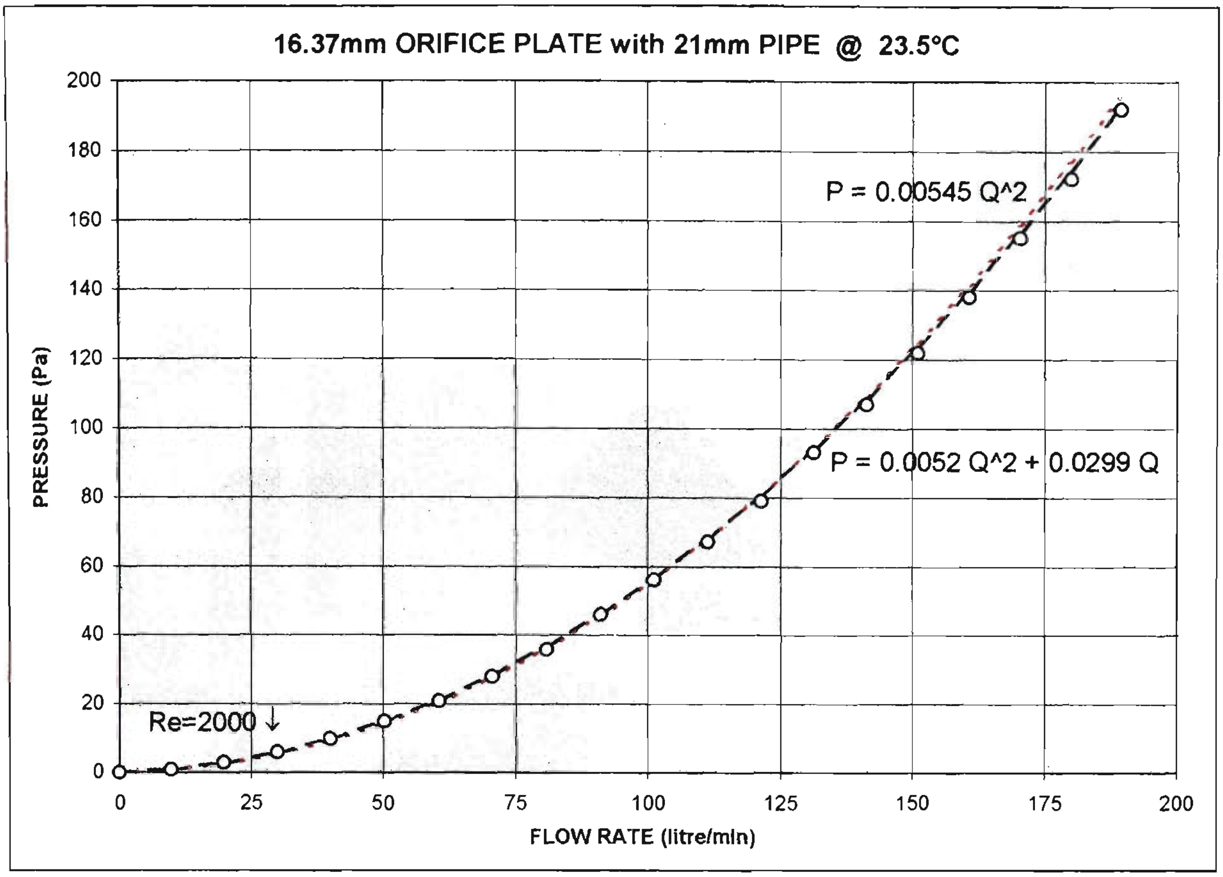

Figure 2.7 - Calibration of 16.37*mm* orifice

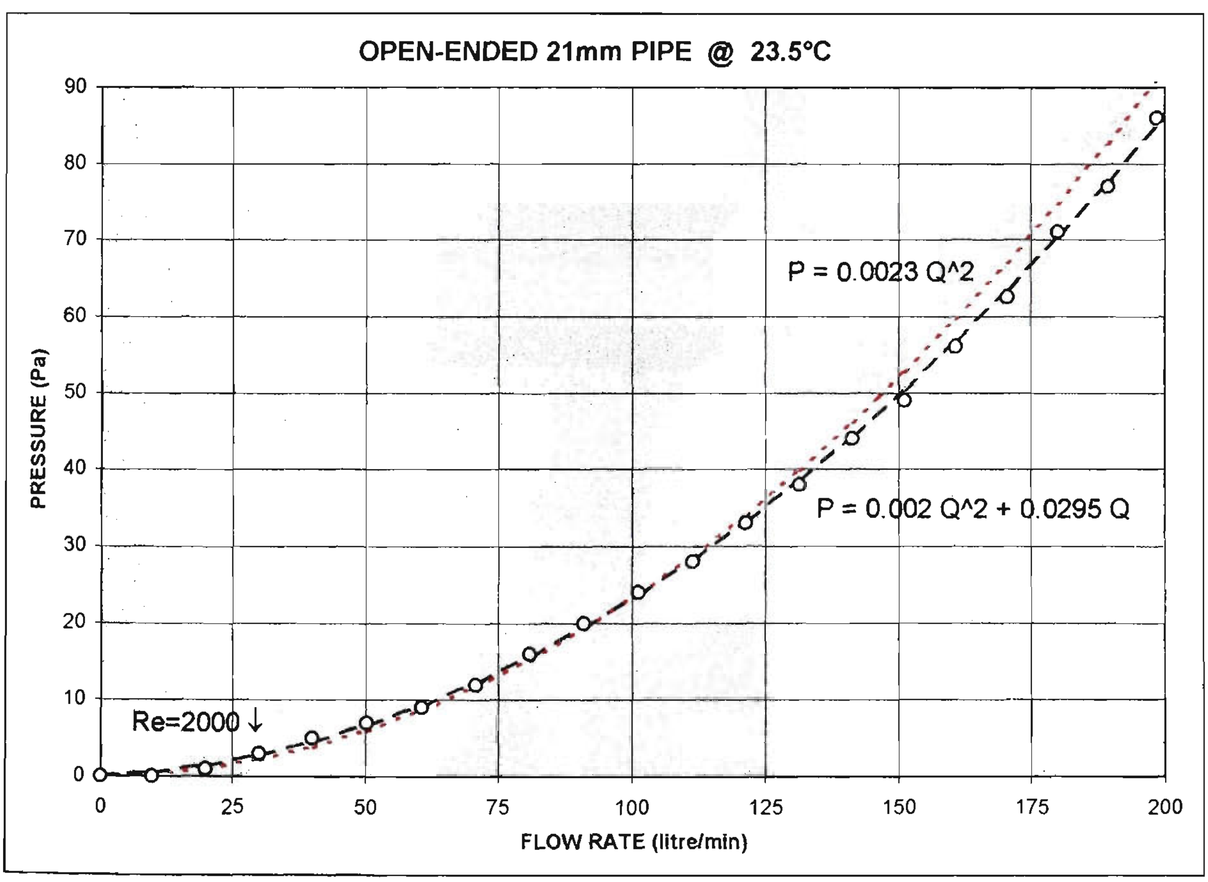

Figure 2.8 - Calibration of pipe open-end (21*mm* orifice)

2.3 ASPIRATORS

The central feature and driving force within an aspirated smoke detection system is the aspirator itself which must be accurately characterised. For any given setting of the aspirator input (defined in terms of the motor supply voltage or the motor speed), it is necessary to measure the pressure developed, throughout the complete range of flow rates.

There are a number of possible settings for the VESDA aspirator, broadly described as "Economy", "Normal" and "Boosted" (E, N, B). These settings are provided to minimise battery consumption (and noise) for smaller systems, or alternatively to reduce smoke transport time for large systems.

In the Xenon-based VESDA detector (Mk3), the aspirator is operated at constant voltage, whereas in the new Laser-based VESDA LaserPLUS detector (Mk4), the same aspirator is operated at constant speed. This results in significantly different characteristics.

For a constant-voltage aspirator, as the flow rate increases, the pressure reduces due to friction within the impeller blade passages. At this higher flow rate the aspirator delivers more power to the airstream, placing a greater load on the motor, so the speed reduces. This speed reduction further reduces the available pressure as a secondary effect.

For a constant-speed aspirator, a tachometer output is used automatically to control an increase in the supply voltage so as to maintain speed and hence deliver more power to the airstream. Although pressure is reduced due to internal friction in the normal manner at high airflows, there is no secondary reduction of pressure due to speed. Consequently the aspirator performance characteristic is "broader" - a higher airflow range is achieved. This improvement is gained at the expense of a higher electrical input power to the motor at these higher flow rates.

A further complication with the original (constant-voltage) aspirator arose from having designed the impeller with only 12 blades. This number produced a high efficiency but also resulted in a mildly excessive noise intensity. Measuring some 52 to 56 dBA at $1m$ (depending on the motor speed and the environmental acoustics), the noise intensity approached that of typical ventilation fans as used in office equipment (such as PC's and photocopiers). Although much of the noise was contributed by the motor cogging, this was exacerbated by the tonal content of the impeller noise (which is a common characteristic of centrifugal air pumps). This was typically in the region of 700 to 800 Hz, again depending upon motor speed. Such a noise level was regarded as excessive in sensitive environments such as recording studios, live theatres, art galleries and libraries.

Various methods were used in an attempt to reduce this sound level without reducing pump efficiency, including the minor staggering of blade separations (by up to ±3°) to reduce resonance. The most effective and simple solution was to double the number of blades, to 24. This had the effect of halving the pressure differential between opposing sides of any given blade. It is this pressure differential, as each blade passes the aspirator volute tongue, that imparts a noisy pressure impulse. These impulses resonate at the blade-passing frequency. By halving the pressure differential, the sound pressure level should be reduced by 6dB (equating to half power). After modifying the impeller, this reduction was in fact recorded, at the standard distance of $1m$ on-axis to the outlet diffuser.

Increasing the number of blades can sometimes improve efficiency by reducing the tendency for flow circulation within the blade passages. This advantage has to be offset against the disadvantage, of increasing the surface friction. Unfortunately it was discovered that on balance, increasing the number of blades reduced the overall efficiency. This was regarded as a price that was worth paying, for quietness.

Consequently the constant-voltage aspirator had 12 blades and the constant-speed aspirator had 24 blades. The experimental results for typical products are shown in Figures 2.9 and 2.10. In each case, three settings are shown. In the case of the constant-voltage aspirator, cutoff pressures of 200, 300 and 400 Pa were selected, representing Economy, Normal and Boosted (E, N, B) operation. In the constant-speed case, the equivalent settings had not been established so speeds of 3000, 3600 and 4200 RPM were selected.

Curves of best fit to the data and their equations are included in Figures 2.9 and 2.10. Some data points indicate a small departure from a simple, smooth curve at low flow rates (around 20*litre/min*), but this modelling error is unlikely to be significant - the departure is small, and systems would rarely if ever operate at such a low flow rate.

It can be seen that at normal operation (300 Pa max or 3600 RPM), the characteristic equations for the constant-voltage and constant-speed aspirators respectively at 23°C were determined as:

Constant-voltage, 12 blade: $$P_{asp} = -0.011\,Q^2 + 0.05\,Q + P_{\max}$$

Constant-speed, 24 blade: $$P_{asp} = -0.0095\,Q^2 + 0.57\,Q + P_{\max}$$

where Q is the flow rate and P_{max} is the cutoff (zero flow) pressure, being 300 and 246 Pa in these two equations respectively. For simplicity in developing the computer model and also to avoid confusion by the model user, it is desirable to define the aspirator setting in terms of this cutoff pressure, thereby allowing the use one equation for the given aspirator, adjusting only the value of the applicable constant (P_{max}).

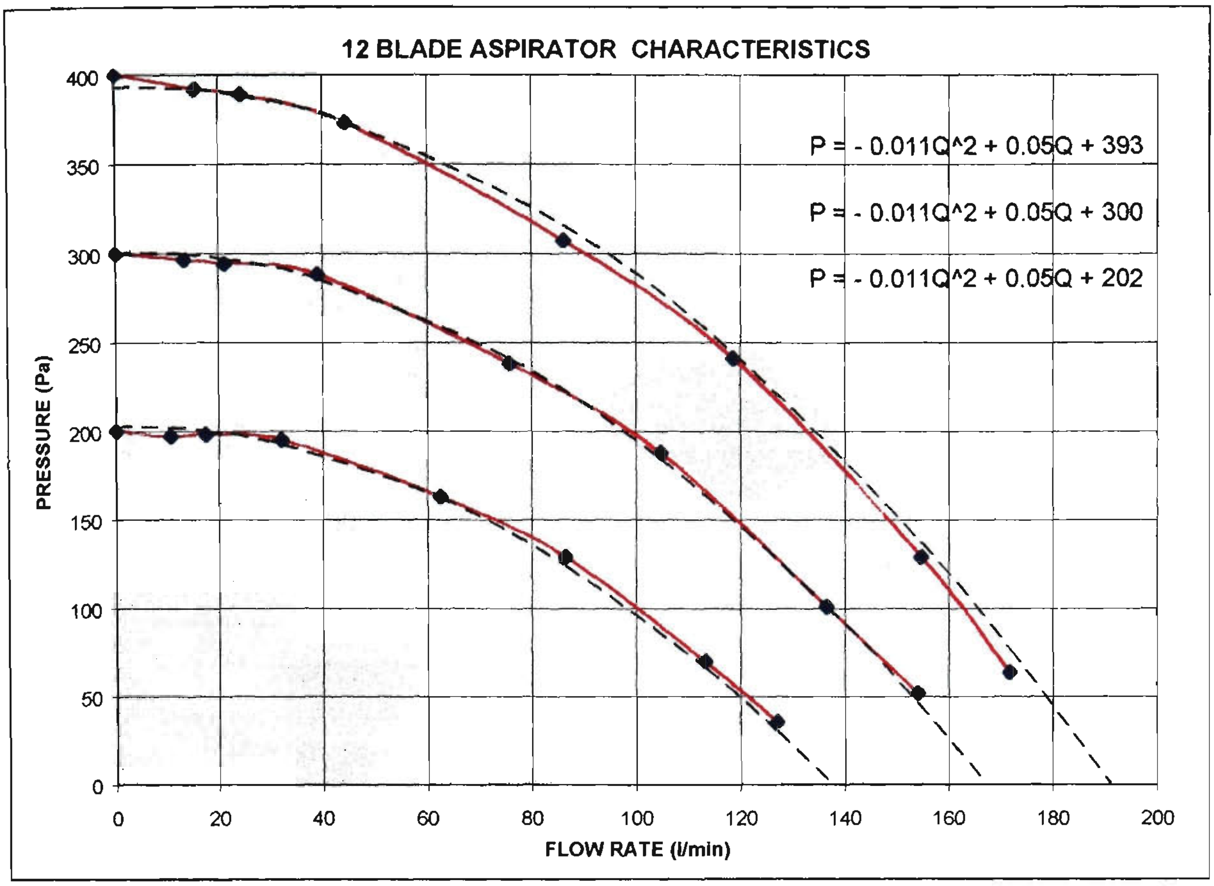

Figure 2.9 - 12 blade aspirator at Economy, Normal and Boost

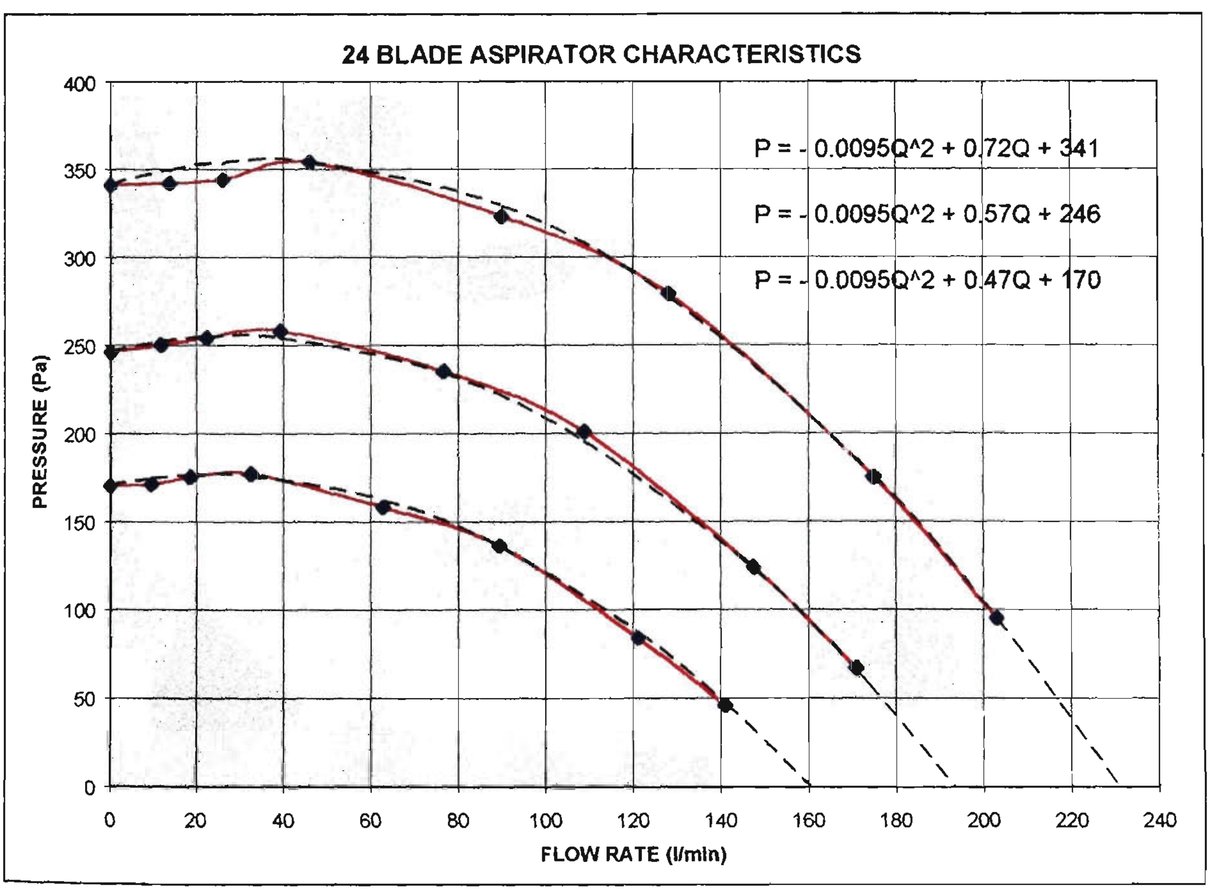

Figure 2.10 - 24 blade aspirator at 3000, 3600 and 4200 RPM

Reasonable consistency across the range of settings was achieved in the case of the constant-voltage aspirator, but a small adjustment to the cutoff pressure constant was required (202 Pa instead of 200 Pa, or 393 Pa instead of 400 Pa). After manually-corrected curve-fitting to the data, as graphed in Figure 2.11, the correction equation for the cutoff pressure is:

$$P_{max,c} \quad = \quad -\,2.5E\text{–}04\ P^2_{max} + 1.105\ P_{max} - 9$$

In the constant-speed case it proved necessary to adjust the linear term (0.47 at 3000 RPM, 0.57 at 3600 RPM or 0.72 at 4200 RPM) without adjusting the other terms. After manually-corrected curve-fitting to the data as graphed in Figure 2.12, this linear term ($Term1$) could be obtained from:

$$Term1 \quad = \quad 1.55E\text{–}06\ P^2_{max} + 6.7E\text{–}04\ P_{max} + 0.3113$$

Because it was proposed that the constant-speed aspirator could be set in terms of speed as well as cutoff pressure, it was necessary to test the relationship of cutoff pressure to speed setting (S_{asp}), as well as the reverse. This has been plotted in Figure 2.12, resulting in the following equations for use in the computer model:

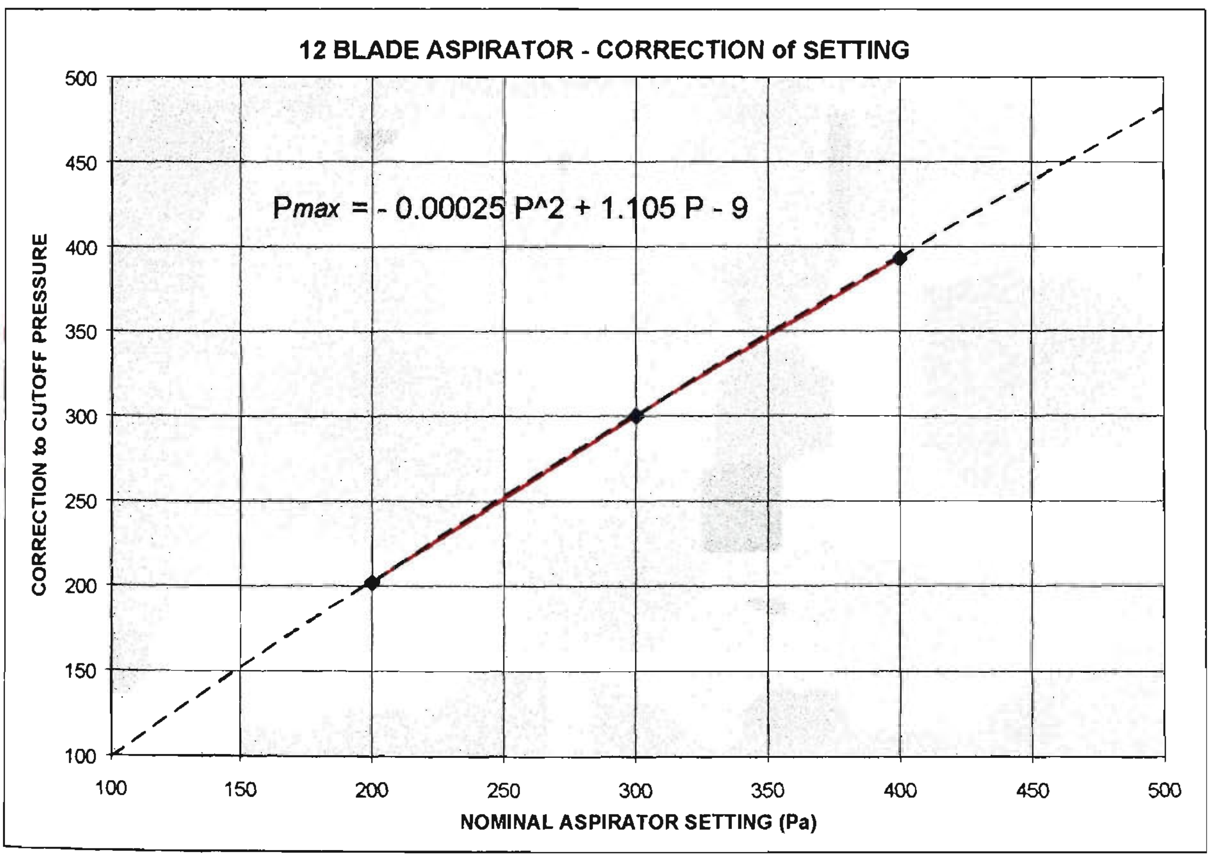

Figure 2.11 - Correction to 12 blade aspirator setting

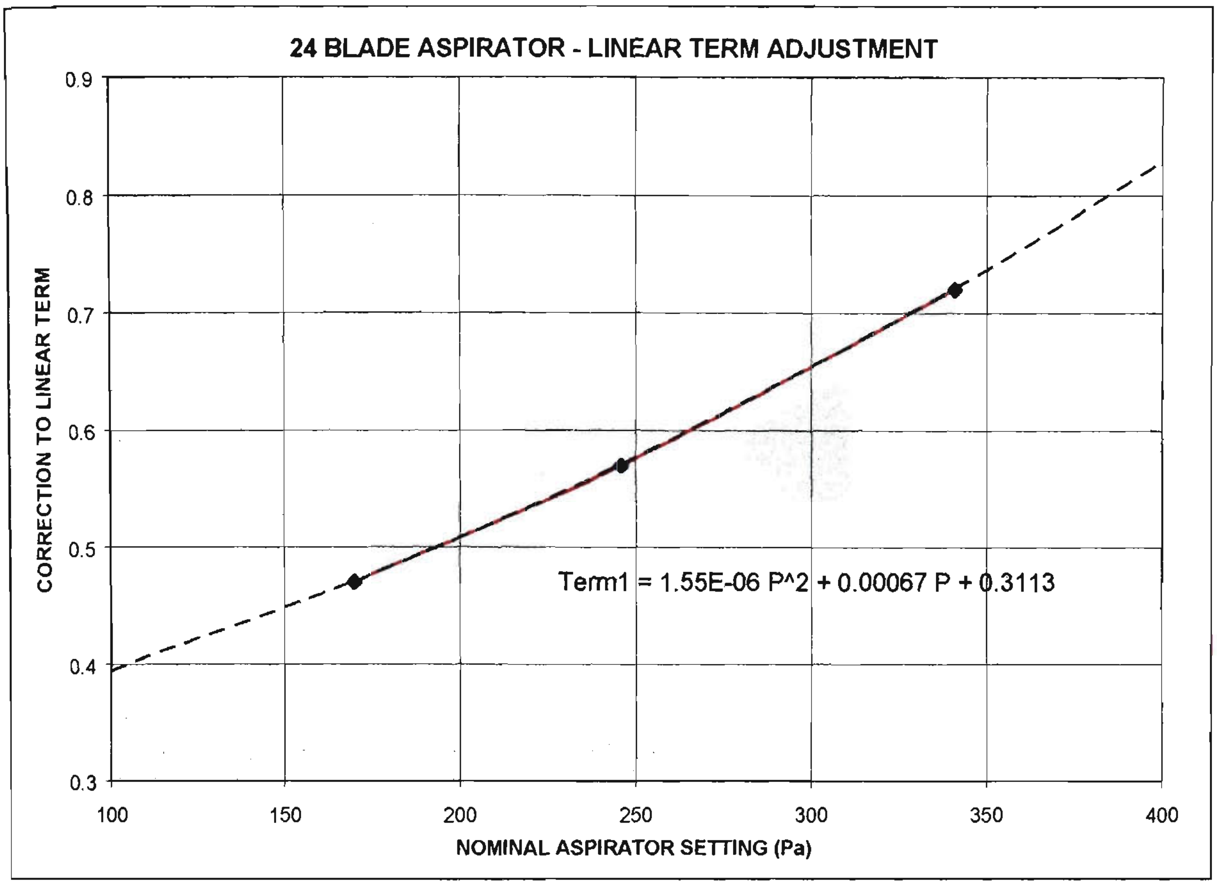

Figure 2.12 - Correction to 24 blade aspirator setting

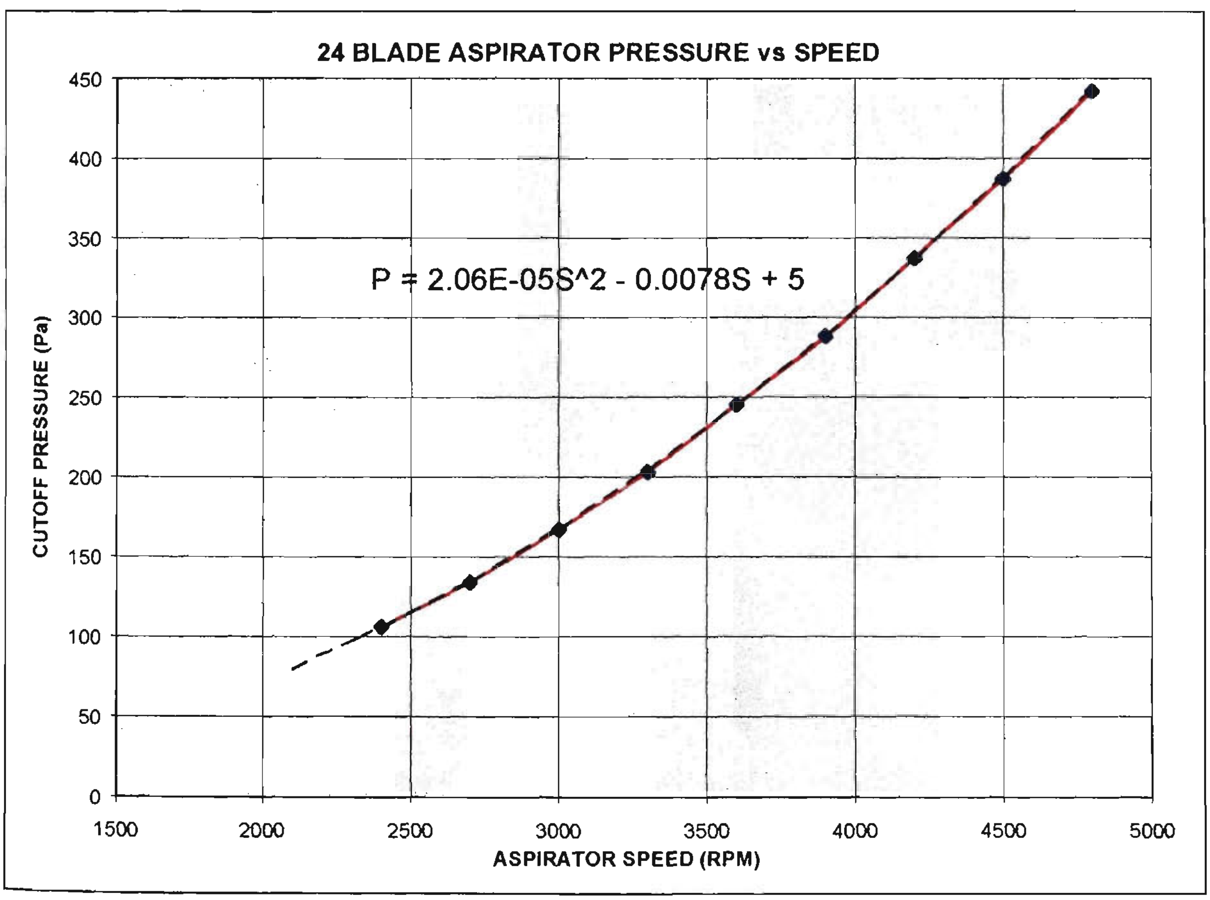

Figure 2.13 - 24 blade aspirator cutoff pressure versus speed

$$P_{\max} \quad = \quad +2.06E\text{-}05\, S_{asp}^2 - 0.0078\, S_{asp} + 5$$

$$S_{asp} \quad = \quad -0.0073\, P_{\max}^2 + 11\, P_{\max} + 1350$$

To establish "equivalent" performance of the two aspirators, the constant speed aspirator can be set to a lower cutoff pressure than the constant voltage aspirator, because of its broader flow range. In this manner, somewhat comparable outcomes for Economy, Normal and Boosted operation can be arranged for each aspirator. This will be discussed in greater detail later, after consideration of the impact of other components within the complete detector package.

In addition to the constant-voltage and constant-speed aspirators, the computer model needs to cater for a range of other types, especially the obsolete VESDA Mk2 fan and the MiniVESDA as illustrated in Figures 2.14 and 2.18. These were characterised as follows:

VESDA Mk2 $\quad P_{asp} = -0.0025\, Q^2 - 0.353\, Q + 118 \quad$ *at 24V DC*

MiniVESDA $\quad P_{asp} = -0.0003\, Q^2 - 0.138\, Q + 48 \quad$ *at 24V DC*

Included in Figure 2.14 for comparison, is the characteristic of the VESDA Mk3 aspirator. The advantage of the newer design is evident, in terms of its higher available pressure across the entire flow range. Moreover, the newer design requires an input power of 2W compared with 5W so that the overall efficiency is some ten times higher. The MiniVESDA is intended for coverage of small areas and is not comparable with other aspirators.

For adaptable computer modelling it is useful to characterise other brands of detector (see Appendix 1). In the two following cases, it was not possible to isolate the aspirator characteristic from the detector loss (and the filter loss in the latter case). The characteristics obtained for the available samples are illustrated in Figures 2.16 and 2.17 while the equations are as follows:

Hart/Analaser $\quad P_{asp} = -0.0037\, Q^2 + 0.157\, Q + 135 \quad$ *at 24V DC*

Stratos $\quad P_{asp} = +0.0002\, Q^2 - 0.38\, Q + P_{\max}$

where $122 < P_{\max} < 224$ in the case of Stratos, according to the available setting which ranges from "1" to "10". However, this setting has been observed to alter during operation. This is thought to be an economy feature (being a 12W fan at 24V DC), but this would make system performance unpredictable. In the case of VESDA Mk2, MiniVESDA and Hart/Analaser, the aspirator performance is affected by supply voltage which is an uncontrolled variable typically within the range 20 to 28V DC. Nevertheless for modelling purposes the above equations are regarded as representative.

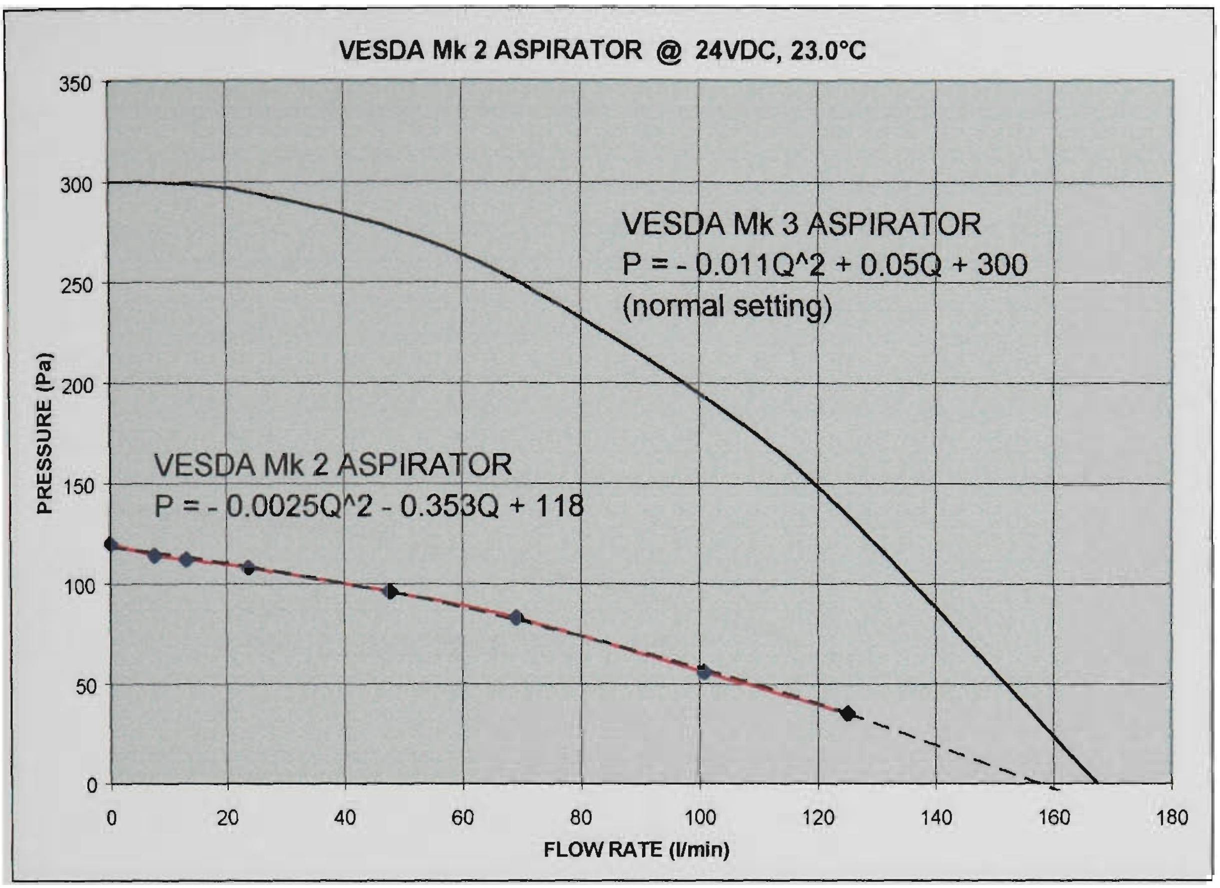

Figure 2.14 - VESDA Mk2 aspirator fan, compared with Mk3

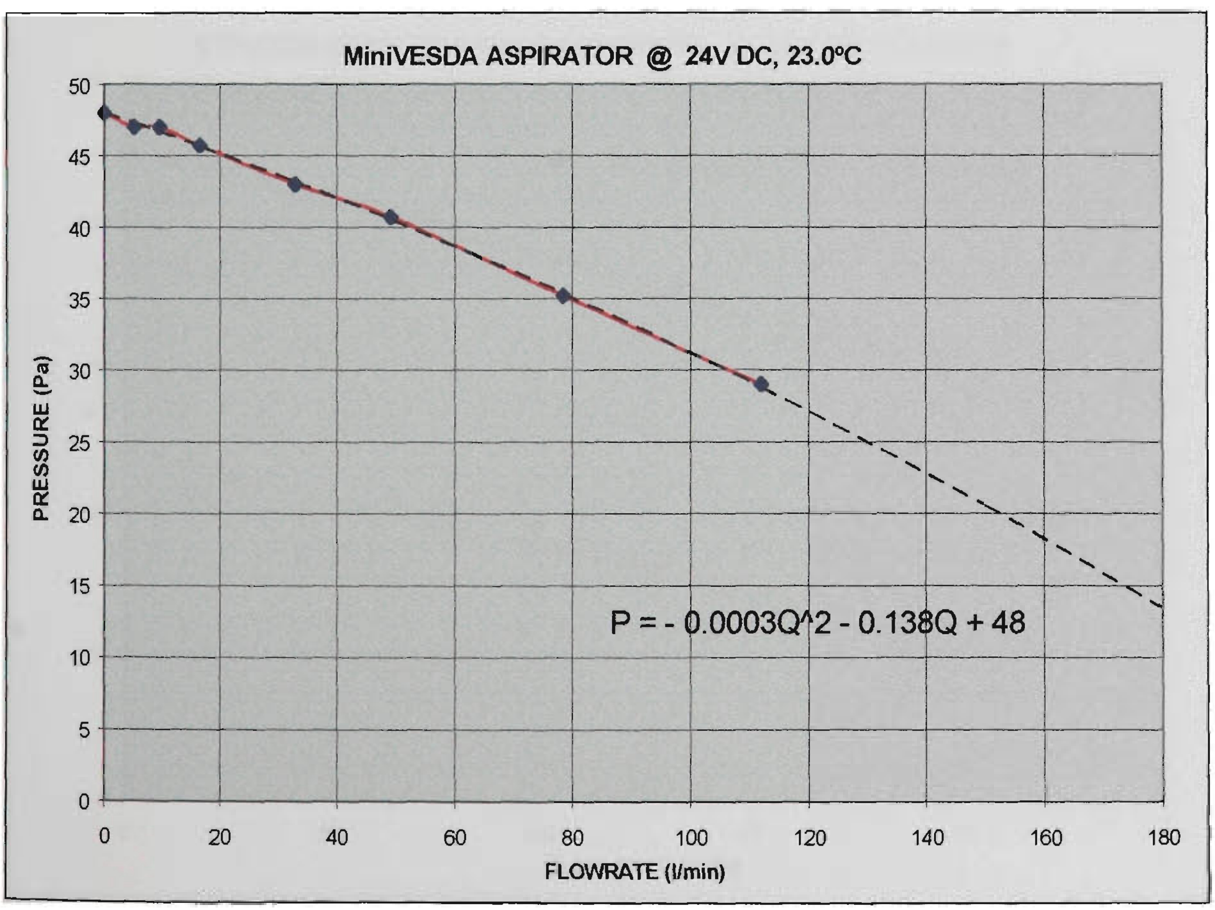

Figure 2.15 - Characteristic of MiniVESDA aspirator fan

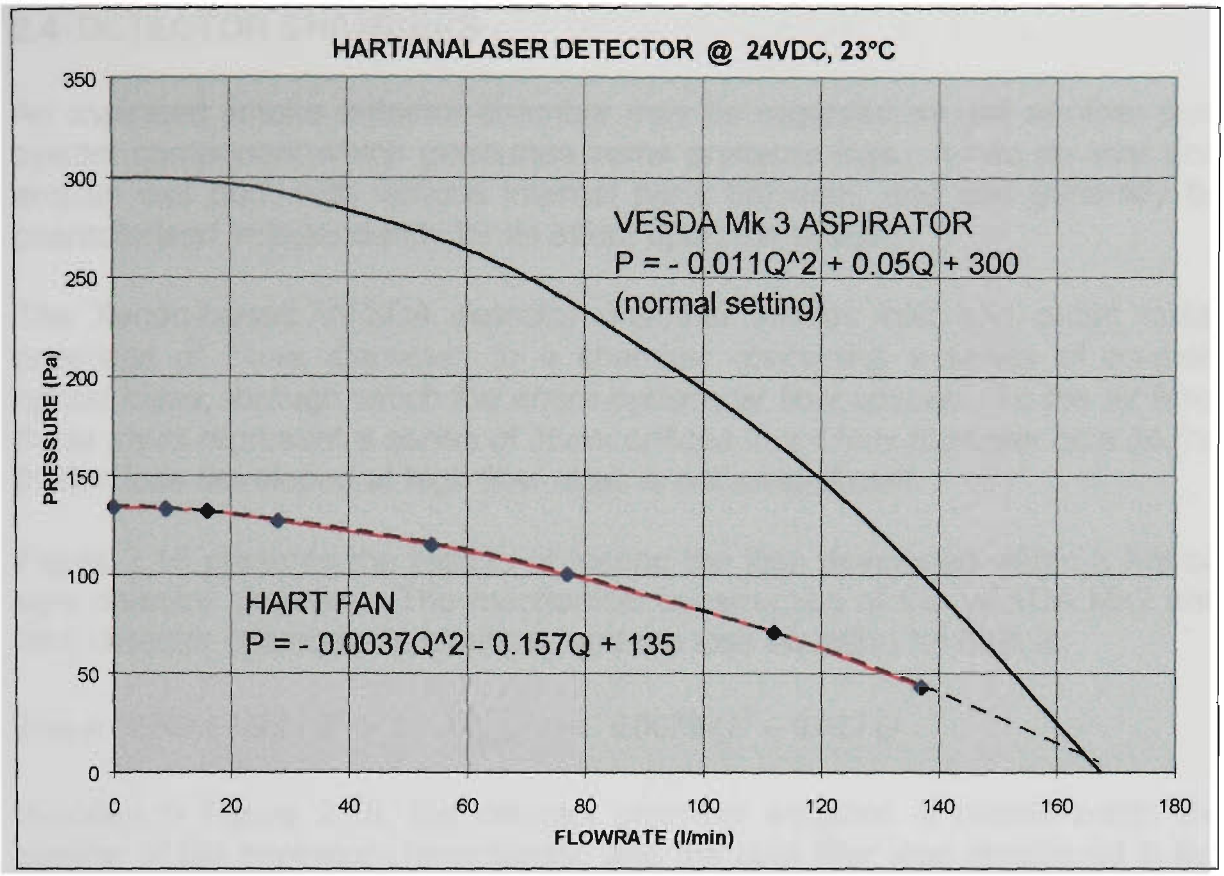

Figure 2.16 - Characteristic of Hart detector

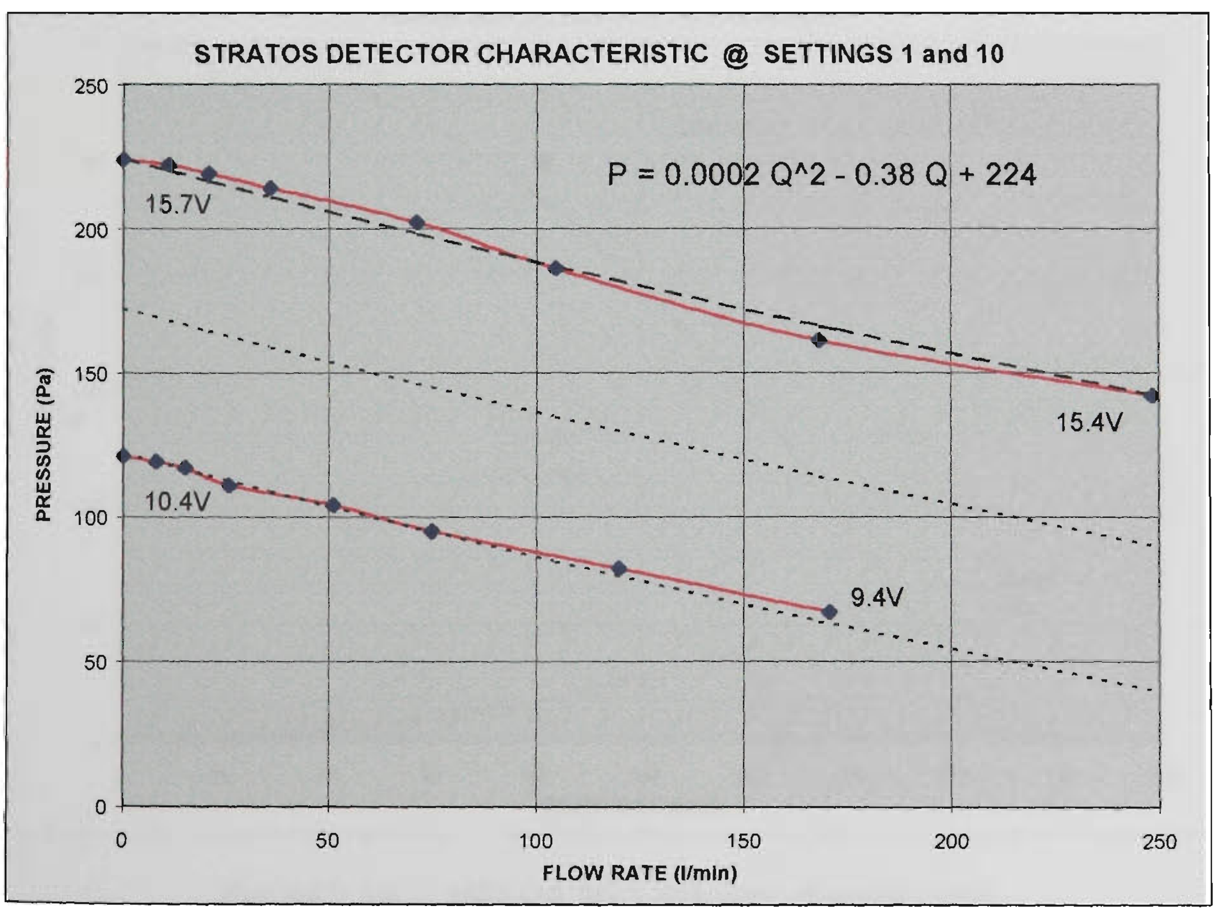

Figure 2.17 - Characteristics of Stratos detector

2.4 DETECTOR CHAMBERS

An aspirated smoke detector chamber may be regarded as just another pipe system component which generates some pressure loss. It has an inlet port and an exit port, with various internal parts between, and can generally be characterised independently for its effect upon the system.

The Xenon-based VESDA detector chamber utilises inlet and outlet radial couplings of $21mm$ diameter, to a chamber containing a series of co-axial optical irises, through which the entire system air flow passes. To the air flow, these irises represent a series of $36mm$ orifices in a $45mm$ diameter pipe so the friction loss developed at high flow rates is not insignificant.

Figure 2.18 presents the results of testing the loss developed within a Xenon type detector chamber. The mechanical construction of the VESDA Mk2 and Mk3 detector chambers is identical, and the loss equation for both is:

Xenon VESDA Mk2 / 3 $\qquad \Delta P_{chmb} \quad = \quad 0.0029\, Q^2 - 0.023\, Q$

Included in Figure 2.18, the detector chamber equation is placed within the context of the aspirator characteristic and the dust filter loss (explained in the next chapter) to present the overall performance of the detector package.

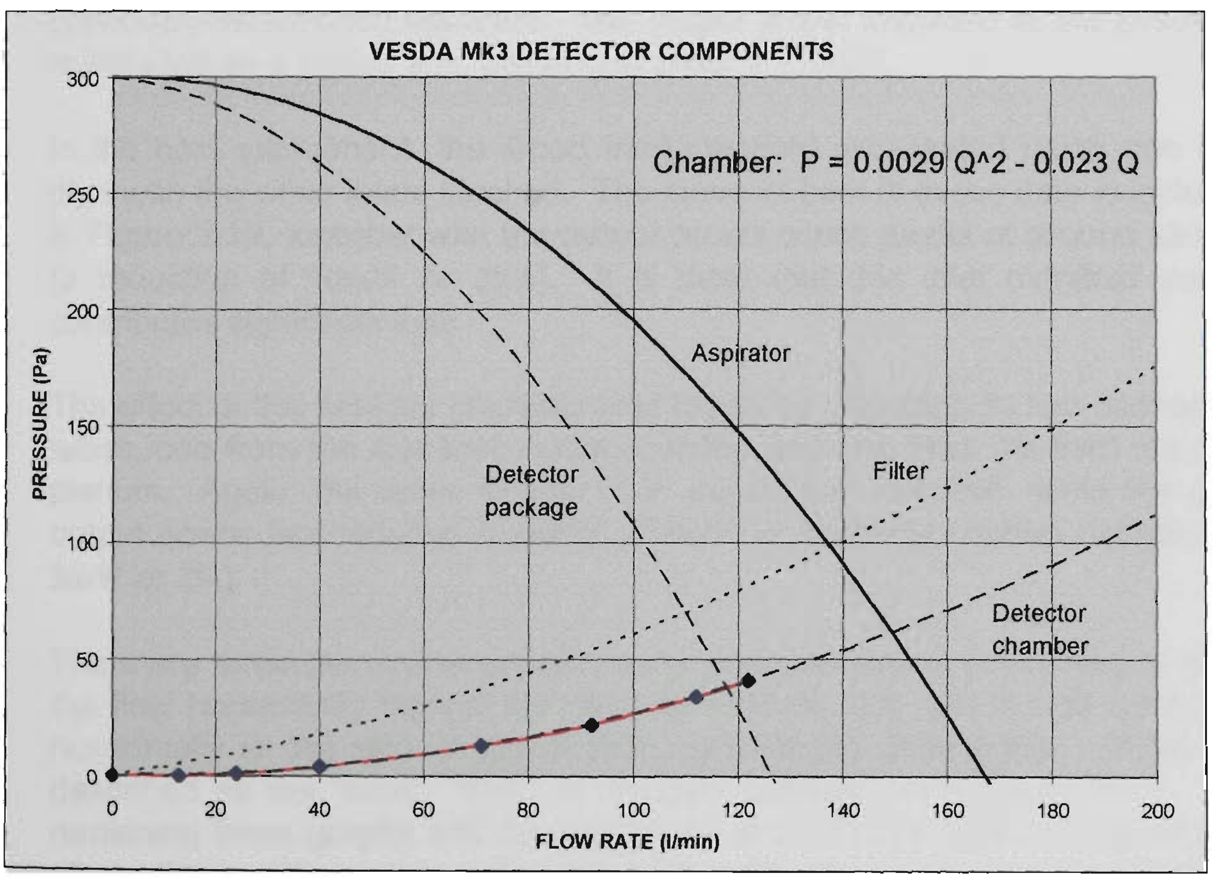

Figure 2.18 - VESDA Mk3 detector chamber loss

By contrast, the Laser-based design of the VESDA Mk4 detector allows for a miniature detector chamber (amongst other benefits). The associated "plumbing" maintains a uniform tube diameter with some bends in the main flow path, with only a small sample (less than 5%) of the total system flow directed through this tubing and the detector chamber. The density of smoke within the sample is no different from the density in the main flow, so there is no degradation in smoke sensitivity. Moreover, dust filtration need only be applied to this small sample, greatly extending filter service life in the field.

This small sample flow is generated by connecting the detector across the aspirator itself to obtain the maximum pressure differential. This serves to overcome relatively high friction losses within the small detector chamber and its associated dust filter. Accordingly, in this case the loss introduced by the detector chamber amounts to a small short-circuit flow affecting the aspirator directly. However, the impact of this can be isolated as a quasi-independent loss equation.

Figure 2.19 illustrates how the impact of the various components of the VESDA Mk4 (or "VESDA LaserPLUS") detector can be isolated at a given aspirator speed. A speed of 3600 RPM was selected as typical and representative. Firstly, the 24-blade aspirator was tested using the standard orifices, test pipe and pressure tapping previously described (as used with all other experiments). This verified repeatability by conformance with the previously-established equation. The output power imparted to the airstream is included as a dotted line, peaking at around 350mW.

In the next experiment, the 4-port inlet manifold was tested using one inlet pipe with the other inlets blocked. The curve of best fit to the data is included in Figure 2.19, together with the output power which peaks at around 280mW (a reduction of 70mW or 20%). It is clear that this inlet manifold design contributes significant loss.

The effect of the detector chamber was tested by attaching its two connecting tubes, one from the aspirator outlet coupling and one from the inlet manifold plenum. Again, the curve of best fit to the data is included, while the peak output power has reduced to about 275mW (a relatively modest reduction of 5mW or 2%).

There are three alternative exhaust outlet ports available, positioned to direct the flow horizontally behind the detector module (e.g. into a wall cavity), or horizontally to the side of the module, or vertically downwards. These are described as the "back", "side" or "bottom" exhaust ports respectively. The remaining three graphs and curves of best fit on Figure 2.19 represent these alternatives. The peak power is about 240, 230 or 215 mW respectively, indicating a reduction of 13, 16 or 22 % respectively. The back exhaust is clearly preferred in terms of efficiency and performance at a given aspirator speed.

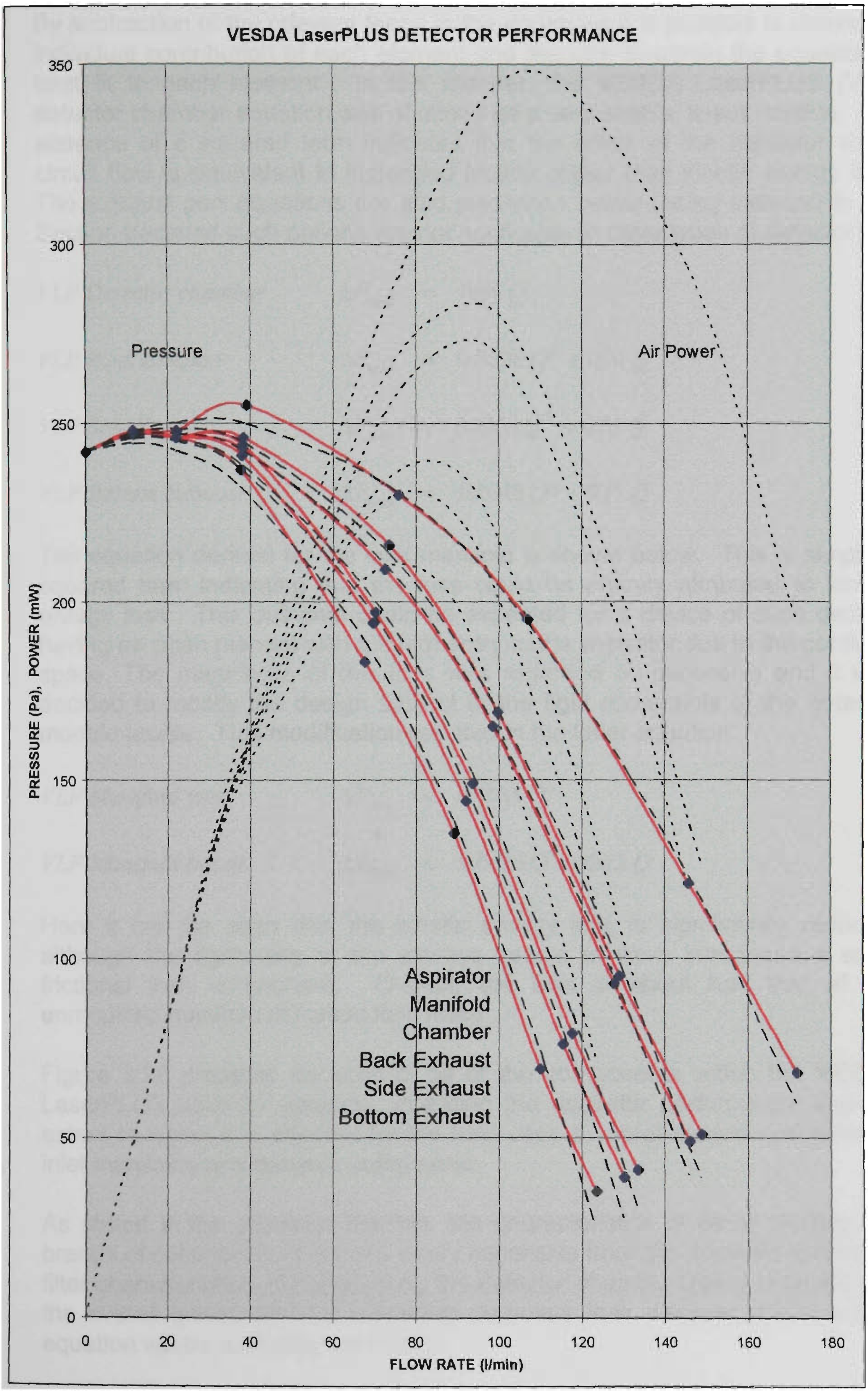

Figure 2.19 - VESDA LaserPLUS characteristics

By subtraction of the relevant terms in the equations it is possible to derive the individual contribution of each element and thereby, to obtain the equation of best fit to each element. In this manner, the VESDA LaserPLUS (VLP) detector chamber equation was obtained as a very simple, linear relation. The absence of a squared term indicates that the effect of the aspirator short-circuit flow is equivalent to increased friction rather than kinetic energy loss. The exhaust port equations are also presented below (being included in this Section because such options are not applicable to other types of detector):

VLP Detector chamber $\quad \Delta P_{chmb} = 0.06\,Q$

VLP Back Exhaust $\quad \Delta P_{back} = 0.0026\,Q^2 + 0.01\,Q$

VLP Side Exhaust $\quad \Delta P_{side} = 0.0035\,Q^2 + 0.01\,Q$

VLP Bottom Exhaust $\quad \Delta P_{botm} = 0.0045\,Q^2 + 0.11\,Q$

The equation derived for the inlet manifold is shown below. This is simply a squared term indicating that the loss could be entirely attributed to kinetic energy loss. This outcome could be expected for a device of such design, having an open plenum with a sharp entry to the aspirator due to the confined space. The magnitude of this loss was regarded as excessive and it was decided to modify the design subject to the tight constraints of the detector module profile. This modification resulted in the latter equation:

VLP Manifold (std) $\quad \Delta P_{man} = 0.0035\,Q^2$

VLP Manifold (mod) $\quad \Delta P_{\mathrm{mod}} = 0.0015\,Q^2 + 0.12\,Q$

Here it can be seen that the kinetic energy loss is significantly reduced, although the tightening of the airways seems to have introduced a small frictional loss component. Overall, the loss is about half that of the unmodified manifold at typical flow rates.

Figure 2.20 presents an audit of all of the components within the VESDA LaserPLUS detector package, including the aspirator performance and the extent to which it is affected by the best case or worst case combination of inlet manifolds and exhaust outlet ports.

As stated in the previous Section, the characteristics of other models and brands of detector head are not easily separable from the aspirator and/or the filter characteristics. Consequently the detector chamber loss is included with the overall losses and for modelling purposes their detector chamber loss equation will be artificially set to zero.

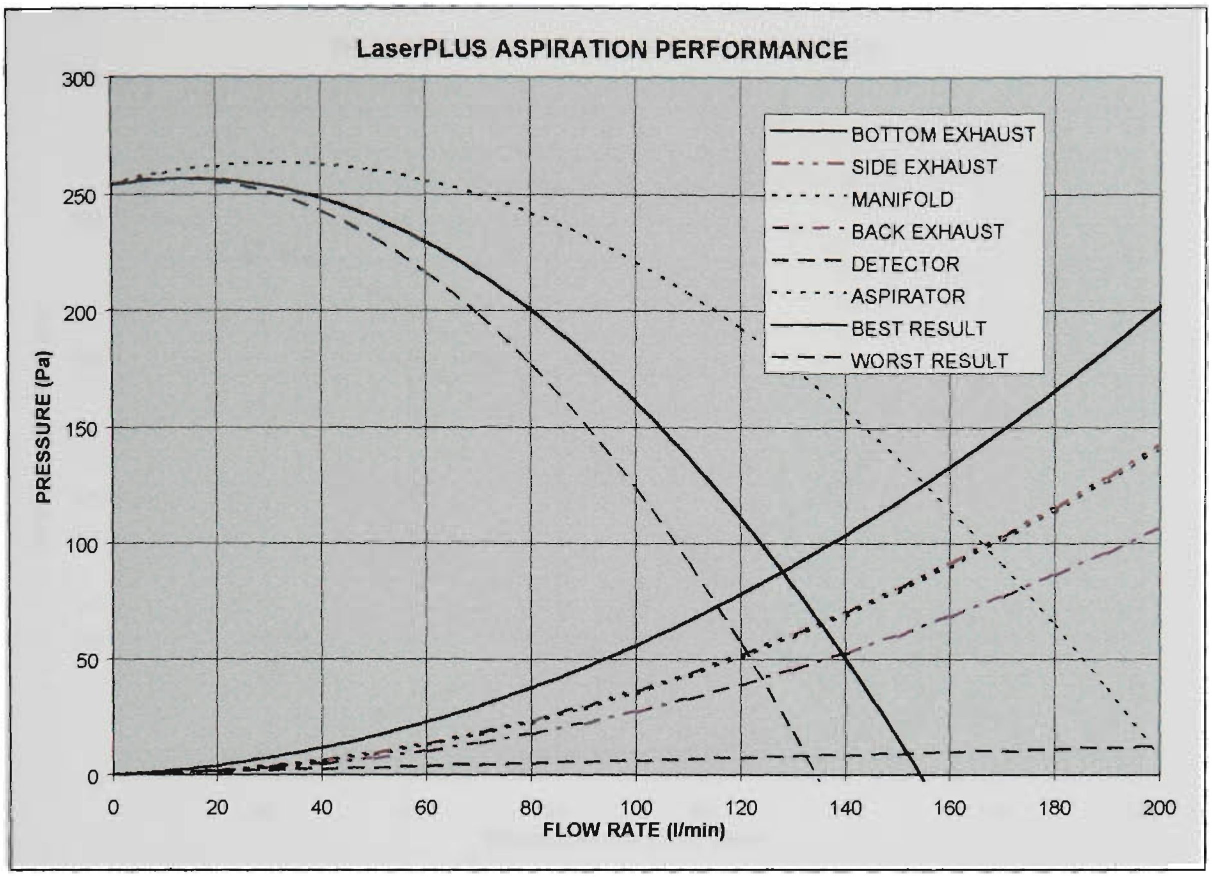

Figure 2.20 - Audit of VESDA LaserPLUS components

2.5 DETECTOR PACKAGE PERFORMANCE

Having obtained the performance characteristics for the complete Xenon VESDA (Mk3) and VESDA LaserPLUS (Mk4) packages, it is now possible to determine the aspirator settings that would provide equivalent system performance from each of these products, when operated in the Economy, Normal or Boosted modes.

The approach is illustrated in Figures 2.21, 2.22 and 2.23. For reference, these graphs include a set of four different system load characteristics representing a range of aspirated smoke detection system configurations (based upon the current version of the computer model, to be substantiated later). Note that the system operating point would be the point of intersection of the aspirator characteristic and the system load characteristic in each case.

Given that the specified maximum aggregate pipe length for any system is $200m$, systems comprising one pipe of $100m$ length, two pipes of $100m$ length and four pipes of $50m$ length, as well as four pipes of $10m$ length have been included. Overall these illustrate the typical span and maximum spread of pressures and flow rates expected for practical systems.

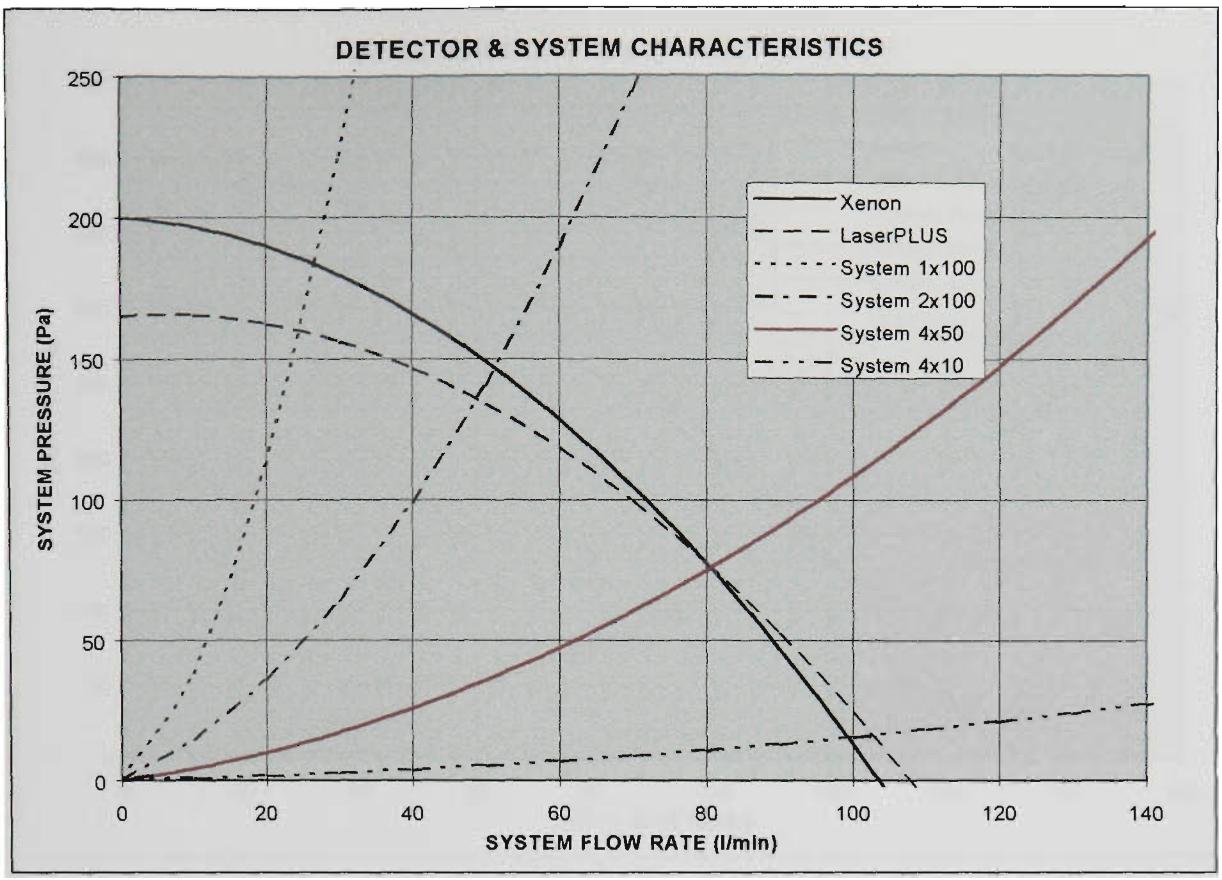

Figure 2.21 - Aspirated system operation at Economy setting

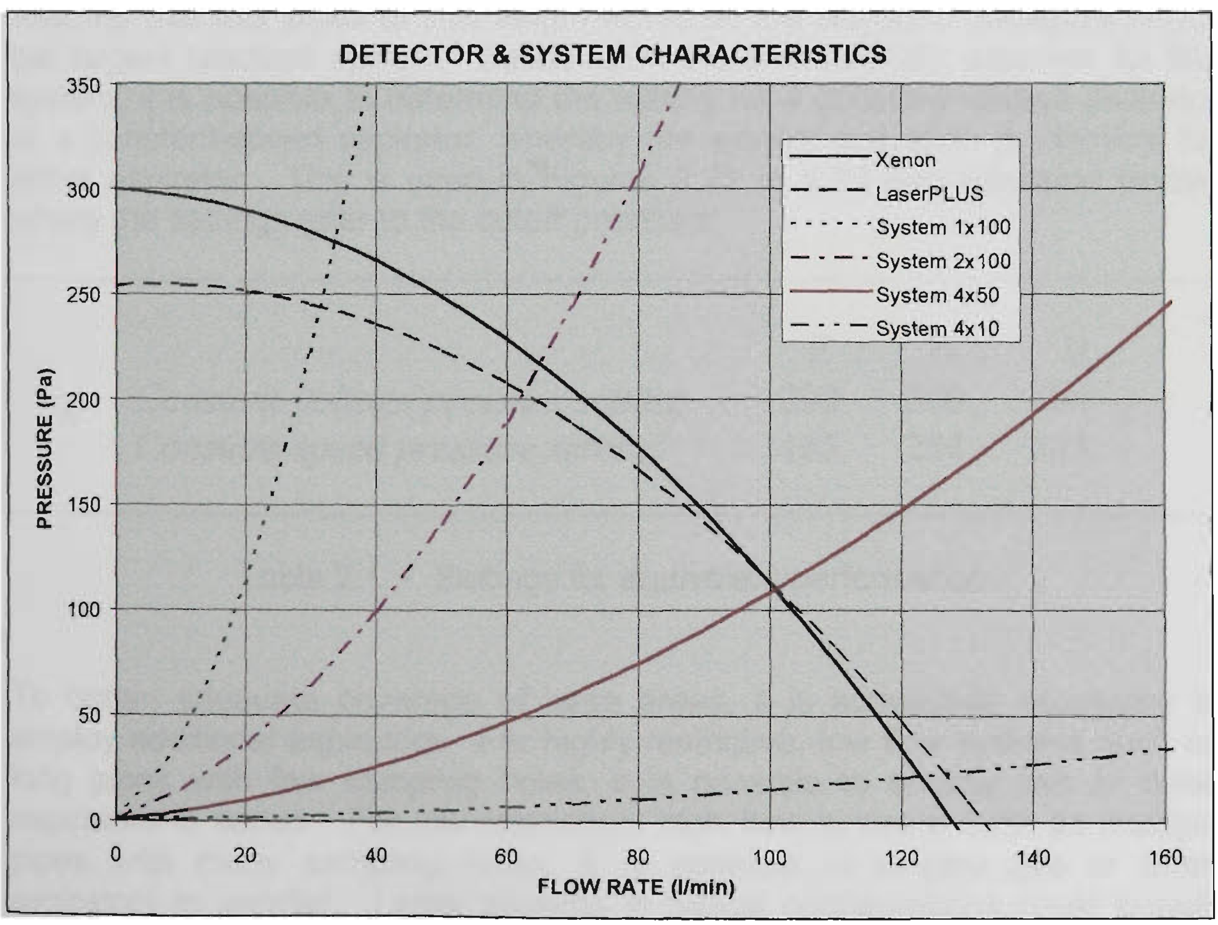

Figure 2.22 - Aspirated system operation at Normal setting

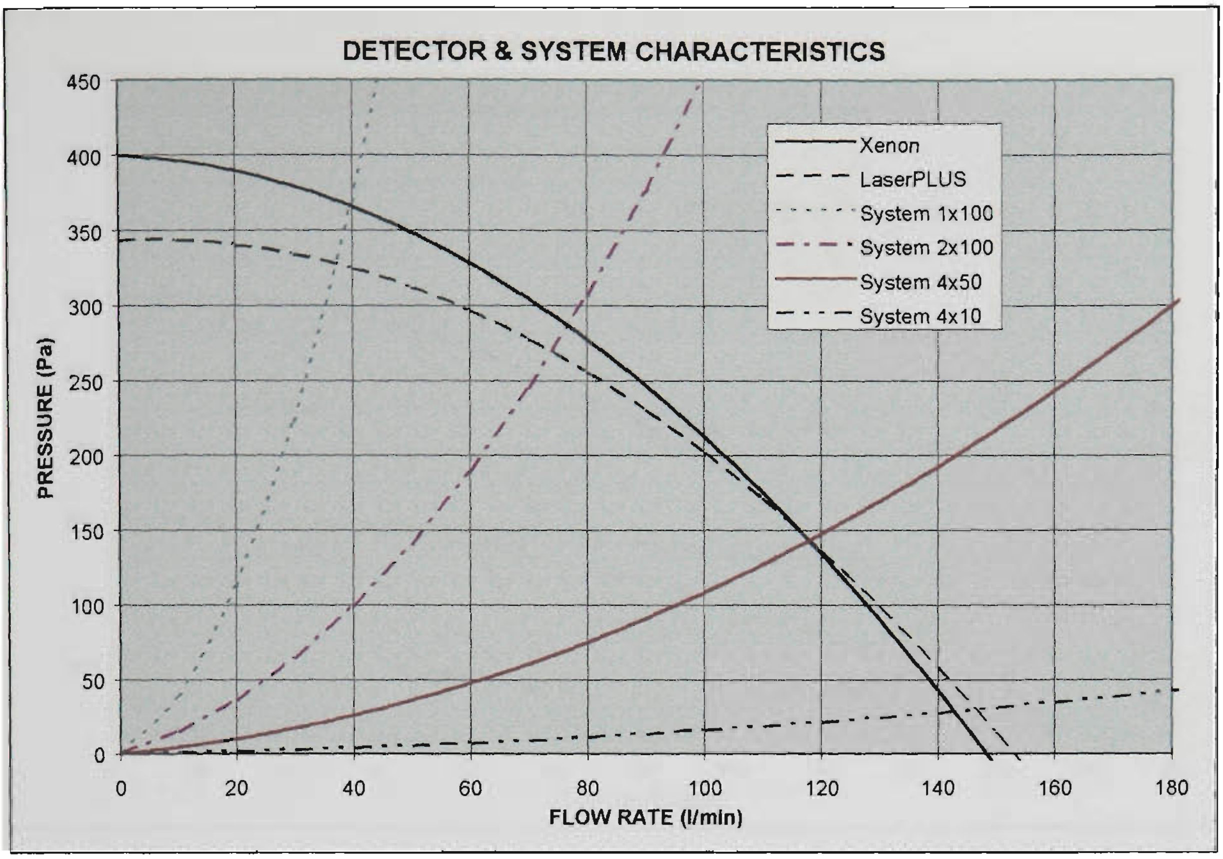

Figure 2.23 - Aspirated system operation at Boosted setting

Assume that four pipes of $50m$ length would be the preferred configuration for the largest practical system. Based upon the characteristic equation for this system, it is possible to determine the setting for a constant-voltage aspirator or a constant-speed aspirator, whereby the system operation is identical for either aspirator. This is used in Figures 2.21 to 2.23 and tabulated below, where the settings refer to the cutoff pressure:

	E	N	B
Constant-voltage pressure setting	200	300	400
Constant-speed pressure setting	165	254	343

Table 2.1 - Settings for equivalent performance

To obtain adequate coverage of large areas, it is sometimes necessary to employ additional aspirators. For highly restrictive, low flow systems such as long pipes with few sampling holes, it is possible to employ two or three aspirators in series. For low restriction, high flow systems such as multiple pipes with many sampling holes, it is possible to employ two or three aspirators in parallel. Large systems in typical configurations could benefit from a series/parallel arrangement of four aspirators.

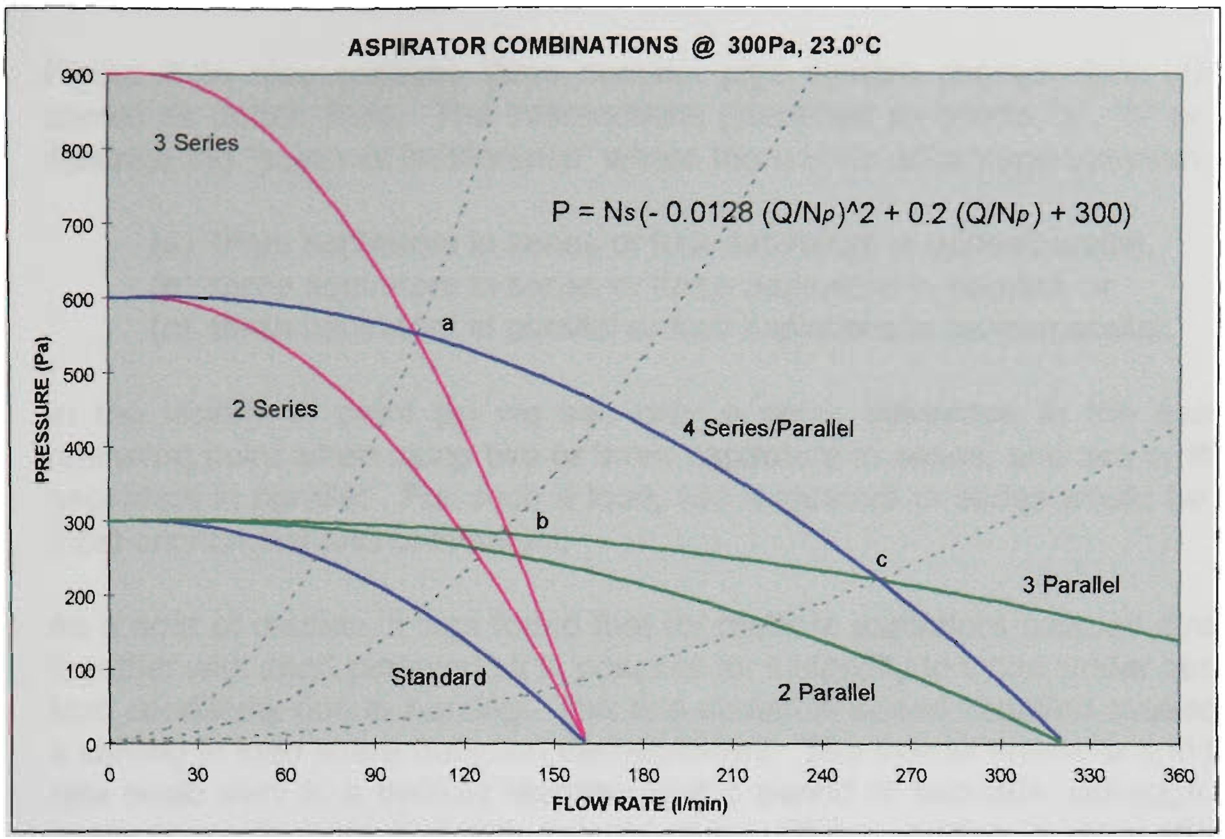

Figure 2.24 - Multiple aspirator combinations

Series, parallel and series/parallel combinations of aspirators were measured with results as shown in Figure 2.24 (which relate to the constant-voltage version). It was established that for two aspirators in **series**, it is appropriate to double the value of P_{max} in the characteristic equation to obtain the system pressure. Such a simple result was not entirely expected because there was a concern about leakage and the level of turbulence in the air delivery from one aspirator to the next.

It was established that for two aspirators in **parallel**, it is appropriate to apply the characteristic equation at half the value of the system flow rate, Q_{system}. Again it had been mistakenly feared that coupling losses and imperfect sharing of the flow would be likely to reduce this figure.

For four aspirators in **series/parallel**, it proved appropriate to apply the characteristic with double the value for P_{max} and half the value for Q_{system}. Accordingly in general terms:

$$P_{system} = N_s \left[K_2 \left(\frac{Q_{system}}{N_p} \right)^2 + K_1 \left(\frac{Q_{system}}{N_p} \right) + P_{max} \right]$$

where N_p is the number of aspirators in parallel (1, 2 or 3) and N_s is the number of aspirators in series (1, 2 or 3). K_2 is the squared-term coefficient and K_1 is the linear term coefficient, both determined experimentally.

Figure 2.24 also contains three nominal pipe system characteristic curves shown as dotted lines. The intersections (identified as points "a", "b" or "c") illustrate the "points of indifference" where there is no advantage between:

(a) three aspirators in series or four aspirators in series/parallel,
(b) three aspirators in series or three aspirators in parallel, or
(c) three aspirators in parallel or four aspirators in series/parallel.

In the vicinity of point (b) we see only a small difference in the system operating point when using two or three aspirators in series, and two or three aspirators in parallel. For such a load, two aspirators in series would be the most economical and convenient.

As a note of caution, it was found that for multiple aspirators coupled directly together with short pipework, it is possible for instability to occur under certain load conditions due to hunting. This is a continual speed variation caused by a shifting in load share between the aspirators. The overall pressure and flow rate could vary in a cyclical manner over a period of seconds, although the average results complied with the above equation. Hunting is reduced with constant-speed aspirators, depending upon the transient response time of the speed controller.

To facilitate comparison of the operation of the complete detector packages offered by the various manufacturers when attached to any given pipe system, the characteristic equations for the aspirator, detector chamber, dust filter, manifold and exhaust have been combined to provide the performance of the overall package in each case. These are presented in Figure 2.25 with reference to a typical pipe system load (solid, rising curve) representing two pipes of $100m$ length.

Included in Figure 2.25 is the characteristic for a VESDA LaserPLUS package in which the inlet manifold has been modified for increased efficiency. This modification involves reshaping of the plenum area in such a manner as to reduce the contained volume and assist the change in flow direction, thereby to minimise eddies and reduce losses due to deceleration and acceleration of the airstream.

The VESDA Mk3, Stratos and Hart/Analaser aspirators are shown operating at their maximum settings, while the VESDA LaserPLUS is shown operating at a particular setting which is below its maximum speed, that would provide equivalent performance to the VESDA Mk3 for the given pipe system.

Figure 2.26 provides a comparison of output power from each of the detector packages. The most efficient operation occurs within a region near the peak of these curves and the principles of good system design would always attempt to "match the pump and load" within this region.

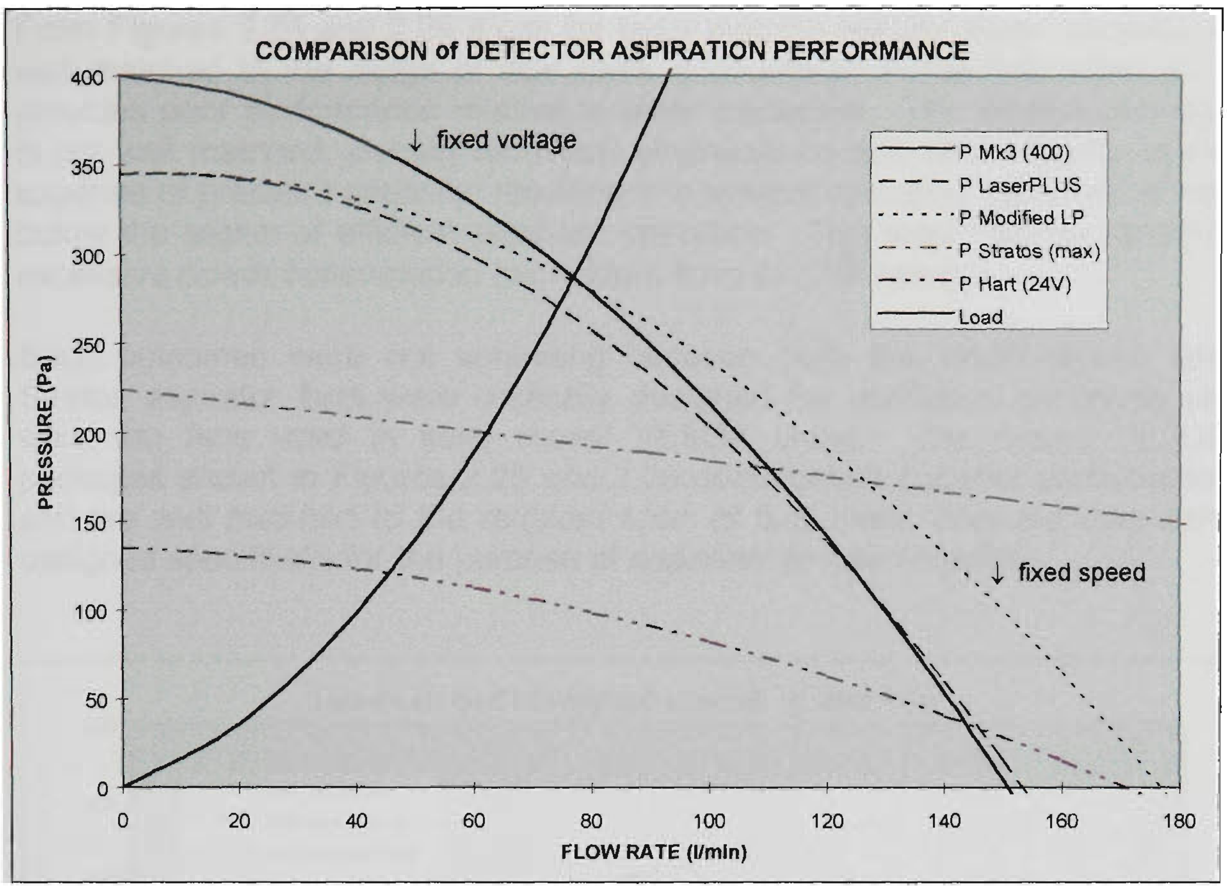

Figure 2.25 - Comparison of detector aspiration performance

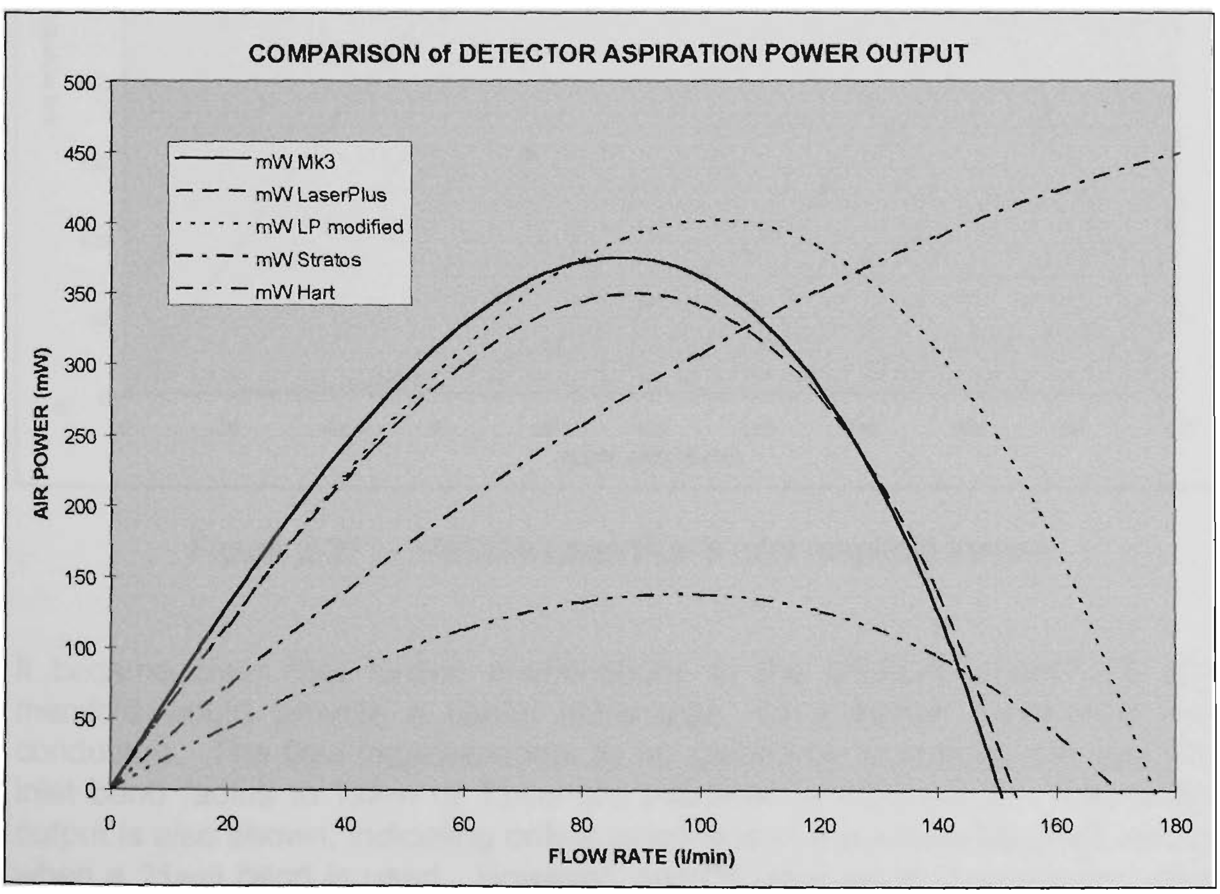

Figure 2.26 - Comparison of detector aspiration power output

From Figures 2.25 and 2.26 it can be seen that the Hart/Analaser package is well matched to the range of flow rates encountered in the field although it provides poor performance relative to other packages. The Stratos package is not well matched, placing too much emphasis on flow rate capacity at the expense of pressure capacity, resulting in a system operating span that is well below the region of efficient aspirator operation. This would further result in excessive power consumption (as evident from its 12W rating).

Such outcomes were not surprising because both the Hart/Analaser and Stratos aspirator fans were originally designed for ventilation purposes (as were the fans used in early model VESDA units). The recent VESDA packages shown in Figures 2.25 and 2.26 demonstrate superior performance and are well matched to the required span of flow rates, because they were designed specifically for the purpose of aspirated smoke detection.

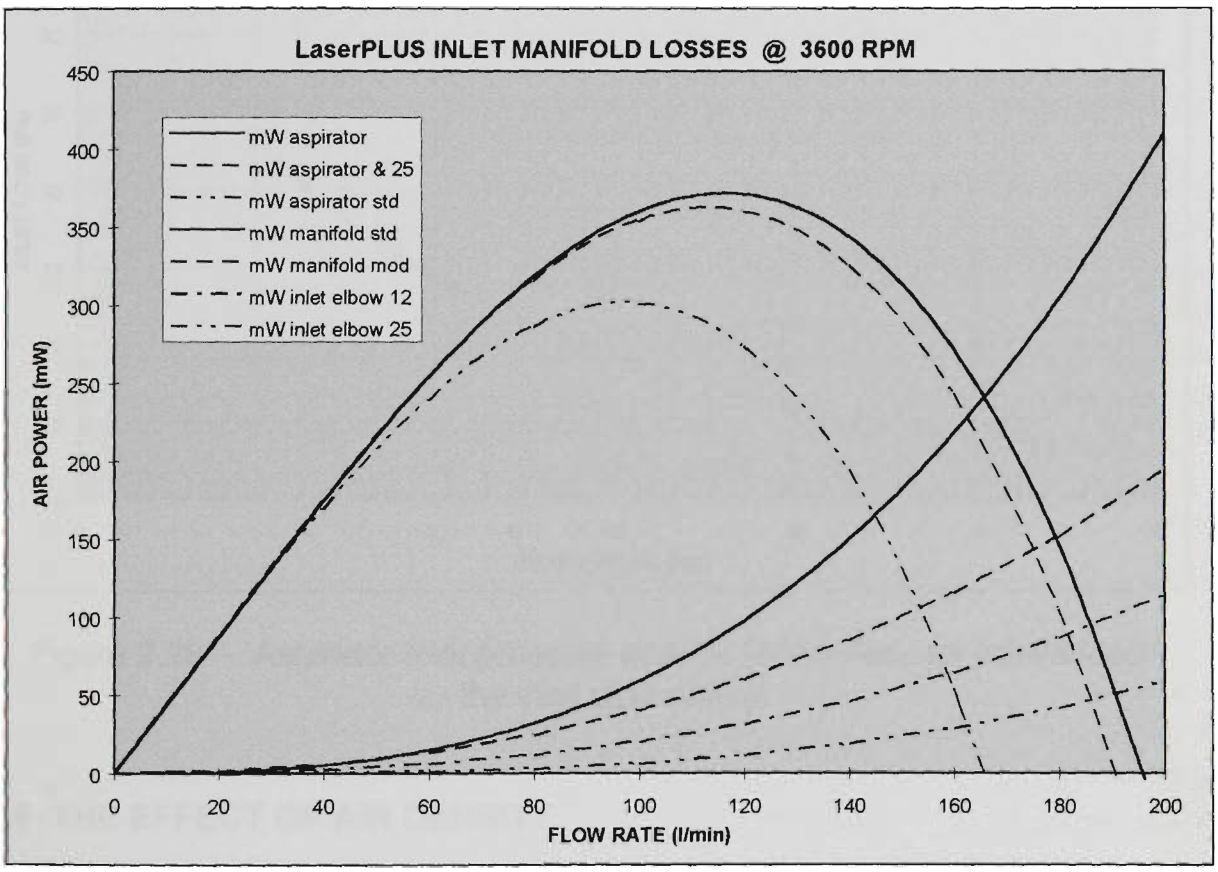

Figure 2.27 - VESDA LaserPLUS inlet manifold losses

It became clear that further modifications to the VESDA LaserPLUS inlet manifold would provide a useful advantage, so a further experiment was conducted. The flow improvements to be gained by increasing the aspirator inlet bend radius to $12mm$ or $25mm$ are indicated in Figure 2.27. The power output is also shown, indicating only a small loss in the attainable performance when a $25mm$ bend is used. However, such a large bend is precluded within the low-profile size of the detector package, so the inlet manifold loss at high flow rates must be overcome with increased motor speed. In the interests of efficiency, in the longer term it would be appropriate to design a flat motor configuration to save space within the detector package, thereby enabling a larger inlet bend radius for the aspirator.

Figure 2.28 presents the pressure drop as a function of inlet radius at a flow rate of $100 litre/min$, the shape of which is representative of the full range of flow rates used with aspirated smoke detection. This shows that the inlet radius should ideally be greater than $20mm$, and that the loss rises sharply for radii less than $10mm$. Where packaging constraints preclude the use of larger radii, the aspirator is required to operate at a higher speed to compensate.

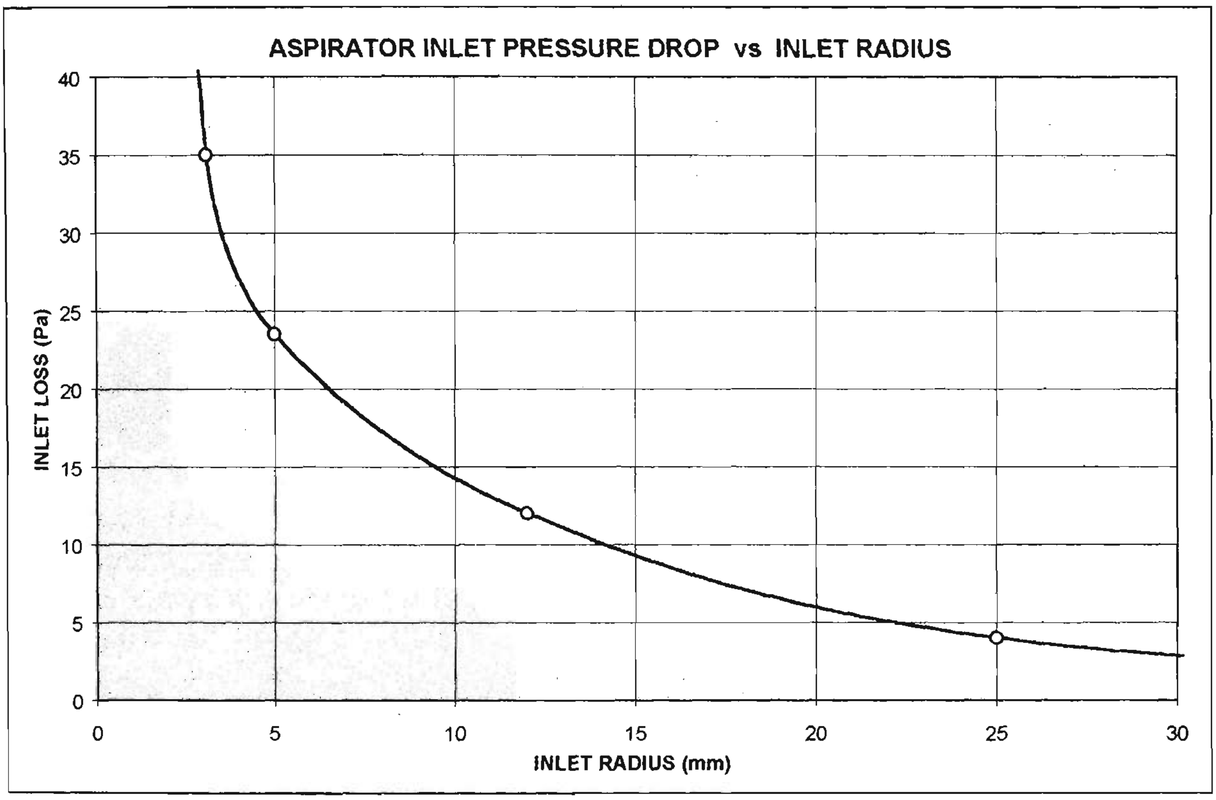

Figure 2.28 - Aspirator inlet pressure drop at $100 litre/min$ as determined by the inlet pipe radius

2.6 THE EFFECT OF AIR DENSITY

The characteristics of passive system components are directly affected by the air density in a known manner. In the case of an active system component (the aspirator), this does not necessarily apply because this is the one component that imparts energy to the system. The net theoretical head (H_{th}) assuming no pre-rotation of the air stream may be obtained from Euler's equation (Stepanoff, 1957 p35):

$$H_{th} = \frac{u_2}{g}\left(u_2 - u_r \cot(\beta_2)\right)$$

where u_2 is the tangential velocity at the impeller periphery, u_r is the radial velocity component of the air flow, β_2 is the impeller outlet angle and g is the acceleration due to gravity. The VESDA aspirator impellers have been designed with radial-tipped blades, so the theoretical total pressure becomes:

$$P_{th} = \rho u_2^2$$

where ρ is the air density. The operating pressure is obtained by taking account of the slip factor (determined by the number of blades), the pitch loss (determined by the blade inlet angle), and the mechanical losses (bearing friction loss and shroud windage). Detailed discussion of these losses is not warranted here, but the interested reader is referred to Cole (1991 Chapter 5). The important point is that for a constant-speed aspirator as used in VESDA LaserPLUS, the pressure developed is proportional to the air density, as indicated below:

$$P_{\max} = K_{asp} \rho u_2^2$$

where K_{asp} is an aspirator coefficient. However, the situation of the constant-voltage aspirator as used in Xenon VESDA Mk3 is quite different, despite having the same physical construction. Depending on the motor torque-speed characteristic and the power supply regulation, as the air density reduces, the impeller loading reduces and the aspirator speed increases. This tends to compensate for the reduced air density. Obviously the opposite occurs as the air density increases, which is again partly compensated for. Accordingly, the aspirator pressure (and the system operating point) will be affected by a change in ambient pressure and/or temperature in a relatively complex manner.

An experiment was conducted using a temperature-controlled chamber at Victoria University of Technology, as a means for inducing a range of air densities. At an elevation of $100ft$, the ambient pressure on the day of the test was $1012millibar$. An aspirator was placed in the chamber, coupled to the test pipe with four-port pressure tap as described in Figure 2.1, together with the same set of seven standard orifices.

By adjustment of the power supply, the setting of the aspirator was fixed at 300Pa at 23°C, being the temperature at which most of the other experiments had been conducted, and being the single most common temperature at which aspirated smoke detection systems are operated. The chamber was operated at -10 to +60 °C in steps of 10°C. At each set temperature, each orifice was attached in turn. After allowing the temperature to stabilise, the pressure developed across the aspirator in each case was measured using a Furness FC012 manometer. Readings below 0°C had to be taken with special care because of a tendency for icing, caused by the humid air entering the chamber each time an orifice was changed. Attempts to take readings at -20°C were abandoned for this reason.

At first, the eight sets of data were plotted together but it was found that the small spread in readings produced a series of graphs that were so closely-matching across the range of flow rates (each separated by a $\approx 1\%$ vertical offset) that they became too cluttered for useful presentation here. However, the maximum operating pressure in each case was reliably determined by inspection of the sets of data. Figure 2.29 presents the results obtained for the maximum aspirator pressure versus temperature. It can be seen that the trend of this data follows a curve that is almost straight (drawn as solid) represented by the following equation, and that all of the data lie within $\pm 0.5\%$ of this curve (dotted):

$$P_{aspV} = P_{23} \left(\rho / \rho_{23}\right)^{0.32}$$

where P_{23} is the reference maximum pressure developed at 23°C and 1012*millibar* (in this case $\rho_{23} = 1.190$). In practice this equation can be used to adjust, not only the maximum pressure, but also the pressure developed at any selected flow rate throughout the aspirator range.

Also included in Figure 2.29 is a curve (dashed) representing a constant-speed aspirator according to Euler's equation, adjusted to coincide with the constant-voltage aspirator at 23°C. Assuming ideal gas behavior, an equation representing the constant-speed aspirator adjustment is:

$$P_{aspS} = P_{23} \left(\rho / \rho_{23}\right)$$

It is evident from the graphs and the equations that the compensatory effect of the constant-voltage aspirator is highly significant, having a gradient one-third that of the constant-speed aspirator. Across the specified operating range of -20 to +60 °C, the constant-voltage aspirator would range from 314 to 289 Pa (a span of 25Pa or 8%) whereas the constant-speed aspirator would range from 351 to 267 Pa (a span of 84Pa or 28%).

However, it should be noted that in the field, the "higher stability" of the constant-voltage aspirator may or may not be an advantage. Whereas this aspirator could provide system performance that is largely independent of ambient conditions, this very compensation mechanism could also render it relatively difficult to detect small changes in system flow rate (using an anemometer within the detector package) caused by pipe leakage or hole blockage (should either unlikely event occur). To some extent this detectability would depend upon the pipe system configuration (the operation of which is also affected by air density), so the possibility should be examined in relation to each site using the system modelling software.

Figure 2.30 presents data similar to Figure 2.29 except that the aspirator pressure appears as a function of air density, so the gradients reverse. The same equations apply to both figures because they are expressed in terms of density and the experiment was conducted at a fixed ambient pressure.

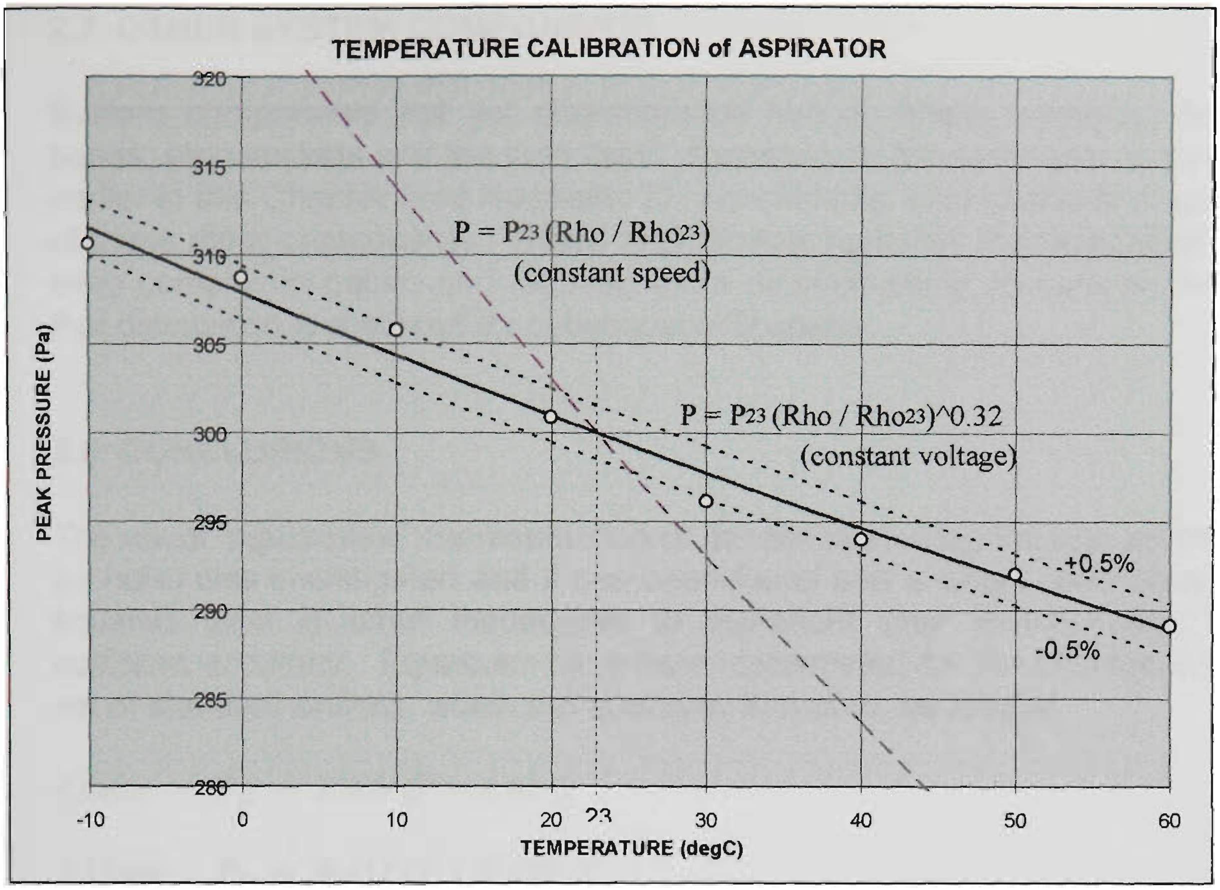

Figure 2.29 - Effect of air temperature on aspirator pressure at a fixed ambient pressure ($1012 millibar$)

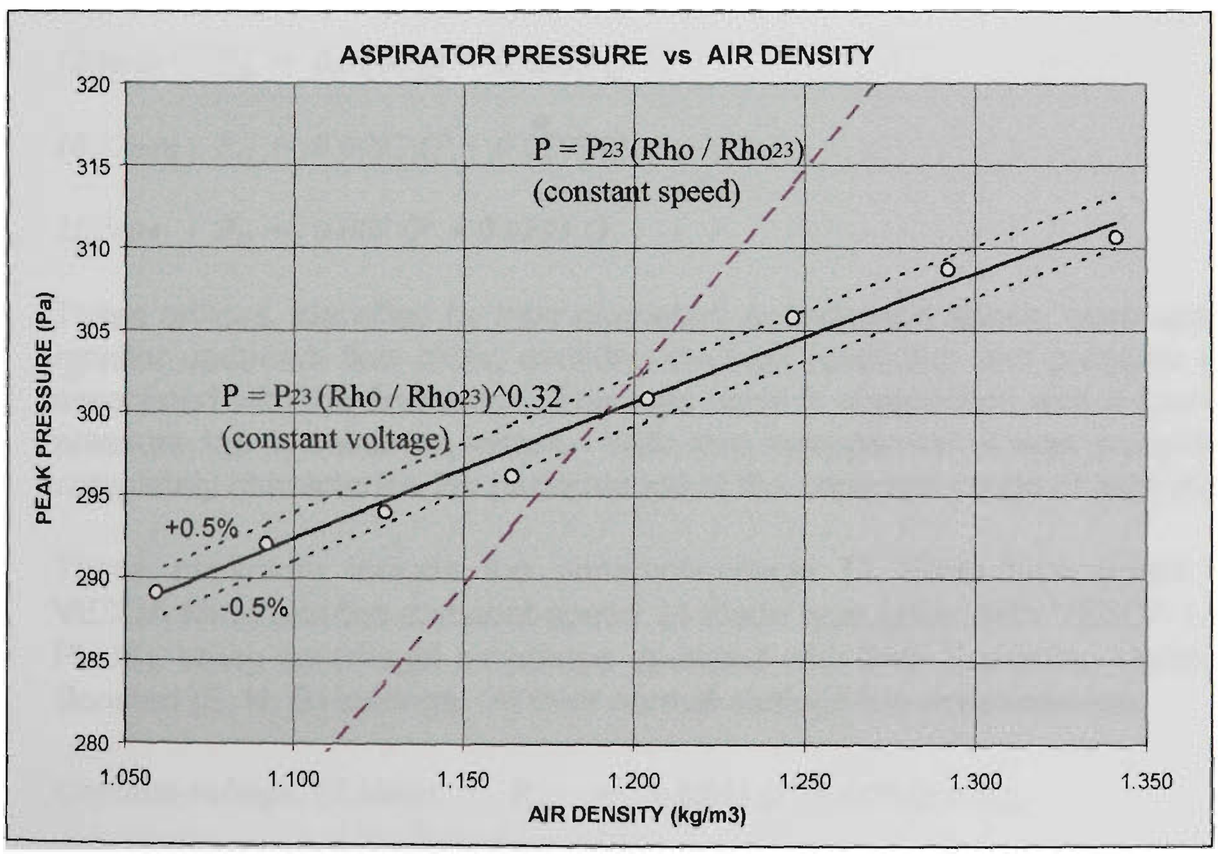

Figure 2.30 - Effect of air density on aspirator pressure

2.7 OTHER SYSTEM COMPONENTS

System components not yet characterised include filters, sampling holes, bends, pipe sockets and the pipe itself. Based upon the technique described earlier in this Chapter (and Appendix 2), experiments were conducted with all of these other components. These experiments revealed characteristics that were complex in nature and required more detailed study, to such an extent that discussion is reserved for subsequent Chapters.

2.8 CONCLUSIONS

The usual "square-law" representation of the pressure drop through an orifice (or hole) was investigated and it has been found that a single coefficient and squared term is often inadequate to represent their characteristic with sufficient accuracy. Equations have been determined for the calibration of a set of standard orifices, which are quadratic in nature, as follows:

4.0mm $P_O = 1.309\,Q^2 + 4.61\,Q$

5.31mm $P_O = 0.652\,Q^2 + 0.039\,Q$

7.37mm $P_O = 0.186\,Q^2 + 0.142\,Q$

10.36mm $P_O = 0.0404\,Q^2 + 0.0849\,Q$

12.9mm $P_O = 0.0166\,Q^2 + 0.0583\,Q$

16.37mm $P_O = 0.0052\,Q^2 + 0.0299\,Q$

21.2mm $P_O = 0.002\,Q^2 + 0.0295\,Q$

These orifices, identified by their diameters as indicated above, were used to monitor upstream flow rates, avoiding the high restriction and pressure drop associated with the flowmeter. This was done in conjunction with a four-port pressure tap to minimise errors. With this arrangement it was possible to completely characterise the performance of the complete range of aspirators.

These aspirators include the constant-voltage 12 blade type (used with VESDA Mk3) and the constant-speed 24 blade type (used with VESDA Laser PLUS), being centrifugal air pumps operated with their Economy, Normal or Boosted (E, N, B) settings. At their normal settings the equations are:

Constant-voltage, 12 blade: $P_{asp} = -\,0.011\,Q^2 + 0.05\,Q + P_{\max}$

Constant-speed, 24 blade: $P_{asp} = -\,0.0095\,Q^2 + 0.57\,Q + P_{\max}$

where the cutoff pressure P_{max} is used to define the "aspirator setting", being 300Pa in the former case and 246Pa in the latter. To characterise their operation at other settings, in the case of the constant-voltage aspirator a small adjustment to the cutoff pressure constant is required:

$$P_{\max,c} = -2.5E{-}04\, P_{\max}^2 + 1.105\, P_{\max} - 9$$

In the constant-speed case it proved necessary to adjust the linear term ($Term1$) without adjusting the other terms:

$$Term1 = 1.55E{-}06\, P_{\max}^2 + 6.7E{-}04\, P_{\max} + 0.3113$$

Because it was proposed that the constant-speed aspirator could be set in terms of speed (S_{asp}) as well as cutoff pressure, the following alternative equations were obtained for use in the computer model:

$$P_{\max} = +2.06E{-}05\, S_{asp}^2 - 0.0078\, S_{asp} + 5$$

$$S_{asp} = -0.0073\, P_{\max}^2 + 11\, P_{\max} + 1350$$

The equations to other aspirators that were characterised for use in the computer model are as follows, three of which do not operate from internally regulated power supplies so their performance at 24V DC is shown:

VESDA Mk2	$P_{asp} = -0.0025\, Q^2 - 0.353\, Q + 118$	*at 24V DC*
MiniVESDA	$P_{asp} = -0.0003\, Q^2 - 0.138\, Q + 48$	*at 24V DC*
Hart/Analaser	$P_{asp} = -0.0037\, Q^2 + 0.157\, Q + 135$	*at 24V DC*
Stratos	$P_{asp} = +0.0002\, Q^2 - 0.38\, Q + P_{\max}$	

Next, the detector chambers were characterised. In the case of the Xenon-type VESDA Mk2 and Mk3, the entire system flow passes through the detector chamber which has the following characteristic:

Xenon VESDA Mk2 / 3 $\quad \Delta P_{chmb} = 0.0029\, Q^2 - 0.023\, Q$

In the case of VESDA LaserPLUS, only a small proportion of the total system flow passes through the detector chamber. This chamber with its inline dust filter has high restriction and is connected across the aspirator to provide maximum pressure differential, thereby producing a mild short-circuit flow. The chamber is characterised by the nett effect it has on the aspirator performance. In addition, this product provides a choice of exhaust ports and there is an inline four-port inlet manifold. An opportunity for significant improvement in the efficiency of this manifold was identified. The equations for each of these individual components are:

VLP Detector chamber	$\Delta P_{chmb} = 0.06\,Q$
VLP Back Exhaust	$\Delta P_{back} = 0.0026\,Q^2 + 0.01\,Q$
VLP Side Exhaust	$\Delta P_{side} = 0.0035\,Q^2 + 0.01\,Q$
VLP Bottom Exhaust	$\Delta P_{botm} = 0.0045\,Q^2 + 0.11\,Q$
VLP Manifold (std)	$\Delta P_{man} = 0.0035\,Q^2$
VLP Manifold (mod)	$\Delta P_{\mathrm{mod}} = 0.0015\,Q^2 + 0.12\,Q$

In the case of the Hart/Analaser detector, the entire system flow passes through the detector chamber but this restriction is included in the aspirator characteristic shown earlier. In the Stratos detector, part of the system flow is diverted past the detector chamber but once again, this feature is included within the aspirator characteristic shown earlier.

The operation of the complete detector package within an aspirated system was considered for all products.

In the case of VESDA Mk3 and VESDA LaserPLUS it was determined that for these two aspirators to provide equivalent performance with a standard pipe system configuration (four pipes of $50m$ length), then the cutoff pressure settings should be as follows:

	E	N	B
Constant-voltage pressure setting	200	300	400
Constant-speed pressure setting	165	254	343

For operating these aspirators in series, parallel or series-parallel combinations to provide rapid smoke transport times in vary large systems, the following equation was determined:

$$P_{system} = N_s \left[K_2 \left(\frac{Q_{system}}{N_p} \right)^2 + K_1 \left(\frac{Q_{system}}{N_p} \right) + P_{\max} \right]$$

where N_s is the number of aspirators in series, N_p is the number in parallel, and where K_2 and K_1 are coefficients peculiar to the given aspirator model.

The various brands of aspirator fan were evaluated in relation to their relative matching to a wide range of system load requirements. The Hart/Analaser package is well matched to the range of flow rates encountered in the field although it provides poor performance relative to other packages. The Stratos package is not well matched, placing too much emphasis on flow rate capacity at the expense of pressure capacity, resulting in a system operating span that is well below the region of efficient aspirator operation. This would further result in excessive power consumption. The two VESDA packages provide the best performance and both are well matched to the required span of flow rates and pressures.

The effect of air density change (caused by ambient temperature and pressure) has been determined theoretically and experimentally. In the case of the constant-speed aspirator, the pressure it develops is directly proportional to the air density, causing a 28% reduction across the specified temperature range of -20 to +60 °C:

$$P_{aspS} = P_{23} \left(\rho \,/\, \rho_{23}\right)$$

The constant-voltage aspirator tends significantly to compensate for changes in air density by altering its speed, causing only an 8% reduction across the same temperature range:

$$P_{aspV} = P_{23} \left(\rho \,/\, \rho_{23}\right)^{0.32}$$

Whereas the constant-voltage aspirator offers the advantage of more-stable system operation, its self-compensation may tend to mask the effects of minor pipe leakage or hole blockage which are monitored-for using an anemometer built into the detector package. Because the rest of the aspirated pipe system operation is also affected by air density, the overall effect can best be considered by application of system modelling software.

CHAPTER 3 - DUST FILTER CHARACTERISATION

3.0 INTRODUCTION

It will be seen that the type of dust filter selected has a significant bearing on the performance of the aspirated system. In some situations, as much as half of the available energy (pressure drop) can be developed across the filter, directly impacting upon the smoke transport time. This changes with filter loading. Accordingly it is important to understand the need for a dust filter and the factors affecting selection or design of the particular type used. In this chapter, a new concept in filter design is developed and experimental results are presented to characterise various types of dust filters.

3.1 THE NEED FOR DUST FILTERS

Dust filters have proven necessary in most aspirated smoke detection sites, to avoid two distinct problems:

- False alarms caused by airborne dust which could be mistaken by the detector for smoke.
- Shortened service interval or reduced sensitivity to smoke due to soiling of the detector internal (optical) components.

Whereas it is possible with sophisticated detection techniques to achieve some degree of discrimination between smoke particles and dust particles based on size, and with good design it is possible to minimise the rate of soiling on detector components that are sensitive, these do not completely eliminate the need for dust filtration.

To consider the role of filters in more detail, it is necessary to understand the nature of the environment that is being monitored. Measurements of particulate mass concentrations have been conducted in cities, with typical results presented in Figure 3.1 (Shaw, 1987).

Here we see the two-humped curve that is apparently common to most cities, and is responsible for visible pollution. Atmospheric smoke particles are generally in the range of 0.01 to 1 μm diameter, generated by automobiles, factories, incinerators and sometimes by forest fires. Atmospheric dust particles are generally in the range of 1 to 100 μm and are generated by construction sites, traffic movement and by wind erosion of pastures. Dust particles can be even larger (as large as sand grains) but these tend not to remain suspended in the air except during a wind storm.

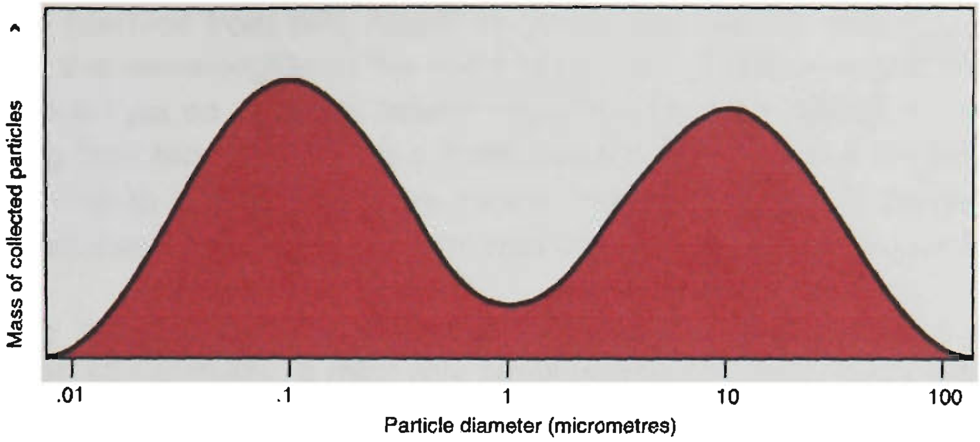

Figure 3.1 - Airborne particle mass distribution in cities (Shaw, 1987)

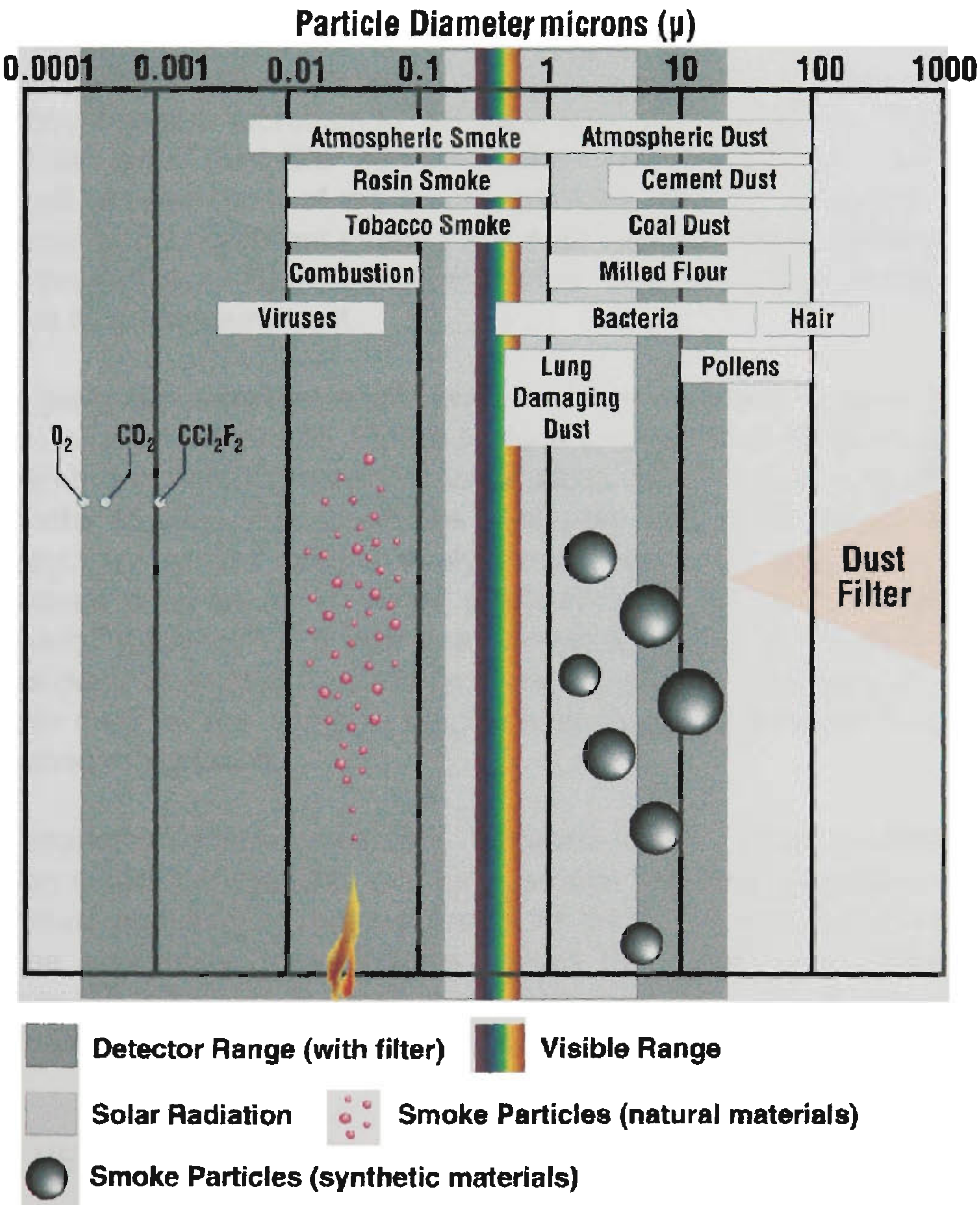

Figure 3.2 - The range of airborne particle sizes (from SRI, 1968)

Figure 3.2 (derived from SRI, 1968) illustrates the relative size of particles in relation to the wavelengths in the solar spectrum. Visible wavelengths range from 0.4 to 0.7 μm so particles smaller than this become difficult to see. Very hot flaming fires tend to produce a huge quantity of very small particles, in the vicinity of 0.05 to 0.5 μm which are mostly invisible. Many of these particles may coalesce or agglomerate to form much larger, visible sizes (soot).

Pyrolysing and smoldering materials lack the heat energy for complete combustion so generally, a relatively small number of relatively large particles (or aerosol droplets) are produced, in the region of 1 to 5 μm or even larger. It is these large particles that must be detected if potential fires are to be announced well in advance of the flaming stage.

To discriminate between small dust particles and large smoke particles which are of comparable size, is therefore a difficult task. Moreover, it has been found in practice that as membrane type filters become partially loaded with dust, they become increasingly efficient at trapping particles of decreasing size. This type of dust filter can eventually become loaded to such an extent that it will remove most of the smoke particles from the airstream. And yet there may be no significant change to the air flow restriction, making detection of an over-efficient filter difficult to detect with the usual anemometry or pressure drop measurement.

Filters generally comprise a thin membrane of cellulose or synthetic fibres, which is pleated to contain a large surface area within a small housing. This thin membrane must complete its work within its small active depth, which is in the order of $1mm$. This requires a small pore size, which would quickly load and begin to remove progressively smaller particles including smoke. In applications such as air or water purification for human consumption, this increasing “efficiency” of a filter is an advantage. The air or water becomes progressively cleaner until such time as the filter loading causes too much pressure drop for the pump to efficiently manage, whereupon the filter must be cleaned or replaced.

With aspirated smoke detection, because of the minor overlap in size between small dust particles and large smoke particles, selection of the most appropriate particle size removal profile for the filter is somewhat critical. This must be accurately controlled throughout the service life of the filter, to maintain the optimum separation of dust from air that continues to carry smoke. Therefore a new approach was required.

3.2 A NEW DUST FILTRATION TECHNOLOGY

Various techniques for dust separation were investigated, based upon the principle of momentum. High velocity particles of various sizes, travelling within a common airstream, have momentum in proportion to their mass. By imparting a sudden change in direction to the airstream, the heavier particles have a greater tendency to resist the change in direction, and can thereby be separated from the main flow. A typical example is the cyclone-type dust separator where centrifugal force is used. Another common type is the impactor where large particles are arrested upon impact with a plate.

Numerous prototypes of differing design were evaluated, employing spinners to develop centrifugal force or labyrinths with sudden changes in direction, but it became clear that there was insufficient energy in the airstream to impart sufficient momentum to the particles, to overcome viscosity drag and produce separation. Because the entire smoke detection system was driven by an aspirator imparting only 1W of power to the airstream, the available power for dust separation was less than 0.5W.

One technology that efficiently cleans air in ventilation systems without restricting the airflow, without a tendency for clogging, without high maintenance requirements and without relatively high energy demand is electrostatic precipitation. This is effective in removing dust, but it is even more effective in removing smoke, so this technology could not be employed.

Having exhausted other avenues, membrane filter technology was considered in greater detail. It became clear that filters do not act like a sieve, where all particles smaller than the pore size pass through. In fact a large proportion of these smaller particles are trapped. This is due to a phenomenon called Brownian Motion. In the literature, an understanding of this began with the discovery of small buoyant particles moving rapidly and randomly on the surface of still water, when viewed under a microscope (Brown, 1827). This understanding was subsequently extended to airborne particles.

Einstein has written three papers devoted to Brownian Motion (Methuan & Co trans., 1926). In 1905 he published the following equation for the average linear displacement (X_p) of a small particle within a given time interval (Θ) (Jorgensen, 1961 p7-20):

$$X_p = \left(\frac{4\, R_u\, T\, C_s\, \Theta}{3\, \pi\, \mu\, N_A\, d_p} \right)^{0.5} \quad \textit{where:} \quad C_s = 1 + \frac{1}{3.75\, P\, d_p} \left(6.23 - 201\, e^{\left(-0.821\, P\, d_p\right)} \right)$$

where T is absolute temperature, R_u is the universal gas constant, C_S is the Stokes-Cunningham-Millikan slip-correction factor, μ is the fluid viscosity, N_A is Avogadro's number, d_p is the particle diameter and P is absolute pressure.

Full discussion of this equation and its various terms is not warranted here, but the application of this equation over a time interval of $1sec$ to a range of particle sizes is presented in Figure 3.3 using a log-log scale. Here we see that the displacement varies strongly in inverse proportion to the particle size, ranging from about $260\mu m$ in the case of a $0.01\mu m$ particle, to only $2\mu m$ in the case of a $10\mu m$ particle.

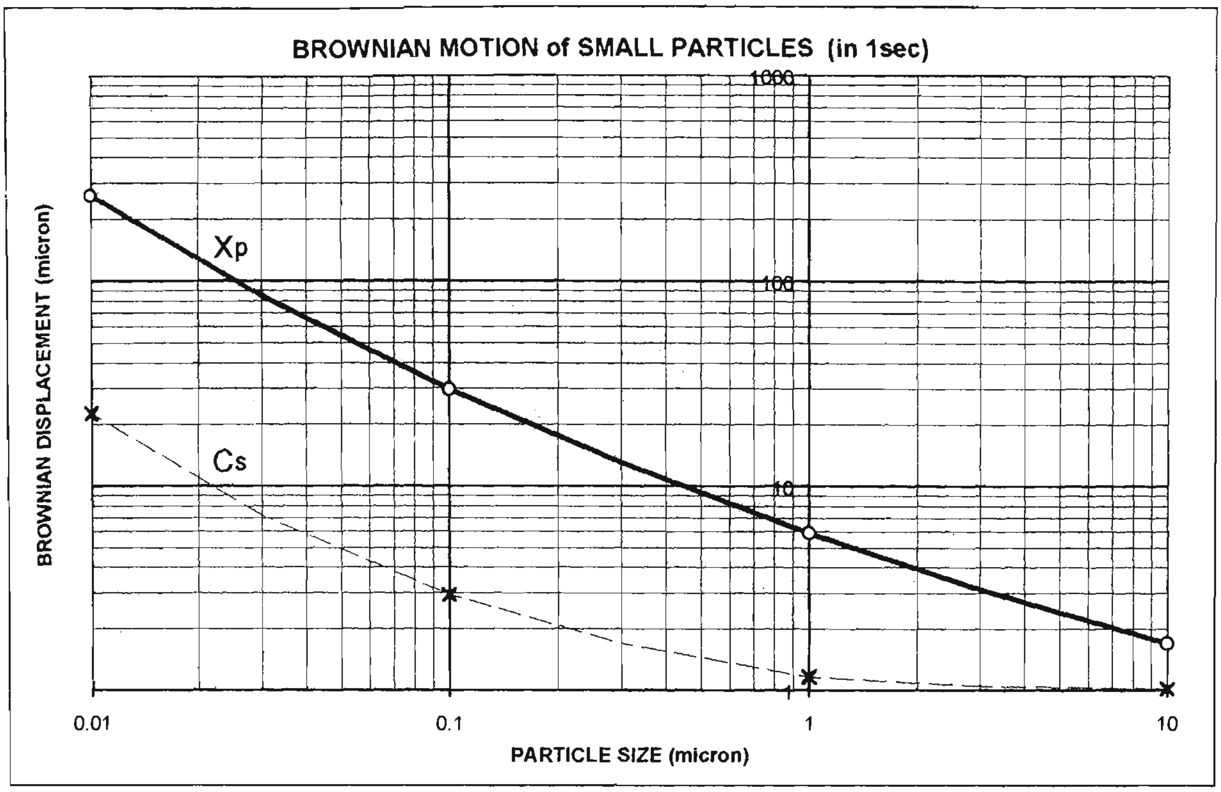

Figure 3.3 - Amplitude of Brownian Motion of particles (data from Jorgensen, 1961)

The significance for current purposes is that small airborne particles can "oscillate" rapidly in a large amplitude compared with their size, apparently due to buffeting by the thermally-induced random motion of air molecules. This motion results in each particle behaving as if it were many times its actual size, so that the "apparent diameter" of the particle is increased to that extent. This is illustrated in Figure 3.4 (based on Paul, 1988). Thus, particles of (say) $0.5\mu m$ diameter could be trapped with a filter pore size of about $5\mu m$.

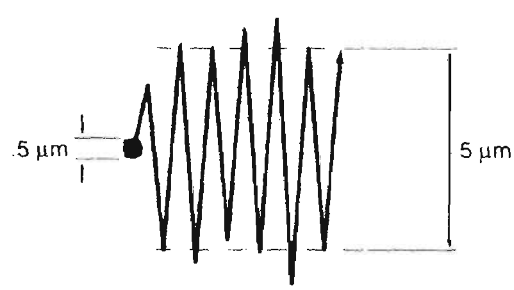

Figure 3.4 - Particle motion in air (Paul, 1988)

This motion is not apparent in liquids such as water, because the viscosity of the fluid is sufficient to dampen the Brownian motion as shown in Figure 3.5 (adapted from Paul, 1988). Therefore in the case of liquids, the filter pore size is closely matched to the size of the particle intended to be removed from the flow. The common perception of filters is based upon experience with liquid filtration, which is often incorrectly assumed relevant to air filtration (this was certainly so in the case of the aspirated smoke detection industry).

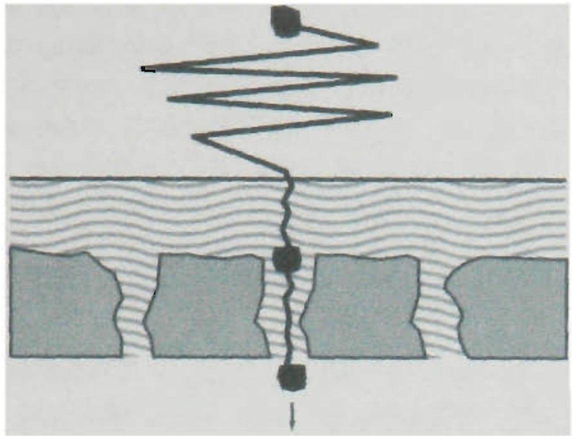

Figure 3.5 - Particle motion in liquid (Paul, 1988)

Figure 3.6 (adapted from Paul, 1988) illustrates at high magnification, the depth of a membrane filter and the mechanism whereby Brownian motion can cause particles, much smaller than the filter pores, to be adsorbed on impact with the filter material (and absorbed by the filter as a whole).

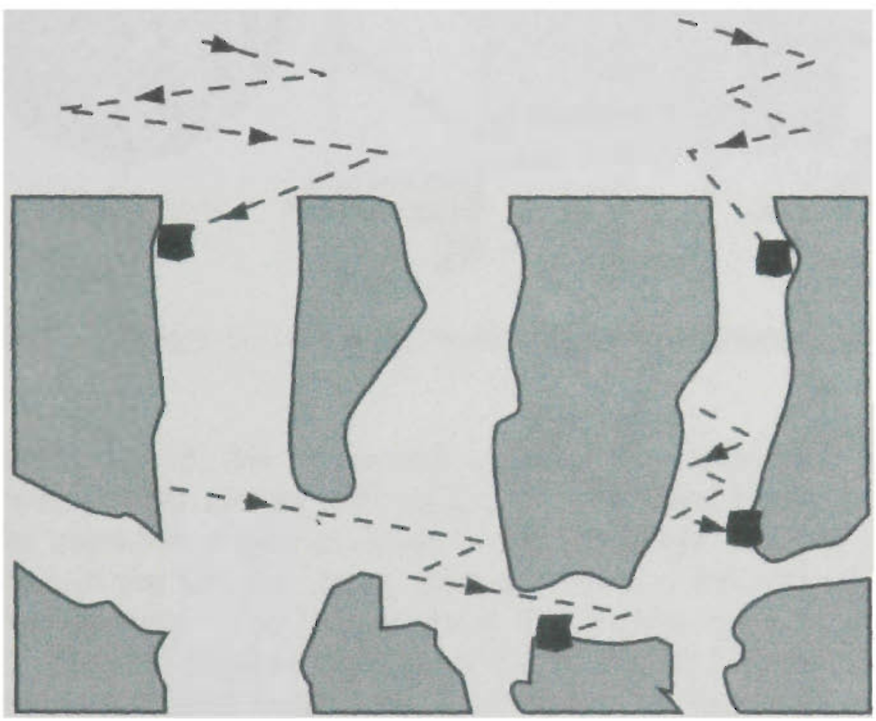

Figure 3.6 - Adsorption of small particles (Paul, 1988)

Accordingly, for dust filtration of air, it became clear that a relatively large pore size could be used effectively. This idea was extended further, to develop a new concept especially for aspirated smoke detection. This technique employs a much thicker (deeper) filter element with an exceptionally large pore size, so that dust particles are progressively removed on a statistical chance basis throughout the large depth.

The material chosen for the depth filter element is composed of open-cell "reticulated" polyester-urethane foam. Whereas the use of this type of foam for dust filtration was known, the concept of carefully-selecting the pore size to maximise the transmission of smoke was new. Using a pore size at least 100 times that of smoke particles, but with a path length equivalent to several hundred pores, Brownian motion is relied upon to arrest dust particles, but with very much less tendency (than a membrane) for dust buildup to reduce the effective pore size and increasingly trap smoke particles over time.

The large pore size results in a greatly reduced pressure drop per unit surface area, such that the surface area can be reduced (from $3000cm^2$ to $50cm^2$), while the filter depth is some 20 to 100 times that of a typical membrane filter.

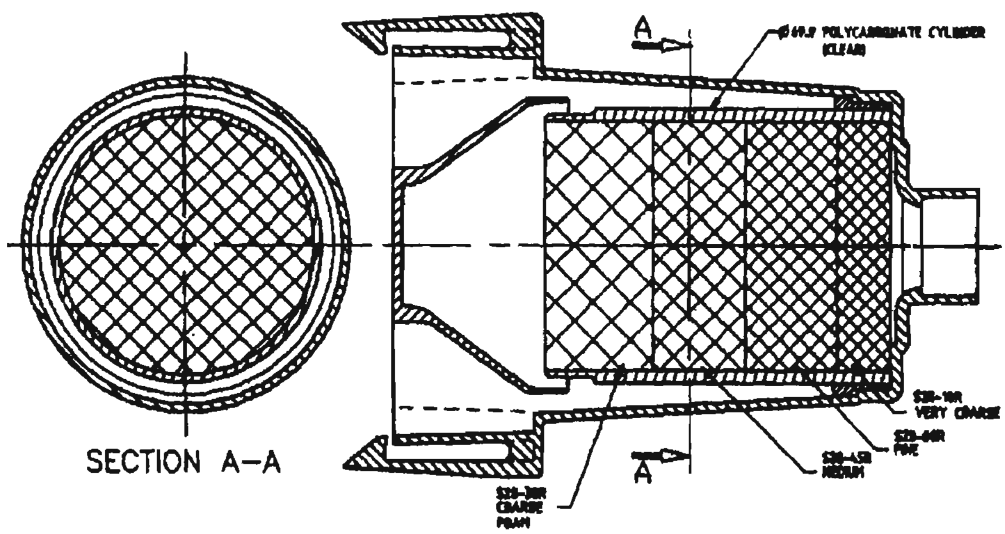

Figure 3.7 - Design of a sleeved, multi-stage filter canister (50% scale)

To increase the service life of the filter canister, it was decided to divide the filter into three or four stages, with reducing pore sizes at each stage. This arrangement traps the largest particles in the first stage, and the not-quite-so-large particles in the second stage, thereby reducing the rate of blockage of the final, fine element. The final element has a pore size at least ten times larger than that of the original membrane, but is at least 20 times deeper. One such arrangement of this removable filter canister is illustrated in Figure 3.7 (drawn sideways). This canister is fitted below a four-port inlet manifold and contains a "spreader cone" to divert heavy debris such as insects to a coaxial side chamber by virtue of their momentum and the force of gravity.

In the final design of the general-purpose depth filter, the sleeve was removed and three filter elements were chosen, being open-cell foam disks of some $80mm$ diameter and $25mm$ depth. The coarse element has an average pore count of 30 per $25mm$, the medium element has 45 and the fine element has 80. Of necessity, the foam filter canister was designed as a compatible replacement for the original pleated-membrane filter canister.

The orientation of the filter canister between the four-port inlet manifold and the VESDA smoke detector is shown in Figure 3.8. The position of the aspirator is also shown. The canister is removable to permit access to the foam filter disks, which can be cleaned by washing in soapy water. Note that filter life could be further extended by bypassing much of the total flow past the filter and detector (as will be explained in Section 3.6), but this proved inconvenient to the four-port manifold design.

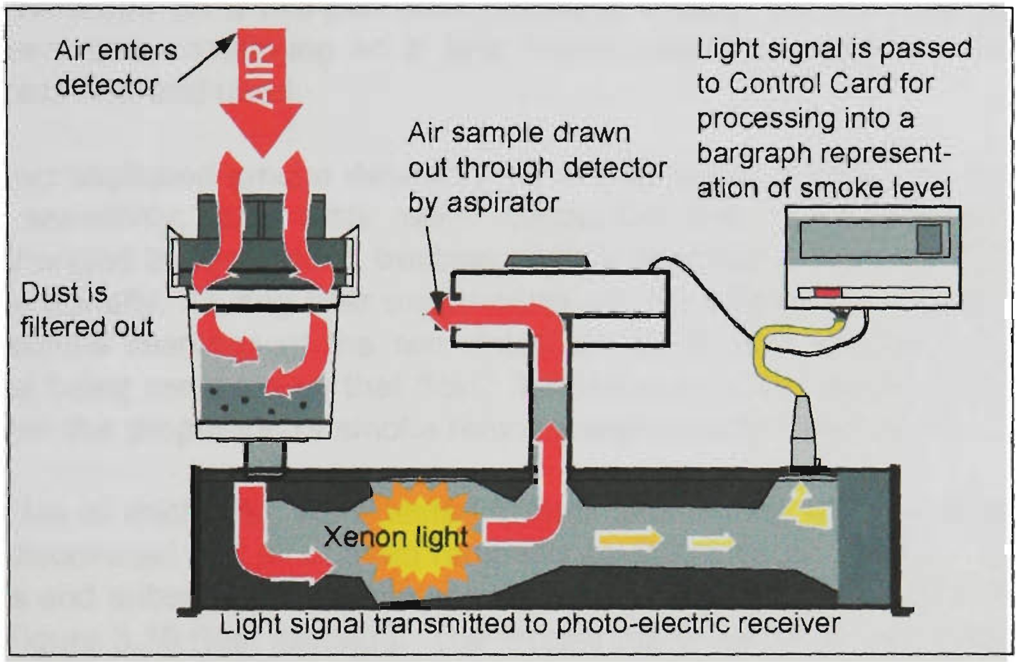

Figure 3.8 - Position of filter, detector and aspirator (IEI Pty Ltd, 1992)

3.3 EXPERIMENTAL TECHNIQUE AND RESULTS

It was necessary to evaluate this new foam filter design comprehensively, along with similar designs using elements of differing pore size. These designs would differ in both filtration efficiency and pressure-drop characteristic. Whereas the most reliable testing involves extensive field trials in many different environments, this would require a program duration measured in years. Commercial issues demanded that an accelerated life testing program be developed to produce results within weeks, with a view to rapid adoption of the new filter design in the field. Experiments were conducted at the premises of Vertec Pty Ltd assisted by Mr Hans Verzijl.

Three types of membrane filter that had been used in the field in large numbers, were used for benchmark comparison - the P1 and P7 from GUD (Victoria), and the type G from Vokes (England). Two types of smoke test in common use for the evaluation of smoke detection systems were the "hot wire test" (a $1m$ length of PVC sheathed wire heated by electric current) and a commercially-available smoke detector test aerosol spray (a pressure-pack can of synthetic smoke aerosol). These were considered most appropriate for the purposes of filter experiments.

The experimental setup comprised a smoke chamber of $2m^3$ internal volume into which the "PVC" or "TEST" smoke was introduced. The smoke within the chamber was kept agitated by a small fan to minimise settling-out. Smoky air from this chamber was passed through a first aspirated smoke detector, then through the filter under test, then through a second aspirated smoke detector, and then through an aspirator which recycled the smoky air back to the chamber. A vent was provided in the chamber to allow the smoke density to slowly dilute, over a period of some $30min$. The smoke detector readings were recorded on a two-pen chart recorder initially, but the data conversion was very time-consuming so in later experiments, an electronic data logger was obtained and used.

The two aspirated smoke detectors were calibrated to verify the matching of their sensitivity, and tests were conducted with the detector positions interchanged to verify good tracking of their readings across the full range of smoke density. During filter experiments, as the smoke level slowly reduced, the relative readings of the two detectors would indicate the proportion of smoke being removed by that filter. The linearity of the result would indicate whether the proportion of smoke removal was density-dependent.

Samples of each filter were tested in their brand-new, clean condition and it was discovered that all of them removed smoke to some degree. The results of this and subsequent experiments are illustrated in Figure 3.9 (PVC smoke) and Figure 3.10 (test aerosol). The smoke transmission for the clean P7 filter was 75% for the PVC test and 68% for the test aerosol. The figures for the clean P1 filter were 81% and 79% respectively. For the clean type G filter, the figures were 90% in both experiments, whereas the clean foam filter provided the best performance at 94% in both experiments. All of these results proved to be linear across the range (0.01 to 0.10 $\%/m$), i.e. the proportion of smoke removal did not depend upon smoke density.

The significance is, that in the worst case, a perfectly clean membrane filter could reduce the effective sensitivity of a smoke detector alarm threshold from (say) $0.10\%/m$ to $0.15\%/m$ which is unacceptable (note that the higher figure represents lower sensitivity). By contrast, the foam filter could provide an effective sensitivity of $0.106\%/m$ which represents an insignificant loss of sensitivity. However, these results apply only to clean filters.

Next, each filter was to be contaminated with dust. It was recognised as important to contaminate each filter with a comparable quantity of dust and that this quantity should represent a high level of contamination. The surface area of each membrane filter was about $3000cm^2$ so it was decided to use a measured quantity of $3000mm^3$ dust, which would blanket the whole surface.

Arizona Dust which is available for filter experiments in various grades was initially tried, however the results showed poor repeatability and this was abandoned. As an alternative, talcum powder was tried. This powder was analysed using a particle sizer-counter and found to have a suitable size range, mostly within 10 to 20 μm.

To contaminate the filter, $3000 mm^3$ of dust or talcum powder was placed inside a holder which was agitated to keep the powder airborne. This laden air was passed through the filter under test, and returned to the holder via an aspirator. This air was recycled until all of the powder had been absorbed by the filter. The same procedure was adopted to contaminate (load) a sample of each type of filter.

The next step was to measure the absorption of both types of smoke, by each contaminated filter, using the same experiment setup that was used for brand new, uncontaminated filters (described above).

There was some concern about the fact that talcum powder can absorb moisture, with a risk that the results could be skewed according to the air humidity. This could affect the size, mass or "stickiness" of the talc particles. Therefore a substitute was found, in Alumina (Al_2O_3) powder. This was available in a controlled particle size range similar to talcum powder. Filters were contaminated with Alumina powder in the same manner as for talcum powder, and then the absorption of the two test smokes was measured.

The next most obvious contaminant was tobacco smoke (although this is becoming a less frequent problem). A quantity of $50 gram$ of tobacco was burned within a holder and passed through a sample of each type of filter, in a similar manner to the powder, for $90 min$. This procedure was repeated with an additional $50 gram$ of tobacco, for each filter.

When the level of smoke absorption in these contaminated filters was measured, it was discovered that a higher smoke reading was obtained on the second, downstream smoke detector, indicating that smoke was being drawn out of the filter (unloading). Retention of moisture from the tobacco was considered largely responsible for this effect.

It was decided to purge each filter with fresh air for $8 hours$. Upon further measurement, a small degree of unloading was still evident so the purging was continued for another $12 hours$. After a total of $20 hours$ purging, there was no further evidence of unloading and so it became possible to measure the absorption of test smoke by each of the filter types.

It was recognised that in a real environment, the filter was likely to be contaminated by a combination of materials, such as tobacco smoke and dust. Therefore it was decided to examine such a combination. Two sets of filters were initially contaminated with tobacco as described above. It was expected that this would make the surface of the filter elements somewhat sticky, and more likely to become clogged, thereby absorbing more test smoke.

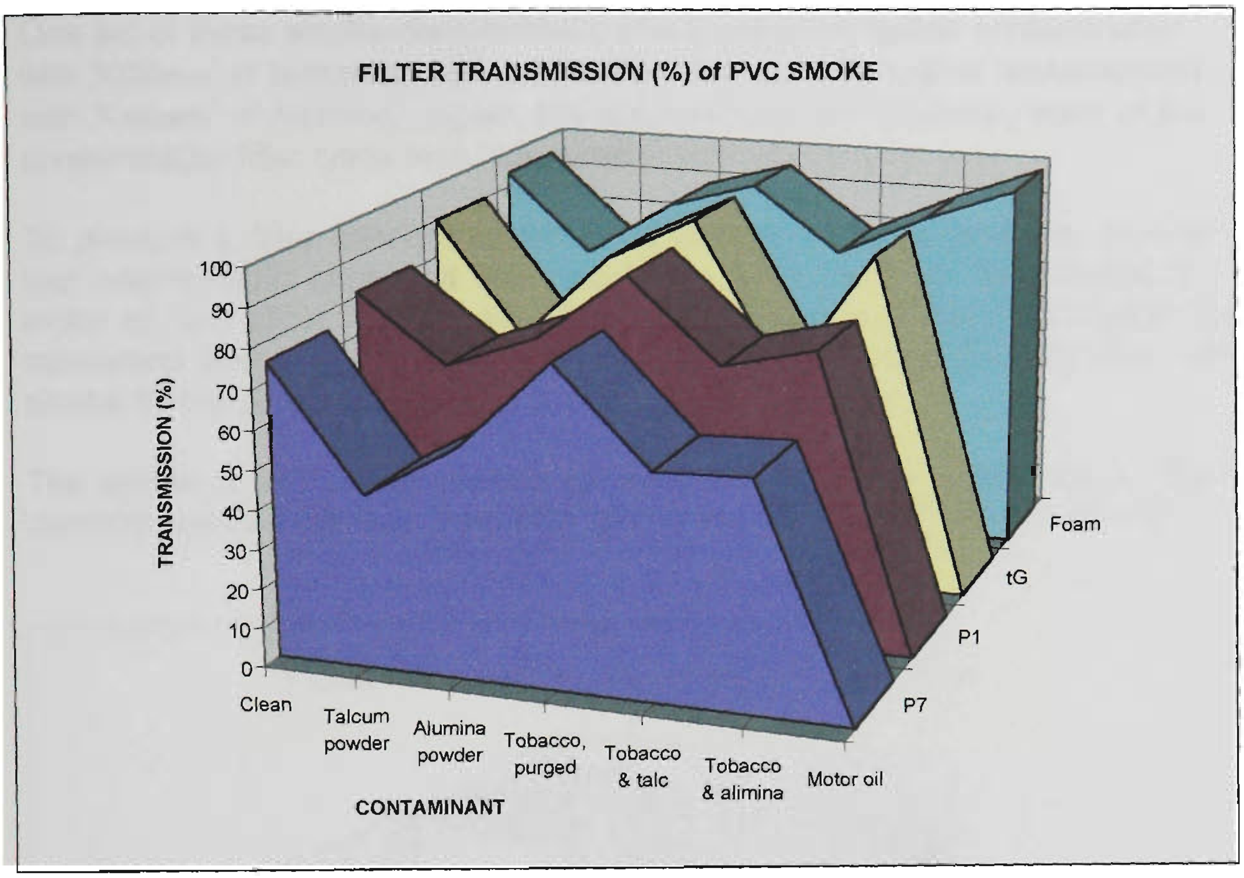

Figure 3.9 - Results of filter experiments with PVC smoke

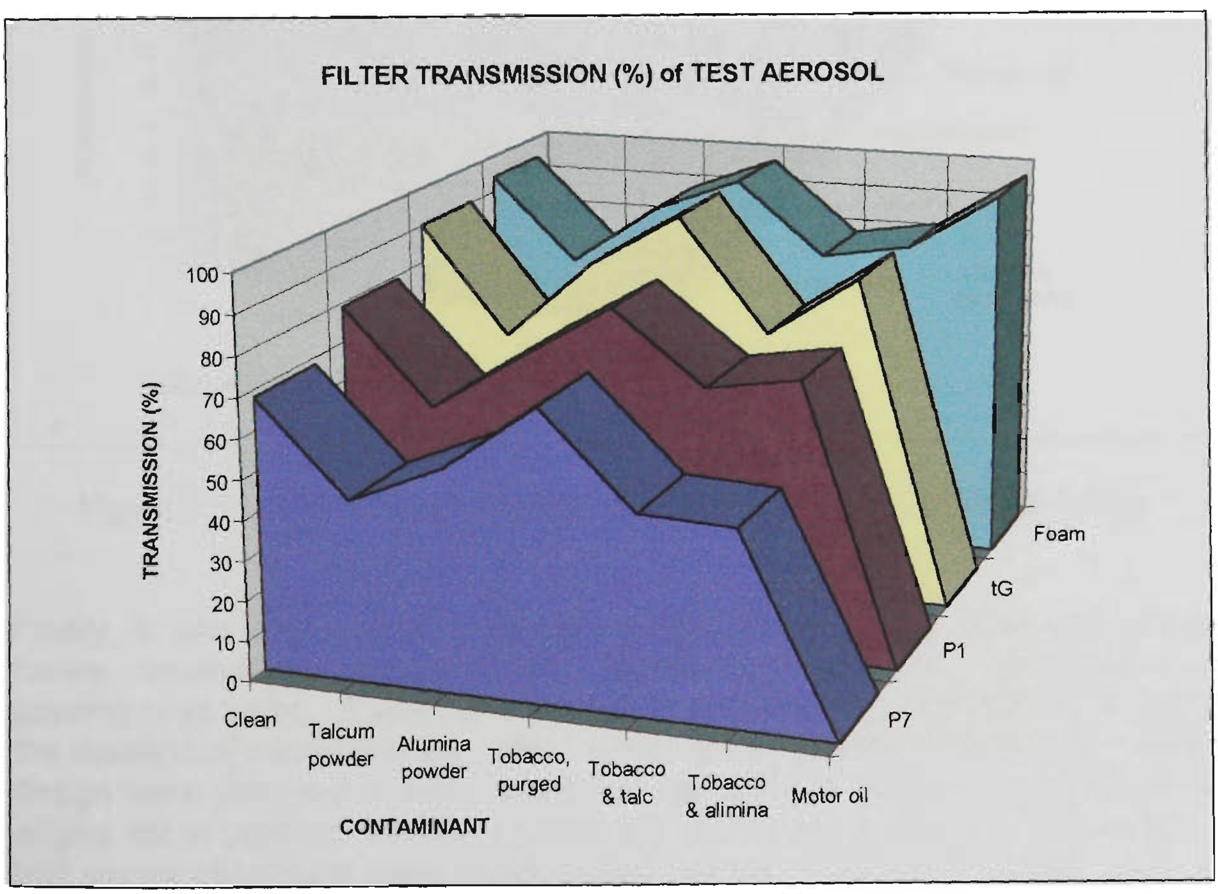

Figure 3.10 - Results of filter experiments with TEST smoke

One set of these smoke-contaminated filters was then further contaminated with $3000mm^3$ of talcum powder, while the other set was further contaminated with $3000mm^3$ of Alumina. Again, the absorption of test smoke by each of the contaminated filter types was measured.

To produce a filter element surface that was as sticky as possible, to which test smoke might adhere, it was decided to soak the foam filter elements in motor oil, and allow this to drain. This experiment could not be conducted for membrane filters, which could not be drained. The absorption of each test smoke by the oil-saturated foam filter was measured.

The results of all the experiments as illustrated in Figures 3.8 and 3.9 clearly demonstrate that the new foam filter technology is superior in all situations.

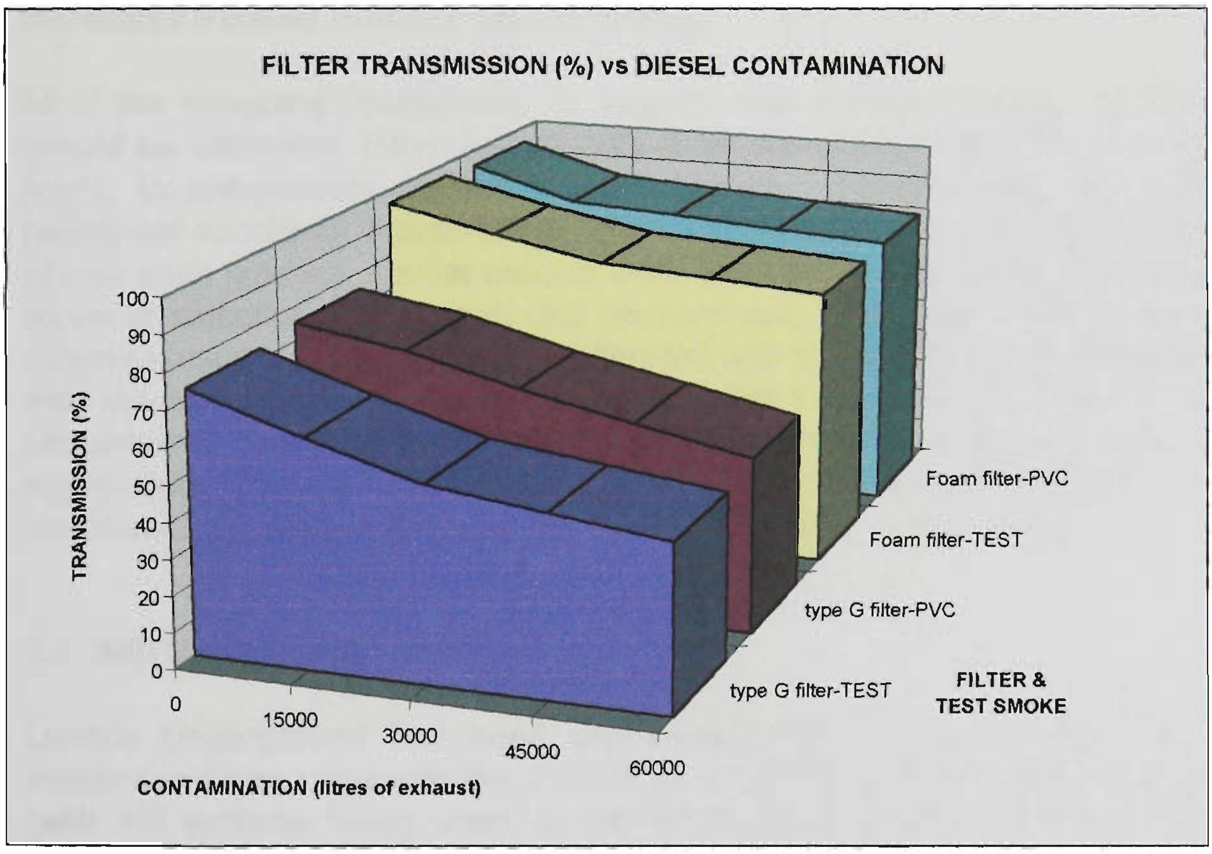

Figure 3.11 - Results of time duration experiment using diesel fumes

Finally, it was known that a significant concern on many sites was diesel fumes, caused by delivery trucks, forklift trucks, standby generators, or passing road traffic. It was decided to adopt a different approach based upon the duration of contamination. New, uncontaminated filters of type G or foam design were attached in turn, directly to the exhaust pipe of an aging diesel engine set to produce $1000 litres$ of exhaust products per minute. Readings of test smoke absorption were taken before the test, $15 min$ into the test, then at $30 min$ and $60 min$. This amounted to a total of $60{,}000 litres$ of contaminating exhaust products for each filter.

The results are shown in Figure 3.11 where it can be seen that the test smoke absorption is not linear with time/contamination. Note that data at $45min$ have been added by interpolation, to permit correct scaling of the chart (the graphics software does not permit a "scattered" axis on 3-D plots). Here it can be seen that the foam filter provides higher transmission of both test smokes and that its rate of reduction in transmission is less steep, tending to flatten over time. By contrast the type G filter always removes more smoke and continues to do so at a greater rate over time.

The significance is, that after considerable contamination by diesel exhaust, a perfectly clean type G membrane filter could reduce the effective sensitivity of a smoke detector from (say) $0.10\%/m$ to $0.22\%/m$ which is intolerable. The foam filter could instead provide an effective sensitivity of $0.125\%/m$ which represents a barely tolerable sensitivity loss.

All of the foregoing results tend to suggest that aspirated smoke detectors should be calibrated (say) 10% to 20% more sensitively than the published figure, to compensate for the filter absorption. Nevertheless, the actual factory-set sensitivity is determined without knowledge of the final destination site for each product. Earlier models were available in a range of sensitivities requiring selection to suit each real environment, based upon testing during commissioning. Later models are calibrated with the filter in place and have a wide dynamic range, permitting alarm thresholds to be set from 0.01 to 20 $\%/m$ obscuration. The most important requirement is that the sensitivity does not significantly <u>change</u> in the long term, which would invalidate the commissioning tests and render the system operation unpredictable.

3.4 INSITU TESTING

London Underground had been experiencing difficulties with the pleated membrane filters used with the VESDA systems installed to cover escalators (with 360 systems being used, in the wake of the disastrous Kings Cross Station fire of 1987). Because of the high volume of people traffic as well as the constant wear on escalators, train wheels and brakes, the environment was such that that the Authority was obliged to change the filters as often as every three weeks. This provided an ideal test site because the service life of a filter would be quickly revealed.

Choosing the most troublesome site, a foam filter was fitted to one VESDA system and a membrane filter was fitted to an adjacent system. The Authority regularly removed each filter to test for smoke absorption and air flow restriction. Their results are presented in Figure 3.12. Whereas the service life of a membrane filter proved to be three weeks before a significant increase in smoke absorption became evident, this period increased to six months in the case of the foam filter, which was entirely satisfactory. In addition, the air flow resistance was superior in the case of the foam filter.

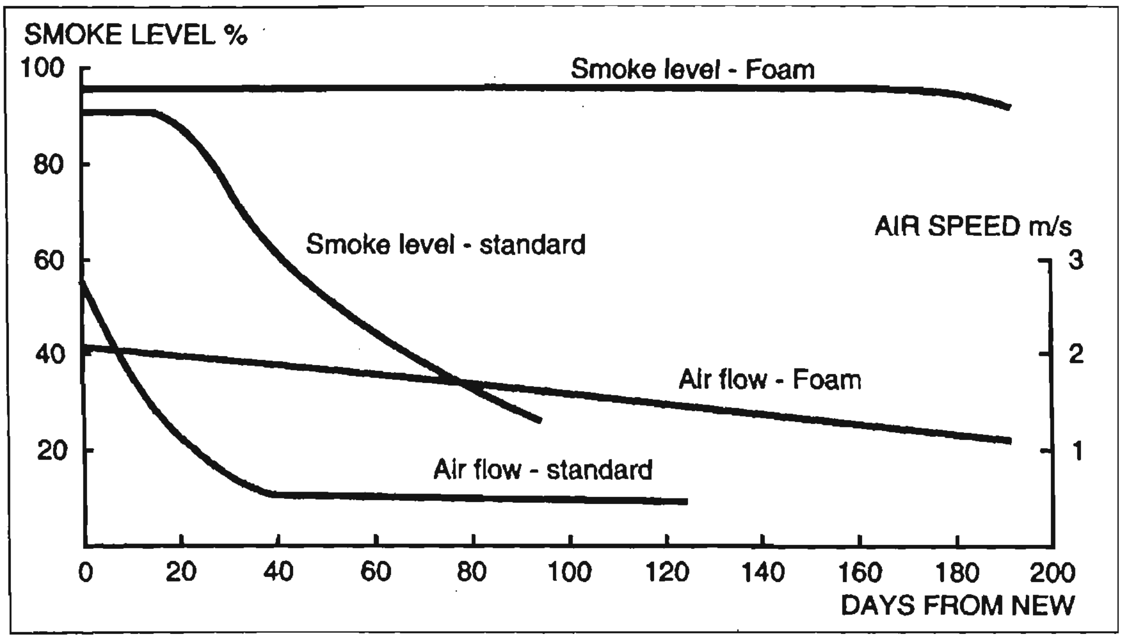

Figure 3.12 - London Underground filter test

Insitu testing was also conducted at three British Telecom sites where the question of contamination from diesel fumes had become a particular issue. After a period of three months it became clear that the foam filter design was superior to the original membrane filters and there proved to be no difficulty in meeting the client's minimum two-year service life criterion.

3.5 CHARACTERISATION OF FILTER LOSS

It is useful to characterise a number of filters of a type that have been used, or are available to be used for a range of environments. For the VESDA Mk3 four-port foam filter assembly including a set of $80mm$ average diameter CMF (coarse-medium-fine) foam filter elements (similar to Figure 3.7 without sleeve and spreader cone), the data are presented in Figure 3.13 and we obtain:

CMF foam filter element $\quad \Delta P_e = 0.00047\,Q^2 + 0.305\,Q$

Container outlet component $\quad \Delta P_o = 0.00220\,Q^2 + 0.031\,Q$

Complete filter assembly $\quad \Delta P_{filter} = 0.00270\,Q^2 + 0.336\,Q$

These data were obtained from differential pressure measurements across the filter housing inlet, the filter element, and the filter housing outlet, as well as the complete assembly for verification of the sum. Surprisingly, no significant pressure drop could be measured at the inlet which represents a smoothly blended but somewhat short manifold diffuser. However, the outlet represents a relatively sudden contraction from about $80mm$ diameter to $21mm$ diameter which introduces comparatively high loss.

It can be seen from Figure 3.13 that for flow rates up to about $155 litre/min$, the filter element loss is less than the outlet loss. The filter element characteristic is also relatively linear, indicating that most of its loss is caused by friction. Note that the loss for the complete assembly does equate to the algebraic sum of the individual equations for the filter element and the filter outlet, as one would expect. This serves to validate the equations.

This experiment was repeated for a filter element composed entirely of fine foam layers (FFF) as presented in Figure 3.13. It is interesting once again to consider the components:

FFF foam filter element	ΔP_e	$=$	$0.00070\,Q^2 + 0.528\,Q$
Container outlet component	ΔP_o	$=$	$0.00210\,Q^2 + 0.018\,Q$
Complete filter assembly	ΔP_{filter}	$=$	$0.00280\,Q^2 + 0.548\,Q$

In this case the filter element loss is much greater, typically twice that of the filter outlet. It is curious that the filter outlet loss is different from the CMF case, particularly in relation to the linear coefficient. This results in a lower loss at any given flow rate, amounting to $6Pa$ at the maximum flow rate (approximately 8% across the range). This is a relatively small variation possibly attributable to a slightly different fit causing a larger clearance between the filter element and the outlet.

Figure 3.15 presents the data for a number of other types of filter. The sleeved foam filter was previously shown in Figure 3.7, and is similar to the CMF except that the foam element diameter is set by the $60mm$ coaxial sleeve within the housing (which reduces the foam cross-sectional area to 56%). Although the "spreader cone", is useful in employing momentum to direct large debris such as insects to a recess outside the sleeve (but within the housing), this cone also increases the loss because it causes the airflow direction to reverse.

The GUD paper element filter is of the original, membrane type, and has the lowest loss of all filters. The empty housing is also included for reference to indicate the least possible loss. The equations obtained for the complete assemblies are as follows:

Sleeved CMF foam filter	ΔP_{filter}	$=$	$0.0066\,Q^2 + 0.622\,Q$
Sleeved CMF, no cone	ΔP_{filter}	$=$	$0.0055\,Q^2 + 0.583\,Q$
GUD membrane filter	ΔP_{filter}	$=$	$0.0014\,Q^2 + 0.068\,Q$
Empty housing	ΔP_{filter}	$=$	$0.0015\,Q^2 + 0.037\,Q$

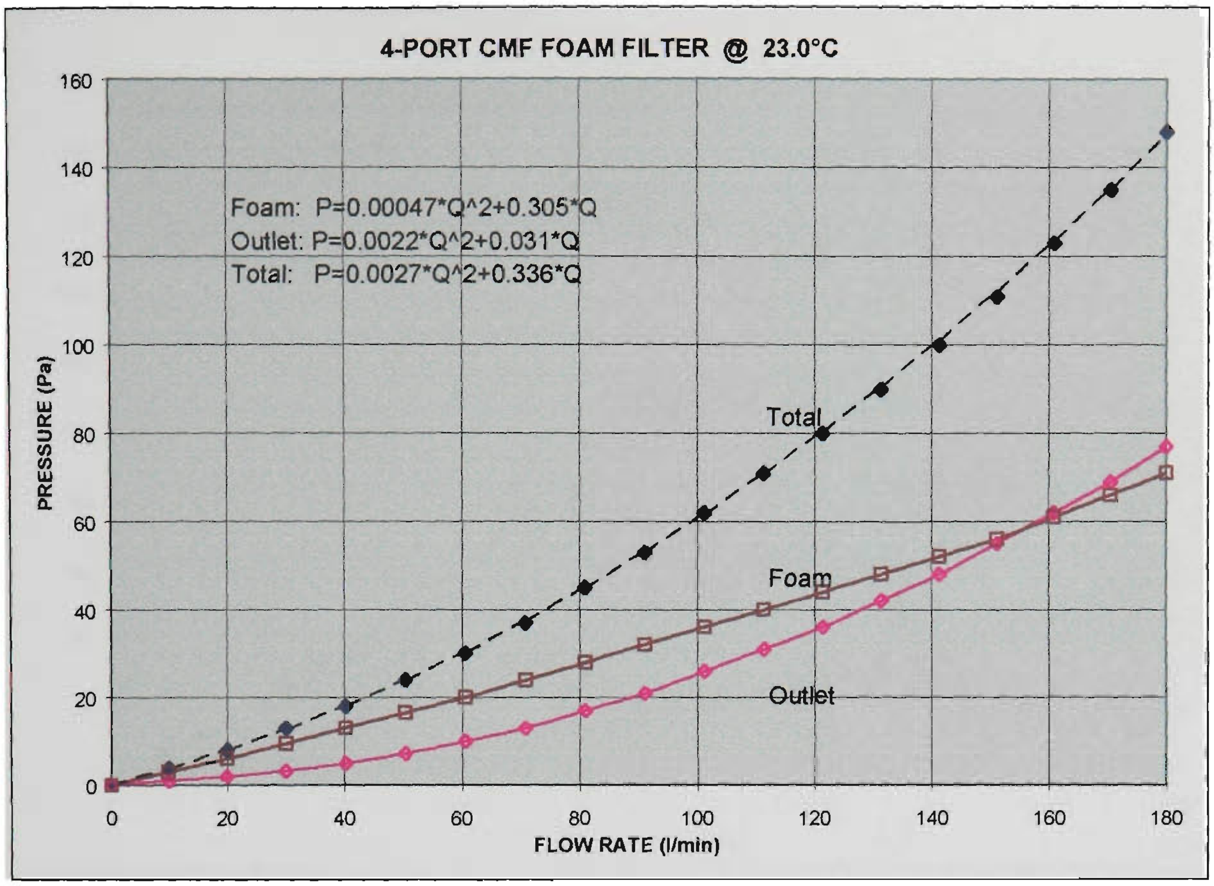

Figure 3.13 - Characterisation of four-port CMF foam filter

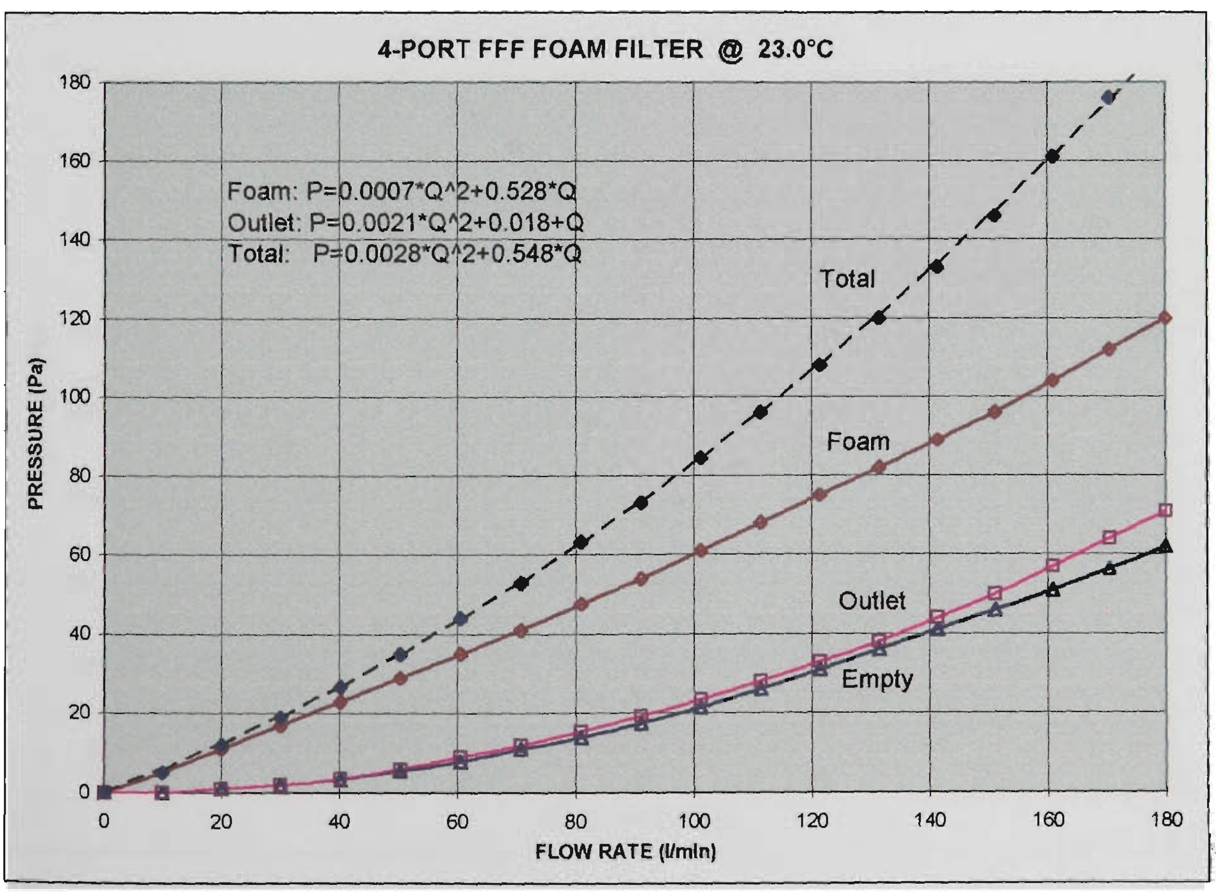

Figure 3.14 - Characterisation of four-port FFF foam filter

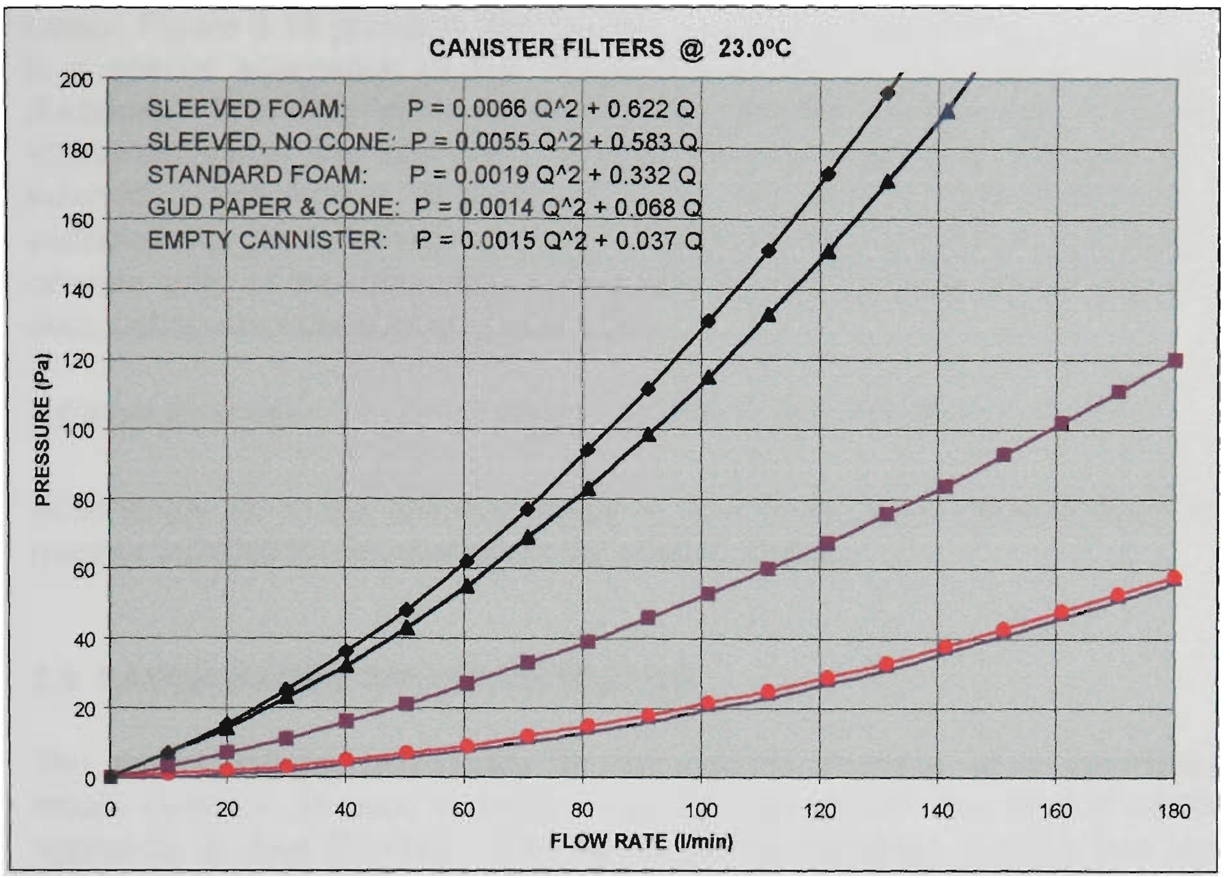

Figure 3.15 - Characterisation of various canister filter arrangements

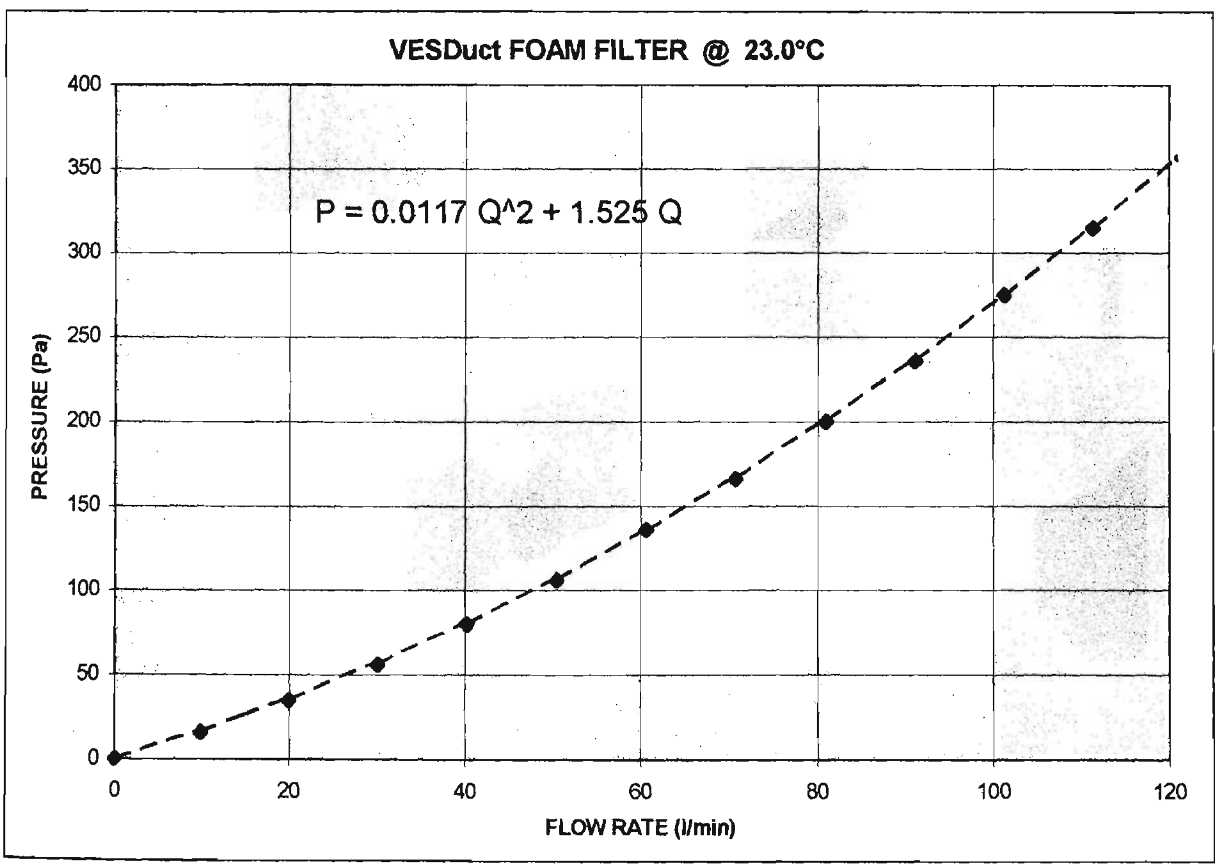

Figure 3.16 - Characterisation of VESDuct foam filter

Lastly, Figure 3.16 presents the data for a VESDuct foam filter. This product is a special adaptation of the VESDA Mk3 detector for use in ventilation ductwork. Providing lower sensitivity, the detector components have been shortened within the chamber, allowing for a coaxial filter element to be inserted. This has a diameter of $50mm$, resulting in high resistance as indicated by the following equation. However, this product is expected to operate only at low flow rates, generated by the dynamic head within the duct, acting on probes (see Figure 4.58).

$$\textit{VESDuct foam filter} \qquad \Delta P_{filter} = 0.0117\, Q^2 + 1.525\, Q$$

Accordingly all of the relevant types of filter have been characterised in a manner suitable for application to the system model.

3.6 LASER-BASED SMOKE DETECTOR

The miniaturisation achievable for the optical chamber of a laser-based smoke detector, as used in the new VESDA LaserPLUS, has offered another approach to dust filtration. The sizing of the aspirated system has been optimised for the range of suitable pipe sizes, operating pressures and flow rates. Whereas this magnitude of flow rate is required in order to achieve a satisfactory smoke transport time, only a small proportion of the resulting smoke sample is required for smoke detection purposes. This means that only this small proportion, on the order of 5% of the available sample, need be tested for smoke density. Therefore it is necessary only to filter this 5% sample, with the 95% balance ducted directly to waste. This provides an opportunity to use a filter some 20 times smaller, or to gain a service interval 20 times longer, or a compromise between these benefits.

Because the VESDA LaserPLUS filter is not installed directly in line with the pipe system flow, it was dealt with as an integral part of the detector itself in Chapter 2.

3.7 CONCLUSIONS

Dust filtration is an essential part of an aspirated smoke detection system, to prevent soiling of the detector (affecting sensitivity) and also to minimise the possibility of unwanted alarms. Membrane filters were found to absorb an excessive proportion of smoke, increasingly over time, to the point where the sensitivity of a system could be dangerously compromised. Extensive evaluation of various possible alternative technologies led to the development of a new filtration method based upon an understanding of Brownian motion. The new design involves thick layers of large-pore reticulated foam within a canister. This multi-layer design results in longer service life, while maximising the capture of dust and minimising the capture of smoke within the filter, thereby preserving the sensitivity of the system.

Evaluation of the new filtration method included challenging the filter with various combinations of contamination products and determining the degree to which smoke was captured. The multi-layer reticulated foam proved superior to other technologies in all cases. The new filter design was independently tested in London Underground where it provided a service life in excess of eight times that of the original filter.

The pressure drop incurred by each of several types or brands of filter have been characterised for inclusion in the computer-based system model. For the VESDA Mk3 four-port, three layer (CMF) foam filter and its component parts we obtain:

CMF foam filter element	ΔP_e	$= 0.00047\,Q^2 + 0.305\,Q$
Container outlet component	ΔP_o	$= 0.00220\,Q^2 + 0.031\,Q$
Complete filter assembly	ΔP_{filter}	$= 0.00270\,Q^2 + 0.336\,Q$

For an alternative form of this filter composed entirely of fine foam layers (FFF) we obtain:

FFF foam filter element	ΔP_e	$= 0.00070\,Q^2 + 0.528\,Q$
Container outlet component	ΔP_o	$= 0.00210\,Q^2 + 0.018\,Q$
Complete filter assembly	ΔP_{filter}	$= 0.00280\,Q^2 + 0.548\,Q$

In this case the filter element loss is much greater, typically twice that of the filter outlet. Other useful equations are:

Sleeved CMF foam filter	ΔP_{filter}	$= 0.0066\,Q^2 + 0.622\,Q$
Sleeved CMF, no cone	ΔP_{filter}	$= 0.0055\,Q^2 + 0.583\,Q$
GUD membrane filter	ΔP_{filter}	$= 0.0014\,Q^2 + 0.068\,Q$
Empty housing	ΔP_{filter}	$= 0.0015\,Q^2 + 0.037\,Q$
VESDuct foam filter	ΔP_{filter}	$= 0.0117\,Q^2 + 1.525\,Q$

Any of the above arrangements will be selectable in the system modelling software.

In the particular case of the VESDA LaserPLUS, the filter is contained within a small branch off the main flow which short-circuits the aspirator to a small extent. The detector chamber is in series with this branch so the effect of the filter has not been separately identified. For system modelling purposes the extent of this short-circuit effect on the aspirator has been characterised in Chapter 2.

CHAPTER 4 - HOLE FLOW CHARACTERISATION

4.0 INTRODUCTION

The characterisation of sampling hole flow rate was expected to be a straight-forward matter involving the calibration of a range of hole sizes in a range of pipe sizes. Investigating a range of hole sizes was required to enable control of hole flow rates at individual locations, with a view to optimising the system balance (i.e. the equalisation of hole flows throughout the system despite the likely unequal pressure distribution).

Investigating a range of pipe sizes was required because the wall thickness of a pipe and the pipe's internal diameter were expected to have a measurable effect on the hole flow rate at a given hole pressure differential. The geometry of the hole (squareness of shoulder and angle of drilling) was also expected to have an influence on flow rate.

It will be shown that characterisation of the sampling hole flow rate is a complex matter involving the pipe upstream flow rate as well as the external "crosswind" velocity, giving rise to the newly-discovered phenomena of "Ultraflow" and "Infraflow" respectively. By superposition, these phenomena significantly alter the hole flow rate due to differential static pressure alone.

4.1 EXPECTED RESULTS

Based upon initial experiments, the hole flow characteristic was expected to have either of the forms shown below:

$$Q_{hole} = A\,\Delta P_{hole}^{0.5} + B\,\Delta P_{hole}$$

$$Q_{hole} = C\,\Delta P_{hole}^{n}$$

where Q_{hole} is the hole flow rate, ΔP_{hole} (or simply P_{hole}) is the differential pressure across the hole, A, B and C are empirically-derived coefficients, and n is an exponent with a value in the range 0.5 to 0.6. As previously explained, text-book values would have $B = 0$ or $n = 0.5$.

It was also expected that these coefficients would be affected by the pipe internal diameter. The hole (typically 2 to 3 mm diameter) penetrates the pipe wall which is relatively thick (also typically 2 to 3 mm) and is analogous to a very short tube. Air flowing through a hole in the pipe wall, or especially when flowing through a hole in the end cap of a pipe, is not unlike the situation of a small pipe which contains a sudden expansion to a large diameter.

Douglas et al (1979, p271), and Roberson and Crowe (1975, p198) use different approaches to show that the head loss (or pressure drop) resulting from a sudden expansion can be determined analytically, as:

$$H_e = (u_1 - u_2)^2 / 2g \qquad or \qquad \Delta P = \rho (u_1 - u_2)^2 / 2$$

where H_e is the head loss or ΔP is the pressure drop, u_1 and u_2 are the average velocities respectively upstream and downstream of the sudden expansion, g is the local acceleration due to gravity and ρ is the air density. This equation appears similar to the loss in dynamic head, except that simple dynamic head loss would have the bracketed terms squared individually. With continuity of flow, the upstream and downstream average velocities are in inverse proportion to the cross-sectional areas of the pipes, so:

$$H_e = \frac{u_2^2}{2g}\left(\frac{A_1}{A_2} - 1\right)^2 \qquad or \qquad \Delta P = \rho \frac{u_2^2}{2}\left(\frac{A_1}{A_2} - 1\right)^2$$

where A_1 and A_2 are the respective pipe cross-sectional areas. This equation satisfies the limits ranging from $A_2 = A_1$ (where the head loss is zero), to $A_2 = \infty$ (where the head loss equates to the total dynamic head). Therefore, if we apply the experience of a pipe expansion to the case of a sampling hole, we would expect the downstream pipe diameter to influence the hole flow coefficients. In particular, we would expect the head loss to be reduced if, for the same sized hole, the pipe diameter is reduced.

The same conclusion would be drawn when flow is considered from the perspective of streamline visualisation. The flow discharge into the pipe from the hole is contained by the pipe walls, thereby confining the expansion of streamlines and reducing the head loss.

4.2 CONSIDERATION OF UPSTREAM FLOW

The above analogy with a sudden expansion, does not hold in the case of a side-wall hole where upstream flow is present. Here, the hole flow provides only a contribution to the total flow (with the downstream flow necessarily greater than upstream). The upstream flow could impact on the hole flow, by virtue of altering the streamlines or altering the "effective diameter" of the pipe downstream. In the latter case, the pipe is not filled by the hole flow alone, in fact for a typical hole, the majority of flow comes from upstream.

There is no known precedent for analysing this combination of flows in the literature. Most pipe networks or systems are used for distribution, involving the discharge of fluids from a number of orifices (with the upstream flow exceeding downstream flow). The current investigation involves induction rather than discharge, so the whole approach to balancing (equalisation of hole flow rates) throughout the network, for example, is different.

Given the expectation that the hole flow coefficients would depend partly upon the pipe diameter, it seemed possible that the upstream flow rate may also have a significant impact upon the coefficients. The objective was to determine the significance, if any, of this upstream flow.

4.3 EXPERIMENTAL TECHNIQUE AND RESULTS

An experimental technique was needed that would detect the effect of upstream flow rate upon hole flow rate. This proved to be a difficult challenge as discussed in Appendix 2, initially resulting in relatively coarse results.

As usual the flowmeter was needed to monitor flow rates downstream of the sampling hole in all experiments. This combined the upstream flow rate and the hole flow rate. Control orifices were used upstream of the sampling hole, in association with the digital pressure gauge, to determine the upstream flow rate. The hole flow rate was then obtained by subtraction. These calibrated orifices (used as end vents) were configured in the manner of Figure 2.1 and a test pipe of $21.2mm$ inside diameter was initially used.

A distance of $3000 \pm 0.5\ mm$ separated the pressure tap from the sampling hole location, with the flowmeter attached by a flexible straight coupling some $1m$ further downstream. The outlet of the flowmeter was attached to the adjustable aspirator bank.

Because the pressure gauge was already committed for use with the standard orifices to measure upstream flow rate during the experiment, then to obtain the differential pressure reading at the hole, the pipe pressure drop was calibrated in advance. This involved another, temporary pressure tap at the proposed location of the sampling hole. Using a $10.36mm$ diameter control orifice at the far end of the pipe, the pipe pressure drop versus flow rate was obtained as shown in Figure 4.1 (note change of gradient at $\mathrm{Re} \approx 2000$).

The resolution of the pressure gauge had become an important issue in the repeatability of the data. After investigating all available alternatives it proved possible to improve the resolution of the pressure gauge. This was done by attaching a digital voltmeter (Fluke type 77 multimeter) with a resolution of 1mV DC, to the output of the pressure transducer. This was calibrated against the display of the pressure gauge. Confidence was boosted when a precisely linear relationship was discovered across the full range, with 4mV representing 1Pa. The zero offset was 980mV so the resulting equation was:

$$P_{gauge} = 0.25\left(R_{mV} - 980\right)$$

where R_{mV} is the voltmeter reading in millivolts. It was noted that the zero offset was subject to drift over a period of hours (due to temperature), so it was necessary to record the zero reading routinely throughout any series of experiments. This was preferable to adjusting the zero-set potentiometer which was stiff and coarse in operation. In addition it proved easier to keep track of each experiment by mentally subtracting 1000mV from each reading before recording same, such that the equation became:

$$P_{gauge} = 0.25\left(R_{mV} + O_{mV}\right)$$

where O_{mV} is the offset which was found to lie within the range of 16 to 24. Accordingly, the resolution of the pressure gauge was improved fourfold.

Temperature drift was known to be a problem with the flowmeter already, associated with its high resolution. Now, temperature stability had become even more critical, if the improved pressure gauge resolution was to be utilised. For this reason, and because the general trend of the data was known (Appendix 2), it was decided to limit the number of control orifices used (i.e. to limit the number of experiment runs) so each experiment could be completed as quickly as possible (limiting the opportunity for system drift). Based upon earlier experiments, the control orifices of 10.36 and 12.9 mm diameter had proven to be the most revealing for current purposes.

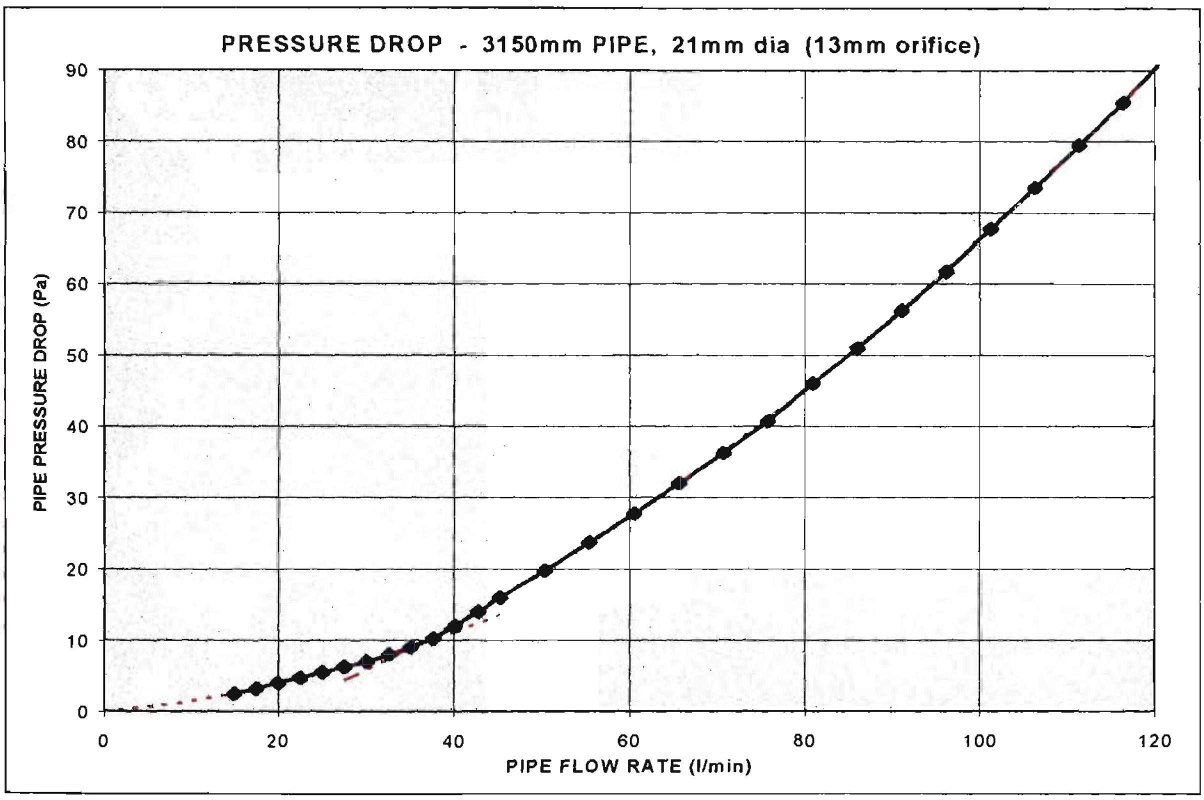

Figure 4.1 - Calibration data for pipe pressure drop

Figure 4.1 presents a graph of the pipe pressure drop obtained with the higher resolution apparatus, using a 4-port pressure tap placed 150mm downstream of the (blocked) hole location (and then scaling the pressure drop by 3000/3150). The equations for the laminar and turbulent regions are:

$$Q_{pipe} < 35: \qquad \Delta P_{pipe} = 0.0042\,Q_{pipe}^2 + 0.11\,Q_{pipe}$$

$$Q_{pipe} > 35: \qquad \Delta P_{pipe} = 0.0037\,Q_{pipe}^2 + 0.38\,Q_{pipe} - 8.9$$

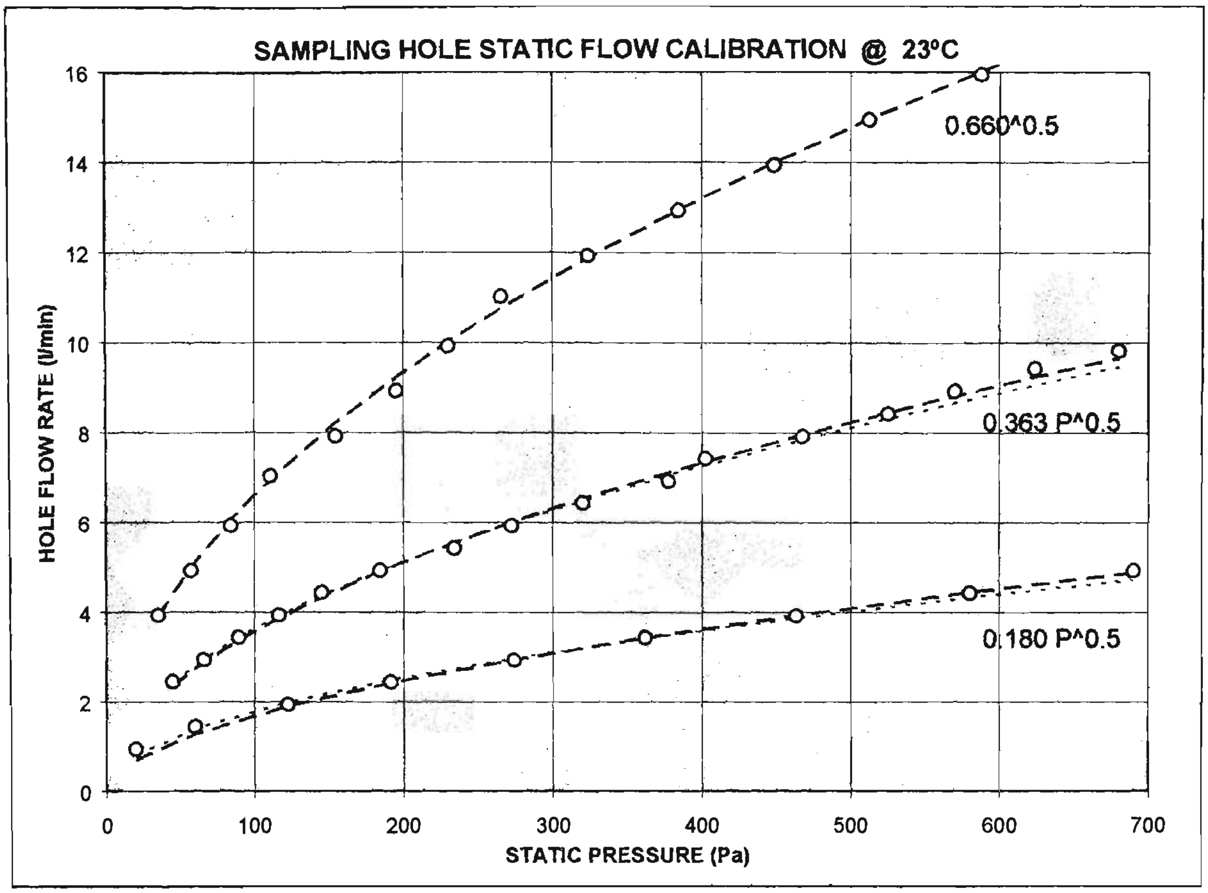

Figure 4.2 - Calibration of sampling holes

Figure 4.2 presents the static flow rate calibration results for the three sampling hole sizes. For current purposes only, we make the assumption that curves of good fit (dashed) can be expressed with an exponent of 0.5 to simplify comparisons or normalisations (the dotted curves use 0.52 and 0.55 which are more accurate at low flow rates). The equations to these curves, and an expression for the general case were determined as follows:

2mm hole: $Q_{stat} = 0.180\,\Delta P_{stat}^{0.5}$

3mm hole: $Q_{stat} = 0.363\,\Delta P_{stat}^{0.5}$

4mm hole: $Q_{stat} = 0.660\,\Delta P_{stat}^{0.5}$

Generally: $Q_{stat} = K_{hole}\,\Delta P_{stat}^{0.5}$

where K_{hole} is the hole coefficient. These results are mutually consistent and because a continuous range of hole sizes was contemplated for use in the field, equations for the hole coefficient were found as a result of applying curves of best fit to Figure 4.2, wherein D_{hole} is the hole diameter (mm):

$$K_{hole} = 0.0391\,D_{hole}^2 + 0.0075\,D_{hole} \qquad (\textit{passes through zero, } R^2 = 0.996)$$

$$K_{hole} = 0.057\,D_{hole}^2 - 0.102\,D_{hole} + 0.156 \qquad (\textit{not through zero, but } R^2 = 1)$$

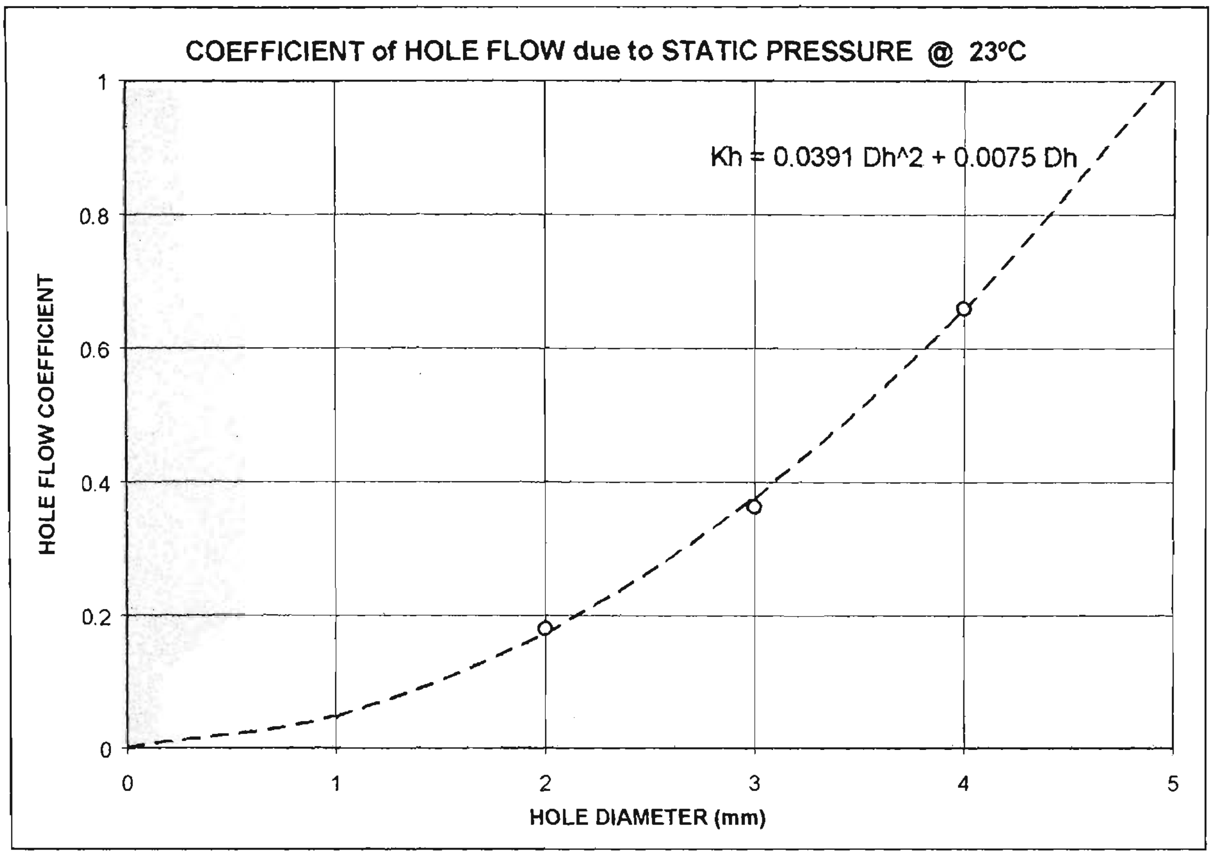

Figure 4.3 - Determination of static hole flow coefficient

Figure 4.3 includes the curve of the former equation (dashed) which appears to be applicable within the range of hole sizes from 1 to 5 *mm*. However, based upon field experience and the results of balancing calculations it can be shown as unlikely, that sizes outside the range of 2 to 4 *mm* will be actually required.

The experimental results for 2, 3, and 4 *mm* holes using control orifices (vents) of nil, 10.36 and 12.9 *mm* diameter are presented in Figures 4.4 to 4.6, together with curves of best fit (dashed). The improved smoothness over initial results (Appendix 4) indicates that the magnitude of error has reduced. Previous experiment runs had been repeated many times in order to improve the accuracy, as determined from the consistency of data points within a set, and between sets. This acted as a check on the experimental technique.

Figure 4.7 presents the current results together, indicating good consistency. Here, three sets of three graphs are presented, with each set corresponding to a given hole size. For a given set, the results for the 12.9 and 10.36 *mm* orifices (simplified to 13 and 10 *mm* respectively) are always above the corresponding graph for the 0*mm* (nil) orifice. Such consistency enhances confidence in the results.

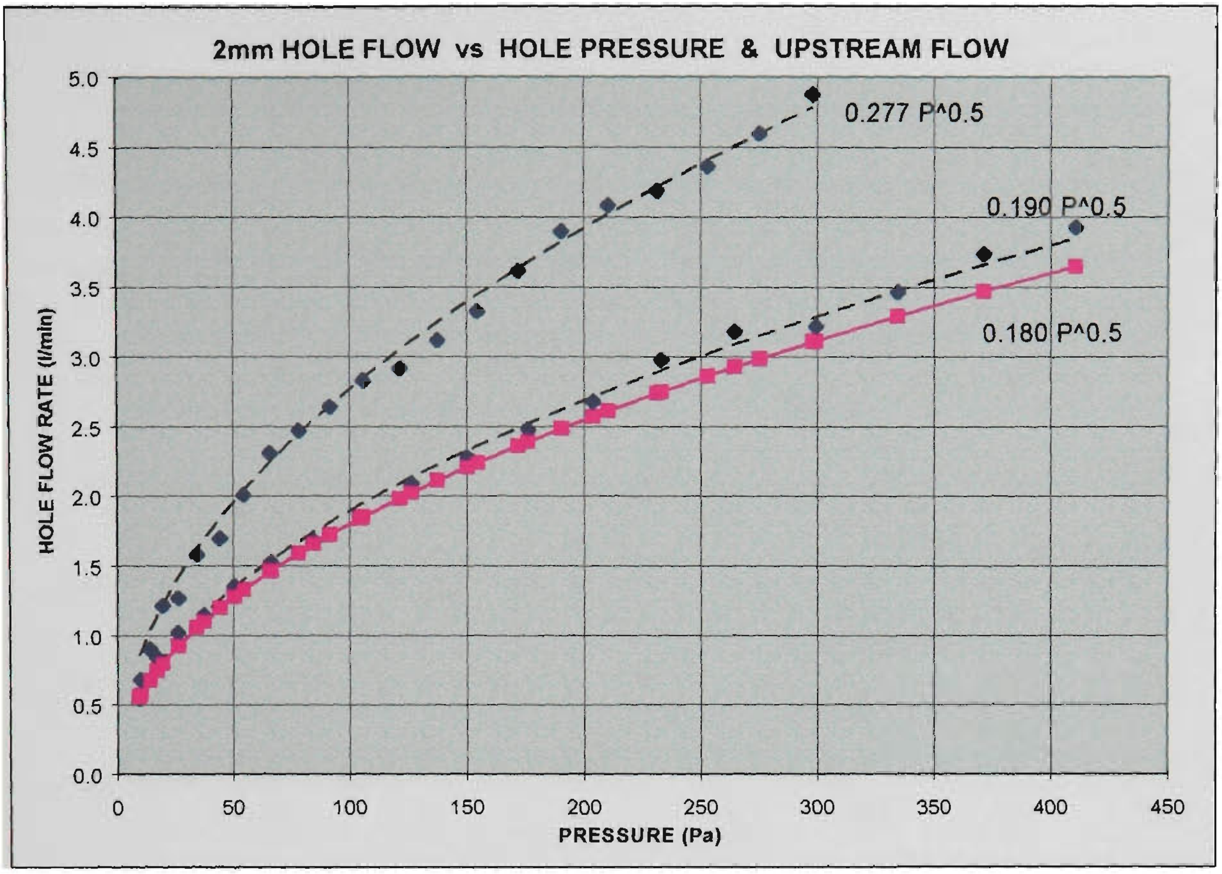

Figure 4.4 - $2mm$ hole flow with upstream flows

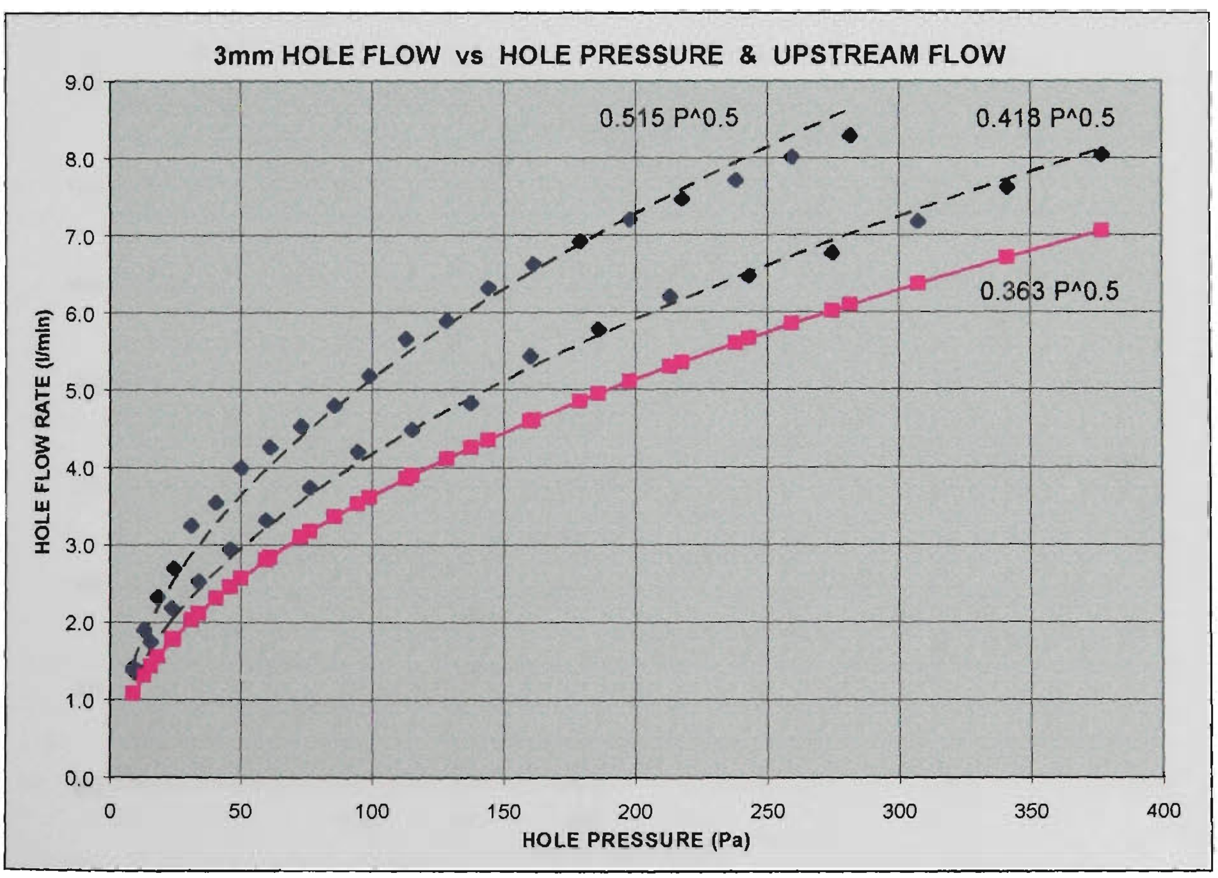

Figure 4.5 - $3mm$ hole flow with upstream flows

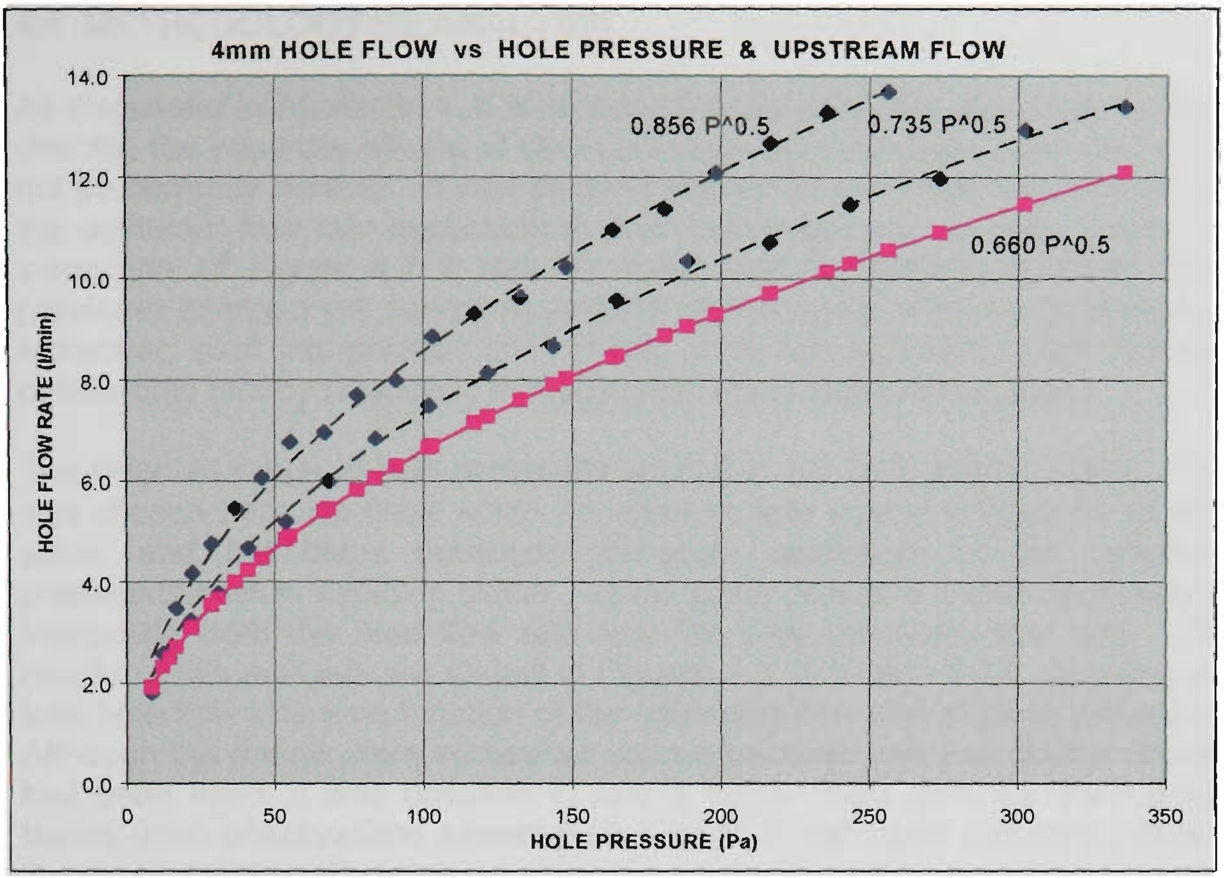

Figure 4.6 - 4*mm* hole flow with upstream flows

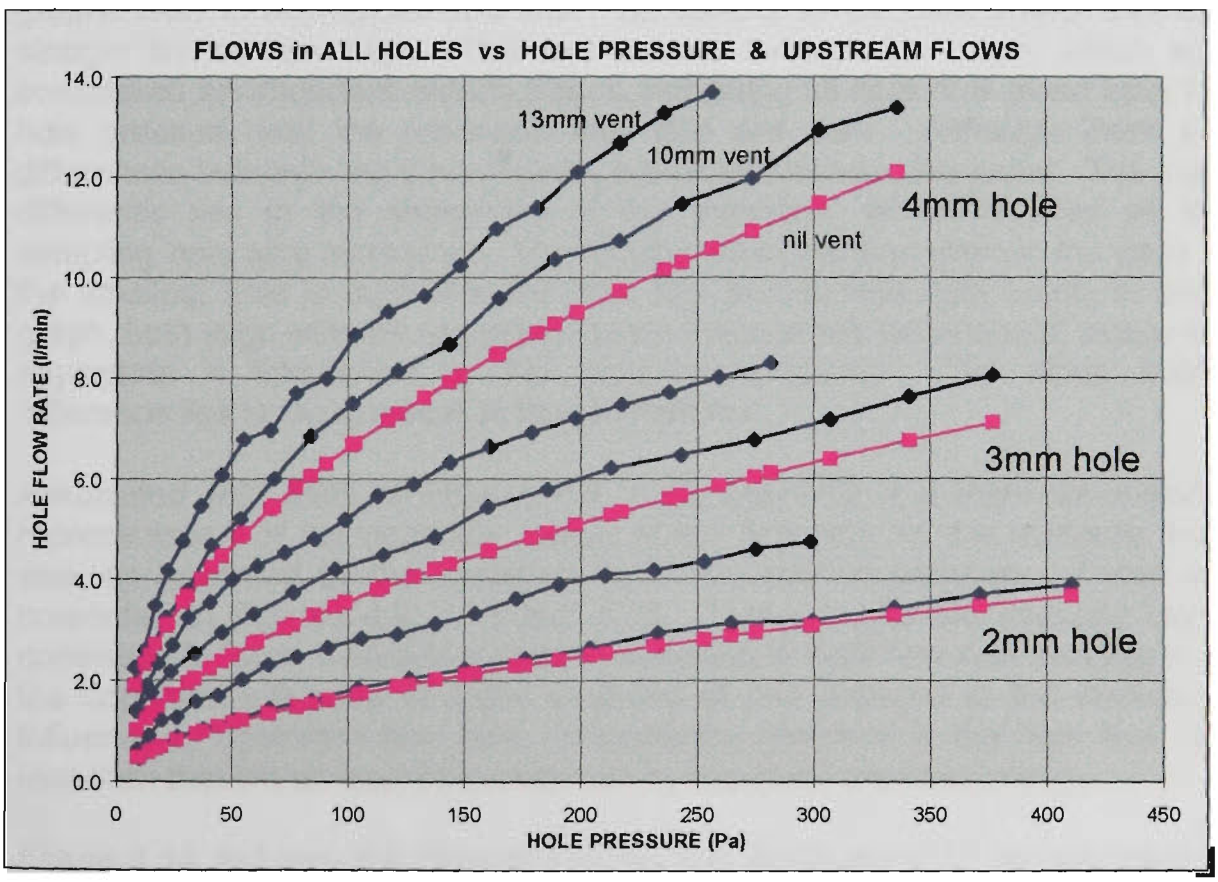

Figure 4.7 - Flow in all holes with upstream flows

4.4 METHODOLOGY OF ANALYSIS

As discussed in Appendix 4, it was found that by using the experimental data directly, the separate effects of static pressure and upstream flow rate would not be correctly isolated. It was decided instead to use interpolation to obtain the upstream flow rate applicable to each hole pressure. In other words, by inspection of Figure 4.7 it can be seen that the vertical gridlines (hole pressure) intersect the curves at points that can be obtained by interpolation. Moreover, such interpolation can provide some improvement to the estimate of hole flow rate by effectively averaging between adjacent readings.

The selected range of hole pressures was 20 to 120 Pa in steps of 20Pa. This was chosen because it fell within the span of both control orifices for all hole sizes, and the steps produced adequate resolution for the graphical presentation while avoiding clutter. At the given pressure it was necessary to interpolate both the hole flow rate and the pipe upstream flow rate. The results of this analysis are shown in Figures 4.8, 4.10 and 4.12, depicting the total hole flow rate as a function of the upstream flow rate at given pressures. Although the results were somewhat coarse because only two control orifices had been used, it was possible to add a further data point for each graph based upon observations whereby no Ultraflow had been detected below a threshold upstream flow rate.

The results proved most interesting. It can be seen that the graphs at low upstream flow rates are essentially horizontal, but at higher flow rates the graphs tend to asymptote to a line. Conformity of the data points with this straight line is very high. This line passes through the origin, which was considered an important validity check, indicating nil hole flow when both the hole pressure and the upstream flow rate are zero. Although there are differences between the three figures, the overall trend is the same. The main difference lies in the sharpness of the transition, which reduces as the sampling hole size increases. The sharpness of the transition in the case of the smallest hole is such that the final and penultimate data points in each graph, both align with the asymptote (note that a small "undershoot" below the asymptote is introduced by the graphics software). The other, subtle difference lies in the gradient of the asymptotes.

Associated with each of Figures 4.8, 4.10 and 4.12 is a three-dimensional representation of the complete model of the flow rate for the particular hole size, as governed by the upstream flow rate and the pressure. These are presented in Figures 4.9, 4.11 and 4.13. These results are mutually highly consistent in form. There is a smooth transition in hole flow rate, ranging from the dominant influence of static pressure at one extreme to the increasing influence of upstream flow rate. Importantly, nowhere is the hole flow rate less than that which would be produced by the static pressure alone.

Figure 4.14 includes the data of Figures 4.8, 4.10 and 4.12 on one page to indicate the relativity and consistency between the three sets of data. For completeness, Fig 4.15 depicts the three sets of results together in three-dimensions to assist comparison (presented side-by-side to avoid clutter).

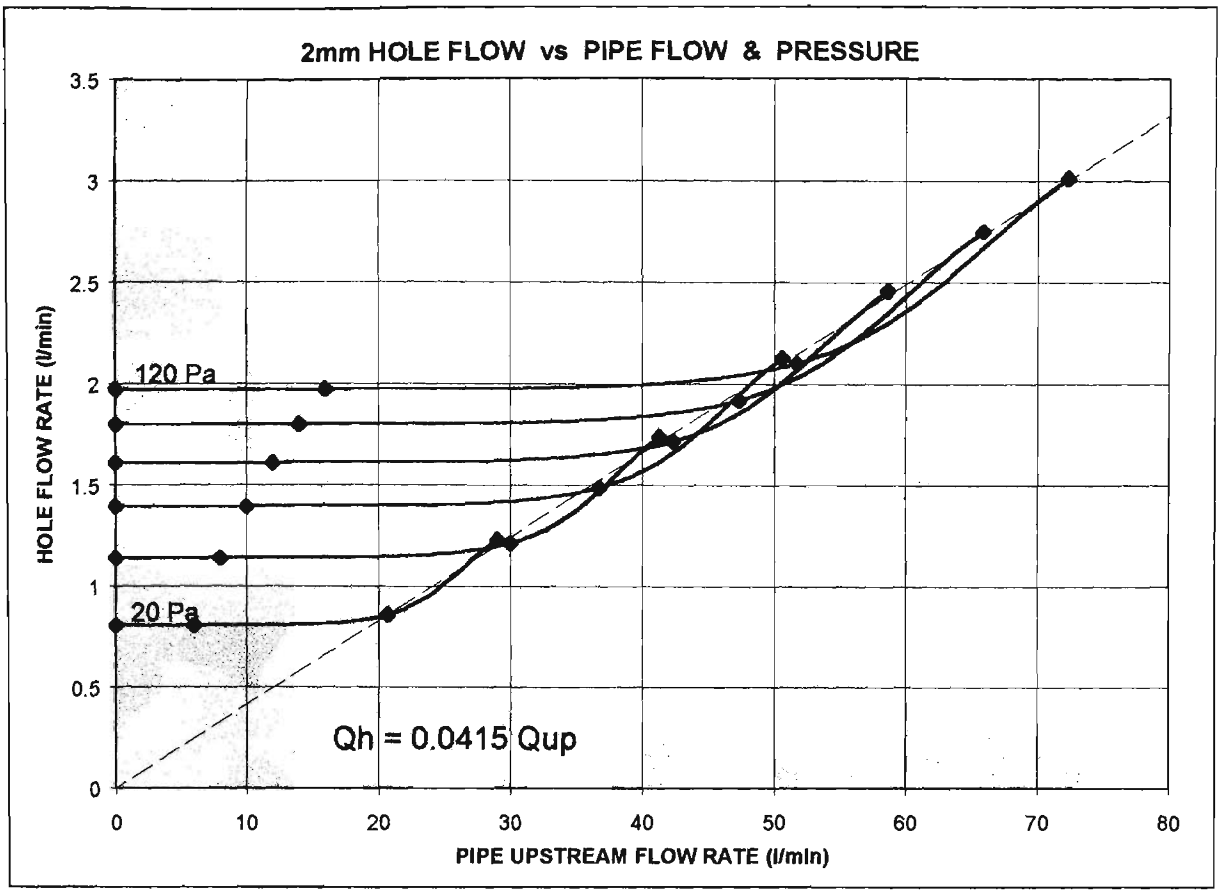

Figure 4.8 - $2mm$ hole flow with $21mm$ pipe

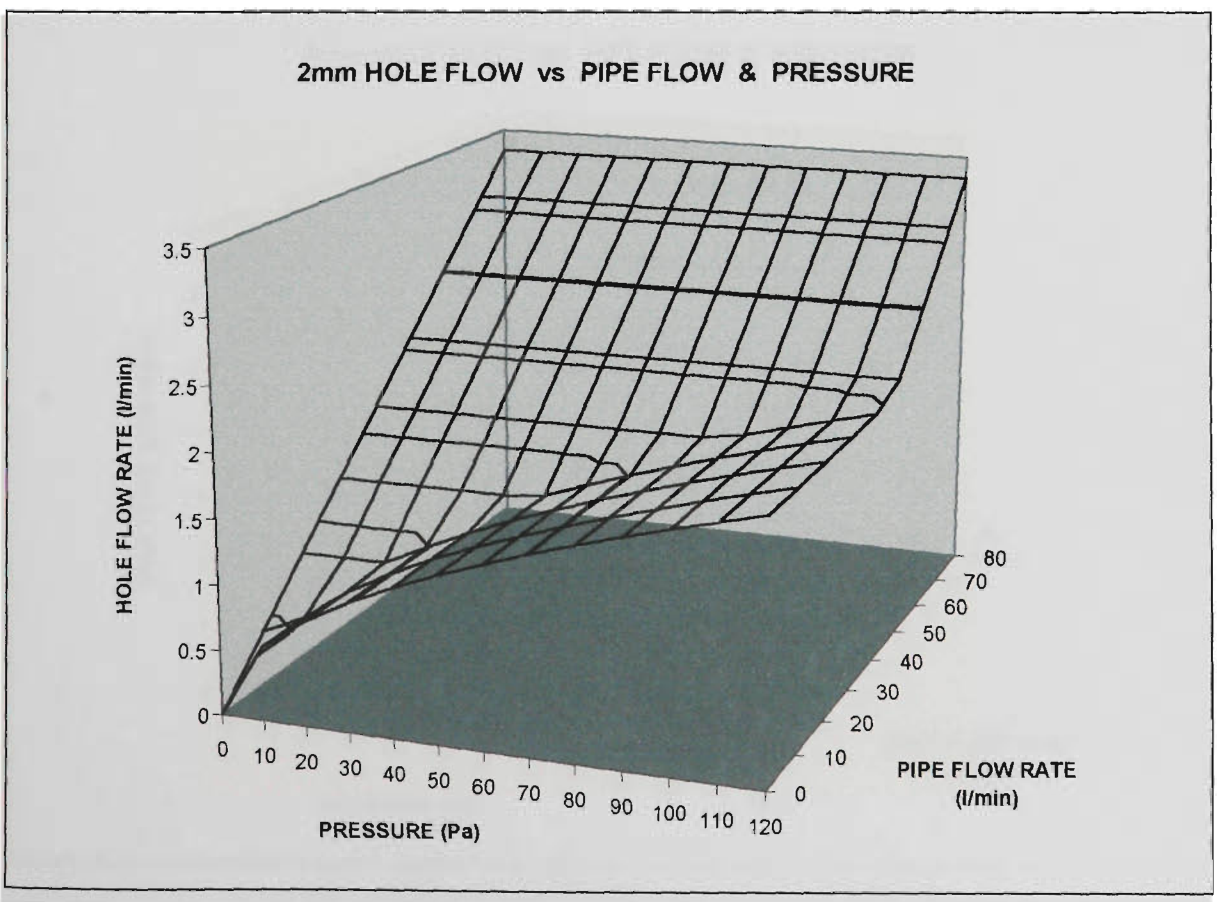

Figure 4.9 - Three-dimensional model for $2mm$ hole

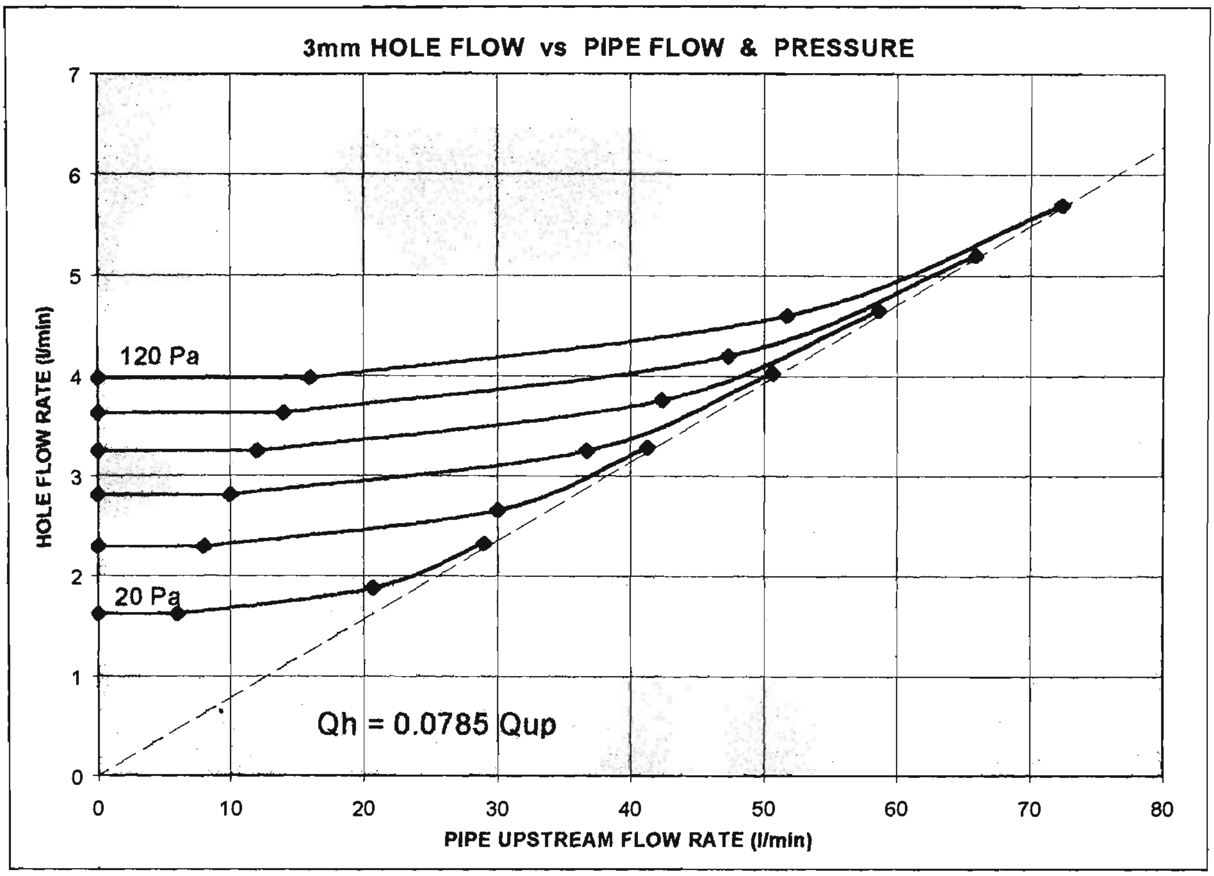

Figure 4.10 - $3mm$ hole flow with $21mm$ pipe

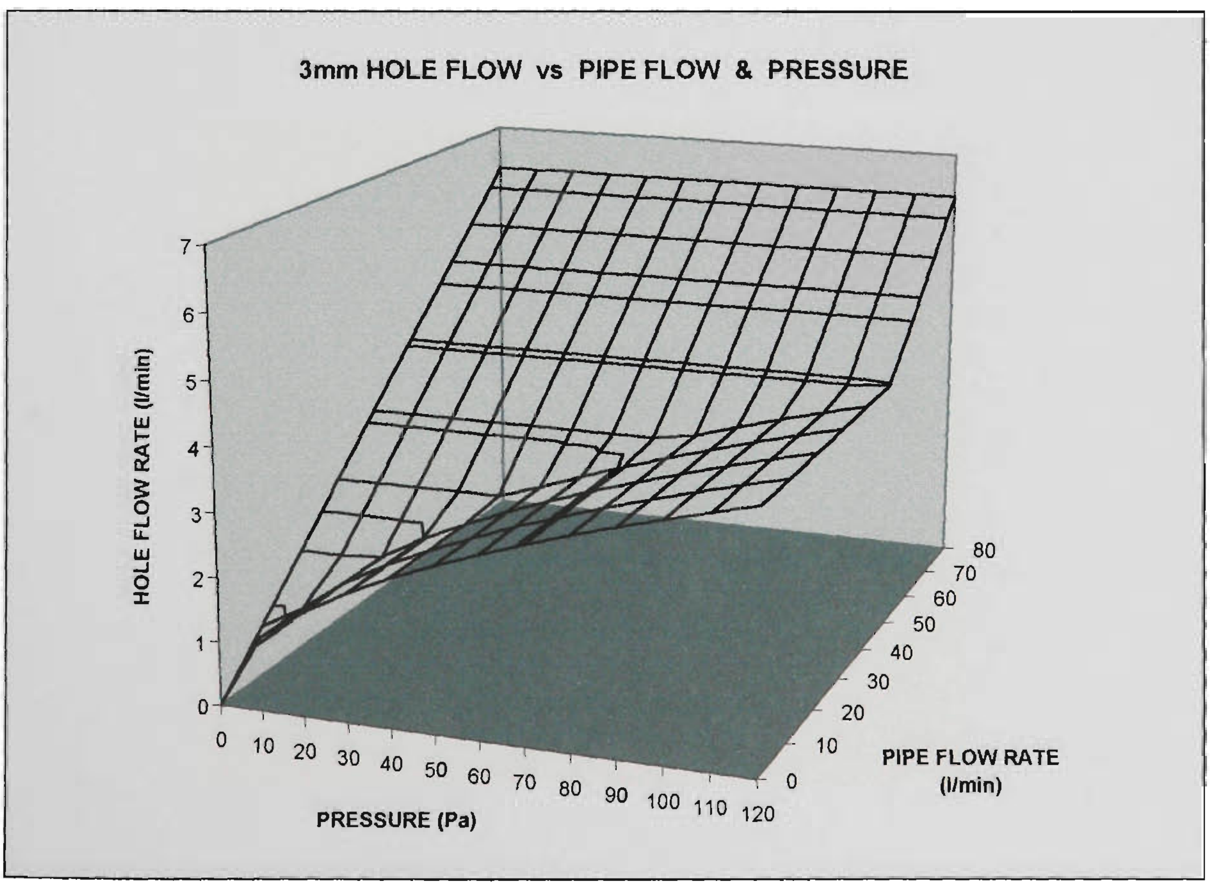

Figure 4.11 - Three-dimensional model for $3mm$ hole flow

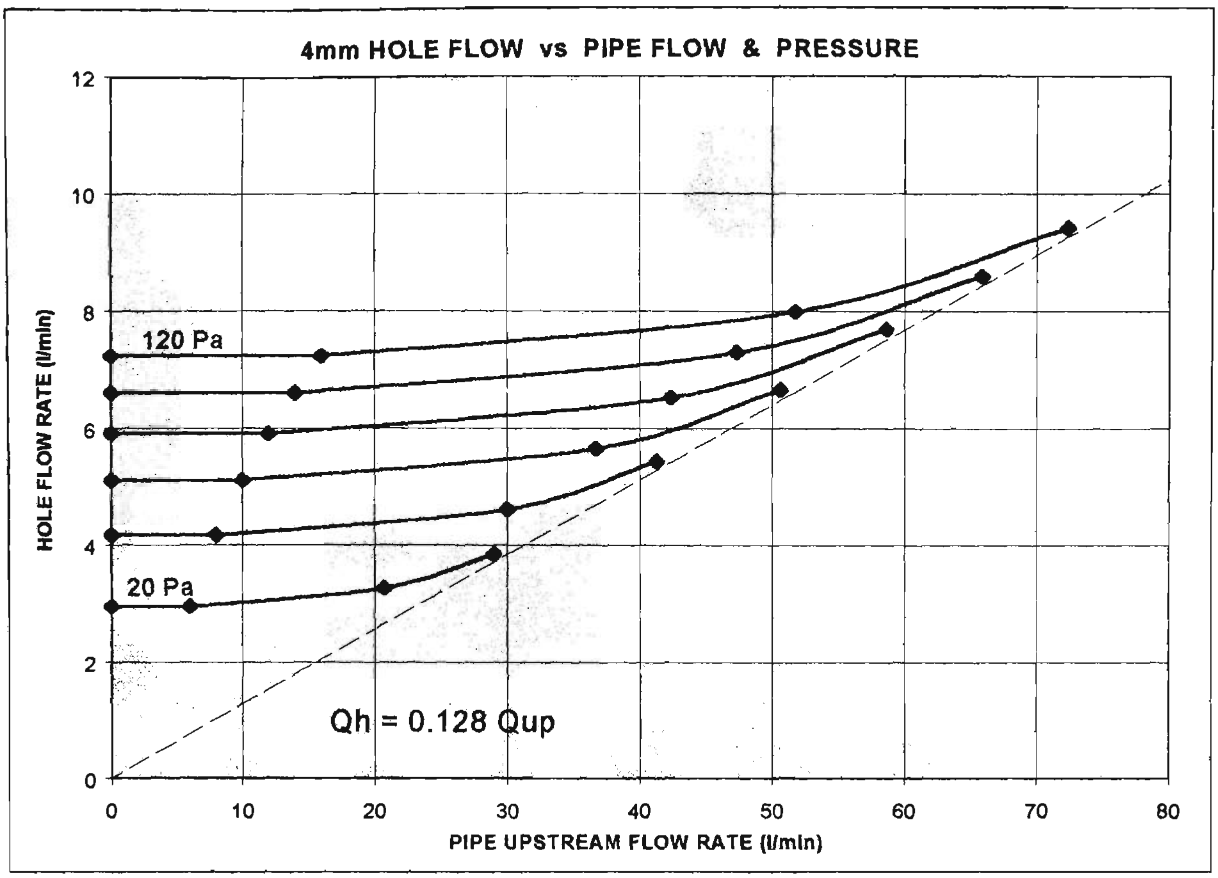

Figure 4.12 - $4mm$ hole flow with $21mm$ pipe

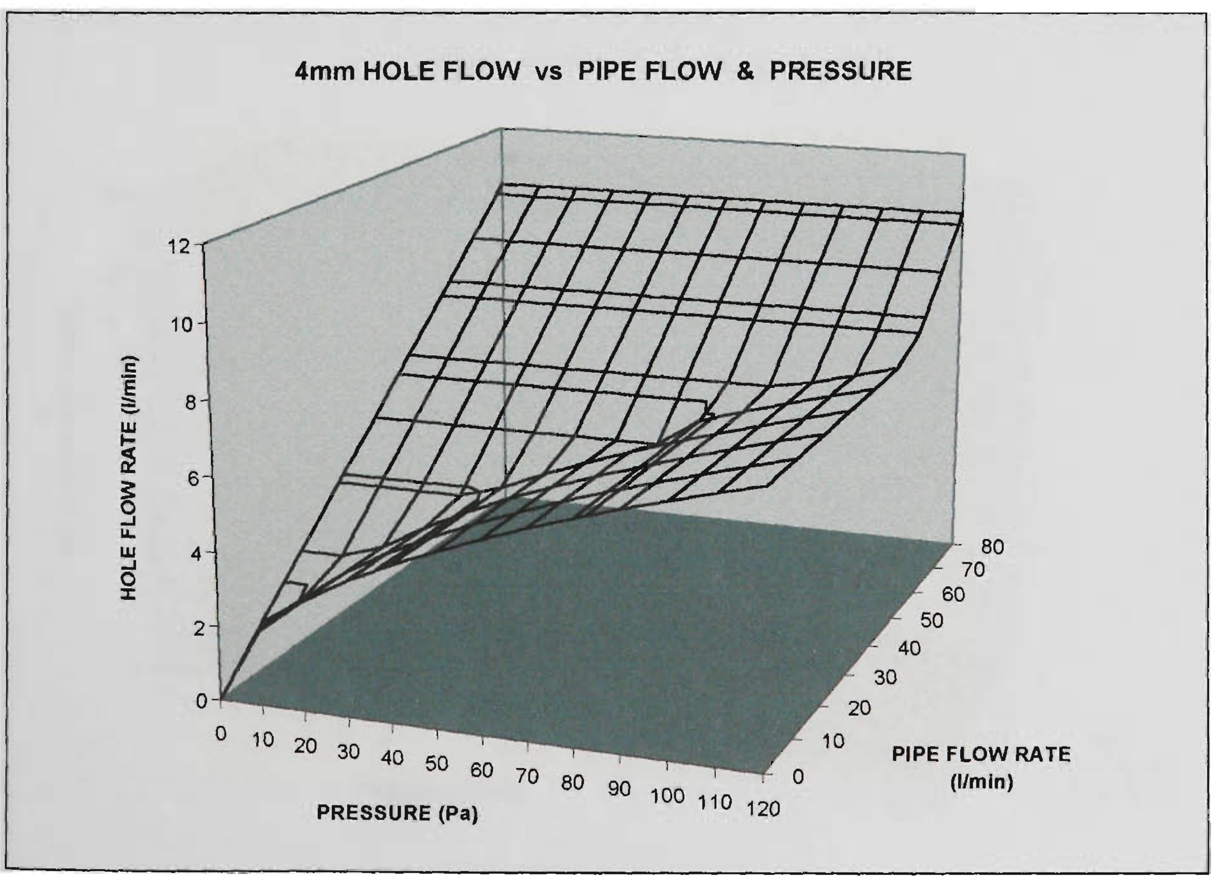

Figure 4.13 - Three-dimensional model of $4mm$ hole flow

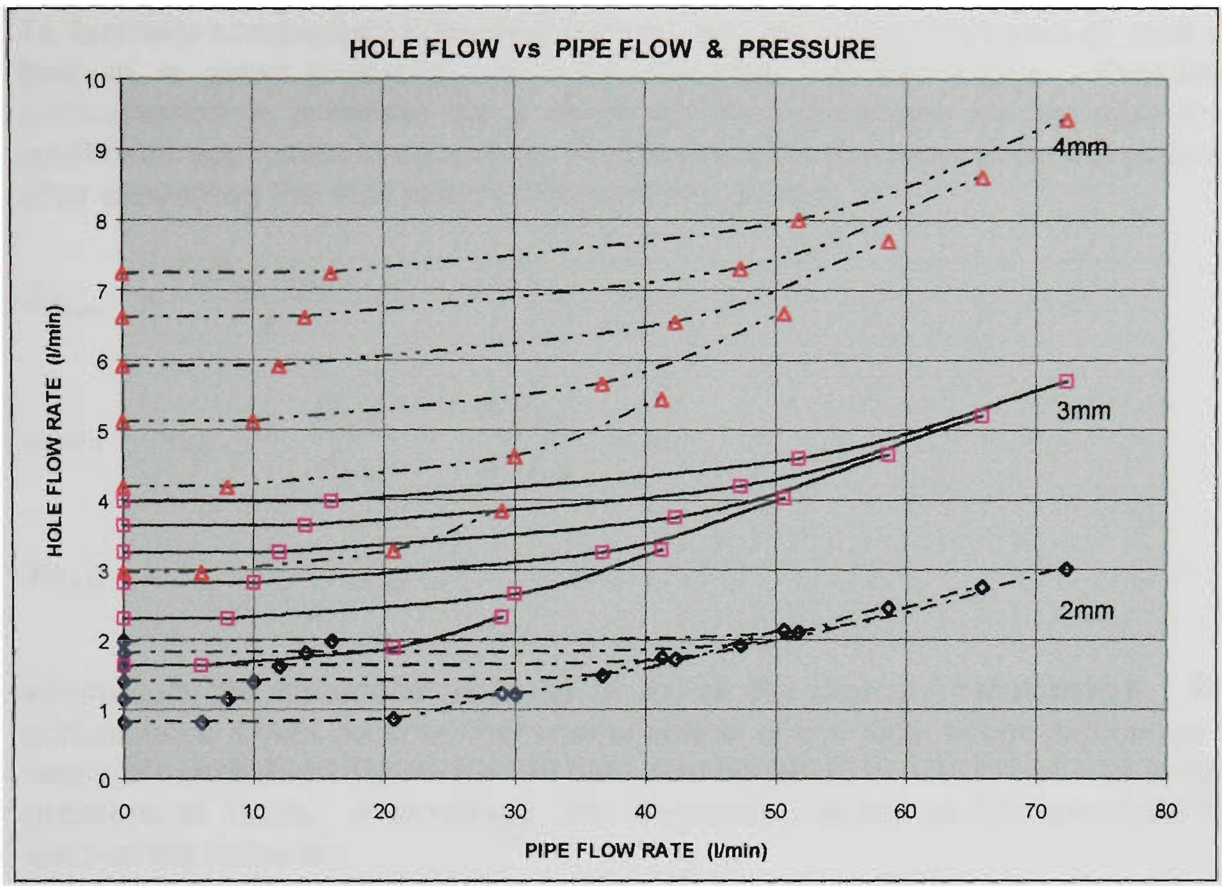

Figure 4.14 - Combined graphs of hole flow rates

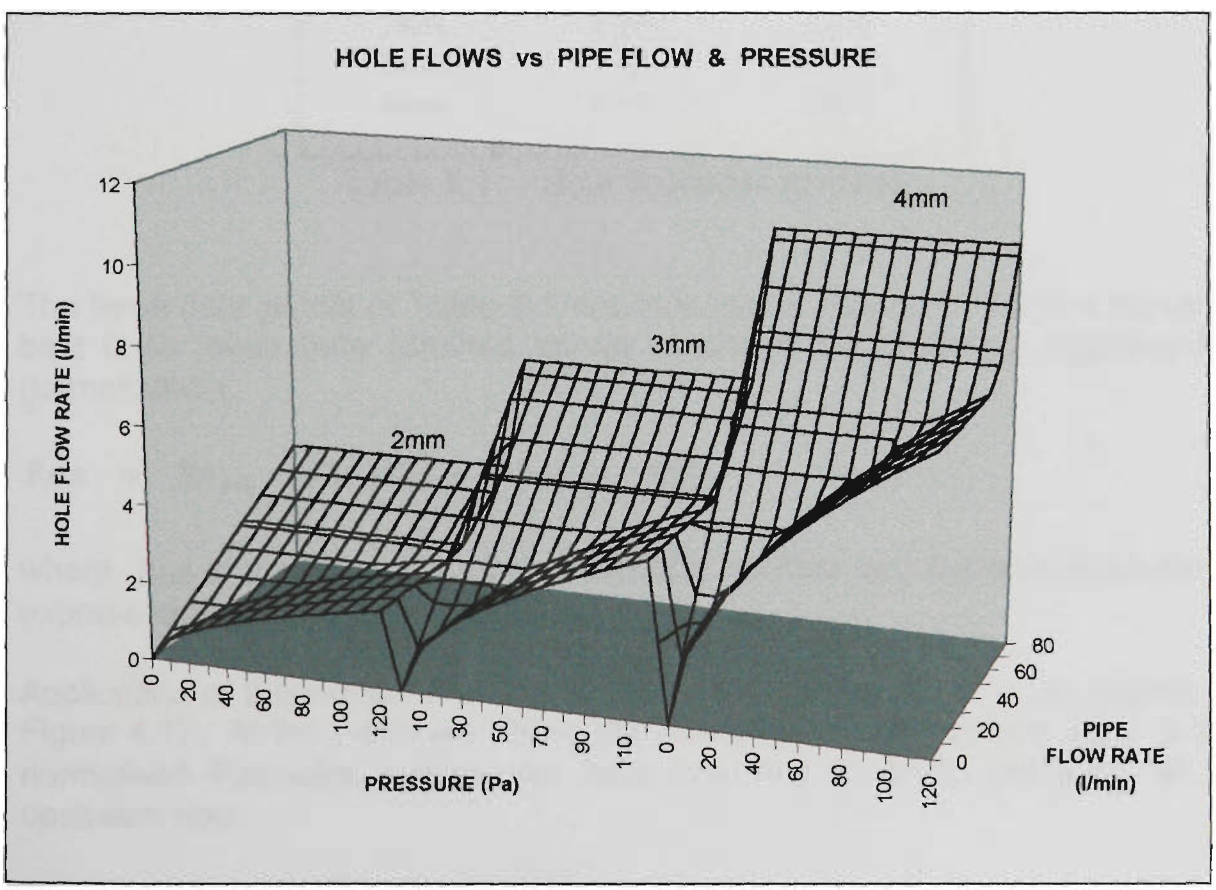

Figure 4.15 - Three-dimensional comparison of hole flows

To facilitate comparison it is necessary to normalise the three sets of data so that, at a given pressure, they are coincident at the y-axis. Typically, normalisation is achieved as a result of dividing-through by the hole flow coefficient applicable to each hole. In this case the divisors will be determined after converting the flow rates to Reynolds numbers:

$$\mathrm{Re}_{hole} = \frac{D_{hole}\, u_{hole}}{k}$$

$$where \quad u_{hole} = \frac{Q_{hole}}{A_{hole}} = \frac{4\, Q_{hole}}{\pi\, D_{hole}^2} \quad so:$$

$$\mathrm{Re}_{hole} = \frac{4}{k\, \pi\, D_{hole}}\, Q_{hole}$$

where k is the kinematic viscosity of air at the ambient temperature. For convenience it was decided that normalisation of the data, when expressed in terms of normalised Reynolds number, should result in a value of 1 at a hole pressure of 100Pa. Accordingly, the Reynolds number at this pressure for each of the holes is:

Hole	Q_{hole}	Re_{hole}
2*mm*	1.80	1274
3*mm*	3.63	1712
4*mm*	6.60	2335

Table 4.1 - Hole flow rates at 100Pa

The three data points of Table 4.1 are included in Figure 4.16 and a curve of best fit to these data (dashed curve) results in the following equation for normalisation:

$$\mathrm{Re}n = \mathrm{Re}_{hole} \,/\, \left(92.5\, D_{hole}^2 - 24.5\, D_{hole} + 953\right)$$

where $\mathrm{Re}n$ is the normalised hole Reynolds number and the hole diameter is expressed in millimetres.

Application of this equation to the data of Figure 4.14 results in the graphs of Figure 4.17. At the y-axis we obtain the following equation where $\mathrm{Re}n_0$ is the normalised Reynolds number for hole flow due to static pressure, at nil upstream flow.

$$\mathrm{Re}n_0 = \mathrm{Re}_{hole0} \,/\, \left(92.5\, D_{hole}^2 - 24.5\, D_{hole} + 953\right)$$

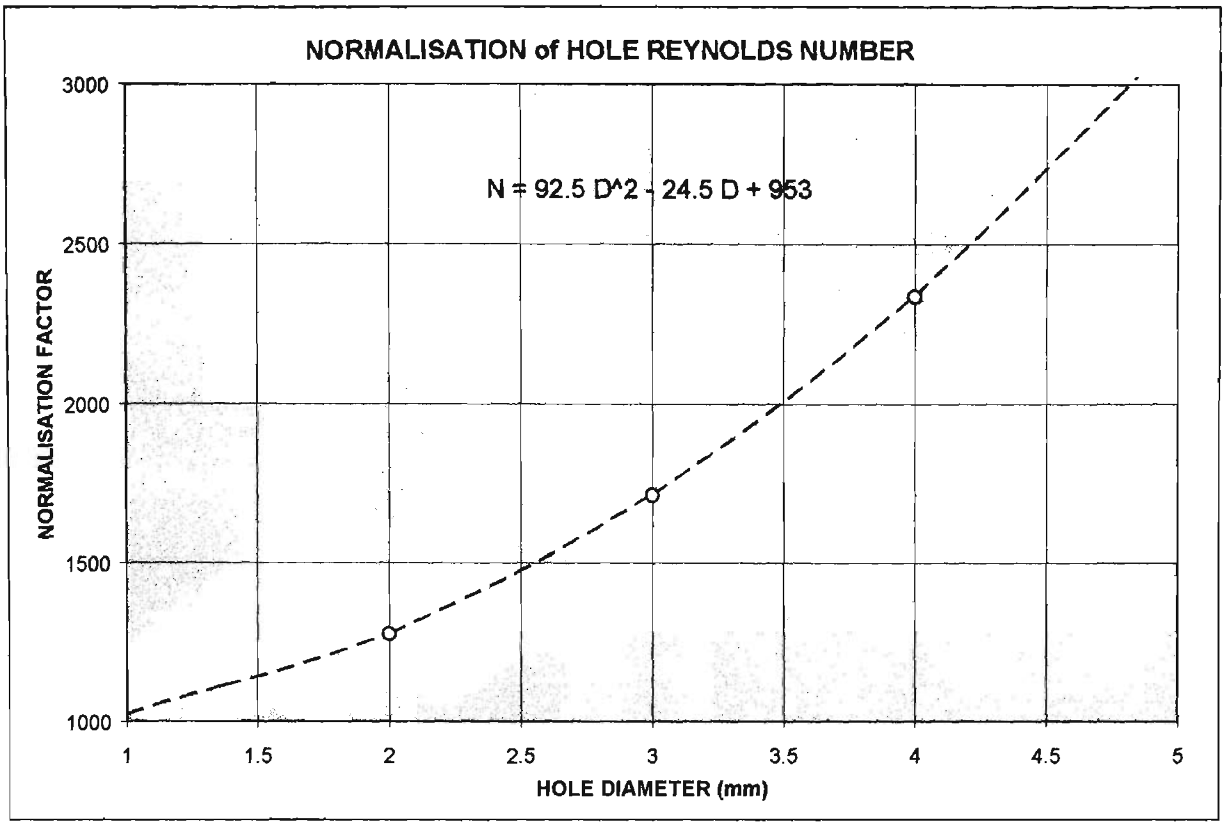

Figure 4.16 - Determination of normalisation factor

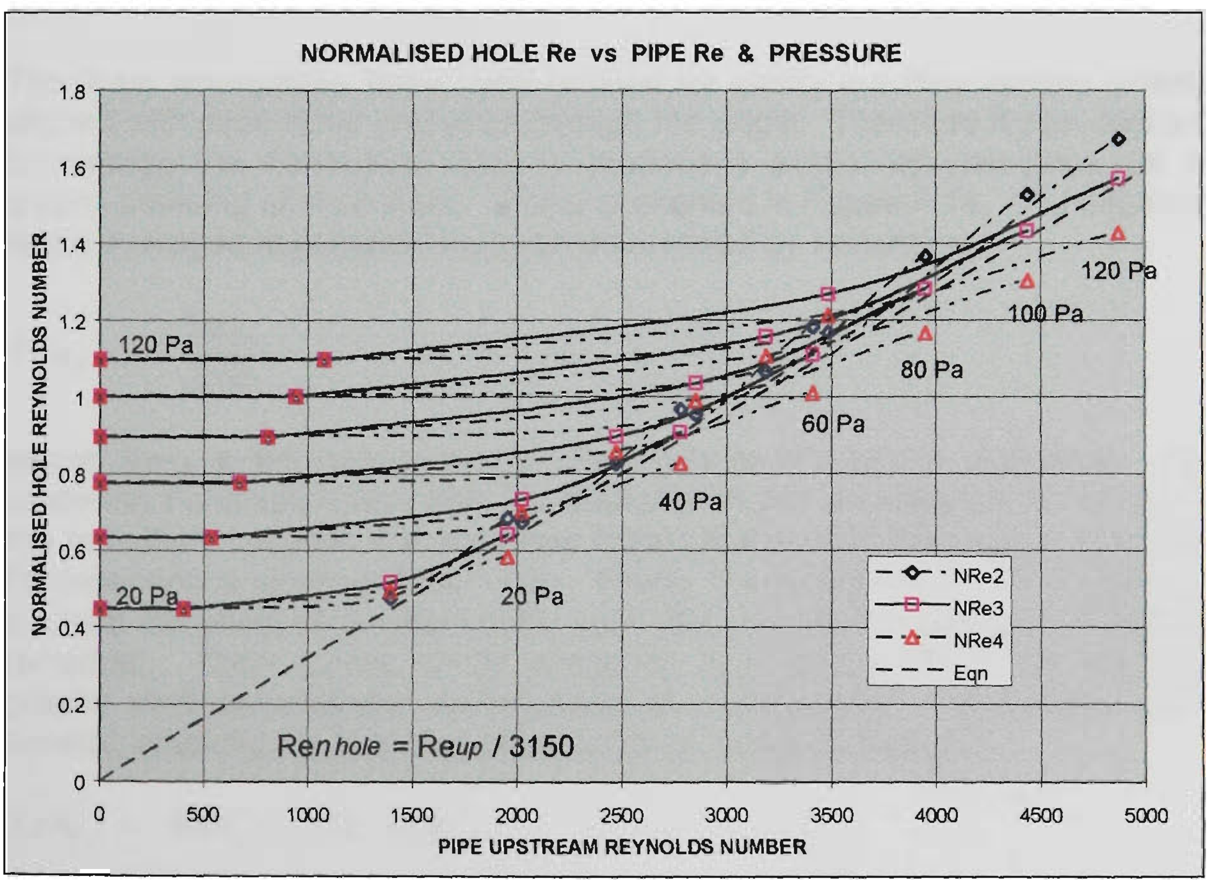

Figure 4.17 - Normalised combined hole flows

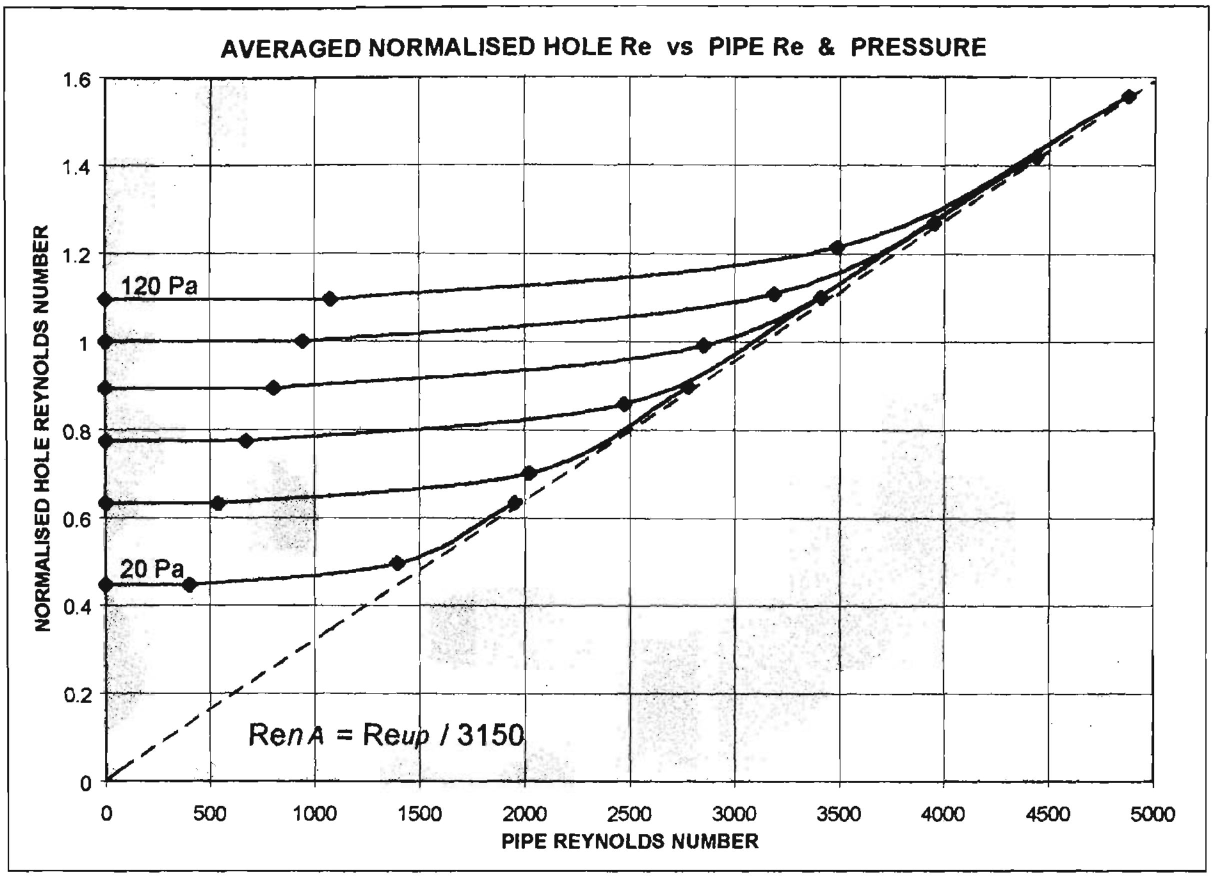

Figure 4.18 - Averaged normalised hole Reynolds number

The three asymptotes have been omitted for clarity but they remain closely aligned with each-other and pass through the origin. Therefore it was decided to average the normalised data to produce a single representative set of graphs covering all hole sizes. This is presented in Figure 4.18. The equation to the averaged asymptote has been determined by inspection :

$$\mathrm{Re}n_A = \frac{\mathrm{Re}_{up}}{3150}$$

where $\mathrm{Re}n_A$ is the normalised hole Reynolds number at the asymptote. For modelling purposes it was also felt desirable to find an equation to represent the transition, between the hole flow dependence upon pressure, through to its dependence upon upstream flow. Firstly, the above equation was used to subtract the effect of the asymptote such that only the transitional component remained. Then curves, or for simplicity, lines of best fit to the resulting graphs were ascertained, as indicated on Figure 4.19. These lines were parallel, enabling the following equation to be applied generally:

$$\mathrm{Re}n_T = \mathrm{Re}n_0 - 2.85E\text{–}04\,\mathrm{Re}_{up} \geq 0$$

where $\mathrm{Re}n_T$ is the normalised Reynolds number component in the transition, which must be set greater than (or equal to) zero. The three components determining the hole Reynolds number have been isolated and for the complete model we simply sum the terms: $\mathrm{Re}n = \mathrm{Re}n_T + \mathrm{Re}n_A$

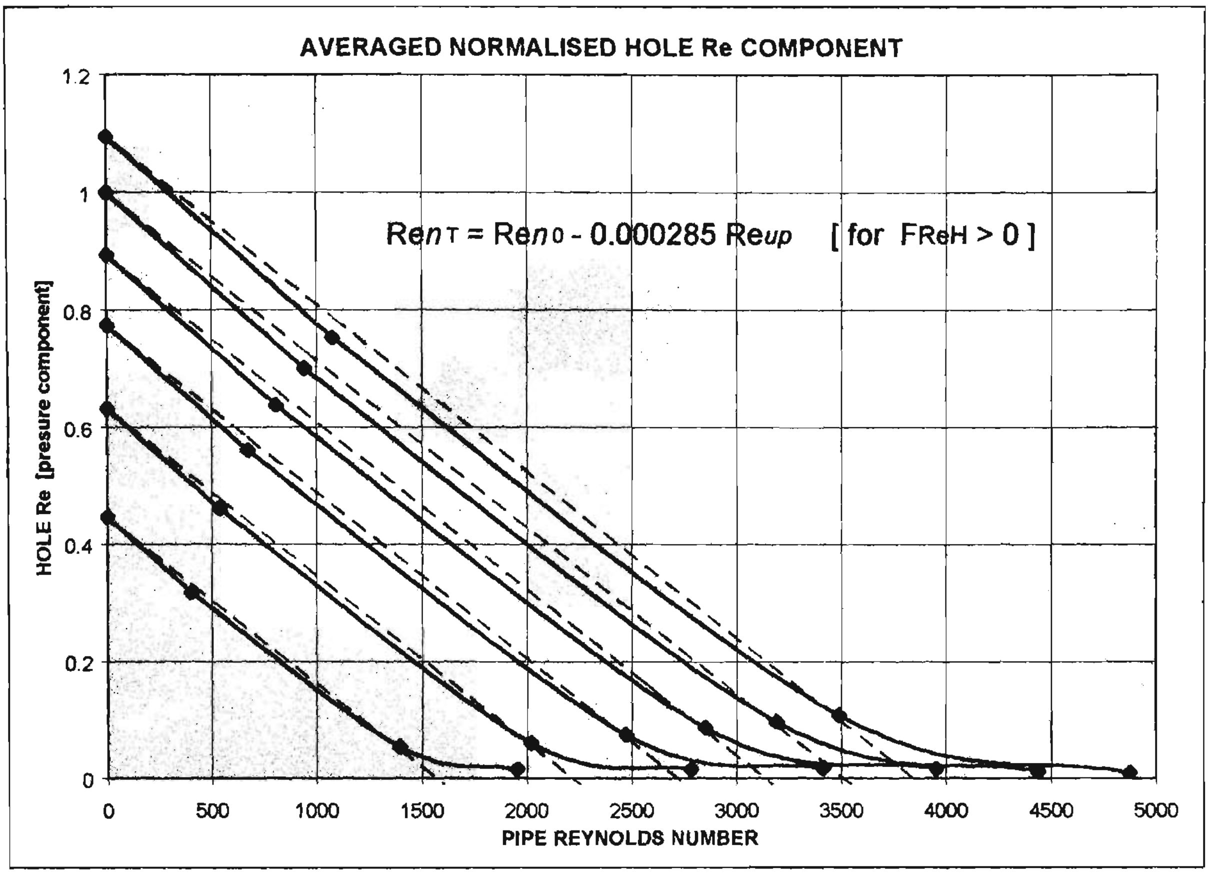

Figure 4.19 - Correction for the transition between hole flow dependence upon pressure, to its dependence upon upstream flow rate

Alternatively, the following equations will obtain the new hole Reynolds number adjusted for Ultraflow, where $\mathrm{Re}\,n_U$ is the larger of $\mathrm{Re}\,n_{AT}$ and $\mathrm{Re}\,n_A$:

$$\mathrm{Re}n_{AT} = \mathrm{Re}n_0 + 2.9E{-}05\mathrm{Re}_{up}$$

$$\mathrm{Re}_{holeU} = \mathrm{Re}n_U \left(92.5\,D_{hole}^2 - 24.5\,D_{hole} + 953\right)$$

4.5 FURTHER CONSIDERATION OF ERRORS

As previously discussed, the resolution and temperature stability of the instrumentation represented a significant potential source of error and it was decided to revisit the data to ascertain whether, despite confirmation by numerous experiments and the overall consistency of the data obtained, the Ultraflow phenomenon could be an artifact of the experimental method.

Figure 4.20 uses the data of Figure 4.12, which was chosen because the $4mm$ hole tends to exhibit the weakest trend toward Ultraflow. With a long term ambient temperature range of 22.5 ±2.5°C, it had been observed that the maximum span of zero-set drift was ±4mV. Given the voltmeter resolution of ±1mV, the data was amended in accordance with a ±5mV adjustment (corresponding to approximately ±1Pa change).

Upon inspection of the data, the main consequence of this artificial pressure adjustment is to alter the **upstream flow rate** values as determined from the calibration of the control orifice. This in turn significantly affects the calculated **hole flow rate**. In contrast, the impact on the graphs caused by altering the **hole pressure** proves to be negligible.

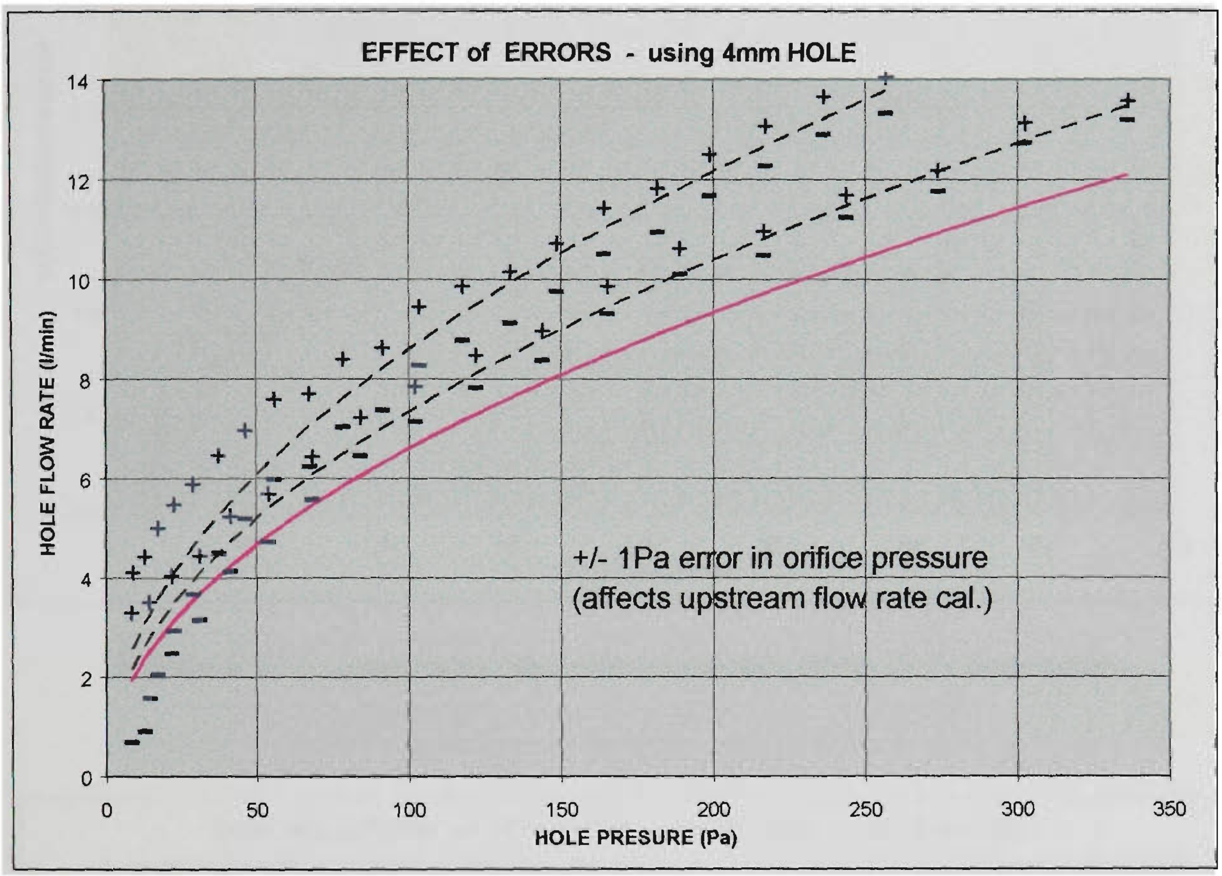

Figure 4.20 - The effect of ±1Pa error spread

Figure 4.20 retains the graphs of best fit to the original data, shown as dashed lines. The amended data points are scattered above and below these graphs (with each "+" point representing +1Pa and each "-" point representing -1Pa). As expected from the earlier discussion, the error band is largest at low pressures, while the data seems more reliable at higher pressures. It appears that the data at higher pressures could be extrapolated down to the low pressure region with reasonable confidence. Overall, the data spread is consistent with the curves of best fit previously obtained, so it does not appear likely that the observed Ultraflow phenomenon is an artifact.

4.6 ALTERNATIVE PIPE SIZES

There was lingering concern about the validity of the foregoing model so it was decided to select a modest change in pipe diameter in anticipation of obtaining similar results. It proved convenient to test a "heavy-duty" pipe of 19.8*mm* internal diameter (13% reduction in area) because it had the same outside diameter, and was easily fitted with the available 4-port pressure taps. The significance of its thicker pipe wall (3*mm*) required consideration.

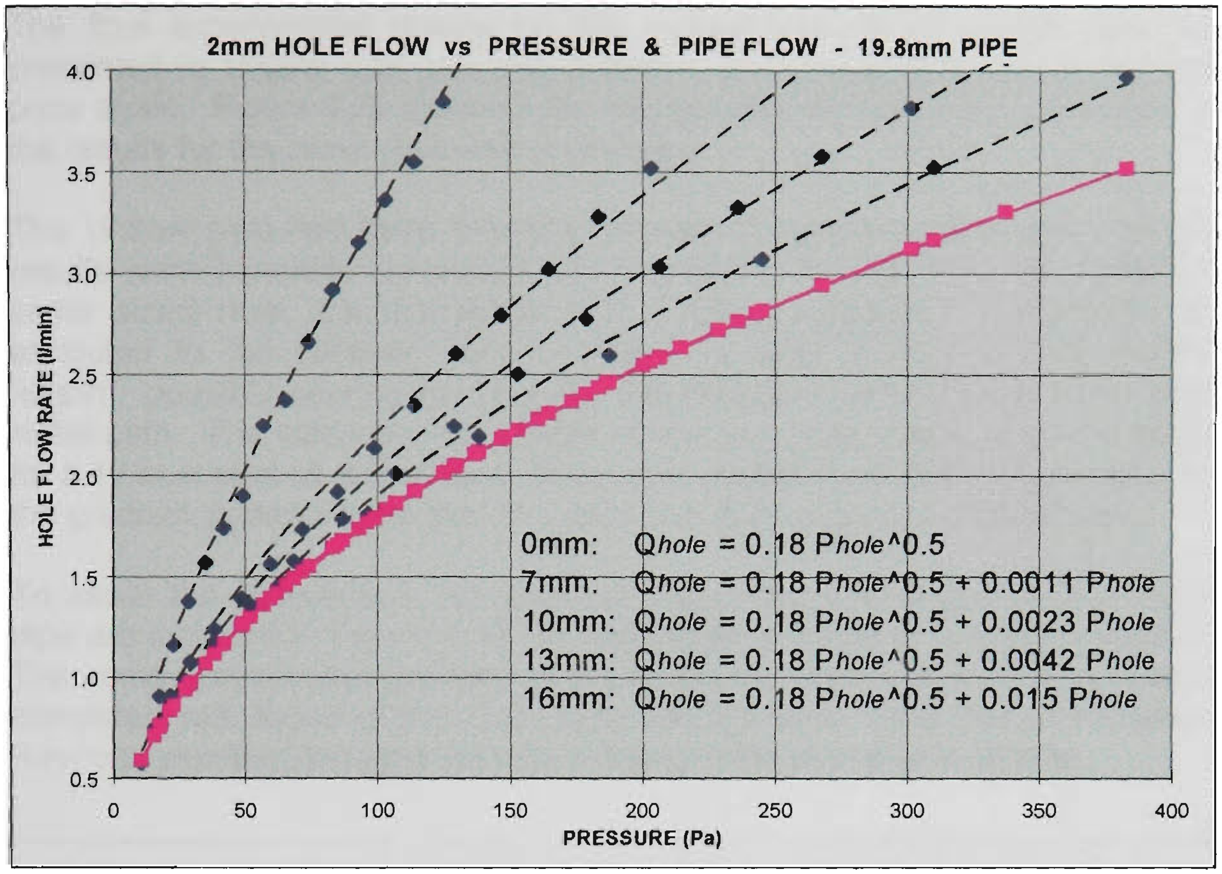

Figure 4.21 - $2mm$ hole flow with upstream flows in $19.8mm$ pipe

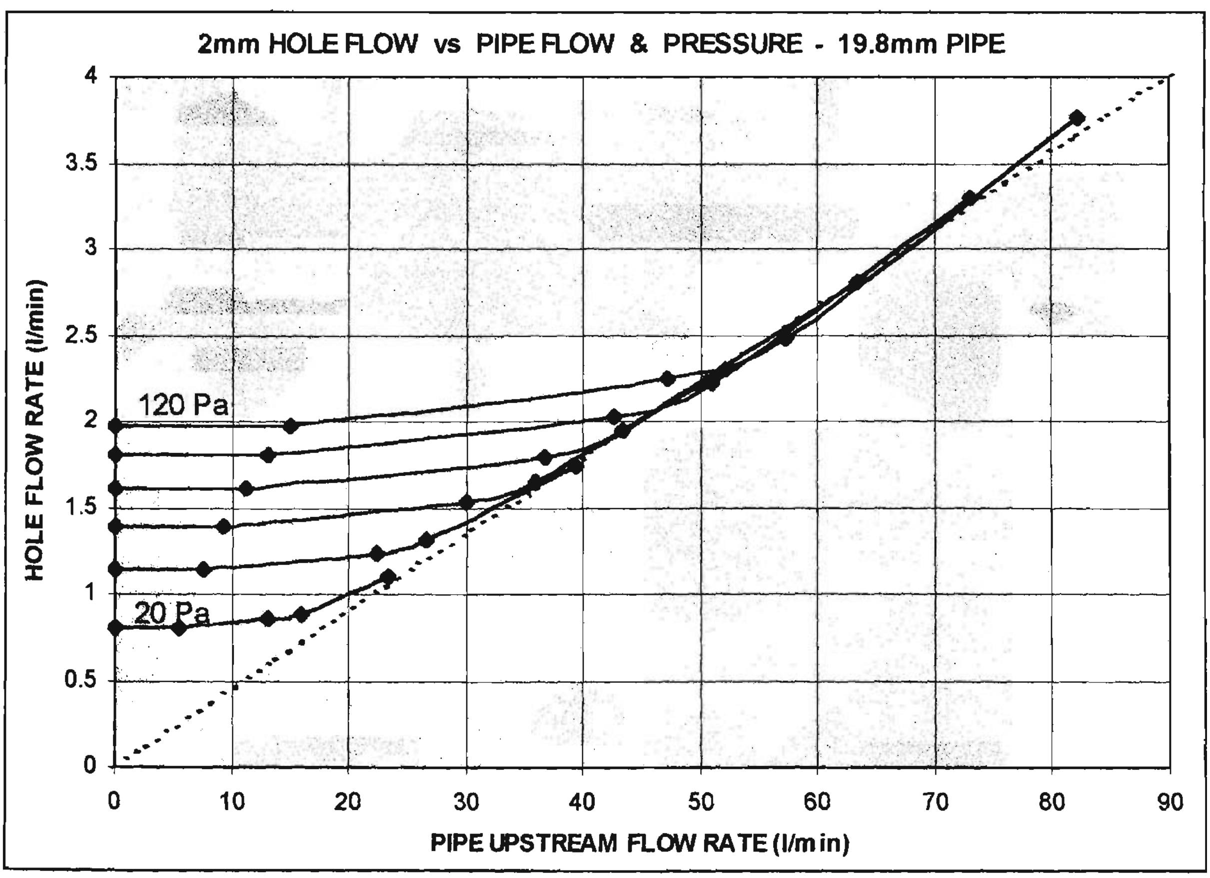

Figure 4.22 - $2mm$ hole flow in $19.8mm$ pipe

The final experimental results for the 19.8*mm* pipe using a 2*mm* hole are presented in Figure 4.21 and the Ultraflow phenomenon is clearly evident once again. Figure 4.22 presents the interpolated results which are similar to the results for the 21*mm* pipe with 2*mm* hole.

The 19.8*mm* pipe had been tested a number of times because, although the results were generally consistent with the results for the 21*mm* pipe with the same sized hole, the asymptote had a higher gradient. This could be attributed to the different wall thickness, causing a hole of 50% greater "depth", possibly serving to maintain the induction jet trajectory in a more radial path. The static flow coefficient of the 2*mm* hole proved to be the same for a 19.8*mm* pipe as it was for a 21*mm* pipe, so the most likely explanation for the gradient appears to be the 13% reduction in pipe cross-sectional area.

To assist the comparison, the previous results for a 2*mm* hole with a 21*mm* pipe are included in Figure 4.23, all expressed in terms of Reynolds number. The somewhat steeper gradient of the asymptote to the 19.8*mm* pipe graphs compared with those of the 21*mm* pipe can be seen. Note that at the same Reynolds number, the pipe velocity is higher if the diameter is smaller.

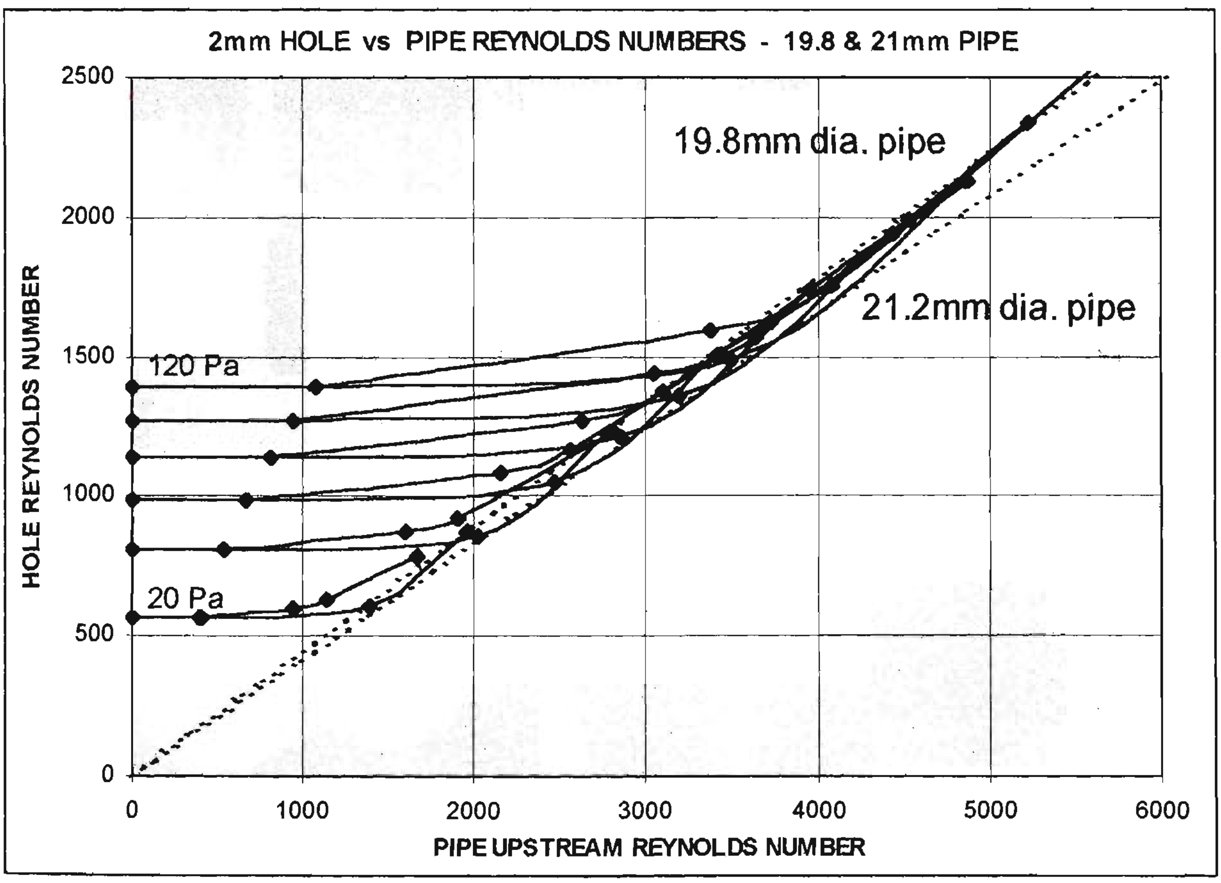

Figure 4.23 - Comparison of 19.8*mm* and 21*mm* pipe results

In order to verify the trend indicated by the 19.8*mm* pipe it was decided to investigate a pipe of significantly smaller diameter, namely 12.4*mm* (34% of the area). Figures 4.24 and 4.25 present the results that were obtained after several verifications.

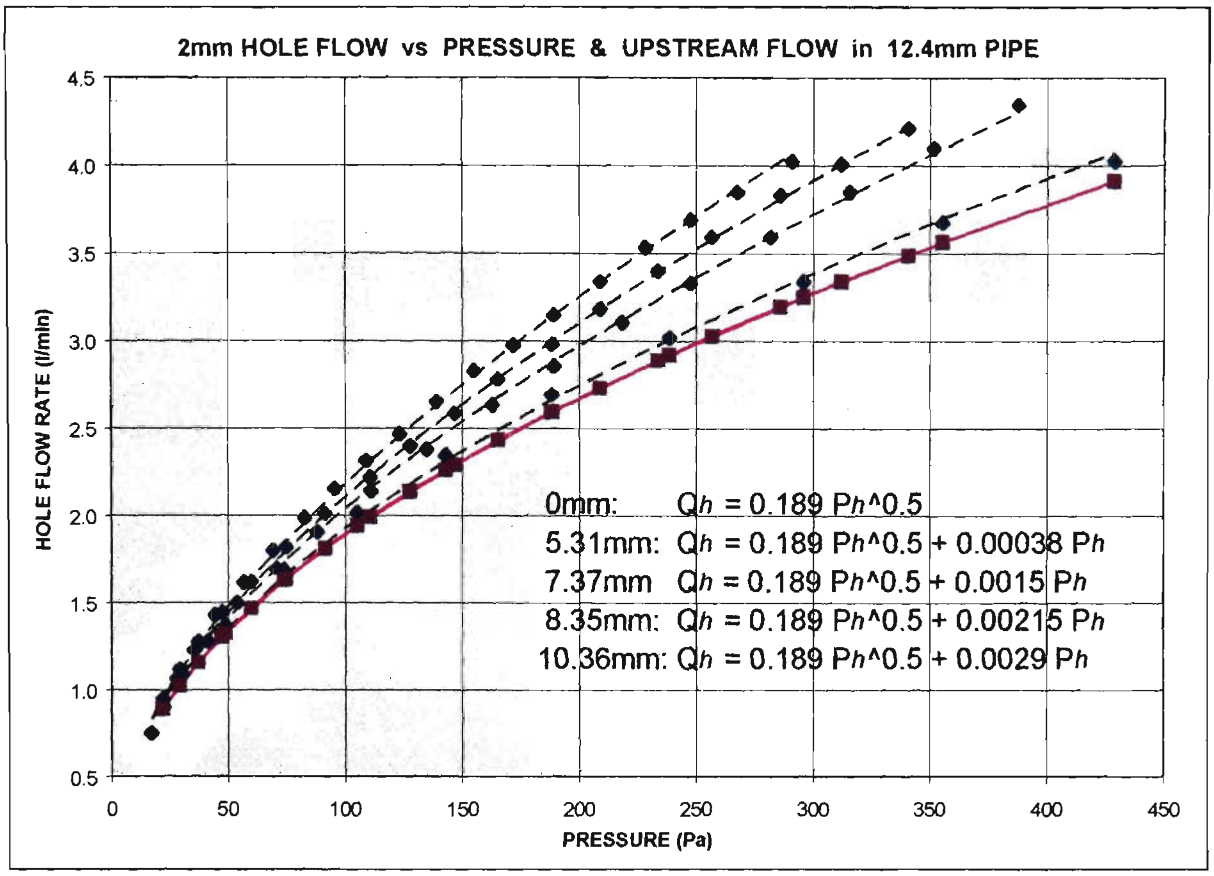

Figure 4.24 - $2mm$ hole flow with upstream flows in $12.4mm$ pipe

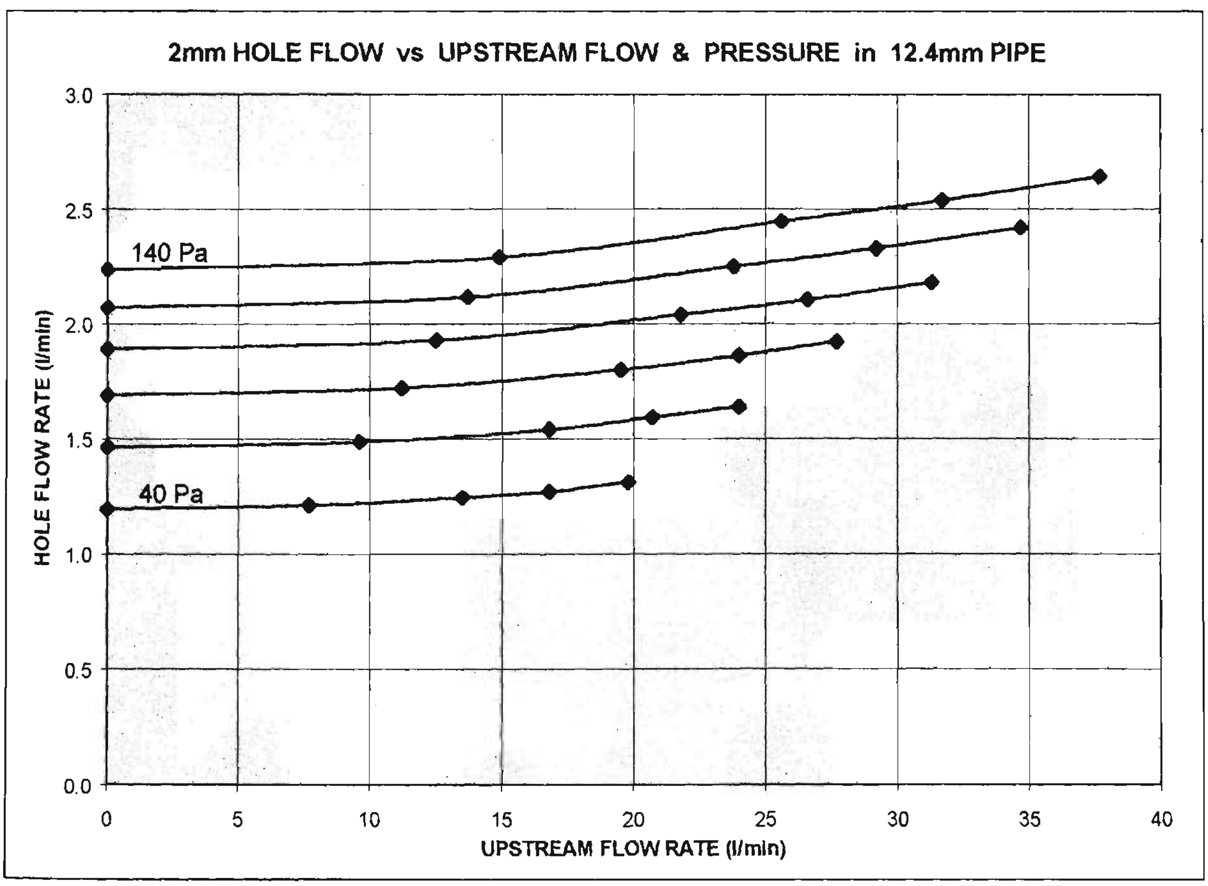

Figure 4.25 - $2mm$ hole flow in $12.4mm$ pipe

It is clear from the results of the 12.4*mm* pipe that the Ultraflow effect is present, but the transition to a steeply rising asymptote seems deferred to higher flow rates than were possible to generate with the apparatus. This is also likely to be the case in the field.

4.7 STATIC HOLE FLOW COEFFICIENT

The above consideration of the significance of pipe diameter leads us back to the suggestion in Section 4.1, that the head loss incurred by air while flowing through a sampling hole of given diameter within a pipe wall, should reduce if it were to discharge into a pipe of smaller diameter. This is because the air, after passing through the hole, would be more confined within a smaller pipe, diffusing to a lesser extent and losing less energy. In order to quantify this effect an experiment was conducted to determine the coefficient applicable to 2, 3 and 4 *mm* holes in all available pipes, from 12.4 to 26 *mm* internal diameter.

In each case the static hole coefficient (i.e. with nil upstream flow) was obtained by using a 1*m* length of each test pipe in the nominated diameter, with the far end blocked and a sampling hole drilled 5*dia* "downstream" of the blocked end. A pressure tapping was made on the meridian of the sampling hole and at 90° radially to it. Curves of best fit to the data were used to determine the static hole flow coefficient in each case.

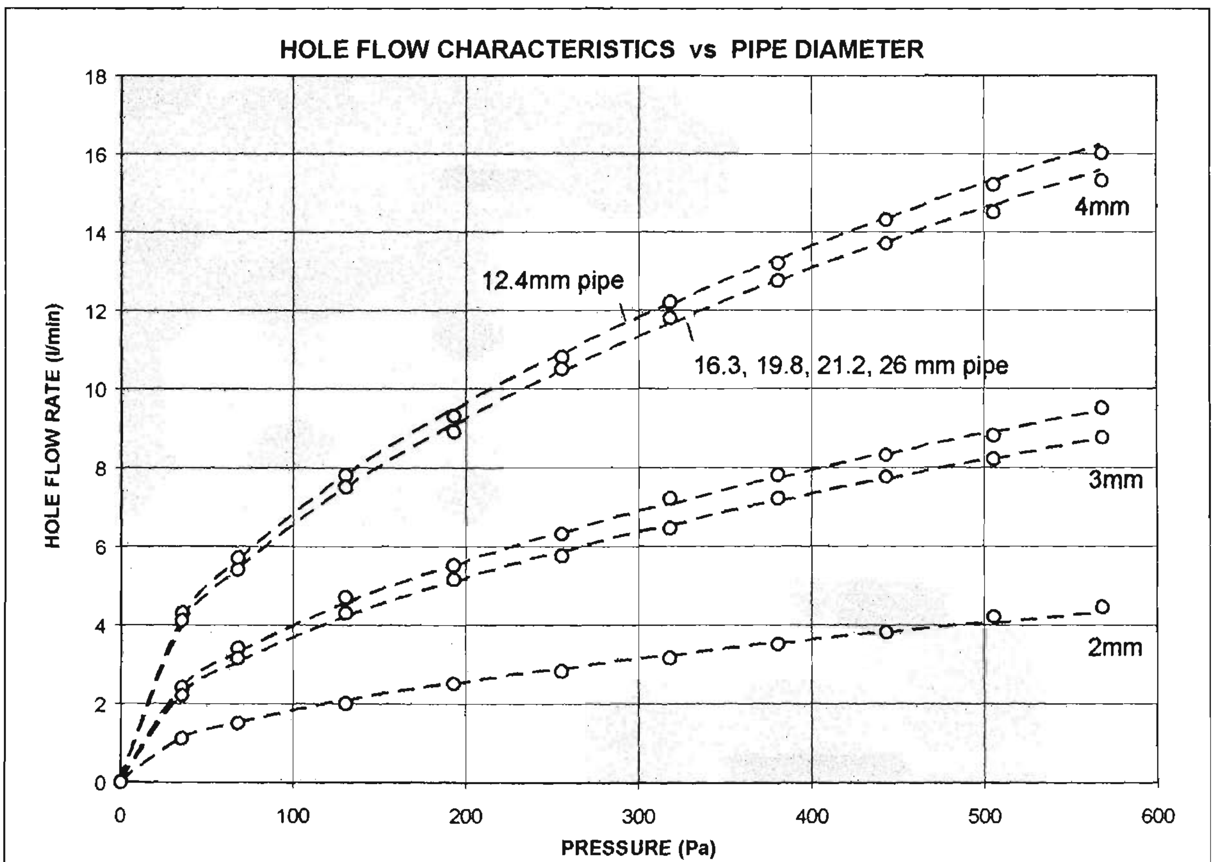

Figure 4.26 - Hole flow characteristics with different pipe diameters

The theoretical upper limit to the value of the hole flow coefficient would occur in the situation where the pipe has the same diameter as the hole. This is equivalent to the case of a large reservoir discharging into a pipe with a sharp transition. It is known that the head loss or pressure drop are given by the following equations, in which the hole flow coefficient, $C_h = 0.5$:

$$H = C_h \frac{u^2}{2g} \quad or \quad \Delta P = C_h \, \rho \frac{u^2}{2} = C_h \frac{\rho}{2} \left(\frac{Q_{hole}}{A_{hole}} \right)^2$$

So therefore:

$$Q_{hole} = A_{hole} \left(\frac{2 \, \Delta P}{C_h \, \rho} \right)^{\frac{1}{2}} = \frac{\sqrt{2} \, A_{hole}}{\sqrt{C_h \, \rho}} \sqrt{\Delta P} = K_{hole} \sqrt{\Delta P}$$

$$K_{hole} = \frac{\sqrt{2} \, A_{hole}}{\sqrt{C_h \, \rho}} = \frac{\sqrt{2} \, \pi \, D_{hole}^2}{4 \sqrt{C_h \, \rho}} = \frac{\pi \, D_{hole}^2}{2 \sqrt{2 \, C_h \, \rho}} = \frac{\pi \, D_{hole}^2}{2 \sqrt{\rho}}$$

Based upon the curves of fit to the data of Figure 4.26 and application of the above equation in the limit case, the dependency of the hole flow coefficient for each sampling hole has been determined as presented in Figure 4.27

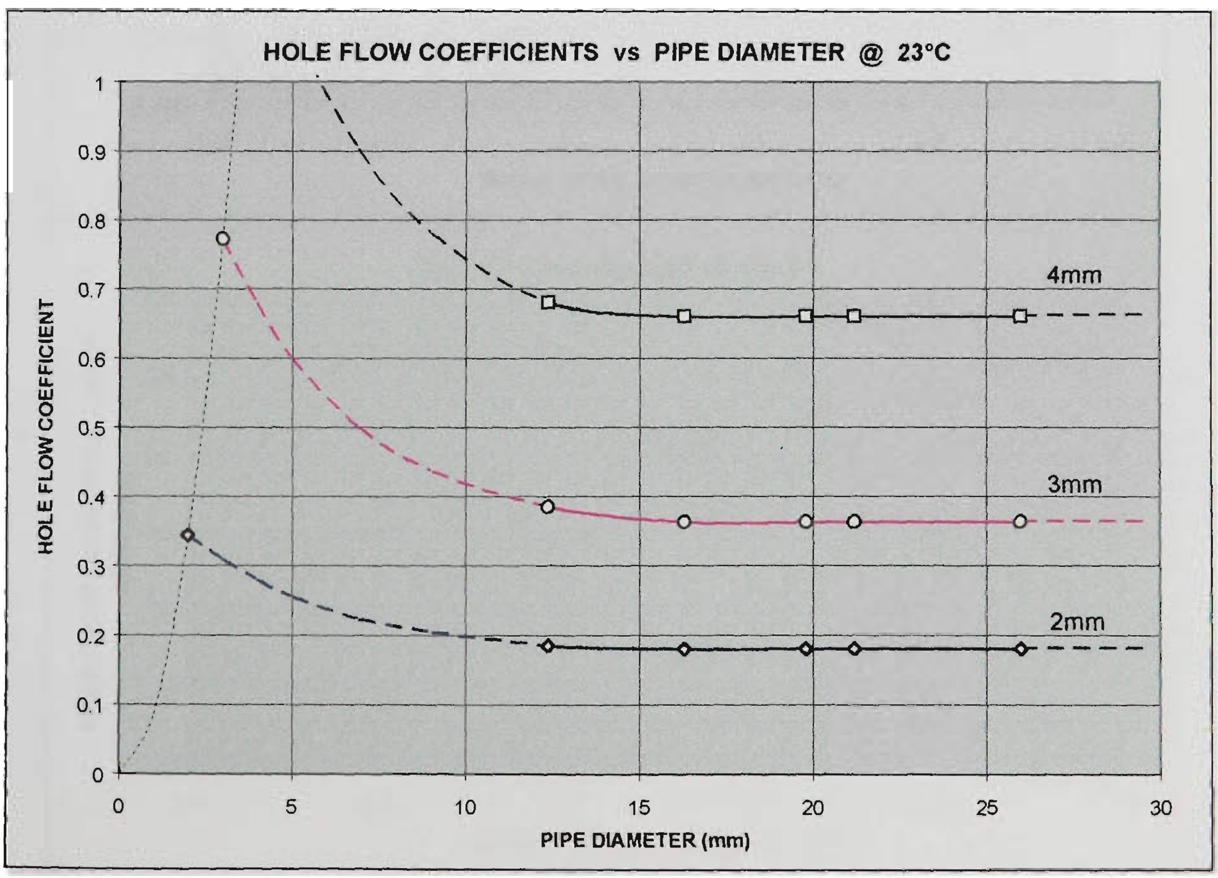

Figure 4.27 - Hole flow coefficient versus pipe diameter

The hole flow coefficient is independent of pipe diameter above 15*mm*. An attempt was made to determine a dimensionless coefficient applicable below 15*mm*, by dividing the hole diameter into the pipe diameter and plotting the hole flow coefficient. Figure 4.28 (a) shows that the resulting graphs do not converge although the curved regions of Figure 4.27 have become linear and are broadly directed at the origin.

In Figure 4.28 (b) the hole coefficient has been divided by the hole cross-sectional area (as measured in m^2 for convenience, however, this is not dimensionless) and these graphs converge only at the point where the hole diameter equals the pipe diameter. Attempts to produce a dimensionless coefficient were unsuccessful, so this course of investigation was abandoned.

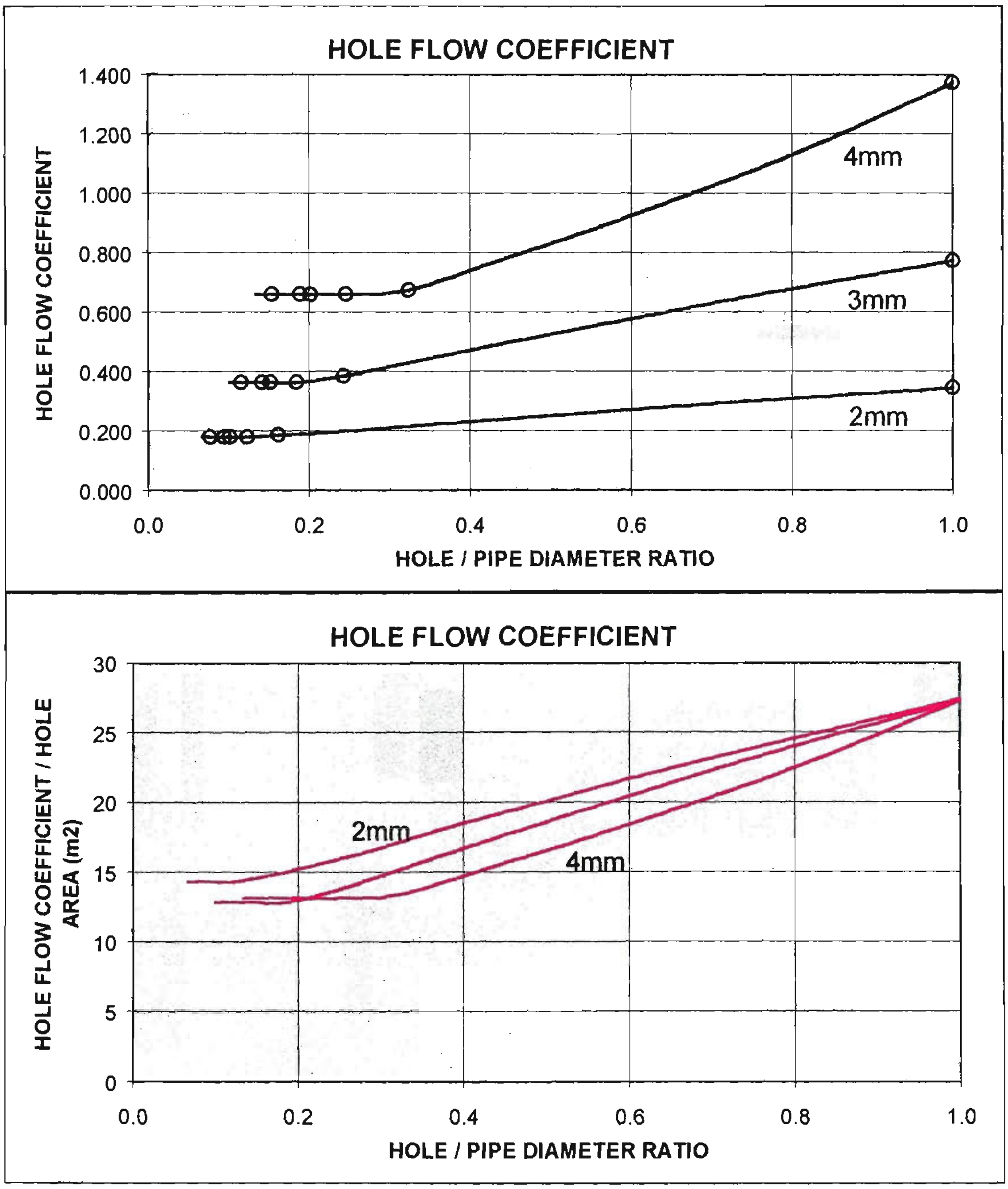

Figure 4.28 (a) and (b) - Attempts to determine a dimensionless hole flow coefficient for pipe diameters below 15*mm*

Importantly Figure 4.27 shows that, even with the largest hole size used, the influence of pipe size upon the hole flow coefficient is not significant above $15mm$ diameter. Therefore in the great majority of applications, within the computer model it will not be necessary to make a correction to the coefficients that were determined in relation to Figure 4.2.

4.8 END VENT CHARACTERISTICS

The sampling hole furthest from the detector is known as the end vent. It is different from all other holes because there is no upstream flow to consider, and hence no question of Ultraflow. More importantly, the vent governs the flow rate in the furthest segment of pipe. Assuming all pipe segments have the same diameter, then the air velocity in the furthest segment is relatively slow compared with all other segments, because segments closer to the detector have a higher flow rate resulting from the flow contribution from a number of upstream holes.

For example, in a perfectly balanced system the velocity in the second-furthest segment is twice that of the furthest, while the velocity in the third-furthest segment is three times, and so on. Therefore the overall (worst case) smoke transport time is most significantly affected by the flow rate in the furthest segment.

One way to maximise the velocity in the furthest segment is to reduce the pipe diameter. However, to reduce the cross-sectional area by a factor of (say) three or four, would incur significant pressure drop which would cause a reduction in the vent flow rate, somewhat defeating the purpose.

The preferred method in the field has been to retain a uniform pipe diameter (which is simpler to install and avoids potentially lossy reduction fittings), and to increase the size of the vent. This causes a relatively larger flow rate in the furthest pipe segment which reduces the overall smoke transport time. The disadvantage is that the vent provides a higher effective smoke sensitivity at that location because smoke entering the vent suffers less dilution than smoke entering any other single hole. However, given that the vent is also the most distant sampling point, involving the longest delay, the higher sensitivity is seen as a form of compensation for the delay.

Additionally, the vent is physically different from a regular sampling hole. It is commonly drilled into the pipe end cap, which has flat surfaces and the hole is coaxial with the pipe centreline. By contrast, a sampling hole forms a saddle shape due to the pipe wall curvature and is drilled at a right angle to the pipe centreline, such that the flow stream must turn through 90° on entering the pipe. The thickness of the materials drilled are also different.

An experiment was conducted using a test pipe of $21.2mm$ internal diameter. The pressure differential (measured five diameters downstream of the vent), was set to various levels within an accuracy of 0.25Pa and the vent flow rate was measured using the same instrumentation as previously described. Measurements were taken using a wide range of vent sizes, in greater detail than was the case for sampling holes, because of the critical nature of this one item in determining the transport time within the system, and because vents tend to be significantly larger than other sampling holes.

The results of the experiment are presented in Figure 4.29, wherein graphs of the equations of best fit to the data have been included (dashed curves). The anticipated curve applicable to a $7mm$ vent has been included (dotted). Figure 4.30 presents similar results taken in the case of a $16.3mm$ test pipe while Figure 4.31presents the results taken in the case of a $12.4mm$ test pipe.

The flow coefficients obtained from the equations of fit to the data in Figures 4.29, 4.30 and 4.31 have been graphed versus vent diameter, as presented in Figure 4.32. It can be seen that there is a negligible departure between the characteristics applicable to the 21.2 and 16.3 mm pipes. However, in the case of the $12.4mm$ pipe, it is clear that a higher flow rate occurs at any given pressure, especially at larger vent diameters. Equations describing curves of best fit to the vent flow coefficients are:

$$12.4mm \text{ pipe: } K_{vent} = 0.0479\,D_{vent}^{2} - 0.0065\,D_{vent}$$

$$21.2mm \text{ pipe: } K_{vent} = 0.0479\,D_{vent}^{2} - 0.0127\,D_{vent}$$

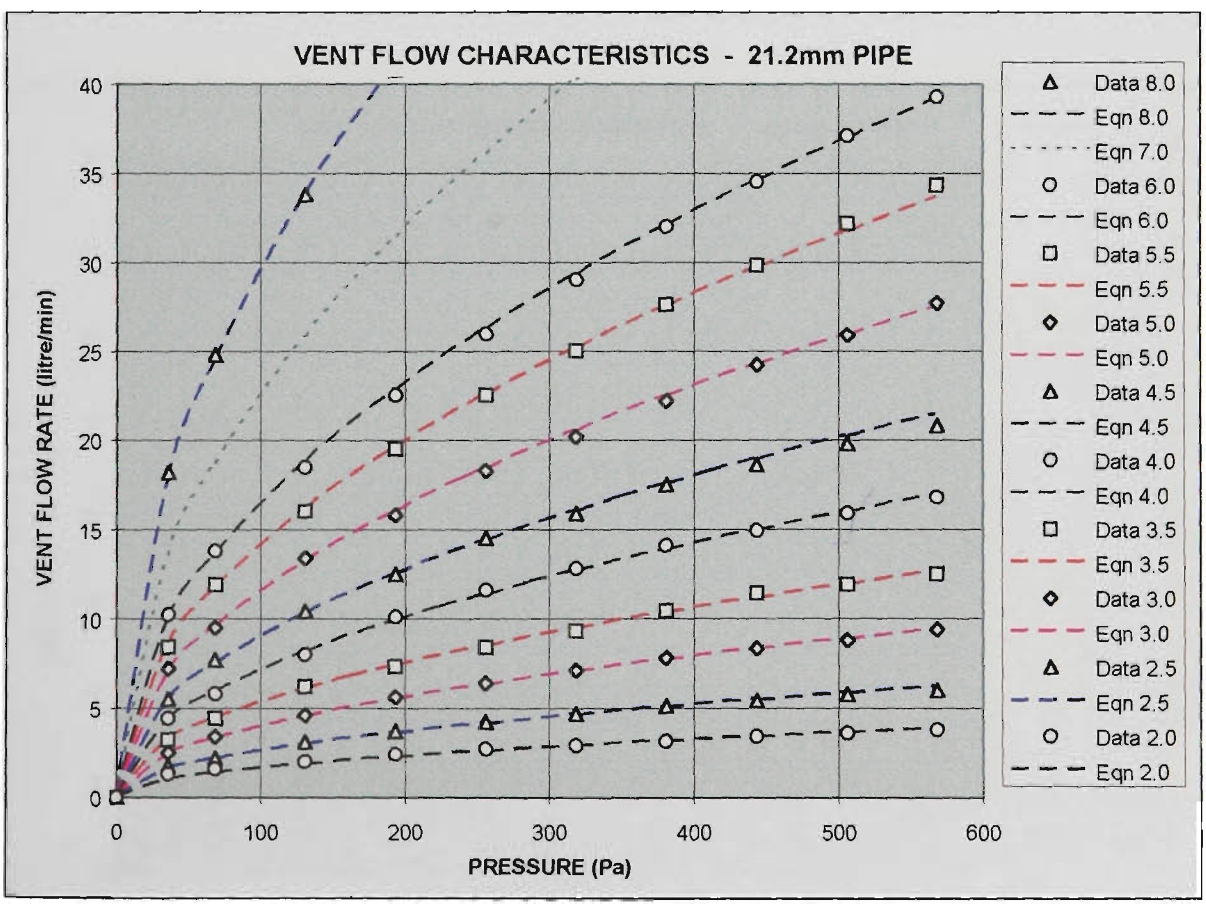

Figure 4.29 - Characteristics of end vents in $21.2mm$ pipe

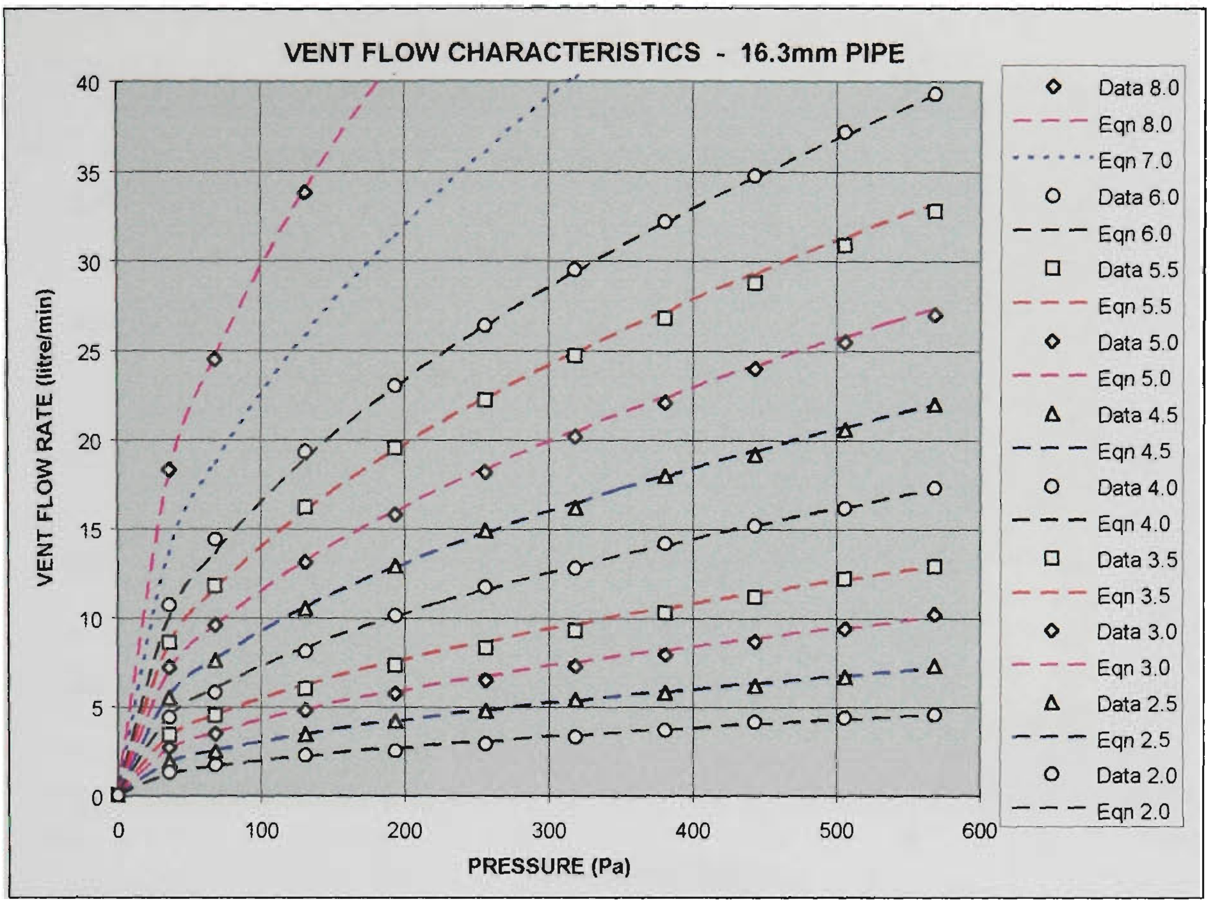

Figure 4.30 - Characteristics of end vents in 16.3*mm* pipe

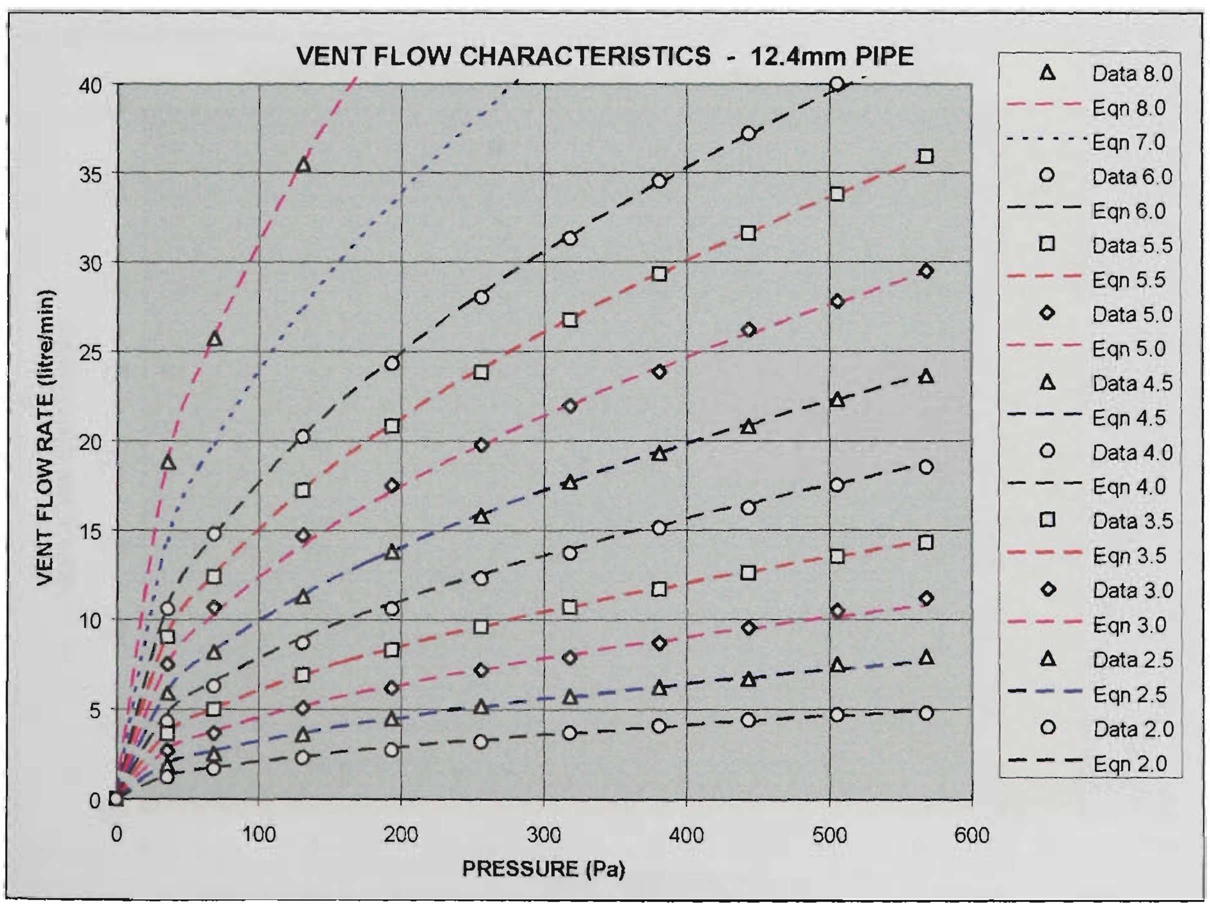

Figure 4.31 - Characteristics of end vents in 12.4*mm* pipe

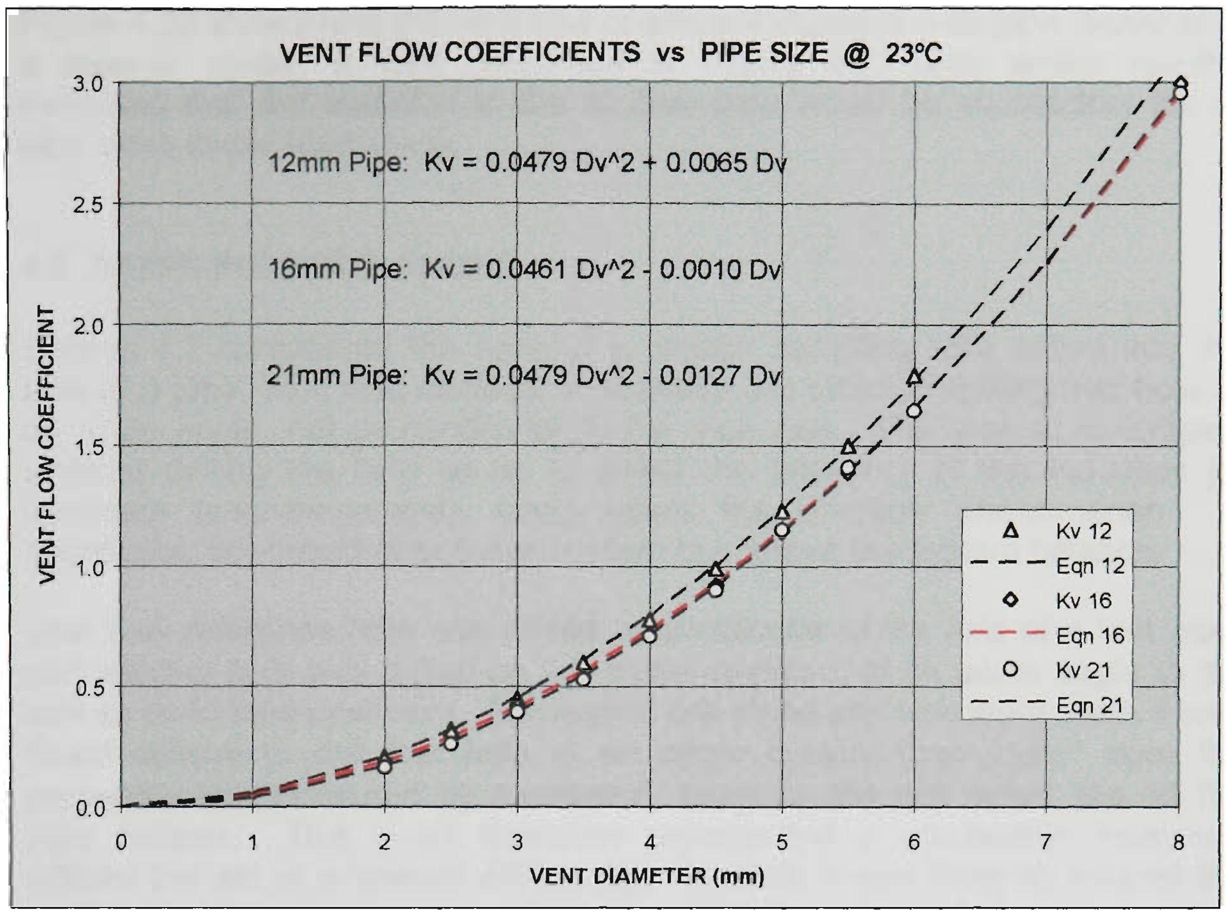

Figure 4.32 - End vent flow coefficients

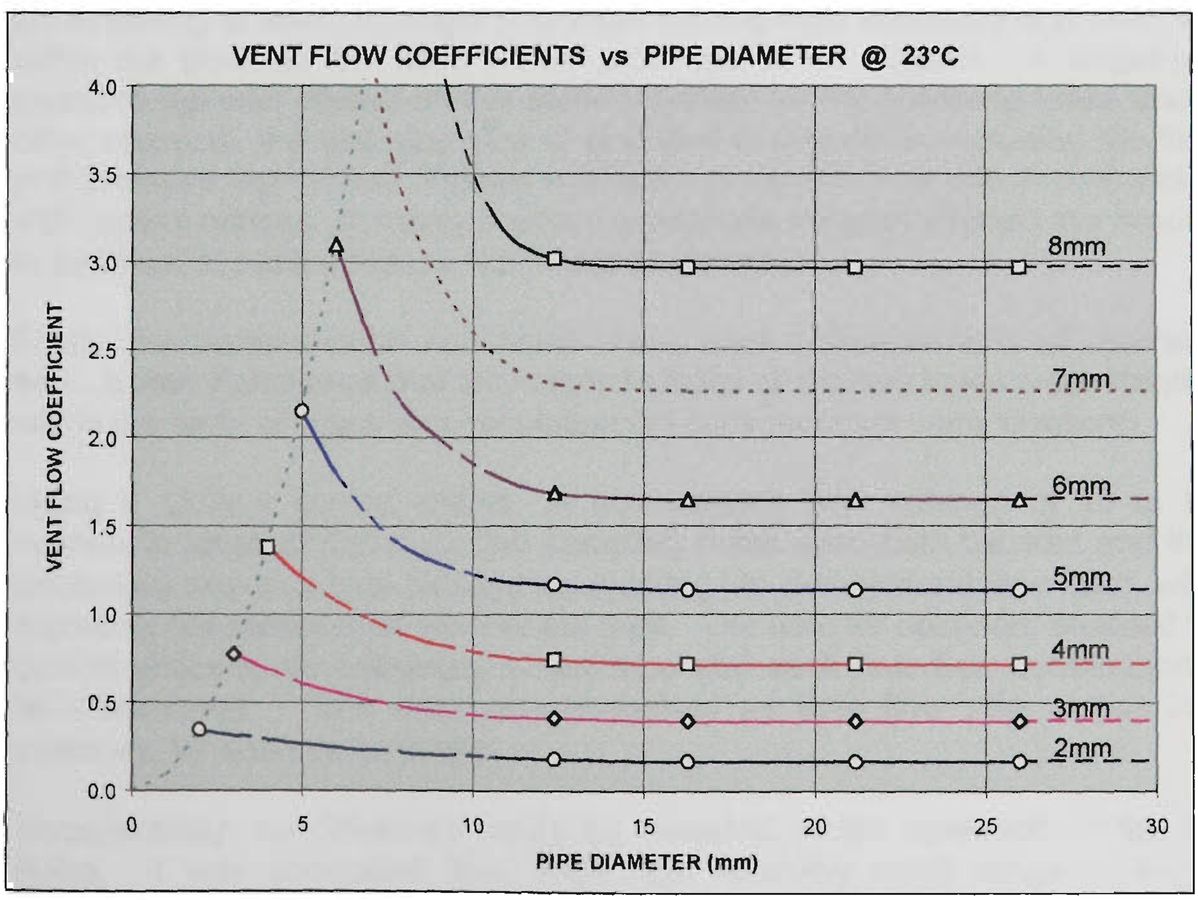

Figure 4.33 - Vent flow coefficients versus pipe diameter

Figure 4.33 shows how the vent flow coefficient changes with pipe diameter in a manner similar to that presented in Figure 4.27 with similar results, indicating that the equation to the $21.2mm$ pipe would be satisfactory for all pipe sizes larger than $15mm$.

4.9 SAMPLING HOLE ANGLE

Section 4.7 considered the case of a regular sampling hole drilled into the side of a pipe, so it was decided to evaluate the effect of drilling that hole at an acute angle, not perpendicular to the pipe axis. This was to investigate whether drilling the hole so as to direct the trajectory of the induction jet upstream (counter-current), could retard the Ultraflow phenomenon. If successful, this would offer a mechanism to improve the system balance.

One $2mm$ reference hole was drilled perpendicular to the axis of a test pipe, and another hole was drilled on the same meridian, at an acute angle to the axis so as to face upstream. Although a drill stand and vice were used, it was found difficult to drill this hole at an angle greater than $13 \pm ½°$ from the perpendicular (measured by protractor), because the drill would slip off the pipe surface. This angle therefore represented a practicable maximum without the aid of a special drilling jig. As such it was likely to exceed the angle at which contractors, using a hand drill, could drill the holes either intentionally or in error.

Special attention had to be given to deburring the acutely-angled hole. The act of drilling at such an angle promoted burring both externally and internally within the pipe, so the bore of the pipe had to be reamed. A single-port pressure tap was placed on the same meridian as the sampling holes and in other respects, the test pipe was of standard configuration including the four-port pressure tap located $3000mm$ upstream to monitor flow rate in conjunction with control orifices. A newly-sourced pneumatic selector allowed the reading to be taken at each pressure tap in rapid succession.

Firstly, the perpendicular and acute holes were calibrated with nil upstream flow. It was discovered that the characteristics of the two holes were identical within the limits of apparatus resolution (all data readings were identical).

Using a $12.9mm$ control orifice, at downstream flow settings of 20 to 120 *litre/min* in steps of *5litre/min*, the sampling holes were both blocked and then unblocked one-at-a-time (always readjusting the downstream flow rate), while recording the pressure at each of the taps. The data so obtained, enabled the control orifice to be calibrated in real time and each hole flow contribution to be determined. The data was presented as hole flow rate versus hole pressure, for each of the holes.

Unexpectedly, no difference could be detected in the operation of the two holes. It was concluded that, within the relatively small range of angles available to orientate the sampling hole, no advantage could be gained in terms of diminishing the Ultraflow phenomenon. It was further concluded that because the pipe wall was relatively thin, rendering the hole depth relatively short, the hole geometry was unable to impart a significant change in jet induction trajectory. The benefit is that the hole flow rate is not sensitive to the angle at which a hole is drilled by a contractor.

4.10 SAMPLING NOZZLES

For the majority of sites, sampling holes take the form of a small downward-facing hole drilled through the wall of an exposed plastic pipe. However, a substantial proportion of sites use concealed pipes. In these cases a nozzle is installed through the ceiling panel, and connected to the pipe via a capillary tube. As illustrated in Figure 4.34, this capillary tube is typically a flexible Nylon tube of $5mm$ internal diameter and 0.5 to $2\ m$ length.

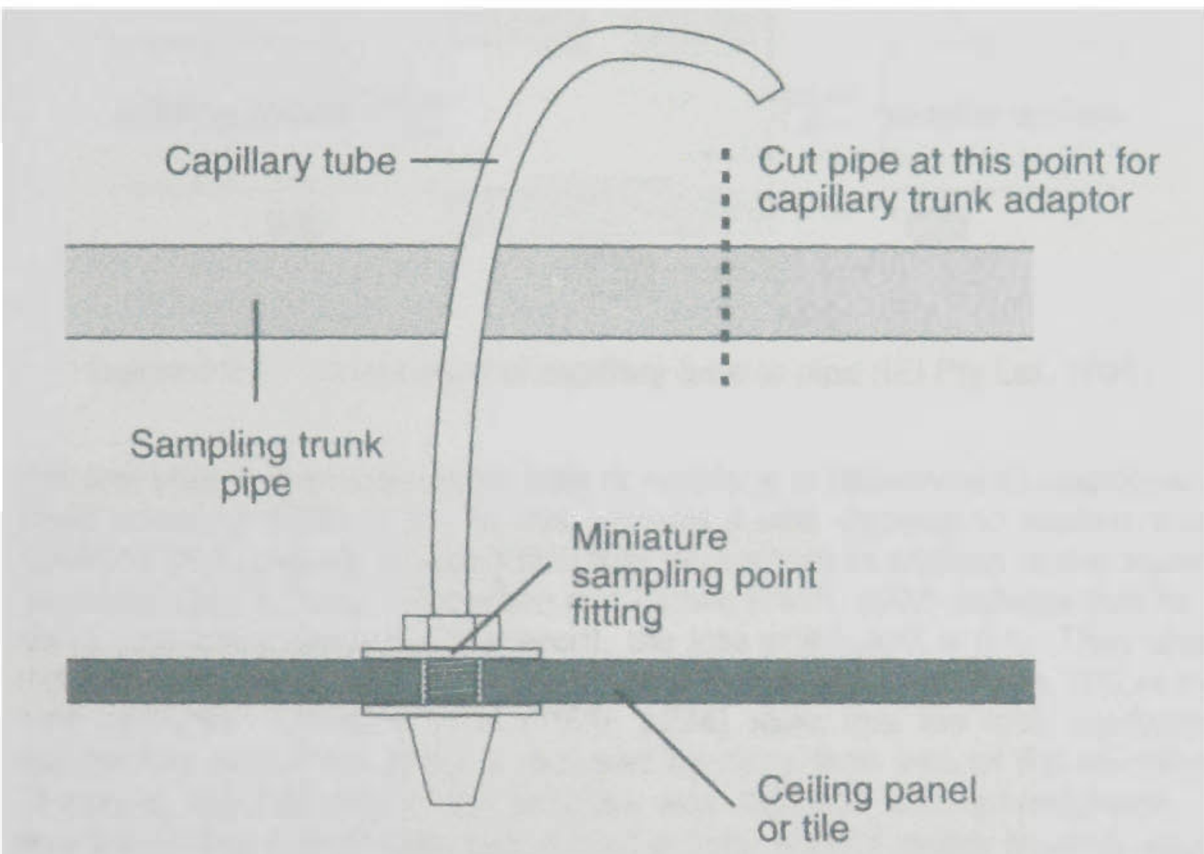

Figure 4.34 - Nozzle and capillary tube (IEI Pty Ltd, 1991)

As illustrated in Figure 4.35, the connection of the capillary tube to the pipe is typically made by using an in-line adaptor, not unlike a "T" connector. The pipe is cut to allow insertion of the adaptor, which is fitted with a capillary tube receptacle.

The investigation of sampling nozzles offers three opportunities to expand knowledge beyond that available from ordinary sampling holes. Firstly, it is possible to install a pressure tap on the capillary tube, thereby obtaining direct measurements of hole pressure. Secondly, the flow metering role of the sampling hole can be isolated from any pipe jet-induction phenomenon (the pipe entry junction can have various geometries and sizes without upsetting the flow-metering function). Thirdly, the nozzle inlet shoulder geometry can be conveniently modified and different nozzles can be readily interchanged without altering or dismantling any other part of the apparatus.

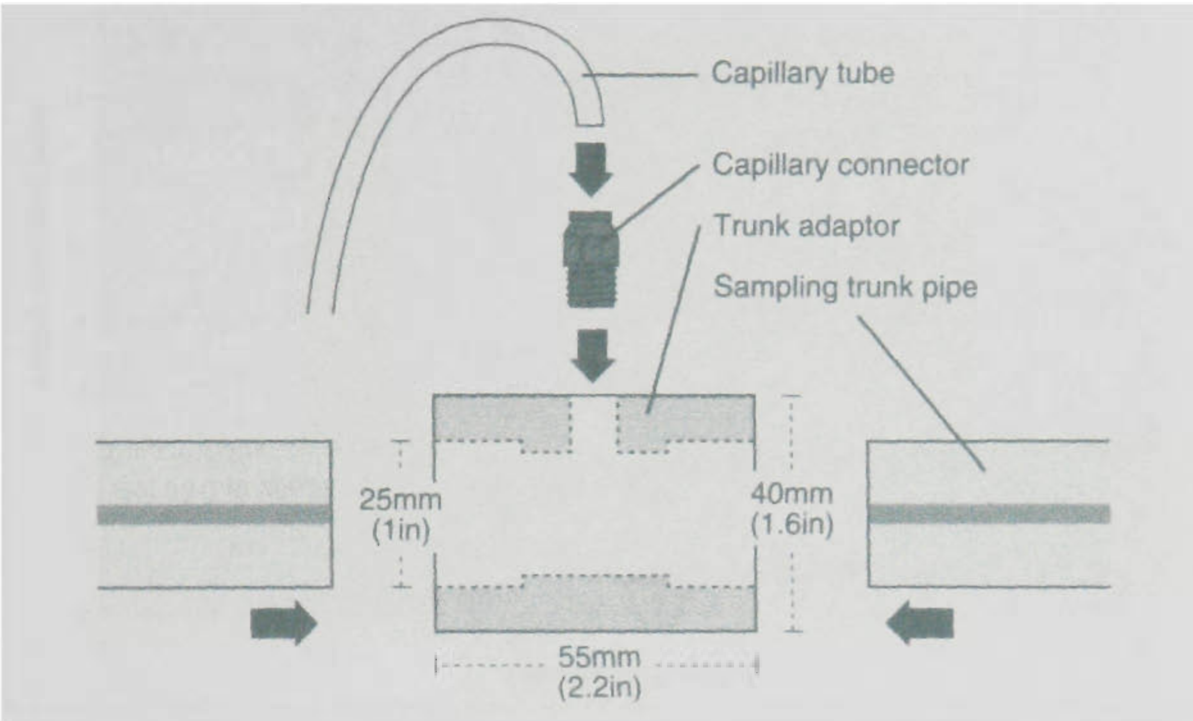

Figure 4.35 - Connection of capillary tube to pipe (IEI Pty Ltd, 1991)

The first step in characterising a hole or nozzle is to determine its response to static pressure differential. At this juncture it was decided to expand such experiments to include rounded shoulder geometries in addition to the square geometry used hitherto. Roberson and Crowe (1975, p305) indicate that for a sharp pipe entry (square-shouldered), the loss coefficient is 0.5. They state that this coefficient is reduced to 0.1 if the shoulder radius exceeds 12% of the hole diameter. Douglas et al (1979, p274) state that the loss coefficient approaches zero if the entry is radiused by more than 14% of the diameter. Therefore, any rounding of the shoulder was regarded with apprehension. It was feared that a technician deburring the hole, without proper training, could dramatically affect the flow metering performance of that hole without actually changing its measurable diameter.

Each capillary nozzle was drilled with a 2, 3 or 4 *mm* hole, being careful to drill coaxially with the certreline of the capillary tube receptacle, while producing square shoulders. One set of these nozzles was carefully reamed to produce shoulder roundings with radii approximately 30% of the hole diameter. This was more than twice the radii considered above, to ensure minimal entry loss. These nozzles were connected in turn to a short capillary tube (100*mm*) with a pressure tap. The experimental results for the various nozzles are presented in Figure 4.36.

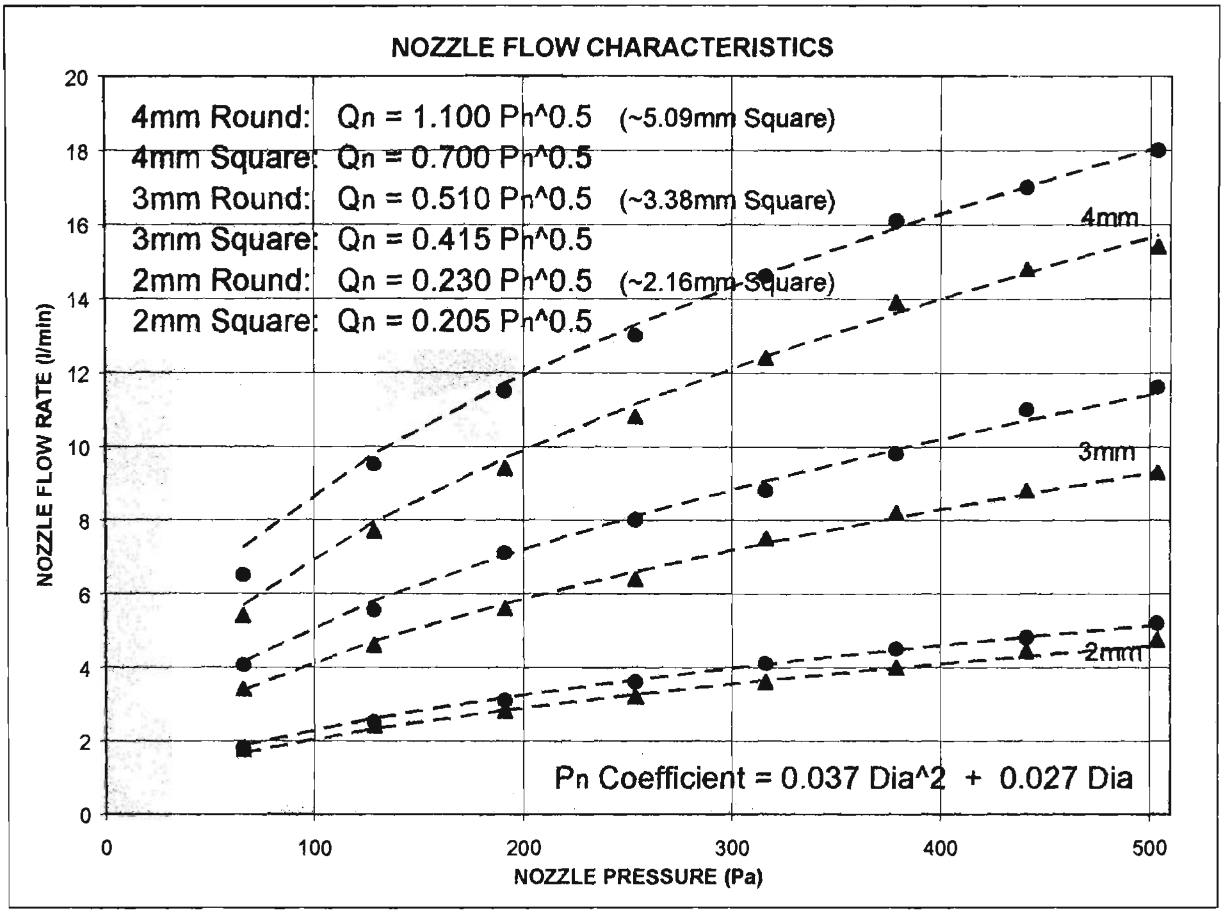

Figure 4.36 - Nozzle flow characteristics

Contrary to the expectation gained from the literature, it was discovered that the hole flow coefficient was not greatly reduced by the rounding, especially for the *2mm* nozzle. The curves of best fit to the data are shown below:

2mm square: $Q_{nozzle} = 0.205\,\Delta P_{nozzle}^{0.5}$

2mm round: $Q_{nozzle} = 0.230\,\Delta P_{nozzle}^{0.5}$ *(≈2.16mm square)*

3mm square: $Q_{nozzle} = 0.415\,\Delta P_{nozzle}^{0.5}$

3mm round: $Q_{nozzle} = 0.510\,\Delta P_{nozzle}^{0.5}$ *(≈3.38mm square)*

4mm square: $Q_{nozzle} = 0.700\,\Delta P_{nozzle}^{0.5}$

4mm round: $Q_{nozzle} = 1.100\,\Delta P_{nozzle}^{0.5}$ *(≈5.09mm square)*

It was noted that the hole flow coefficients were consistent and an equation of best fit to the square-shouldered nozzle coefficients was determined:

$$K_{nozzle} = 0.037\,D_{nozzle}^2 + 0.027\,D_{nozzle}$$

By interpolation of this equation it was possible to determine the equivalent square nozzle size for each rounded nozzle. These are included above. It is concluded that the flow rate through each nozzle is significantly affected by its internal geometry, particularly the capillary tube receptacle, such that the entry rounding has reduced significance. This is good news inasmuch as rounded nozzles can be used, with the advantages of reducing dust buildup in the hole and removing a tendency to whistle.

As a next step the pipe pressure drop was recalibrated and the calculated pressure inside the pipe, at the capillary adaptor, was compared with the reading at the capillary pressure tap, using the pneumatic selector. Close agreement was found, after experiments using 7.37, 10.36 and 12.9 *mm* control orifices. Figure 4.37 presents the results for a square 2*mm* nozzle and the Ultraflow phenomenon remains evident.

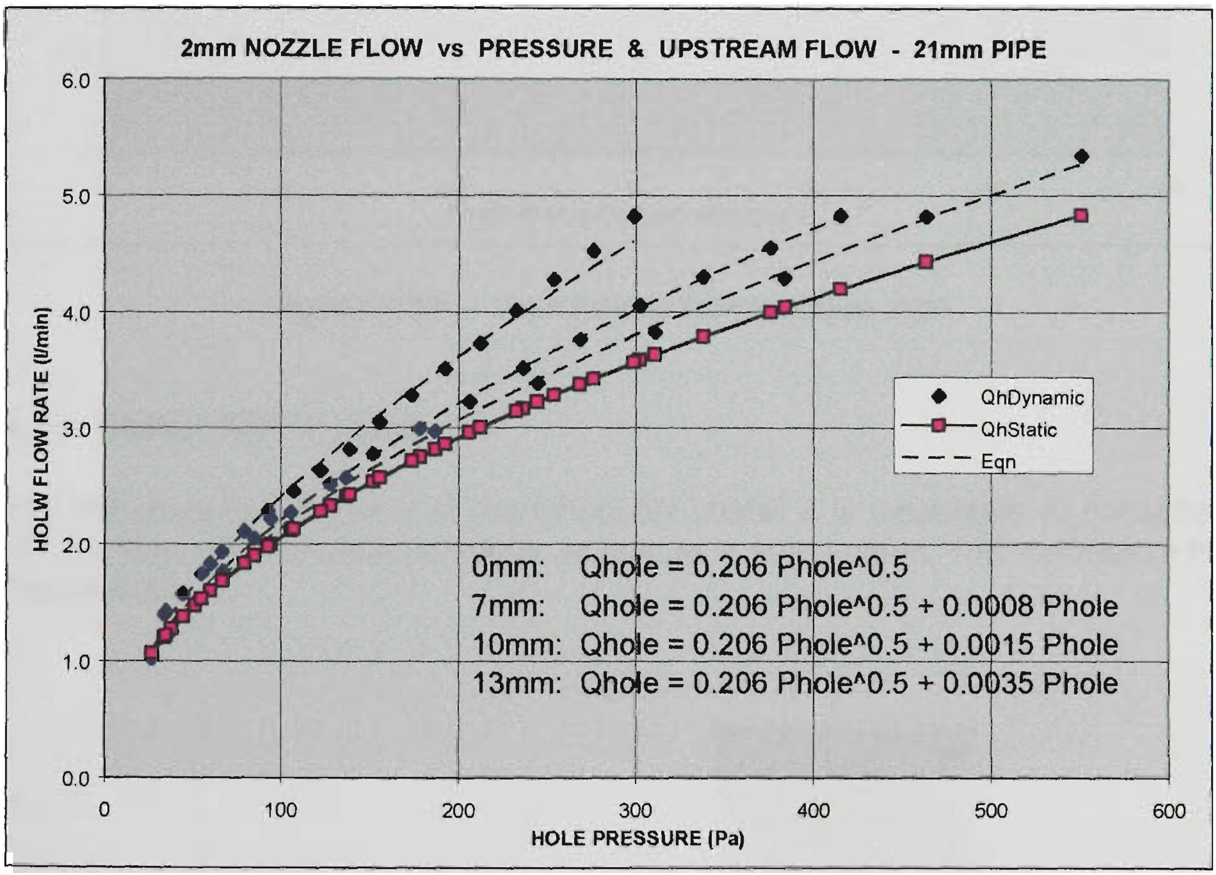

Figure 4.37 - 2*mm* nozzle flow with upstream flows

However, on interpolation to quantify the Ultraflow effect, as presented in Figure 4.38, it was discovered that the onset of Ultraflow had been deferred to higher flow rates than was the case for the regular sampling hole (dashed line). This is attributed to the fact that the pipe adaptor presents a large opening (matching the capillary tube, at 5*mm*) to the pipe wall and the mixing of flows would be more diffuse. That is, with this opening being more than six times the cross-sectional area, the average jet induction velocity (and momentum) would be reduced by the same factor and the nozzle flow would be less likely to penetrate towards the core of the pipe upstream flow.

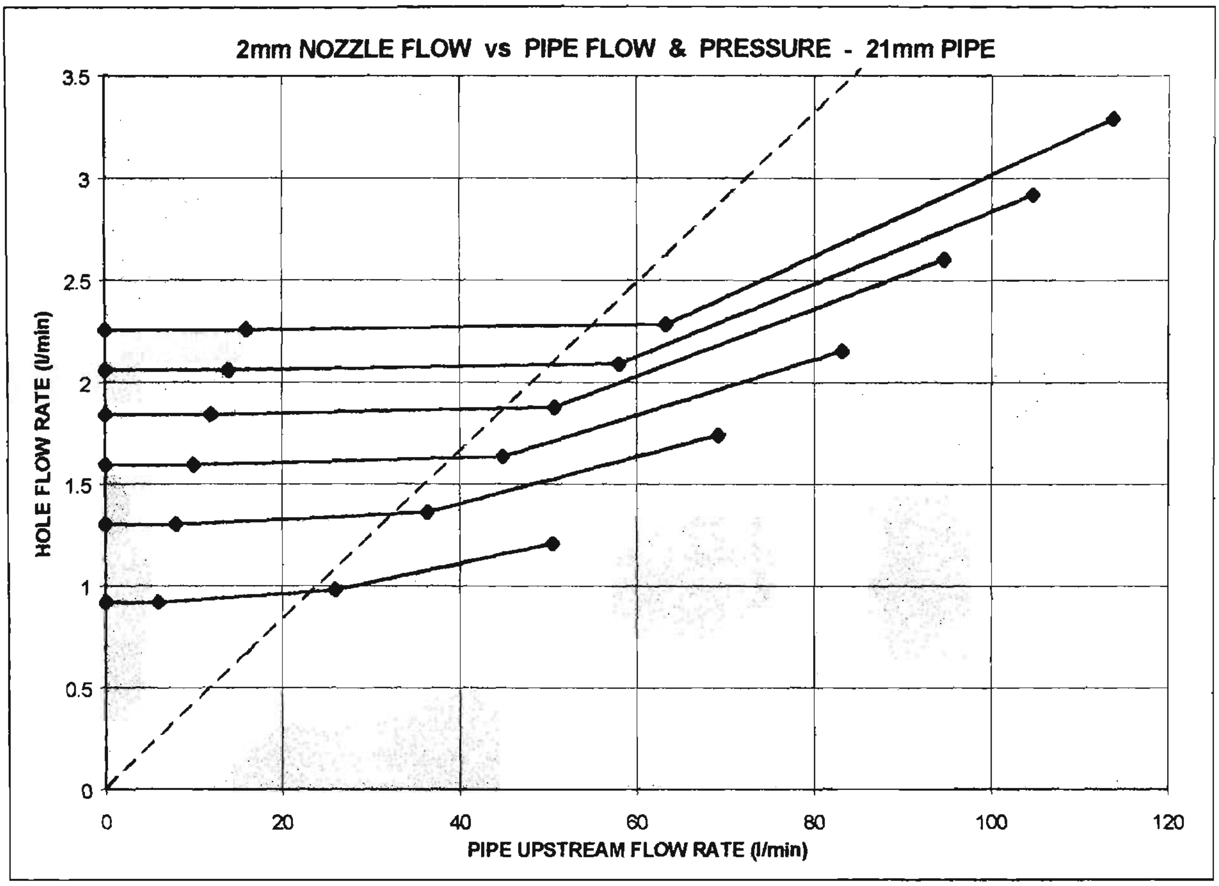

Figure 4.38 - $2mm$ nozzle flow in $21mm$ pipe

4.11 CAPILLARY TUBES

For efficiency in operation of the computer model it is necessary to consider the capillary tube and its sampling nozzle as a sub-system, with reference to Figure 4.39.

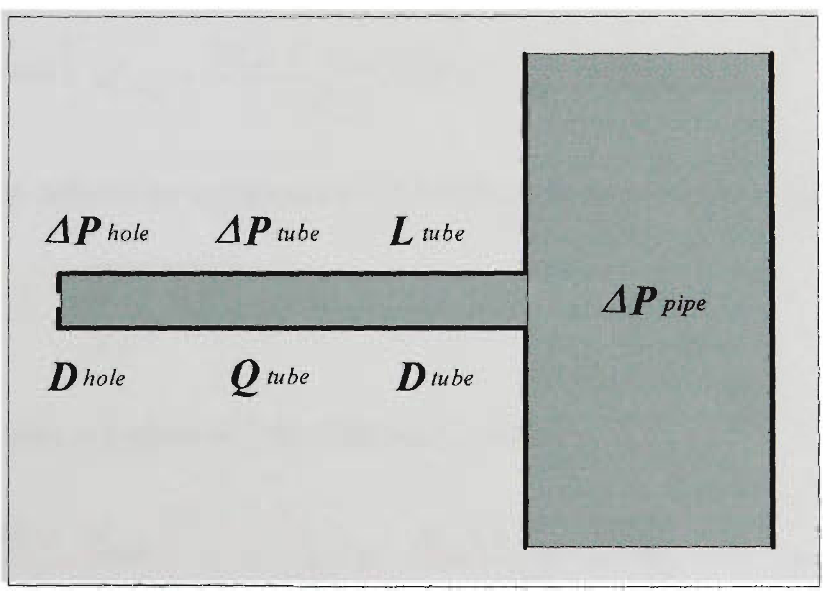

Figure 4.39 - Capillary tube parameters

Firstly, consider the sampling nozzle (hole). We have previously obtained:

$$Q_{nozzle} = K_{nozzle} \, \Delta P_{nozzle}^{0.5} \qquad so:$$

$$\Delta P_{nozzle} = \left(\frac{Q_{nozzle}}{K_{nozzle}} \right)^2 = \left(\frac{60000 \, A_{nozzle}}{K_{nozzle}} \right)^2 u_{nozzle}^2 = \left(\frac{15000 \, \pi \, D_{nozzle}^2}{K_{nozzle}} \right)^2 u_{nozzle}^2$$

where the term 60000 provides conversion from *litre/min* to m^3/sec so that the velocity is in *m/sec* when the nozzle flow coefficient values of Figure 4.36 are used. The capillary tube has typically $5mm$ ($0.005m$) internal diameter and the flow rate is low (a few litres per minute), so the flow regime will always be laminar. The tube is typically at least $200dia$ in length so the flow regime should be well-developed throughout much of its length. Therefore we can use the Hagen-Poiseuille equation to obtain the pressure drop along the tube (Douglas et al. 1979 p251):

$$\Delta P = \frac{128 \, \mu \, L \, Q}{\pi \, D^4} \qquad where \qquad Q = \frac{\pi \, D^2}{4} u \qquad so:$$

$$\Delta P_{tube} = \frac{32 \, \rho \, k \, L_{tube}}{D_{tube}^2} u_{tube} = \frac{32 \, \rho \, k \, L_{tube}}{D_{tube}^2} \left(\frac{D_{nozzle}}{D_{tube}} \right)^2 u_{nozzle}$$

Now by the summation of relative pressures:

$$\Delta P_{pipe} = \Delta P_{nozzle} + \Delta P_{tube} = \left(\frac{15000 \, \pi \, D_{nozzle}^2}{K_{nozzle}} \right)^2 u_{nozzle}^2 + \frac{32 \, \rho \, k \, L_{tube} \, D_{nozzle}^2}{D_{tube}^4} u_{nozzle}$$

so we can obtain the quadratic equation in u_{nozzle} :

$$\left(\frac{15000 \, \pi \, D_{nozzle}^2}{K_{nozzle}} \right)^2 u_{nozzle}^2 + \frac{32 \, \rho \, k \, L_{tube} \, D_{nozzle}^2}{D_{tube}^4} u_{nozzle} - \Delta P_{pipe} = 0$$

which can be solved by application of the known solution to a quadratic:

$$u_{nozzle} = \frac{-b \pm \sqrt{b^2 - 4 \, a \, c}}{2 \, a}$$

where a, b, and c represent the following terms:

$$a = \left(\frac{15000 \, \pi \, D_{nozzle}^2}{K_{nozzle}} \right)^2 \qquad b = \frac{32 \, \rho \, k \, L_{tube} \, D_{nozzle}^2}{D_{tube}^4} \qquad c = -\Delta P_{pipe}$$

By substitution we can obtain the equation for nozzle flow rate as follows:

$$Q_{nozzle} = \pi \, D_{nozzle}^2 \left(\left(t_1^2 + 4\, t_2 \, \Delta P_{pipe} \right)^{\frac{1}{2}} - t_1 \right) \Big/ 8\, t_2$$

where the terms $t_1 = b$ and $t_2 = a$ (above). This nozzle flow rate equation can be readily applied within the computer model because all of the parameters would be known. It has been found that the negative possibility before the square root term does not apply.

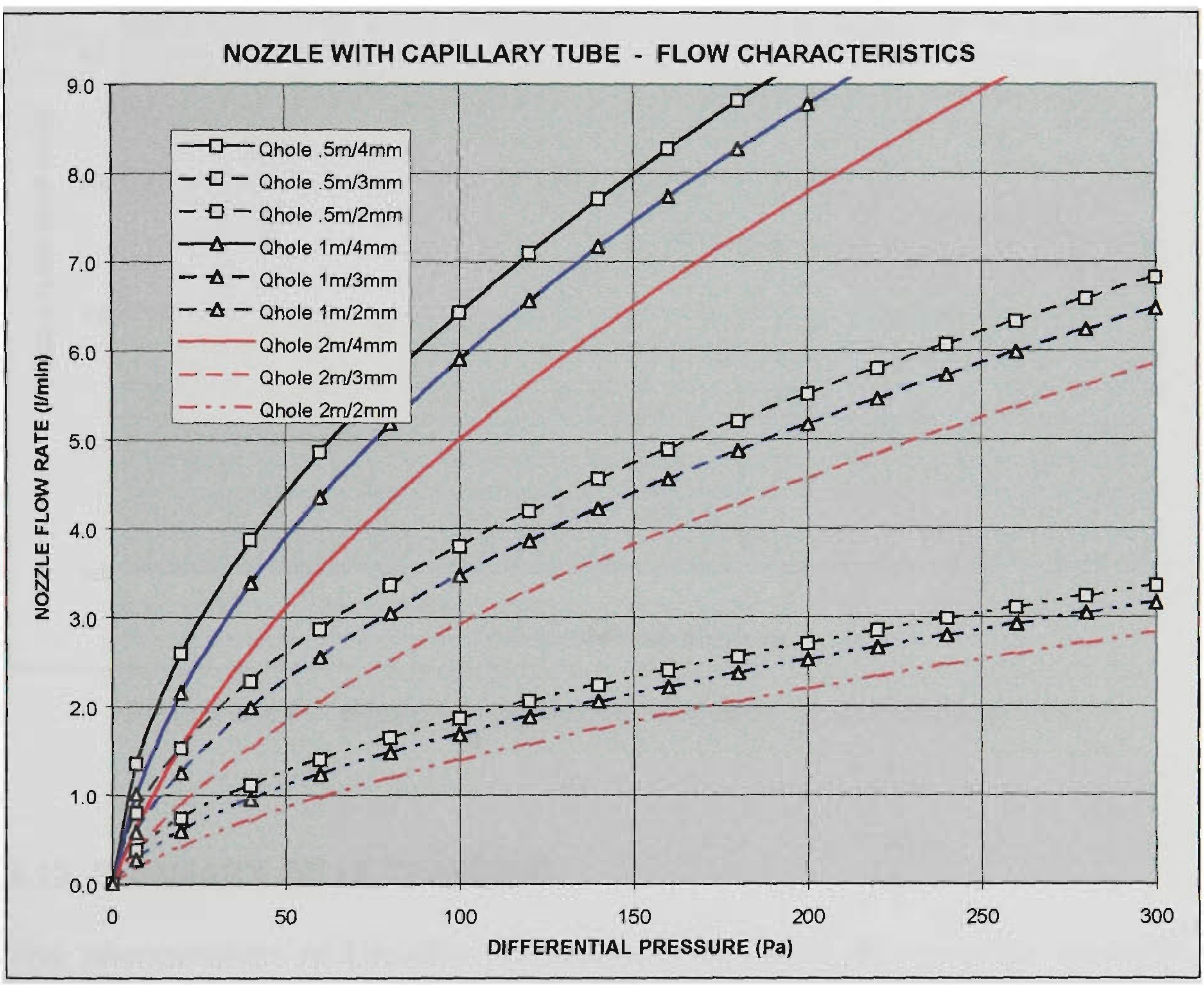

Figure 4.40 - Capillary nozzle flow rate as determined by the combination of the hole diameter and the capillary tube length at a given pressure

Noting that the most common capillary tube arrangement has used a *2mm* hole with a *1m* length tube of *5mm* internal diameter, Figure 4.40 presents the results of applying these equations to a range of capillary tube lengths (0.5, 1.0 and 2.0 *m*) and nozzle hole sizes (2, 3 and 4 *mm*). The curve representing the *1m/3mm* combination occupies the central position among the graphs. There is a tendency for the curves to be grouped by hole size but otherwise the trends are difficult to see.

Figure 4.41 has been produced to clarify the effect of capillary tube length for each of the three hole sizes specified. To avoid clutter, these graphs are limited to two selected differential pressures - 100 and 200 Pa. Here we see that at a given pressure, the flow rate reduces only gradually with increasing tube length, and that the hole diameter is the dominant parameter. Note that the y-axis values relate to a capillary tube of zero effective length (equating to the characteristics of Figure 4.36).

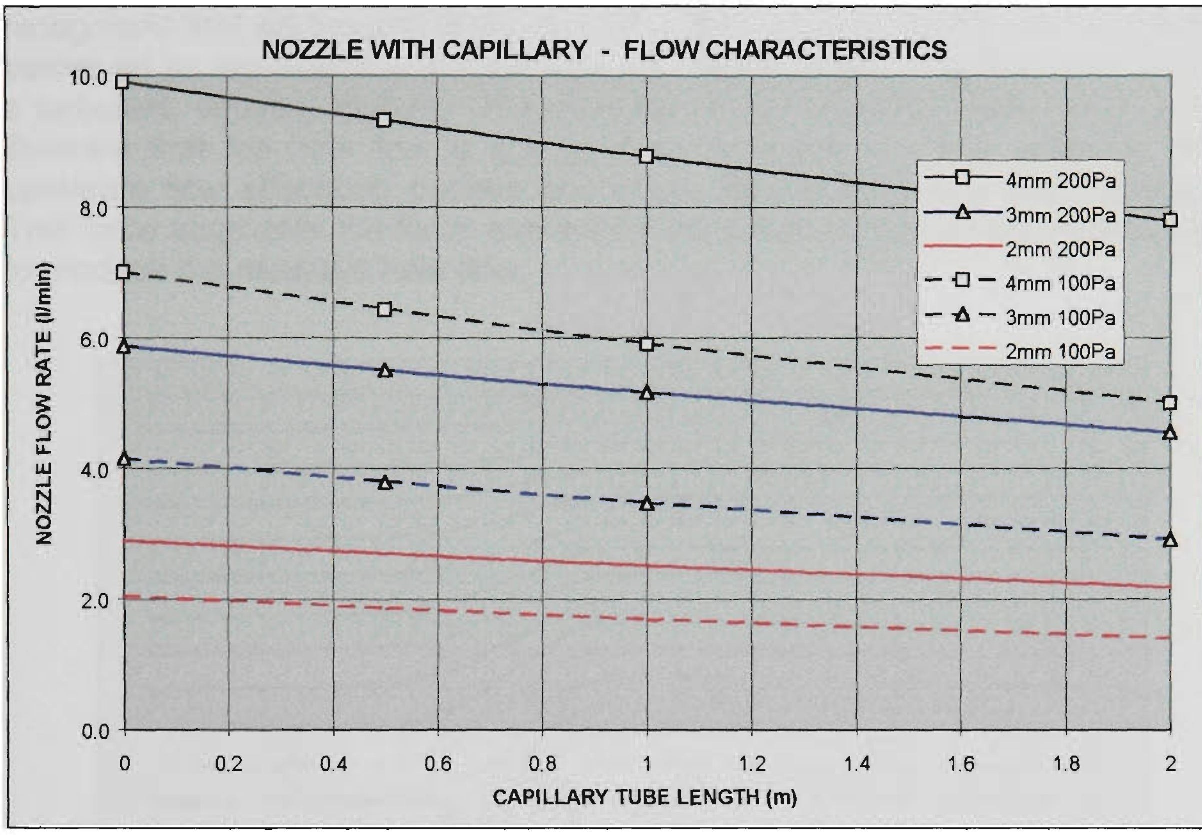

Figure 4.41 - Effect of capillary tube length on nozzle flow rate

4.12 SUMMARY OF ULTRAFLOW

The phenomenon of Ultraflow has been discovered whereby the expected hole flow rate caused by static pressure, is exceeded because of the upstream flow rate in the pipe. At any given pressure, this Ultraflow (as a component of the total hole flow) initially increases in small measure as the upstream flow rate increases. Then an upstream flow rate threshold is reached, above which the hole flow rate increases linearly with upstream flow rate, becoming independent of pressure.

In the case of a typical sampling hole (2 to 4 *mm* diameter) in a typical pipe (21*mm* diameter), this threshold can be obtained in terms of the normalised hole Reynolds number, being the pipe Reynolds number divided by 3150. The circumstances that determine this threshold gradient (3150) are not clear except that, at a given Reynolds number, the onset of Ultraflow is deferred as the pipe radius is reduced (pipe velocity increased), or as the sampling flow velocity entering the pipe is reduced (e.g. with a capillary adaptor) - in both cases reducing the penetration of the induction jet.

Figure 4.42 has been constructed in an attempt to visualise, simplistically, the process that may generate Ultraflow. Here, the upstream flow streamlines are shown travelling from left to right, and encountering the hole flow jet that enters the pipe from below. For clarity the "boundary" between the flows is shown as a dashed streamline, although in practice, substantial mixing is expected. In this and other respects the streamlines are idealised and it is recognised that eddies are likely to exist. The streamlines are perhaps best perceived as representing the average path of packages of air that may be in a turbulent, eddying motion. The purpose of this simplified view, then, is to illustrate that the hole flow is <u>entrained</u> by the upstream flow, whereby the upstream flow effectively pushes and drags the incoming flow into the pipe. This force augments the force exerted by the pressure differential, combining to produce the resultant hole flow.

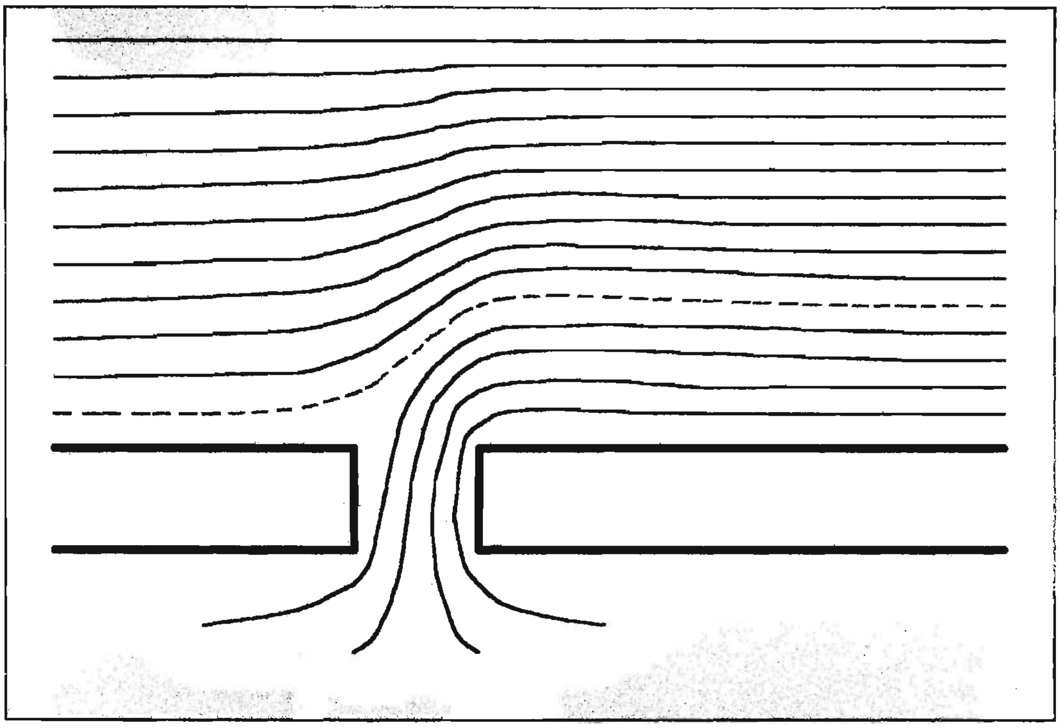

Figure 4.42 - Simplified 2-D visualisation of the entrainment of a hole flow induction jet into a pipe stream

Recognition of Ultraflow as potentially an entrainment phenomenon has led in logical sequence to a theoretical analysis which is developed in Section 4.14, but it was found that this analysis would depend upon first completing an analysis of the pressure drop caused by the induction jet which is discussed in Section 4.13.

4.13 ACCELERATING THE INDUCTION JET

The volume of air that is continuously induced into and through the sampling hole, will firstly acquire velocity in the radial direction towards the centre of the pipe, under the force of ambient air pressure. Because of the momentum acquired, this induction air will tend to form a jet which penetrates the pipe airstream. This airstream will exert a distributed force upon the jet, deflecting its path and accelerating it in the pipe longitudinal direction, from zero until it reaches the pipe stream velocity. This acceleration force adds to the pressure drop in the segment of pipe in the immediately vicinity of the sampling hole. If this pressure drop is significant, it will affect the accuracy of pressure distribution calculations throughout the aspirated pipe system.

With reference to Figure 4.42 a control volume that fills the pipe in the vicinity of the sampling hole has been constructed and presented in Figure 4.43. This includes the upstream flow rate (Q_{up}), the downstream flow rate (Q_{dn}) and the jet flow rate (Q_{jet}) which is also the hole flow rate.

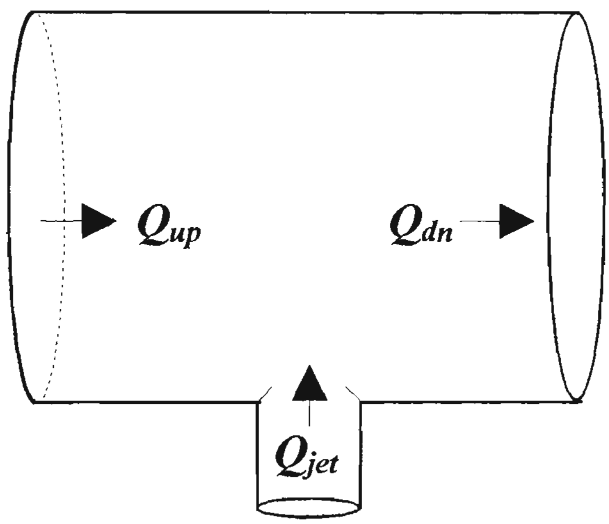

Figure 4.43 - Control volume for
a hole induction jet

Assuming steady flow and a uniform velocity at all points in a given cross-section, the force exerted in the direction of Q_{up} because of the jet (with negligible wall friction loss) is given by the momentum equation:

$$F_{jet} = \dot{m}_{dn}\, u_{dn} - \dot{m}_{up}\, u_{up} = \rho\, A_{dn}\, u_{dn}^2 - \rho\, A_{up}\, u_{up}^2$$

substituting $u = Q/A$ and $\delta P_{jet} = F_{jet}/A_{pipe}$, and where $A_{up} = A_{dn} = A_{pipe}$:

$$\delta P_{jet} = \rho \left(\frac{A_{dn}}{A_{pipe}} \left(\frac{Q_{dn}}{A_{dn}} \right)^2 - \frac{A_{up}}{A_{pipe}} \left(\frac{Q_{up}}{A_{up}} \right)^2 \right) = \rho \left(\frac{Q_{dn}^2 - Q_{up}^2}{A_{pipe}^2} \right)$$

since $Q_{dn} = Q_{up} + Q_{jet}$ we obtain:

$$\delta P_{jet} = \rho \left(\frac{\left(Q_{up} + Q_{jet}\right)^2 - Q_{up}^2}{A_{pipie}^2} \right)$$

which can be shown as dimensionally correct and can be solved for a range of values of Q_{up} and Q_{jet}. A graph of this pressure drop would have a parabolic form, and, because its value depends upon both the upstream flow rate and the hole flow rate, a family of curves would be required to represent it.

In developing this equation, steady flow and a uniform velocity at all points in a given cross section were assumed. In reality a curved velocity profile is likely to exist in relation to Q_{up} which may be a developing or fully-developed laminar or turbulent flow profile. Given that, on passing through the control volume the profile is completely disturbed by the hole flow jet, the velocity profile for Q_{dn} is assumed to be that of plug flow, as is the profile for Q_{jet} (which develops over a very short displacement).

It is known that a momentum correction factor β can be applied, to take account of the velocity profile relating to Q_{up}. By integration of the momentum at all points on the velocity profile, Vardy (1990, p186) shows that in the case of a fully-developed laminar flow regime, this factor is 1.33, while Douglas et al. (1979, p121) state that in the case of fully-developed turbulent flow, this factor can be taken as 1.02 (based upon the Prandtl one-seventh power law). Thus the complete equation becomes:

$$\delta P_{jet} \quad = \quad \rho \left(\frac{\left(Q_{up} + Q_{jet}\right)^2 - \beta\ Q_{up}^2}{A_{pipe}^2} \right)$$

An experiment was conducted in an attempt to confirm this theoretical result as well as to add credence to the experimental method. The apparatus was set up using a $4m$ length of straight pipe, ahead of a test segment containing a $3mm$ sampling hole. The actual diameter chosen for this hole is not significant – a hole of another size would require another differential pressure to produce a given hole flow rate, but it is the hole flow rate (not the differential pressure) that is of current interest. Put another way, the pressure differential through the hole (ΔP) is not directly relevant to the pipe pressure drop (δP_{jet}). Therefore, a $3mm$ hole is representative of other hole sizes.

Pressure taps were placed just one diameter upstream and downstream of the hole. High accuracy in the results was not expected because the small pressure drop in the space of two diameters would represent a challenge to the resolution of the pressure gauge. However, the acceleration was expected to be complete within one pipe diameter (if not one hole diameter - see Figure 4.42) and it was felt important to minimise the separation of the pressure taps, so that the pressure drop due to jet acceleration would not be swamped by that of pipe friction.

The test segment was connected to the flowmeter and to a bank of aspirators providing adjustable pressure. Measurements of the pressure drop between the two tappings were taken for the maximum practicable range of pipe flow rates, with the sampling hole either held open or blocked. The latter condition provided the pressure drop due to pipe friction alone (to be subtracted from the reading obtained with the hole open). The ambient pressure differential at the sampling hole was also recorded.

The experiment technique was perfected using a completely open-ended pipe ($21.2mm$) and repeated using $12.9mm$ and $10.36mm$ control orifices. The equations of Figure 4.5 were used to obtain the hole flow rates in the presence of upstream flow, taking due account of Ultraflow. In using these control orifices, at any given pipe flow rate it was possible to obtain changes by a factor of two in the differential pressure at the sampling hole. For example, at a downstream flow rate of $90 litre/min$, the differential pressures were 95, 180 and 340 Pa for the 21.2, 12.9 and 10.36 mm orifices respectively. Accordingly the hole flow rate was substantially different in each case. This would enable us to distinguish whether the pipe pressure drop is dependent on hole flow rate as well as pipe flow rate.

In order to obtain measurable results the experiment was conducted at flow rates no less than $40 litre/min$, so the minimum Reynolds number was 2400, and the applicable value for the momentum correction factor (β) was 1.02 at most.

The results are presented in Figure 4.44, in terms of incremental pipe pressure drop versus hole flow rate. Given the instrument resolution of 0.25Pa, there is good correlation amongst the three sets of measured data (shown as points), and between these data and the theoretical curves. Here, the dotted curves represent $\beta = 1.00$ while the solid curves represent $\beta = 1.02$.

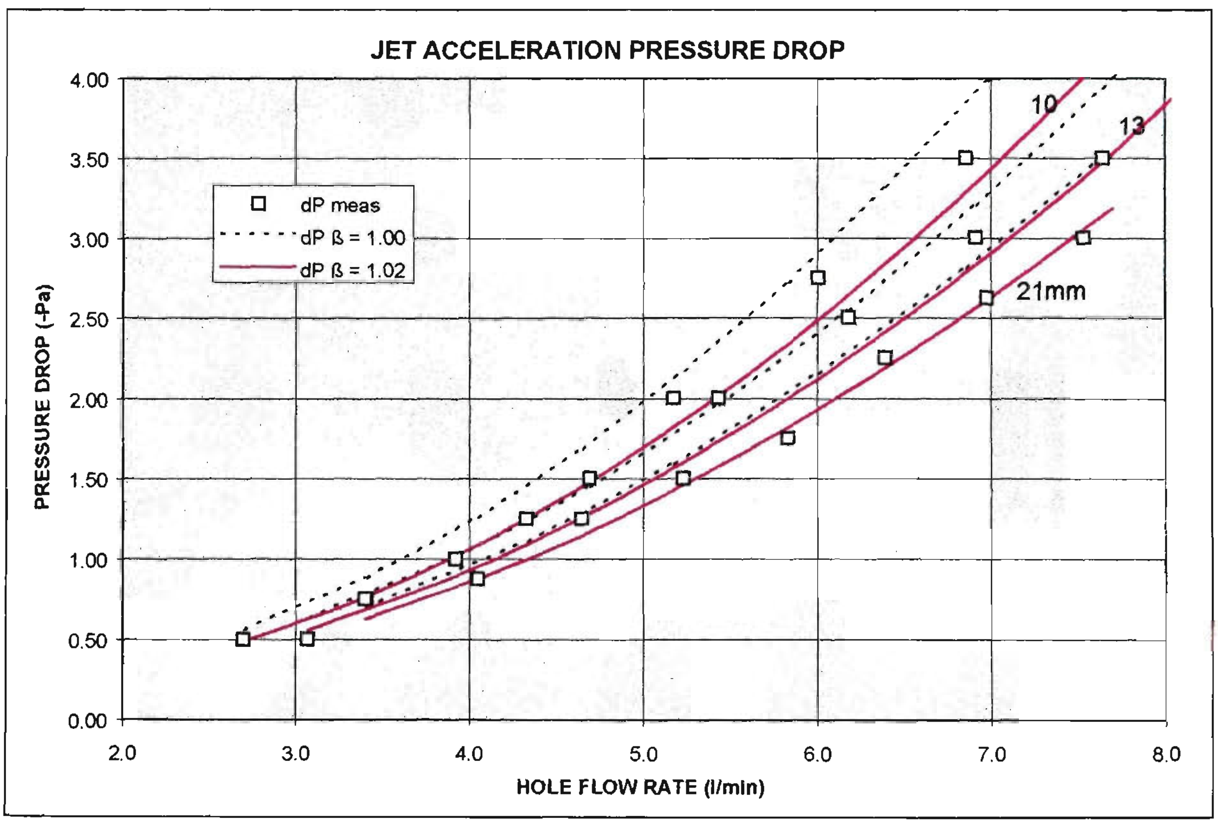

Figure 4.44 - Pressure drop due to acceleration of the induction jet - comparison of theoretical and measured results

It is evident that the effect of the momentum correction factor is on the order of half a Pascal at most (i.e. if the incoming flow regime was fully-developed). However, the measured data tend to align somewhere between the $\beta = 1.00$ set and the $\beta = 1.02$ set, indicating that the flow regime was not fully-developed. Overall, the pressure drop is on the order of a few Pascal.

Given the experiment methodology used in this and related experiments it can be assumed that the pressure drop due to jet acceleration is included in the overall pipe pressure drop readings and serves to increase the apparent friction factor. This is dealt with in Chapter 5.

4.14 THE ENTRAINMENT PHENOMENON

The entrainment of flow through a sampling hole and into the pipe as illustrated in Figure 4.42 may be modelled by analogy with a jet ejector pump. A schematic diagram for such a pump is shown in Figure 4.45, in which region 1 refers to the upstream, motive flow, N refers to the nozzle, S the suction port, T the throat, and 2 the diffuser discharge. These labels will be used as suffixes in the equations that follow.

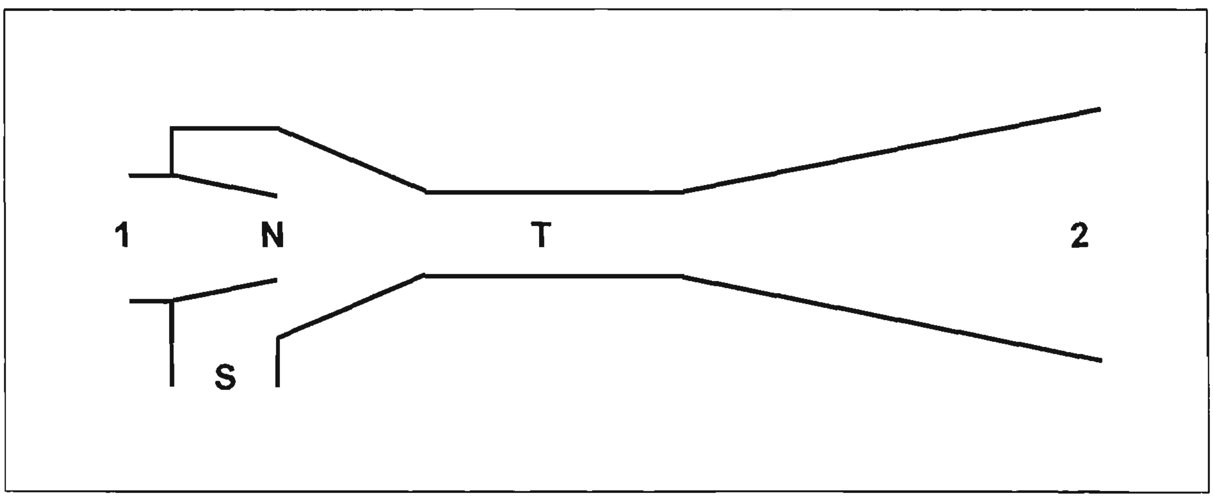

Figure 4.45 - Schematic diagram of jet ejector pump

Jumpeter (1976, p61) has analysed the operation of such pumps in a manner similar to the following, with surface friction regarded as insignificant. Firstly, the energy equation is written for the region of the nozzle:

$$\frac{P_1}{\rho_1 g} + \frac{u_1^2}{2g} = \frac{P_S}{\rho_1 g} + \frac{u_N^2}{2g}$$

Upstream of the nozzle, all energy is considered to be in the form of static head, so $u_1^2 << u_N^2$ and the term u_1^2 can be eliminated (assumption 1). Therefore we can obtain the "operating head":

$$\frac{u_N^2}{2g} = \frac{P_1 - P_S}{\rho_1 g}$$

Across the diffuser at the nozzle discharge, Jumpeter states that the energy equation may be written for the mixed fluid streams as follows:

$$\frac{P_S}{\rho_2 g} + \frac{u_T^2}{2g} = \frac{P_2}{\rho_2 g} + \frac{u_2^2}{2g}$$

At the discharge (region 2) it is assumed that all velocity head is converted to static head, so $u_2^2 << u_T^2$ and the term u_2^2 can be eliminated (assumption 2). Therefore we can obtain the "discharge head":

$$\frac{u_T^2}{2g} = \frac{P_2 - P_S}{\rho_2 g}$$

The ratio of the operating head to the discharge head (R_H) is:

$$R_H = \frac{u_N^2 / 2g}{u_T^2 / 2g} = \frac{u_N^2}{u_T^2} = \frac{(P_1 - P_S)/\rho_1 g}{(P_2 - P_S)/\rho_2 g}$$

And when the fluids are the same (have the same density and temperature):

$$R_H = \frac{H_1 - H_S}{H_2 - H_S}$$

expressed in terms of head (m). Now, the entrainment conditions immediately downstream of the nozzle may be defined by the momentum equation:

$$\dot{m}_1 u_N + \dot{m}_S u_S = (\dot{m}_1 + \dot{m}_S) u_T$$

It is assumed that the velocity of approach at the suction inlet is zero in the downstream direction, so u_S is zero or insignificant (assumption 3) and we obtain:

$$\dot{m}_S = \dot{m}_1 \left(\frac{u_N}{u_T} - 1 \right)$$

The "weight operating ratio" (R_W) is therefore:

$$R_W = \left(\frac{\dot{m}_S}{\dot{m}_1} \right) = \frac{u_N}{u_T} - 1$$

Now, the term u_N^2/u_T^2 has been previously defined as the head ratio (R_H) so:

$$R_W = \sqrt{R_H} - 1$$

The "volume ratio" (R_Q) is thus obtained:

$$R_Q = \frac{Q_S}{Q_1} = R_W \frac{specific\ gravity_1}{specific\ gravity_2} = \sqrt{R_H} - 1 = \sqrt{\frac{\Delta P_{1S}}{\Delta P_{2S}}} - 1$$

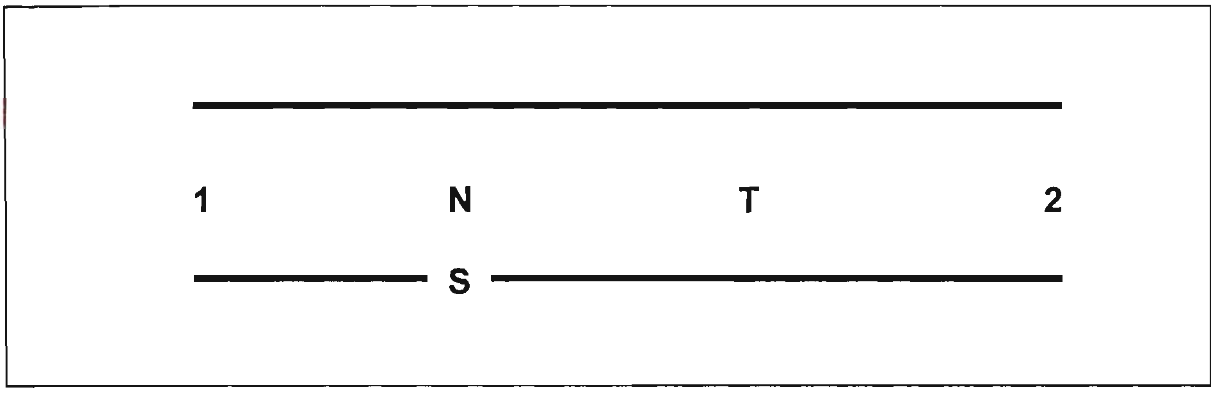

Figure 4.46 - Sampling hole considered as a jet pump

Consider now the special case of a sampling hole drilled into the side wall of a pipe as depicted in Figure 4.46. There are a number of differences in this configuration from that of the jet ejector pump, so the assumptions need to be revisited. In the absence of an inlet nozzle and an outlet diffuser, assumptions 1 and 2 cannot be made. Therefore, without eliminating terms u_1^2 and u_2^2 we obtain a revised equation for the ratio of operating head to discharge head:

$$R_H = \frac{u_N^2 / 2g}{u_T^2 / 2g} = \frac{(P_1 - P_S)/\rho g + u_1^2 / 2g}{(P_2 - P_S)/\rho g + u_2^2 / 2g}$$

Assumption 2 (that $u_2^2 << u_T^2$) is not valid because in practice $u_2 = u_T$ given that no outlet diffuser is used (and noting that average velocities are involved). Nevertheless, application of assumption 1 (that $u_1^2 << u_N^2$) is not completely invalid because it is likely that $u_N > u_1$ as a result of the effective deflection and squeezing of the upstream flow as it encounters the jet flow (see Figure 4.42). Therefore an empirical coefficient of entrainment (C_{jet}) is introduced for modifying the impact of the pipe upstream velocity head:

$$R_H = \frac{(P_1 - P_S)/\rho g + C_{jet}\, u_1^2 / 2g}{(P_2 - P_S)/\rho g + u_2^2 / 2g}$$

Here, in the special case of a sampling hole, P_S is zero (relative atmospheric pressure) and $P_2 = P_1 + \delta P_{jet}$ where δP_{jet} is the jet acceleration pressure drop as determined previously in Section 4.13, namely:

$$\delta P_{jet} = \rho \left(\frac{\left(Q_{up} + Q_{jet}\right)^2 - \beta Q_{up}^2}{A_{pipe}^2} \right)$$

so that, after adopting consistent subscript labeling:

$$R_H = \frac{P_{up} / \rho + C_{jet}\, u_{up}^2 / 2}{\left(P_{up} + \delta P_{jet}\right) / \rho + \left(Q_{up} + Q_{jet}\right)^2 / 2 A_{pipe}^2}$$

which is implicit in R_H because:

$$Q_{jet} = Q_{stat} + Q_{ultra} = Q_{stat} + Q_{up}\left(1 - \sqrt{R_H}\right)$$

which also takes into account the superposition of hole flows due to static pressure and Ultraflow (entrainment), and reverses the negative according to the convention adopted for relative pressure. Therefore it is necessary to provide an iterative solution. Nested iteration is required because the hole flow rate is incremented by entrainment which in turn increments the jet acceleration pressure drop, which in turn affects the value of R_H.

In computing the theoretical data it was found that the graphical results were of the same form as the experimental results seen in Figure 4.10, including the asymptotic trends. It can be shown that after making the necessary iterative computations, close agreement with all of the experimental results (Figures 4.8, 4.10, 4.12, 4.22 and 4.25) is obtained using the following equation for the coefficient of entrainment:

$$C_{jet} = \frac{2}{\left(D_{hole} + 1\right)\left(D_{pipe} / 21.2\right)^{0.8}}$$

with diameters expressed in mm. Figure 4.47 presents the results of application of the above four equations to the situation of a $3mm$ hole in a $21mm$ pipe, with static pressure increments of 20Pa from 20 to 120Pa in conformity with the experimental results of Figure 4.10.

It can be seen that the form and magnitude of the theoretical results of Figure 4.47 are consistent with the experimental results of Figure 4.10, including the asymptotic approach of the data to a straight line through the origin. For brevity, the results obtained for all other pipe and hole diameter combinations are included in Appendix 4, where the close match of the theoretical data to the asymptote originally obtained from the relevant experimental data, is readily apparent. Taking account of experimental error, the results are consistent with a minimum possible value for C_{jet} of unity, which is applicable to the case of a diffuse induction jet (capillary tube adapter).

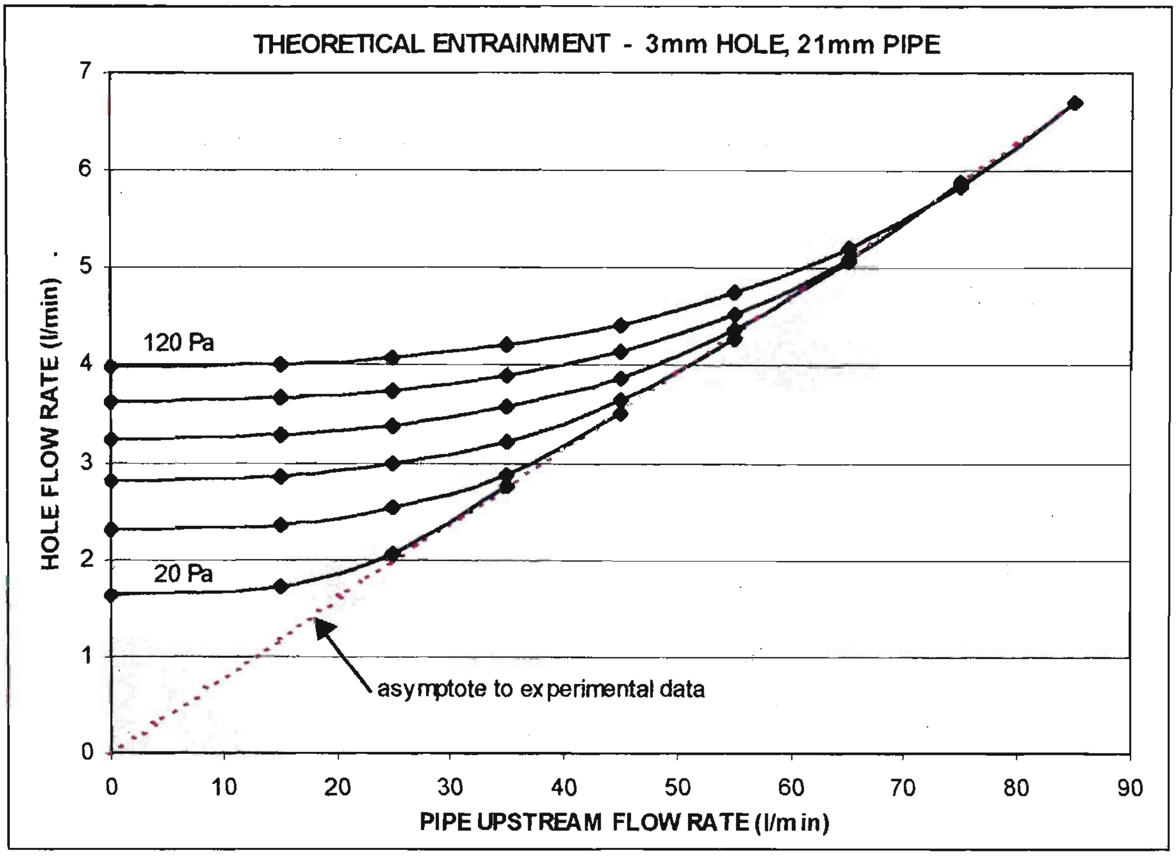

Figure 4.47 - Theoretical model of the Ultraflow phenomenon resulting from entrainment by the pipe flow superimposed on the hole flow due to static pressure differential

It can be shown that the approximate gradient of the asymptotes for the full range of pipe and hole sizes used may be obtained from the following equation:

$$G_{asym} = \left(0.0433\, D_{hole} - 0.0471\right)\left(2.487 - 0.0704\, D_{pipe}\right)$$

or more accurately from:

$$G_{asym} = \left(0.0063\, D_{hole}^2 + 0.0057\, D_{hole} + 0.005\right)\left(0.0013\, D_{pipe}^2 + 0.1135\, D_{pipe} + 2.822\right)$$

where $Q_{asym} = G_{asym}\, Q_{up}$ and which has the value 0.0415 in the case of Figure 4.47 (and Figure 4.10). The hole flow rate in the presence of upstream flow, cannot attain a value below this asymptotic value (nor fall below the flow rate attributable to the static pressure differential).

It may be concluded that a theoretical basis has been determined which supports the existence, form and magnitude of the Ultraflow phenomenon. In addition it has been noted that if the equations are applied to pipe upstream flow rates and pressures that are higher than was possible to develop in the experiment apparatus, the "asymptote" is in fact a tangent to a family of parabolas that model the Ultraflow phenomenon.

4.15 THE EFFECT OF EXTERNAL AIR FLOWS

Pipes are sometimes installed in areas that can have high ventilation flows such as within air conditioning ducts, within floor plenums or simply at ceiling level in open areas. An example of a typical duct monitoring method is shown in Figure 4.48, where pipes are inserted into the duct, using the dynamic pressure to drive air samples through a slot in each pipe. Microchip wafer fabrication plants (clean rooms) have air velocities of several metres/sec spanning large volumes. Perhaps the most demanding application has pipes mounted externally aboard railway wagons travelling through the Eurotunnel at speeds up to 130*km/h* (36*m/sec*). Typically however, external air velocities rarely exceed 10*m/sec*. It was considered important to gain an understanding of the impact of such velocities on the effectiveness of sampling holes.

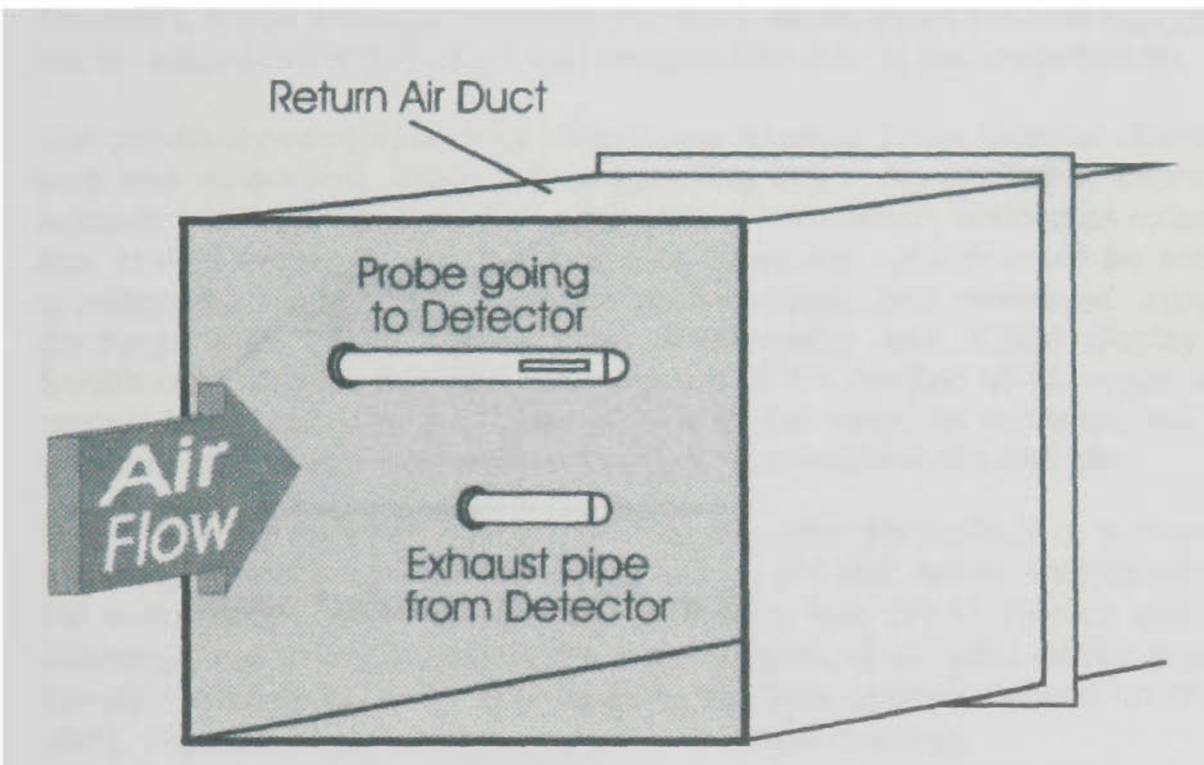

Figure 4.48 - Duct sampling example (Vision Products, 1997)
(offset, unequal length slotted pipes
with domed ends are shown)

Douglas et al (1979, p318) illustrate that for a long cylinder (or pipe) within an airstream, the pressure on the forward-facing quarter of the body is higher than the rearward-facing and side-facing three-quarters of the body. At high Reynolds numbers, the greatest reduction in pressure occurs at the sides, approximately at a right angle to the flow direction (if not slightly forward of a right angle). As a point of reference for the current investigation, the applicable Reynolds number at 20°C and at a velocity of 10*m/sec* is:

$$Re = \frac{D_p \, u_w}{k} = \frac{0.025 * 10}{1.5 * 10^{-5}} \approx 17{,}000$$

where D_p is the pipe external diameter and u_w is the external "wind" velocity. This value of Reynolds number lies within the "intermediate" range ($90 < Re < 10^5$) where the eddies formed behind the cylinder would break away, alternately on either side, to be washed away by the main airstream. Schlicting (1951/87, p21, p427) indicates that the surface pressure generated around the meridian of a long cylinder can be obtained from:

$$P - P_0 \quad = \quad C_\theta \, \rho \, u^2 \, / \, 2$$

where the coefficient C_θ ranges from +1 to approximately -2.5 according to the angular position around the cylinder, and ρ is the air density. This equation yields pressures in the order of +60 to -150 Pa, which are quite significant, being of similar magnitude to the pipe internal pressures. Therefore, it was expected that external flows would affect the hole flow rates but the magnitude of this effect was unquantified prior to this investigation.

The previously-used apparatus using 21*mm* internal, 25*mm* external diameter pipe was assembled, using a 2*mm* sampling hole. An additional, separate aspirator was used as a blower to generate a "crosswind", defined as external flow at right angles to the pipe axis. The crosswind velocity could be set by adjusting the voltage of a separate power supply, and monitored using a discharge pipe, fitted with a vane anemometer and digital display (a Schiltknecht Mini Air 2). The discharge could be directed at all angles with respect to the pipe axis and hole. A wind tunnel would be preferred, but the turbulent discharge was considered not unrepresentative of a real site.

Firstly, with nil crosswind, the hole flow rate was set to 2, 3 or 4 *litre/min* (resulting in hole differential pressures of 125, 275 and 460 Pa respectively) in the experiment. Then, the crosswind velocity was set to 10*m/sec* and the discharge was directed towards the hole meridian, at all radial angles around the pipe in steps of 22.5°, referenced to the hole position defined as 0° (or 360°). Figure 4.49 presents the results of the data obtained.

The results in Figure 4.49 appear consistent with the expected pressure distribution around a cylinder (discussed above). In a typical site the normal orientation for a hole is vertically downwards. The usual orientation of ventilation air flow toward aspiration pipes is horizontal (across a ceiling or through a duct or plenum). Therefore it is both appropriate and prudent to adopt the worst case scenario, which occurs for a crosswind angle of 90° or slightly less.

It should be noted that, while crosswind (by definition) is directed at a right angle to the pipe longitudinal axis, external flows could occur at any other angle in the horizontal plane. However, further experiments have indicated that the greatest reduction in hole flow occurs for external flow at a right angle to the pipe axis (and at about 90° to the hole radial), i.e. crosswind.

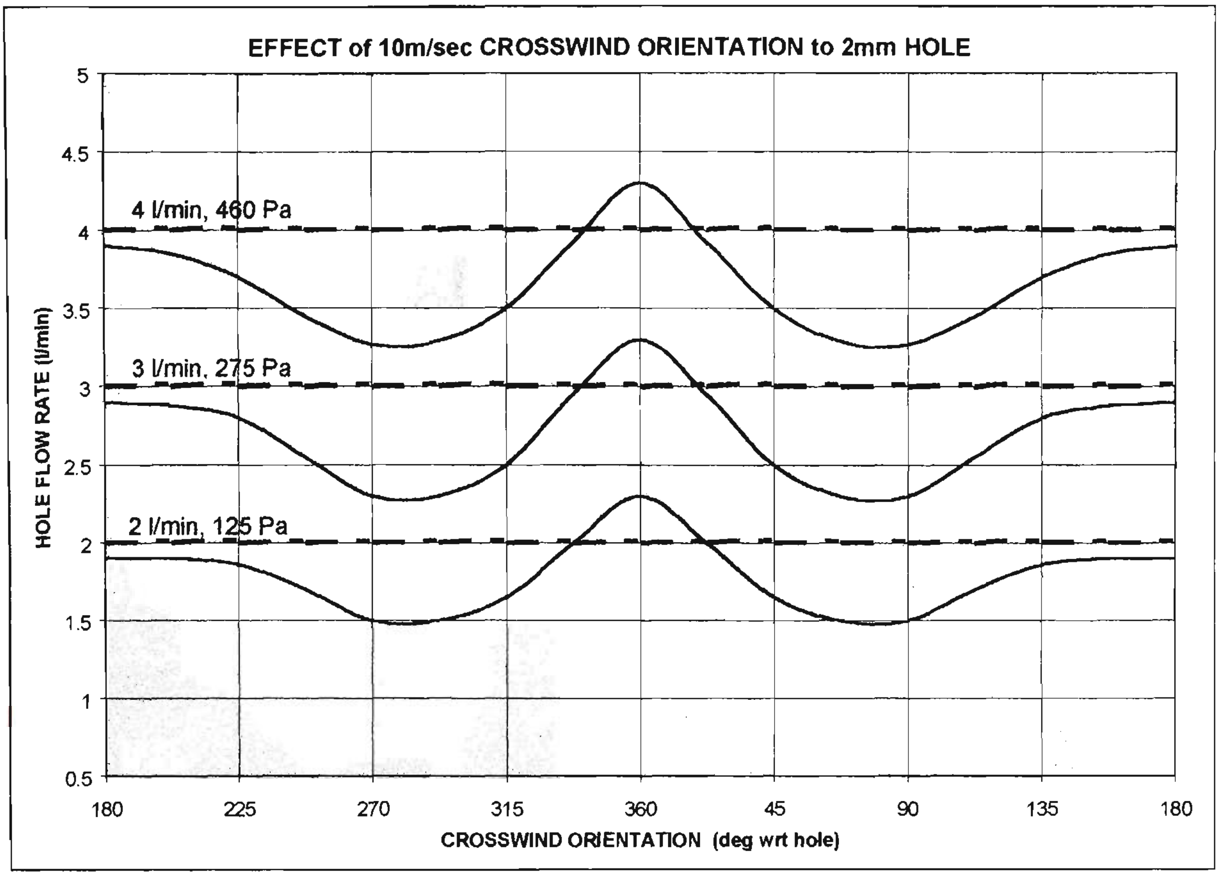

Figure 4.49 - Impact of external flows on hole flow rates

Figure 4.49 shows that a crosswind of $10 m/sec$ would typically reduce the hole flow rate by some 0.5 to 0.75 *litre/min*. This phenomenon of crosswind causing a reduction in hole flow is termed "Infraflow" (as distinct from Ultraflow, discussed previously) and would have significant implications for system balancing, especially if the crosswind velocity varies throughout the aspiration zone and/or with time (e.g. ventilation could be turned off after hours, or the system, or part thereof could be subject to wind gusts or draughts in unsealed buildings or outdoor locations).

Having selected the crosswind angle of $90°$ for subsequent experiments, measurements were taken for the full range of hole pressures, with crosswind velocities ranging from 0 to 12 *m/sec* in steps of $2 m/sec$. Figure 4.50 presents the results obtained in terms of hole pressure and flow rate. As indicated on the graph, at a crosswind velocity of $10 m/sec$ the hole flow rate may be characterised as almost linear above 100Pa. An equation of best fit is:

$$Q_{holeC10} \quad = \quad -1.5E\text{–}06\,\Delta P_{hole}^{2} + 0.0057\,\Delta P_{hole} + 0.9 \qquad (\Delta P_{hole} > 100)$$

where $Q_{holeC10}$ is the hole flow in the presence of crosswind at $10 m/sec$. Figure 4.51 presents the same results in terms of crosswind velocity, where the reduction in hole flow due to crosswind seems almost linear, particularly at the higher pressures.

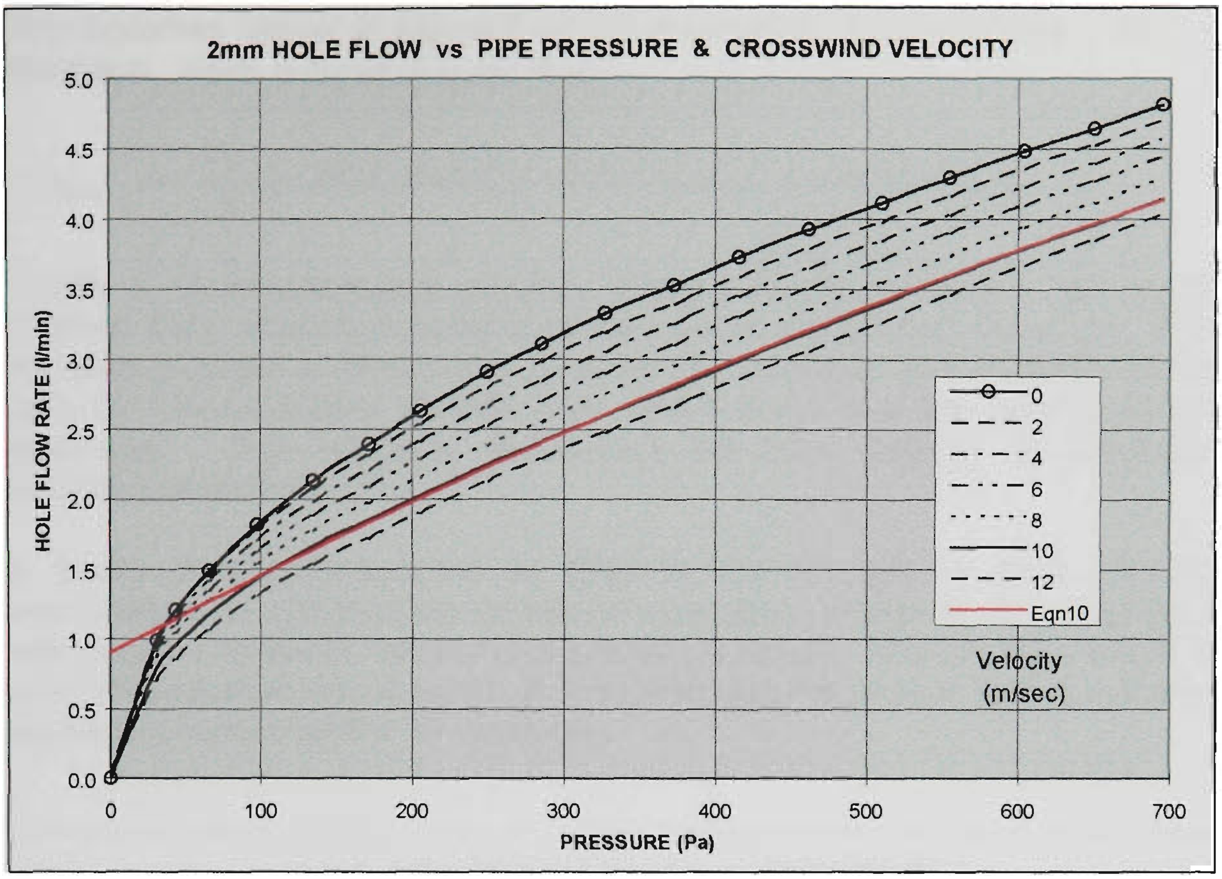

Figure 4.50 - Reduction in hole flow (versus pressure) due to crosswind

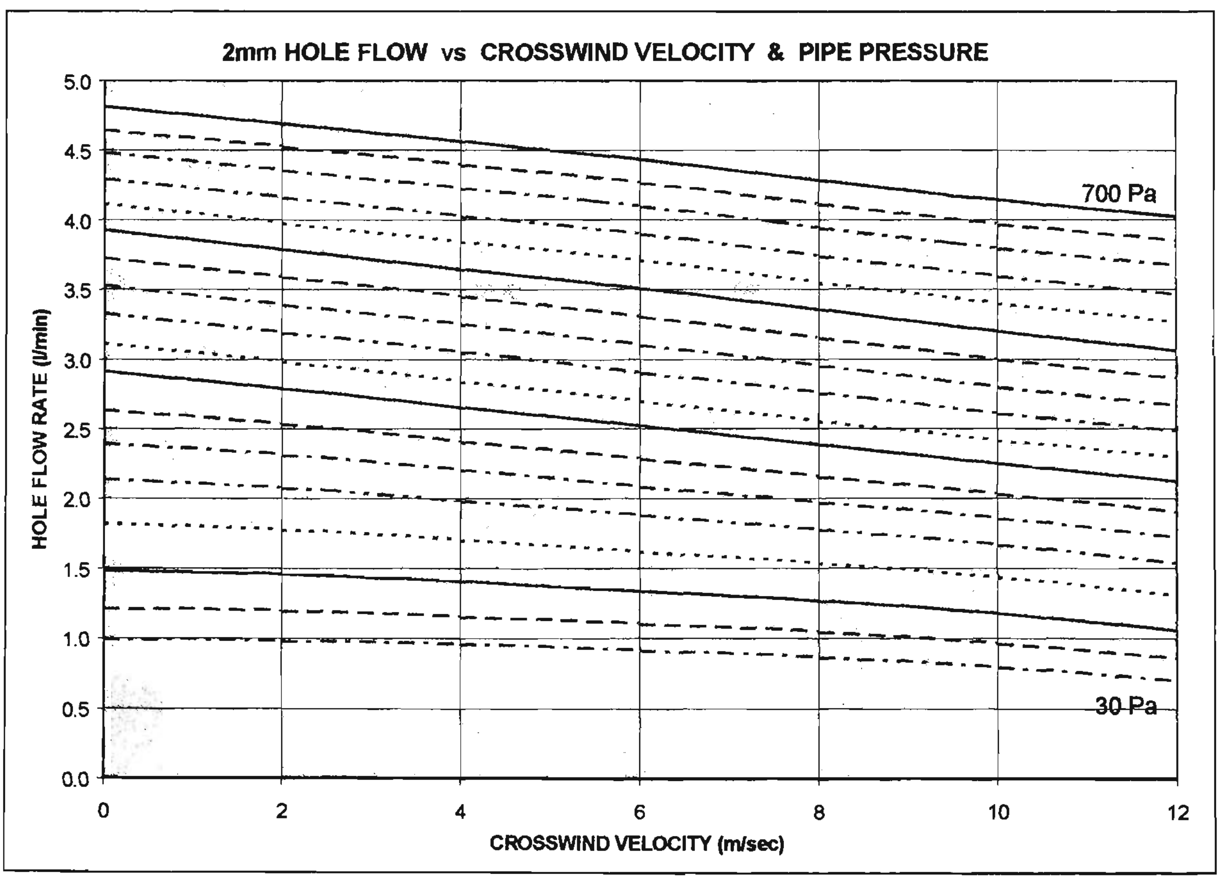

Figure 4.51 - Reduction in hole flow due to crosswind velocity

This becomes clearer in Figure 4.52 which presents the incremental hole flow reduction. Here, a curve of good fit is:

$$\Delta Q_{holeC} = \frac{U_C}{8}\left(-3.92E{-}09\,\Delta P_{hole}^3 - 6.7E{-}06\,\Delta P_{hole}^2 + 0.00381\,\Delta P_{hole}\right)$$

where U_c is the crosswind velocity. This equation is graphed in Figure 4.52 (dashed line), showing a good fit to the data at a crosswind of $8m/sec$. This equation provides a compromise fit to all the other data, as indicated with the data for $12m/sec$ (upper dashed line), where there is a discrepancy at low pressures. This negative discrepancy becomes positive at crosswind velocities below $8m/sec$.

A family of equations could be fitted to the six sets of data, allowing interpolation for intermediate crosswind velocities. However, for simplicity it was decided to adopt the above equation generally. The errors involved in using this equation would be small compared with the error of having, hitherto, applied no compensation for crosswind.

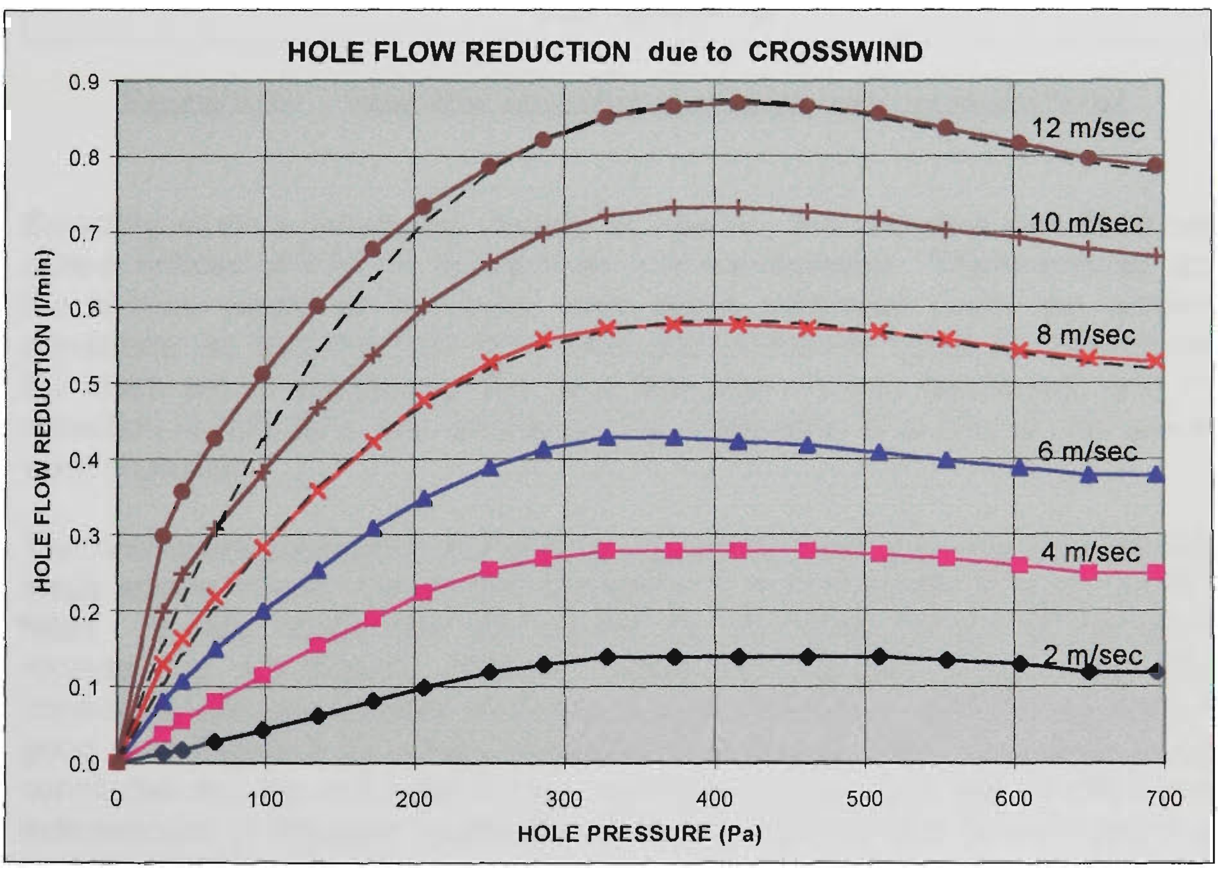

Figure 4.52 - Incremental hole flow reduction due to crosswind

The crosswind experiments to date had involved no upstream pipe flow. It was considered essential to extend the experiments to represent real installed systems, which have upstream pipe flows to varying extents at each hole.

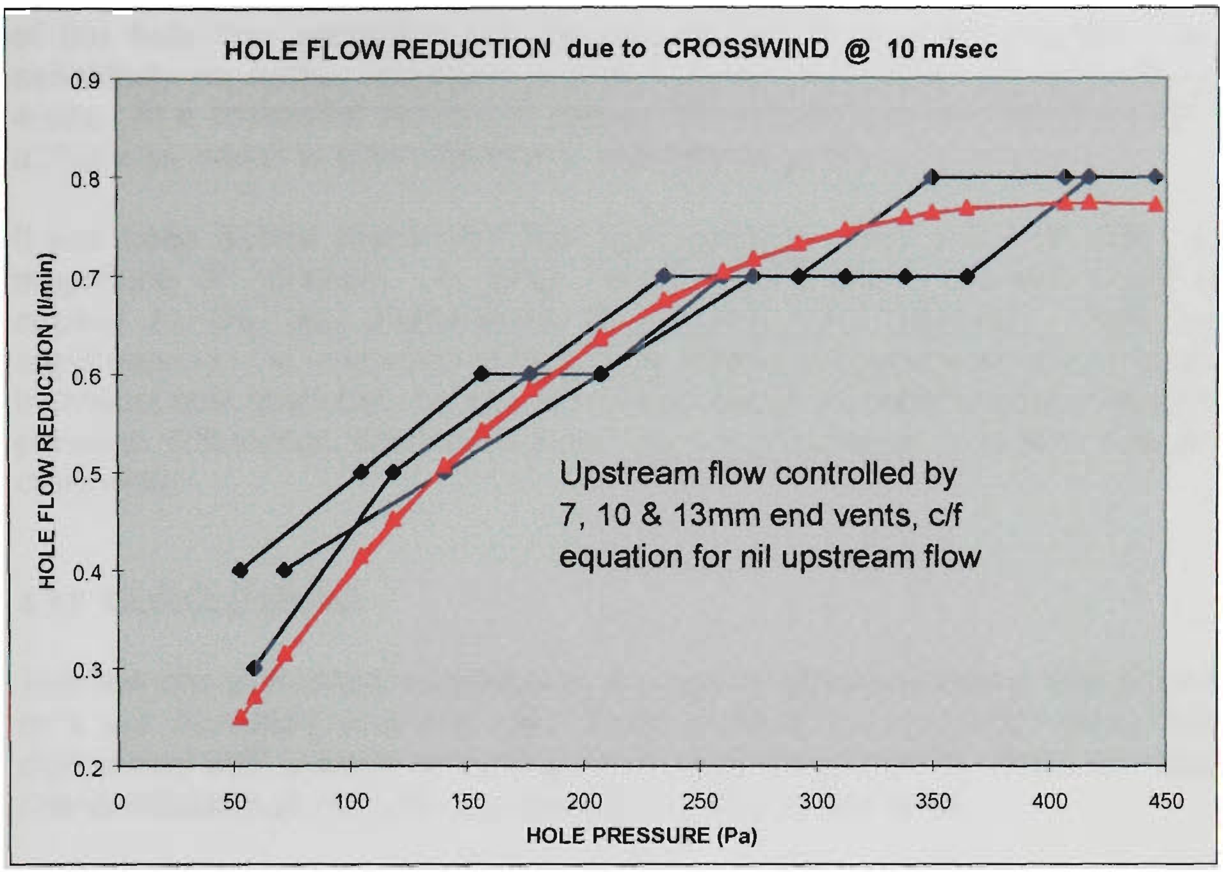

Figure 4.53 - Hole flow reduction correlated with upstream flows

Selecting again a crosswind velocity of $10 m/sec$, the test pipe was fitted with control orifices of 7.37, 10.36 and then 12.9 mm diameter. These orifices, and the $3000mm$ length of test pipe, were again calibrated under the ambient conditions, so that the hole flow rates and pressures could be determined. For each set of conditions, the hole flow rate without crosswind, and the reduction in hole flow rate caused by the application of a $10 m/sec$ crosswind, were recorded.

The results are presented in Figure 4.53, where it can be seen that the data steps appear coarse due to the resolution of the flowmeter at such low flow rates. It was noted that the results for the three control orifice sizes, representing significantly different ranges in upstream flow rates, were consistent with one-another and in turn, were consistent with the equation of good fit to Figure 4.52 (which involved nil upstream flow). Therefore it was concluded that the reduction in hole flow due to crosswind, the Infraflow, was independent of the pipe upstream velocity. This outcome is convenient for system modelling purposes.

4.16 SUMMARY OF INFRAFLOW

The phenomenon of Infraflow has been discovered whereby the expected hole flow rate caused by static pressure, can be reduced as a result of external flows. This reduction is greatest for external flows oriented mutually at right angles to the pipe axis and to the hole meridian radial. The magnitude of the hole flow reduction can be represented by a cubic equation, with essentially no further reduction in hole flow as pressures rise above about 400Pa. At a crosswind velocity of $10 m/sec$ the maximum hole flow reduction is $0.73 litre/sec$ which is quite significant, representing 21%.

It has been further discovered that pipe upstream flow does not affect the magnitude of Infraflow. In other words, superposition theorem could be applied to the two phenomena of Infraflow and Ultraflow. This has significance in the balancing of hole flows throughout a pipe system, whereby individual hole flows may be higher or lower than that predicted from the static pressure differential, depending upon the magnitudes of upstream flow and crosswind.

4.17 CONCLUSIONS

The flow characteristics applicable to a range of typical sampling hole sizes (2 to 4 mm diameter) and end vent sizes (2 to 8 mm diameter) have been determined and general equations have been developed to model the static flow coefficients at room temperature (23°C) and at sea level:

$$Q_{stat} = K_{hole}\,\Delta P_{stat}^{0.5} \quad where \quad K_{hole23} = 0.057\,D_{hole}^2 - 0.102\,D_{hole} + 0.156$$

$$Q_{stat} = K_{vent}\,\Delta P_{stat}^{0.5} \quad where \quad K_{vent23} = 0.0479\,D_{vent}^2 - 0.0127\,D_{vent}$$

whereas at all other temperatures and ambient absolute pressures:

$$K_{hole} = K_{hole23}\sqrt{\frac{\rho_T}{\rho_{23}}} \quad and\ obviously \quad K_{vent} = K_{vent23}\sqrt{\frac{\rho_T}{\rho_{23}}}$$

A typical pipe internal diameter is $21mm$ but if this is reduced below $15mm$, the hole or vent flow coefficient begins to increase, resulting in higher flow rates at any given pressure differential. In the limit, as the pipe diameter is reduced to match the hole or vent diameter, the flow coefficient becomes:

$$K_{hole} = \frac{\pi\,D_{hole}^2}{2\sqrt{\rho}}$$

Capillary tube nozzles, used to penetrate the ceiling in systems where the pipework is concealed, have been characterised in a similar manner so that:

$$Q_{stat} = K_{nozzle}\,\Delta P_{stat}^{0.5} \quad where \quad K_{nozzle23} = 0.037\,D_{nozzle}^2 + 0.027\,D_{nozzle}$$

The effect of altering the inlet geometry by rounding the shoulder to the extent of approximately 30% of the hole radius, was investigated with a view to minimising the possibility of dust buildup or whistle noise. This causes a 2, 3 or 4 mm rounded hole to behave as a 2.16, 3.38 or 5.09 mm square-shouldered hole respectively. The expectation based upon the literature, was that the change in flow coefficient would be much greater, requiring the use of smaller holes (defeating the purpose). As matters stand, rounding of the inlet is a suitable option.

To include the effect of the capillary tube in combination with the nozzle, the following equation may be applied on the assumption of laminar flow:

$$Q_{nozzle} = \pi \, D^2_{nozzle} \left(\left(t_1^2 + 4 \, t_2 \, \Delta P_{pipe} \right)^{\frac{1}{2}} - t_1 \right) \Big/ 8 \, t_2$$

where the terms t_1 and t_2 are obtained from:

$$t_1 = \frac{32 \, \rho \, k \, L_{tube} \, D^2_{nozzle}}{D^4_{tube}} \qquad t_2 = \left(\frac{15000 \, \pi \, D^2_{nozzle}}{K_{nozzle}} \right)^2$$

Within the typical range of tube sizes (0.5 to 2 m length and 5mm diameter), the hole diameter has the dominant effect over the tube length in determining the flow rate. However, the flow rate gradually and linearly falls toward zero as the tube length increases toward infinity (Figure 4.41).

The phenomenon of **Ultraflow** has been discovered whereby the expected hole flow rate caused by static pressure, is exceeded because of the upstream flow rate in the pipe. At any given pressure, this Ultraflow (as a component of the total hole flow) initially increases in small measure as the upstream flow rate increases. Then (within the bounds of practicable system flow rates and pressures) an upstream flow rate threshold is reached, above which the hole flow rate increases more strongly, and linearly with upstream flow rate, having become largely independent of pressure.

To quantify this effect, the Reynolds number representing the hole flow may be normalised using the following equation applicable to all hole diameters (in the size range of current interest). For convenience this is set to have a value of 1 at a pressure differential of 100Pa:

$$\mathrm{Re}\,n_0 = \mathrm{Re}_{hole0} \, / \left(92.5 D^2_{hole} - 24.5 D_{hole} + 953 \right)$$

The transitional increase in hole flow rate (averaged over all hole sizes) is:

$$\mathrm{Re}\,n_{TA} = \mathrm{Re}\,n_0 + 2.9E\text{–}05 \, \mathrm{Re}_{up}$$

At increased upstream flow rates this equation will intersect with the Ultraflow threshold (in practice the data tightly asymptote to this threshold). In the case of a typical sampling hole (2 to 4 mm diameter) in a typical pipe (21mm diameter), this threshold (or asymptote) can be obtained in terms of the normalised hole Reynolds number as follows:

$$\mathrm{Re}\,n_A = \frac{\mathrm{Re}_{up}}{3150}$$

At a given Reynolds number, the threshold is deferred as the pipe radius is reduced (the pipe velocity is increased), or as the sampling flow velocity entering the pipe is reduced (e.g. with a capillary adaptor) - in both cases reducing the penetration of the induction jet. The revised hole Reynolds number after adjustment for Ultraflow becomes as follows, where Re_{nU} is the larger of Re_{nTA} and Re_{nA}:

$$\mathrm{Re}_{holeU} = \mathrm{Re}_{nU} \left(92.5\,D_{hole}^2 - 24.5\,D_{hole} + 953\right)$$

An explanation for the cause of the phenomenon of Ultraflow is proposed in terms of the entrainment of hole flow by the main pipe flow (see Figure 4.42). A combination of the ambient pressure differential and entrainment by the pipe upstream flow causes a jet of air to be induced into the main pipe flow, causing disturbance to the flow regime. Each quantum of air comprising the induction jet must be accelerated to reach the velocity of the main pipe flow. This acceleration force causes an additional pressure drop in the vicinity of the hole, for which an equation has been derived theoretically. The effect of the pipe velocity profile has also been considered by reference to a momentum correction factor, so the resulting equation provides a satisfactory match to experimental data:

$$\delta P_{jet} = \rho \left(\frac{\left(Q_{up} + Q_{jet}\right)^2 - \beta\, Q_{up}^2}{A_{pipe}^2} \right)$$

where Q_{up} is the upstream flow rate, Q_{jet} is the jet (or hole) flow rate and β is the momentum correction factor applicable to the upstream velocity profile.

The entrainment phenomenon has been investigated theoretically with reference to a partly analogous jet ejector pump and consistent results have been obtained, including the asymptotic nature of the phenomenon. Based upon the above calculation for the jet acceleration pressure drop, the ratio of operating head to discharge head (R_H) has been derived theoretically as:

$$R_H = \frac{P_{up}/\rho + C_{jet}\,u_{up}^2/2}{\left(P_{up} + \delta P_{jet}\right)/\rho + \left(Q_{up} + Q_{jet}\right)^2 / 2A_{pipe}^2}$$

where:

$$C_{jet} = \frac{2}{\left(D_{hole} + 1\right)\left(D_{pipe}/21.2\right)^{0.8}}$$

and where C_{jet} is an empirical coefficient of entrainment which is introduced to correct for the deflection of the pipe upstream flow path by the impinging jet. After extensive consideration of all the experimental results (Figures 4.8, 4.10, 4.12, 4.22 and 4.25), very close agreement is obtained. The equation for R_H is implicit because:

$$Q_{jet} \;=\; Q_{stat} + Q_{ultra} \;=\; Q_{stat} + Q_{up}\left(1 - \sqrt{R_H}\right)$$

which takes into account the superposition of hole flows due to static pressure and Ultraflow (entrainment). Therefore it is necessary to provide an iterative solution. Nested iteration is required because the hole flow rate is incremented by entrainment which in turn increments the jet acceleration pressure drop, which in turn affects the value of R_H.

The effect of drilling the sampling hole at an angle (other than a right angle) to the pipe, was discovered to have negligible effect on the hole flow coefficient. Apparently because the pipe wall thickness is too small to impart a significant change in the induction jet trajectory, control of this angle does not provide a means for controlling the magnitude of Ultraflow.

The phenomenon of **Infraflow** has been quantified whereby the expected hole flow rate caused by static pressure, can be reduced as a result of external flows. This reduction is greatest for external flows oriented mutually at right angles to the pipe axis and to the hole meridian radial. The magnitude of the hole flow reduction can be represented by a cubic equation:

$$\Delta Q_{holeC} \;=\; \frac{U_C}{8}\left(-3.92E{-}09\,\Delta P_{hole}^3 - 6.7E{-}06\,\Delta P_{hole}^2 + 0.00381\,\Delta P_{hole}\right)$$

where U_c is the crosswind velocity. It is noted that essentially no further reduction in hole flow occurs at any crosswind velocity (up to $12m/sec$) as the pressure differential rises above about 400Pa. At a crosswind velocity of $10m/sec$ the maximum hole flow reduction is $0.73 litre/sec$ which is quite significant, representing 21%.

It has been further discovered that pipe upstream flow does not affect the magnitude of Infraflow, so that the two phenomena of Ultraflow and Infraflow can be applied by superposition.

The components of an aspirated smoke detection system are interactive. In applying the above results to correct the individual hole flow rates, this alters the flow rate in individual sections of pipe, affecting the pipe pressure drop, thereby altering the pressure distribution around the system. This can affect the system balance and therefore, the relative sensitivity of individual sampling holes, while establishing a new system operating point and affecting the calculation of smoke transport times.

CHAPTER 5 - DETERMINATION OF FRICTION FACTOR

5.0 INTRODUCTION

For the purpose of calculating the head loss in aspirated pipes, this Chapter begins with a review of the accepted procedure for determining the friction factor applicable to round pipes. The significance of the flow regime as determined by flow stability and damping is discussed. A method for the determination of friction factor in disturbed or developing flow regimes is discussed. Results are obtained for friction factor in terms of the degree of disturbance induced into the flow regime.

5.1 PUBLISHED DATA

As indicated in Chapter 1, the accepted approach to calculation of friction loss in round pipes is to apply an appropriate equation such as that of Darcy-Weisbach (which is repeated here for convenience):

$$H = f \frac{L}{D} \frac{u^2}{2g}$$

where H is the head loss (*metres*), f is the friction factor (*dimensionless*), L is the pipe length (*metres*), D is the pipe internal diameter (*metres*), u is the average air velocity (*m/sec*), and g is the acceleration due to gravity. This equation can be applied to laminar or turbulent flow by selection of an appropriate value for the friction factor. These values were empirically derived in terms of Reynolds number and published many decades ago, as indicated in the "Moody chart" which is reproduced for convenience in Figure 5.1 (Roberson, 1975 p298).

As previously stated in Chapter 1, Reynolds number within a round pipe is obtained from the following equation:

$$\mathrm{Re} = \frac{D\,u}{k}$$

where k is the kinematic viscosity (*m^2/sec*). Reynolds number is defined as the ratio of inertial force to viscous force acting upon the fluid (air). This provides an indication of the degree to which the flow is damped.

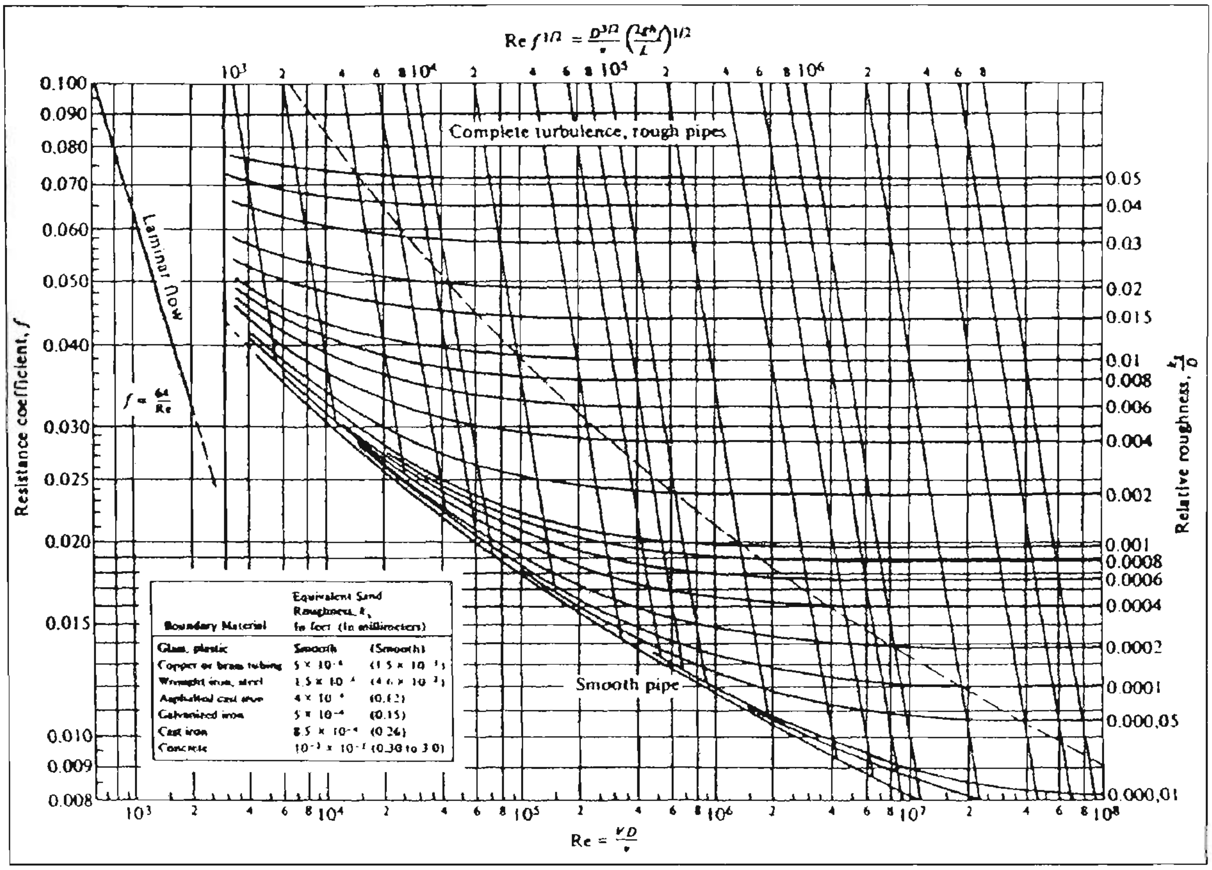

Figure 5.1 - "Moody chart" of friction factor in round pipes (Roberson, 1975), indicating the region of uncertainty for 2000<Re<3500

For example, if a small pocket of air is forced out of alignment with the main airstream because of some disturbance, then if the viscous force exceeds the inertial force, the disturbance energy of the pocket will tend to dissipate (as heat) such that the pocket is drawn into line with the main flow. In this case the motion is damped, which is typical of fully-developed flows at Reynolds numbers less than about 2000.

Alternatively, if the viscous force is not large enough to overcome the inertial force, then the pocket will tend to continue and spread its effect to neighboring air pockets. In this case its motion is undamped, which is typical of fully-developed flows at Reynolds numbers in excess of about 3500.

Damped motion tends toward stability and hence laminar flow. Undamped motion tends toward instability and hence turbulent flow. Where the ratio approaches critical damping, the flow regime (laminar or turbulent) is very much dependent upon the physical conditions. If the pipe is long and smooth without disturbances such as sockets or bends, then laminar flow can be maintained for Reynolds numbers up to about 2300 or a little higher. If the pipe has significant disturbances, then steady laminar flow may not be possible for Reynolds numbers of 1500 or even lower. Consequently, over a significant range of values, Reynolds number alone does not necessarily indicate the flow regime accurately.

As indicated on the Moody chart reproduced in Figure 5.1, it is widely accepted that for laminar flow, at all Reynolds numbers less than about 2000, the friction factor (or resistance coefficient) can be calculated simply:

$$f = \frac{64}{\mathrm{Re}}$$

It is also widely accepted that for turbulent flow, at all Reynolds numbers greater than about 3500, the Moody chart can be used to obtain the friction factor provided that the internal surface roughness is known. This roughness can be defined as a ratio of the internal surface contour amplitude, to the pipe internal diameter. It can be seen that for a Reynolds number of 3500, the friction factor can vary by a factor of two depending on the roughness. This magnitude of variation increases at higher Reynolds numbers.

As indicated in Figure 5.1, at Reynolds numbers from 2000 to 3500 the friction factor is not generally included in published data. However in 1933, Nikuradse published the data shown in Figure 5.2 (Roberson, 1975 p296) for which the surface roughness was introduced by adhering sand grains of particular sizes to the pipe walls. These data have previously been used for the modelling of aspirated pipe systems and the design of the aspirator (Cole, 1991).

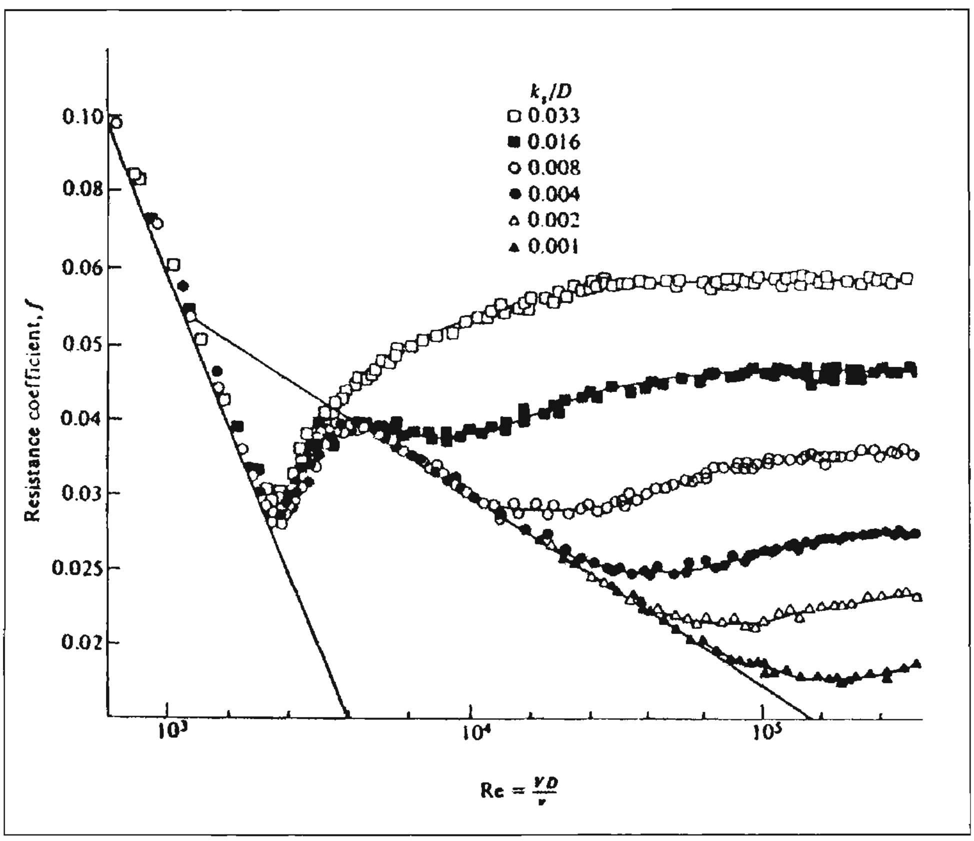

Figure 5.2 - Friction factors in the flow-transition region (Nikuradse 1932)

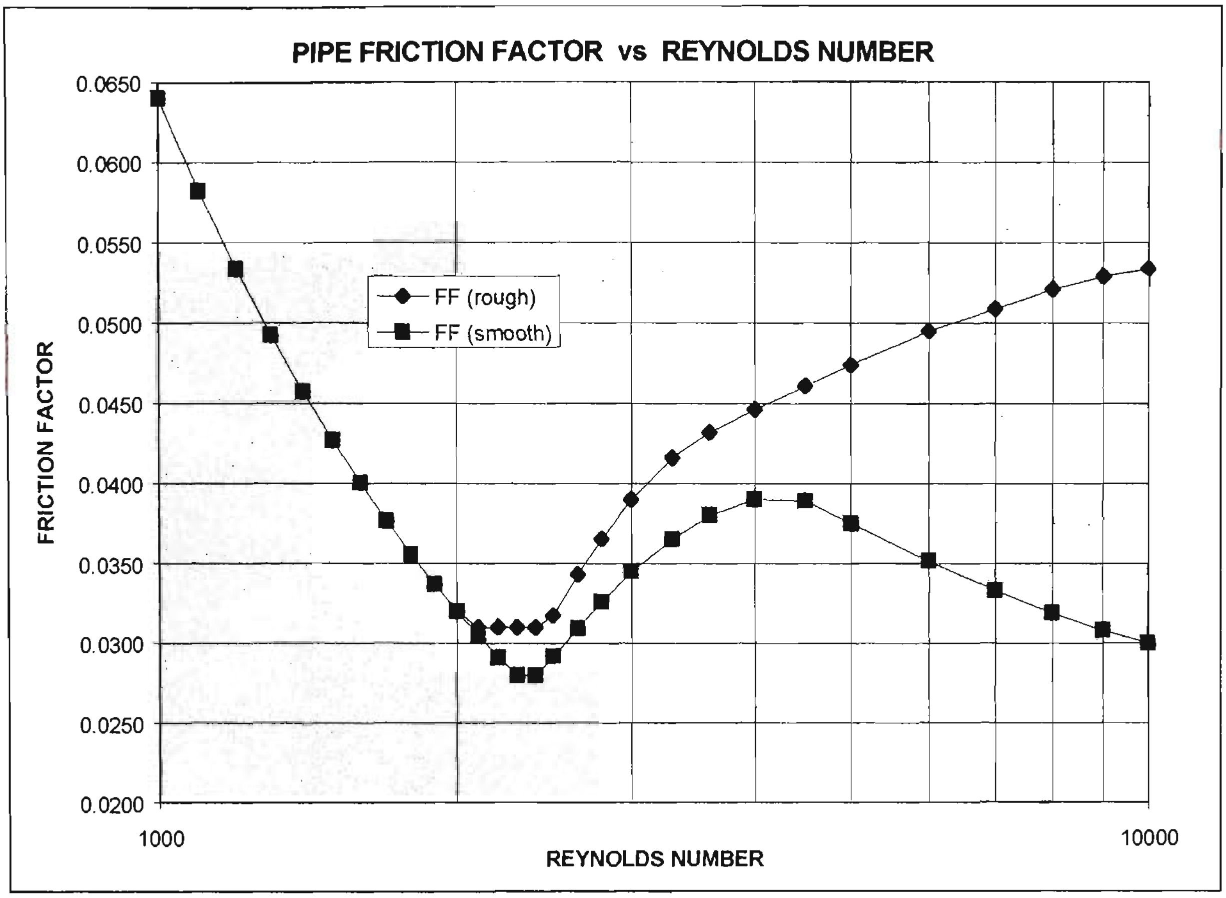

Figure 5.3 - Approximations to the Nikuradse data for friction factor

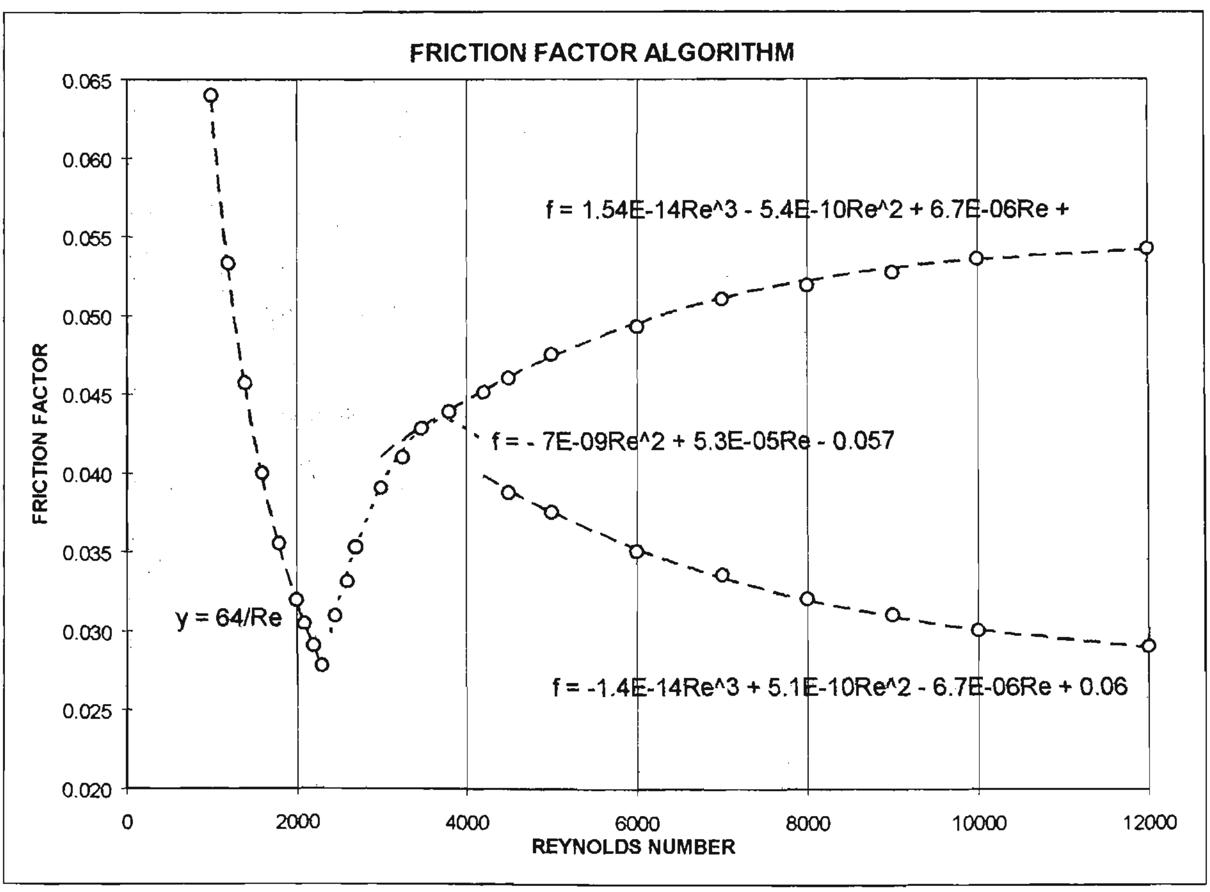

Figure 5.4 - Curves of best fit to Nikuradse data

These data were found to be difficult to apply with accuracy because they were presented graphically with poor scale delineation (logarithmic). Figure 5.3 is the result of very careful inspection of the Nikuradse data, relating to very smooth (lower curve) and very rough pipes, for $1000 < \mathrm{Re} < 10{,}000$.

Early investigations within this project indicated that the data pertaining to smooth pipes did not produce calculated results that were in agreement with experimental results. Better agreement was obtained from the data pertaining to rough pipes. To suit computer modelling, some curves of best fit to the Nikuradse data were developed, as presented in Figure 5.4. As discussed in Section 2.2, these curves of best fit were initially obtained using the Microsoft Excel curve-fitting routines, the results of which had to be painstakingly refined due to rounding errors in the equations it presented. This analysis has resulted in the following algorithm for rough pipes:

$\mathrm{Re} < 2100$: $$f = \frac{64}{\mathrm{Re}}$$

$2100 < \mathrm{Re} < 2460$: $$f = 0.0310$$

$2460 < \mathrm{Re} < 3480$: $$f = -7E\text{–}09\,\mathrm{Re}^2 + 5.3E\text{–}05\,\mathrm{Re} - 0.057$$

$\mathrm{Re} > 3480$: $$f = +1.54E\text{–}14\,\mathrm{Re}^3 - 5.4E\text{–}10\,\mathrm{Re}^2 + 6.7E\text{–}06\,\mathrm{Re} + 0.0254$$

This algorithm was used quite effectively in a computer program that will be described later. As a software option, an alternative algorithm for smooth pipes could be selected, but the calculated results based on this algorithm indicated a greater departure from experimental data at high flow rates (in the region above $\mathrm{Re} = 3000$). Furthermore, over an extended period of use, even the rough pipe algorithm did not always appear to be sufficiently accurate when comparing the computer calculated results with site test results. Accordingly it was decided to conduct an investigation into the friction factor obtained with pipe systems typical of those expected to be used in aspirated smoke detection systems.

5.2 EXPERIMENTAL TECHNIQUE AND RESULTS

The "standard" pipe is $25mm$ external, $21mm$ internal diameter PVC electrical conduit that is available in $4m$ lengths and may have a socket at one end. To obtain a representative example of smooth pipe, it was necessary to avoid interruptions due to joints (sockets), bends or other sources of disturbance to the air flow. Therefore a $4m$ section of pipe was selected, with pressure tappings (as described in Figure 2.4) positioned $3000mm$ apart (being $500mm$ from each end). The internal diameter was measured at the ends using electronic calipers, at $21.2mm$ ($0.0212m$), and was assumed to be constant. It was proposed that the average velocity would be determined from the quotient of the measured flow rate (Q) and cross-sectional area (A). This area is in turn determined by the pipe internal diameter (D). Accordingly:

$$\text{Re} = \frac{D\,u}{k} = \frac{D\,Q}{k\,A} = \frac{4\,D\,Q}{k\,\pi\,D^2} = \frac{4\,Q}{k\,\pi\,D}$$

Substituting for $k = 1.513E\text{-}05$ at 20°C and converting the flowmeter reading from *litre/min* to m^3/sec (a factor of precisely 60,000 i.e. $6E04$), we obtain:

$$\text{Re} = \frac{4}{1.513E{-}05 * 3.1416 * 0.0212 * 6E04}\,Q = 66.16\,Q$$

To obtain results in terms of pressure drop instead of head loss, we include the density term (ρ) and amend the Darcy-Weisbach equation to:

$$\Delta P = \rho\,f\,\frac{L}{D}\,\frac{u^2}{2}$$

Transposing to obtain the friction factor, then substituting for u and A :

$$f = \frac{\Delta P}{\rho}\,\frac{2\,D}{L}\left(\frac{A}{Q}\right)^2 = \Delta P\,\frac{2\,D}{\rho\,L}\left(\frac{\pi\,D^2}{4\,Q}\right)^2 = \frac{\Delta P}{Q^2}\,\frac{2\,\pi^2\,D^5}{16\,\rho\,L}$$

Now substituting for $D = 0.0212$, $L = 3.000$ and $\rho = 1.204$ at 20°C, with flow rate again expressed in *litre/min*:

$$f = \frac{\pi^2\,D^5}{8\,\rho\,L}\,\frac{\Delta P}{Q^2} = \frac{3.1416^2 * 0.0212^5 * 3.6E09}{8 * 1.204 * 3.000}\,\frac{\Delta P}{Q^2} = 5.283\,\frac{\Delta P}{Q^2}$$

Thus it is possible to measure the pressure drop obtained for a $3m$ length of pipe over a wide range of measured flow rates, and apply the above equations to obtain the Reynolds numbers and friction factors. The main potential source of error (apart from the instrumentation) would be the air density which is dependent upon ambient temperature and ambient pressure (weather and altitude).

The pressure tappings in the test pipe were connected to the Yokogawa differential pressure gauge. The test pipe was connected to the Furness flowmeter and thence to one or two aspirators in series, operated from a fully adjustable regulated power supply. Care was taken to ensure that the pipe was straight.

To ensure that the flow regime would be fully-developed, an additional $4m$ length of pipe was connected to the inlet of the test pipe. This provided an entry length of $4.5m$ prior to the first pressure tap. The temperature according to a digital thermometer was noted as 20.2°C which was regarded as 20°C for experimental purposes.

Initially the results were obtained in steps of *5litre/min* up to *160litre/min*. The flow readings were adjusted in accordance with the flowmeter calibration curve discussed in Chapter 2.

It was discovered that the pressure gauge had insufficient resolution to provide reliable readings at low flow rates, so it was decided to find the flow rate at which the pressure gauge reading would just change, in steps of 1Pa up to 20Pa or more. The point at which the pressure reading would just increment for a rising flow rate, was tested against the point at which the pressure reading would just decrement for a reducing flow rate. With painstaking care it was possible to note one flow rate reading for each pressure change, with an uncertainty of *one* in the least significant digit position.

The results obtained for the smooth pipe with $4.5m$ entry length were tabulated and graphed, together with the $f = 64/\mathrm{Re}$ curve pertaining to fully developed laminar flow which was included for reference. It became of immediate concern that the data was a poor fit to this reference curve at low flow rates. It was then recognised that because the pressure gauge could only be set to "zero" using a coarse and stiff screwdriver adjustment, this zero-setting could be inaccurate within as much as ± 1Pa, affecting all readings by such an offset. Therefore, it was proposed to adjust all of the pressure readings for this offset. With this particular experiment it was noted that for all readings above 3Pa, an offset of -0.7Pa was necessary and sufficient to produce readings that were consistent with the laminar flow equation.

After making this correction, the minimum value for the friction factor within the transition region was 0.0320 (at Re= 2200) while the peak value was 0.0397 (at Re=2800). By inspection of Figure 5.5 it was possible to derive (manually) a curve of best fit to the turbulent flow region (dotted line), namely:

$$f \;=\; 0.357 / \mathrm{Re}^{0.275}$$

To fit the transitional flow region, it would be necessary to develop an algorithm. To provide a clearer understanding of this region, the data are presented over a narrower flow range in Figure 5.6.

The effect of having a short entry length was tested by removing the initial $4m$ pipe, resulting in a $500mm$ entry length. This was considered somewhat more-representative of a real situation in which the airflow regime entering the pipe section would be disturbed by a nearby bend or socket. These results are presented in Figure 5.7. Here it can be seen that the transition region is significantly skewed when compared with Figure 5.6, with a minimum friction factor of 0.0340 (at Re=2300) and a peak of 0.0382 (at Re=3100).

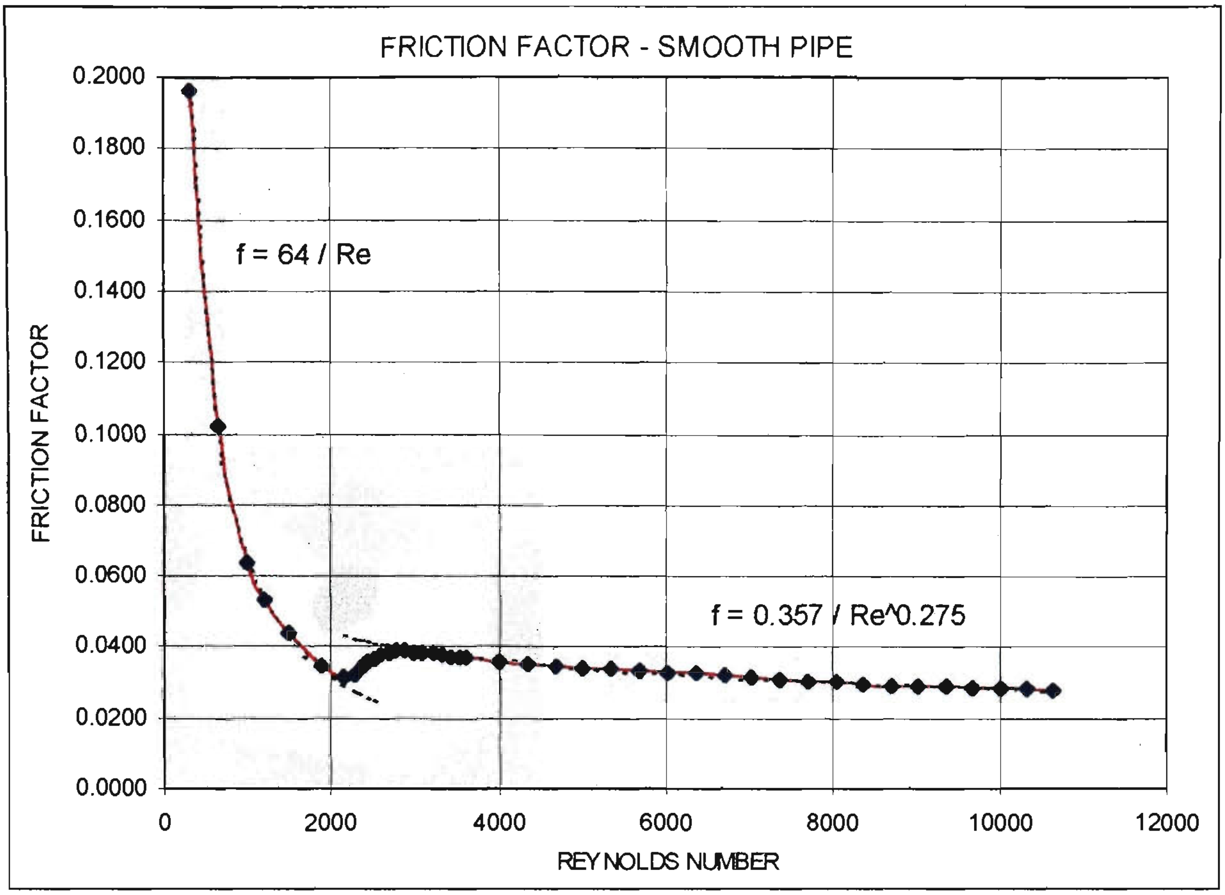

Figure 5.5 - Measured friction factor in smooth round pipe

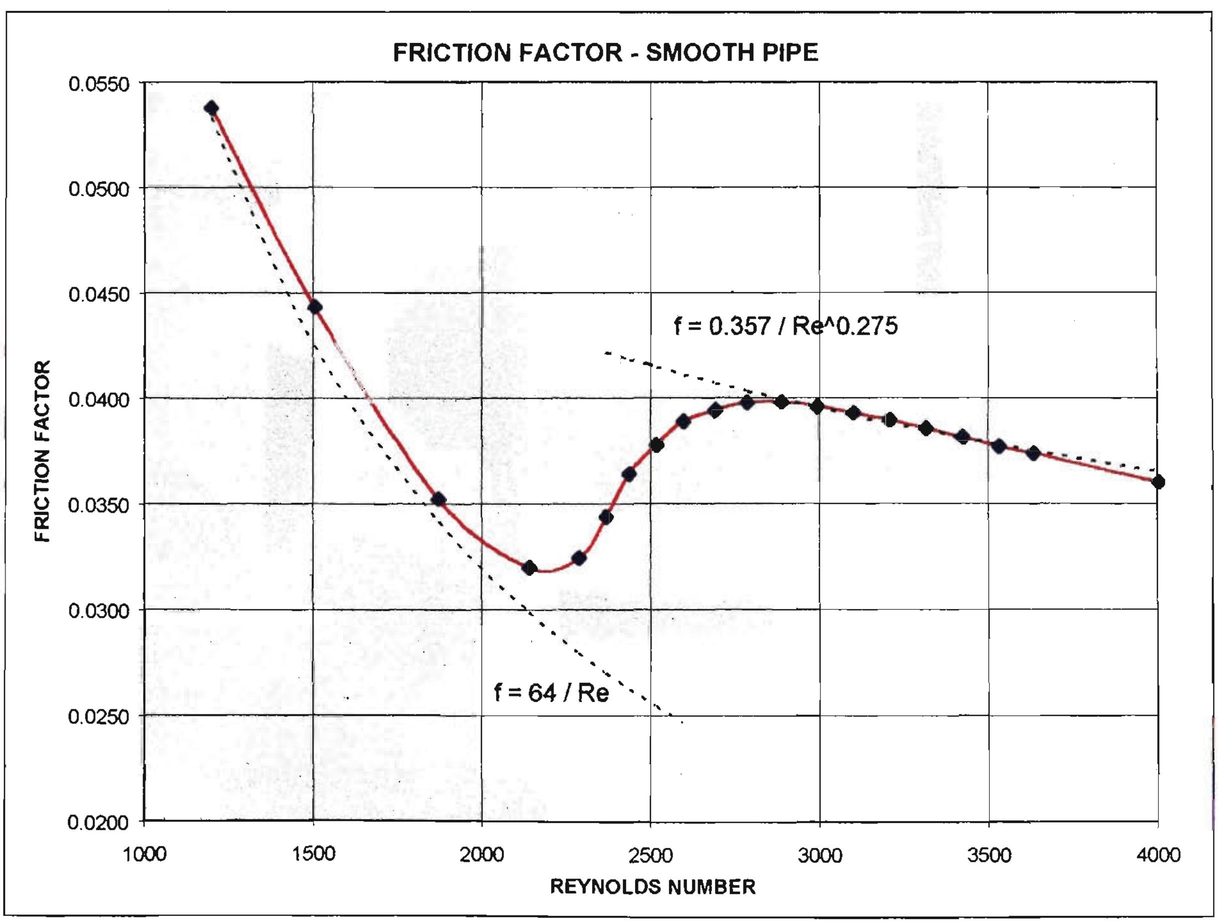

Figure 5.6 - Measured friction factor for $1000 < Re < 4000$

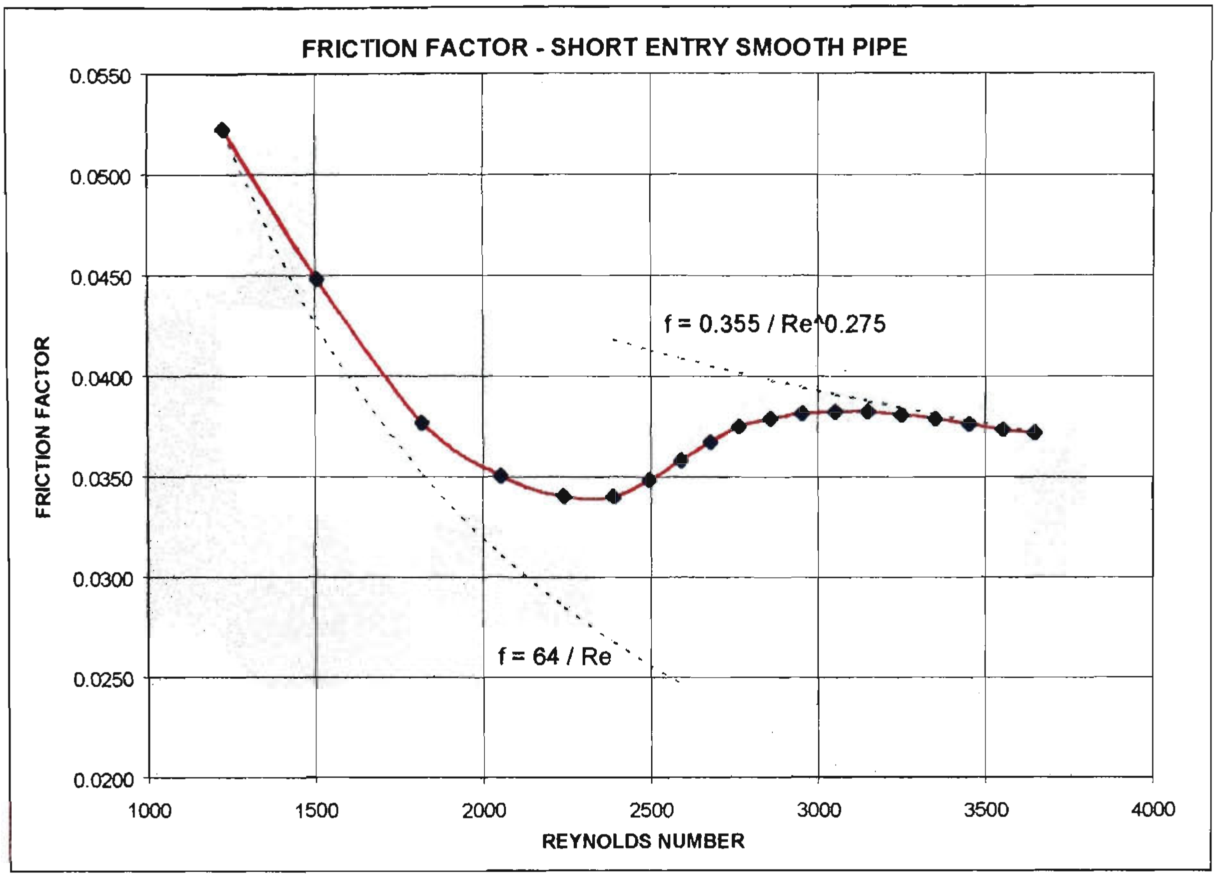

Figure 5.7 - Friction factor with disturbed flow regime

The next experiment involved a typical pipe socket. In this case another (identical) pipe was selected, which had a socket molded onto one end. This pipe was cut into two halves and rejoined using the socket, so that the socket was in the middle of the $4m$ overall length. Then pressure tappings were positioned $500mm$ from each end of this socketed test pipe, $3000mm$ apart, in the same manner as for the original (smooth) test pipe discussed above.

Figure 5.8 presents the data for the socketed pipe, wherein the zero-offset of the pressure readings have again been adjusted to achieve consistency with the laminar flow equation (at low Reynolds numbers). Here the minimum value of the friction factor in the transition region was 0.0322 (at Re=2200) while the peak value was 0.0409 (at Re=2900). The curve of best fit to the turbulent flow region (at higher Reynolds numbers) was:

$$f \quad = \quad 0.372 \,/\, \mathrm{Re}^{0.275}$$

This showed that the friction factor in the turbulent region was (0.372 / 0.355) i.e. 4.2% higher than for the smooth pipe. This difference was not as great as expected from the original Nikuradse data, but would nevertheless be quite significant in determining the pressure distributions in the segments of pipework close to the detector (where high flow rate occurs). This would in turn influence the remainder of the pipe. Note that a pipe of $100m$ length would have at least 25 sockets.

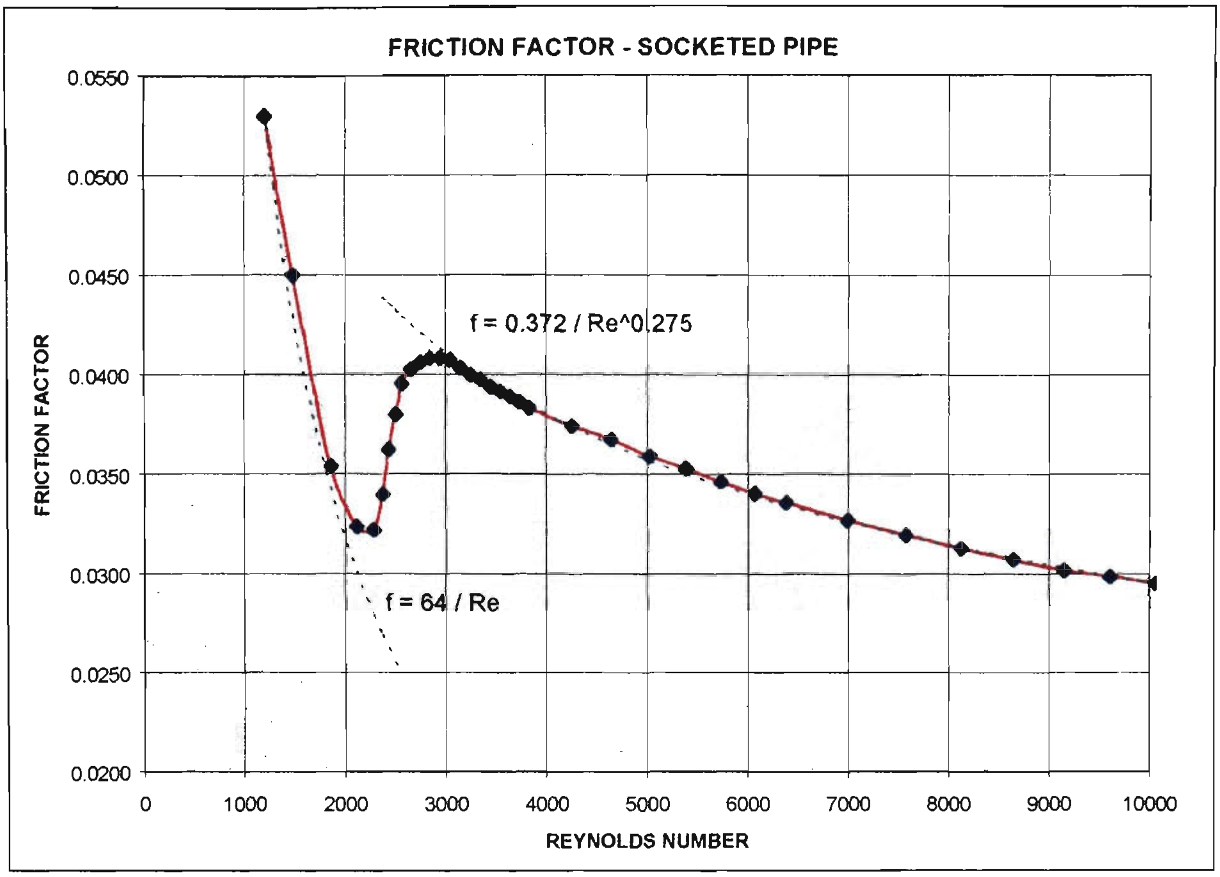

Figure 5.8 - Friction factor with socketed pipe, $1000 < Re < 10{,}000$

As a note of caution, it can be shown that if the pressure readings were not adjusted by -0.7Pa throughout the range as described, then the curve of best fit becomes $f = 0.47/Re^{0.3}$ with a peak value in the transition region of 0.0428, which is 4.9% higher. As previously discussed, there would be a substantial mismatch in the laminar flow region. If instead the readings were adjusted by -0.5Pa (being half of the finest resolution step), then the curve of best fit becomes $f = 0.39/Re^{0.28}$ with a peak value in the transition region of 0.0414, but even this adjustment would not produce good conformity with the laminar flow curve (because part of the data passes beneath the curve). Thus pressure readings could provide a significant source of error and consistency checks need to be rigorously applied. It is assumed that the laminar flow curve at low Reynolds numbers is so fundamental and well-established that it can be relied upon (as the best-case scenario).

Figure 5.9 presents the data within a narrower flow range, for comparison with Figs 5.6 and 5.7. Again it is clear that the friction factor within the transition region is significantly affected by the physical conditions.

For the next series of experiments, a *2mm* hole was drilled *100mm* upstream of the first pressure tap in the socketed test pipe. The induction jet of air entering the pipe would disturb the flow regime to some extent, in a manner typical of an installed pipe system.

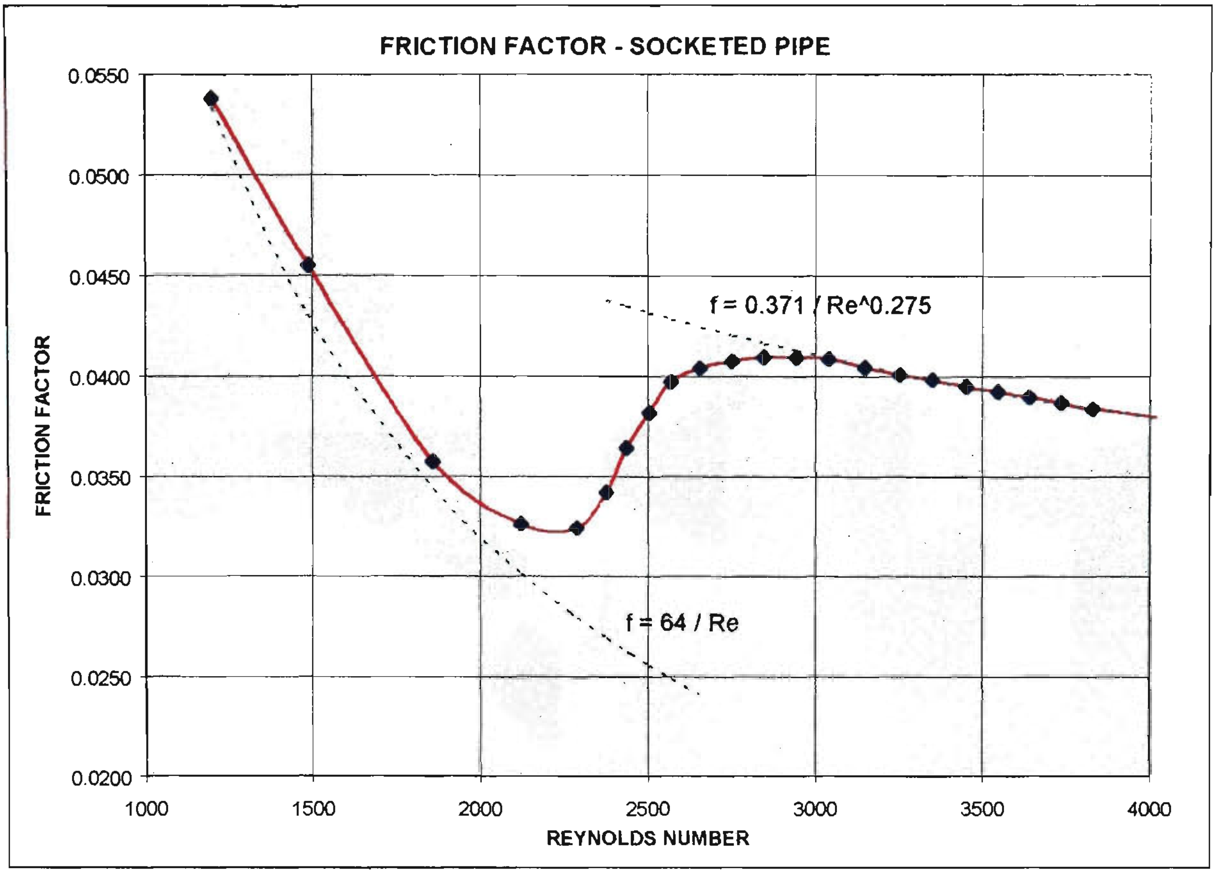

Figure 5.9 - Friction factor with socketed pipe, $1000 < \mathrm{Re} < 4000$

It was considered important to simulate the position of the hole, to represent its location in the pipe at various distances from the detector. The significant difference that occurs as a consequence of its position is the relative quantity of upstream flow compared with sampling hole flow.

By throttling the far end of the test pipe, the upstream flow rate could be adjusted. Thus, at a given pressure setting at the sampling hole, the quantity of air introduced by the sampling hole (as a proportion of the upstream pipe flow), would change. Not only would this proportion represent differing positions along the pipe, it would also establish differing degrees of disturbance to the upstream flow regime caused by the sampling hole induction jet. A convenient outcome of this approach was that the degree of disturbance to the pipe flow regime, could be adjusted without need to alter the sampling hole size.

The standard orifice plates discussed in Chapter 2 were chosen to provide a set of end vents with eight different throttle settings, representing the pipe flow rate at different locations along virtually the entire length of a typical pipe system. Pressure and flow rate readings were taken throughout the transition region, based upon a range of pressure drops from 5 to 16 Pa along the $3000mm$ segment of test pipe. This corresponded to Reynolds numbers from about 1500 to 3000. This range incorporated a -1Pa zero-error correction in the pressure gauge readings.

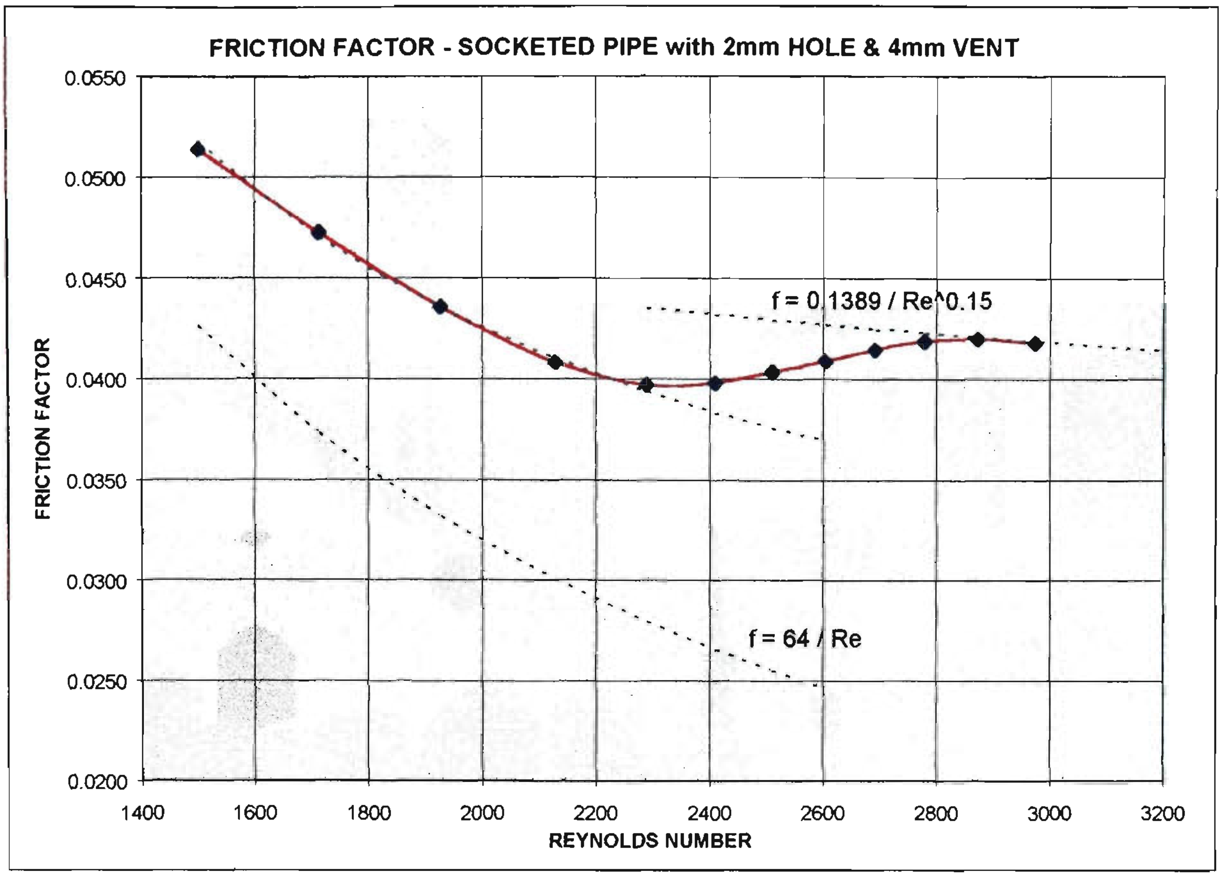

Figure 5.10 - Friction factor after highest flow disturbance ($4.0mm$ vent)

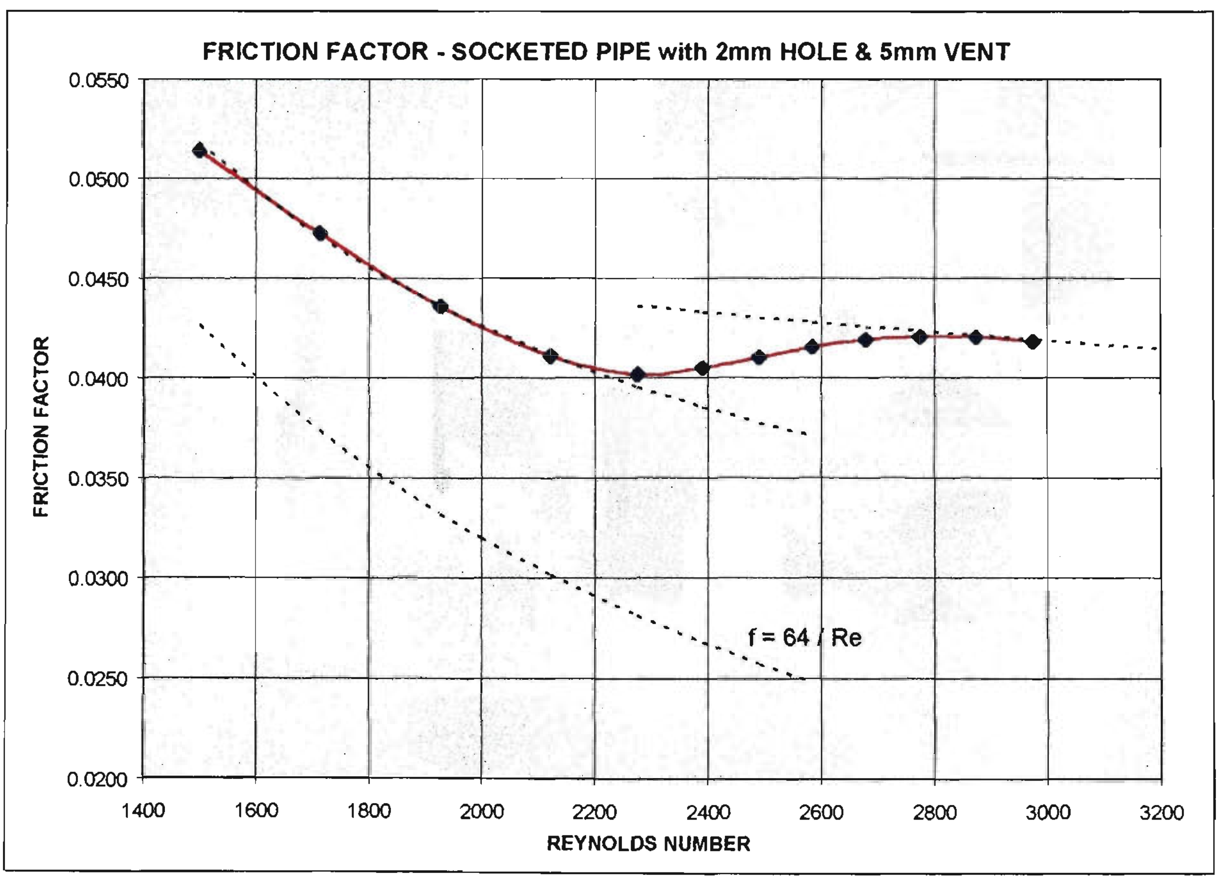

Figure 5.11 - Friction factor after high flow disturbance ($5.31mm$ vent)

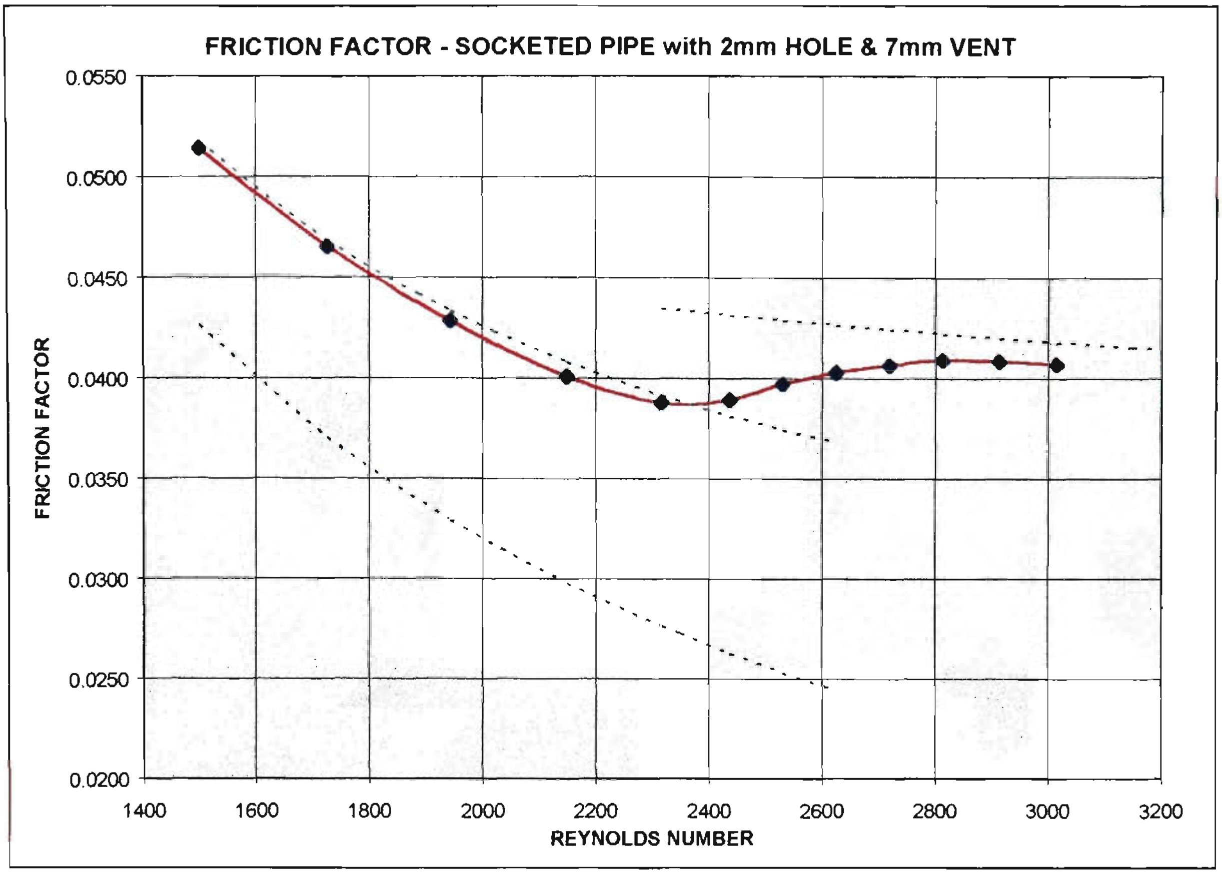

Figure 5.12 - Friction factor after moderate flow disturbance ($7.37mm$ vent)

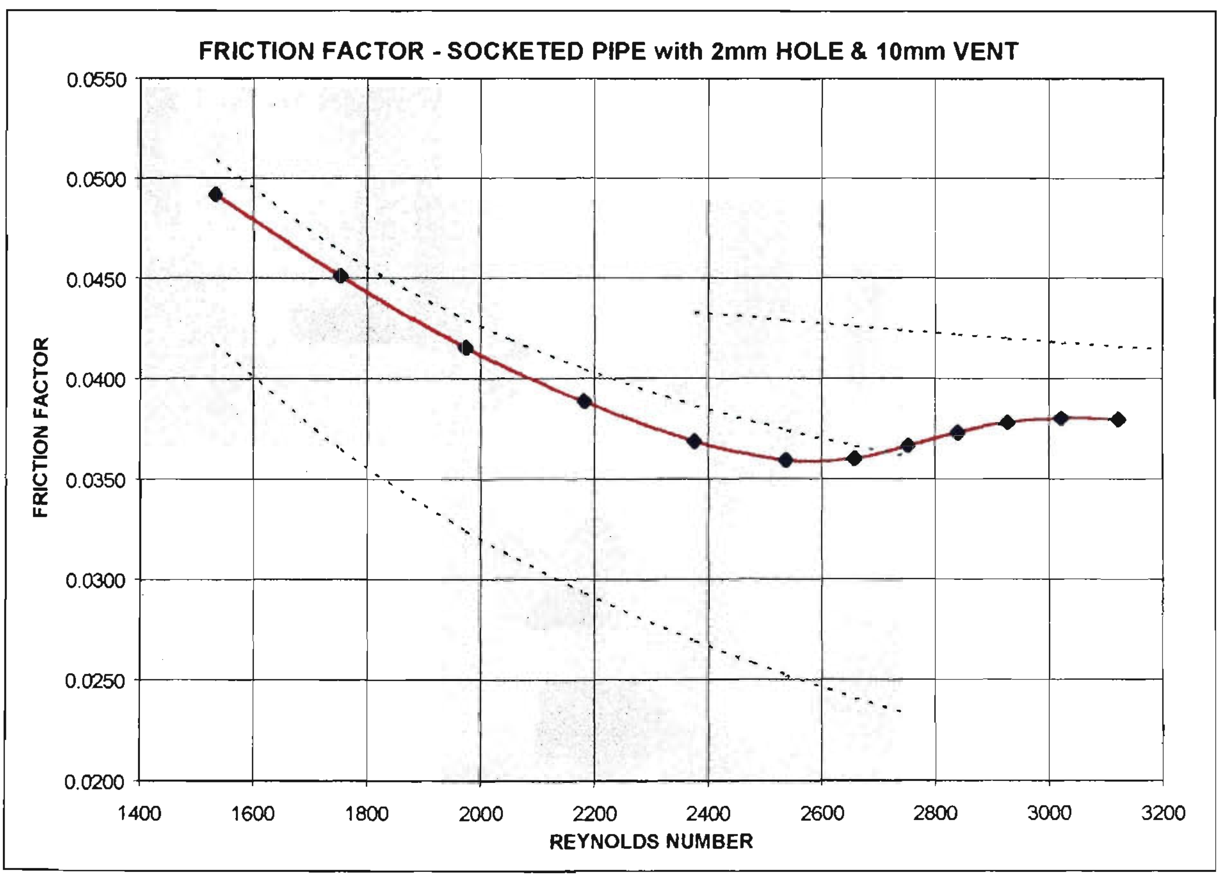

Figure 5.13 - Friction factor after moderate flow disturbance ($10.36mm$ vent)

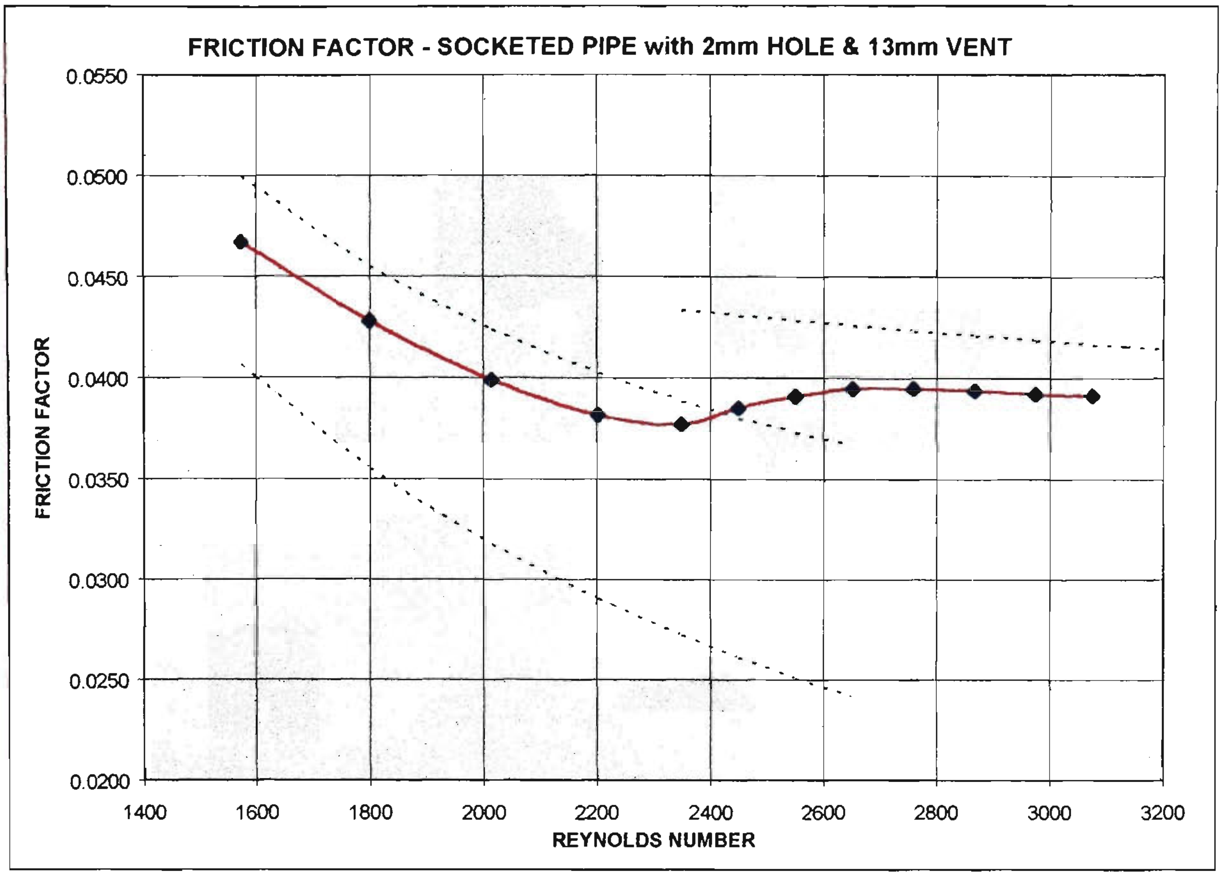

Figure 5.14 - Friction factor after small flow disturbance ($12.9mm$ vent)

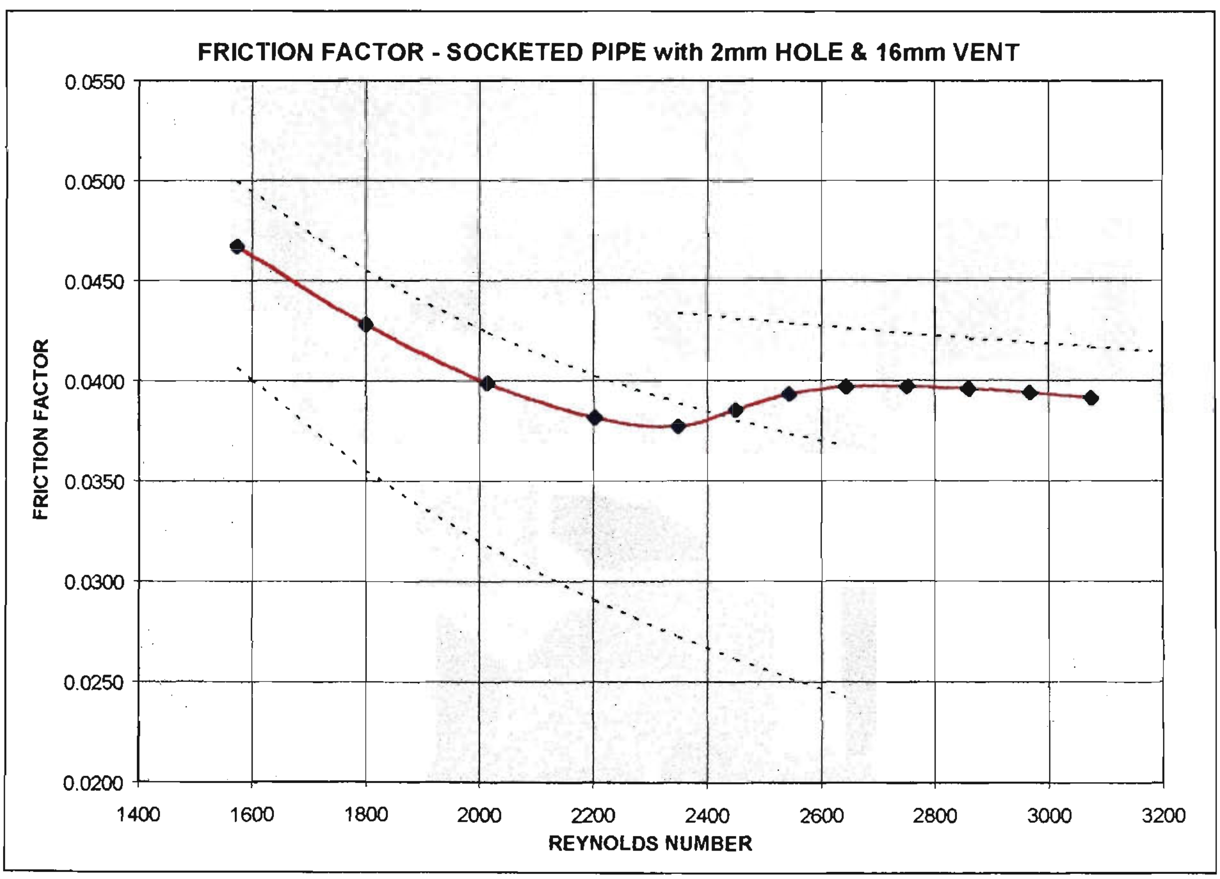

Figure 5.15 - Friction factor after minimal flow disturbance ($16.37mm$ vent)

The results are presented in Figures 5.10 to 5.15, for the 4.0 to 16.37 *mm* end vents respectively. The 21.2*mm* end vent was also tested but the results were identical to the 16.37*mm* vent. On these graphs, the standard $f = 64 / \mathrm{Re}$ curve is included for reference. So too is the $f = 0.1389 / \mathrm{Re}^{0.15}$ curve from Figure 5.10. This enables the relative movement of the friction factor data in relation to these equations, to be seen from graph to graph.

Whereas the movement of the friction factor data in relation to the end vent size was interesting, this was not yet in a form that could be directly applied to a pipe system. It was necessary to determine the actual ratio of flow entering the hole in each case, compared with the main pipe flow.

For each reading, the pressure in the pipe beside the hole was measured. In a separate experiment, the flow versus pressure characteristic of the hole was determined, as presented in Figure 5.16. Although these readings were taken over a wide pressure range of 100 to 1000 Pa, the flow rates ranged from only 1.8 to 5.5 *litre/sec*. The flowmeter resolution produced coarse data, but the most credible curve of good fit was determined (manually, because it could not be generated by Excel). For simplicity this curve is presented as a single term equation (necessitating two significant digits in the exponent):

$$Q = 0.132\ \Delta P^{0.54}$$

The total flow rate (downstream of the hole) was available from the flowmeter. Given the differential pressure across the hole, the hole flow rate could be calculated and expressed as a ratio of the total flow rate for each reading. This resulted in a remarkably convenient outcome. The percentage flow contributed by the hole was virtually the same at all flow rates, for a given end vent size. This implies that the flow characteristic of each vent has a similar shape to that of the hole, so that the flows "track" each other. This hole flow rate ratio was regarded as the percentage disturbance to the main flow. The results obtained are tabulated in Table 5.1. For comparison, the percentage hole-to-vent area ratio is included:

End Vent size	Area ratio	Disturbance
4.0 *mm*	25.0 %	18.1 %
5.31 *mm*	14.2 %	11.9 %
7.37 *mm*	7.4 %	6.7 %
10.36 *mm*	3.7 %	3.5 %
12.9 *mm*	2.4 %	2.5 %
16.37 *mm*	1.5 %	1.9 %
21.2 *mm*	0.9 %	1.3 %

Table 5.1 - Disturbance level (L_D) caused by 2*mm* hole

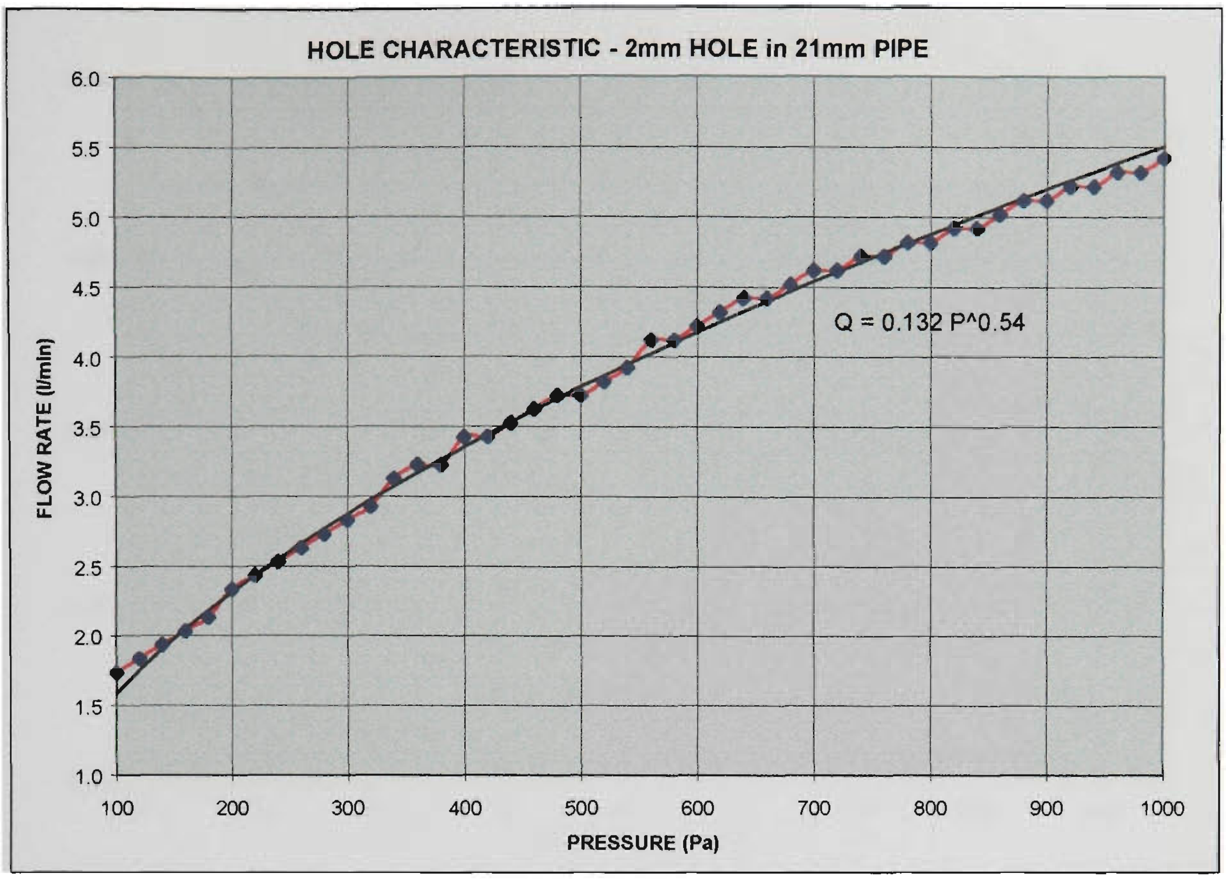

Figure 5.16 - Flow characteristic for $2mm$ sampling hole

In order to present the graphical data on one sheet for comparison (while plotting with different line styles to distinguish each set of data), it was necessary to employ quadratic interpolation of the data in Figures 5.9 to 5.15 to the nearest increment in Reynolds number, in steps of 100. This produced an array of 144 elements, providing data from $Re = 1500$ up to $Re = 3200$ for each of the eight disturbance levels (including zero disturbance).

The resulting series of graphs are presented in Figure 5.17, with each graph representing a different disturbance level (L_D labelled as "Dis") . Whereas this does indicate the wide overall spread between the data, it is difficult to identify the trends. Therefore the data array has been "sliced" in the other dimension and is presented in Figure 5.18, where each graph now represents a different Reynolds number. Upon careful study, this gives a clearer indication of the variations in friction factor. Evidently the friction factor remains stable for all disturbances in excess of about 8%. Below this level, the relationship is quite complex, but neighboring sets of data are all consistent.

To further clarify the picture, the data were graphed three-dimensionally as shown in Figure 5.19. Here we can see a surface describing the friction factor under all conditions. This is presented in a finite-element wire-grid format but the disturbance axis is distorted because Excel cannot handle "scattered" data with this type of graph. The resulting scale of disturbance is similar to logarithmic.

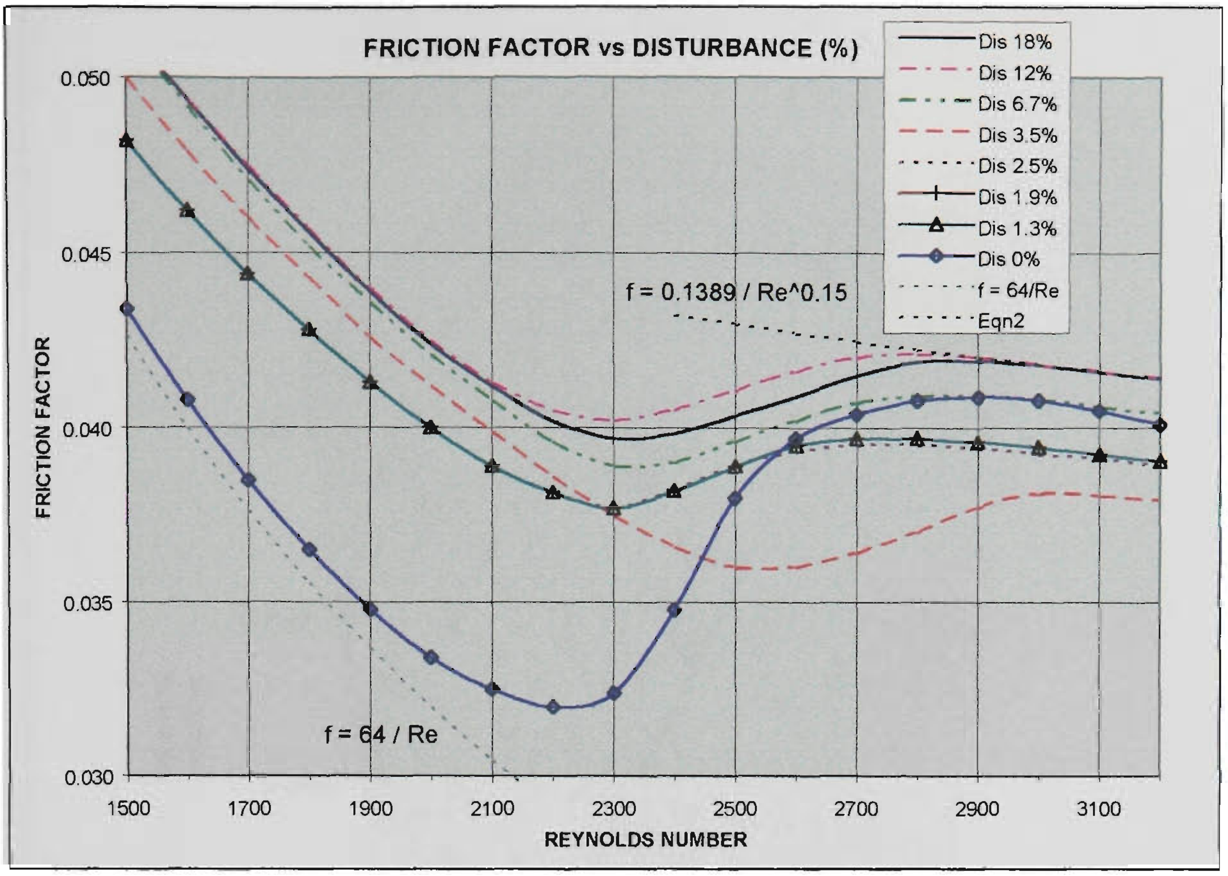

Figure 5.17 - Friction factor vs disturbance level (%)

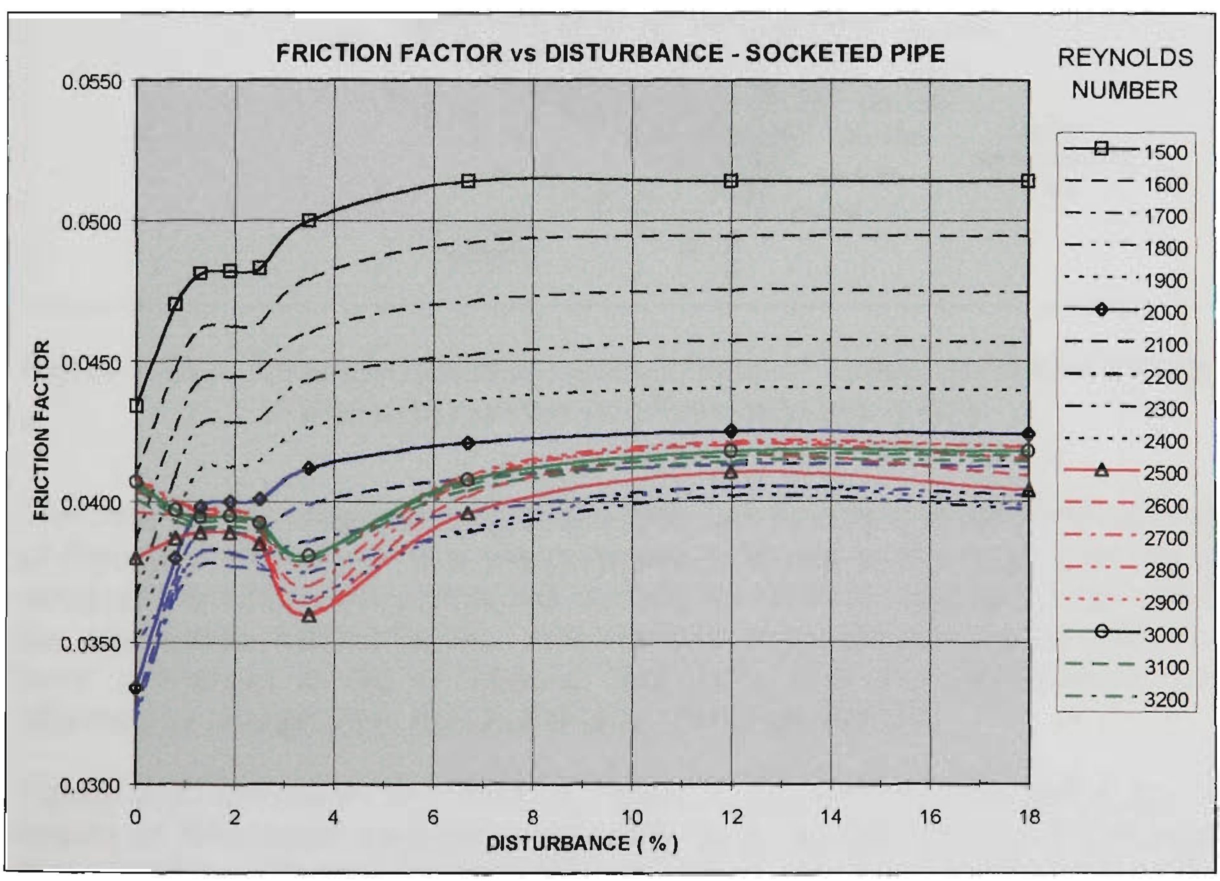

Figure 5.18 - Friction factor vs disturbance

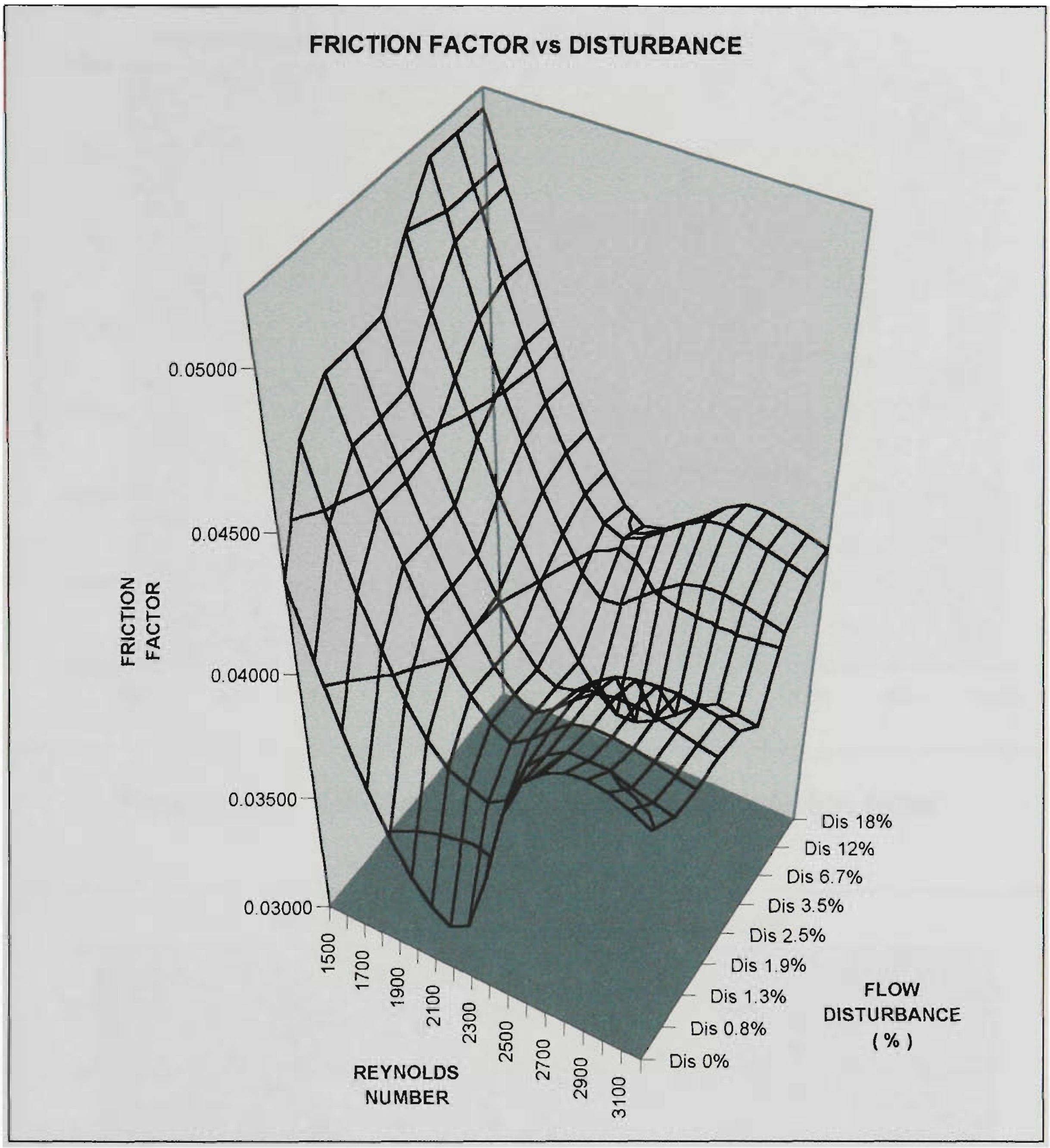

Figure 5.19 - Three-dimensional representation of friction factor as a function of Reynolds number and flow-disturbance level

The best overall understanding of the data can be obtained by studying each of Figures 5.17 to 5.19. For the purposes of a computer model, it would be adequate to interpolate across the surface elements of Figure 5.19 to obtain the appropriate friction factor. This method treats the surface as though it were composed of flat or skewed tiles, such that intervening points are obtained by interpolation across the face of the relevant tile.

Figure 5.20 compares the data of Figure 5.3 (which was based upon the results of Nikuradse) originally used, with data obtained for highly disturbed flow (11.9%). Clearly, the simplistic approach assuming undisturbed fully-developed flows was quite inadequate, involving significant errors. The magnitude of error is shown in Figure 5.21, ranging from -31 to +53%.

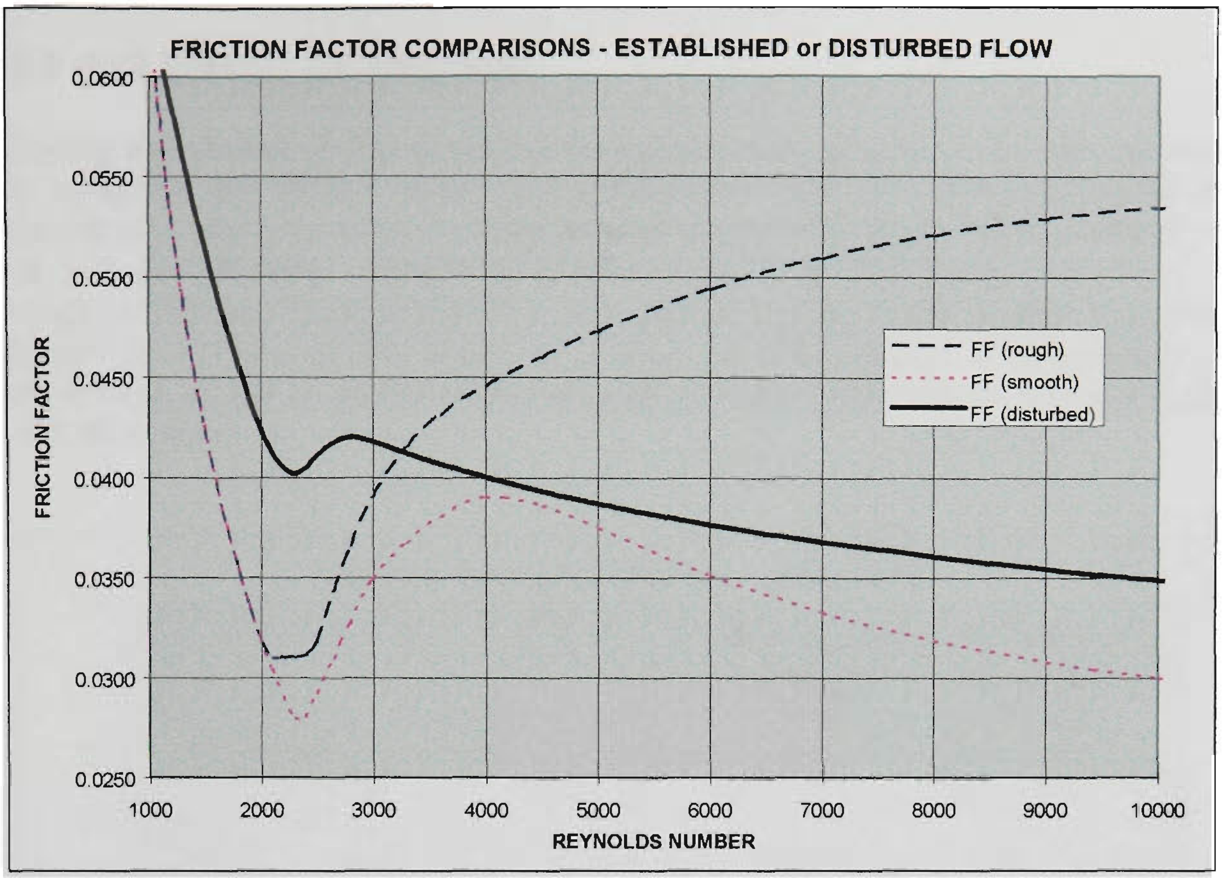

Figure 5.20 - Effect of high flow disturbance on friction factor

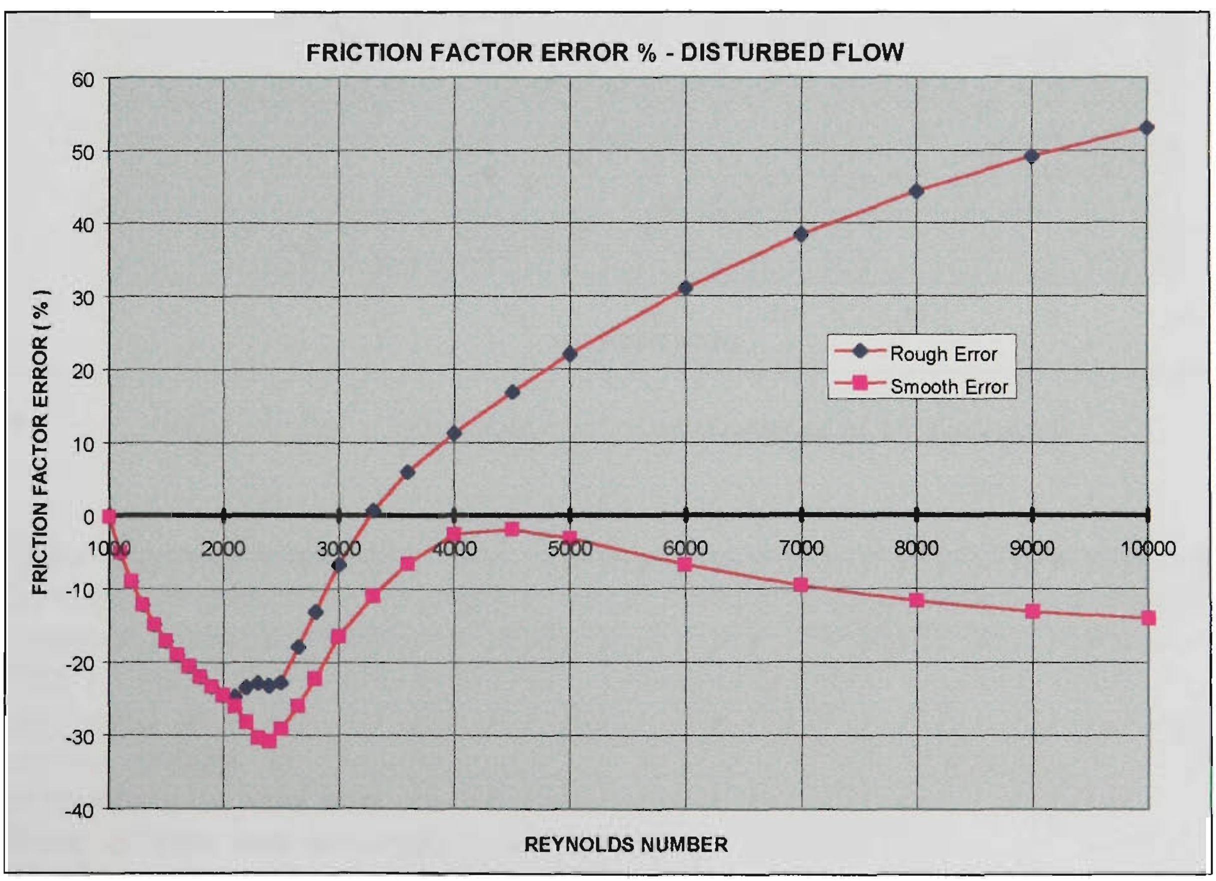

Figure 5.21 - Errors involved by using “undisturbed” friction factor

5.3 THE EFFECT OF PIPE SIZE

During the course of the experiments described in Chapter 4, it was possible to examine the friction factor applicable to a pipe of significantly different diameter, namely 12.4*mm*, in order to substantiate the results obtained for pipe of 21.2*mm* diameter. Whereas the measurements had been taken over a length of 3000*mm* in the case of 21.2*mm* diameter pipe, it was decided to use a length of 1755*mm* in the case of 12.4*mm* diameter pipe. This ensured a consistent length in terms of the number of diameters represented (namely, 142 diameters).

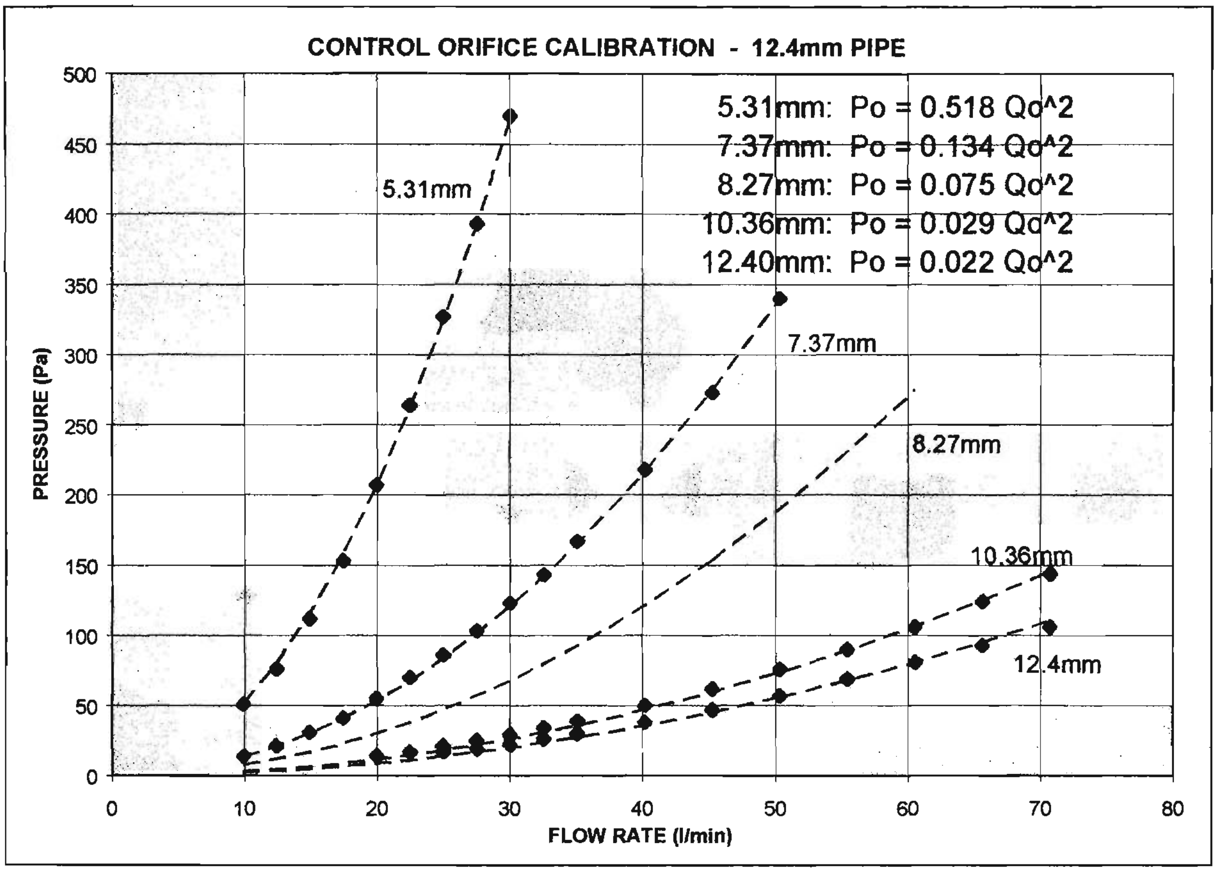

Figure 5.22 - Calibration of control orifices in 12.4*mm* pipe

Given a pipe diameter of 12.4*mm*, the larger available control orifices could not be used. In order to obtain a good spread of disturbance levels it was decided to use a 1.0*mm* sampling hole initially, and then to drill this out to 1.5 and 2 *mm*. The 1.0 and 1.5*mm* holes were used in conjunction with an open-ended pipe (regarded as a 12.4*mm* control orifice), while the 2*mm* hole was used with control orifices of 12.4, 10.36, 8.27, 7.37 and 5.31*mm*, representing higher proportions of hole flow, i.e. increasing levels of disturbance. Calibration of these orifices was undertaken and presented in Figure 5.22. The curves of best fit to these data based upon adopting a square characteristic were:

5.31*mm* orifice: $P_o = 0.518\, Q_o^2$

7.37*mm* orifice: $P_o = 0.134\, Q_o^2$

8.27*mm* orifice: $P_o = 0.075\, Q_o^2$

10.36*mm* orifice: $P_o = 0.029\, Q_o^2$

12.4*mm* orifice: $P_o = 0.022\, Q_o^2$

Minimal disturbance was represented by blocking the sampling hole and using an open-ended pipe. Using a 1.0*mm* hole with an open-ended pipe represented a disturbance level of 1.2%. The 1.5*mm* hole with open-ended pipe represented 2.8%. In the case of the 2*mm* hole when used in conjunction with the various control orifices, the disturbance levels were 4.9%, 5.4%, 6.5%, 7.9%, 13.0% and 18.0%.

Figure 5.23 presents the results obtained for the extreme cases of minimal and maximal disturbance. The dotted lines are included for comparison with the results of the 21.2*mm* pipe. Although the pipe cross-sectional area is only 34% of the original, the results are quite similar. This would be expected from similarity laws, given that the results are expressed in terms of non-dimensional parameters. This outcome suggested that the experimental technique was valid and the results could reasonably be translated to other pipe sizes.

Figure 5.24 presents the complete set of results obtained for a wide range of disturbance levels. These sets of data are mutually consistent and to assist comparison with the data of Figure 5.17 (applicable to 21.2*mm* diameter pipe), the data of Figure 5.24 is re-presented in Figure 5.25 with a matching span of Reynolds numbers and friction factor.

This data array is presented yet again in Figure 5.26, but "sliced" in the other dimension for comparison with Figure 5.18. The actual Reynolds numbers used, and the intervals between the graphs, are different when comparing Figure 5.26 with Figure 5.18. Despite this difficulty, the comparison reveals a remarkable similarity in structure. For example, note the consistent "dip" at the 2 to 3 % disturbance level and the relative "flatness" above the 8% level. The magnitudes are also comparable, for example, at a Reynolds number of $Re = 1700$; for a 21.2*mm* pipe the friction factor is 0.0475 for disturbance levels above 8% which is similar to the result for the 12.4*mm* pipe.

Figure 5.27 is a three-dimensional representation of the data and this bears similarity to Figure 5.19 in general. The curious central "furrow" in the surface of Figure 5.19 at a disturbance level of 3.5% is not evident in that of Figure 5.27, but it was not possible to take data at precisely this level in the case of the 12.4*mm* pipe (data being taken either side, at 2.8 and 4.9 %).

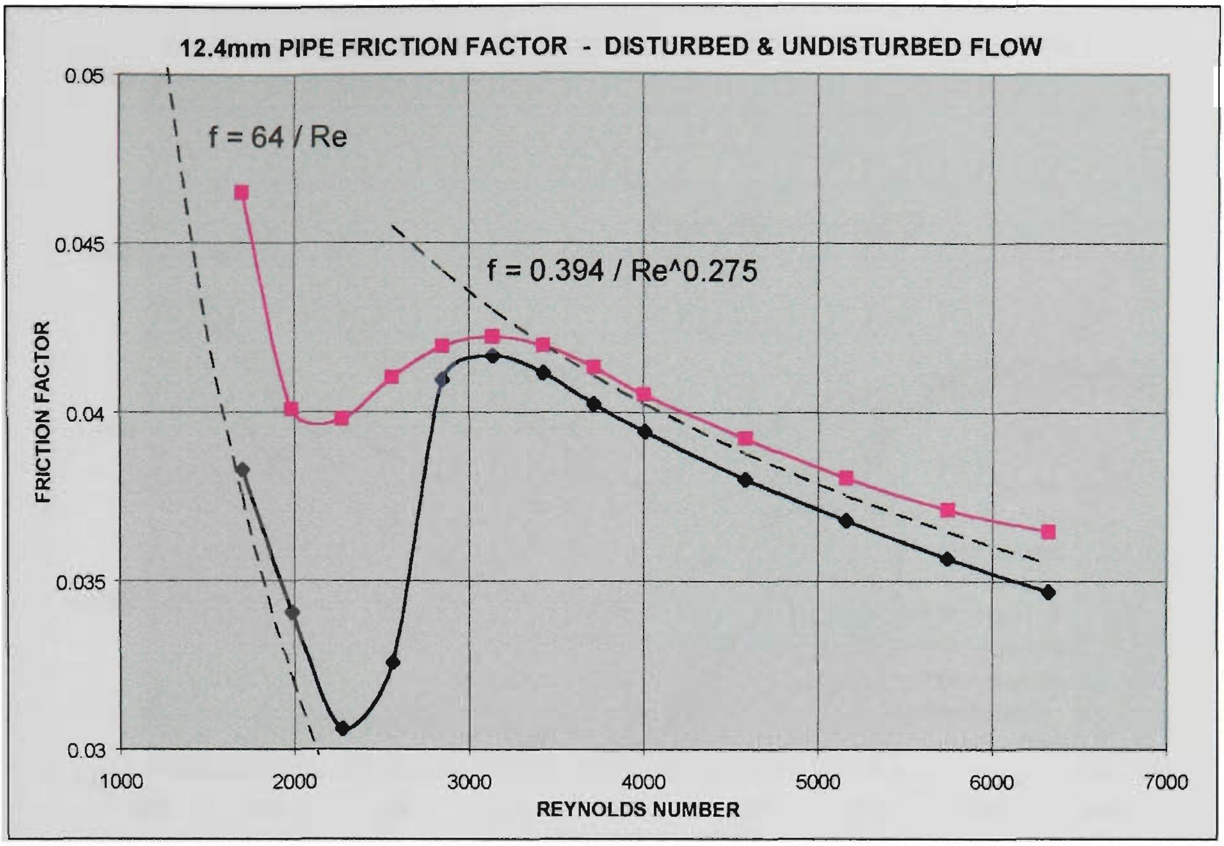

Figure 5.23 - Friction factor for extreme flows in 12.4*mm* pipe

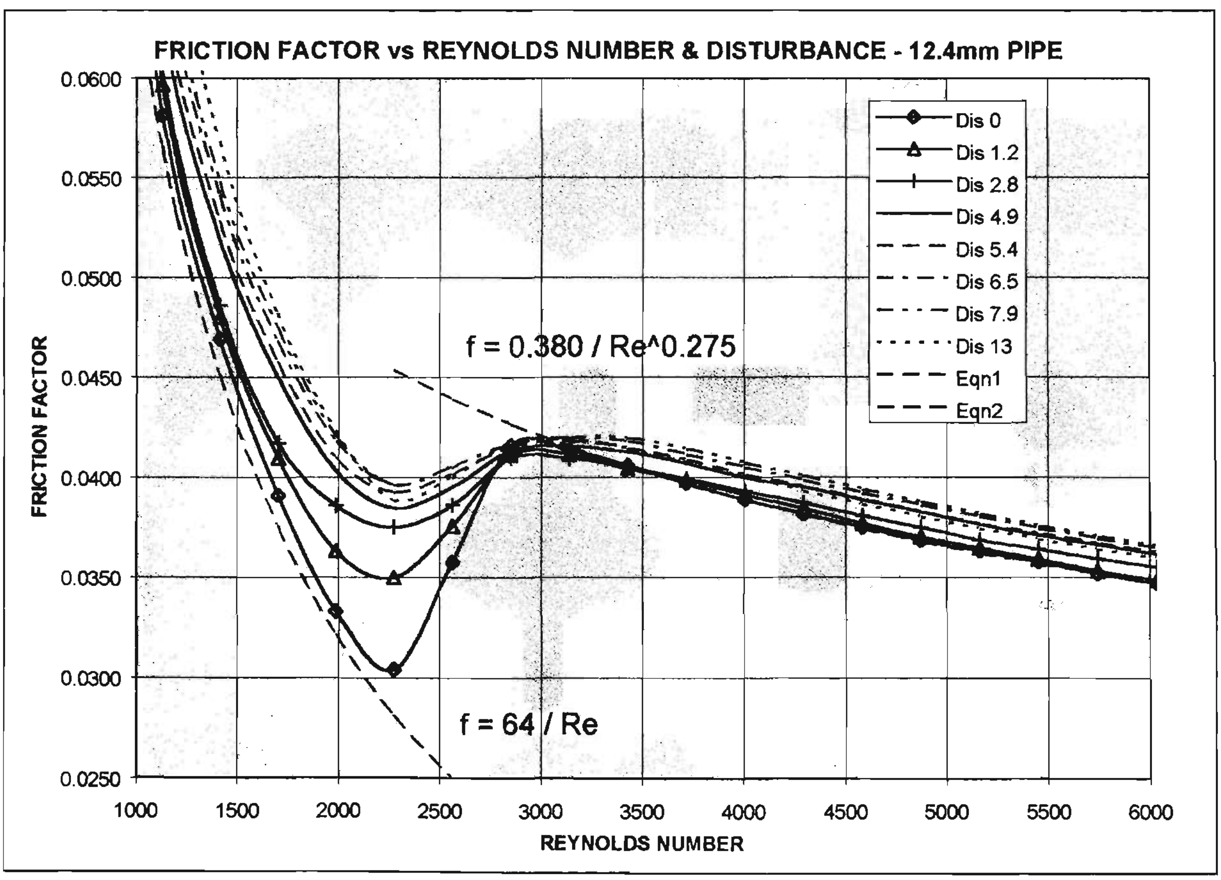

Figure 5.24 - Friction factors in 12.4*mm* pipe for various disturbance levels

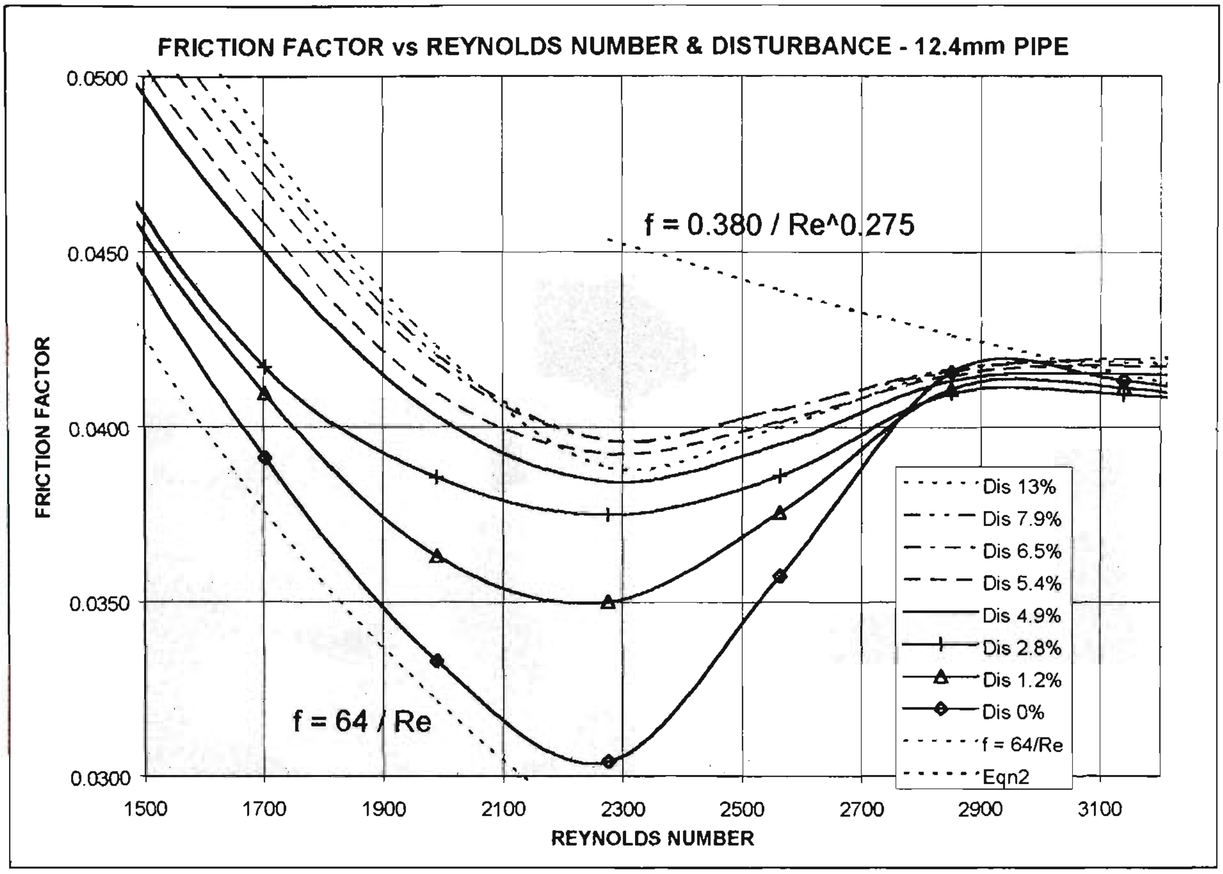

Figure 5.25 - Friction factors in 12.4*mm* pipe (1500 < Re < 3200)

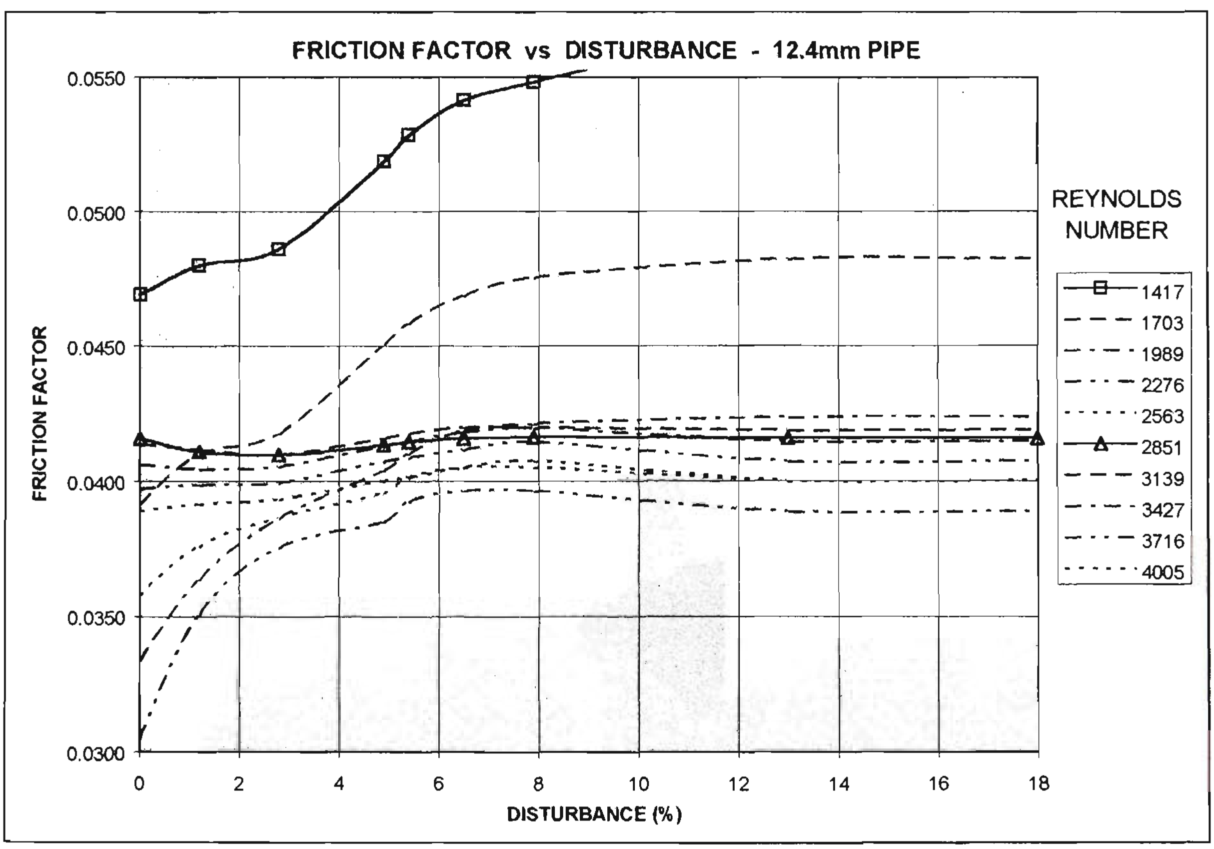

Figure 5.26 - Friction factor versus disturbance in 12.4*mm* pipe

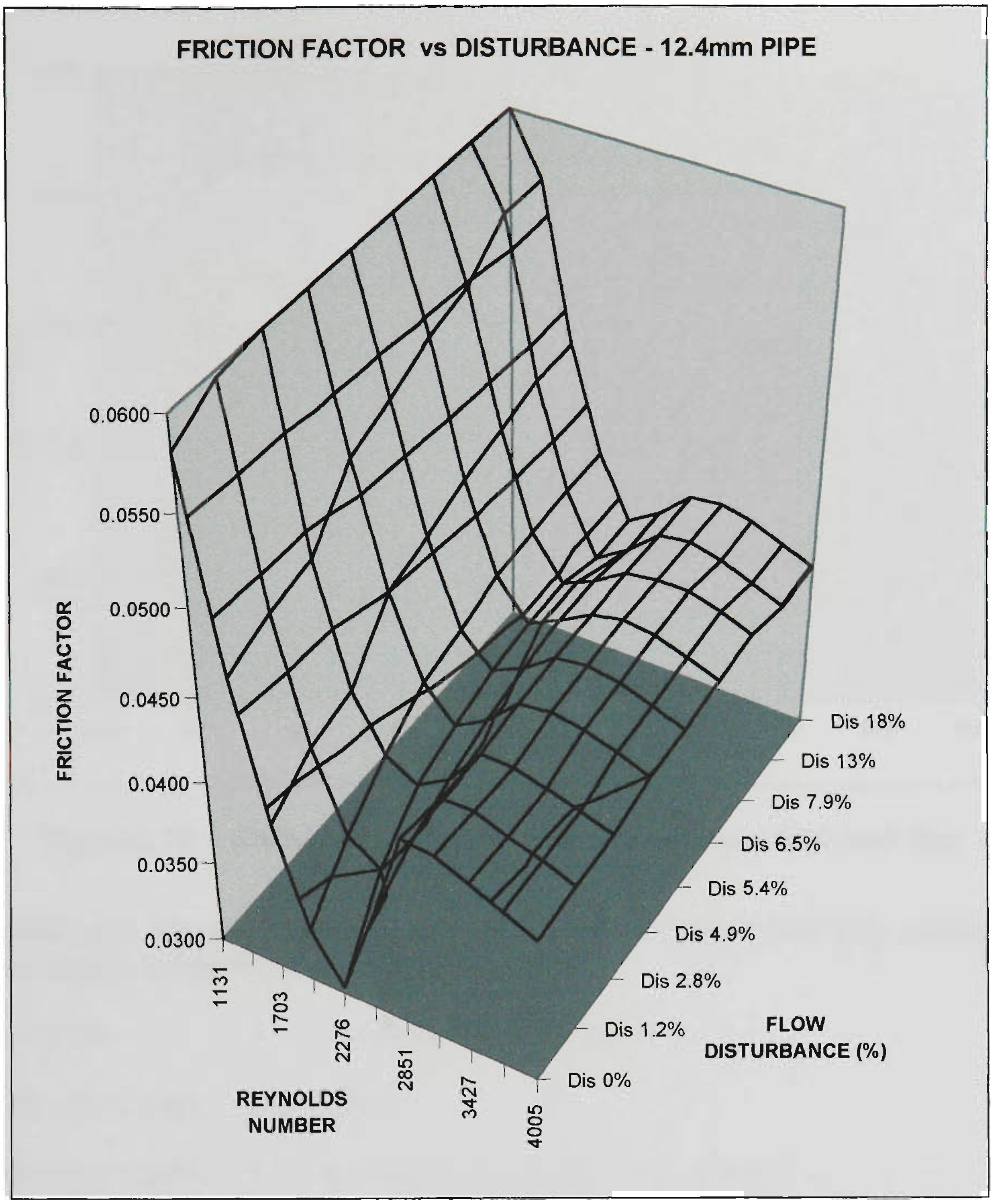

Figure 5.27 - Three-dimensional representation of friction factor as a function of Reynolds number and disturbance level in $12.4mm$ pipe

In view of the consistency obtained between the friction factor data for two pipes of such large size difference, the data pertaining to the $21.2mm$ pipe with maximum disturbance (from Figure 5.10) are again presented in Figure 5.28, as representing the worst-case situation for all commonly-used pipe sizes. This can be compared with the friction factor data available from the literature, relevant to completely undisturbed flows. Equations of best fit to these maximally-disturbed flow data have been developed and the related curves (shown dashed) have been included in Figure 5.28.

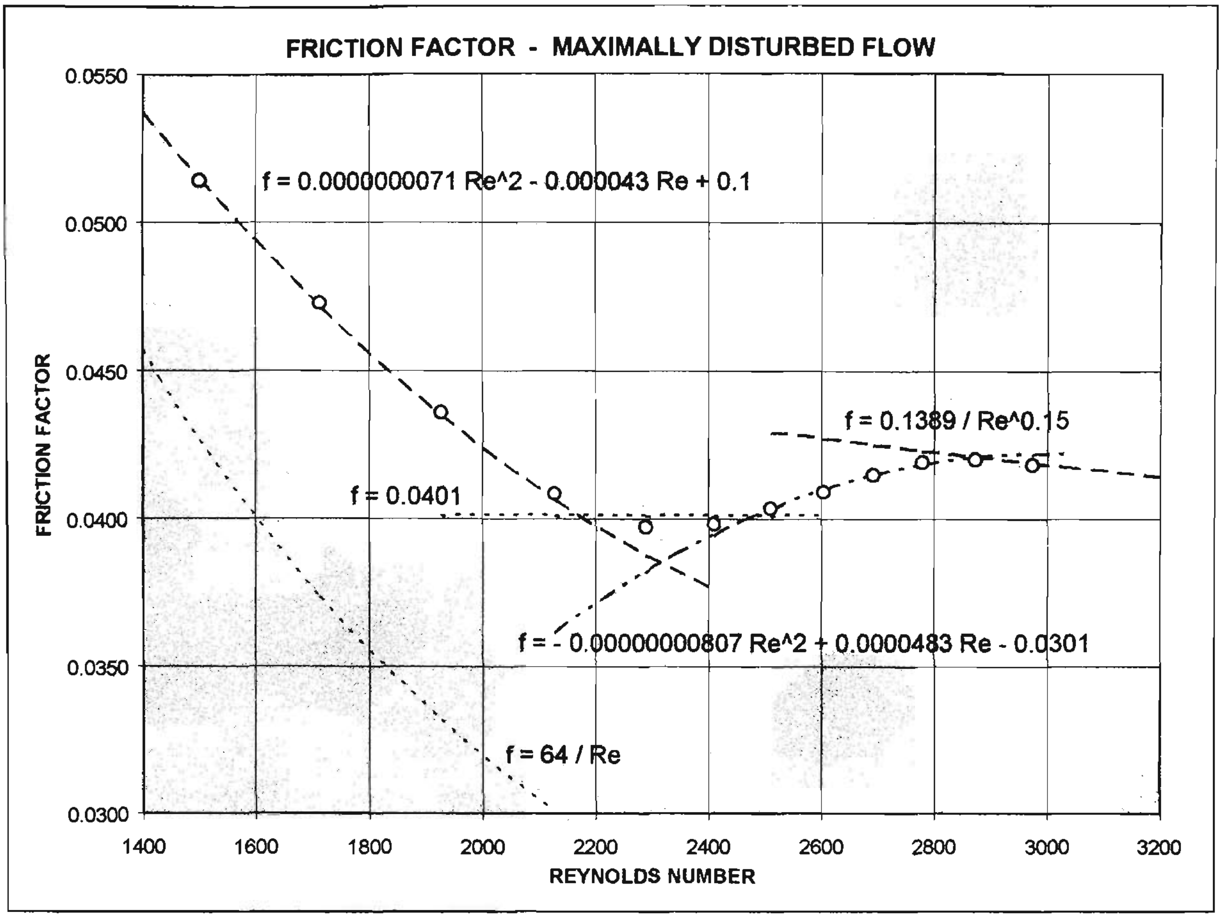

Figure 5.28 - Determining friction factor for maximally disturbed flow

Based upon Figure 5.28 the algorithm for modelling the maximally-disturbed flow regime would proceed as follows:

Re < 2170: $f = 7.1E\text{-}09\ \mathrm{Re}^2 - 4.3E\text{-}05\ \mathrm{Re} + 0.1$

2170 < Re < 2480: $f = 0.0401$

2480 < Re < 2875: $f = -8.07E\text{-}09\ \mathrm{Re}^2 + 4.83E\text{-}05\ \mathrm{Re} - 0.0301$

Re > 2875: $f = 0.1389 / \mathrm{Re}^{0.15}$

5.4 THE EFFECT OF BENDS

It had been anticipated that 90° pipe bends should be characterised in much the same manner as other pipe system components, as discussed in Chapter 2, resulting in a quadratic equation. However, experiments revealed that the impact of bends on the system as a whole is rather more complex and significant than a simplistic approach would reveal. To determine this impact, a bend was inserted in the middle of a $4m$ length of $21.2mm$ diameter test pipe which had a four-port pressure tap mounted $0.5m$ from each end, producing a $3000mm$ test segment. The pressure drop for a range of bend sizes (radii) over a range of flow rates was measured and is presented in Figure 5.29.

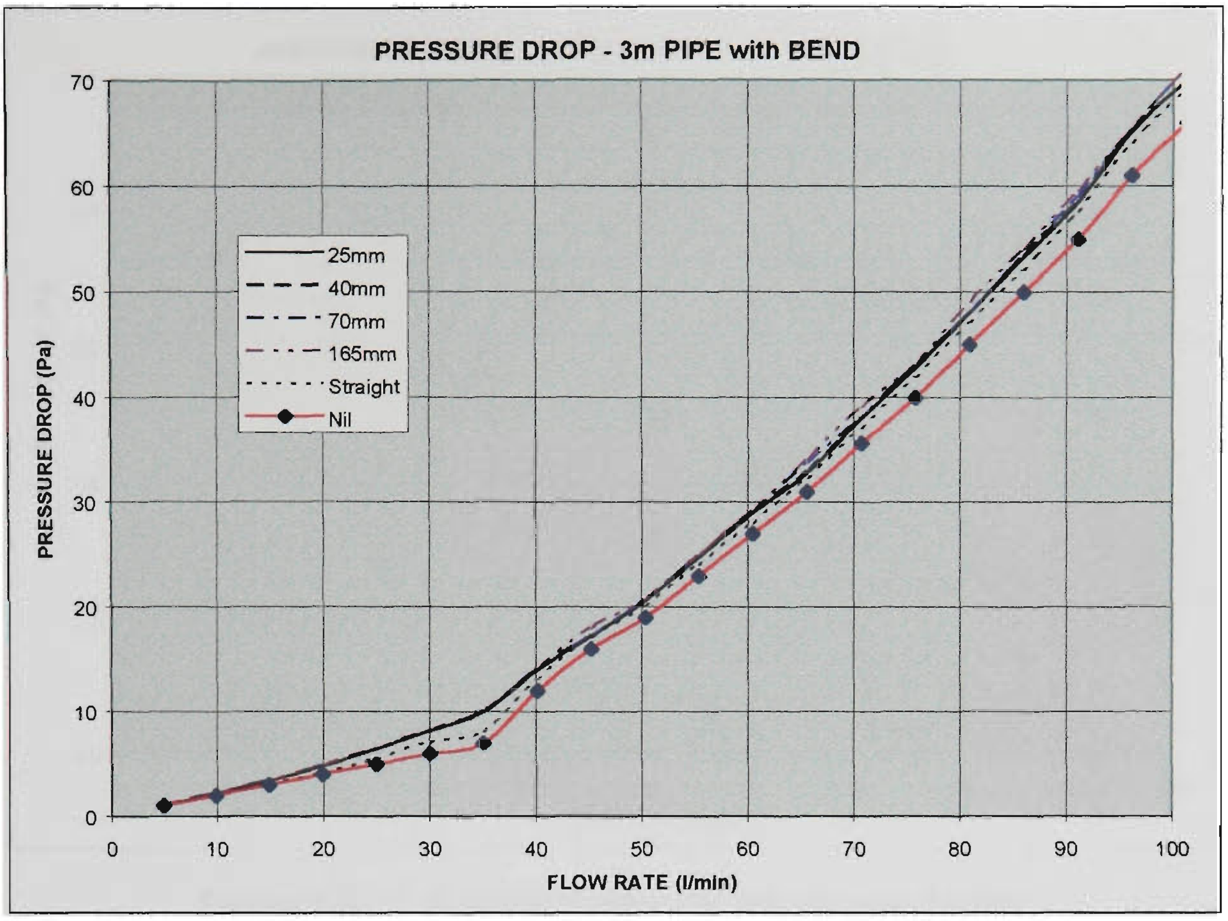

Figure 5.29 - Pressure drop in bends of various radii

For reference, Figure 5.29 includes the pressure drop incurred for the $3000mm$ test pipe without any bend fitted (being the lowest, solid curve with data points included - these points are excluded in other curves to avoid clutter). It had been anticipated that there would be a gradual increase in pressure drop as the bend radius was reduced, because of the increasingly sharp change in direction of air flow (incurring kinetic energy loss due to momentum change).

The remarkable result from these experiments, involving bend radii of 25, 40, 70 and 165 mm is that the pressure drop at a given flow rate is almost identical for each bend size. For example, at a flow rate of $100 litre/min$, the pressure drop is 71Pa for all bend radii except for $25mm$ which has a pressure drop of 70Pa (all other readings at a given flow rate are also within 1Pa). It was noted that the bends of larger radius are physically longer, thereby incurring additional frictional loss, but this seemed unlikely to so perfectly counter-balance the effect of the sharpness in change of flow direction.

All bends share a common feature, namely a pair of sockets, one at each end. It was postulated that the pressure drop due to the sockets alone could dominate either of the above effects. Therefore a $100mm$ length of pipe was obtained, in which the ends had been heated and expanded to form a pair of sockets, identical to those provided on bends. The measurement results are included in Figure 5.29 (dotted line), and the pressure drop is typically only 1Pa less than that of the $25mm$ bend (being 69Pa at $100 litre/min$).

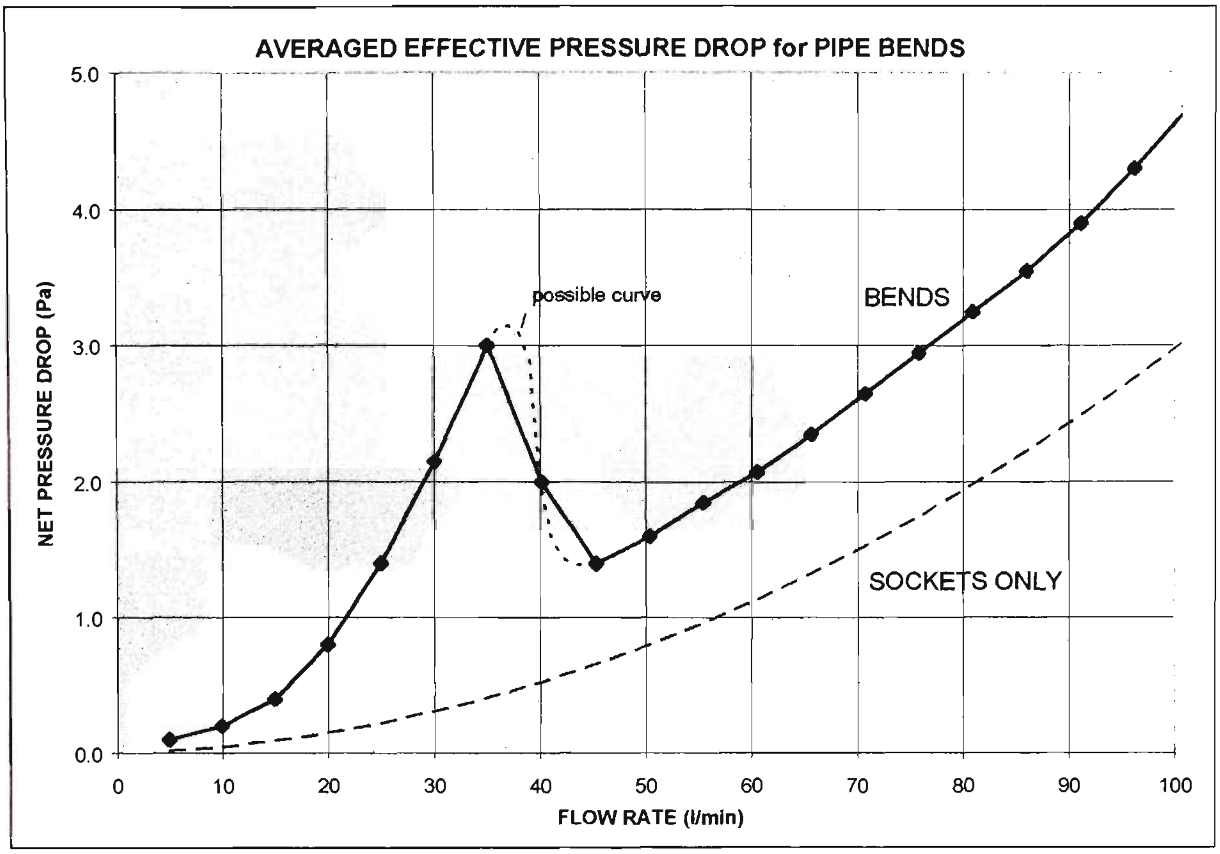

Figure 5.30 - Averaged pressure drop in pipe bends

Figure 5.30 shows the incremental increase in pressure drop due to a bend. This is obtained by subtracting the pressure drop for the $3000mm$ test pipe, from that obtained when a bend is inserted. The (almost identical) results for all of the bend radii have been averaged to represent the general case. The important features to note in this graph, are the surprisingly sharp discontinuity that occurs at *35litre/min*, where the pressure drop begins to fall, until reaching another sharp discontinuity at *45litre/min*. These discontinuities can only be explained by the impact of the bend in disturbing the flow regime.

Included in Figure 5.30 as a dashed curve is the pressure drop due to the short length of straight pipe containing a pair of sockets. The discontinuities noted above are not evident, confirming that sockets alone do not disturb the flow regime significantly, although they do cause pressure drop. This finding is important because it means that the precise location of sockets (without bends) is not required to be known in order to model the development of the flow regime (which affects smoke transport time, as considered in Chapter 6).

In verification of this important finding the data of Figures 5.6 and 5.9 have been combined in Figure 5.31 to compare directly, the effect of including a single socket in the middle of a smooth $3000mm$ test pipe. Here we see that divergence occurs only in the transition and turbulent flow regimes. This has been established as a characteristic of rough pipes and is consistent with the finding of Cole (1991, p27), who states that the effect of sockets is to increase the effective roughness of the pipe. However, it is now possible to add the finding that the flow regime is not significantly disturbed by sockets.

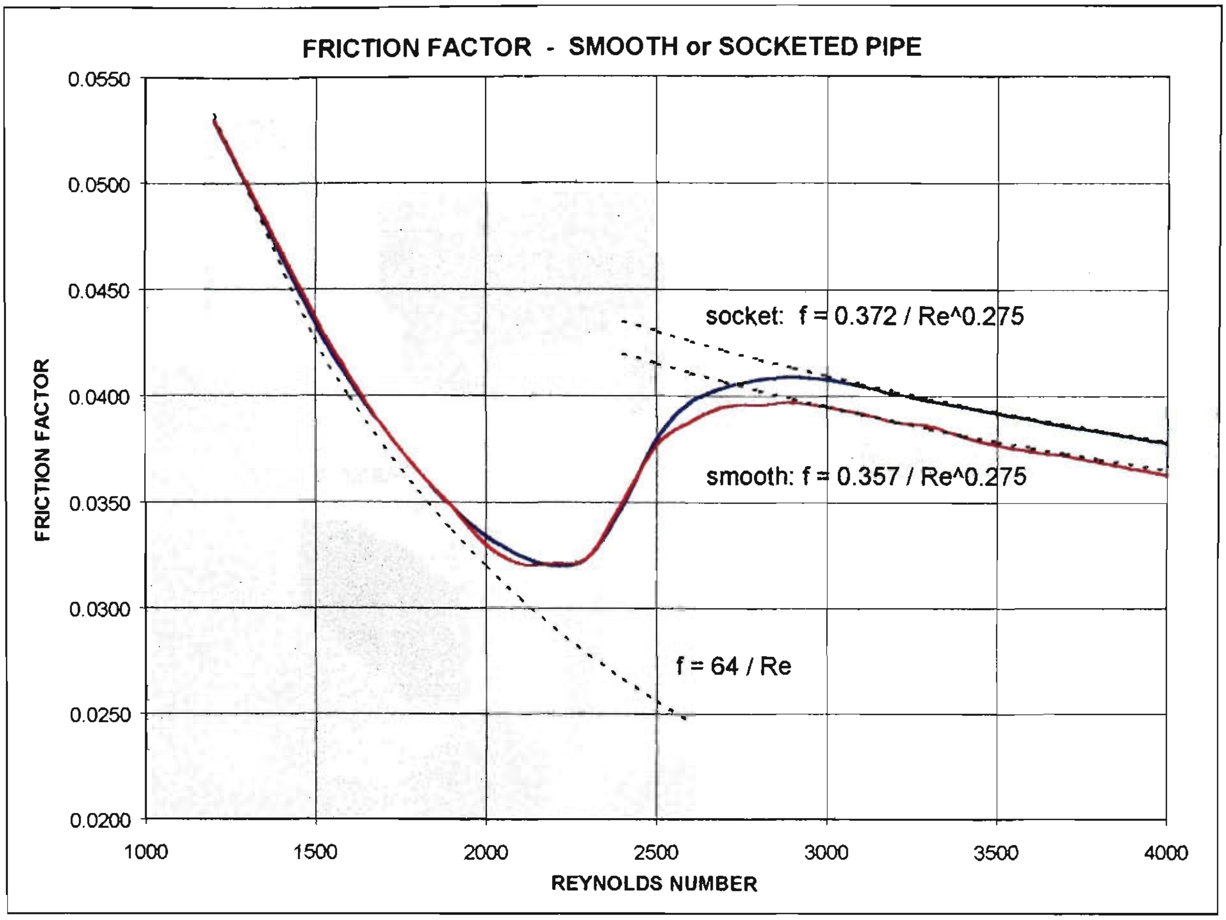

Figure 5.31 - Effect of a socket on friction factor

Figure 5.32 presents the data of Figure 5.30 expressed in Reynolds number. Here we see that the first discontinuity occurs near $\mathrm{Re} = 2300$ which is the point of transition from a laminar flow regime within the test pipe and bend. This transition is evidently complete near $\mathrm{Re} = 3000$. An algorithm to characterise the effect of a single bend of **any** radius has been developed from Figure 5.32 as follows (given that $25mm$ radius is the minimum size for a pipe of $21.2mm$ internal, $25mm$ external diameter):

$\mathrm{Re} < 2300$: $\quad P_{bend} = 9.4E\text{-}11\ \mathrm{Re}^3 + 3.5E\text{-}07\ \mathrm{Re}^2$

$2300 < \mathrm{Re} < 3000$: $\quad P_{bend} = 1.766E\text{-}6\ \mathrm{Re}^2 - 0.0118\ \mathrm{Re} + 20.9$

$\mathrm{Re} > 3000$: $\quad P_{bend} = 8.7E\text{-}08\ \mathrm{Re}^2 + 5.5E\text{-}05\ \mathrm{Re} + 0.455$

An important point to note is that the impact of a bend is more significant than the careful measurement of pressure drop immediately across the bend itself would reveal (such measurement results only in the third of the above equations). From a systems viewpoint the bend disrupts the flow regime within the neighboring segments of pipe, resulting in a characteristic that is rather more complex than a single quadratic equation. Accordingly, the impact of bends on friction factor will be considered, later.

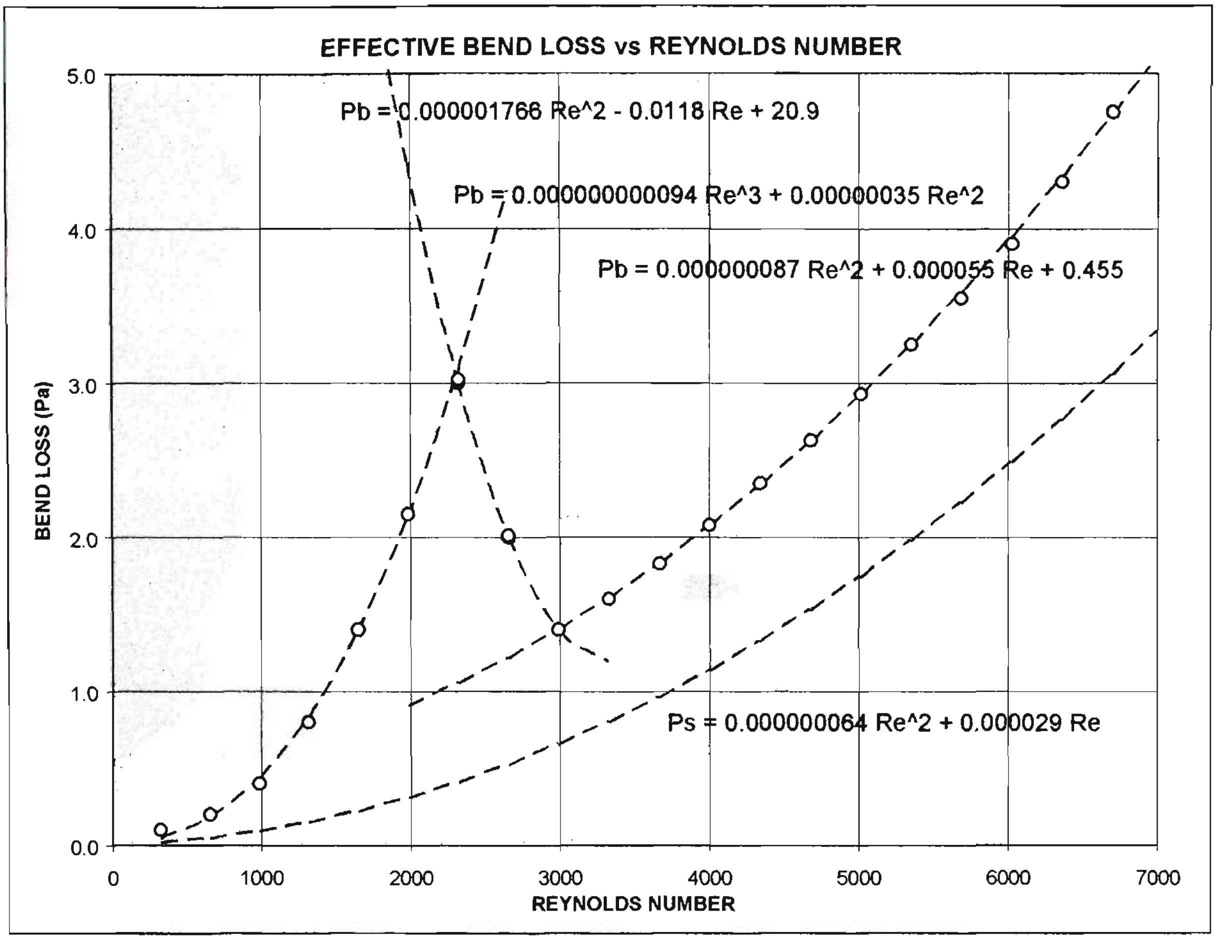

Figure 5.32 - Incremental bend loss versus Reynolds number

The next experiment investigated the effect of multiple bends. These are typically required where a straight run of pipe must avoid a ceiling beam or duct, so four bends are used in close proximity. In view of the above results it was anticipated that the effect of increasing the number of bends at one location would **not** necessarily involve using the result of the above algorithm, multiplied by the number of bends in the immediate vicinity. This is because the flow regime, having already been disturbed by the first bend in the sequence, is unlikely to be further disturbed to the same additional extent by the next bend. The effect of additional bends was therefore expected to have diminishing significance to the flow regime.

The single bend used in the previous experiment was replaced with either two or four bends. The option of three bends was not employed because of the physical difficulty in placing the pipework, because such an arrangement is rarely used in the field, and because it became evident that such data would not add significantly to an understanding of the characteristics.

The experimental results for 0, 1, 2 and 4 bends are presented in Figure 5.33 where it can be seen that the pressure drop increases broadly in proportion to the number of bends used. The similarity and consistency between these sets of results can best be seen in Figure 5.34 which shows the incremental pressure drop due to bends after subtraction of the test pipe pressure drop.

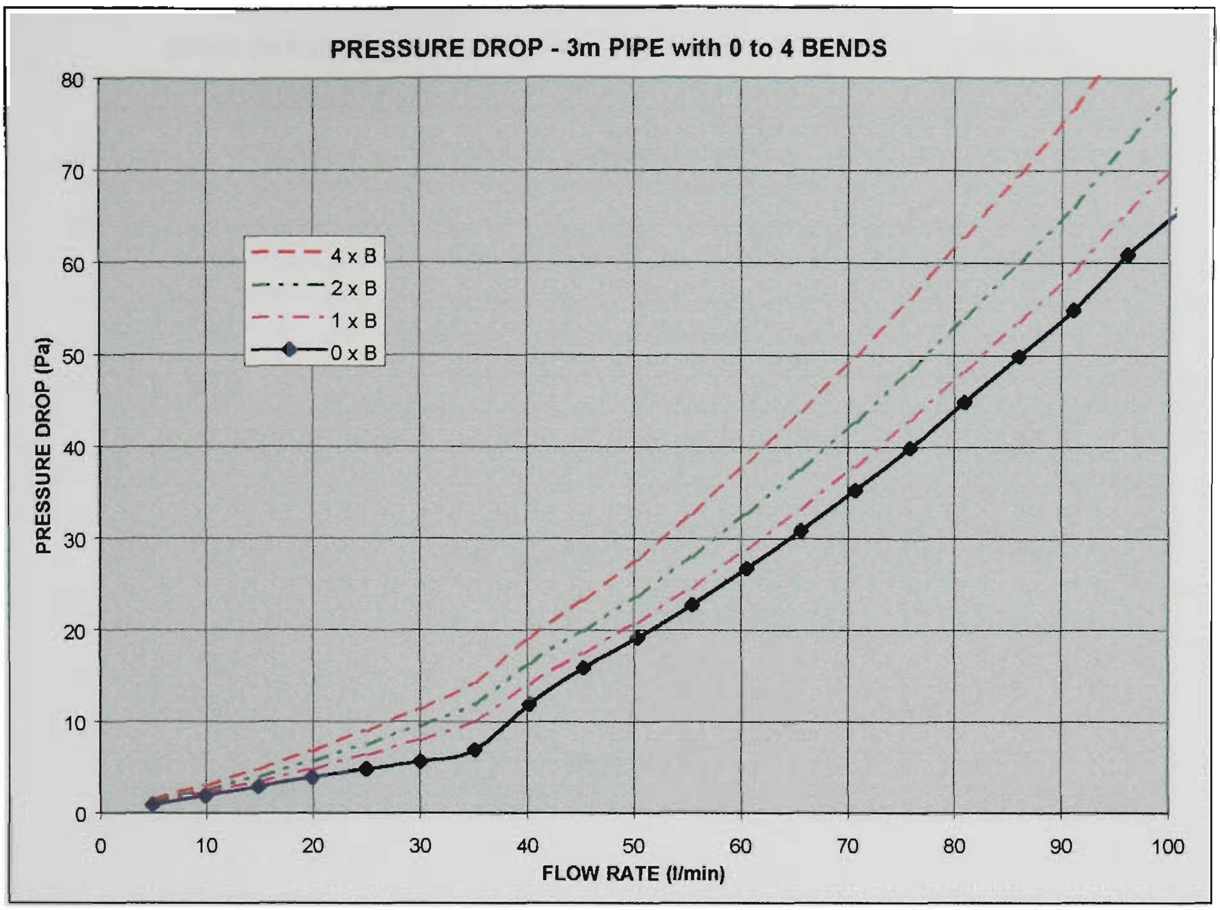

Figure 5.33 - Pressure drop for multiple bends

Discontinuities in the curves are once again evident at 35 and 45 *litre/min.* However, it is noted that if the complex pressure drop characteristic of a single bend is subtracted from the data obtained for multiple bends, then simple curves result, as graphed with dotted curves in Figure 5.34.

Greater clarity of the significance of this result is provided in Figure 5.35. Here, the incremental effect of using bends in addition to the first bend is shown. The consistency of these data have made it possible to interpolate the likely characteristic of a three-bend arrangement with reasonable confidence. Equations for the incremental effect of bends are as follows:

One more bend: $P_{bend2} = P_{bend} + 9.5E\text{-}08\ Re^2 + 6.0E\text{-}04\ Re$

Two more bends: $P_{bend3} \approx P_{bend} + 2.0E\text{-}07\ Re^2 + 8.5E\text{-}04\ Re$

Three more bends: $P_{bend4} = P_{bend} + 3.0E\text{-}07\ Re^2 + 0.0011\ Re$

Generally: $P_{bendN} \approx P_{bend} + 1.0E\text{-}07\ N_b\ Re^2 + (2.5E\text{-}04\ N_b + 3.5E\text{-}04)\ Re$

where the algorithm to obtain P_{bend} is as previously determined from Figure 5.32 and where N_b is the number of additional bends in close proximity.

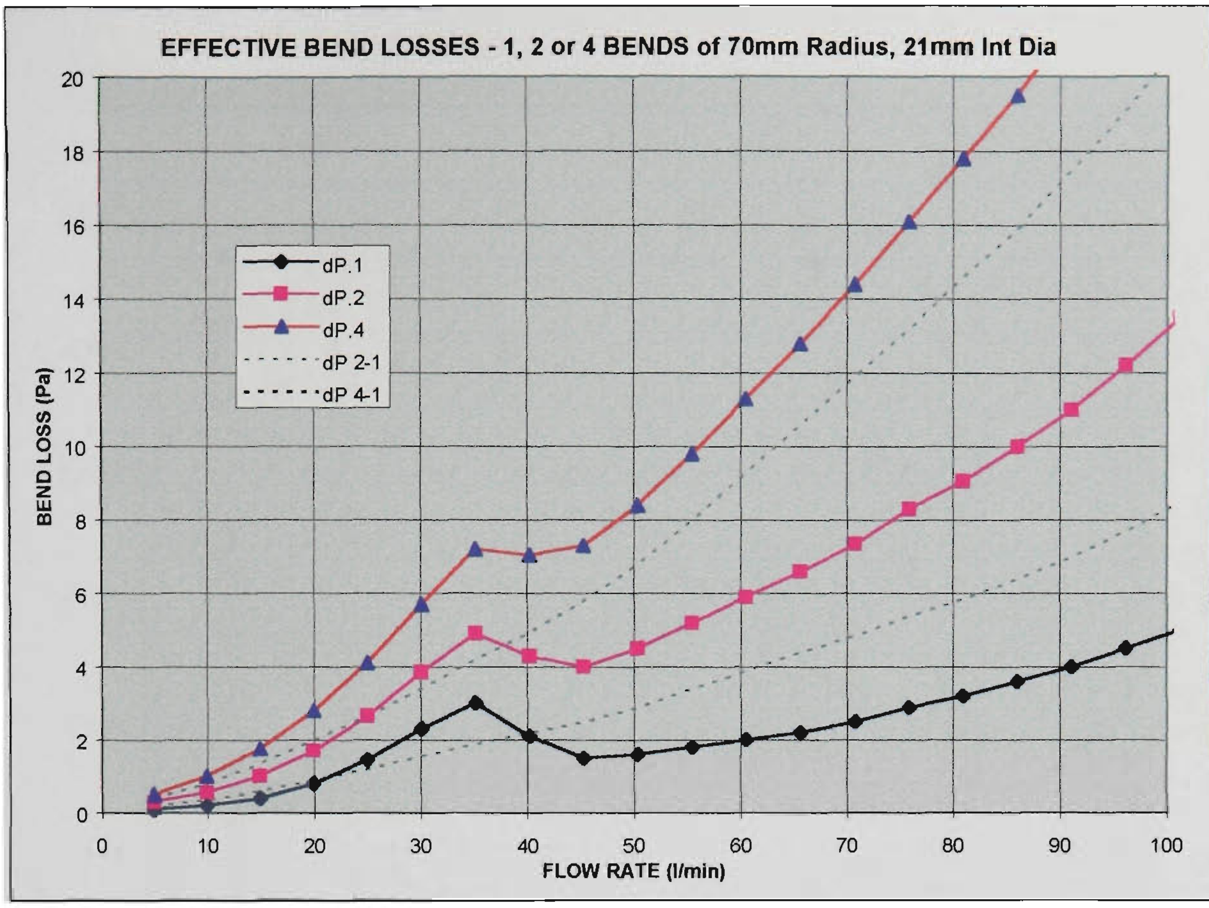

Figure 5.34 - Pressure drop due to multiple bends

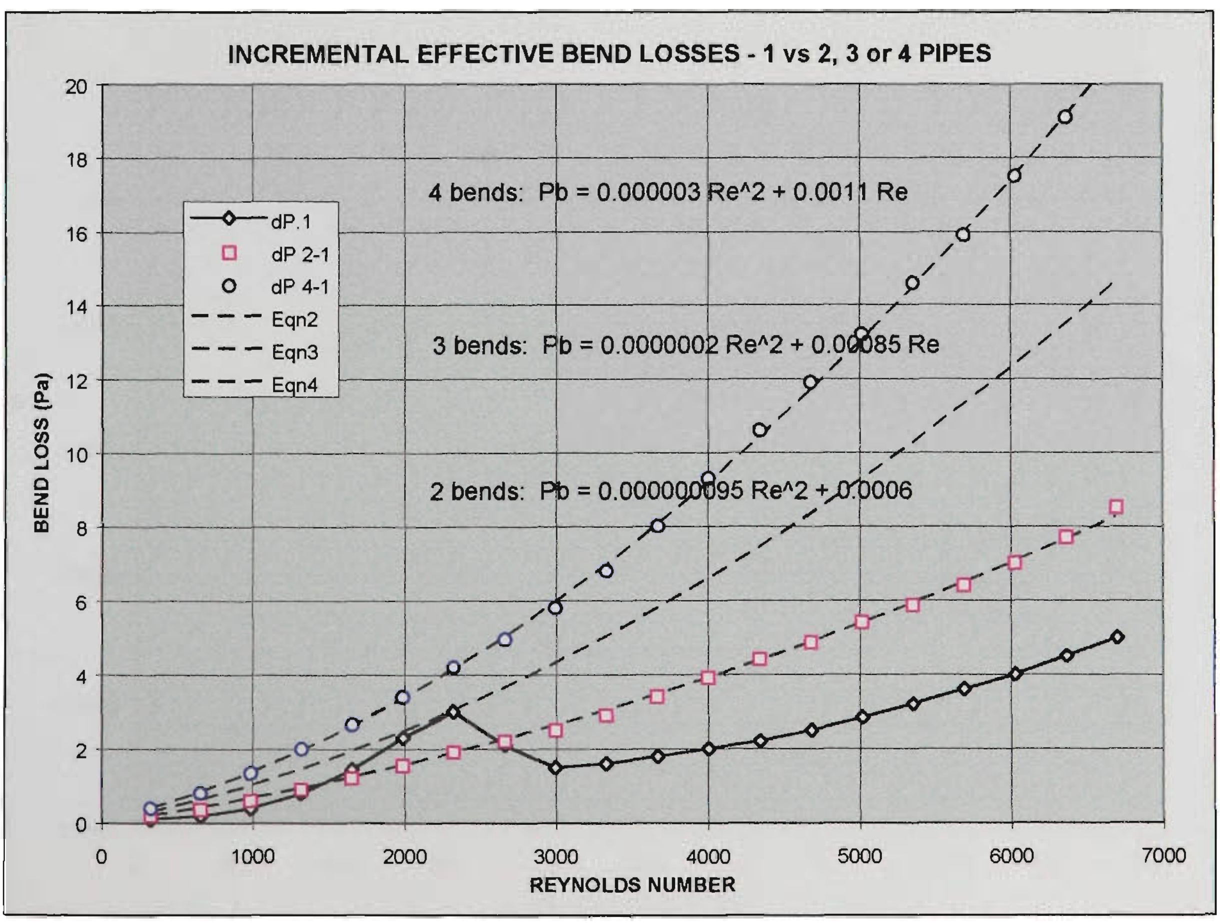

Figure 5.35 - Incremental pressure drop with multiple bends

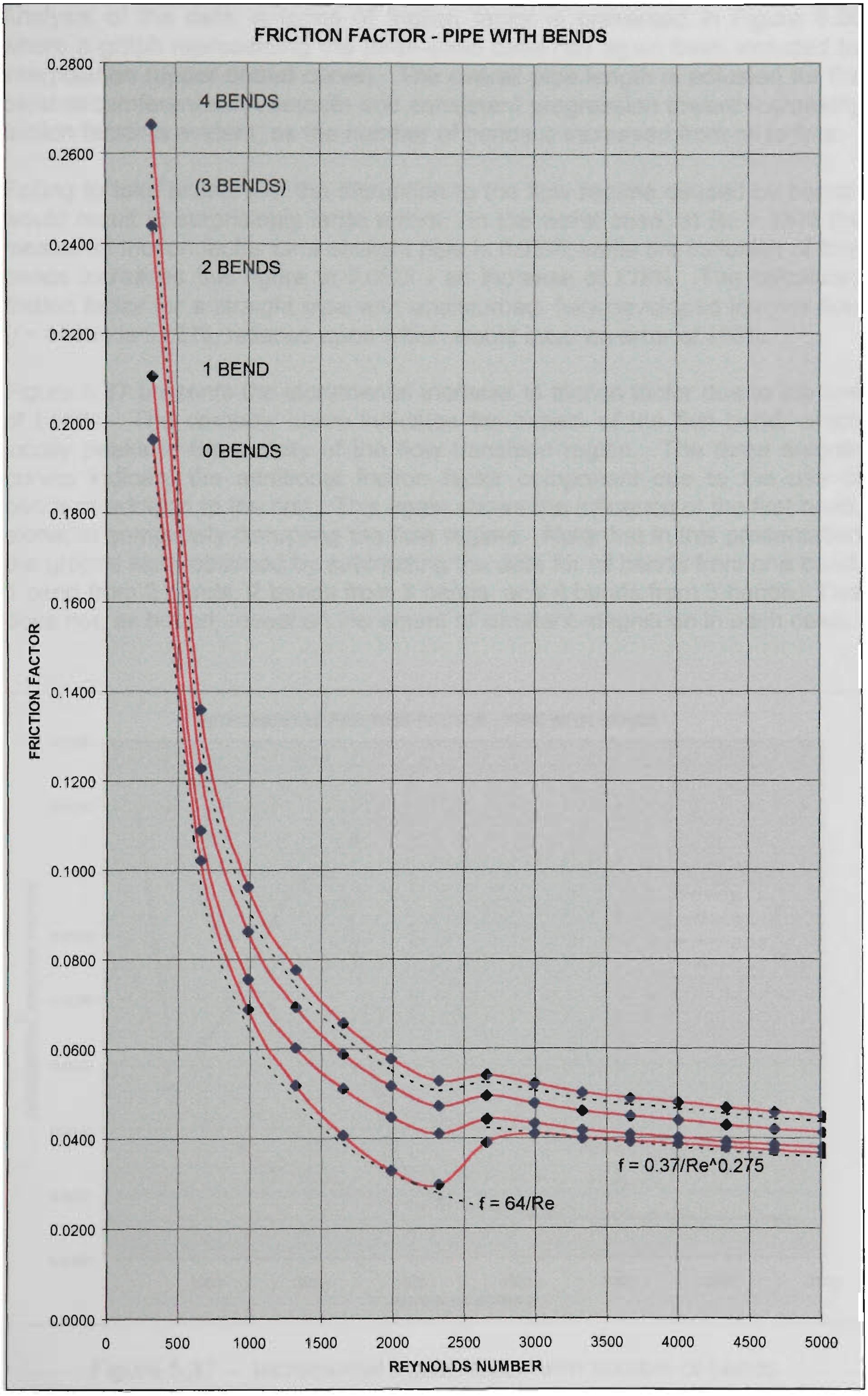

Figure 5.36 - Friction factor for a pipe with bends

Analysis of the data in terms of friction factor is presented in Figure 5.36 where a graph representing the three-bend case has again been included by interpolation (upper dotted curve). The overall pipe length is adjusted for the bend circumference. A smooth and consistent progression toward increasing friction factor is evident, as the number of bends is increased from nil to four.

Failing to take account of the disruption to the flow regime caused by bends, would result in surprisingly large errors. In the worst case, at Re = 2300 the measured friction factor for a straight pipe is 0.0296, while the inclusion of four bends increases this figure to 0.0527 - an increase of 178%. The calculated friction factor for a straight pipe with undisturbed, fully developed laminar flow ($f = 64/\mathrm{Re}$) is 0.0278, reliance upon which would incur an error of 190%.

Figure 5.37 presents the incremental increase in friction factor due to the use of bends. The complex curve indicates the impact of the first bend, which locally peaks in the vicinity of the flow transition region. The three smooth curves indicate the additional friction factor component due to the use of bends in addition to the first. This again shows the influence of the first bend, alone, in completely disrupting the flow regime. Note that in this presentation the graphs were obtained by subtracting the data for nil bends from one bend, 1 bend from 2 bends, 2 bends from 3 bends, and 4 bends from 3 bends. This does not, as hoped, reveal an increment of constant magnitude in each case.

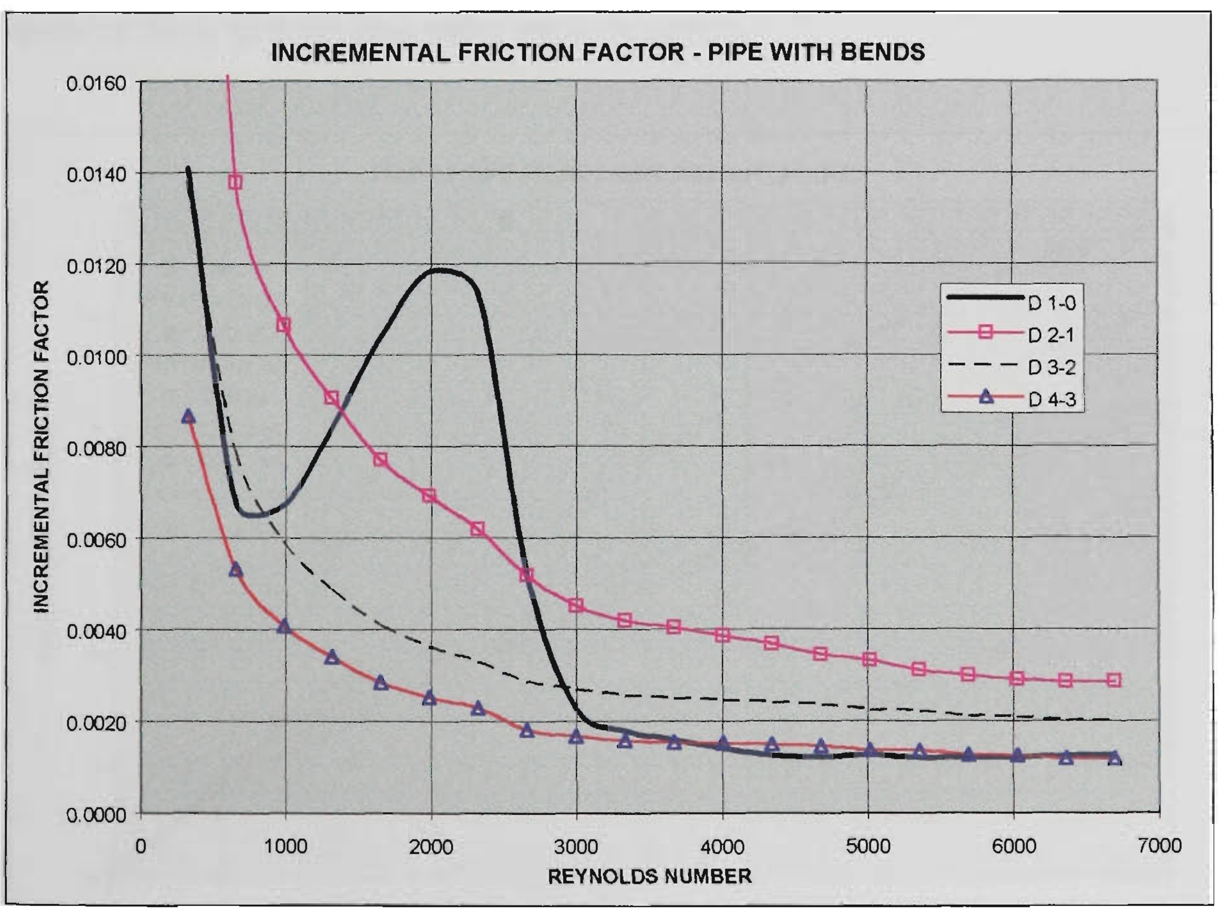

Figure 5.37 - Incremental friction factor with number of bends

5.5 COILED CAPILLARY TUBES

Hitherto, calculation of the pressure drop in capillary tubes has been regarded as a straightforward matter because, at typical flow rates, the flow regime is laminar and the tube length is often several hundred diameters. However, a complication arises from the fact that the tubing is supplied in coils and tends to retain significant curvature after installation. Moreover, this springy flexible tubing is generally installed with plenty of slack to assist fitting-off and maintenance. As a result, capillary tubes are rarely straight. For this reason, they should be treated as a continuous sweeping bend.

An experiment was conducted to determine the effect on pressure drop (or friction factor) for a range of coil radii. A $1.6m$ length of $5.8mm$ internal diameter tube was fitted with two pressure taps $1000mm$ apart ($0.3m$ from each end). The far end was left open with the other end attached to an adapter, which was in turn coupled to the usual test pipe, flowmeter and aspirator. Both pressure taps were coupled to the pressure gauge to obtain the differential pressure. The tube was initially held straight (infinite coil radius) by fixing it to the bench, and subsequently pulled into circular shapes of 4, 2, 1 and 0.67 m equivalent circumference (representing a quadrant, a semicircle, a full circle, and a circle overlapped by a half). These correspond to coil radii of respectively 110, 55, 27 and 18 tube diameters, covering the maximum expected range of field use. Pressure settings of zero to 200Pa were used in steps of 20Pa, and the flow rates were recorded.

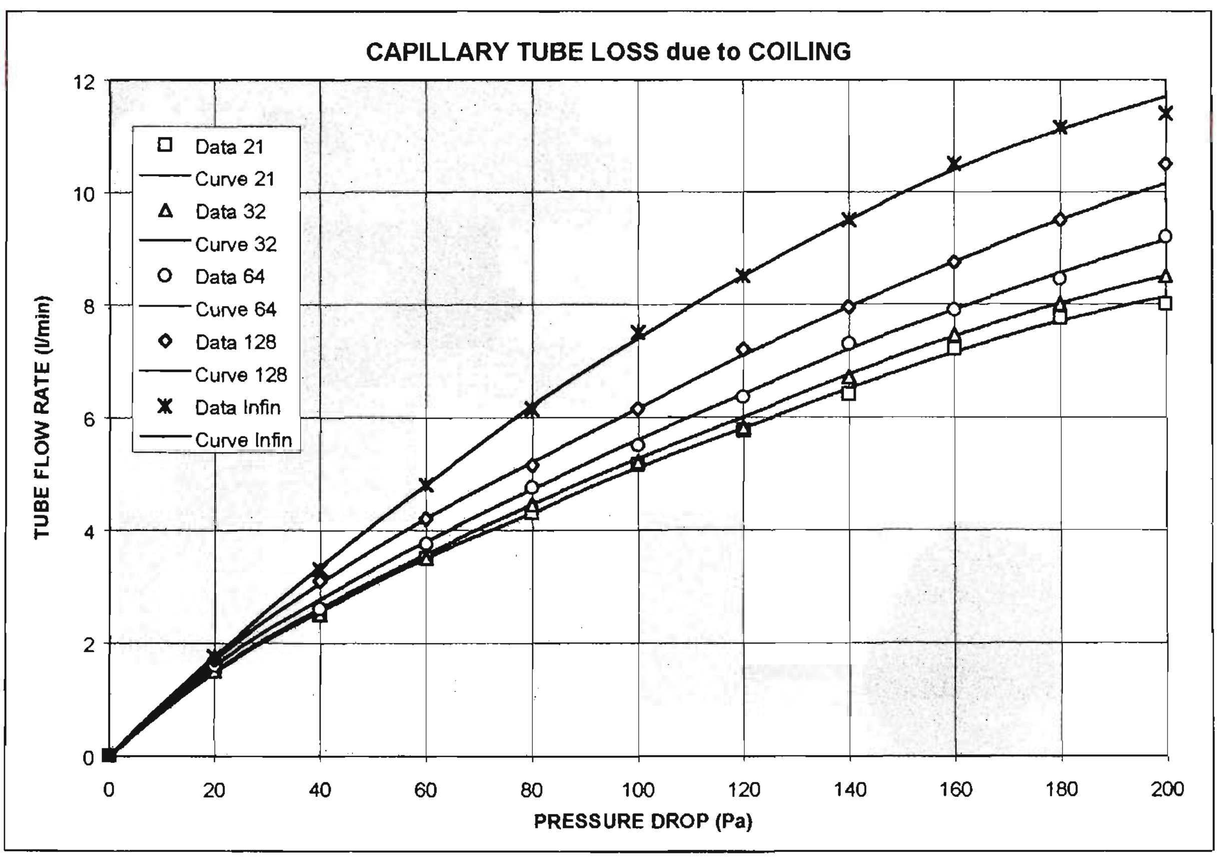

Figure 5.38 - Measurement of capillary tube loss for various coil radii

The results are presented in Figure 5.38 together with manually-smoothed curves of good fit. The fit is not so good at the higher pressures because the flow regime there has entered the turbulence transition phase. It is evident that a significant increase in pressure drop results from reducing the coil radius - for example, at a flow rate of $8 litre/min$ the pressure drop increases from 110 to as much as 195 Pa (a 77% increase).

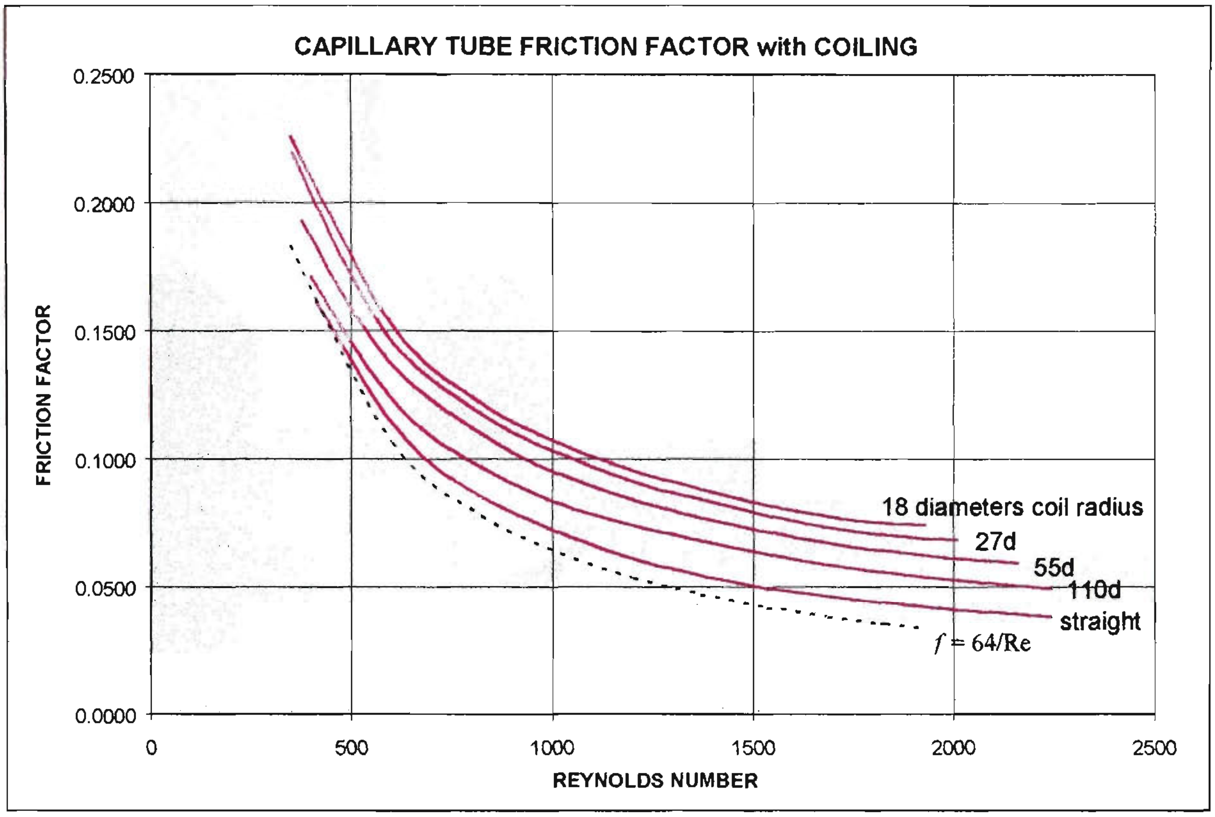

Figure 5.39 - Friction Factor versus Reynolds number for coiled tubing

In Figure 5.39 the friction factor is presented in terms of Reynolds number, where the effect of reducing coil radius is clearly seen. The curve $f = 64/\mathrm{Re}$ is included for reference (dotted), which is similar to, but does not exactly match the curve representing straight pipe because the flow regime is initially disturbed. By normalisation of all these curves it has been possible to determine a Coil Friction Correction Factor due to the tube coiling radius. The results obtained are presented in Figure 5.40, and an equation of best fit within the span of results has been determined as:

$$F_C = 1 + C_C \,\mathrm{Re} \qquad \text{where:}$$

$$C_C = -1.07\,E{-}10\,R_C^3 + 4.1\,E{-}08\,R_C^2 - 6.95\,E{-}06\,R_C + 7.4E{-}04 \geq 1.3E{-}04$$

F_c is the dimensionless Coil Friction Correction Factor, C_c is the correction coefficient and R_c is the coil radius in tube diameters. This Factor provides the increase in friction factor, and it should asymptote to a value of $1 + 1.3E\text{-}04\ \mathrm{Re}$ as the coil radius approaches infinity, for initially disturbed laminar flow (but for ideal undisturbed flow it would asymptote to unity).

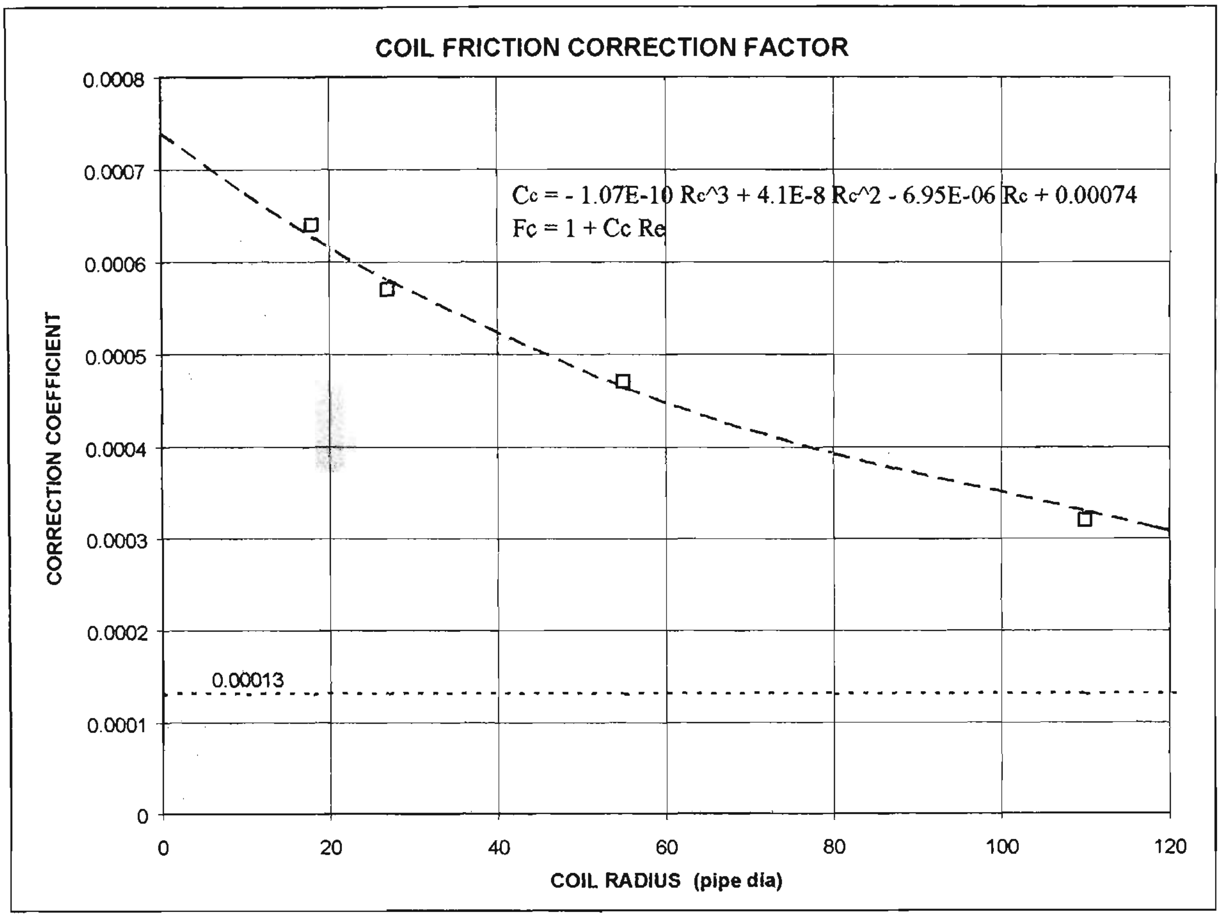

Figure 5.40 - Coil Friction Factor due to tube coil radius (asymptotes to $1 + 0.00013$ Re at infinite radius)

Overall it is possible to state that the effect of a typical degree of tube coiling is approximately to double the pressure drop in the tube at a given flow rate, compared with a smooth straight tube with undisturbed flow.

Accordingly it is necessary to revisit Section 4.12 which considered the combination of a sampling nozzle and capillary tube on the assumption of straight tubing and undisturbed flow. By inspection of those equations it can be shown that the solution:

$$Q_{nozzle} = \pi D^2_{nozzle} \left(\left(t_1^2 + 4\, t_2\, \Delta P_{pipe} \right)^{\frac{1}{2}} - t_1 \right) \Big/ 8\, t_2$$

may continue to be used provided that the Coil Friction Correction Factor is taken into account by amendment of the tube friction factor which occurs in the equation for t_1 such that:

$$t_2 = \left(\frac{15000\, \pi\, D^2_{nozzle}}{K_{nozzle}} \right)^2 \quad \text{and:} \quad t_1 = \frac{32\, F_C\, \rho\, k\, L_{tube}\, D^2_{nozzle}}{D^4_{tube}}$$

To some extent, effects such as coiling may be compensated for within the dynamics of the system. For example, tightening the coil radius increases the friction loss and tends to cause a reduced pressure across the nozzle. This produces a lower nozzle flow rate. The associated reduction in tube flow rate reduces the pressure drop, tending to increase the pressure across the nozzle. This in turn, increases the nozzle flow rate. Therefore, to evaluate the net significance of the coiling effect, a sensitivity analysis was conducted. Extreme values of nozzle size (2 and 4 *mm*) and capillary tube length (0.4 and 4 *m*) were selected in the four possible combinations, while a consistent pressure of 250Pa was selected.

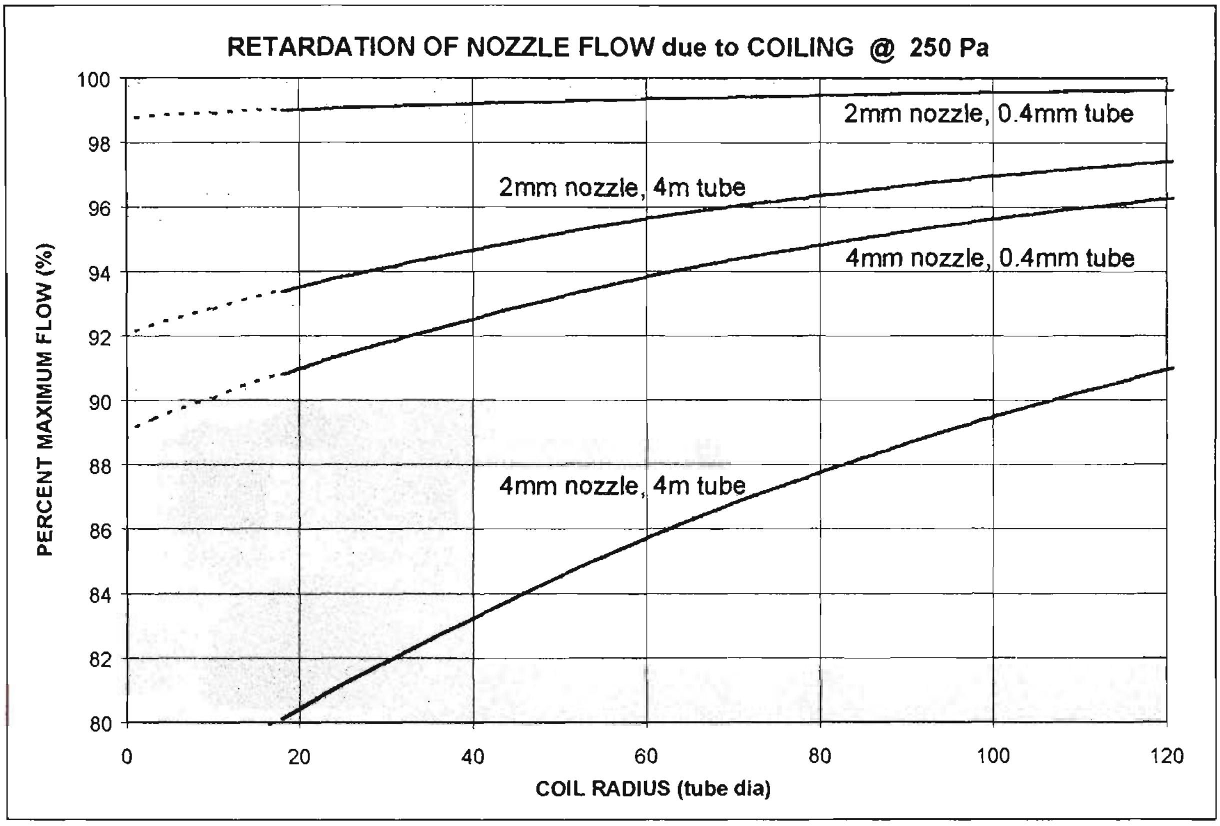

Figure 5.41 - Effect of coil radius on nozzle flow at 250Pa

The results of this analysis are presented in Figure 5.41. For a small nozzle with a short tube the flow rate is reduced in the vicinity of 0.5 to 1 %. If the tube is long, the flow rate for a small nozzle is reduced in the vicinity of 3 to 8 %. With a large nozzle and short tube, the flow rate is reduced in the vicinity of 4 to 11 %. If the tube is long, the flow rate for a large nozzle is reduced in the vicinity of 9 to 23 %.

It is not unexpected that the effect of coiling is more pronounced at relatively high nozzle flow rates and with long tubes. However, this effect has now need quantified. In the absence of field data, a coil radius of 60*dia* will be assumed for the purposes of the computer model.

5.6 CONCLUSIONS

In pipe flow, the head loss due to friction (or the pressure drop) scales with the length to diameter ratio (L/d), the fluid velocity head ($u^2/2g$) and the friction factor (f). In the case of a fully-developed laminar flow regime the friction factor can be obtained from the *pipe* Reynolds number ($f = 64/\mathrm{Re}$). In the case of a fully-developed turbulent flow regime the friction factor is generally obtained from published empirical data (Moody chart). In the case of fully-developed flow in the transition region (approximately $2000<\mathrm{Re}<3500$), values for the friction factor are not generally included although the data of Nikuradse (1932) have been used.

It has been discovered that these published data are not appropriate for use in aspirated pipe systems because of frequent disturbances to the flow regime induced by pipe bends or sampling holes. New data have been obtained experimentally, which provide the friction factor applicable to straight pipe within a range of Reynolds numbers ($400<\mathrm{Re}<4000$) and levels of disturbance appropriate to aspirated smoke detection systems. These data were broadly confirmed as a result of further experiments conducted with pipe of much smaller diameter.

The level of disturbance (L_D) is calculated as a ratio of the air flow rate induced by a sampling hole (Q_{hole}), to the upstream flow rate in the pipe (Q_{pipe}). The friction factor increases as the disturbance level increases, until about 8% disturbance, beyond which there is no significant further increase in friction factor. An algorithm for determining the friction factor applicable to maximally-disturbed flows ($L_D > 8\%$) is:

$\mathrm{Re} < 2170$: $f = 7.1E\text{-}09\ \mathrm{Re}^2 - 4.3E\text{-}05\ \mathrm{Re} + 0.1$

$2170 < \mathrm{Re} < 2480$: $f = 0.0401$

$2480 < \mathrm{Re} < 2875$: $f = -\ 8.07E\text{-}09\ \mathrm{Re}^2 + 4.83E\text{-}05\ \mathrm{Re} - 0.0301$

$\mathrm{Re} > 2875$: $f = 0.1389 / \mathrm{Re}^{0.15}$

while an algorithm for determining the friction factor applicable to mildly disturbed flows ($1 < L_D < 3\ \%$ *approx.*) is:

$\mathrm{Re} < 2200$: $f = 64/\mathrm{Re} + 4.3E\text{-}06\ \mathrm{Re} - 0.005$

$2200 < \mathrm{Re} < 2380$: $f = 0.0378$

$2380 < \mathrm{Re} < 2780$: $f = -\ 1.8E\text{-}08\ \mathrm{Re}^2 + 9.78E\text{-}05\ \mathrm{Re} - 0.0931$

$\mathrm{Re} > 2780$: $f = 0.1305 / \mathrm{Re}^{0.15}$

Figures 5.17 and 5.18 may be used to provide the friction factor at intermediate levels of disturbance by interpolation. The errors involved in using published data (Moody chart, Figure 5.1) to determine the friction factor, which assume undisturbed, fully-developed flow regimes, can be as large as

-30 to +53 % within the range of Reynolds numbers from 1000 to 10,000.

Whereas the above equations were derived from the experimental results of 21.2*mm* pipe, consistent results were obtained for 12.4*mm* pipe.

In the particular case of pipes containing 90° bends, the impact on friction factor has also been determined. It was discovered that one bend is sufficient completely to disturb the flow regime whereby additional bends in the immediate vicinity do not further disturb the flow regime. The pressure drop due to one bend, and additional bends has been quantified in terms of Reynolds number. It was also discovered that the pressure drop caused by a bend is independent of the bend radius. This is because the pressure drop is dominated by the pair of sockets necessarily provided at each end, and to a lesser extent because the smaller radius bends have a shorter length which tends to compensate for their sharper change in flow direction.

An algorithm describing the pressure drop incurred by the first bend at a particular location is:

Re < 2300:	$P_{bend} = 9.4E\text{-}11\ Re^3 + 3.5E\text{-}07\ Re^2$
2300 < Re < 3000:	$P_{bend} = 1.766E\text{-}6\ Re^2 - 0.0118\ Re + 20.9$
Re > 3000:	$P_{bend} = 8.7E\text{-}08\ Re^2 + 5.5E\text{-}05\ Re + 0.455$

Equations for the incremental effect of additional bends in the immediate vicinity of the first bend are as follows:

One more bend:	$P_{bend2} = P_{bend} + 9.5E\text{-}08\ Re^2 + 6.0E\text{-}04\ Re$
Two more bends:	$P_{bend3} \approx P_{bend} + 2.0E\text{-}07\ Re^2 + 8.5E\text{-}04\ Re$
Three more bends:	$P_{bend4} = P_{bend} + 3.0E\text{-}07\ Re^2 + 0.0011\ Re$
Generally:	$P_{bendN} \approx P_{bend} + 1.0E\text{-}07\ N_b\ Re^2 + (2.5E\text{-}04\ N_b + 3.5E\text{-}04)\ Re$

where N_b is the number of additional bends. Failing to take account of the disruption to the flow regime caused by bends, would result in surprisingly large errors. In the worst case, at Re = 2300 the measured friction factor for a straight pipe is 0.0296, while the inclusion of four bends increases this figure to 0.0527 - an increase of 178%. The calculated friction factor for a straight pipe with undisturbed, fully developed laminar flow (f = 64/Re) is 0.0278, reliance upon which would incur an error of 190%.

Within a straight pipe segment, the effect of sockets (without bends) is to increase the friction factor so that the pipe becomes effectively rough. However, the flow regime is not significantly disturbed so the precise location of sockets would not need to be known when modelling the smoke transport time of an aspirated system (refer Chapter 7). This provides a very important simplification to the model in terms of the requirements for data entry.

Whereas the flow regime disturbance induced by pipe bends or sampling holes is expected to dissipate over some distance along a pipe, the typical separation of pipe bends and sampling holes is of similar magnitude to the scale of the experimental apparatus, so it is proposed to apply the above sets of algorithms and equations throughout an aspirated pipe system.

The equations that were developed in Chapter 4 to model capillary tubes and nozzles acting in combination, have been improved to take into account the fact that capillary tubes are rarely straight. The effect of coiling the tubes can be to increase the pressure drop significantly. The dimensionless Coil Friction Correction Factor (F_c) has been developed to describe this increase in terms of coil radius (R_c which is expressed as a ratio of tube radii). The equation is:

$$F_C = 1 + C_C \,\mathrm{Re} \qquad \text{where:}$$

$$C_C = -1.07E{-}10\, R_C^3 + 4.1E{-}08\, R_C^2 - 6.95E{-}06\, R_C + 7.4E{-}04 \geq 1.3E{-}04$$

This also describes the increase in friction factor above that of undisturbed flow in straight pipes, while the range of differential pressures, nozzle and tube dimensions are such that flow regime is likely to be laminar. The equation for modelling the capillary tube and nozzle combination then becomes:

$$Q_{nozzle} = \pi\, D_{nozzle}^2 \left(\left(t_1^2 + 4\, t_2\, \Delta P_{pipe} \right)^{\frac{1}{2}} - t_1 \right) \Big/ 8\, t_2$$

where:

$$t_2 = \left(\frac{15000\, \pi\, D_{nozzle}^2}{K_{nozzle}} \right)^2 \qquad \text{and:} \qquad t_1 = \frac{32\, F_C\, \rho\, k\, L_{tube}\, D_{nozzle}^2}{D_{tube}^4}$$

Overall, the effect of a typical degree of tube coiling ($60dia$) can be approximately to reduce the flow rate in the tube at a given differential pressure by as much as 14% (Figure 5.41).

CHAPTER 6 - DETERMINATION OF CORE VELOCITY

6.0 INTRODUCTION

As discussed in Chapter 1, within an aspirated pipe system a significant proportion of smoky air is contained within the central region (core) of pipe flow, where the velocity is highest. This was confirmed by using a smoke tracer and finding consistency between experimental data and theoretical calculations. Therefore, modelling of the smoke transport time from the hole to the detector will be largely determined by the core velocity and it is necessary to obtain reliable estimates of this velocity under all conditions within aspirated pipe systems.

6.1 THE NATURE OF CORE VELOCITY

It is known that in the case of fully-developed laminar flows, the core velocity ($u_{core} = u_{max}$) can be twice the average velocity (u_{avg}), whereas in the case of fully-developed turbulent flows, the core velocity can be some 20 to 30% faster than the average velocity. This is based upon the well-established profiles of velocity as illustrated in Figure 6.1 (Duncan 1974 p404).

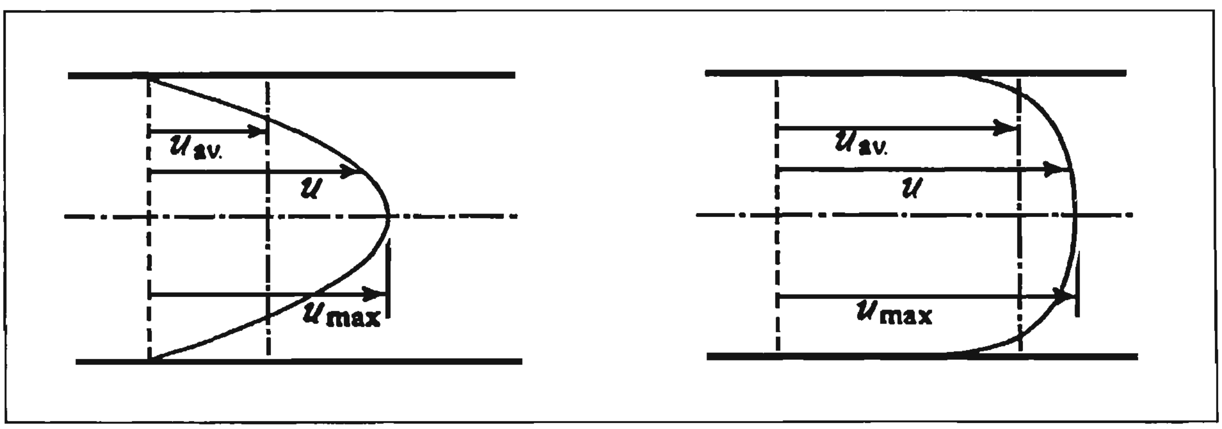

Figure 6.1 - Velocity profiles for fully-developed laminar and turbulent flow regimes in round pipes (Duncan 1974)

However, these velocity profiles are not developed immediately. Consider an open-ended pipe. At the inlet, the core velocity is the same as the average velocity, so the velocity profile is flat (plug flow). Just inside the pipe, the air in close contact with the pipe wall is retarded by surface friction. At increasing distance from the wall surface, shear stresses cause a diminishing degree of retardation of the air, forming a laminar boundary layer.

This boundary layer is defined as the region near the surface (or boundary) of an object in which the fluid has its velocity retarded, because of shearing resistance caused by the surface coupled with the viscosity of the fluid. The extent of the boundary layer is defined as the distance from the surface at which the fluid velocity is either 99% of the free-stream velocity (Roberson and Crowe 1975 p255) or 99.5%. In this project 99% will be used.

The thickness of this boundary layer increases with distance along the pipe. With incompressible flow and conservation of mass, the retardation of the air velocity near the pipe walls is matched by an acceleration of the air velocity in the central region of the pipe. As the boundary layer approaches the pipe centreline, the core velocity approaches its maximum. In the case of laminar flow this maximum is twice the average velocity and a parabolic velocity profile is established.

In the case of turbulent flow regimes, at a critical point along the pipe, the laminar boundary layer breaks into turbulence. The boundary layer thickness then grows more rapidly and turbulent flow within the pipe as a whole becomes fully-developed in a shorter distance than for laminar flow.

These situations are illustrated in Figure 6.2 (Douglas et al. 1979, p285). The critical point is determined by the ***entry*** Reynolds number calculated according to the displacement along the pipe (not the pipe diameter).

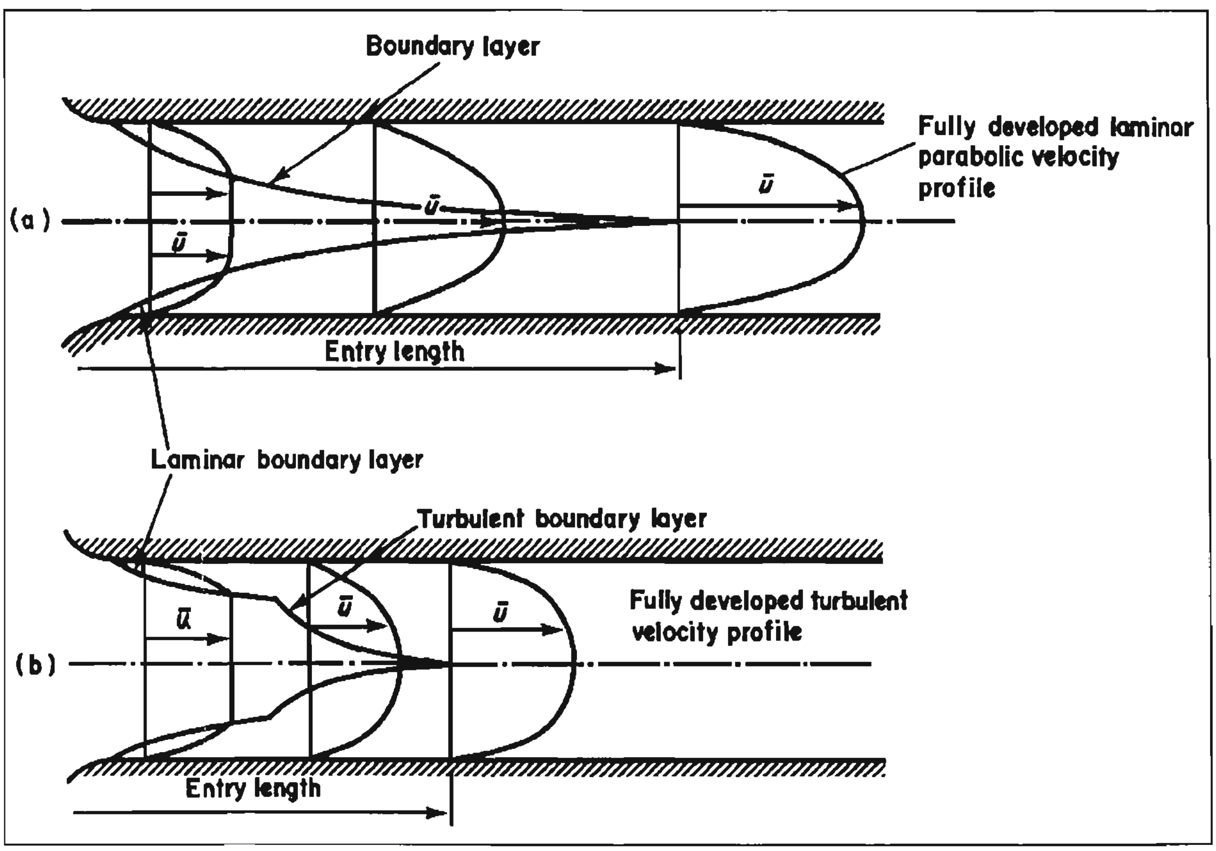

Figure 6.2 - Development of laminar and turbulent flow profiles with distance along a pipe (Douglas et al. 1975)

It is noted that development of a turbulent boundary layer also corresponds with the development of a thin, viscous-flow sub-layer in contact with the pipe surface. Detailed study of this layer is not required for the purpose of determining the core velocity.

6.2 DETERMINING CORE VELOCITY by EMPIRICAL METHOD

A method was described in Chapter 1 for obtaining the envelope of possible core velocities as shown in Figure 1.10 (Cole 1991a, p27), ranging between u_{avg} and u_{max}. This envelope served to verify the data, given that no reading should fall outside it. (In subsequent testing, this fact revealed some problems with certain flowmeters which did produce data outside the envelope, leading to the purchase of more-reliable instrumentation as discussed in Appendix 2).

At a given ***pipe*** Reynolds number in Figure 1.10, the measured core velocity proved to be less than the theoretical maximum, due to pipe bends and sockets which would regularly disturb the flow regime. This data related to a pipe of $26mm$ internal diameter without sampling holes, while a $100m$ pipe length had been employed to improve the timing accuracy (resolution).

In the case of a pipe of the same length but with $21mm$ internal diameter, Cole (1991a, p32) obtained the data presented in Figure 6.3. It can be seen that the measured core velocity is comparatively low in relation to the theoretical maximum, indicating that the effect of disturbances was greater than that of Figure 1.10. Cole attributed this principally to the available pipe bends which were of significantly sharper radius than that applicable to Figure 1.10.

As an initial approach to modelling an aspirated smoke detection system, the data of Figure 6.3 was converted according to the applicable Reynolds numbers and used in a computer program (to be described later), to calculate the smoke transport time by including the following steps:

(1) The local flow rate in each segment of pipe was calculated, including the contribution of flow from the local sampling hole at the local pressure differential.

(2) The Reynolds number and average velocity in each pipe segment were obtained directly from the flow rate (and pipe diameter).

(3) An algorithm based upon the data of Figure 6.3 was used to estimate the core velocity in each pipe segment.

(4) The increments of time delay within each pipe segment were obtained from the core velocity and segment length.

(5) The smoke transport time was then available by summing the increments.

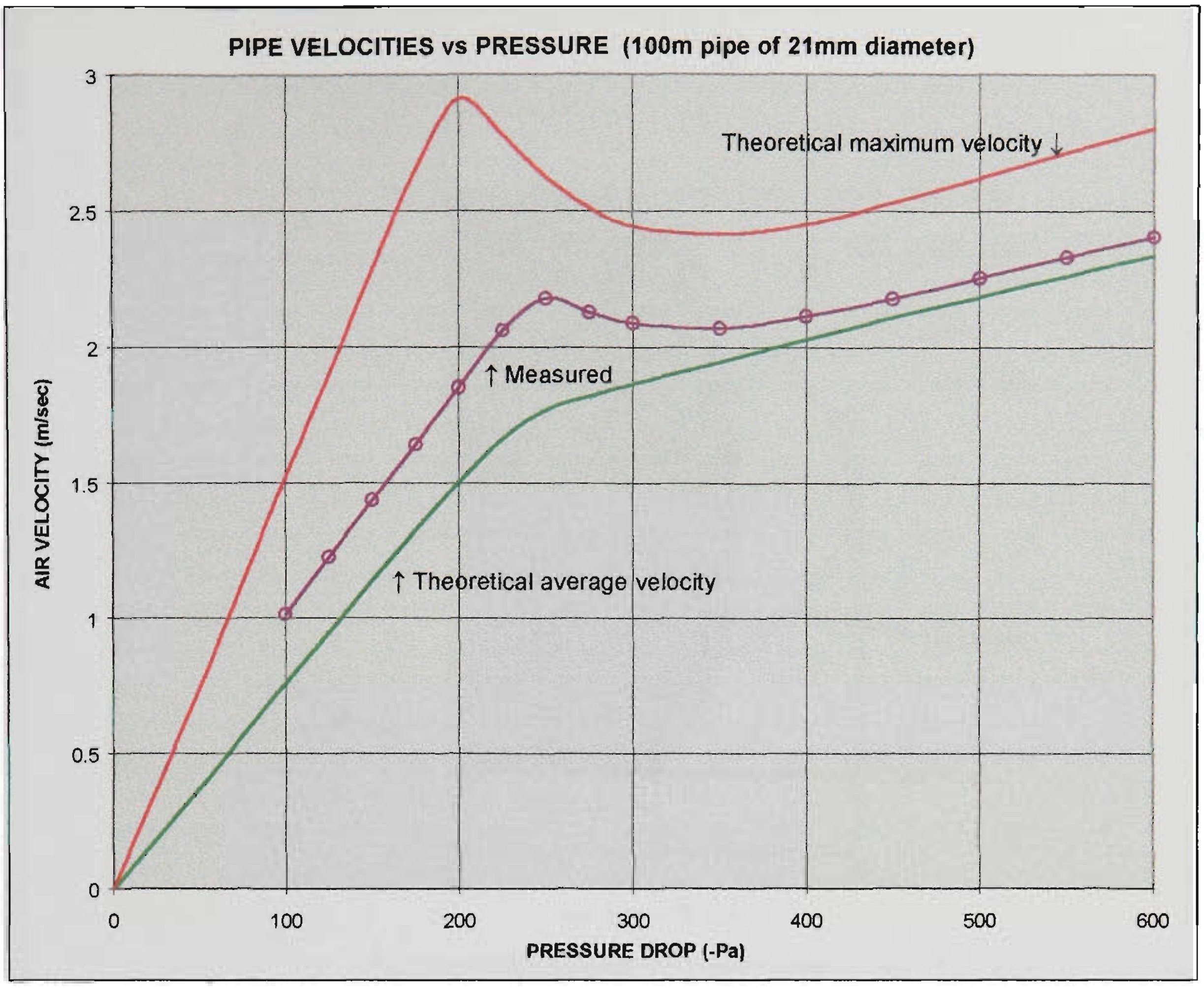

Figure 6.3 - Average, maximum and measured air velocities in $21mm$ pipe

6.3 DETERMINING CORE VELOCITY by THEORETICAL METHOD

By comparing the modelling results with some installed systems, the above empirically-based method was found to have acceptable accuracy using pipes of $21mm$ internal diameter. However, given the proportionally different results of Figures 1.10 and 6.3, this methodology was considered unlikely to be sufficiently accurate for other pipe diameters, unless special algorithms were developed for each pipe size. It was considered preferable (more reliable) to develop a general equation or algorithm to cover pipes within a complete range of sizes and materials likely to be used (worldwide), not all of which could be tested individually and in advance of their usage.

More-accurate velocity profiles for turbulent flows have been published by Miller (1983), as reproduced by Mott (1990, p287) and shown in Figure 6.4. However, these apply to fully-developed flows. Miller has also presented greater detail on the ratio of average velocity to maximum velocity, as shown in Figure 6.5. Here it can be seen that for fully-developed turbulent flow, the (inverted) velocity ratio u_{max}/u_{avg} actually varies from about 1.29 to 1.16 for *pipe* Reynolds numbers of 4000 to 1,000,000 respectively in the case of smooth pipe, or it varies from about 1.29 to 1.22 in the case of rough pipe.

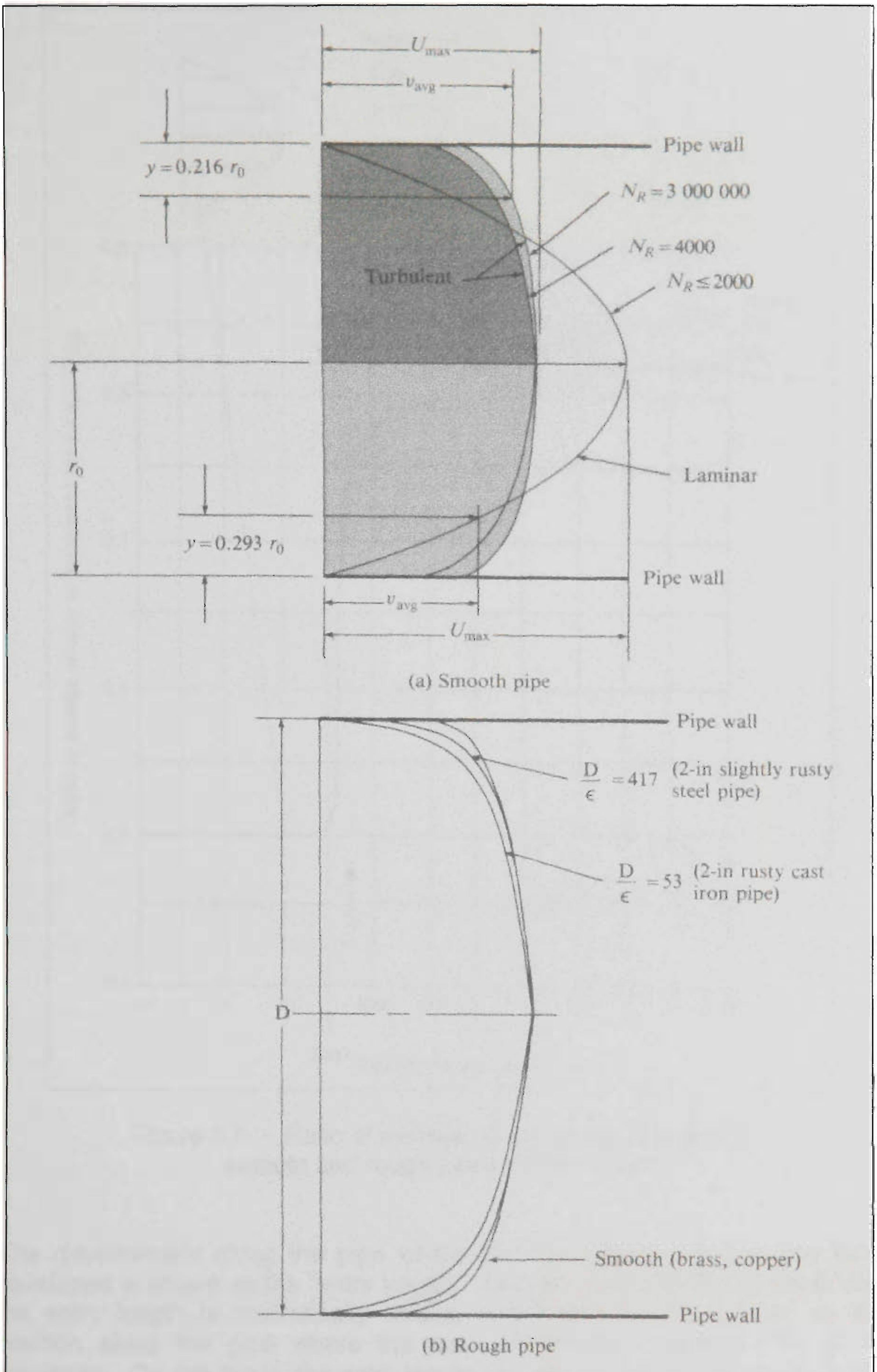

Figure 6.4 - Velocity profiles in laminar and turbulent flow, with (a) smooth and (b) rough pipe (Miller 1983)

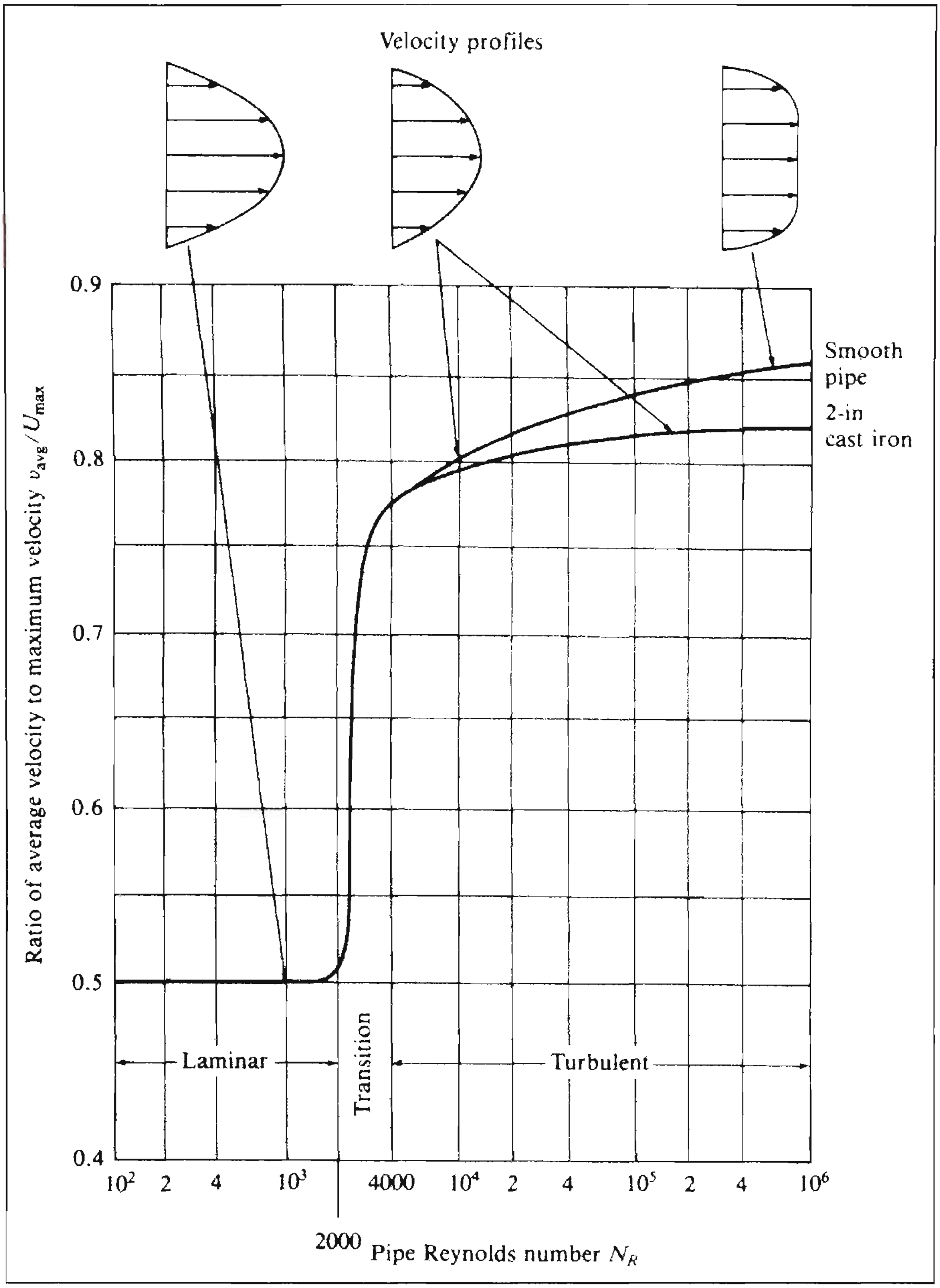

Figure 6.5 - Ratio of average to maximum velocity for smooth and rough pipes (Miller, 1983)

The displacement along the pipe where the flow regime has become fully-developed is known as the "entry length". Douglas et al. (1979) contends that the entry length is theoretically infinite, and it is generally defined as the position along the pipe where the core velocity has reached 99% of its maximum. On this basis, the entry length for laminar flow is estimated as 120 pipe diameters (120*dia*) while that of turbulent flow is estimated as 60*dia*.

Because the core velocity is not established at u_{max} until beyond the entry length, it has been helpful to use a term to describe the local value of the core velocity, namely u_{core} which would always lie between u_{avg} and u_{max}. Particularly in the case of disturbed flow regimes, the exact shape of the boundary layer growth curve applicable to the entry length of a pipe has not been accurately established, and is often disregarded on the basis that the entry length is insignificant in long pipes. In the case of aspirated detection systems, this simplification cannot be made because each sampling hole represents a fresh disturbance.

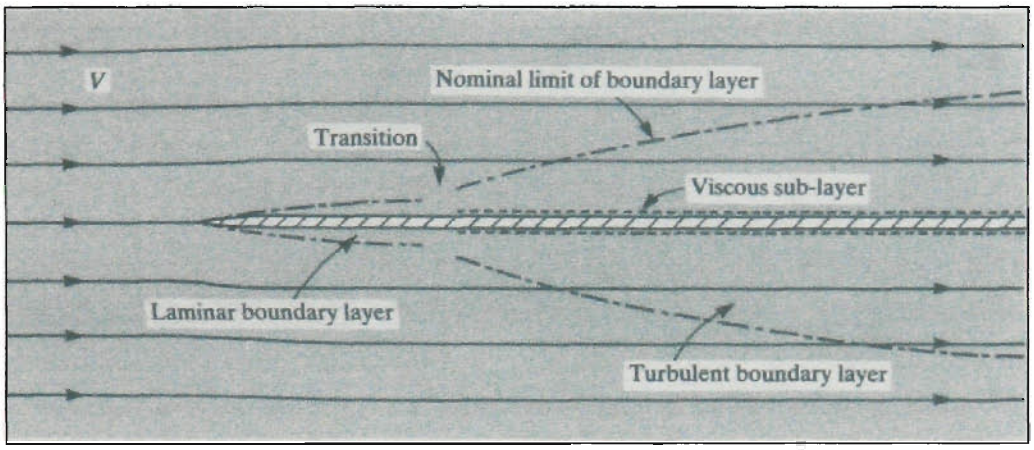

Figure 6.6 - Development of a laminar and turbulent boundary layer over a smooth flat plate at zero incidence (Vardy, 1990)

As a starting point for quantitative analysis; when viewed in longitudinal cross section a pipe entry wall may be likened to a flat plate, the flow characteristics of which have been well-researched. Vardy (1990 p88) has illustrated the development of a boundary layer over a flat plate as shown in Figure 6.6. This Figure has similar features to Figure 6.2. Vardy states that in the case of steady flow parallel to a thin flat plate, the boundary layer thickness B at a displacement S from the leading edge has been shown by Blasius to satisfy:

$$\frac{B}{S} = 4.93\left(\frac{S\,u}{k}\right)^{-1/2} \qquad \text{so:} \qquad B = 4.93\sqrt{\frac{S\,k}{u}}$$

where $(S\,u\,/\,k)$ is the *entry* Reynolds number. To examine the applicability of this equation, let us assume the standard entry length of 120 diameters for laminar flow. It is implied that as Reynolds number (and average velocity) is increased, this entry length should be maintained, until the upper limit for laminar pipe flow is reached. This critical point should correspond to a *pipe* Reynolds number of about $2000 < \mathrm{Re} < 2200$. Selecting $\mathrm{Re} = 2100$, we can obtain an approximation to the critical average velocity for a pipe of $21mm$ ($0.021m$) diameter:

$$\mathrm{Re} = \frac{D\,u_{avg}}{k} \qquad \text{so:} \qquad u_{avg} = \frac{k\,\mathrm{Re}}{D} = \frac{1.5 * 10^{-5} * 2100}{0.021} = 1.5 m/sec$$

At this velocity the Blasius equation provides the following boundary layer thickness, wherein the entry length at $120dia$ equates to $2.52m$:

$$B \;=\; 4.93\sqrt{2.52*1.5*10^{-5}/1.5} \;=\; 0.025m$$

Unfortunately this result is more than twice the expected result of $0.0105m$ (being the pipe radius). Working backwards, this equation predicts an entry length of $0.45m$ or $20dia$ which is unlikely in view of the $120dia$ expected. Moreover, for a given free stream velocity this equation has the form:

$$B \;\alpha\; S^{1/2}$$

from which we would expect the shape of the boundary layer to follow a square-root pattern. However, this does not satisfy the condition that the entry length is "theoretically infinite", whereby the boundary layer approaches the pipe centreline asymptotically. It seems clear that in the case where the flow is constrained by pipe walls, the boundary layer growth pattern is different from that of a flat plate, because the opposing wall has a significant influence.

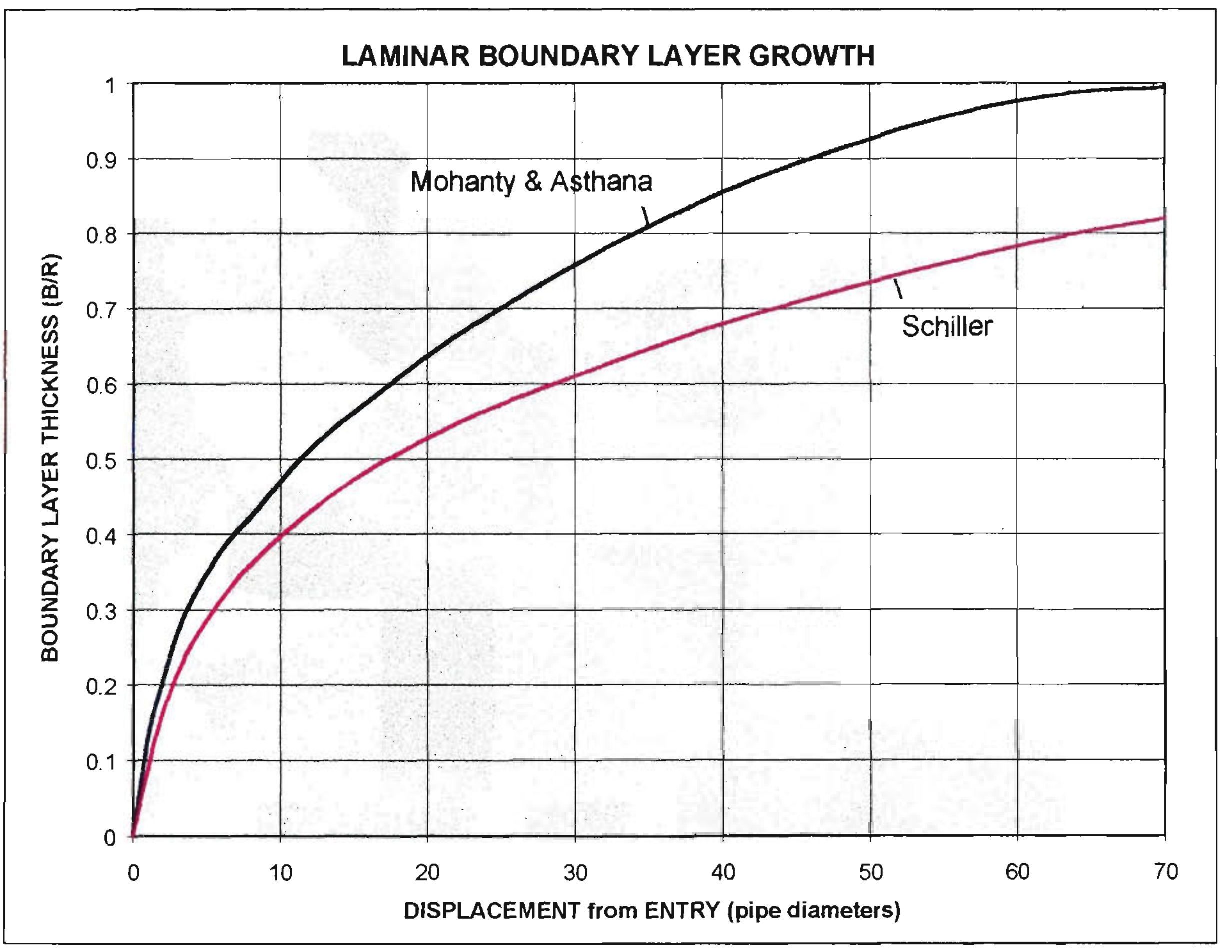

Figure 6.7(a) - Boundary layer growth at the pipe entry for idealised laminar flow (Mohanty and Asthana 1978)

Mohanty and Asthana (1978) have undertaken a theoretical and experimental study of the laminar entrance flow in a smooth pipe, some results of which are presented in Figure 6.7(a). They compare their results with the theory of Schiller. However, these results are applicable to the idealised conditions of a completely smooth, bellmouth pipe entry causing negligible disturbance.

The basis for the initial version of the computer model was, that for the boundary layer to approach the centreline asymptotically, its equation was expected to have the form of a natural exponential (common to many natural phenomena such as electrical or thermal energy transfer), namely:

$$B = \frac{D_{pipe}}{2}(1 - e^{-\frac{S}{s}})$$

where D_{pipe} is the pipe internal diameter. It can be shown that this equation reaches 99% of its final value when the displacement ratio $S/s = 4.6$. The shape of this curve is represented in Figure 6.7 (b), below a curve representing the Blasius equation. Because the latter indicated an entry length of only $20dia$, a further square-root curve has been developed to intersect with the exponential curve, at the point where the boundary layer thickness is 99% of the pipe radius at a displacement of $120dia$.

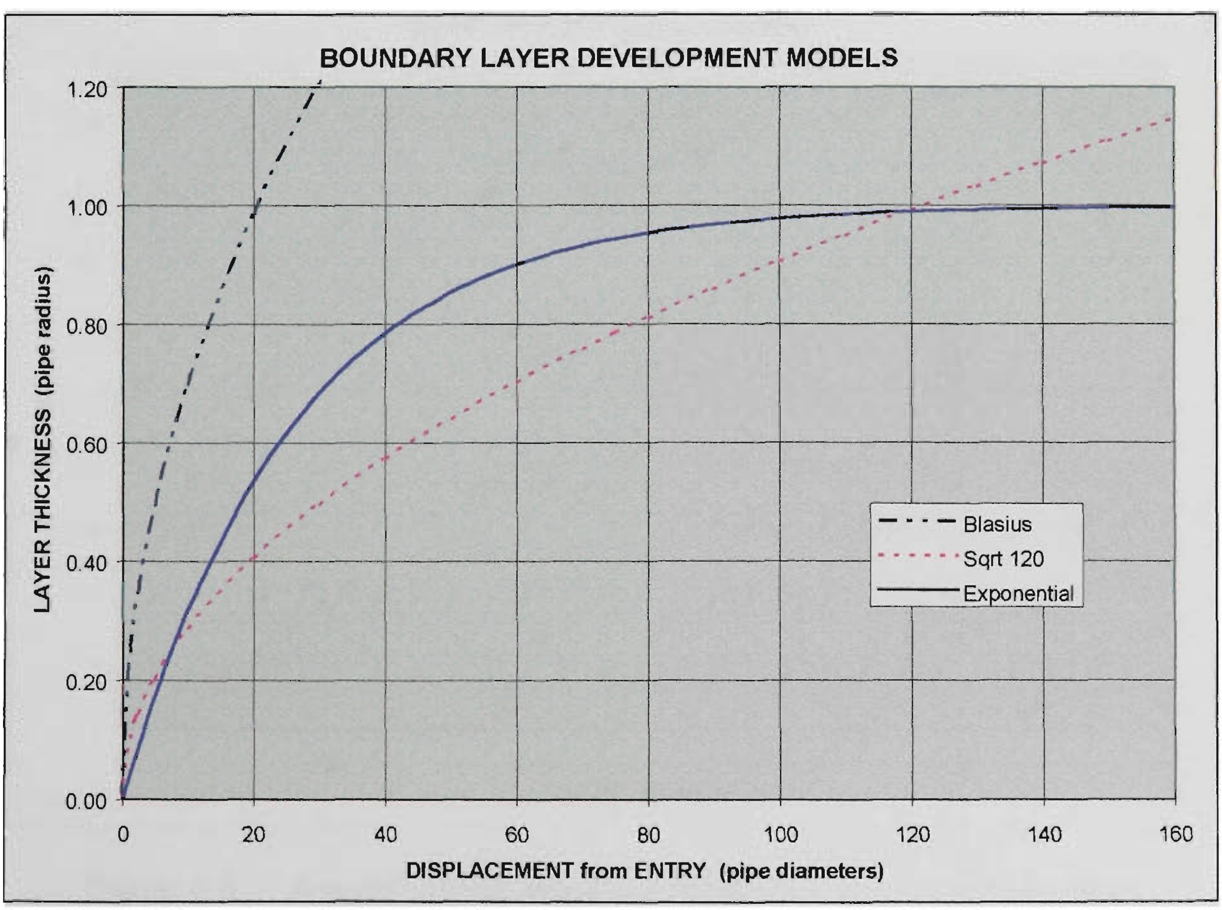

Figure 6.7(b) - Square-root and exponential models for boundary layer growth throughout the entry length

There is a significant difference in shape between the square-root and exponential curves. The most important is the "failure" of the square-root curve to asymptote to the pipe centreline. In addition, the square-root curve has a blunt profile at the pipe entry - in fact it can be shown that the square-root curve produces an infinite gradient at the threshold, whereas the exponential curve indicates a much more gradual growth.

Being directly related to the boundary layer thickness, the core velocity growth coefficient as a function of average velocity was expected to have a similar exponential form, rising from a minimum of unity to a maximum of two.

As noted in Chapter 1 (Section 1.2.2), a number of researchers have published experimental or theoretical data describing the core velocity growth profile under idealised (smooth) pipe entry conditions. The CFD work of Martinuzzi and Pollard (1989) at a high Reynolds number (380,000) shows close agreement with the experimental data of Barbin and Jones (1963), and general agreement with that of Nikuradse (1932).

Sparrow, Lin and Lundgren (1964) report their numerical results along with those of Atkinson, Goldstein, Targ and Langhaar, as presented in Figure 6.8 The x-axis is proportional to displacement, being obtained from the Darcy-Weisbach equation transposed to dimensionless form.

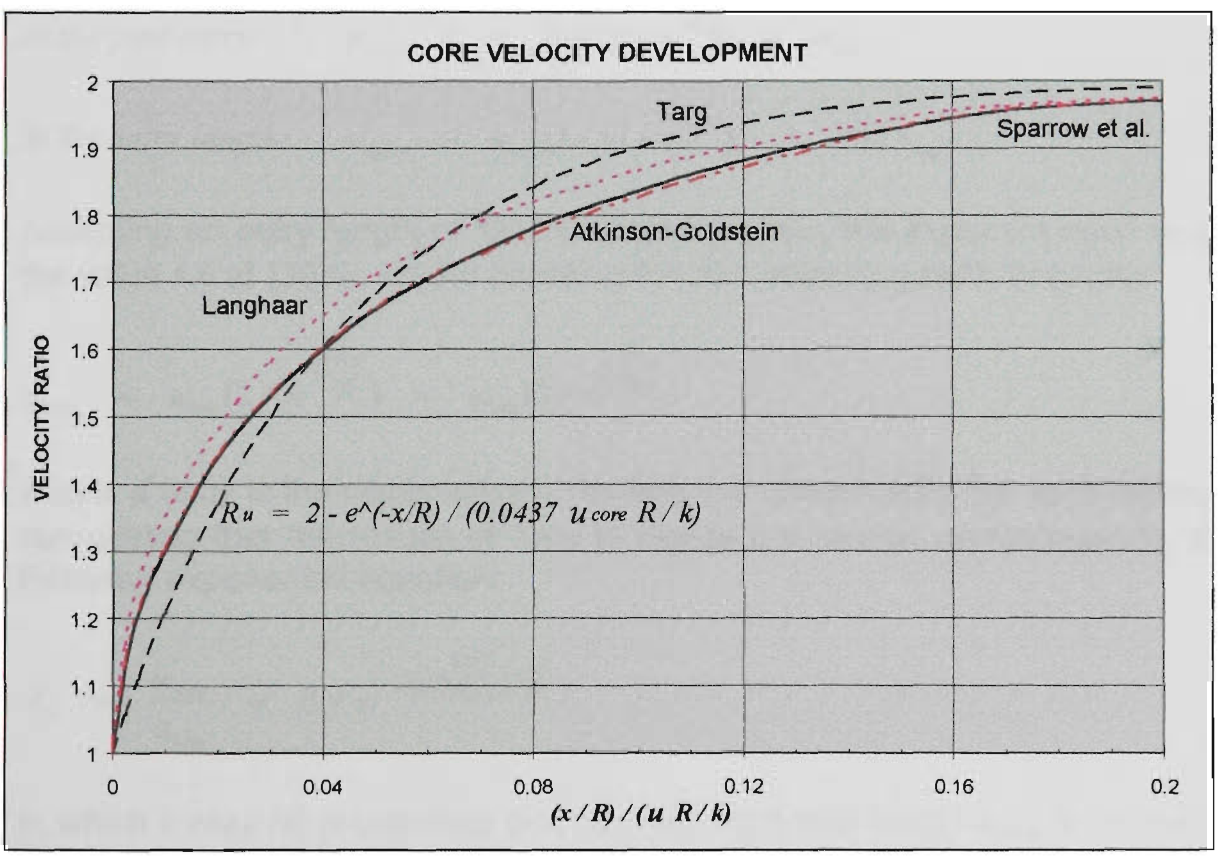

Figure 6.8 - A summary of results from various researchers on core velocity profile development with idealised laminar flow (Sparrow et al. 1964)

Sparrow et al. have used a momentum equation to model the velocity growth profile in round pipes, again under idealised conditions. They propose that this can be modelled as the sum of two terms, the first representing the fully-developed velocity profile and the second representing the transient condition prior thereto. Their velocity solution has the following form:

$$R_u \;=\; 2\left(1-\left(\frac{r}{R}\right)^2\right)+\sum_{i=1}^{\infty}\frac{4}{\alpha_i^2}\left(\frac{J_0(\alpha_i\, r/R)}{J_0(\alpha_i)}-1\right)e^{\alpha_i^2\, X}$$

Detailed discussion of this equation is not warranted here, but a numerical solution to the core velocity growth profile is included in Figure 6.8 (solid curve). However, despite the broad consistency among the various sets of predictions, it can be shown that at a Reynolds number of 2000 for example, the entry length is calculated at 32.5 diameters, which is significantly shorter than expected for laminar flows. Moreover, their ideal pipe entry conditions are likely to produce results significantly at variance from those associated with completely-disturbed flows.

Accordingly, for current purposes it was initially decided to evaluate an exponential model. As previously stated, this was expected to rise from a minimum of unity to a maximum of two (actually 1.98 i.e. 99% of 2):

At the pipe entry: $\quad u_{core} \;=\; u_{avg}(1+(1-e^{-0})) \;=\; u_{avg}$

At the entry length: $\quad u_{core} \;=\; u_{avg}(1+(1-e^{-4.6})) \;=\; 1.98\, u_{avg}$

Accepting an entry length of $120dia$ for laminar flow, the exponent must reach the value 4.6 at $120dia$, so the equation for core velocity growth becomes:

$$u_{core} \;=\; u_{avg}(2-e^{-\frac{4.6\,d}{120}}) \;=\; u_{avg}(2-e^{-\frac{d}{26}})$$

where d (dia) is the displacement. Indeed it is observed by the application of curve-fitting that the results of Targ in Figure 6.8 can be represented by the following exponential equation:

$$R_u \;=\; \frac{u_{core}}{u_{avg}} \;=\; 2-e^{-\frac{x/R}{0.0437\, u_{core}\, R/k}}$$

in which it may be recognised that $d = x/R$ and that $0.0437\, u_{core}\, R/k$ has a set value in normal circumstances. Thus it has the same shape as the exponential curve of Figure 6.7 currently proposed.

Now, to obtain the time delay for a given package of air travelling at a local velocity (du) over an infinitesimal pipe displacement (ds):

$$du = \frac{ds}{dt} \qquad \text{i.e.} \qquad dt = \frac{1}{du} ds$$

By substitution of the core velocity equation, we obtain the following integral for elapsed time over a displacement of d diameters:

$$T = \int_{s=0}^{s=n} \frac{1}{u_{avg}(2 - e^{-\frac{d}{26}})} ds = \frac{1}{u_{avg}} \int_{o}^{n} \frac{ds}{2 - e^{-\frac{d}{26}}}$$

This may be solved by application of the known integral transform:

$$\int \frac{dx}{a + b e^{px}} = \frac{x}{a} - \frac{1}{ap} \ln(a + b e^{px})$$

Substituting $x = n,\ a = 2,\ b = -1,\ p = -1/26$ we obtain:

$$T_{lam} = \frac{1}{u_{avg}} \left(\frac{d}{2} + \frac{1}{2/26} \ln(2 - e^{-\frac{d}{26}}) \right)$$

$$= \left(d + 26 \ln(2 - e^{-d/26}) \right) / 2\, u_{avg}$$

This core velocity growth equation was used in the initial version of the computer modelling program for laminar flow regimes. As distinct from previous methods used, including those of Taylor (1984) and Notarianni (1988), the smoke transport time was now related to the length of the pipe segment in a non-linear manner as governed by the extent to which the boundary layer would develop.

As previously stated, in the case of turbulent flow, the boundary layer is expected to grow in the same manner as for laminar flow until at a critical distance along the pipe, the boundary layer breaks into turbulence. This distance is determined by the *entry* Reynolds number. Here, the Reynolds number is obtained from the following where S (m) is the entry length:

$$\mathrm{Re}_e = \frac{S\, u_{avg}}{k} \qquad \text{so:} \qquad S = \frac{k\, \mathrm{Re}_e}{u_{avg}}$$

Roberson and Crowe (1975, p259) state that the boundary layer transition from laminar to turbulent flow can be expected at an *entry* Reynolds number of 500,000 but if the approach flow is turbulent and/or the surface is rough, transition will occur at a lower Reynolds number. Douglas et al. (1979, p286) also indicate that this transition is often quoted to occur at $\mathrm{Re}_e = 500{,}000$, but this figure is considerably reduced if the surface is rough. He states: "For $\mathrm{Re}_e < 100{,}000$ the laminar layer is stable, however, at $\mathrm{Re}_e \approx 200{,}000$ it is difficult to prevent transition." If flow disturbance increases the effective roughness or promotes the onset of transition, it could conceivably reduce the minimum figure to 50,000. Such a broad range of potential uncertainty (50,000 to 500,000) presents difficulty in accurate modelling.

Accepting that the entry length of $120dia$ is maintained throughout the laminar flow range, until the lower limit of transitional flow is reached, then this entry length can be applied to the critical average velocity that was discussed earlier. It was established that for a pipe of $21mm$ diameter this velocity is about $1.5m/sec$, from which the *entry* Reynolds number can be obtained:

$$\mathrm{Re}_e = \frac{S\, u_{avg}}{k} = d\,\frac{D\, u_{avg}}{k}$$

Whereas the *entry* Reynolds number can be calculated easily by substitution of the critical average velocity together with the other known data, by inspection we see that this number can be obtained directly from the *pipe* Reynolds number:

$$\mathrm{Re}_e = d\,\mathrm{Re} = 120 * 2100 = 252{,}000 \quad \text{say} \quad 250{,}000$$

This result is broadly consistent with the statements by Roberson and Crowe, and by Douglas et al. (discussed above), which would be satisfied by any entry length within the range of about 50 to 200 dia. Therefore it was concluded that a maximum entry length of $120dia$ could be applied.

At average velocities higher than about $1.5m/sec$, the boundary layer would break into turbulence prior to reaching a displacement of $120dia$, and would then grow towards the pipe centreline at a faster rate. In the limit, it was expected that for completely turbulent flow regimes, the entry length would reduce to $60dia$.

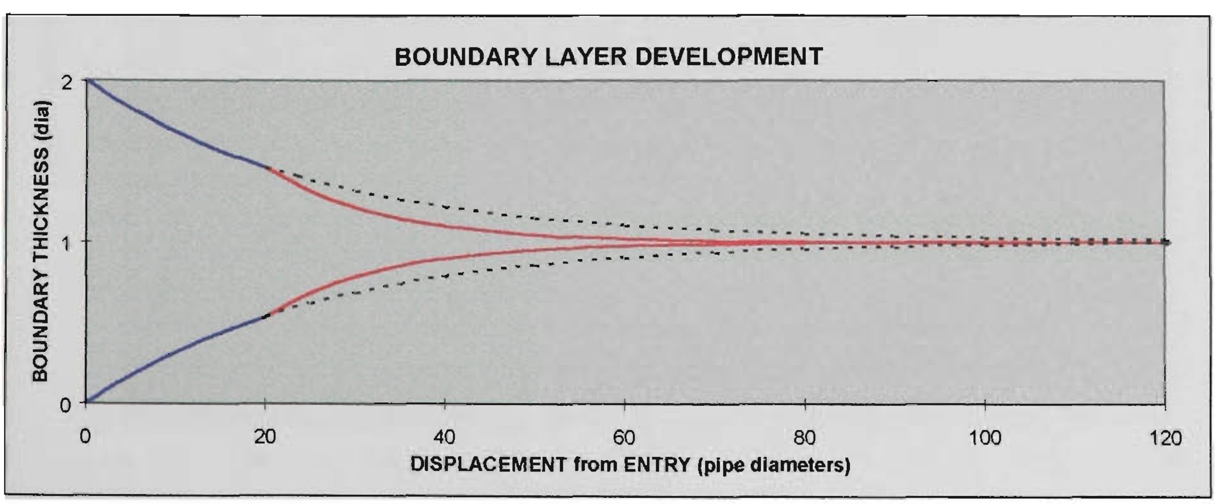

Figure 6.9 - Exponential model for transitional boundary layer growth

Figure 6.9 is a graphical representation of the growth in the boundary layer thickness on both sides of a pipe longitudinal section, according to the exponential equations. This depicts an initially laminar boundary layer that breaks into turbulence at $20dia$ and develops an entry length of $80dia$. Also in accordance with the exponential model, the dotted line represents the boundary layer development within a displacement of $120dia$ in the event that turbulence does not occur. There is close similarity between this Figure and Figure 6.2, providing some confidence in the model

Furthermore, it is noted that in the works of Campos-Silva et al. (1992) and Al-Ali and Selim (1993) they depict the boundary layer growth profile as quite similar in shape to Figure 6.9, although their models are restricted to laminar flow, do not depict the point of transition, and are restricted to a hydraulically-smooth pipe inlet so that the flow regime is completely undisturbed.

Yakhot and Orszag (1993) produced a numerical simulation to the velocity growth profile in the case of developing turbulent flow regimes, in which they claim close agreement with the results of Barbin and Jones (1963) as discussed in Chapter 1. Again, both sets of results are restricted to a hydraulically-smooth pipe inlet so that the flow regime is completely undisturbed, and the effect of boundary layer transition is not indicated. However, the core velocity growth profile is certainly closer to an exponential form than a square-root form.

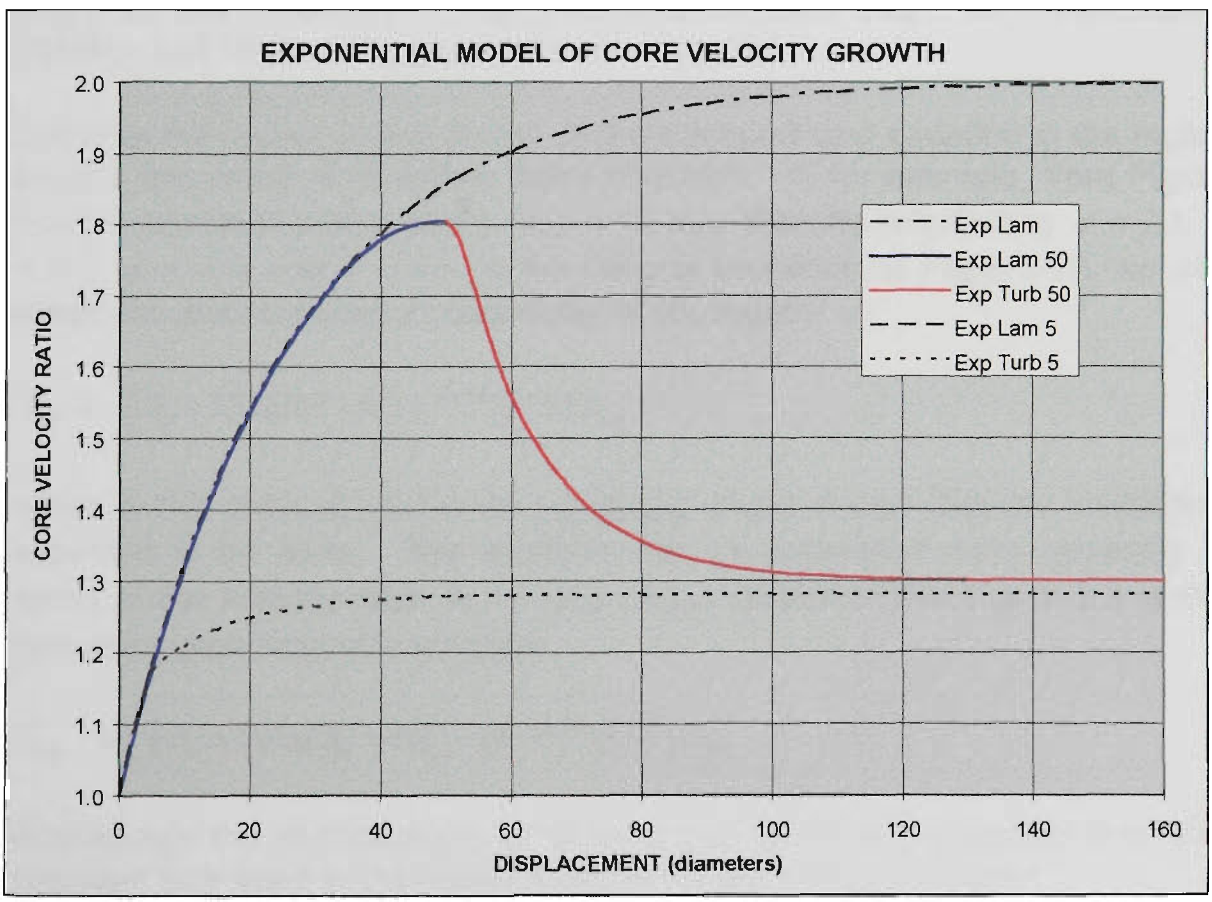

Figure 6.10 - Expected core velocity growth profiles including the effect of the boundary layer transition

Application of the current exponential model directly to the core velocity growth profile is illustrated in Figure 6.10, which shows the core velocity ratio ($R_u = u_{core} / u_{avg}$) as a function of displacement. Firstly, the exponential growth in core velocity ratio within a laminar flow regime is shown, reaching 99% of its final value in $120dia$.

Next, the situation where the boundary layer breaks into turbulence at $50dia$ is shown. Here the core velocity ratio initially grows in the same manner as in the laminar flow case, but at $50dia$ it has reached a value of about 1.8 which is well above the ratio expected for turbulent flow (say 1.3). Therefore, beyond this point the core velocity falls exponentially from 1.8 to 1.3, within a further displacement of $60dia$ (reaching 99% of its final value at $110dia$).

Note that because in practice the onset of turbulence is somewhat gradual, the transition is depicted as smooth, producing a rounded peak to the graph at a value of about 1.8 instead of 1.85.

Finally, the hypothetical situation where the boundary layer transition occurs at $5dia$ is shown. Here, the laminar growth curve has reached a value of only about 1.18, being less than the final value of (say) 1.28. Therefore, beyond the point of transition the core velocity **grows** exponentially from 1.18 to 1.28 within the next $60dia$ (reaching 99% of its final value at $65dia$). This situation would be expected only at high Reynolds numbers (e.g. Re = 250,000/5 = 50,000) - well beyond the range of current interest.

Consider the impact of this model on the transport time equation in the region beyond the onset of boundary layer transition. If, for example, from Figure 6.5 the maximum core velocity $u_{max} = 1.3\, u_{avg}$ then by substituting $a = 1.3$, $b = 0.3$, $p = -4.6 / 60 = -1/13$ in the integral transform of Page 6-12, we can obtain the smoke transport time delay in this region:

$$T_{tur} = \left(d_t + 13\ln(1.3 - 0.3\, e^{-d_t/13})\right) / 1.3\, u_{avg}$$

where in this case, d_t (dia) is the <u>remaining</u> length of pipe (beyond transition), expected to be $60dia$. This equation can be expressed more generally in terms of the velocity ratio $R_u = u_{max} / u_{avg}$ obtained from Figure 6.5 at the governing *pipe* Reynolds number:

$$T_{tur} = \left(d_t + 13\ln(R_u - (R_u - 1)\, e^{-d_t/13})\right) / R_u\, u_{avg}$$

Accordingly the methodology for determining the smoke transport time with turbulent flow used in the initial computer program was as follows:

(1) At the given flow rate in the pipe, calculate the average velocity and the *pipe* Reynolds number.

(2) At the average velocity, calculate the displacement (in pipe diameters) at which the boundary layer becomes transitional ($Re_e = 250{,}000$).
(3) Use the core velocity growth equation applicable to a laminar boundary layer to obtain the transport time up to that point.
(4) Use the core velocity growth equation applicable to a transitional or turbulent boundary layer using the velocity ratio R_u relevant to the given *pipe* Reynolds number, to obtain the transport time for the remainder of the pipe length.
(5) Sum the results of steps (3) and (4) to obtain the segment transport time.

6.4 LASER VELOCIMETRY

Having regard to Chapter 1 and the discussion of Figures 1.15 and 1.16 in particular, it was decided that a detailed experimental analysis should be undertaken to determine or confirm the true shape of the core velocity growth curve at various Reynolds numbers. An experimental program was required, to measure the two-dimensional velocity profile of air flowing through a circular pipe at various distances downstream of a disturbance, and at each Reynolds number, thereby to determine equations describing the growth in core velocity versus displacement from that disturbance. The disturbance could be introduced by the pipe entry, a bend or a sampling hole.

To monitor the air flow in such detail, it was proposed to "seed" the air stream with smoke particles. If each particle is borne by its surrounding package of air, then the particle motion can provide a reliable indication of the air motion. If the particle has sufficiently low inertia, then its motion could accurately describe turbulent flow and eddies.

The most appropriate apparatus for detection of the particle motion would utilise a laser beam, in order to obtain the small "target" (or probe) volume that is necessary to isolate an individual particle. At a given instant in time the impinging laser light is scattered off a particle in a three-dimensional pattern of intensity that depends upon the light wavelength, the particle size, its shape (and orientation and fractal dimension if not spherical), the refractive index, and the polarisation of the light beam.

The available apparatus uses Laser Velocimetry (LV), often described as Laser Doppler Anemometry (LDA). This instrument relies upon backscatter to detect a representative proportion of the scattered light, with sufficient sensitivity to monitor the presence and velocity of the particle.

Lawson (1997) describes this apparatus as utilising the Doppler effect, which is a phenomenon whereby the light scattered off a moving particle is slightly shifted in frequency (and wavelength, in inverse proportion). This shift is directly proportional to the particle's velocity. Accordingly a moving particle that passes through the target volume is detected, and the frequency shift of this received signal provides a direct indication of the particle velocity.

As a general principle, stable detection of a Doppler shift requires a splitting of the carrier (laser beam) to produce a reference channel which is mixed with the measuring channel, to produce a detectable beat frequency (heterodyne). However, in the case of LV, in order to enhance the sensitivity and resolution of the apparatus, the laser beam is split into two intersecting beams of equal intensity, to produce an interference fringe pattern at their intersection (i.e. at the target). A typical arrangement of LV apparatus is illustrated in Figure 6.11 (Lawson, 1997).

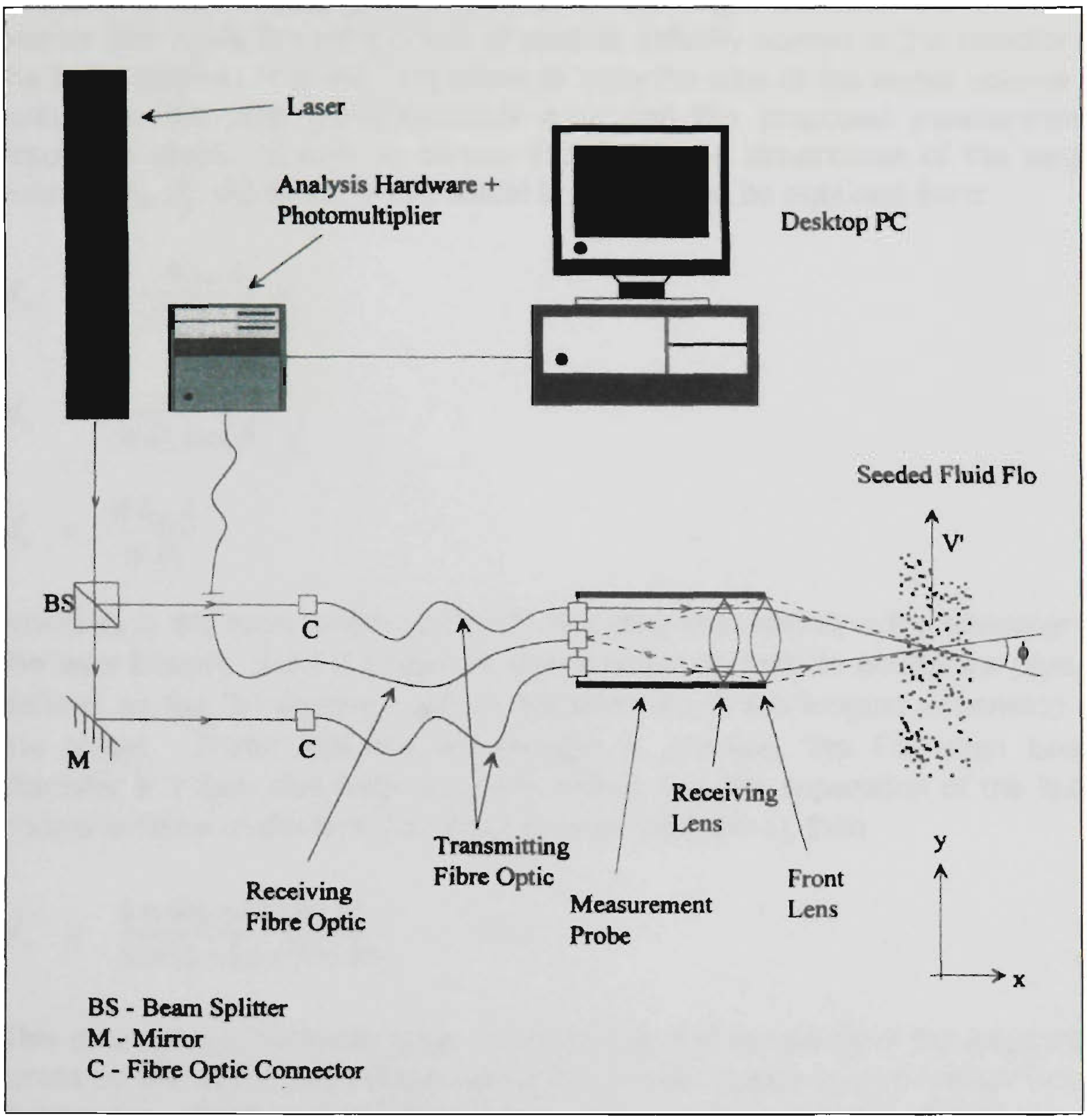

Figure 6.11 - Laser Velocimetry apparatus (Lawson, 1997)

This fringe pattern of light and dark volumes can be likened to a picket fence, across which a stick is dragged to produce a buzzing sound. The spacing of the pickets is fixed by the wavelength and angle of intersection. The buzz frequency is directly proportional to the velocity at which the stick is dragged. With LV this "buzz" is manifested as a scattered-light intensity modulation.

Bremhorst (1995) describes the operation of LV apparatus in terms of the fringe pattern within the target, stating that a heterodyne is generated in the scattered light as the particle passes through the interference fringes. Both he and Lawson agree that if the refractive index of the fluid is unity (standard air) then the frequency f_D detected at the receiver is given by:

$$f_D = \frac{2\,u_p}{\lambda}\sin\left(\frac{\phi}{2}\right)$$

where λ is the wavelength of light, ϕ is the angle between the two laser beams and u_p is the component of particle velocity normal to the bisector of the laser beams. It is also important to note the size of the target volume in relation to the pipe cross-sectional area and the proposed measurement resolution steps. It can be shown that the three dimensions of the target volume (d_x, d_y, d_z) which is ellipsoidal in shape, can be obtained from:

$$d_x = \frac{4\,L_F\,\lambda}{\pi\,D_l\sin(\phi/2)}$$

$$d_y = \frac{4\,L_F\,\lambda}{\pi\,D_l\cos(\phi/2)}$$

$$d_z = \frac{4\,L_F\,\lambda}{\pi\,D_l}$$

where L_F is the focal length of the LV targeting lens and D_l is the diameter of the laser beams. For LV purposes, the direction of traverse across the pipe is defined as the "x" direction, which corresponds to the longest dimension of the target. Given that the wavelength is $514.5nm$, the Gaussian beam diameter is $1.4mm$, the focal length is $400mm$ and the separation of the laser beams is $50mm$ at the lens (i.e. each is $25mm$ off centre), then

$$d_x = \frac{4 * 400 * 514.5 * 10^{-6}}{3.1416 * 1.4 * 25/400} \approx 3mm$$

This dimension is relatively large, even though the sensitivity of the apparatus would be low at the extremities where the volume tapers to zero (which would reduce the effective size below $3mm$). Because the primary intention is to model the core velocity growth, most accuracy is required at the centre of the pipe. With reference to Figure 6.4 it was expected that the shape of the velocity profile would always be relatively blunt at the pipe core, and in fact the worst case challenge for a large target to resolve would be for fully-established laminar flow, where the profile is parabolic (the sharpest profile).

Figure 6.12 (a) shows a parabolic velocity profile, normalised so that the maximum velocity $u_{max} = 1$ and the pipe radius $r_{pipe} = 1$ (with zero at centre). A conservative approximation to the maximum velocity (at the centre of the pipe) could be obtained by averaging all of the velocities within close proximity to the pipe centre, defined as the core of the pipe flow. The smaller the core radius can be, then the more accurately this average would approach the true value.

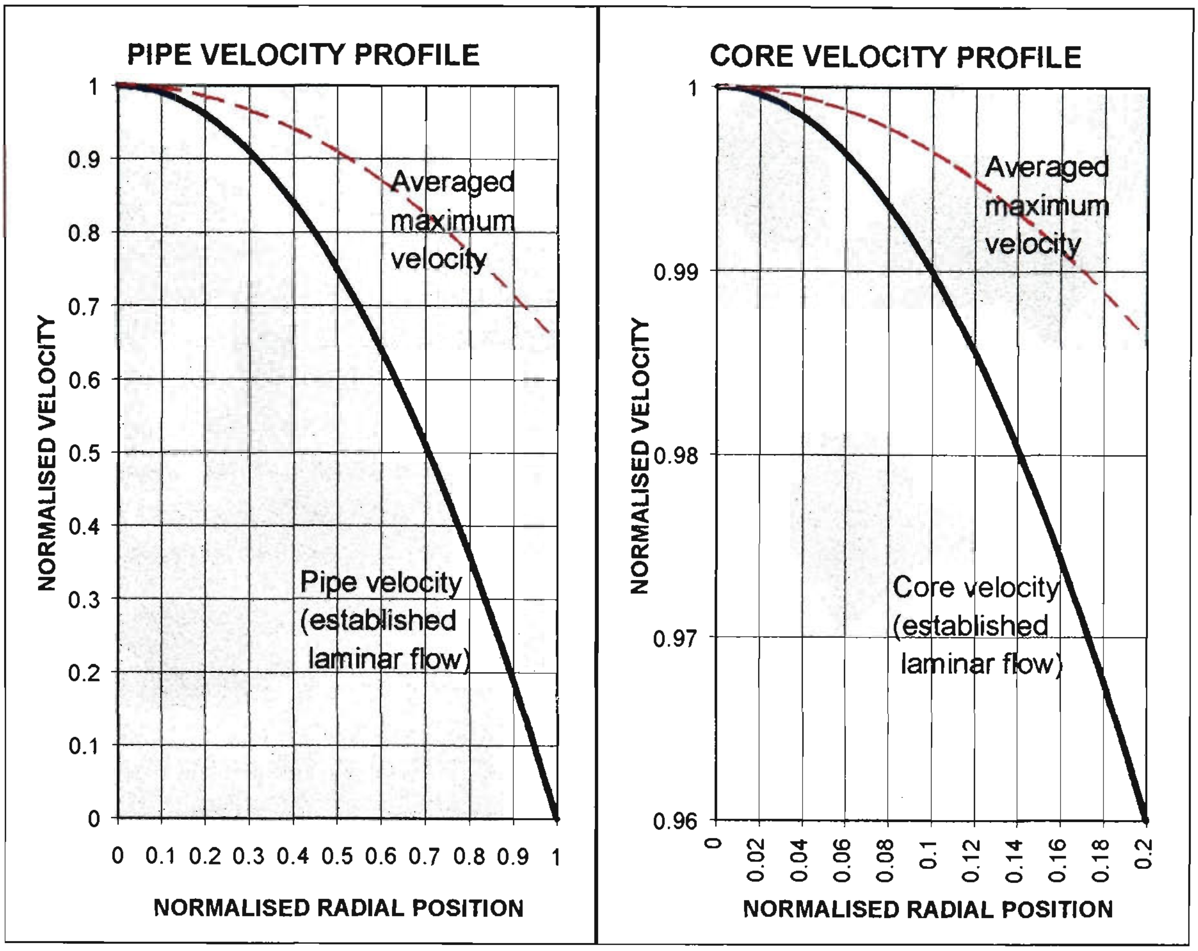

Figure 6.12 - Velocity profile for fully-developed laminar flow and for the averaged maximum velocity, taken over (a) the pipe and (b) the core region

Figure 6.12 (a) includes as a dashed curve, the locus of the approximations to the maximum velocity, that would be obtained by averaging the core velocities that occur within a target size of given radius. In the extreme case this means that if the target were as large as the pipe, then the approximation to the maximum velocity (obtained by averaging all the velocities over this whole radius), would be $0.656\ u_{max}$ or 66% of the true value (an error of -34%).
In Figure 6.12 (b) we see the effect on the same parameters when the radial position is limited to $0.2\ r_{pipe}$. Interestingly, Figures 6.12 (a) and (b) are self-similar in shape.

Given an effective target length of $3mm$ then, when positioned in the centre of the pipe, the applicable target radius is $1.5mm$. For this size the maximum velocity approximation would be $0.993\ u_{max}$ which represents an error of only 0.7%. An equation to this locus has been determined as:

$$u_{\max Avg} = 1 - 0.3436\left(\frac{r_{target}}{r_{pipe}}\right)^2$$

such that the error introduced by the target size would be:

$$E_{u.\max} = 34.36\left(\frac{r_{target}}{r_{pipe}}\right)^2 \quad \%$$

However, an error of 0.7% assumes equal sensitivity of the target, right out to $1.5mm$ radius, whereas the laser light intensity has a Gaussian distribution. Signals received from the extremities of the target would tend to be lost in noise (reducing the 0.7% figure). Moreover, the accuracy of the LV is stated as "typically better than 1%" (Lawson, 1997), which exceeds the error due to target size. Given that the majority of measurements would not involve fully-established laminar flow anyway (such that the core velocity profile would be blunt), it was decided that the error in measurement of the maximum velocity would be minimal. It was decided to adopt traverse steps of $1.5mm$.

6.5 EXPERIMENTAL TECHNIQUE AND SETUP

LV apparatus utilising a 2W CW laser was available for use at Melbourne University, at the G.K. Williams Cooperative Research Centre for Extractive Metallurgy. The difficult process of alignment of the transparent glass, polycarbonate or acrylic pipes with the apparatus was undertaken by Tim Berrigan (Laboratory Technician).

It proved necessary to use the LV in conjunction with a clear glass pipe. Early experiments used clear acrylic and polycarbonate pipes, but the surface defects proved excessive, resulting in poor signal-to-noise ratios at the LV receiver. The glass tube consisted of two $1.5m$ lengths of $25mm$ outside, $21.4mm$ inside diameter, welded together and special care was necessary to ensure its cleanliness at all times. Straightness of the tube was also important, to ensure accurate longitudinal traverses of the target, so the tube was set in the trough of a $2m$ optical bench.

The air was seeded with smoke particles from a smoldering mosquito coil, selected for its fairly constant rate of smoke generation, at low levels, with minimal risk of fire hazard. However, the coil produced a discomforting, somewhat pungent odour and smoldered with stratified filaments of smoke that could waft across the target, causing wide variations in particle count rate. To restrict the smoke leakage within the laboratory and to produce a more homogenous smoke volume, the coil was placed in a clear plastic box of $160 litre$ capacity. The open end of the glass pipe was extended $20mm$ inside the box, through a loose-fitting hole.

The far end of the glass pipe was connected via a smooth flexible hose to the Furness digital manometer (as used in previous experiments), to ensure consistency in results. This was in turn connected to the bank of four aspirators in series-parallel, controlled by an adjustable power supply. The outlet of the aspirators was connected to an exhaust pipe so that the smoke could be ducted outside the building.

A 3-axis (x,y,z) computer-controlled robotic mount was used to traverse the LV probe and its target in steps of $1.5mm$ along a radial path within the pipe. This increment allowed seven radial positions to be used, commencing with a point beyond the centreline and then withdrawing the target radially towards the wall in $1.5mm$ increments. It proved difficult to precisely identify the position of the target in the radial dimension due to refraction by the glass wall, so this approach ensured that the true centre of the pipe was included within the traverse. Although it would have been possible to traverse completely across the pipe diameter from one wall to the other, this would nearly double the data taken and involve excessive time on the valuable equipment. Therefore it was necessary to make the low-risk assumption that the velocity profile was symmetrical about the centreline (only an obvious defect would prevent this).

At each position, the velocities of 2000 particles passing through the target were recorded for subsequent processing. On withdrawing the target radially, the last position at a given displacement from the pipe entry tended to involve the pipe wall partially within the target volume, such that readings became difficult. For these positions close to the pipe wall, it could take half an hour to obtain the 2000 readings.

This process was repeated at each of several displacements along the pipe. Measurements <u>within</u> the first five diameters were not always consistent, probably because of the vena contracta, so after conducting a number of experiments it was decided to use displacement increments of five diameters ($107mm$) along the pipe, defining the open end as the zero datum. The maximum possible length of a single traverse was $1m$ so it was decided to take readings at nine displacements in one complete pass. Subsequently the equipment was reset to cover the next contiguous segment of pipe, thereby covering a total of $90dia$ in pipe length.

Accordingly, a typical set of readings comprised seven positions at nine displacements, in each of two pipe segments, producing a matrix of 126 elements (data sets). This was repeated for six different pipe flow rates set at 10, 20, 30, 40, 50, and 60 *litre/min*, producing some 756 data files. In addition, many sets of readings were repeated using different setups in an endeavor to improve accuracy and to confirm repeatability, bringing the total number of files requiring individual analysis to more than 1000. Each such file included the velocities of 2000 particles, bringing the aggregate volume of such data to over 2,000,000 readings.

Each reading can be inspected and histograms can be plotted for each set of 2000 readings. The histogram software provides the mean velocity of each set, together with the root mean square (RMS) turbulence which represents the fluctuation in velocity (three standard deviations from the mean). Generally, an RMS turbulence level of around 5% indicates excellent results.

6.6 ANALYSIS OF GROUPED RESULTS

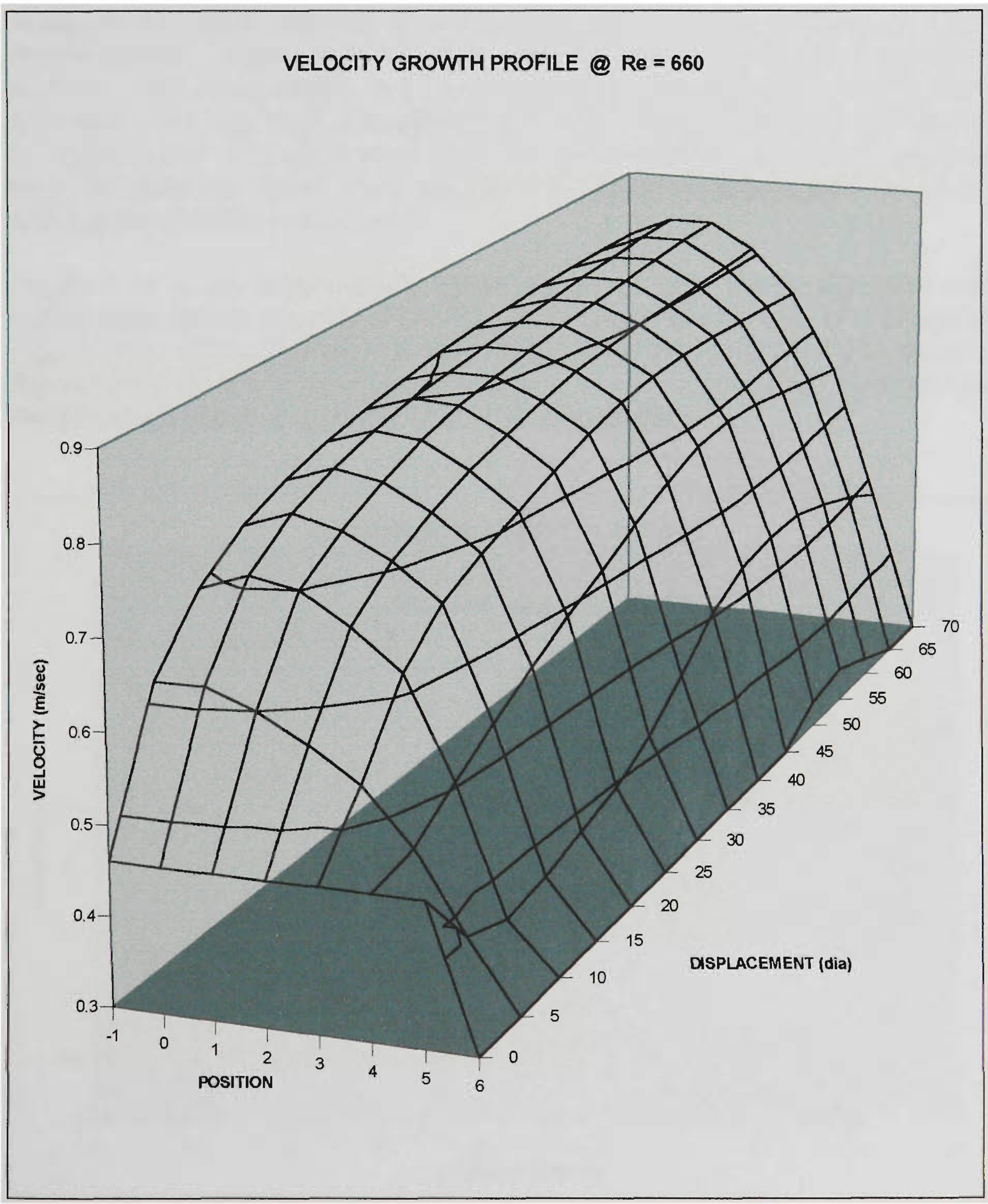

Figure 6.13 - 3-D representation of velocity growth at Re = 660

Being located and discussed in Appendix 6 for convenience, Figures A6.1 (a) to (n) graphically present the velocity results obtained for a pipe flow rate of $10 litre/sec$, corresponding to $\text{Re} = 660$. Each result represents the average among a set of 2000 readings as discussed above. Accordingly, Figures A6.1 (a) to (n) describe the lateral velocity profile at each displacement, as well as the RMS turbulence results.

Figure 6.13 is a three-dimensional (3-D) representation of all the data in Figures A6.1 (a) to (n). Because of a minor setup misalignment discussed in Appendix 6, the data associated with displacements of $50dia$ and more, were realigned (in radial position) to achieve consistency with the data at lower displacements. Then, all of the data were interpolated to achieve a smooth surface. This interpolation has been done three-dimensionally, that is, each amended point has been interpolated between neighboring points in both the "x" (radial) and "y" (displacement) axes. The resulting smoothed data has been included (as dotted lines) among the graphs of Figures A6.1 (a) to (n) and a good correlation is evident.

Figure 6.14 is the core velocity growth curve for $\text{Re} = 660$ (dotted line with hollow data points) obtained from the smoothed three-dimensional surface of Figure 6.13. For reference, the data obtained for the core velocity in each of Figures A6.1 (a) to (n) have been included (solid line and points), to show that the smoothed curve is consistent with the original data.

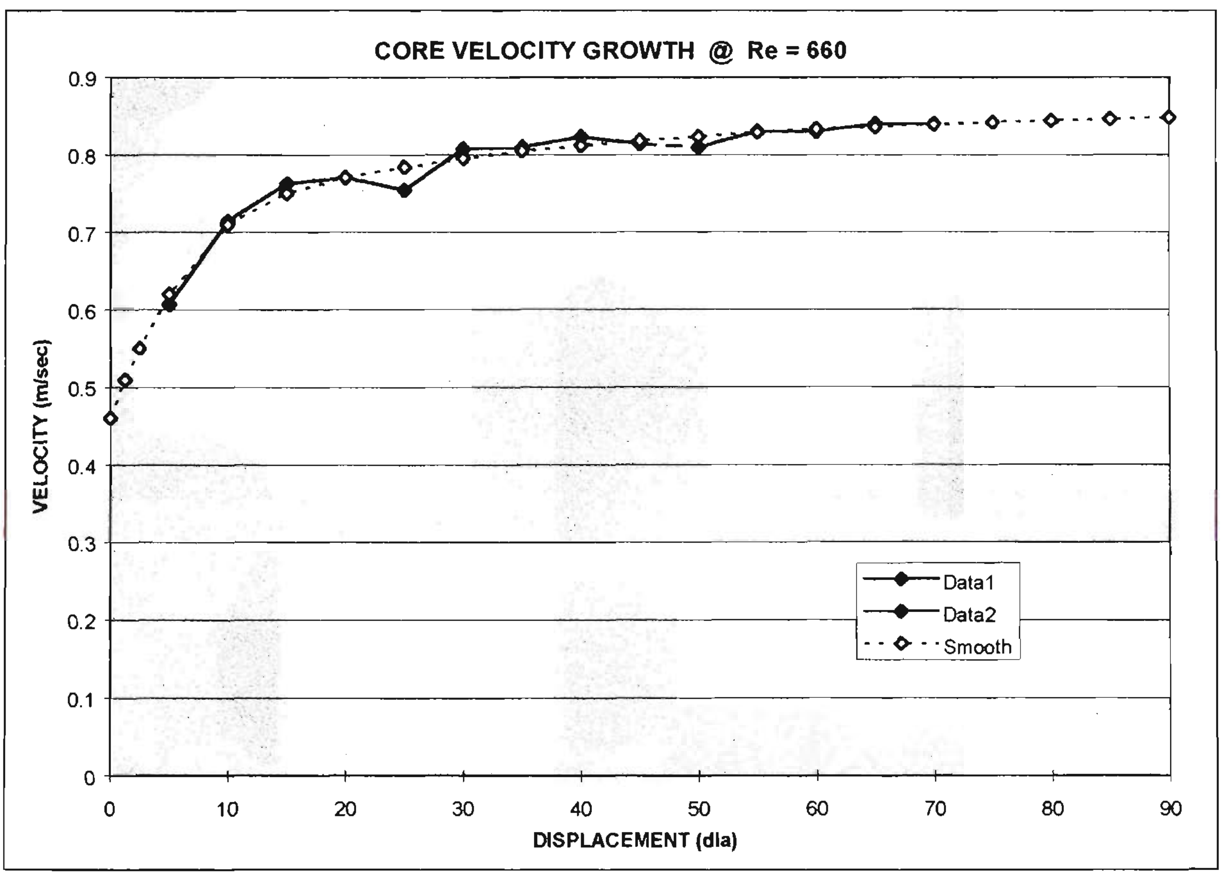

Figure 6.14 - Core velocity growth curve at $\text{Re} = 660$

The next experiment involved the same setup as before except that the flow rate was increased to $20 litre/min$, such that $Re = 1320$. The results of the analysis of all the data recorded appear in Figures A6.2 (a) to (r), which extend out to a displacement of $90 dia$.

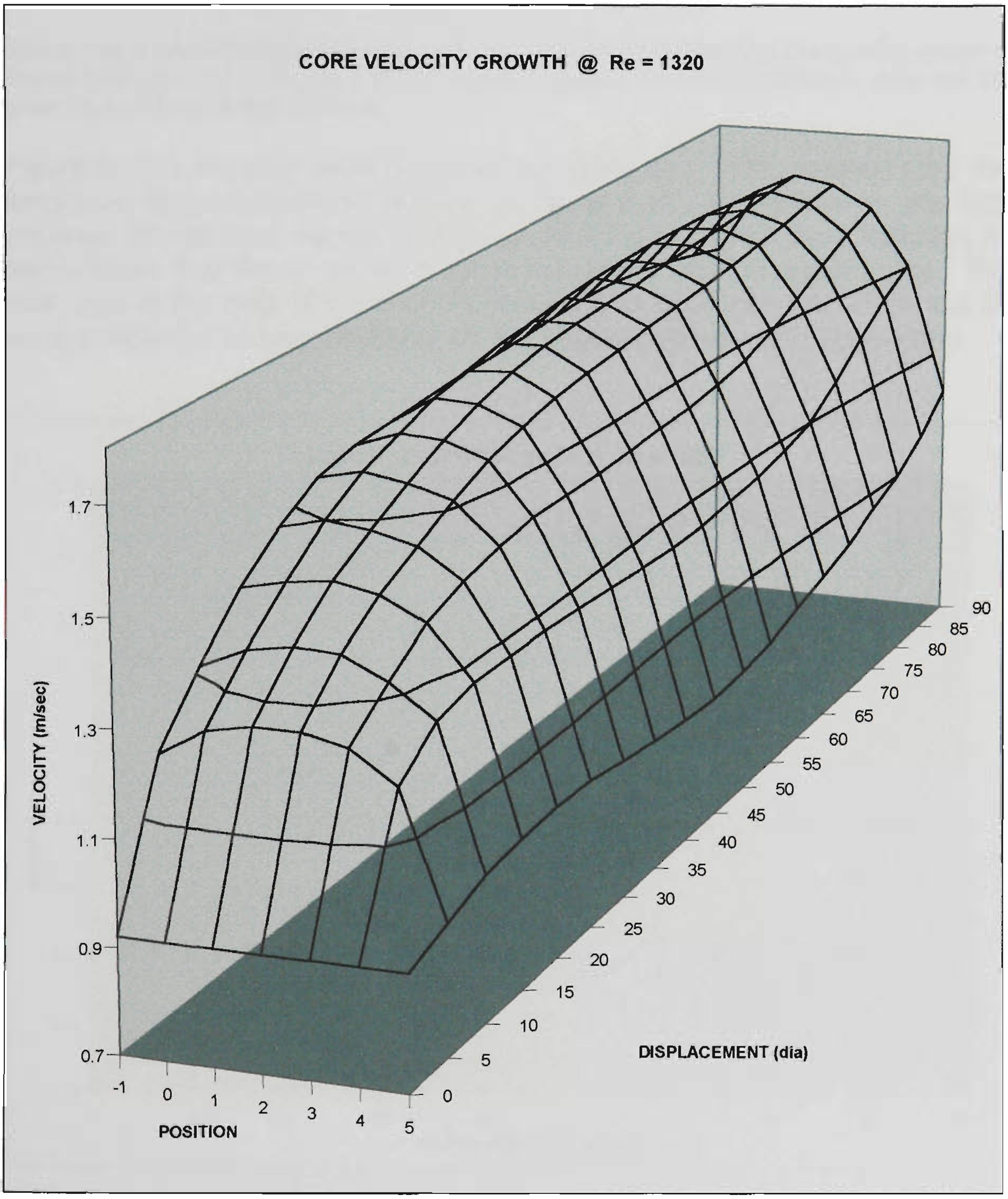

Figure 6.15 - 3-D representation of velocity growth at $Re = 1320$

Figure 6.15 is the 3-D representation of the data in Figures A6.2 (a) to (r) which has been smoothed in the manner previously described. Again, the smoothed data has been included among the graphs of Figures A6.2 (a) to (r), and in the case of Figures A6.2 (h), (j) and (o) there is a significant departure between the data and the smoothed curve. Such departures generally correspond to increased RMS turbulence readings, suggesting local soiling or imperfections in the glass.

Taking into account the different axes used, it is interesting to compare the surface shape of Figure 6.15 with that of Figure 1.15. There is a level of consistency between them but the growth curve is somewhat different.

Figure 6.16 is the core velocity growth curve for Re = 1320 obtained from the smoothed three-dimensional surface of Figure 6.15. For reference, the data obtained for the core velocity in Figures A6.2 (a) to (r) has been included, to demonstrate that the smoothed curve is consistent with the original data. The local dips in the data of Figure 6.16 occurring at displacements of 50 and 80 *dia* are regarded as imperfections, for the reasons discussed in Appendix 6.

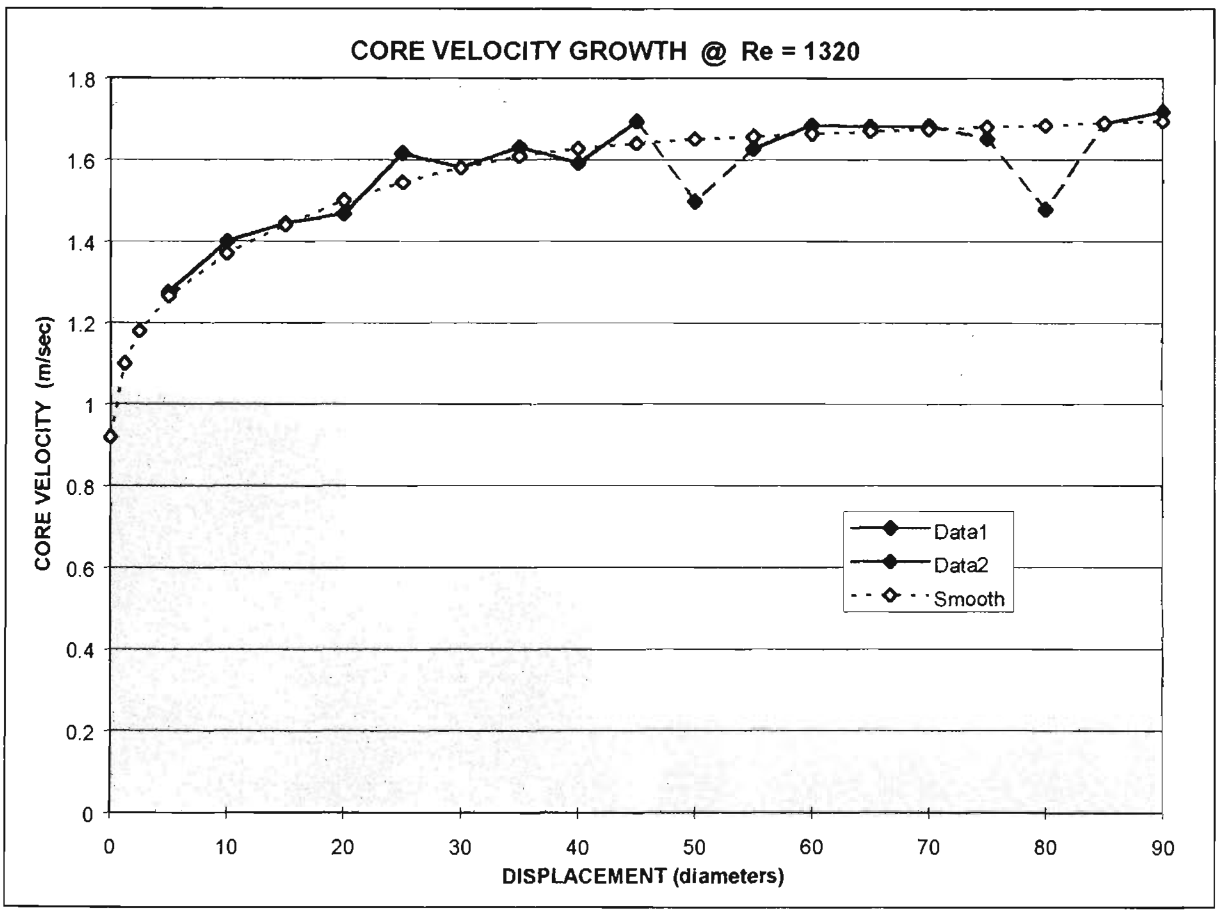

Figure 6.16 - Core velocity growth curve at Re = 1320

The next experiment again involved the same setup except that the flow rate was increased to $30 litre/min$, such that $\mathrm{Re} = 2000$. The results of the analysis of all the data recorded appear in Figures A6.3 (a) to (r), which again extend out to a displacement of $90 dia$.

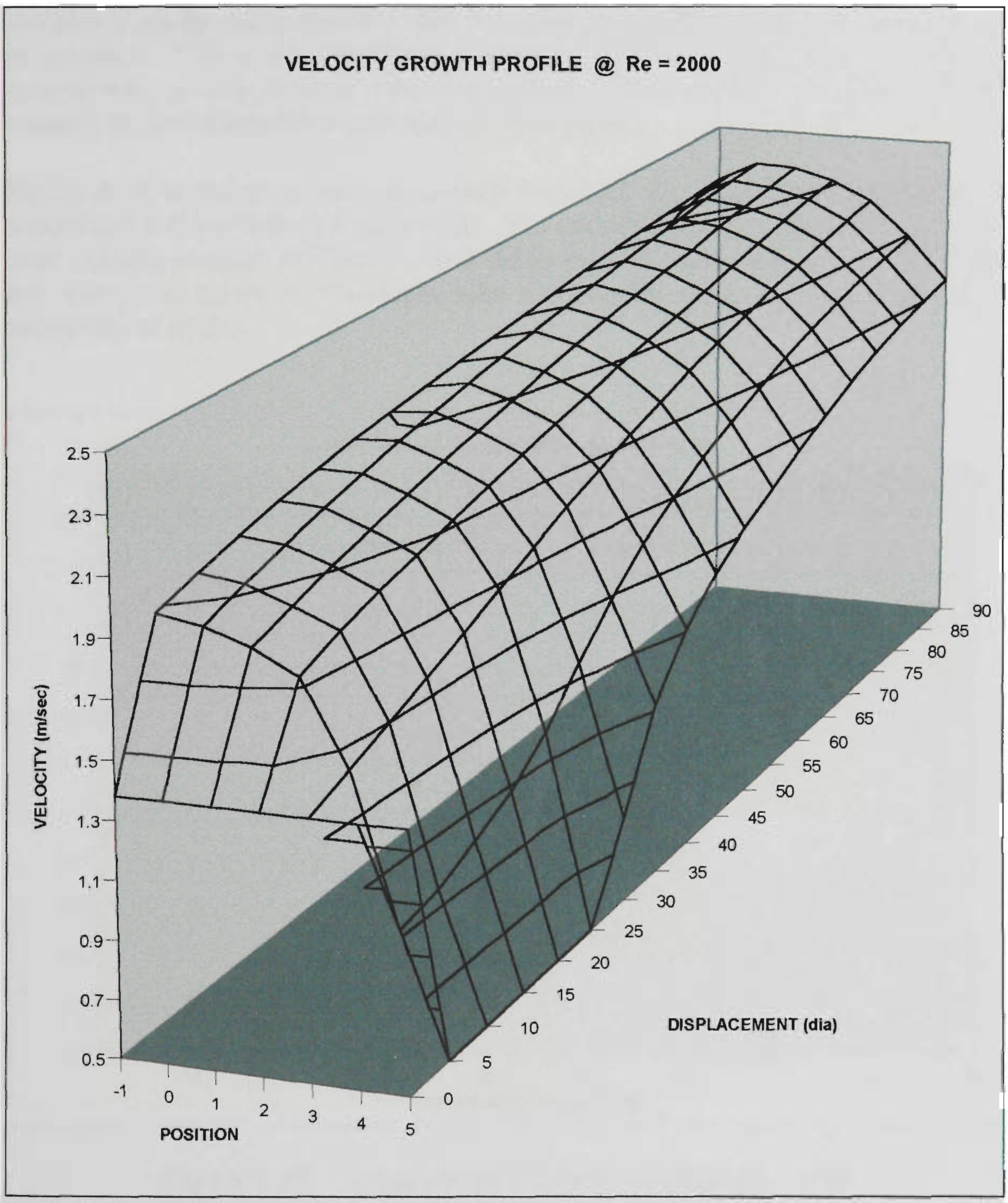

Figure 6.17 - 3-D representation of velocity growth at $\mathrm{Re} = 2000$

Upon inspection of Figure 6.17, it is apparent that the axis of longitudinal traverse of the target may not be perfectly aligned with the pipe axis, such that the local maxima of core velocity shifts from position -1 to 0. Such shifts within any 3-D surface have been accounted for in determining growth curves.

It should also be noted that Figure 6.17 (and the other 3-D representations) indicate a steep rise within the first five diameters followed by a sharp change in gradient. This sharp change is a drafting aberration caused by the relative coarseness of the surface resolution used in this region, coupled with the inability to use scattered x-axis data in 3-D graphs.

Figure 6.18 is the core velocity growth curve for $Re = 2000$ obtained from the smoothed 3-D surface of Figure 6.20. For reference, the data obtained for the core velocity in each of Figures A6.3 (a) to (n) has been included, to show that the smoothed curve is consistent with the original data (with the understood exception at $80dia$).

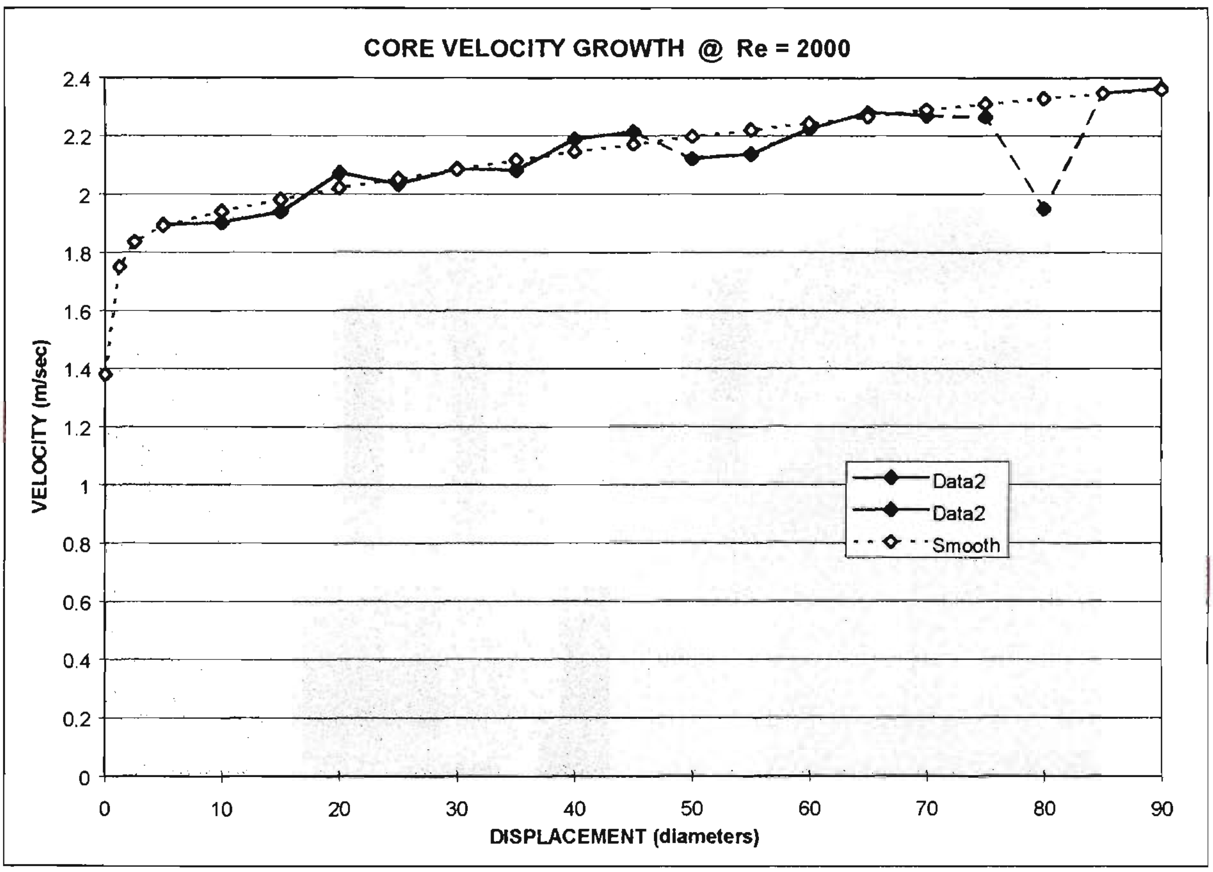

Figure 6.18 - Core velocity growth curve at $Re = 2000$

For the next experiment the flow rate was increased to $40 litre/min$ using the same setup as previously used, such that $\mathrm{Re} = 2660$. The results of the analysis of all the data recorded appear in Figures A6.4 (a) to (r), extending out to a displacement of $90 dia$.

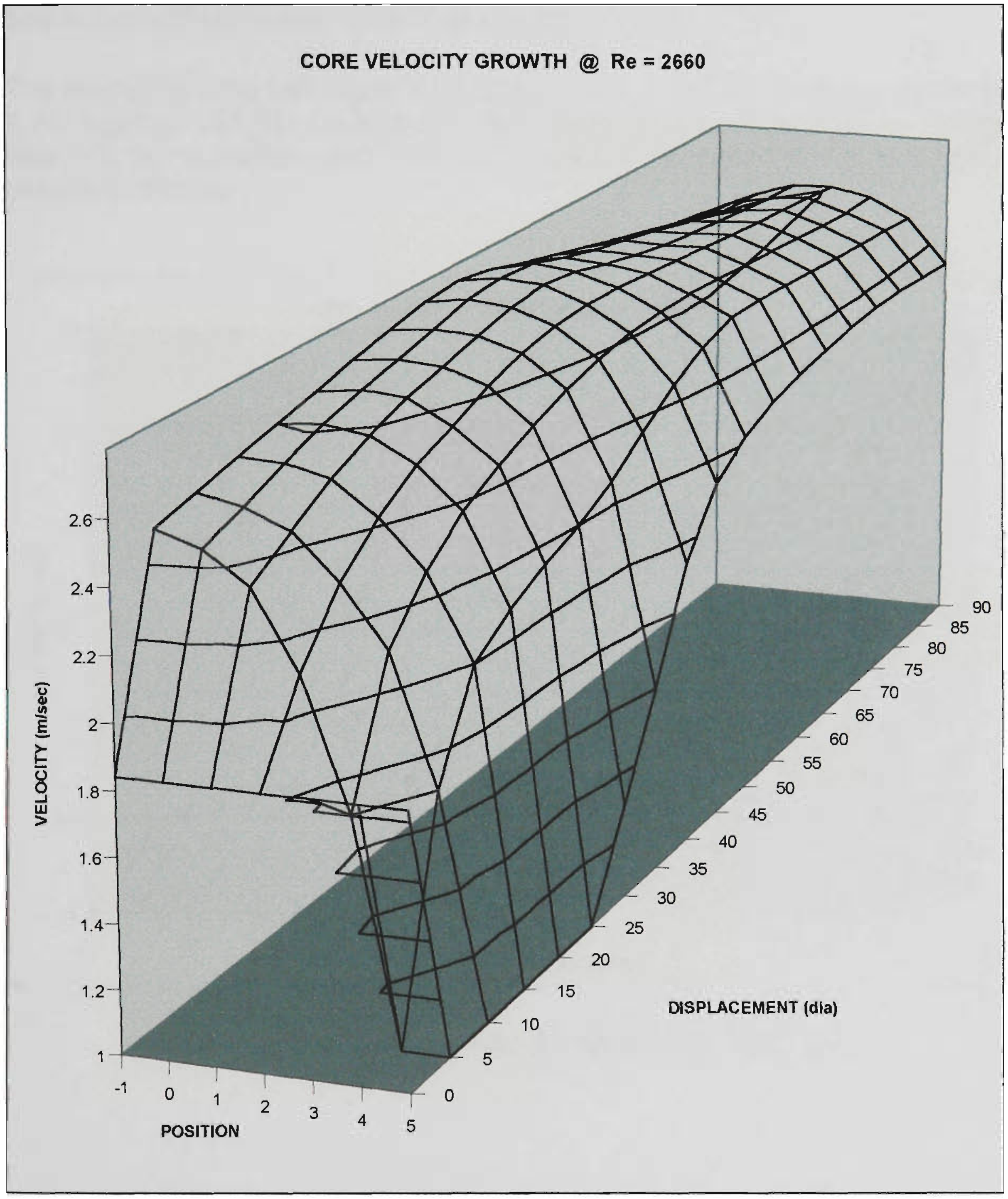

Figure 6.19 - 3-D representation of velocity growth at $\mathrm{Re} = 2660$

The smoothed 3-D representation of the velocity growth as presented in Figure 6.19 is interesting, in that it shows a steady rise similar to that of Re = 2000, but then there is a hump in the vicinity of 40 to 50 *dia*. By about 90*dia* the core velocity seems to have reduced and stabilised at a fixed level. Of course, the Reynolds number Re = 2660 is in the transition region so it is expected that the hump is caused by the transition from laminar to turbulent flow in the boundary layer (refer Figure 6.8(b)).

The smoothed core velocity growth curve for Re = 2660 is presented in Figure 6.20, together with the core velocity data from Figures A6.4 (a) to (r). These data are not a perfect match to the curve but the existence of a hump is difficult to dismiss.

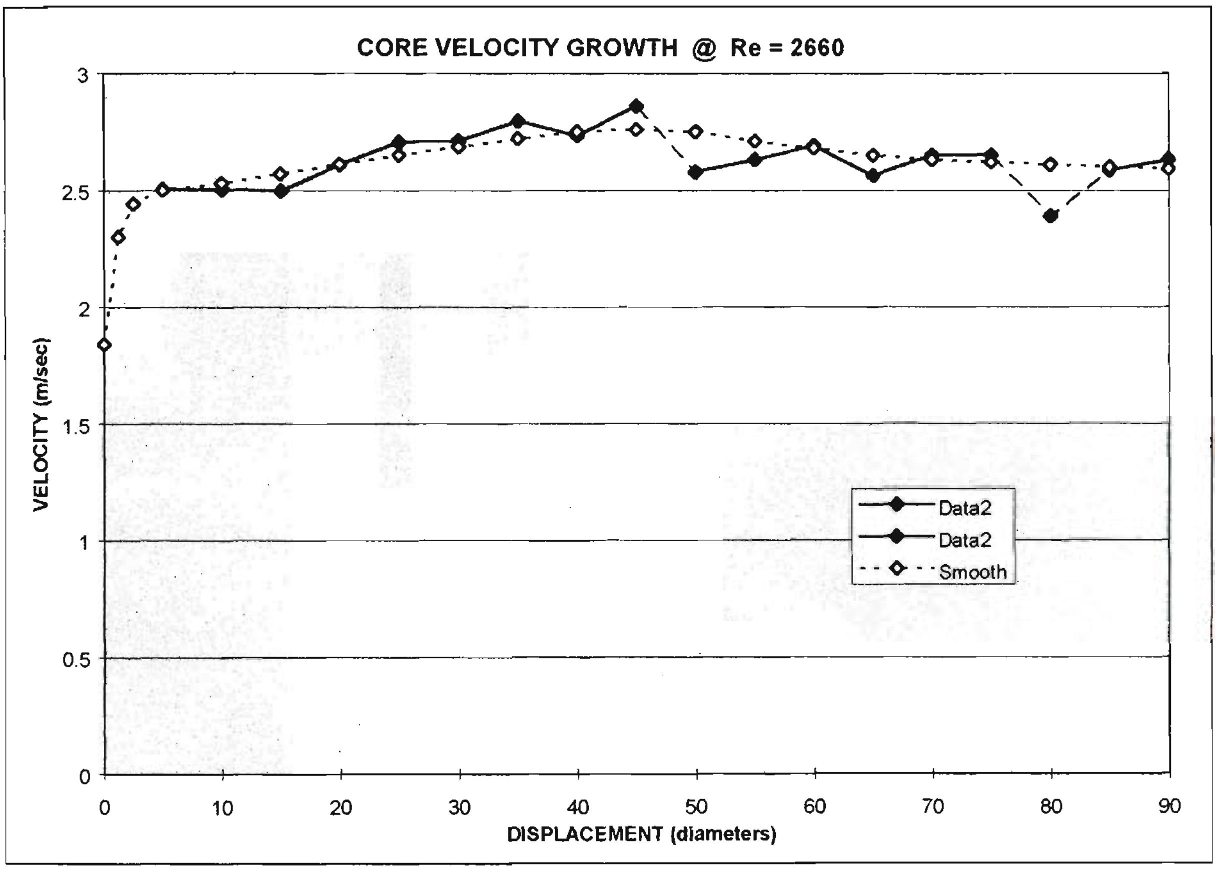

Figure 6.20 - Core velocity growth curve at Re = 2660

The next experiment required increasing the flow rate to $50 litre/min$ without otherwise altering the setup, such that $Re = 3330$. The results of the analysis of all the data recorded appear in Figures A6.5 (a) to (r), extending out to a displacement of $90 dia$.

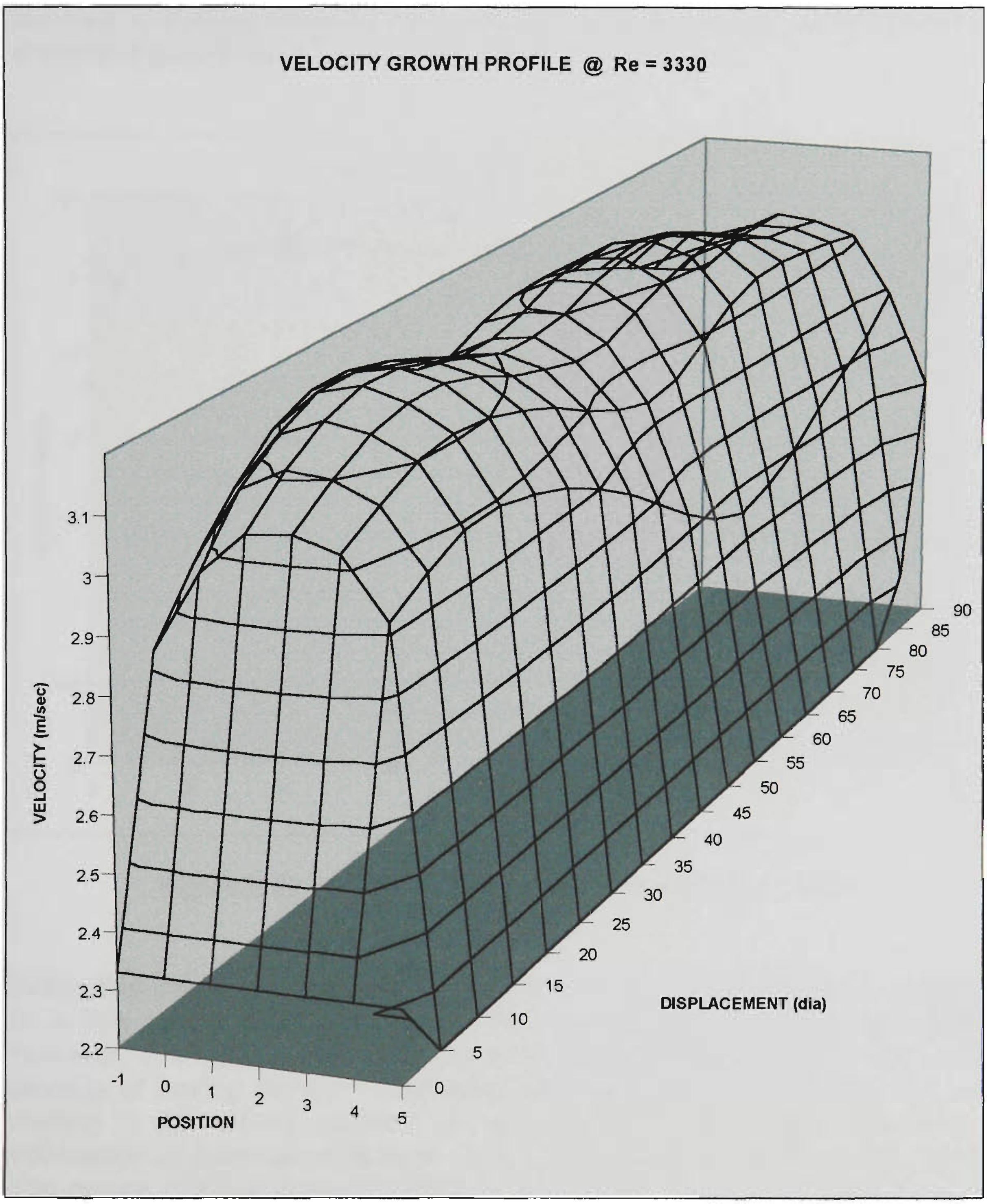

Figure 6.21 - 3-D representation of velocity growth at $Re = 3330$

However, this representation reveals a curious double-hump of low amplitude. There was no explanation for the formation of a double hump (unless there was some unknown acoustic resonance effect) so it was decided to adopt a curve that smoothed these out into a single low hump. Despite this need for what might be described as a second-order smoothing, there is considered to be a high degree of consistency in the data, and that the smoothed result provides a suitable basis for determining the core velocity growth curve as shown in Figure 6.22.

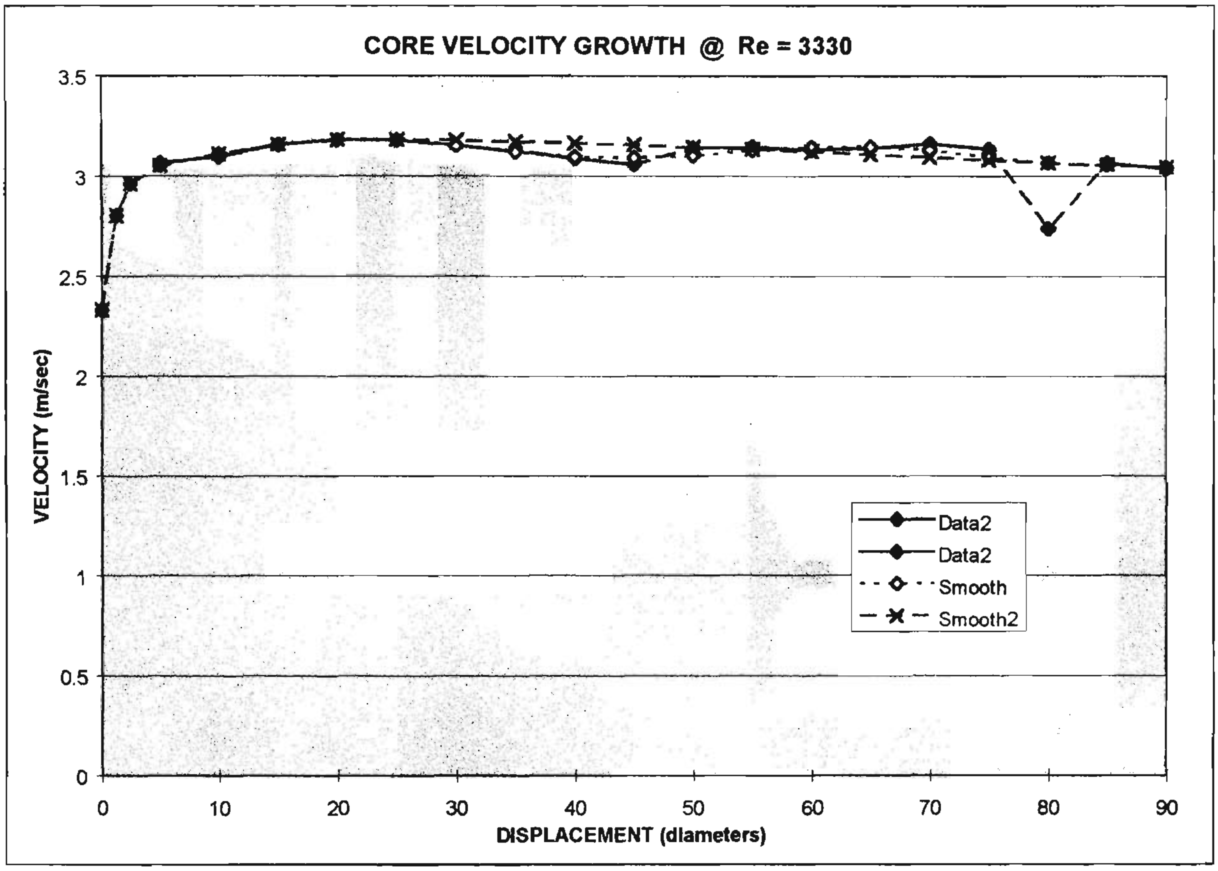

Figure 6.22 - Core velocity growth curve for $\mathrm{Re} = 3330$

Within this phase of experiments it remained only to obtain the data pertaining to a flow rate of $60 litre/min$ using the same setup, such that $\mathrm{Re} = 4000$. However, in a repeat of the misfortune that beset the data for $\mathrm{Re} = 660$, in the process of having the $\mathrm{Re} = 4000$ data files transferred to CDROM, the files relating to the second segment of pipe were lost. Fortunately the velocity information at displacements from 50 to 70 *dia* had been recorded separately. The results of the analysis of all the data recorded appear in Figures A6.6 (a) to (o).

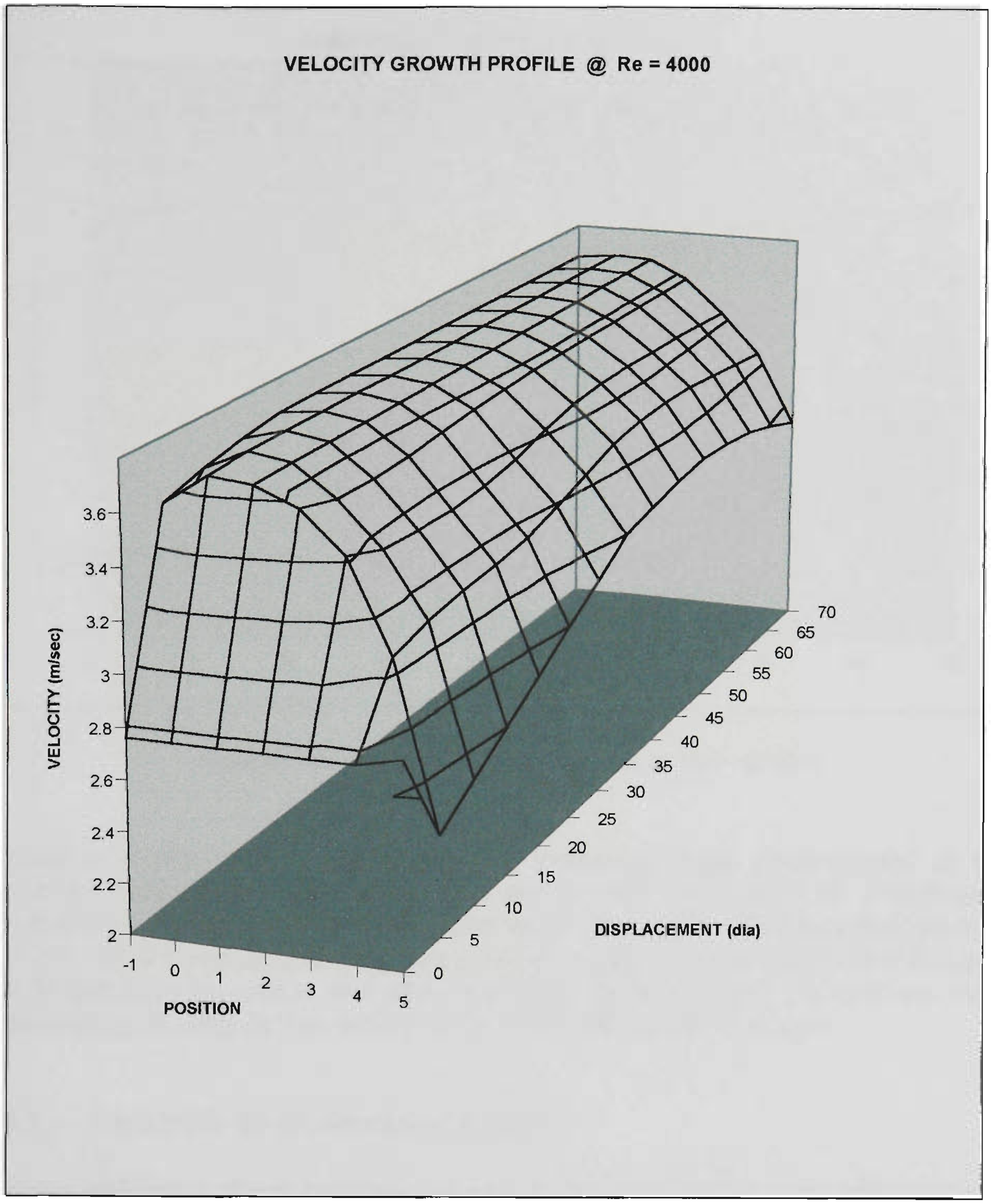

Figure 6.23 - 3-D representation of velocity growth at $\mathrm{Re} = 4000$

Whereas at $\mathrm{Re} = 3330$ the core velocity appears to reach a final, stable value barely within the 90 diameter displacement shown, at $\mathrm{Re} = 4000$ the velocity growth is characterised by a sharp rise to a value of $3.67 m/sec$ within only $5 dia$, and thereafter, stabilises at about this value. The average velocity is $2.81 m/sec$ so $u_{max} / u_{avg} = 1.31$ (or $u_{avg} / u_{max} = 0.77$), which is in close agreement with the data of Miller shown in Figure 6.5. This growth curve suggests that in the case of turbulent flow (beyond the transition region), the core velocity is established at its maximum value almost instantaneously.

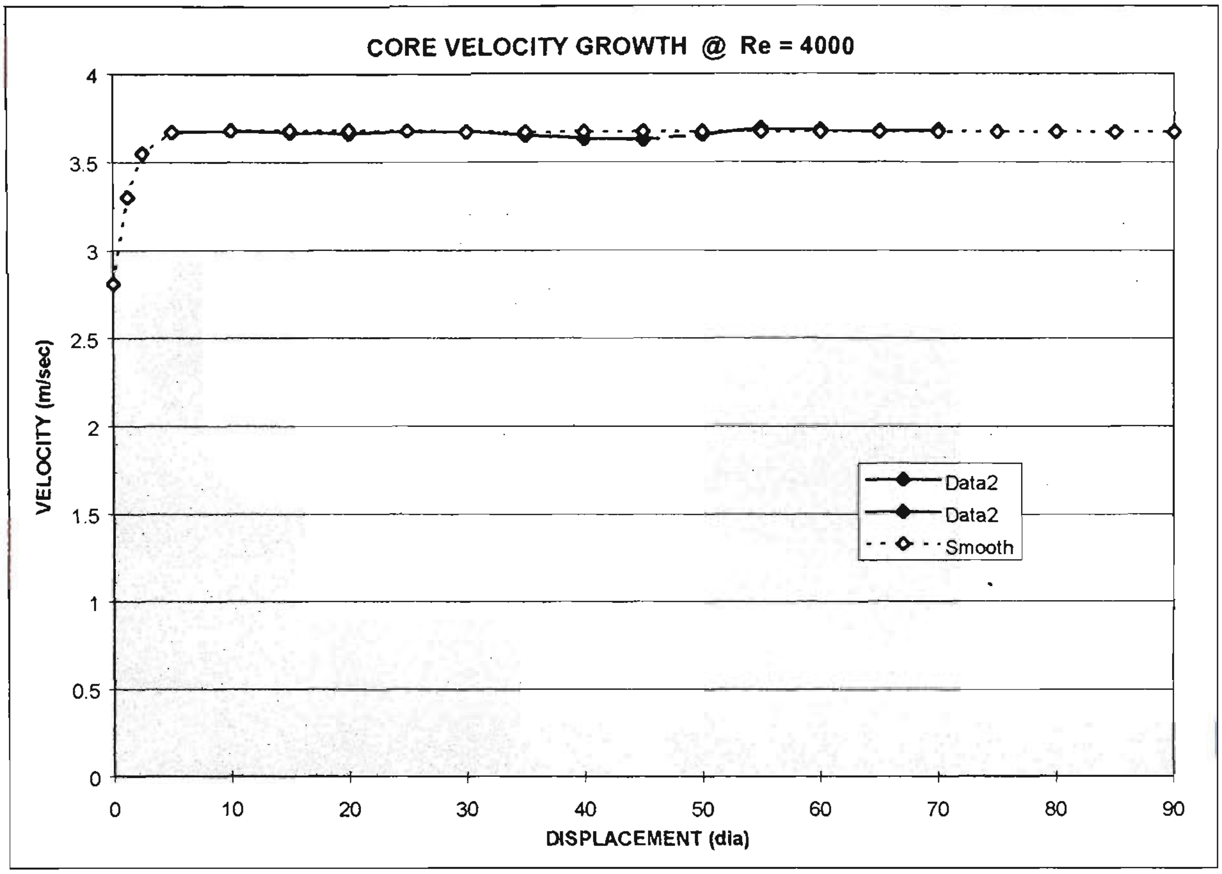

Figure 6.24 - Core velocity growth at Re = 4000

Such a sudden rise in core velocity, indicating rapid development of a turbulent flow regime was unexpected and in view of Figure 1.11, it seemed more likely that the velocity would peak within 20 or 30 *dia* and fully develop by 50*dia*. To a minor degree this shape could be perceived to exist within Figure 6.24 but such a trend is lost within the error band. Overall the data are too consistent, to dismiss the validity of the smoothed curve as shown.

6.7 - ANALYSIS OF OVERALL RESULTS

The significance of the turbulence data has been previously commented upon as a guide to the accuracy of the measurements taken. Figure 6.25 presents a summary of the normalised turbulence data taken at the core of pipe flow, at each Reynolds number and at all displacements. This shows remarkable consistency in the overall trends which promotes confidence in the data.

In the case of the higher Reynolds numbers, a low level of turbulence is maintained throughout the pipe length. At lower Reynolds numbers, it is notable that the turbulence data reduces within the first 15*dia*, indicating initial dissipation of the effects of the disturbance induced by the sharp pipe entry and in particular, by its associated vena contracta. At higher displacements the turbulence level increases slowly. This is interpreted as a natural consequence of the development of the core velocity toward a laminar, parabolic velocity profile, whereby there is intermittency in the velocity as described by Schlicting (1951/1987, refer Figure 1.14). It follows that such intermittency would be of larger magnitude when the flow tends toward a laminar regime, because of the greater difference between the average and core velocities. Accordingly, overall we should expect to see higher turbulence levels at lower Reynolds numbers and at higher displacements, which is indeed shown in Figure 6.25. Therefore it was considered that the data obtained for core velocity should be reliable.

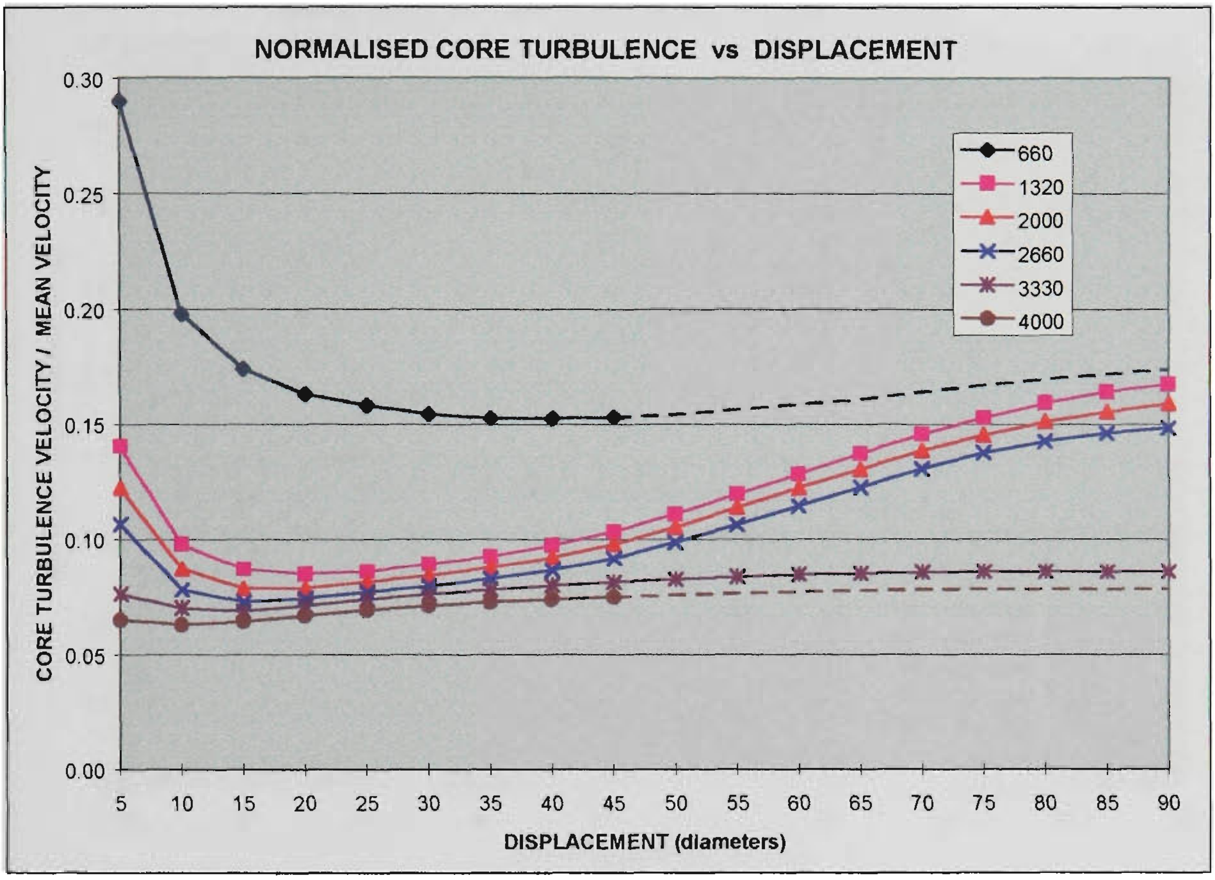

Figure 6.25 - Normalised LV core turbulence data (smoothed)

Consistency of results is considered the most important guide to their credibility and so all six smoothed core velocity growth curves have been normalised as a ratio of average velocity and presented in Figure 6.26. Here we see that there is a remarkable consistency among the graphs inasmuch as the progression from Re = 660 through to Re = 4000 seems entirely progressive and mutually supportive.

At low Reynolds numbers, the growth is initially steep but gradually reduces in steepness, reaching $R_u = u_{core} / u_{avg} = 1.75$ by 35*dia* and continuing to grow toward 2.0. At increasing Reynolds numbers, the initial growth is even steeper until, by about 5*dia*, the growth rate suddenly reduces substantially. By Re = 2660 the growth peaks at 40 or 50 *dia* and then falls to $R_u \approx 1.39$. At Re = 3330 the peak subsides sooner (after 30*dia*), reaching a final value of $R_u \approx 1.31$. Thus the shape of the curve for Re = 4000 is consistent with all the other curves. Also included in Figure 6.26 are two curves, shown dotted, representing the equations for laminar and turbulent flow regimes (as illustrated in Figure 6.10) that were used in the initial computer model. Although these equations bear some broad similarity to the data obtained, there is an obvious difference in the steepness of the curves and the sharpness of the change in gradient.

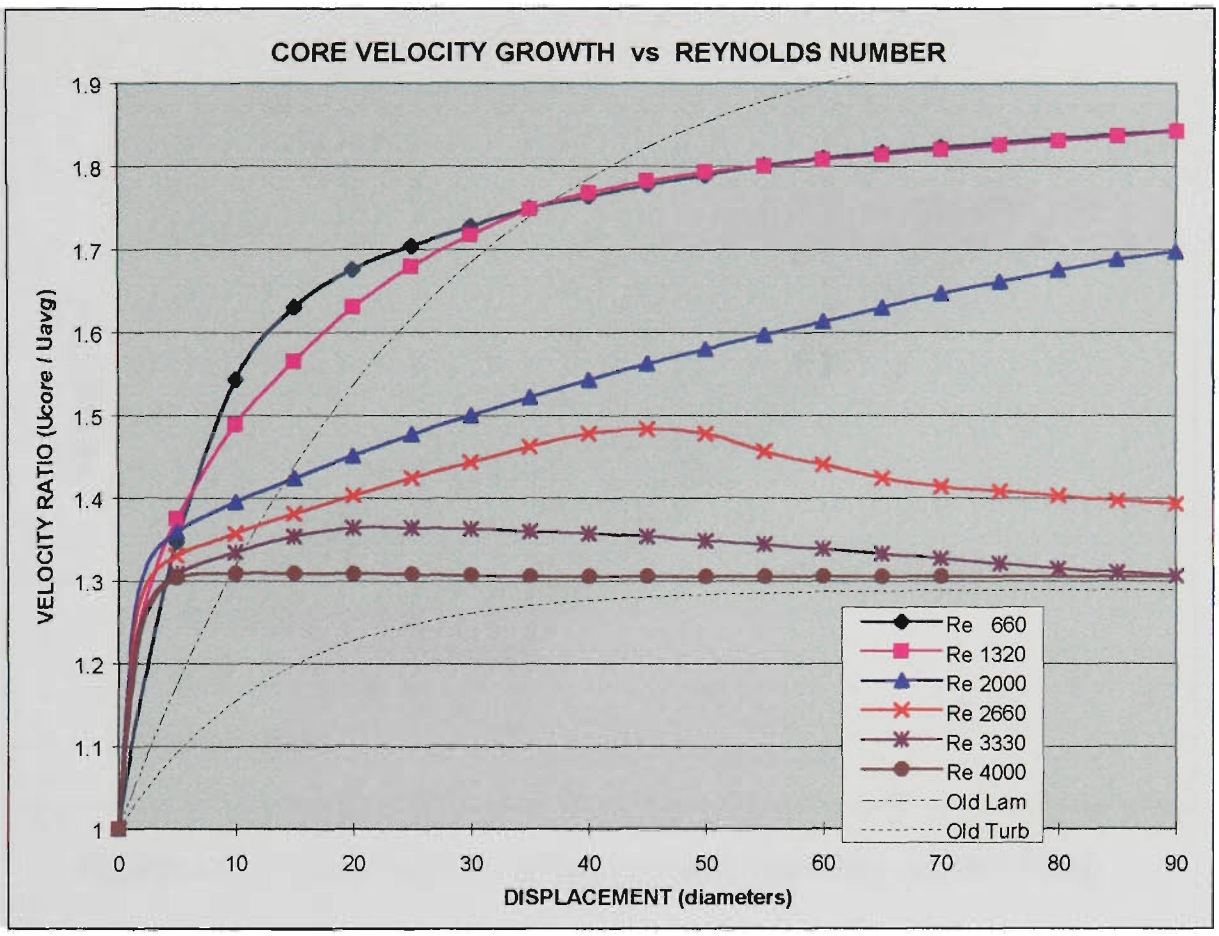

Figure 6.26 - Normalised velocity growth curves

In view of all the foregoing results and analysis it was considered that the graphs of Figure 6.26 provided a suitable basis for the development of a new computer model. Figure 6.27 is a 3-D representation of the smoothed curves in Figure 6.26. This demonstrates that when these curves are converted to a 3-D matrix, it is possible to use 3-D interpolation over the surface to estimate the value of u_{core} based upon the value of u_{avg} and the associated value of Reynolds number. It was noted that at high displacements, the core velocity ratio reaches the same value at the extremes of Reynolds numbers used, i.e. the curve value for $\mathrm{Re} = 660$ matches that of $\mathrm{Re} = 1320$, and the curve value for $\mathrm{Re} = 3330$ matches that of $\mathrm{Re} = 4000$. Thus it was considered appropriate to extrapolate beyond these extremes to provide a reasonable estimate of the growth curve values at $\mathrm{Re} < 660$ and $\mathrm{Re} > 4000$. This extrapolation has been included in Figure 6.26, to indicate the validity of such extrapolation.

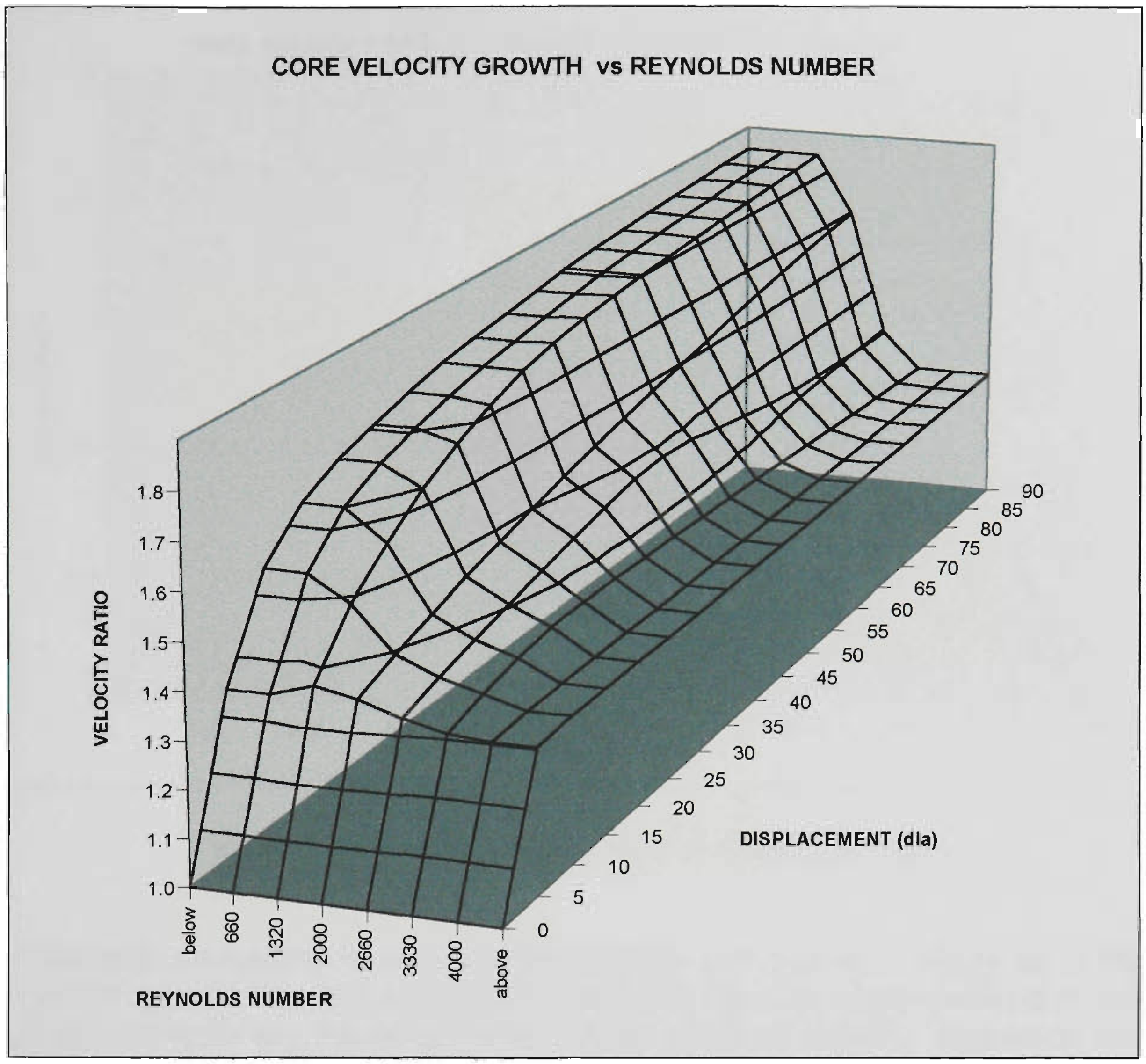

Figure 6.27 - Core velocity growth versus Reynolds number (3-D)

The available graphics package is unable to present Figure 6.27 as a smooth surface and, as previously noted, it is unable properly to represent a scattered axis. Fortunately in this case the steps in Reynolds number are equal. To gain a better picture of the shape of this surface, it has been "sliced" at 90*dia* and presented in Figure 6.28. The shape of this slice supports the assumption previously described, about the validity of extrapolation to lower and higher Reynolds numbers.

As a basis for verification of the results obtained, a dotted line graph has been included in Figure 6.28 to represent the core velocity ratio for fully developed flows in smooth round pipes, as deduced from the data of Nikuradse (1932) and presented in Figure 1.13. This graph bears resemblance to the right-hand part of the slice, but there is a 3% (i.e. 1.31 / 1.27) difference in values. This could possibly be explained by the higher accuracy of modern equipment. The left-hand part of the slice reaches a velocity ratio of about $R_u = 1.85$ at 90*dia* and this is consistent with the expectation of eventually reaching a value of $R_u = 2.0$ at higher displacements.

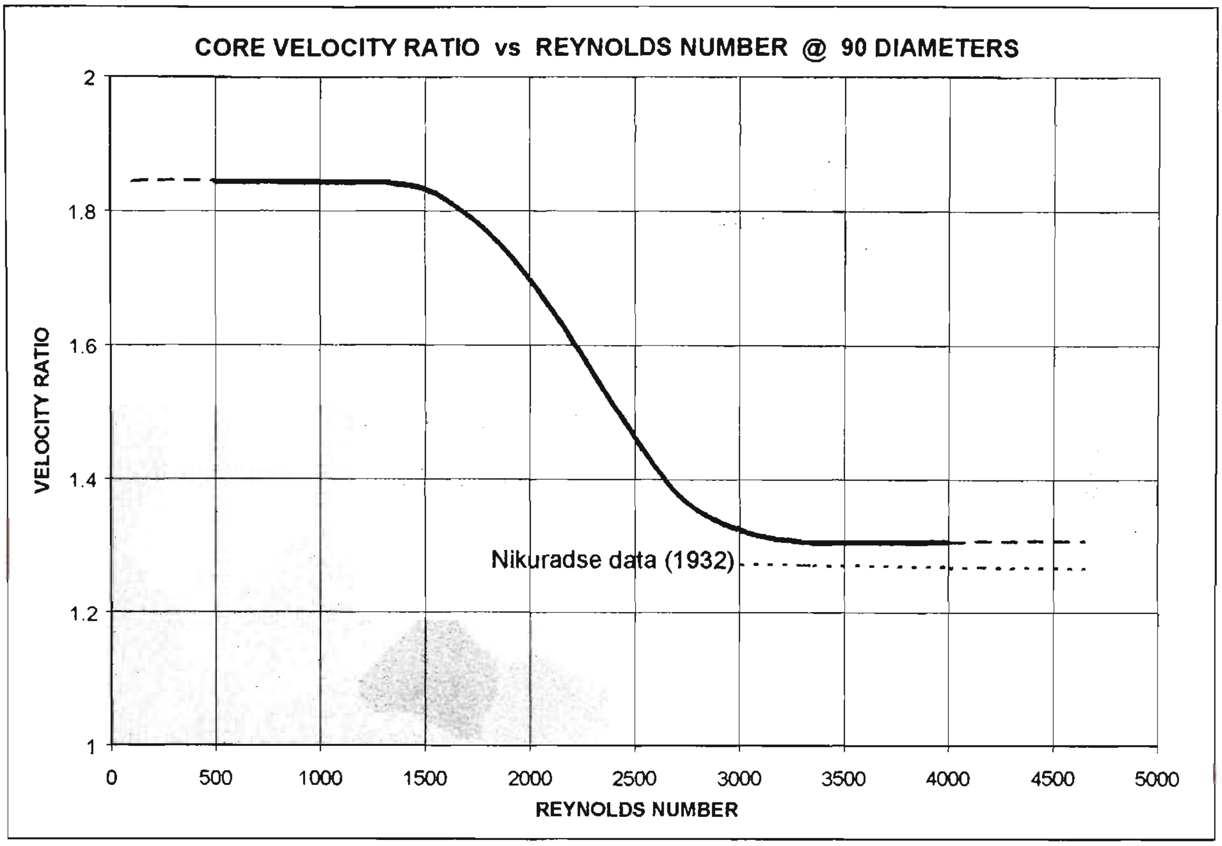

Figure 6.28 - Core velocity ratio at ninety diameters

Preferably, smoothing of the complete surface of Figure 6.27 would be in the manner represented by Figure 6.28, in order to improve approximations to the growth curve for any Reynolds number in the range of interest. This would still involve 3-D interpolation between the data points represented in Figure 6.27 which, in a computer model would require a substantial data matrix. Before committing to this method it was decided to evaluate another approach. At a given Reynolds number this involved directly calculating the elapsed time versus displacement, since this was the parameter sought for modelling purposes.

For this calculation a straight line approximation between adjacent data points was taken (this assumes that over a small increment of displacement, the increase in velocity may be regarded as linear). The elapsed time (T_x) is obtained from the distance (x) divided by the average velocity. If at the first point, the velocity is u_1 and at the second point the velocity is u_2 , and given that the increment of distance is five diameters ($x = 5\,D_{pipe}$), then:

$$T_x = \frac{x}{(u_1 + u_2)/2} = \frac{10\,D_{pipe}}{u_1 + u_2} \quad \textit{so generally} \quad T_x = \frac{10\,D_{pipe}}{u_x + u_{x+1}}$$

By applying the data of Figure 6.26 to this calculation it was possible to progressively sum the elapsed times at each increment of displacement, in order to obtain the graphs of Figure 6.29.

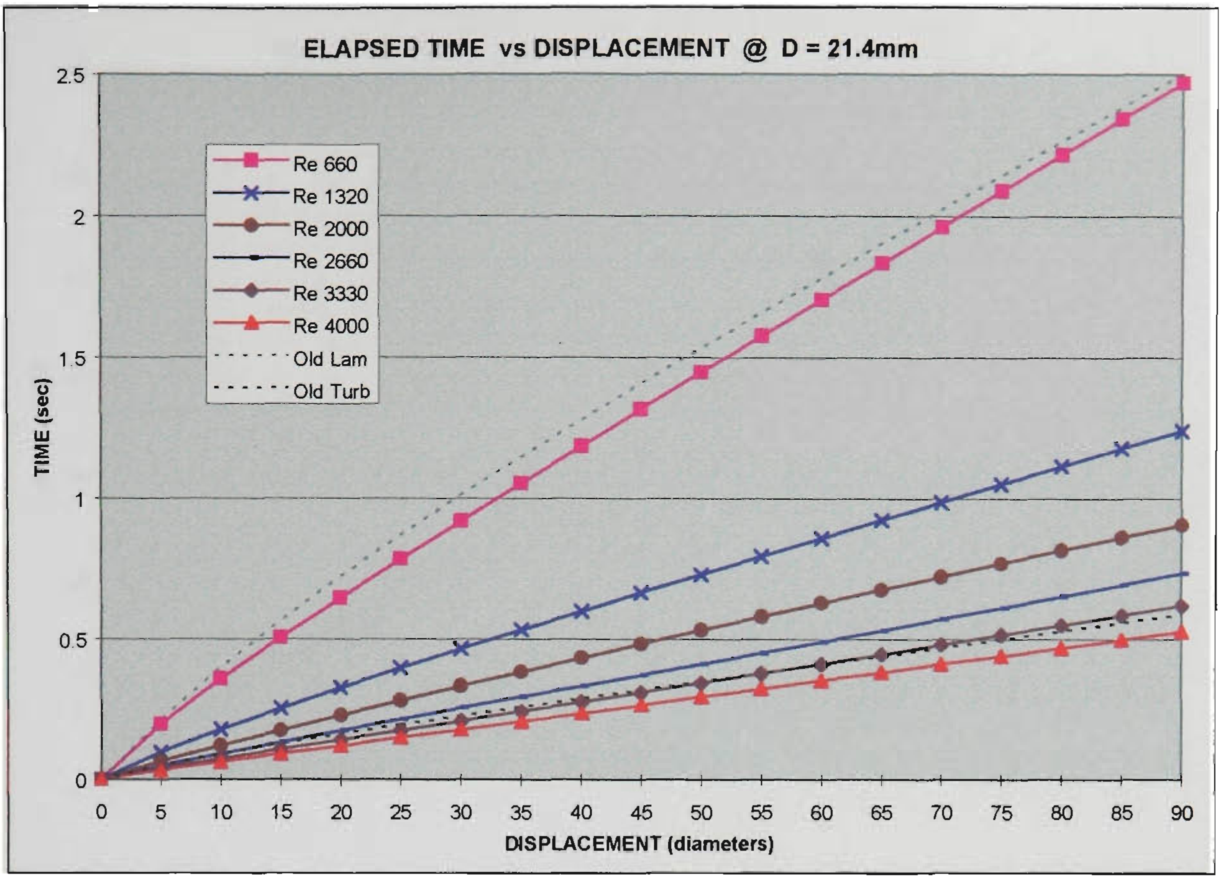

Figure 6.29 - Elapsed time versus displacement and Reynolds number

The remarkable feature of Figure 6.29 is that, despite the complex shape of the various curves shown in Figure 6.26, the graphs of elapsed time appear quite linear (due to integration). Included for reference in Figure 6.29 are two dotted curves representing the elapsed times that would result from using the original exponential equations for velocity growth in developing laminar and turbulent flow regimes (refer Figure 6.9). These graphs are also quite linear and we now see why the original equations could give reasonably accurate results in some circumstances (but not all).

In an attempt to collapse all of the graphs in Figure 6.29 to one line, the equation for elapsed time was amended to:

$$T_x = \frac{10\,D_{pipe}}{\left(R_{Ux} + R_{Ux+1}\right)U_{avg}} = F_T\,\frac{D_{pipe}}{U_{avg}}$$

where R_{Ux} is the velocity ratio at displacement x and F_T is a dimensionless new term; "Time Factor". The results of applying this Time Factor equation appear in Figure 6.30, where it can be seen that the spread of gradients among the graphs has substantially reduced over that of Figure 6.29.

Figure 6.31 is a 3-D presentation of the results in Figure 6.30, which could be used for 3-D interpolation of the Time Factor to obtain the elapsed time. These data have been sliced at all displacements to obtain Figure 6.32.

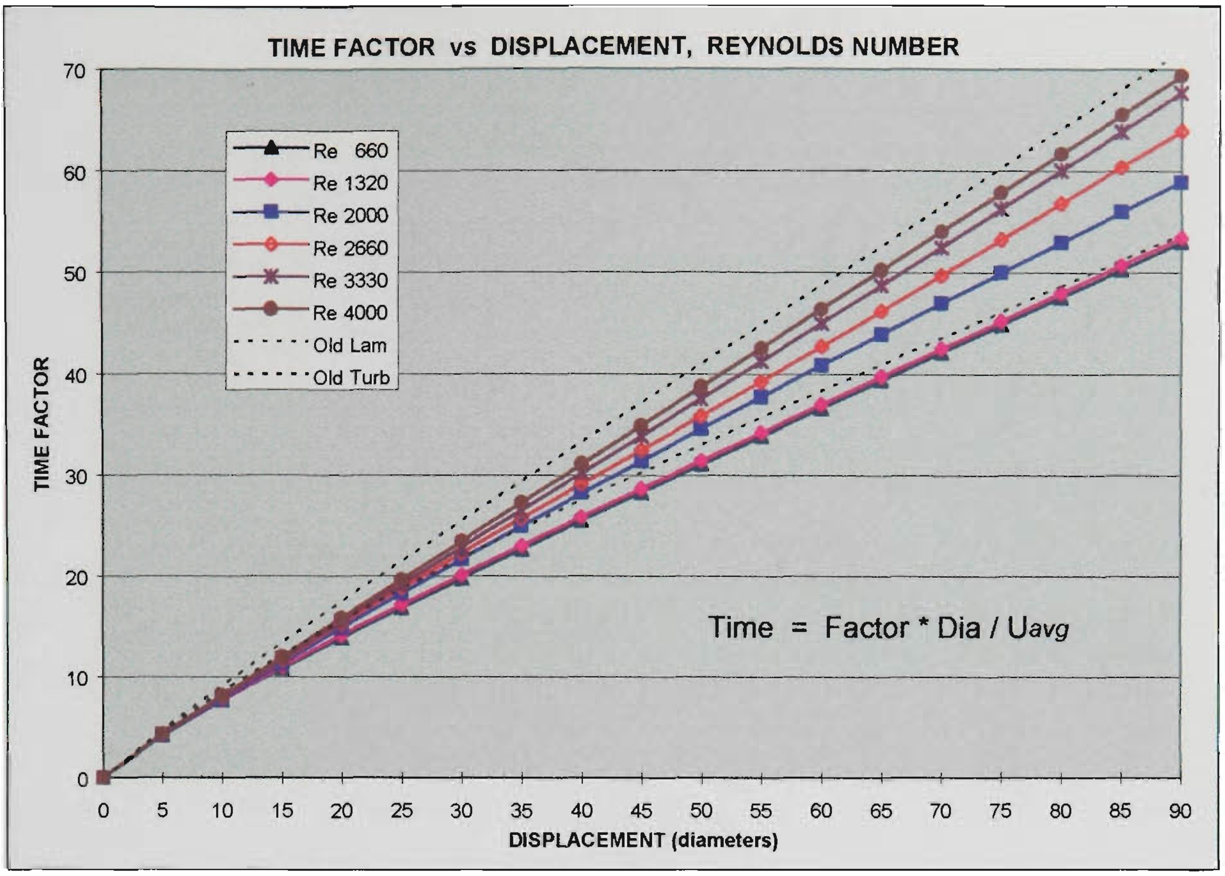

Figure 6.30 - Time Factor versus displacement

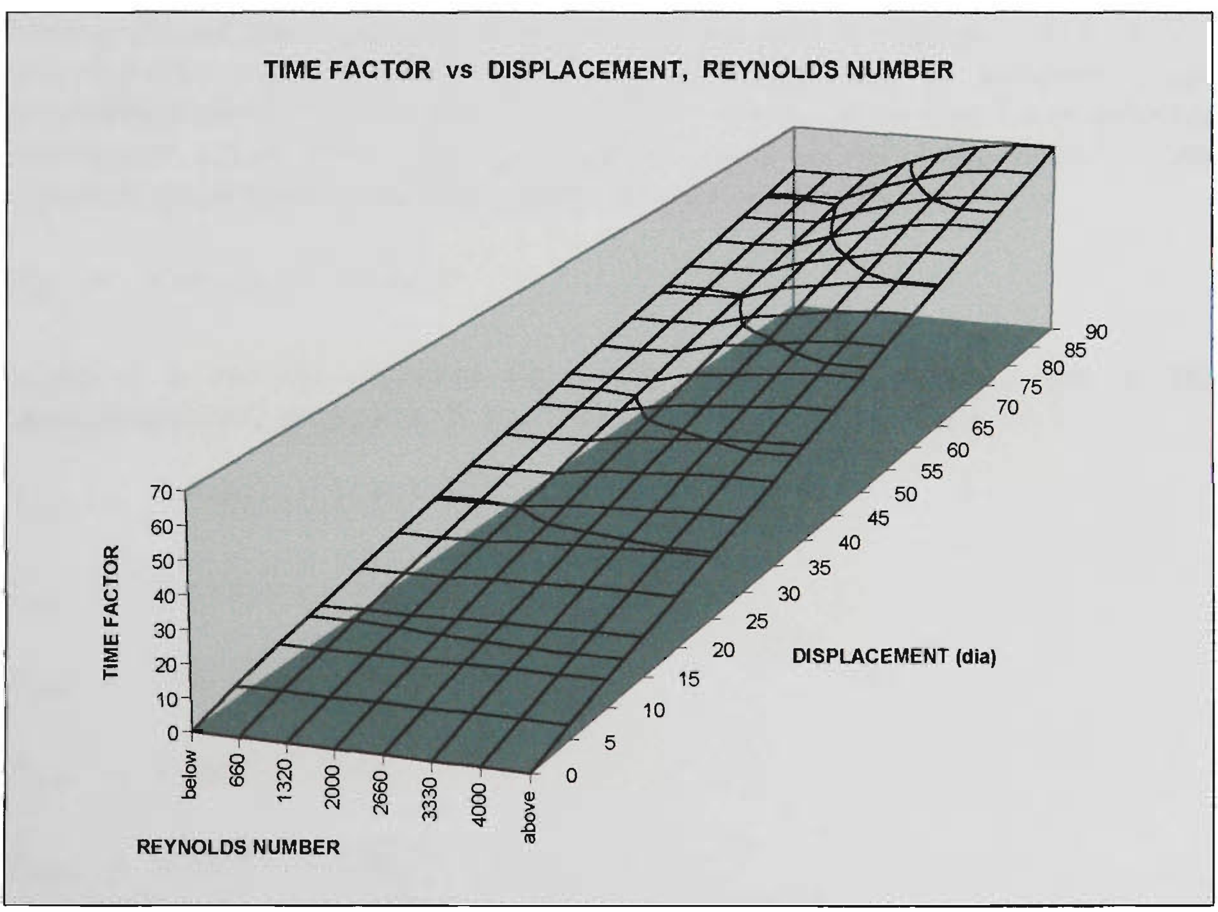

Figure 6.31 - 3-D representation of Time Factor versus Reynolds number

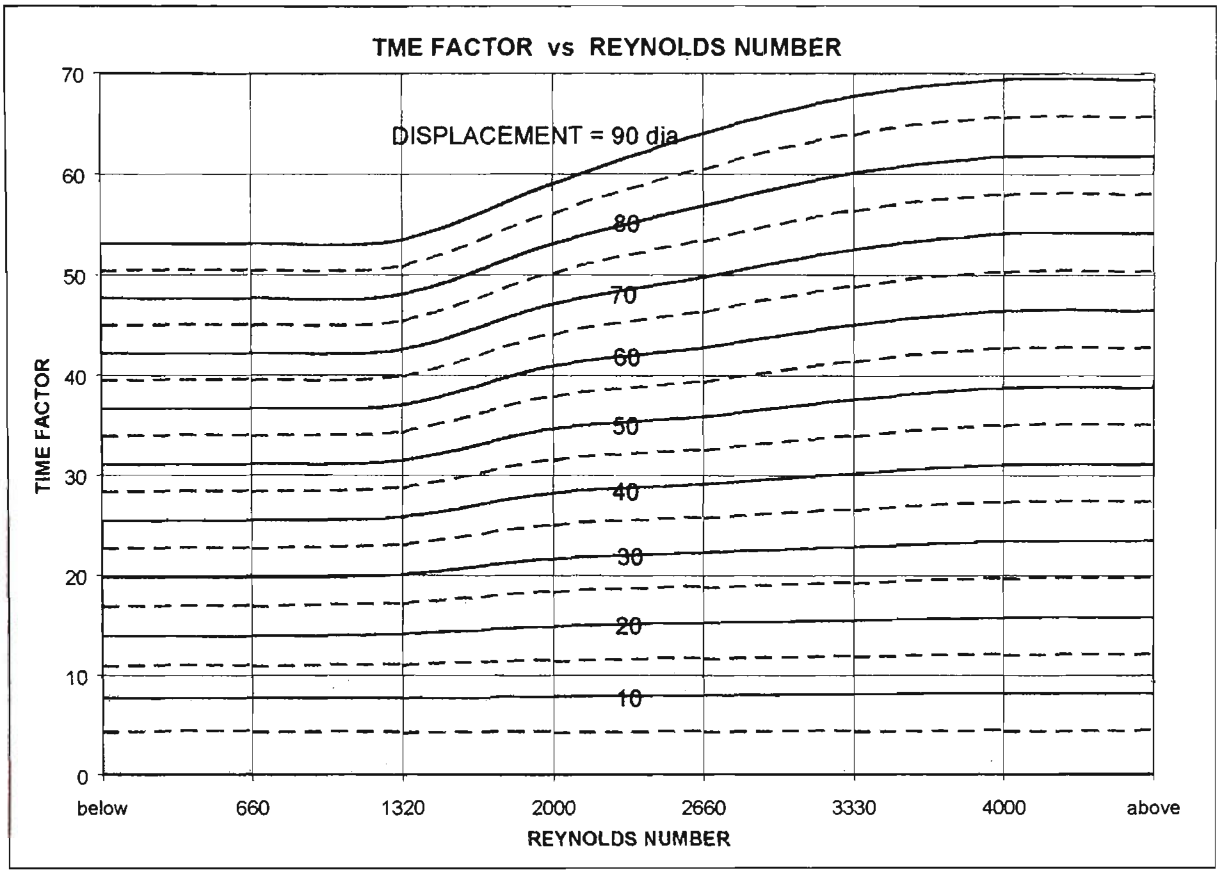

Figure 6.32 - Time Factor versus Reynolds number at various displacements

Having viewed the various presentations of the data in Figures 6.30 to 6.32 it was decided that the most convenient approach was to establish linear approximations to the curves in Figure 6.30. It was noted that the graphs are convergent below about $15dia$ and the equation to the Time Factor in this region at any Reynolds number (within the range used) is:

$$F_{Re} = -0.0078\, d^2 + 0.881\, d$$

where d is the displacement (dia). At higher displacements and at the applicable Reynolds numbers, the Time Factor may be obtained from:

$$F_{0660} = 0.5500\, d + 3.350$$

$$F_{1320} = 0.5552\, d + 3.502$$

$$F_{2000} = 0.6200\, d + 3.100$$

$$F_{2660} = 0.6952\, d + 1.400$$

$$F_{3330} = 0.7451\, d + 0.600$$

$$F_{4000} = 0.7655\, d + 0.500$$

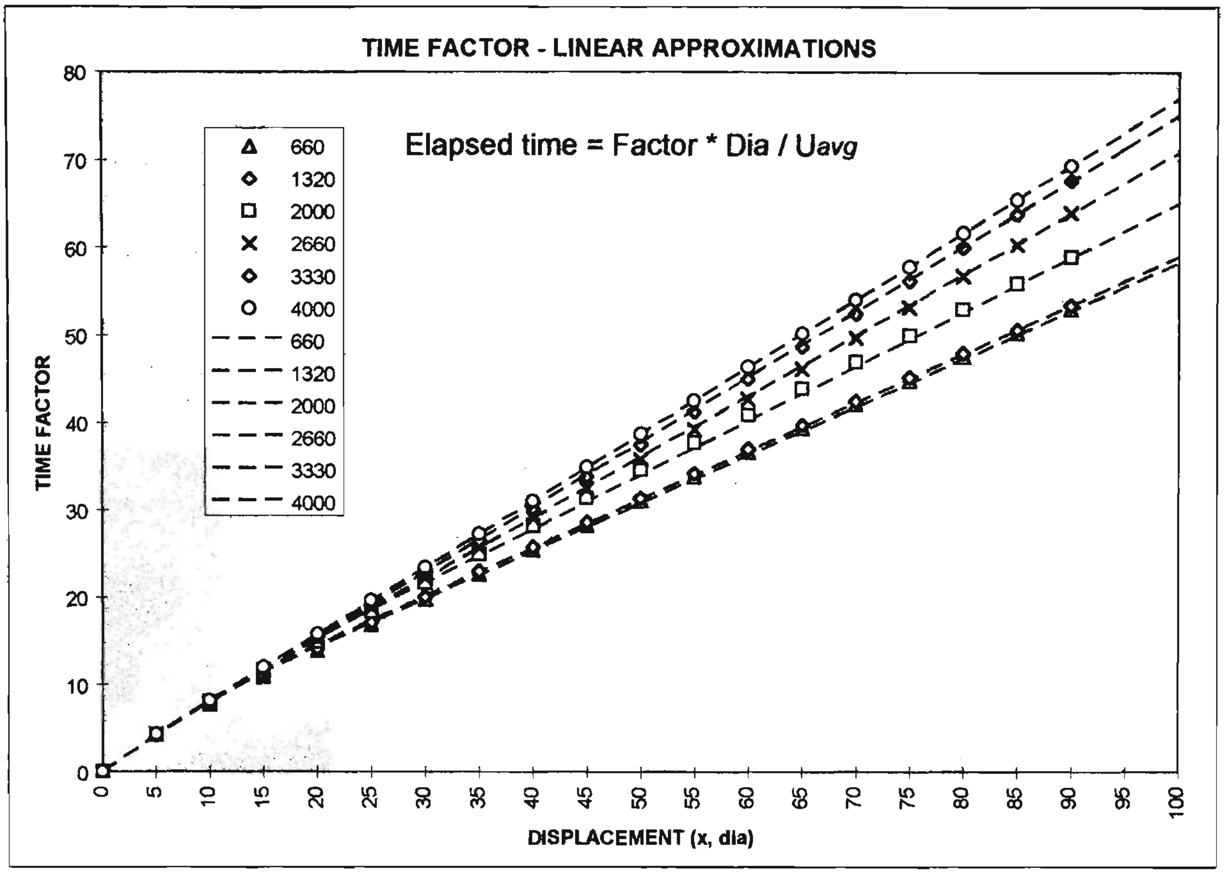

Figure 6.33 - Linear approximations to the Time Factor

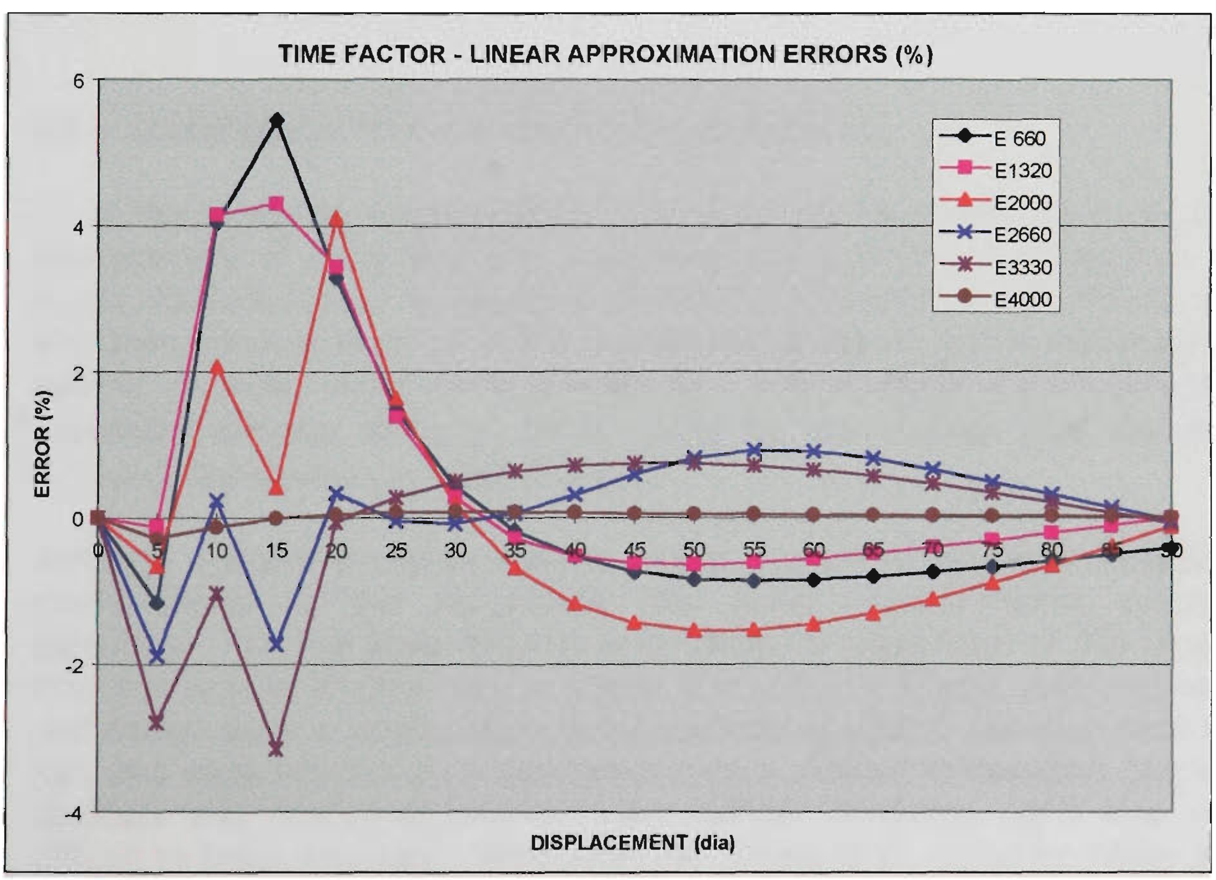

Figure 6.34 - Errors from linear approximations to the Time Factor

Figure 6.33 shows the linear approximations to the various curves, compared with the data points which are also displayed. At this view the errors seem small so it was decided to graph the magnitude of the errors involved. These errors are presented in Figure 6.34. In this analysis the "error" value is the percentage of divergence between the data and the linear approximations, but it must be remembered that these "data" are the result of smoothing the original LV measurements.

Accordingly, in Figure 6.34 we see that the error is contained within about +5% to -3%, with the majority of points lying just within ±1%. By typical standards in fluid dynamics experiments, this magnitude of error represents quite a good result.

Two alternative derivations of a Time Factor are presented in Appendix A6.7 and A6.8, based upon the following equations, but it is argued that these do not provide a satisfactory improvement:

$$T_x = F_T \frac{D_{pipe}}{u_{avg}} = \frac{F_T \, D^2_{pipe}}{k \, \mathrm{Re}}$$

$$T_x = F_T \frac{D^2_{pipe}}{k \, \mathrm{Re}^{0.85}}$$

6.8 - CONSIDERATION OF LONG PIPE SEGMENTS

All of the foregoing experimentation and analysis has been confined to a displacement of $90 dia$ and it is necessary to consider the implications of longer displacements. In aspirated smoke detection systems, although the displacement may reach up to $10m$ between sampling holes, the separation of sockets or bends would rarely exceed $4m$. With a diameter of $21.4mm$ this separation equates to some $190 dia$, while for the smallest pipe yet used ($12.4mm$), this equates to some $320 dia$.

Although it would be appropriate to extend the LV experiments to include displacements of this magnitude, this would present some practical difficulties. Not the least difficulty is to obtain a glass tube of this length. Whereas several lengths may be joined, this requires a lathe able to contain and control such a length, there is the problem of optical distortion near the join, and most importantly a long glass tube is difficult to transport (through corridors and doorways) and to mount without breakage. It is also very difficult to clean internally. Moreover, the experiments would be costly and time-consuming on the apparatus and its laboratory, which is heavily in demand for other projects. Therefore, before proceeding with such a challenge, it was decided to investigate the validity of extrapolating the available data.

Figure 6.35 represents an extrapolation of the curves in Figure 6.26, out to $400dia$. Although this represents a very long extrapolation from $90dia$, the curves follow the "trajectory" implicit in the data and it is difficult to see that the extrapolations could be significantly different from those shown. In other words, it is assumed that the overall shape of the velocity growth curve is determined during the first $90dia$ and, given that the boundary layer transition is already encompassed, there is no reason to expect that the trend already established by $90dia$, could be significantly altered thereafter. Put yet another way, any significantly different extrapolations would put a distinct change in gradient in the curves, which would be difficult to explain.

In the particular case of the curve for $\mathrm{Re} = 2000$, a close fit to the data was obtained using the equation:

$$R_u = \frac{u_{core}}{u_{avg}} = 2 - 0.655\, e^{(-d/113)}$$

where the displacement, d is at least $5dia$. It was also found consistent to converge the extrapolations applicable to lower Reynolds numbers with this curve, meeting at about $270dia$. It is noted that all three curves, representing a laminar flow regime, asymptote to a final value of 2.0 (at infinity), and reach 99% of this value (1.98) at a displacement of $400dia$. This is a remarkable result in view of the $120dia$ stated in the literature (Douglas et al. 1979, p285).

The reason for this large discrepancy is the level of disturbance to the flow regime. Douglas et al. (as well as Martinuzzi and Pollard, Figure 1,11) assumed an aerodynamically smooth entry which would generate minimal entry disturbance without a vena contracta. Our experimental apparatus deliberately used a sharp entry and it is not surprising that the severe disturbance introduced, would take a significantly longer displacement to dissipate. This phenomenon can be restated in terms of boundary layer development which, at low Reynolds numbers, evidently takes three to four times greater distance to establish in the case of initially disturbed flows.

Figure 6.36 presents the projected Time Factor (based on $T_x = F_T\, D_{pipe} / u_{avg}$) versus displacement out to $400dia$. The dotted lines are extended graphs of the linear approximations of closest fit to the data up to $90dia$. It is clear that in a number of cases, these approximations do not match the projections well.

With reference to Figure 6.35 it can be seen that for the transition and turbulent regions (commencing near $\mathrm{Re} = 2000$), the velocity growth has reached its final value by (say) $100dia$. Therefore, for these regions it is possible to use the Time Factor equation out to $100dia$, and assume constant core velocity thereafter.

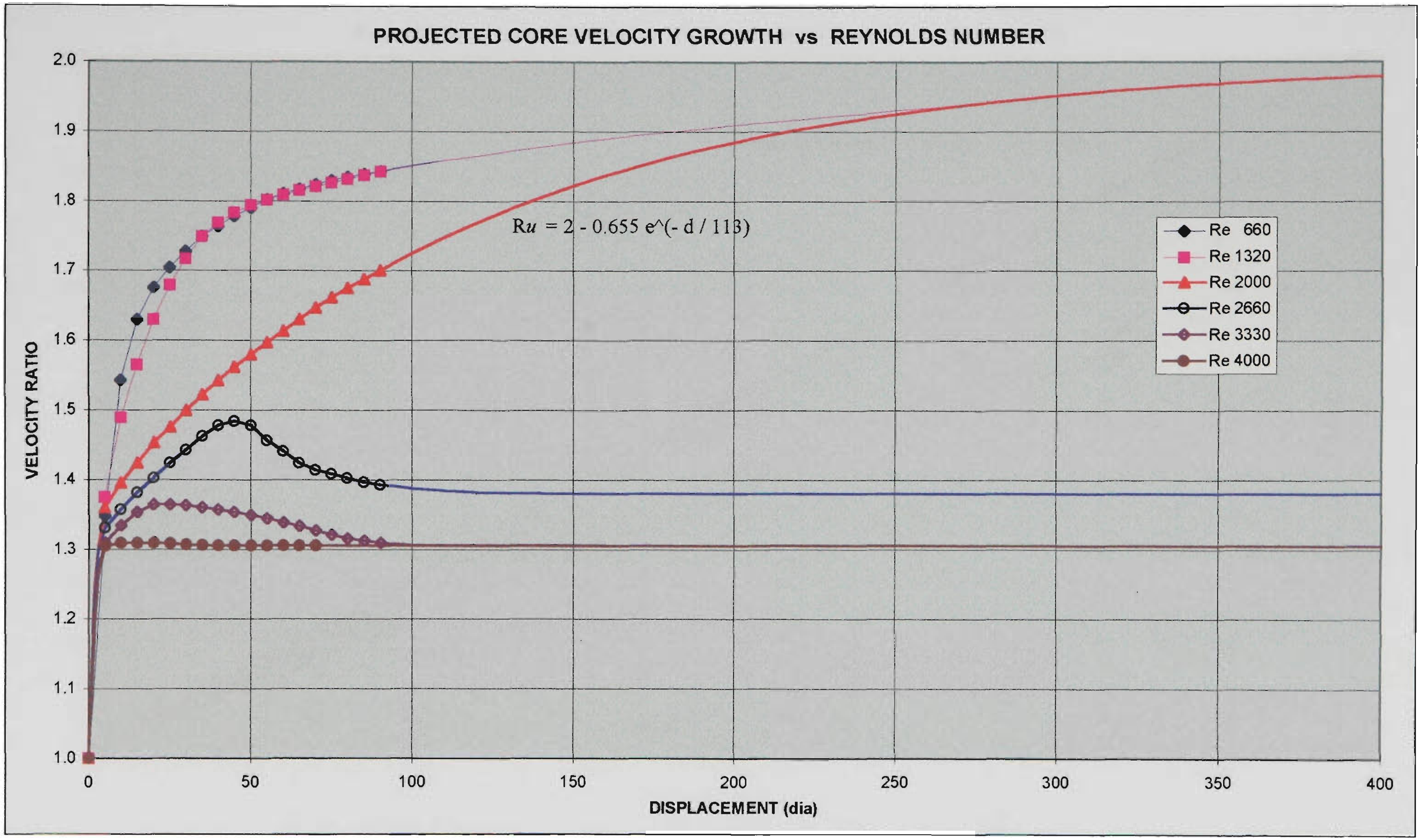

Figure 6.35 - Core velocity growth projected out to $400dia$

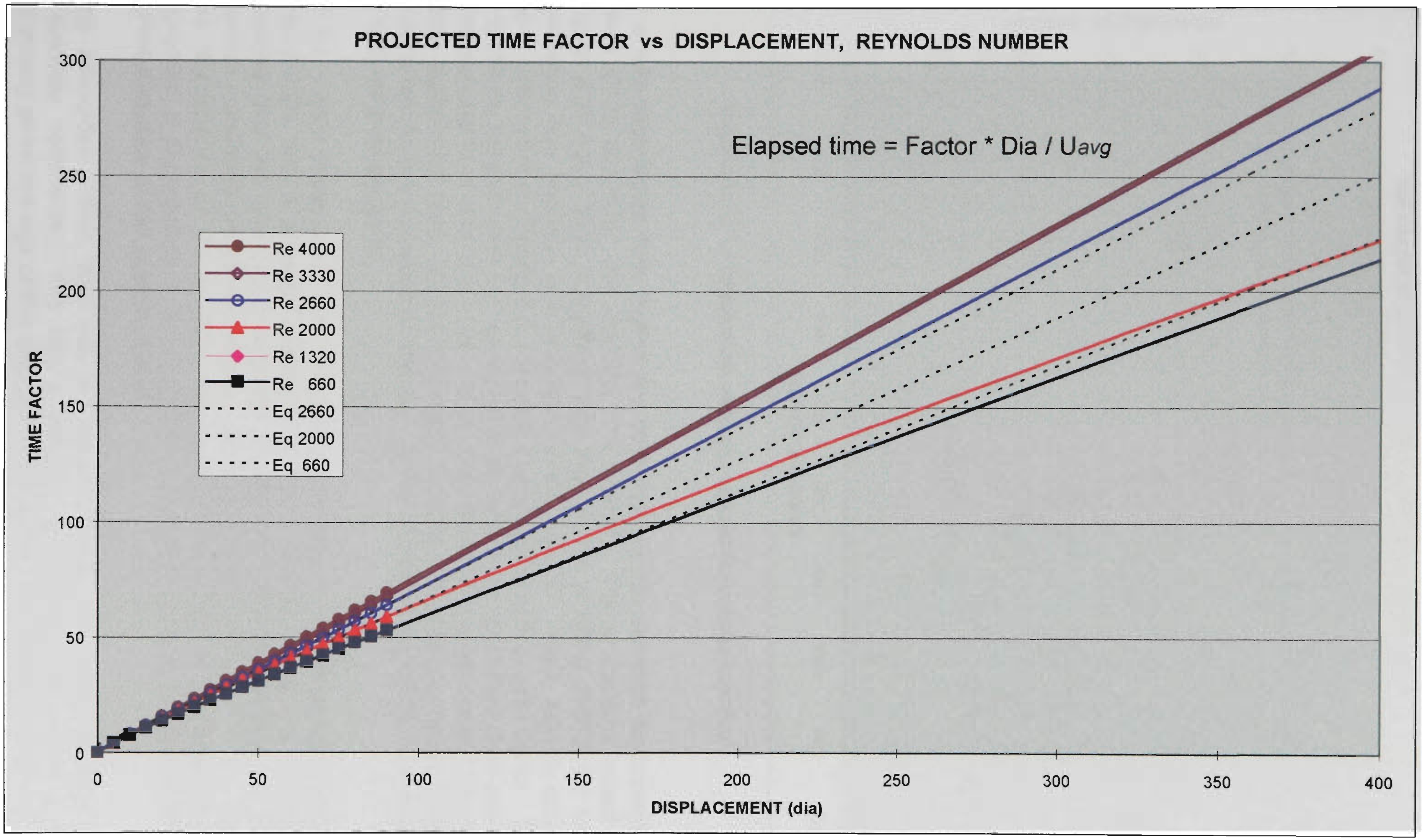

Figure 6.36 - Time Factor projected out to $400dia$

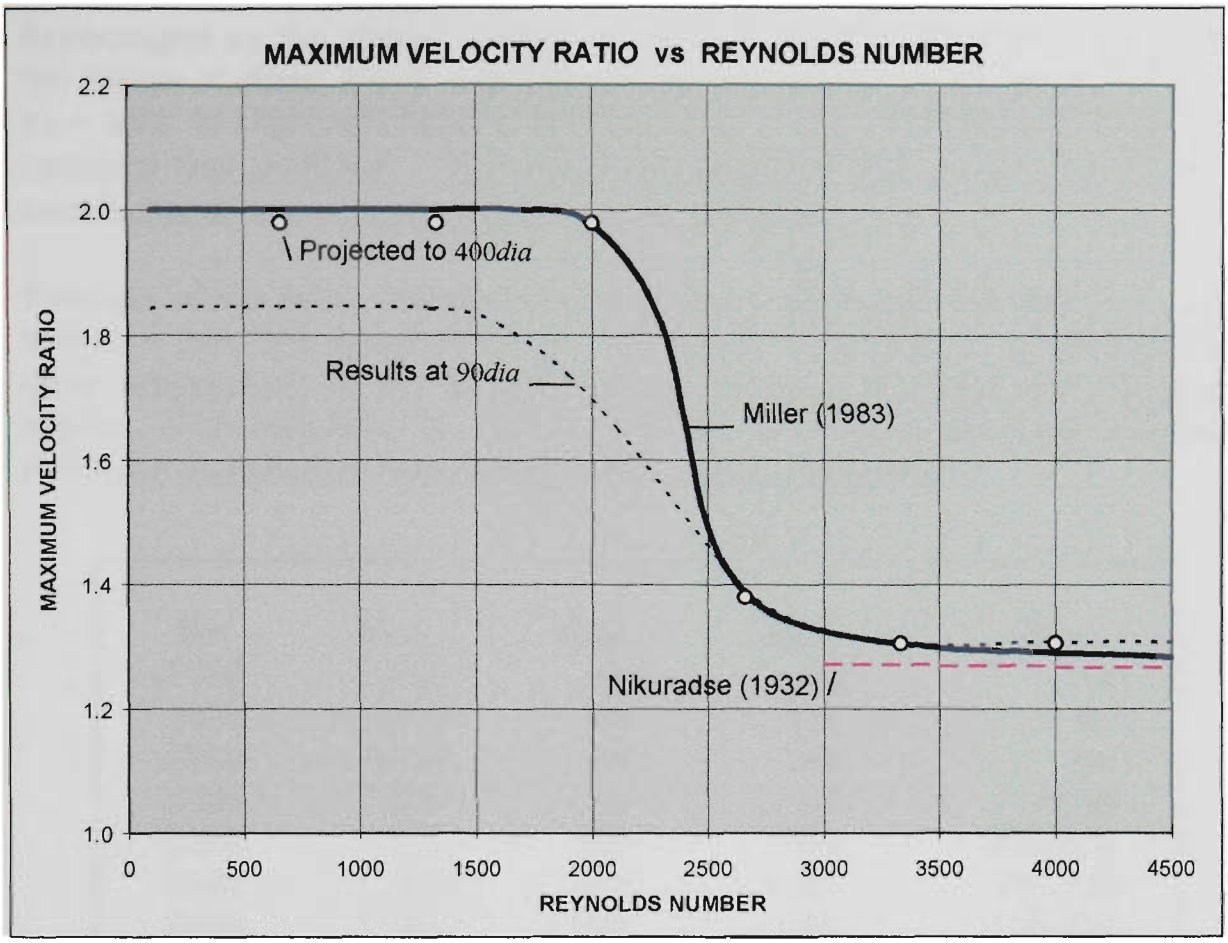

Figure 6.37 - Maximum velocity versus Reynolds number

In a fully-established flow regime the core velocity has reached its maximum value (or by definition, has reached 99% thereof). The projections based on Figure 6.35 have been compared with the results of Miller (1983) for fully-developed flow regimes, and presented in Figure 6.37. Here, Miller's results were obtained from Figure 6.5, inverted and graphed with a solid curve. The projections (based upon LV results) are shown as six individual data points, representing Re = 660, 1320, 2000, 2660, 3330 and 4000 respectively. There is close agreement here. At low Reynolds numbers the data represent 99% of Miller's results (as expected at 400*dia*). In the transition region the correlation is also surprisingly good.

At Re = 4000 there is a small discrepancy of about 1%. Referring back to Figure 6.26, the LV data are available to 70*dia* (instead of 90), and it is quite possible that the true curve may fall slightly at higher displacements, in a manner consistent with the maximum velocity quoted by Miller. In any case this discrepancy of 1% is within the limits of accuracy of the experiment. Moreover, a discrepancy of this magnitude is unlikely to have significant effect on the accuracy of the system model.

The Nikuradse (1932) data has also been included for reference and, as previously commented, this has a small (-3%) discrepancy which is not surprising given the age of the data (the likely accuracy of instrumentation).

Encouraged by the strong correlation between the projected LV results and the results of Miller, it was decided to adjust the core velocity growth curve for $Re = 4000$ to align with Miller's results ($Ru_{max} = 1.290$) for the fully-developed turbulent flow condition. The projected results for this curve beyond $70dia$ were adjusted accordingly, and presented in Figure 6.38.

Because of the large change in curve shapes occurring between $Re = 2000$ and $Re = 2660$ (the onset of transitional flow), it was decided to visualise the likely progression of the velocity growth curves throughout the transition region. With reference to Figure 6.37, the following correlations between Reynolds number and maximum velocity ratio are tabulated:

Re	Ru_{max}	d_{250k}	d_{peak}	Re_{eT}
≤1800	2.000	n/a	n/a	n/a
2000	1.980	n/a	n/a	n/a
2200	1.900	n/a	n/a	n/a
2320	1.800	114	318	700,000
2390	1.700	105	110	262,900
2440	1.600	102	80	195,200
2490	1.500	100	63	156,870
2660	1.380	94	45	119,700
3000	1.326	83	33	99,000
3330	1.306	75	25	83,250
4000	1.290	63	16	64,000

Table 6.1 - Velocity ratios, nominal boundary layer transition displacements and *entry* Reynolds number

By referring to Section 6.3 it was expected that the boundary layer transition for undisturbed flows should occur when the *entry* Reynolds number is in the vicinity of $Re_e = 250{,}000$, and is likely to occur at a significantly lower value where a high level of flow disturbance exists. Included in Table 6.1 is the new term, d_{250k}, being the displacement for which the *entry* Reynolds number reaches 250,000. This term is not applicable to laminar flow regimes (the first three rows, and possibly the fourth - shown in smaller font size). For transitional and turbulent flow regimes, it provides a point of reference for each growth curve, defining a distance within which the core velocity should have peaked (u_{peak}) and commenced its fall towards its final value (u_{max}).

This peaking effect is most obvious in Figure 6.35 at $Re = 2660$ and, with reference to the *entry* Reynolds number it is possible to visualise the likely progression of the local peaking of core velocity at other Reynolds numbers within the transition region. The result of this analysis is presented in Figure 6.38, where a locus connecting the estimated peak velocities has been included, while the relevant displacements (d_{peak}) are included in Table 6.1.

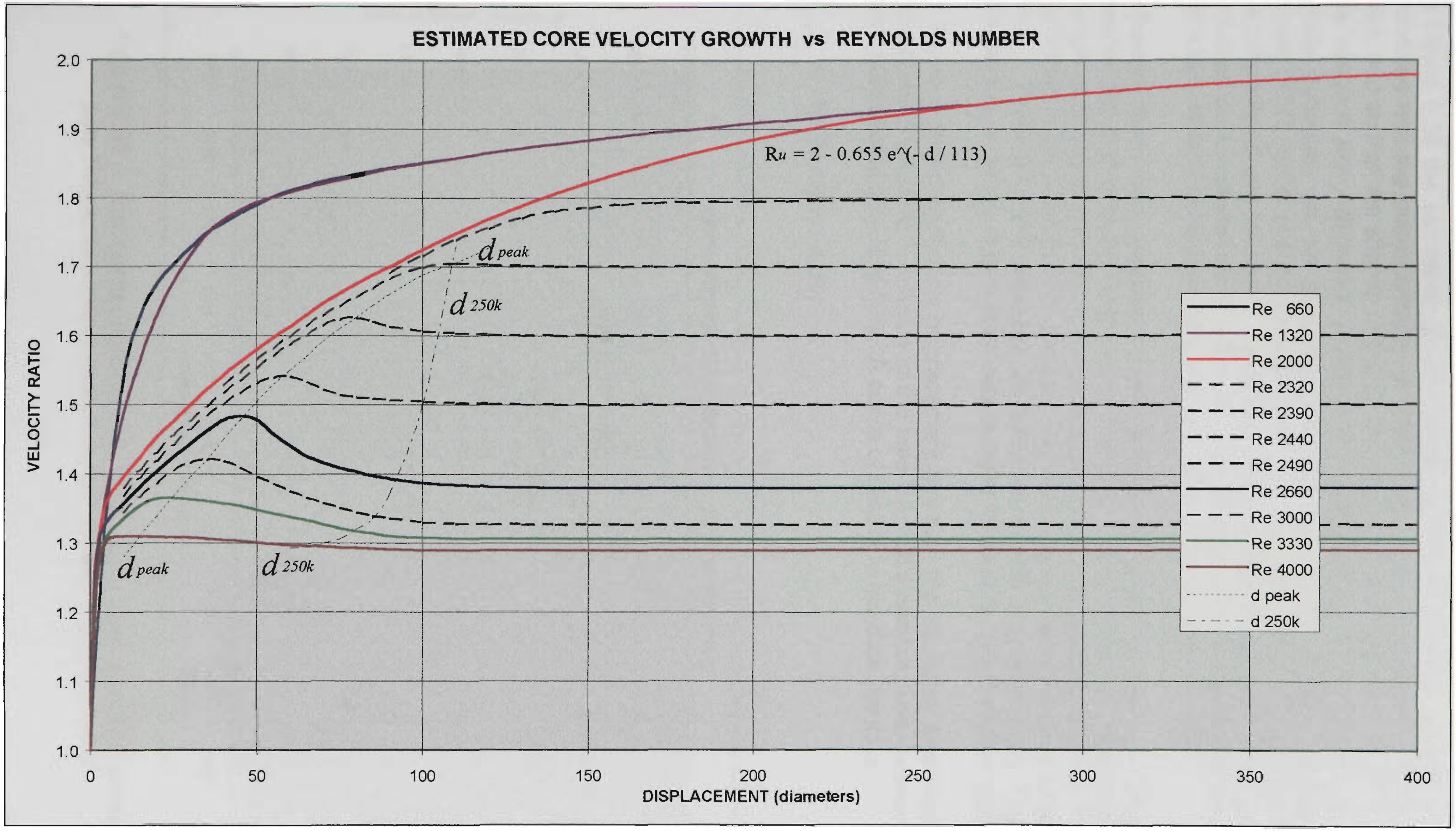

Figure 6.38- Estimated core velocity growth curves throughout transition region (for initially-disturbed flows)

In Figure 6.38 the estimated growth curves have been devised so that the peak velocities and the displacements at which they occur are consistent with the LV data, and so that the shapes of the curves are consistent with each other and with the relevant *entry* Reynolds numbers (as indicated by the d_{250k} and d_{peak} loci). These estimates are all consistent with the values reported by Roberson and Crowe (1975 p259) and by Douglas et al. (1979 p286), given the fact that highly disturbed flows are involved. Note that the results tabulated for $\mathrm{Re} = 2200$ are included for completeness but this is a borderline case, at the threshold of the transition region where boundary layer transition may, or may not occur.

Whereas there had previously been difficulty in obtaining the *entry* Reynolds number applicable to boundary layer transition (being uncertain within the wide margin of 50,000 to 500,000), it is now apparent that this figure is not fixed in value but varies in accordance with the *pipe* Reynolds number and the level of disturbance. Table 6.1 now provides an estimate of this transition *entry* Reynolds number Re_{eT} in terms of *pipe* Reynolds number for initially-disturbed flow regimes.

In Figure 6.39 the estimated displacement at which the boundary layer becomes transitional is graphed in relation to the *pipe* Reynolds number, and we see that a hyperbolic relationship emerges. A curve of best fit to the data points is:

$$d_{peak} = 8.9\,\mathrm{Re}/(\mathrm{Re} - 2150)$$

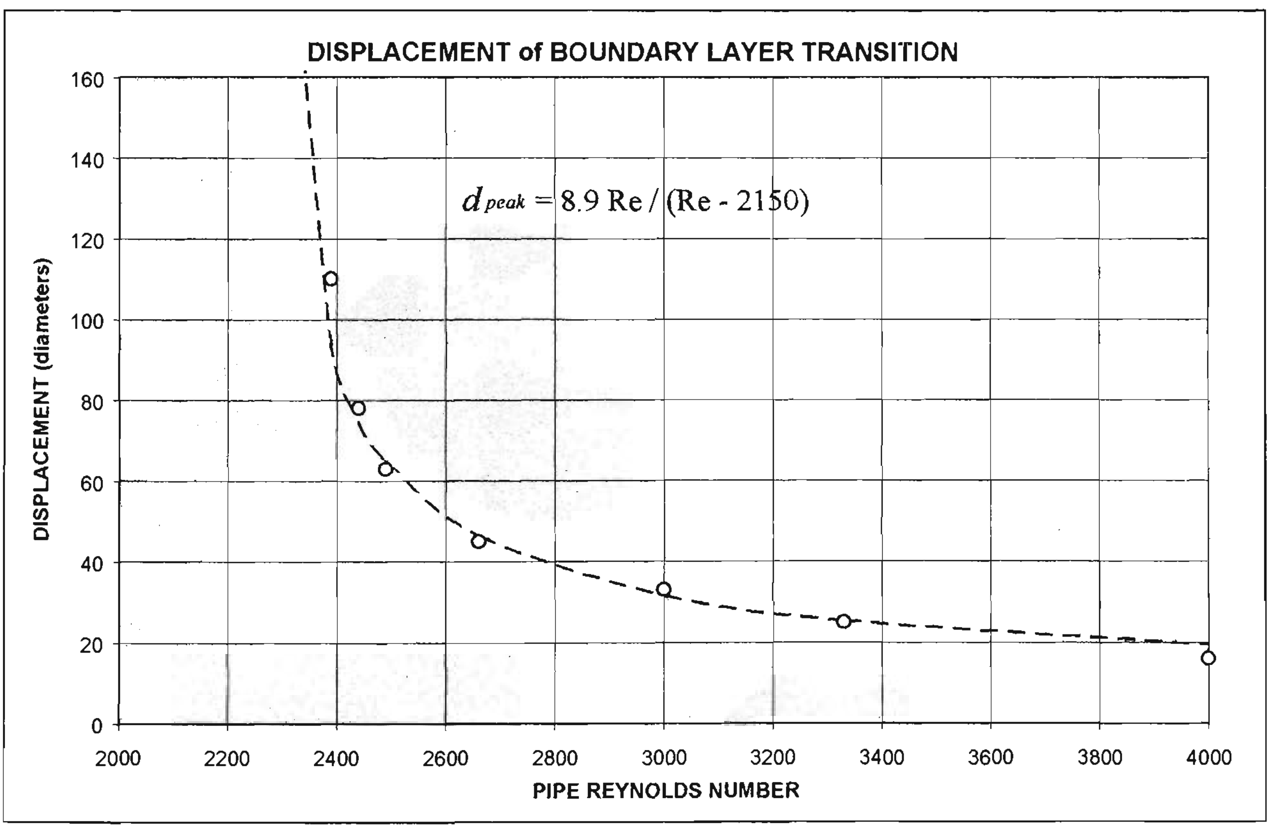

Figure 6.39 - Estimated displacement of boundary layer transition versus *pipe* Reynolds number, resulting from initially-disturbed flows

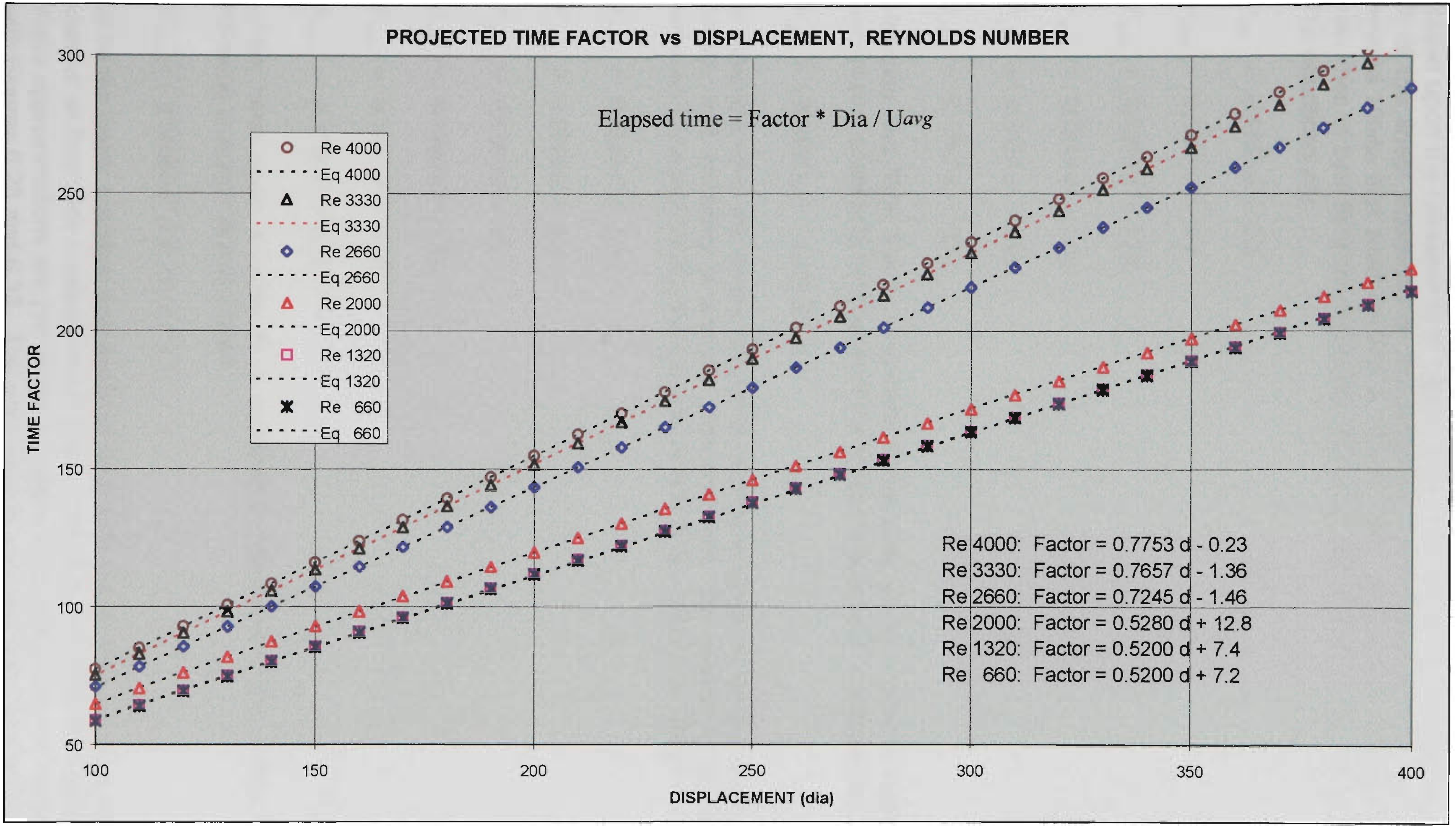

Figure 6.40 - Linear approximations to Time Factor extended to displacements > $100dia$

Based upon the refinements of Figure 6.38 it is possible to address the poor fit of the linear equations to the projected Time Factor at displacements beyond $100dia$ that were evident in Figure 6.36. Figure 6.40 now presents new lines of best fit to the projected data from 100 to 400 dia (shown dotted). The equations are:

$$F_{660} = 0.5200\,d + 7.2$$

$$F_{1320} = 0.5200\,d + 7.4$$

$$F_{2000} = 0.5280\,d + 12.8$$

$$F_{2660} = 0.7245\,d - 1.46$$

$$F_{3330} = 0.7657\,d - 1.36$$

$$F_{4000} = 0.7753\,d - 0.23$$

However, the Time Factor projection in the case of $\mathrm{Re} = 2000$ is relatively curved and a better fit is obtained if the following quadratic is substituted:

$$F_{2000} = -0.00011\,d^2 + 0.579\,d + 8.3$$

In obtaining all of the above equations relating to displacements in excess of $100dia$, and ensuring a smooth transition with the equations applicable between $15dia$ and $100dia$, the latter have now been refined as follows:

$$F_{660} = 0.5550\,d + 3.3$$

$$F_{1320} = 0.5550\,d + 3.5$$

$$F_{2000} = 0.5280\,d + 13$$

$$F_{2660} = 0.6940\,d + 1.15$$

$$F_{3330} = 0.7460\,d + 0.30$$

$$F_{4000} = 0.7720\,d + 0.10$$

where once again a better fit is obtained in the case of $\mathrm{Re} = 2000$ if the following quadratic is substituted:

$$F_{2000} = -0.00066\,d^2 + 0.701\,d + 1.1$$

while the linear equation applicable to $\mathrm{Re} = 3330$ (i.e. $0.7460\,d + 0.30$) can be used at all Reynolds numbers below $15dia$. The errors incurred by using all of these approximations are presented in Figure 6.41, which may be compared with Figures 6.28 and 6.33. The error span is very low, lying well within $\pm 1\%$

above $25dia$ and within $\pm 5\%$ worst case. These errors are not cumulative. Pipe segment lengths below $25dia$ (typically $0.5m$) are rarely used except where closely-spaced holes are positioned in front of a ventilation grille (where pipe lengths are short and smoke transport time is not an issue).

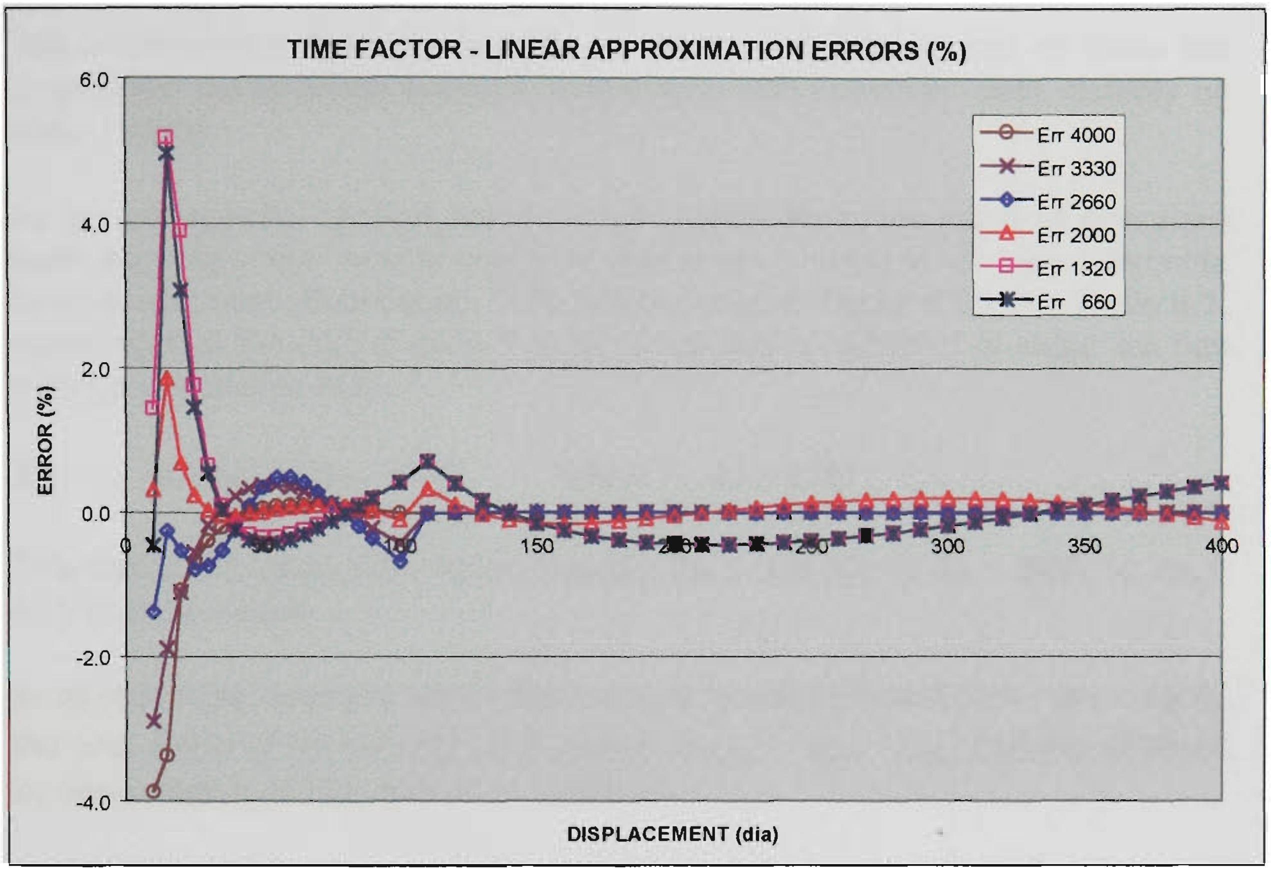

Figure 6.41 - Errors for linear approximation to Time Factor

6.9 CONCLUSIONS

After extensive experimental work and analysis, a model has emerged (Figure 6.38) that describes the core velocity growth profile throughout the laminar, transitional and early turbulent flow regimes, where such flows are initially disturbed. Note that in practice the core velocity refers to the average velocity within a small central region of the pipe as defined by the LV target size ($1.5mm$ radius, involving only a small error due to the blunt core profile). This model indicates that for laminar flows, the core velocity does not reach 99% of its final value until a displacement of some $400dia$. This compares with a figure of $120dia$ quoted in the literature, applicable to undisturbed flows.

For example at $\mathrm{Re} = 2000$, beyond $5dia$ the developing core velocity ratio rises in accordance with the following equation, which reaches the value 1.98 at $400dia$:

$$R_u = 2 - 0.655\, e^{(d/113)}$$

In the case of transitional and turbulent flow regimes, the core velocity initially rises to a peak value (at a displacement corresponding to the boundary layer transition) and then falls, reaching 101% of its final value within some 100*dia*. This compares with a figure of 60*dia* quoted in the literature, applicable to undisturbed flows.

The experimental data are limited to maximum displacements of 90*dia* but projections out to 400*dia* achieve consistency with published data, notably by Miller (1983).

As an unexpected consequence of the investigation, the point of boundary layer transition (for initially-disturbed flows) as a function of *pipe* Reynolds number has been discovered. This is presented in Figure 6.39 and Table 6.1, revealing that the critical *entry* Reynolds number is not fixed in value but has a range obtainable from:

$$\mathrm{Re}_e = 8.9\,\mathrm{Re}^2 / (\mathrm{Re} - 2150) \qquad \textit{where} \qquad \mathrm{Re} > 2350$$

This ranges in value from approximately $\mathrm{Re}_e = 250{,}000$ at $\mathrm{Re} = 2400$, to $\mathrm{Re}_e = 64{,}000$ at $\mathrm{Re} = 4000$.

At all Reynolds numbers within the range of current interest ($400 < \mathrm{Re} < 4000$), the final value of the velocity ratio (where $\mathrm{Ru}_{max} = u_{max} / u_{avg}$) can be obtained by interpolation of Figure 6.37 or Table 6.1.

A simplified method of approximation to the smoke transport time (T_T) has been derived and the new dimensionless coefficient, Time Factor (F_T), has been defined for use in the following equation:

$$T_T = F_T \frac{D_{pipe}}{u_{avg}}$$

which can be applied with significantly greater accuracy than previous methods. Linear approximations to the Time Factor curves at each Reynolds number have been developed (Figures 6.33 and 6.40) and these show a significant improvement in the cumulative error involved in determining the smoke transport time. At displacements less than 15*dia* the Time Factor is obtained from:

$$F_T = -0.0078\,d^2 + 0.881\,d$$

at all *pipe* Reynolds numbers up to 4000. At higher displacements the Time Factor may be obtained from the linear approximation:

$$F_T = t_1\,d + t_0$$

where the gradient and offset terms t_1 and t_0 may be obtained from Table 6.2 (below), requiring different sets of values within the range 15 to 100 *dia*, and above 100*dia*. However, at Re = 2000, a closer approximation to the Time Factor may be obtained from the following quadratic equations:

$$15 < d < 100 \qquad F_{2000} = -0.00066\,d^2 + 0.701\,d + 1.1$$

$$d > 100 \qquad F_{2000} = -0.00011\,d^2 + 0.579\,d + 8.3$$

The Time Factors applicable to intermediate values of Reynolds number are obtained by interpolation. This does not involve large errors because of the relatively small divergence among the equations.

	$15 < d < 100$		$d > 100$	
Re	t_1	t_0	t_1	t_0
660	0.5550	3.30	0.5200	7.20
1320	0.5550	3.50	0.5200	7.40
2000	0.6200	3.10	0.5280	12.80
2660	0.6940	1.15	0.7245	-1.46
3330	0.7460	0.30	0.7657	-1.36
4000	0.7720	0.10	0.7753	-0.23

Table 6.2 - Time Factor parameters

CHAPTER 7 - DEVELOPMENT OF A SYSTEM MODEL

7.1 INTRODUCTION

Having characterised all the components necessary to model an aspirated pipe system it remains to adapt and consolidate these components within a system framework and to validate the integration methodology by applying the model to particular examples, and to judge its advantages over previous methods.

7.2 SMOKE TRANSPORT TIME

To develop a system model, an aspirated pipe of $21.4mm$ internal diameter with segment lengths of $100dia$ ($214mm$) is selected for convenience. The flow through each sampling hole, including the end vent is assumed to be $10 litre/sec$. In practice this requires holes of some $4mm$ diameter which could be finely adjusted in conjunction with the local pressure differential to obtain precisely the flow rate required. Accordingly the flow rate in each successive segment of pipe is 10, 20, 30 *litre/sec*, etc. At the stated pipe internal diameter, the average velocity in each segment is 0.463, 0.926, 1.389 *m/sec*, etc. and the Reynolds numbers are 660, 1320, 2000, etc. By selecting six sampling holes and pipe segments, the complete range of Reynolds numbers of current interest is embraced.

The instantaneous core velocity (u_{core}) is obtained from the product of the average velocity (u_{avg}) and the velocity ratio (R_u). At each applicable Reynolds number, this ratio is available from Figure 6.38 at all required displacements. Note that in practice the core velocity refers to the average velocity within a small central region of the pipe as defined by the LV target size ($1.5mm$).

The result of using this methodology is presented in Figure 7.1, graphed as a contiguous series of solid curves. This is to be compared with the anticipated, conceptual core velocity growth pattern presented in Figure 1.16 which has a similar general form. The core velocity in each segment increases in accordance with the profile established in Figure 6.52 until the next sampling hole is encountered. Here, the core velocity is shown as being reset immediately to the local average velocity (including the local hole flow contribution at that point), thereafter to commence regrowth toward its new maximum value.

It is yet to be established that the core velocity would reset completely, attaining the local average velocity momentarily. It is possible that the core velocity could reset to a somewhat higher value, depending upon the level of disturbance to the flow regime caused by the sampling hole's induction jet. However, there is evidence obtained throughout the extensive experimental program, that the flow regime is very easily disturbed. In Chapter 5 we saw that one bend is sufficient to disturb (reset) the flow regime completely.

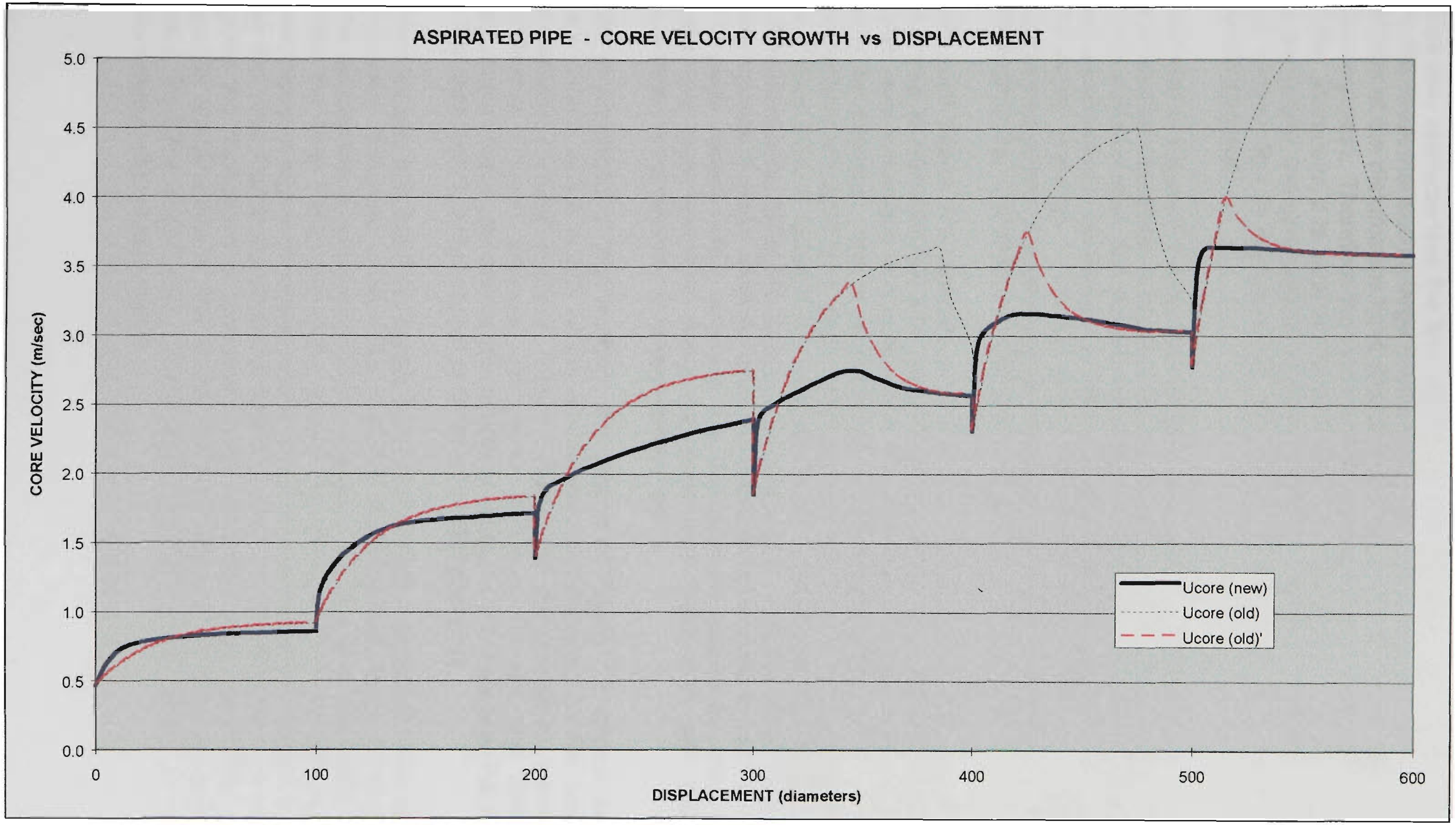

Figure 7.1 - Core velocity growth curve for an aspirated pipe with six sampling holes

This view characterises the flow regime as very fragile. Such a view is reinforced by the result that such a large displacement - some $400dia$ - is required before the effects of the disturbance have dissipated to less than 1% (in the case of laminar flow regimes). Therefore the core velocity is assumed to reset completely at each hole. Moreover, it is apparent from Figure 7.1 that within the overall scale of the pipe system, the core velocity spends very little time at the "reset velocity" (seen as vertical dips in the graph) so any error introduced by such an assumption would be small.

Included in Figure 7.1 as a fine, dotted curve series is the outcome of using the exponential equations of Figure 6.8(b) previously used in the modelling software. Here it can be seen that there is agreement in broad principle but there would be significant errors introduced by the exponential model especially at the higher Reynolds numbers. These errors are significantly reduced if the newly discovered points of boundary layer transition are obtained from Table 6.1 (rather than using $Re_e = 250{,}000$), as indicated by the dashed curve series.

Although Figure 7.1 presents a model of the core velocity growth profile, it is required to translate this into smoke transport time. By integrating the velocity over each increment of displacement, the cumulative transport time ("Sigma T") may be obtained. This is presented as a solid curve in Figure 7.2 ("new"). The cumulative transport time graph obtained from the Time Factor equations related to Figure 6.34, is included for comparison as a dashed curve ("linear"), but the close correlation hides this beneath the solid curve. Included as a dotted curve is the equivalent graph obtained from the exponential equations used in the initial computer model ("old"), whereas the improvement gained by using the new boundary layer transition points (obtained from Table 6.1) with those initial equations is indicated by a dashed curve (" old' ").

When presented in that manner, the graphs of Figure 7.2 appear in general agreement, so the quality of the models are best analysed on the basis of the associated cumulative errors. Figure 7.3 presents the cumulative transport time difference ("Delta") between the results of Figure 7.1 and the Time Factor equations ("new"), as well as the results of using the initial exponential equations ("old" and "old' "), all expressed in terms of percentage error.

Here we see that the Time Factor equations provide a significant improvement in the error. Whereas, even when using the new boundary layer transition points, the exponential equations produce cumulative errors within the range of -12 to +8%, the Time Factor equations reduce this span to -2 to +3% (with a reducing error span at higher Reynolds numbers). The improvement in accuracy provided by the Time Factor equations represent a factor of four or better. Nevertheless, given the fluctuation in cumulative error along the pipe, depending upon the special combinations of pipe system parameters it can be expected that in some sites, the initial model could, coincidentally, produce results that are in reasonable agreement with measurements.

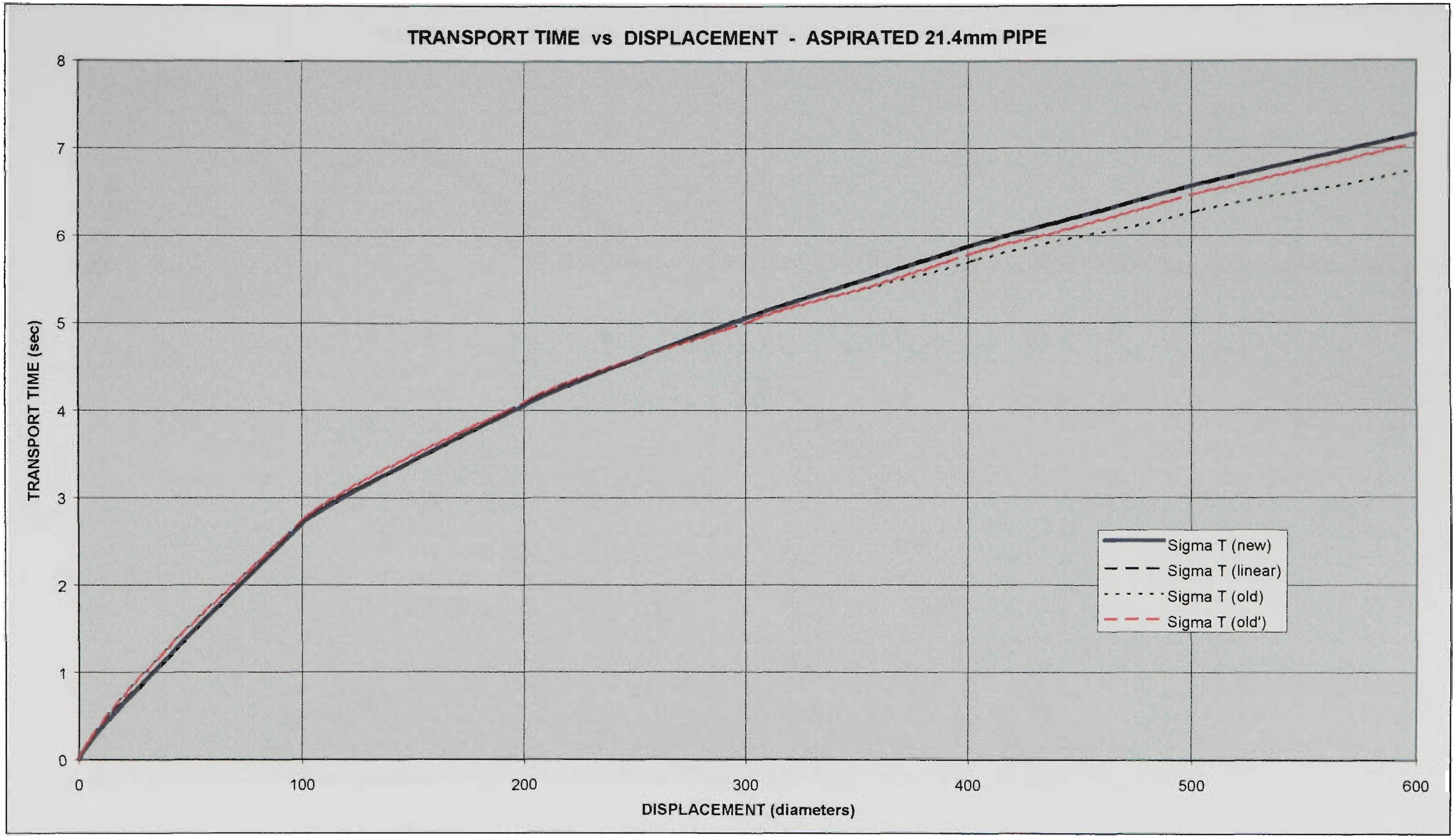

Figure 7.2 - Three models for cumulative smoke transport time versus displacement

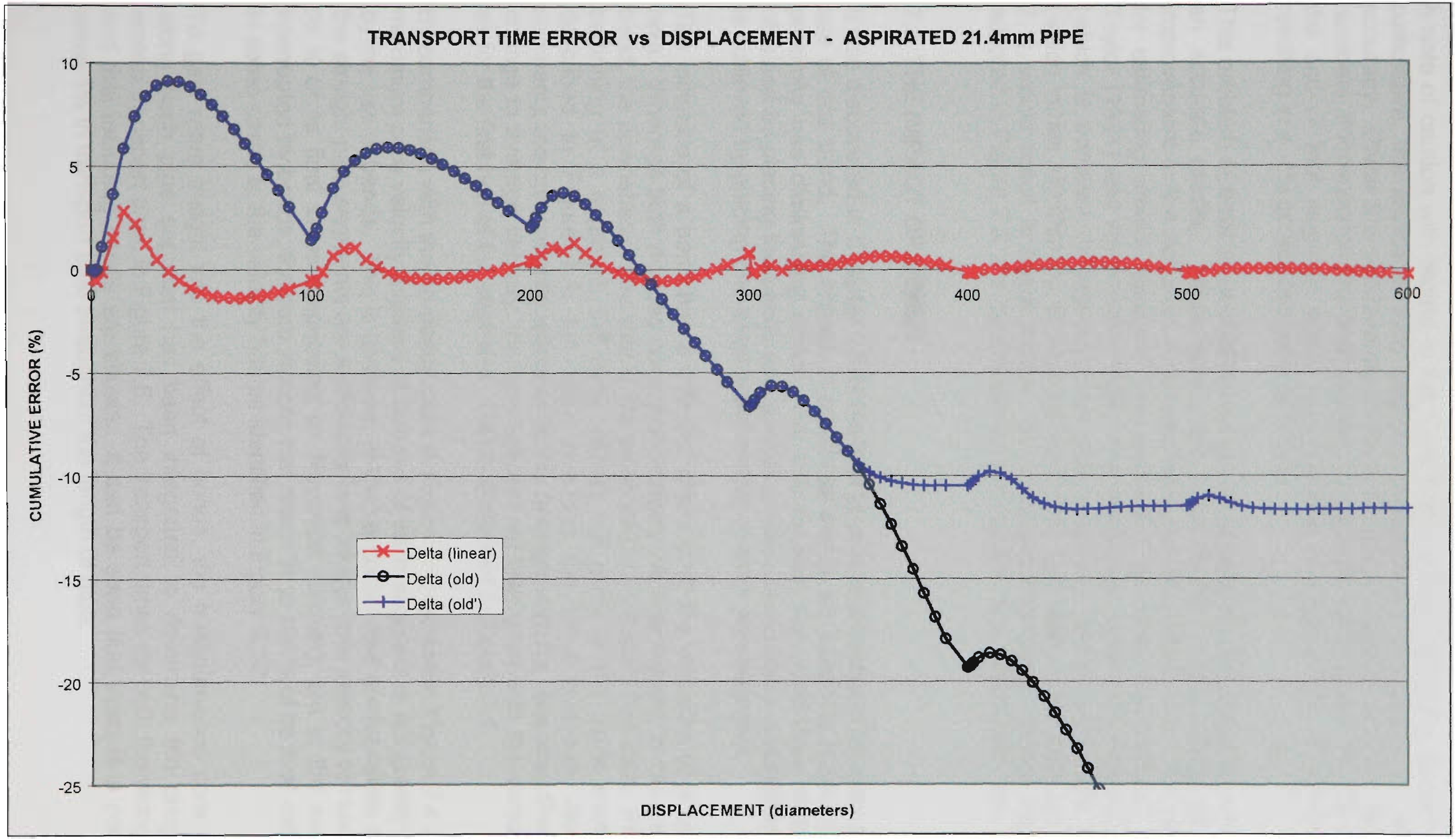

Figure 7.3 - Cumulative errors associated with smoke transport time models

A note of caution with regard to the Time Factor model: Because the errors are cumulative, the choice of pipe segment displacement can affect the apparent accuracy. Given the non-linearity of the error graph, especially at low Reynolds numbers, if for example the first segment length was halved, then the -2% error at the end of that segment would carry-forward throughout the remaining pipe, resulting in a -2% cumulative error at $600dia$.

This problem of error accumulation serves to emphasise the importance of using an accurate model. Nevertheless the Time Factor model offers significant improvement in the accuracy of smoke transport time prediction. The methods for estimating smoke transport time published by other researchers, notably Taylor (1984) and Notarianni (1988), that are based upon the average velocity (which is constant throughout each pipe segment), rather than core velocity (which varies significantly throughout each pipe segment as illustrated in Figure 7.1), would result in larger errors. For example if average velocity had been adopted in Figure 7.2, the cumulative time would be $11sec$ rather than $7sec$.

7.3 THE IMPACT OF BENDS

It was discovered in Chapter 5 that the flow regime is completely disturbed by the use of one bend. The impact of additional bends (or sampling holes) in close proximity has diminishing effect. For this reason, the worst-case situation is obtained by placing the bends and sampling holes at maximum separation. This is achieved by placing one bend in the middle of each pipe segment.

The inclusion of a bend has a different effect from the inclusion of a sampling hole. Whereas both devices completely disturb the flow regime, in the case of a bend, the downstream flow rate is the same as the upstream flow rate. From the beginning of a segment, the core velocity will grow in the same manner as described in Figure 7.1, but upon reaching the bend (half-way along the segment), the core velocity will reset to the average velocity. Because there is no change in average velocity, the core velocity will then grow with the same profile as for the first half of the segment. This is illustrated in Figure 7.4.

By comparison with the no-bends case in Figure 7.1, we see in Figure 7.4 that the maximum core velocity attained at the end of each segment is not greatly altered by the use of bends. This is because, in the particular pipe configuration chosen, the straight pipe segments are sufficiently long for the core velocity to reach 85 to 99 % of its final value (depending on Reynolds number), but in the segments interrupted by bends, the core velocity can reach 79 to 106 % of its final value, due in some cases to the velocity humps identified in Figure 6.52.

To gain more insight into the effect of bends, the instantaneous core velocity along each pipe segment has been integrated to determine the progressive smoke transport time, in Figure 7.5. The transport times for both the straight pipe and that including bends are shown. It can be seen that there is a penalty of some 5% in transport time throughout the length of pipe.

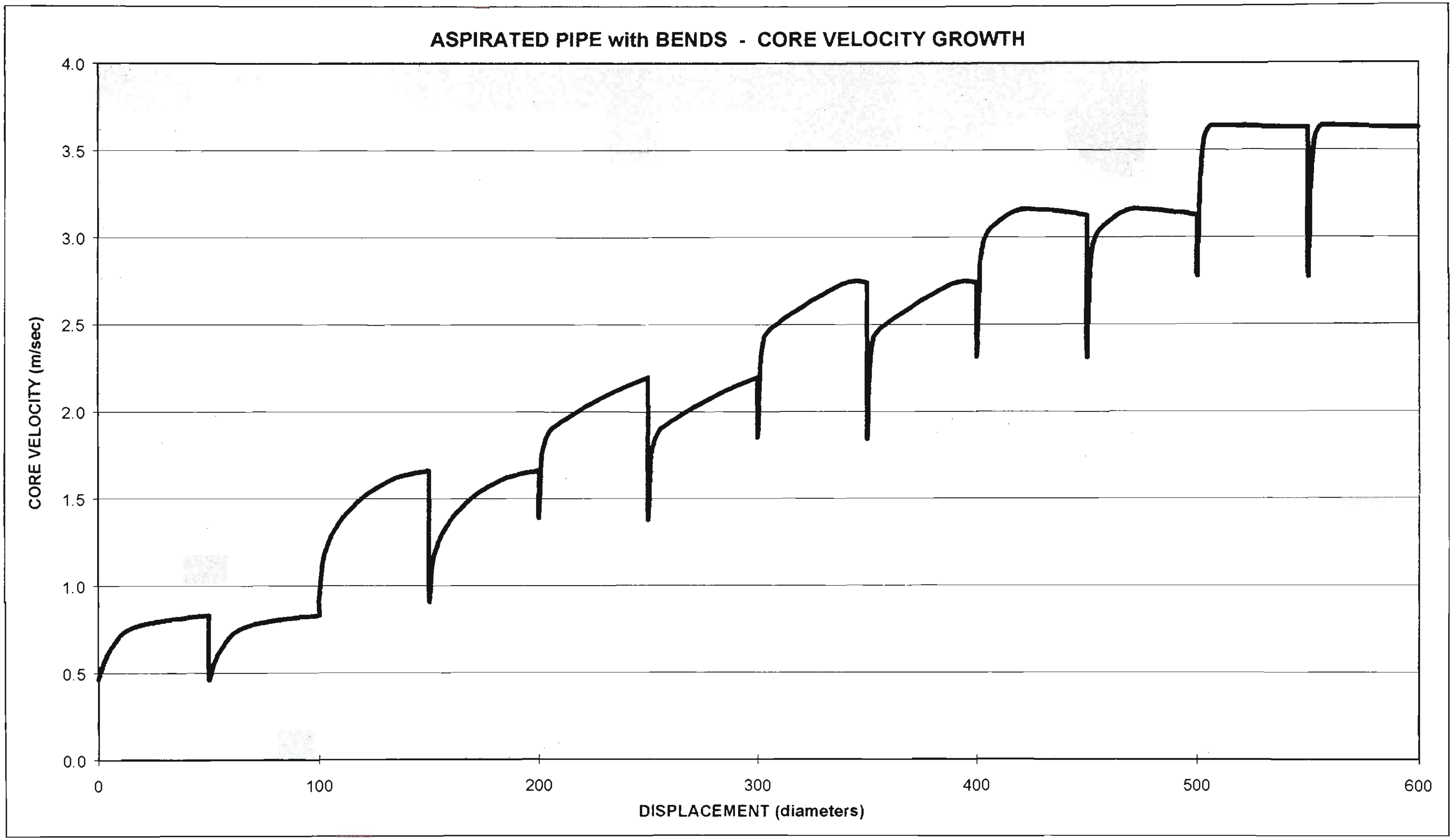

Figure 7.4 - Core velocity growth curve for an aspirated pipe with six sampling holes and bends

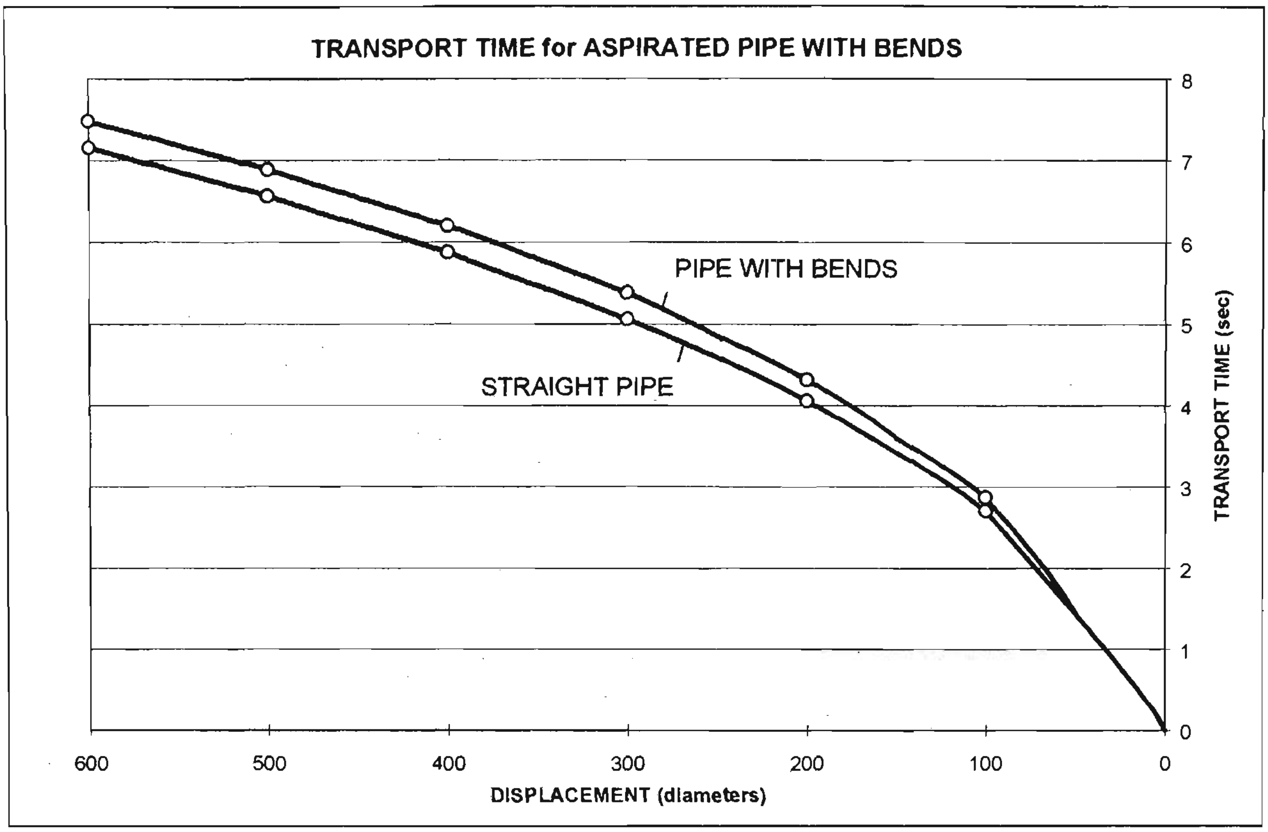

Figure 7.5 - Smoke transport times, with and without bends

In Figure 7.4 the average velocity increases in the direction from left to right, which is also the direction of air flow towards the detector. Figure 7.5 adopts the same convention whereby the air flow direction is also from left to right, which is achieved by reversing the horizontal axis scale. This facilitates a recognition of the smoke transport time from any individual sampling hole to the detector. The position of each hole is represented by a round hollow marker, and the pipe displacement is measured in the direction away from the detector. Thus, the smoke transport time in the case of the penultimate sampling hole for instance, located $500dia$ from the detector, is $6.6sec$ (straight pipe) or $6.9sec$ (with bends). Note that such times are relatively short, which is consistent with a pipe of only $12.8m$ total length (given that typical pipes run to $100m$ with smoke transport times of 60 to 90 sec).

7.4 - SMOKE CONCENTRATION EFFECTS

The foregoing analysis effectively assumes a smoke detector of extremely high sensitivity such that the arrival of, effectively, the first molecule of smoke is detected and reported instantaneously. Although it was understood that in practice, some delay should be incurred as a result of the need for a buildup in smoke concentration to reach a detectable density, this delay had yet to be quantified. Experience gained from initial experiments pointed to a factor of about 1.25 (time penalty of 25%), which will now be examined.

Consider the flow of smoke-laden air through a sampling hole and its entrainment into the pipe stream as illustrated in Figure 4.42. As stated in Chapter 1, at the early stages of pyrolysis or smoldering, the mass concentration of airborne products of thermal decomposition (smoke) is very low. At a typical concentration of 100μg/m^3 (about half-scale on a nephelometer), the visible smoke particulates represent only 0.000001% of the air mass per unit volume. At such low concentration, having emanated from a relatively low temperature source and after travelling some distance to the sampling hole, this smoke will have cooled to ambient temperature. Consequently the conditions of flow rate and pressure established for the sampling hole with clean air, are not significantly changed in the presence of such cool and diffuse smoke.

In transport phenomena (heat and mass transfer), a study of the mechanisms of momentum transport (Newton's law of viscosity) and energy transport (Fourier's law of heat conduction) would not significantly improve the model, whereas diffusivity and mass transport (Fick's law of diffusion) could be considered for modelling the mixing of smoke with the pipe stream, as a binary system. This law is often applied to fluids that are stationary or in laminar flows. Typical applications involve evaporation, boiling and gas diffusion. Turbulent flow regimes are handled by using time-smoothed equations, while new techniques would need to be developed for modelling disturbed, developing flows in laminar, transitional and turbulent flow regimes.

Fick's law also requires empirical data on the diffusivity of one species within another. Obtaining such data for a comprehensive range of types of smoke (i.e. a matrix of fuels, temperatures and oxygen availability) would represent a large project. Data available from fire safety research is relevant to high temperature fires, producing hot smoke and convection forces. More importantly, if prior knowledge of the smoke species is required for accurate modelling, then the behavior of the smoke detection system would be unpredictable in a real environment, because the fuel is rarely known in advance (i.e. rarely is a single material the source of risk or ignition). Moreover, Fick's law is based upon the density of the two species involved. The low concentration of smoke particulates due to pyrolysis or smoldering means that the two species (smoke and air) in the binary system have effectively the same density (within 1 part in 10^5), so the mixing phenomenon may need to be considered as a trinary system. Faced with such obstacles it was decided to proceed as follows.

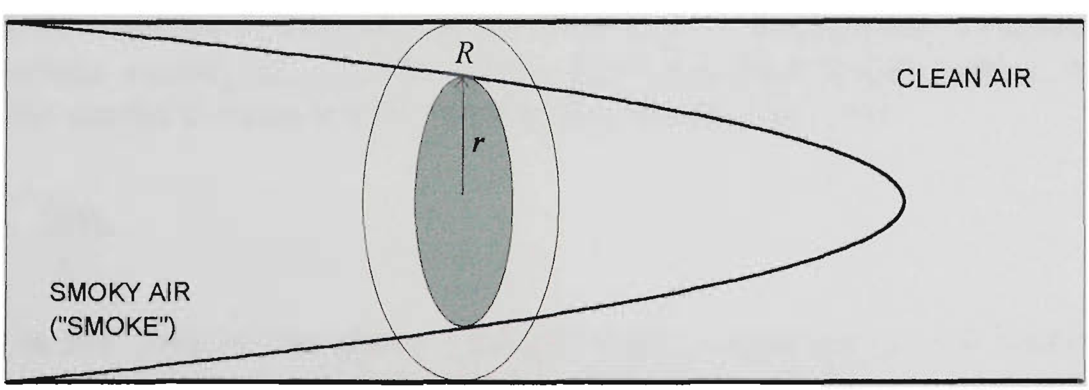

Figure 7.6 - Cross-section through a velocity profile assuming no mixing of smoke with clean air

Consider a laminar flow regime within a round pipe, in which the velocity profile builds towards a parabolic shape as shown in Figures 6.2 and 6.4. If for the purpose of discussion, we disregard any mixing of the smoke with clean air that previously filled the pipe, then smoke introduced at the far end of the pipe would be confined within the 3-D velocity profile "envelope", with that profile surrounded by clean air. In due course this smoke/air "boundary" would pass a stationary observer positioned to view the pipe cross-section well downstream. A small proportion of the smoke (confined within the central core of flow) would reach the observer quickly, in accordance with the core velocity which reaches twice the average velocity. The proportion of smoke passing the observer's cross-section would then build in accordance with the shape of the velocity profile.

Let the initial concentration of smoke introduced into the pipe be C_I. Downstream, as illustrated in Figure 7.6, the actual smoke concentration (C_S) at any cross-section along the velocity profile can be obtained from the initial smoke concentration (C_I), multiplied by the ratio of the circular cross-sectional area of the velocity profile (a_P), to the cross-sectional area of the pipe (A_P), as follows:

$$C_S = C_I \frac{a_P}{A_P} = C_I \left(\frac{r}{R}\right)^2$$

where r is the radius of the parabolic profile at any given displacement and R is the pipe radius. The smoke concentration in relative percentage terms is:

$$C_{s\%} = 100\left(\frac{r}{R}\right)^2 \qquad or \qquad r = R\left(\frac{C_{S\%}}{100}\right)^{\frac{1}{2}}$$

If we assume a large displacement whereby the laminar flow regime is fully-developed and the velocity profile is parabolic, then an equation for the velocity at a given radius is:

$$u_r = 2\,u_{avg}\left(1-\left(\frac{r}{R}\right)^2\right)$$

where, for example in the case of the $21mm$ pipe at a Reynolds number of 1320, the average velocity (u_{avg}) is $0.926 m/sec$. At a specified radial position, the time taken for smoke to travel the length of a pipe segment (L_{pipe}) is:

$$T_r = \frac{L_{pipe}}{u_r}$$

which in the case of the above example using a typical segment length of $4m$ equates to $2.16 sec$ at the core (where $r = 0$), i.e. $T_0 = 2.16$. We may now obtain the percentage increase in time (in excess of the time that would be taken for smoke within the core), for smoke located at a given radius to reach the end of the segment:

$$T_{r\%} \quad = \quad 100\,\frac{T_r}{T_0} \quad = \quad 100\,\frac{u_{core}}{2\,u_{avg}\left(1-\left(\frac{r}{R}\right)^2\right)} \quad = \quad \frac{100}{1-C_S} \quad \%$$

This also equates to the percentage increase in time required (the time penalty), for a given smoke concentration threshold to be reached at a given displacement.

In the case of a fully-developed turbulent velocity profile we can apply the Schlicting equation to the Nikuradse data at $\mathrm{Re} = 4000$ as discussed in relation to Figure 1.12 (instead of Prandtl's more-general one-seventh power law):

$$u_r \quad = \quad 1.29\,u_{avg}\left(1-\frac{r}{R}\right)^{\frac{1}{6}} \qquad \textit{so therefore:}$$

$$T_{r\%} \quad = \quad 100\,\frac{T_r}{T_0} \quad = \quad 100\,\frac{u_{core}}{1.29\,u_{avg}\left(1-\frac{r}{R}\right)^{\frac{1}{6}}} \quad = \quad \frac{100}{\left(1-\sqrt{C_S}\right)^{\frac{1}{6}}}$$

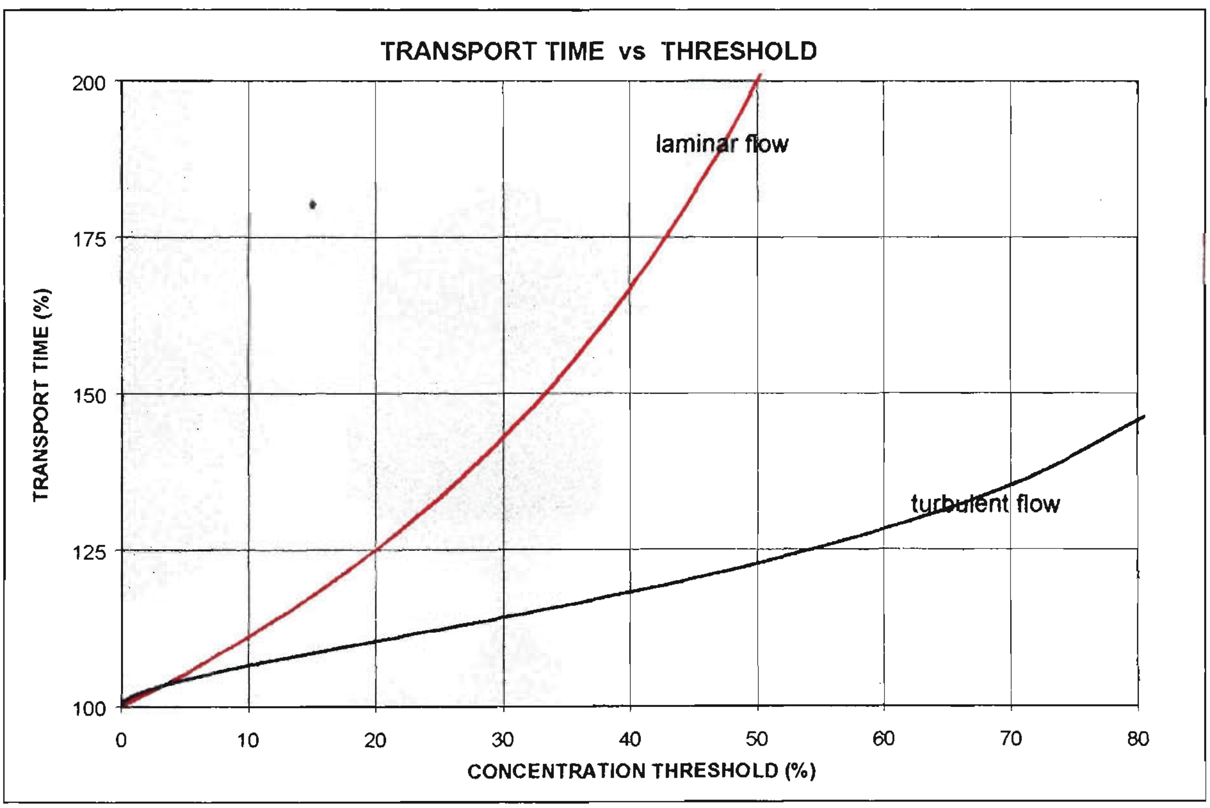

Figure 7.7 - Time penalty incurred by smoke concentration threshold

The graphs in Figure 7.7 use the above equations to show the percentage increase in transport time resulting from a given smoke concentration threshold, for fully-developed laminar or turbulent flow regimes. Here for example, it can be seen that a transport time of 125% (time penalty of +25%) occurs for a smoke concentration threshold of 20% in the case of laminar flow, or 54% in the case of turbulent flow. Although this analysis has yet to suggest why a timing discrepancy of specifically +25% should occur across the full range of applicable Reynolds numbers, it does suggest that the time penalty should be significant and could well be of the order of +25%.

There was no evidence of a reduction in sensitivity, with increasing distance of the smoke injection point from the detector. This would have implied progressive condensation or settling-out of smoke particles on the pipe walls en-route. Such an effect would only increase the above discrepancy (given that the turbulent flow regimes are closer to the detector).

Two assumptions were made in the analysis producing the graphs of Figure 7.7 - (a) that there is no mixing at the smoke/air boundary and (b) that the flow regime is fully developed. Firstly, in order to consider the effect of initially-disturbed, developing flow regimes, the LV data of Chapter 6 is revisited.

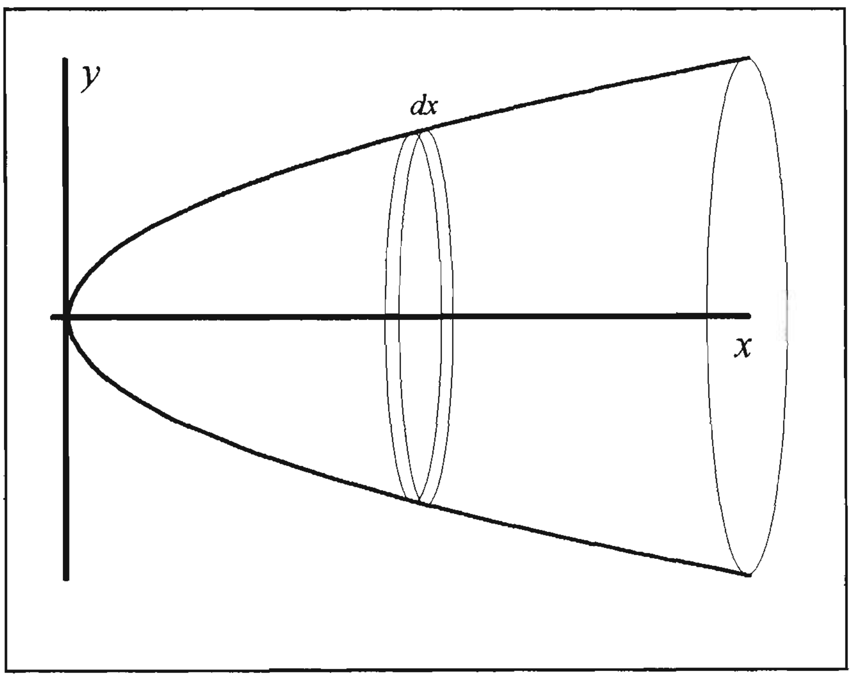

Figure 7.8 - Obtaining the solid of revolution of the parabolic volume

Selecting $\mathrm{Re} = 1320$ representing the middle set of results obtained for laminar flow, the velocity profiles at each displacement have been examined to develop equations of best fit to the data. It is understood that for conservation of mass (and incompressible flow), the contained volume under the curved 3-D surface of the velocity profile boundary, must have the same value at all stages of development (regardless of the surface shape). This volume can be determined from the solid of revolution. With reference to Figure 7.7 it is known that the volume of a solid of revolution (V_r) is obtained from:

$$V_r = \int_a^b \pi \ y^2 \ dx$$

where $y = f(x)$. In the case of fully-developed flow where the surface is parabolic, this function can be expressed as $y = R\ (u_{core}\ x)^{1/2}$ where in this case $u_{core} = 2\ u_{avg}$, so:

$$V_r = \int_0^1 \pi \ R^2 \left(u_{core}\ x\right)^{\frac{2}{2}} dx = \pi \ R^2 \ u_{core} \int_0^1 x \, dx = \frac{\pi \ R^2}{2} \ u_{core} = \pi \ R^2 \ u_{avg}$$

At the other extreme, in the case of plug flow at the pipe entry, the volume of the solid of revolution is a cylinder, where $y = R$ and where $u_{core} = u_{avg}$, so:

$$V_r = \pi \ R^2 \ u_{core} = \pi \ R^2 \ u_{avg}$$

which satisfies having the same volume as that of the parabolic profile. If all intermediate velocity profiles (each having a unique value of u_{core}) can be expressed as a power law (using the exponent n_x), then generally:

$$V_r = \int_0^1 \pi \ R^2 \left(u_{core}\ x\right)^{\frac{2}{n}} dx = \pi \ R^2 \ u_{core}^{2/n} \int_0^1 x^{2/n} \, dx = \frac{\pi \ R^2 \ u_{core}^{2/n}}{1 + 2 / n_x}$$

where for all values of u_{core} and n_x, conservation of mass and volume requires:

$$\frac{\pi \ R^2 \ u_{core}^{2/n}}{1 + \left(\dfrac{2}{n_x}\right)} = \pi \ R^2 \ u_{avg}$$

Now at each displacement, the value of u_{core} is known from the LV results of Chapter 6. Therefore, to maintain the requirement of a constant volume there is a unique value of the exponent, n_x, at each displacement until the point is reached where $n_x = n_\infty = n$ (effectively, beyond $x = 400dia$):

$$n_x = \frac{2}{\left(\dfrac{u_{core}^{2/n}}{u_{avg}}\right) - 1} \quad \text{where } n = 2 \text{ so:} \quad n_x = \frac{2}{R_u - 1}$$

Figure 7.9 illustrates the result of using the above equation to determine the value of the velocity profile exponent (n_x) at any given displacement, based upon the value of the core velocity ratio (R_u) obtained from the LV results. Note that both the exponent and the ratio asymptote to a value of 2 at infinity (effectively, again, beyond $400dia$).

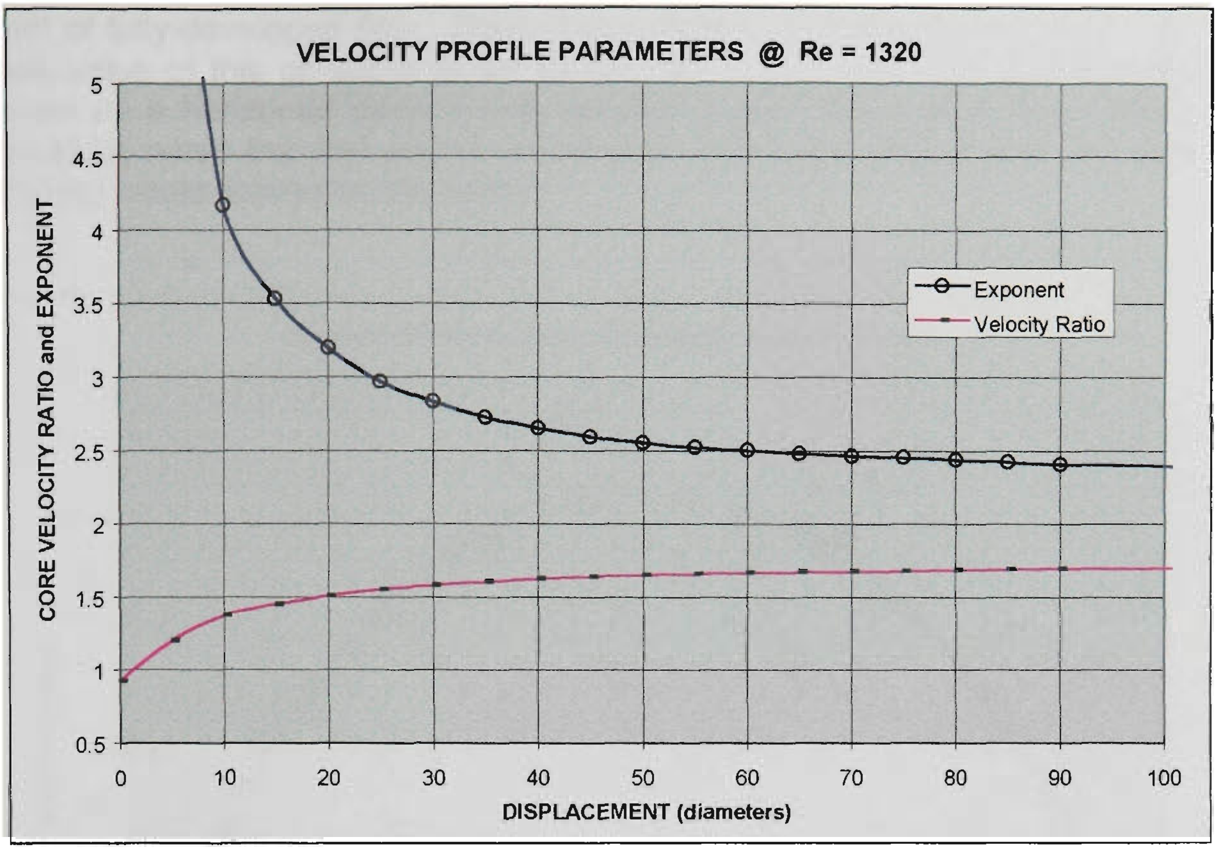

Figure 7.9 - Core velocity ratios and exponents applicable to a Universal power-law approximation to the developing velocity profiles at $\mathrm{Re} = 1320$

Having previously determined an equation for the velocity at a given radius in a fully developed laminar flow regime, a universal power law applicable throughout the developing stage of the regime can now be expressed as:

$$u_r = R_u\, u_{avg}\left(1 - \left(\frac{r}{R}\right)^{n_x}\right) = R_u\, u_{avg}\left(1 - \left(\frac{r}{R}\right)^{\frac{2}{R_u - 1}}\right)$$

where u_r is the velocity at radius r (R_u being a function of displacement, at the given Reynolds number). The curves generated from the above equation were compared with the LV results of Figures A6.2 (a) to (r) at each displacement. A good and consistent fit was achieved throughout the sets of data, particularly from 5 to 75*dia*, generally matching the dotted curves which represent the smoothed results. (It should be noted that the initial approach used for this analysis, was to determine curves of fit to the smoothed data. This led to a recognition that a power law equation could be applied universally, stimulating the above analysis.)

An advantage of the universal power law equation is that it can be used to generate complete curves that can fill-in the gaps in the LV data (especially near the pipe walls). The outcome of this work is presented in Figure 7.10, which includes the complete set of velocity profiles from 0 to 90*dia* in steps of 5*dia*. To include projections beyond 90*dia* would clutter the figure, except that the profile at 400*dia* (dashed parabola) has been included to indicate the shape at the nominal point of fully-developed flow. (Note that if Figure 7.10 were normalised then the peak value of this parabola would be 99% of 2 i.e. 1.98). The profile at $0dia$ is shown as a horizontal dashed line, indicating plug flow at the entry. Again, it should be noted that the volume under each 3-D curve (based upon the solid of rotation) would always be the same.

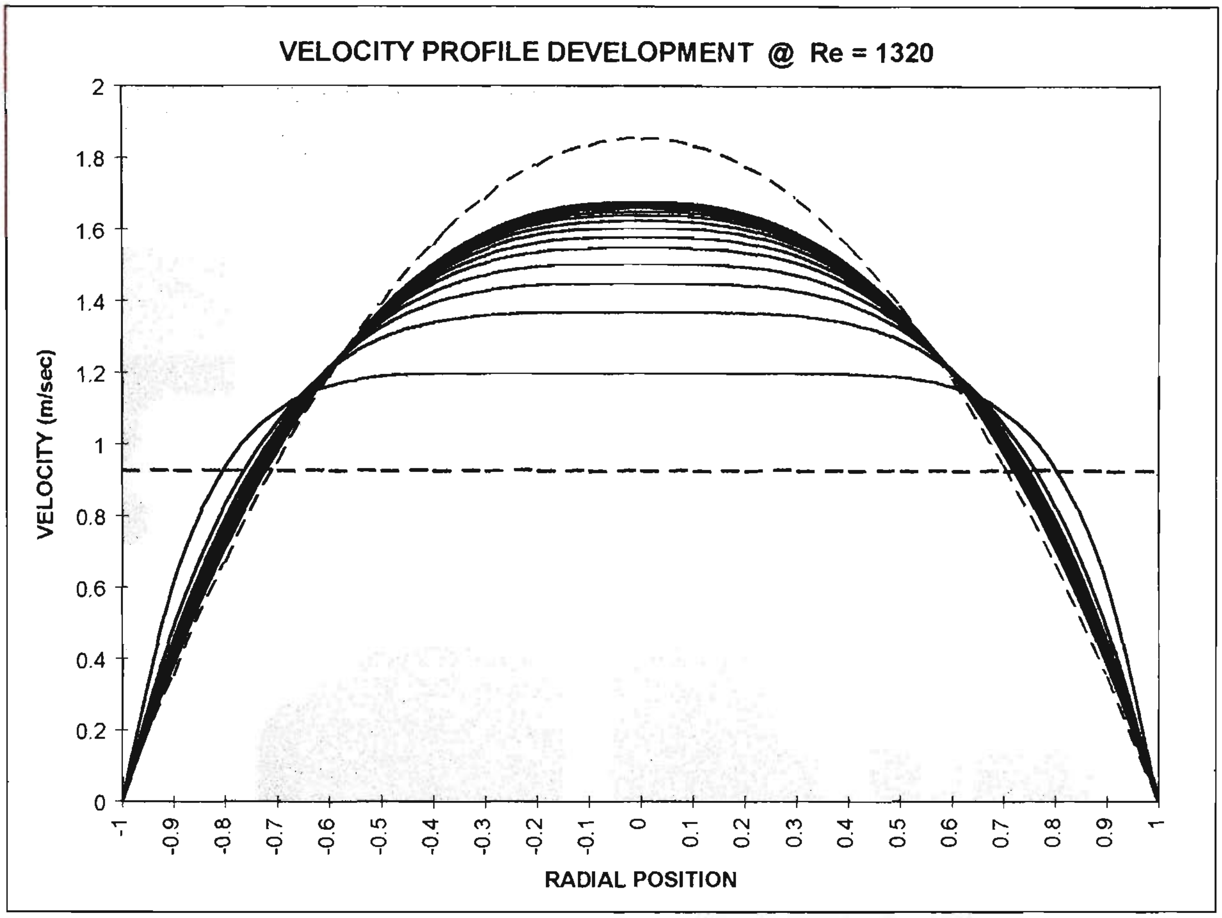

Figure 7.10 - Developing velocity profiles at $Re = 1320$ utilising the universal power law

To illustrate more-clearly the development of the velocity profile, Figure 7.11 presents the results of Figure 7.10 in a 3-D progression, using a finer horizontal resolution than was possible in Figure 6.15 (the LV results for $Re = 1320$).

The universal power law equation can now be applied to the analysis methodology of Figure 7.7, to obtain the time penalty at all stages of laminar flow regime development, as shown in Figure 7.12. In this presentation, each graph represents a particular displacement and we see that only a small time penalty is incurred at small displacements (this would seem obvious in absolute terms but here, we are discussing percentage terms). The small size of this penalty is because the velocity profile is relatively flat (or blunt) there. Nevertheless in real aspirated pipe systems, displacements of less than $100dia$ are rarely encountered.

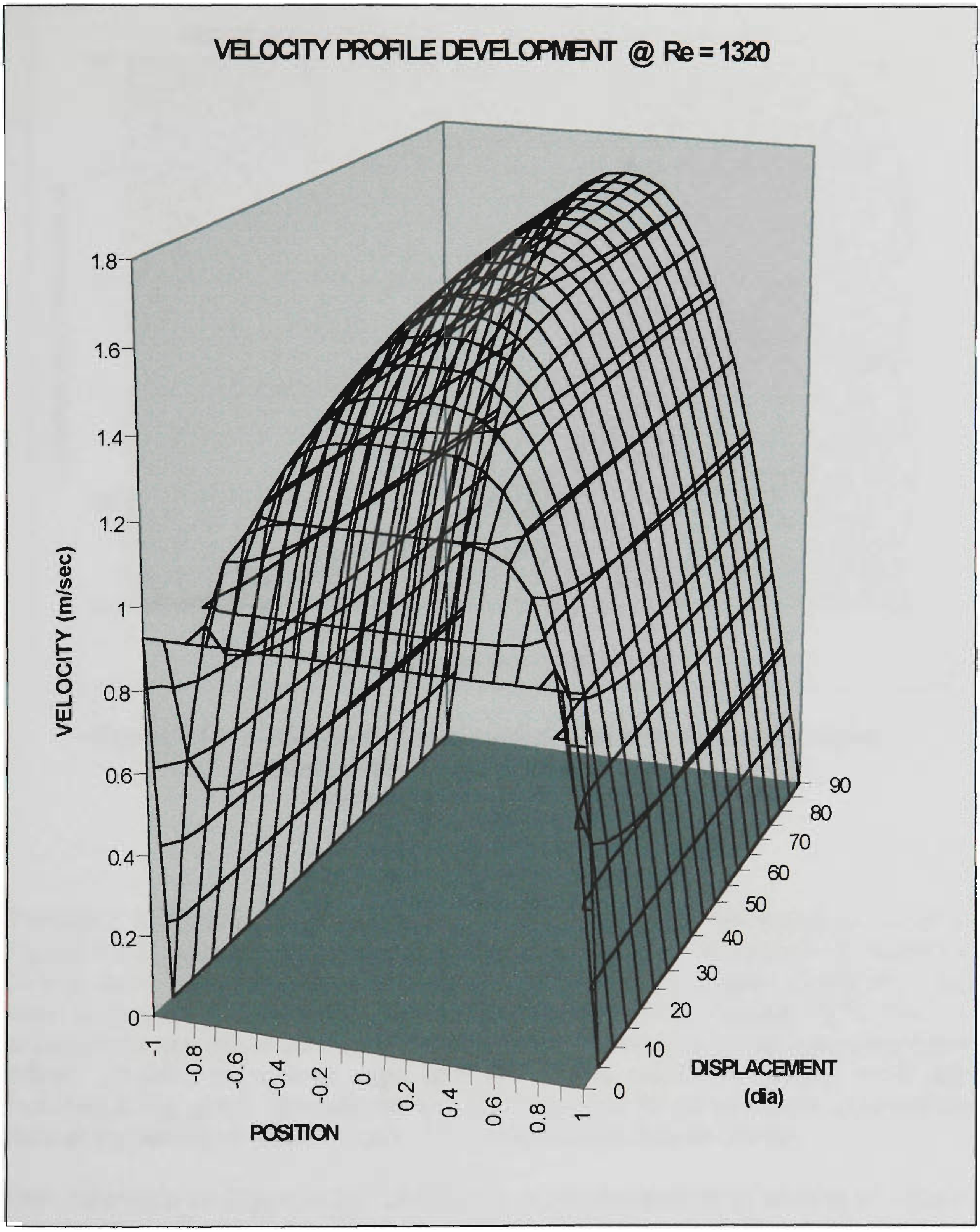

Figure 7.11 - A 3-D view of the velocity profile development over a displacement of $90dia$ (fully-developed at $400dia$) within a round pipe at $\mathrm{Re} = 1320$ based upon a universal power law (lateral) and the core velocity growth profile of Figure 6.38 (longitudinal)

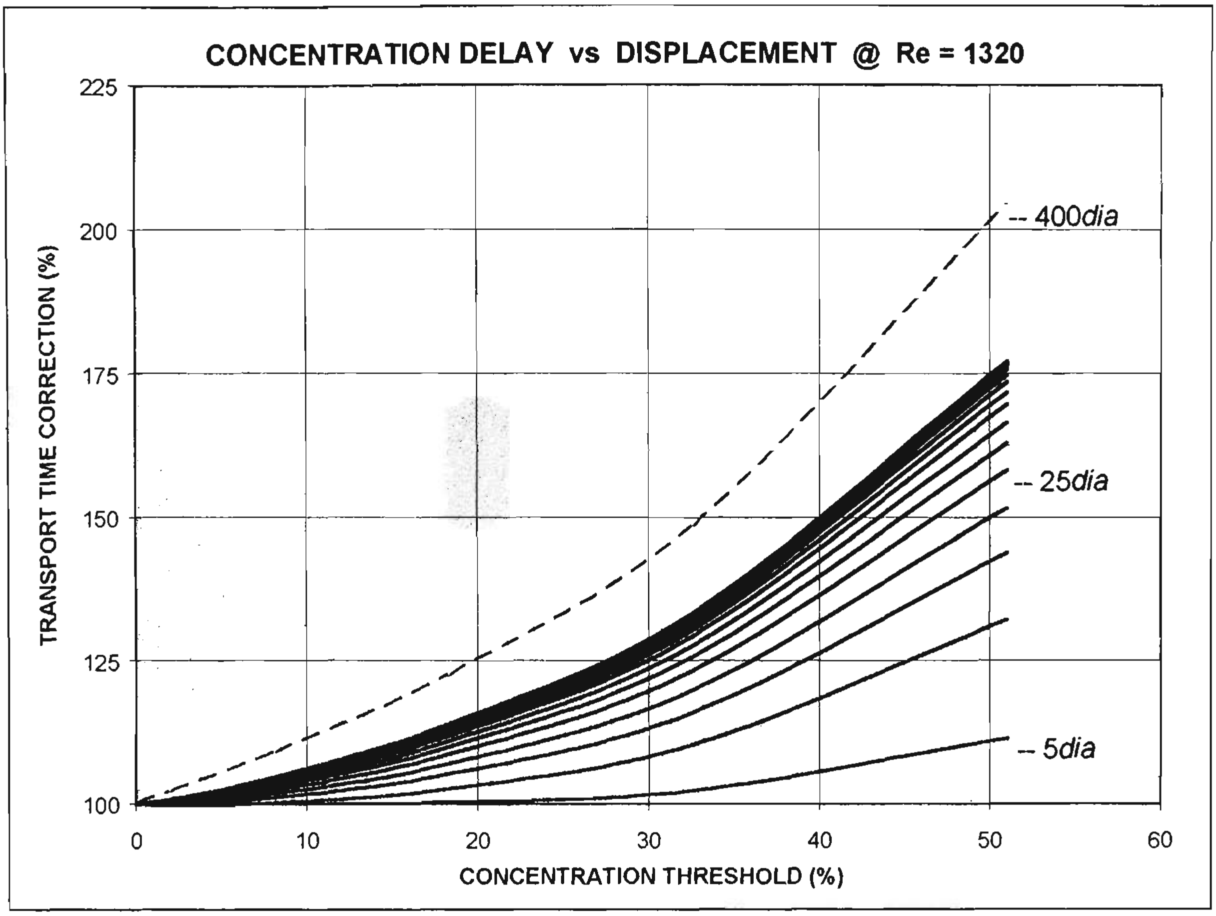

Figure 7.12 - Transport time correction (%) required due to smoke concentration detection threshold (%) for a developing laminar flow regime

Therefore the same results have been presented in an alternative manner in Figure 7.13, with each graph representing a particular threshold of detection (where such non-integers as 18.4, 32.7 or 51.0 % concentration result from the data conversion). To avoid clutter, the data points derived from the LV experiments are identified on the 51.0% graph only, beyond which, projections are made. These projections align with the known results at 400*dia*, which are included in the graph spreadsheet but not displayed (to do so would compact the data at the left-hand side of Figure 7.13 which would reduce clarity).

With reference to Figure 6.38, particularly at displacements in excess of 100*dia*, the results of Figure 7.13 could be expected to apply to all Reynolds numbers within the laminar flow region. In addition, in Figure 7.13 we see that after some 100*dia* the curves are almost flat and linear. For both of these reasons, at the displacements typically used in the field (100–400 *dia*), the required smoke concentration to reach the detection threshold would be essentially constant throughout the segments of pipe for which a laminar flow regime applies. Therefore, the use of a fixed correction factor (such as +25%) would be appropriate for the computer model.

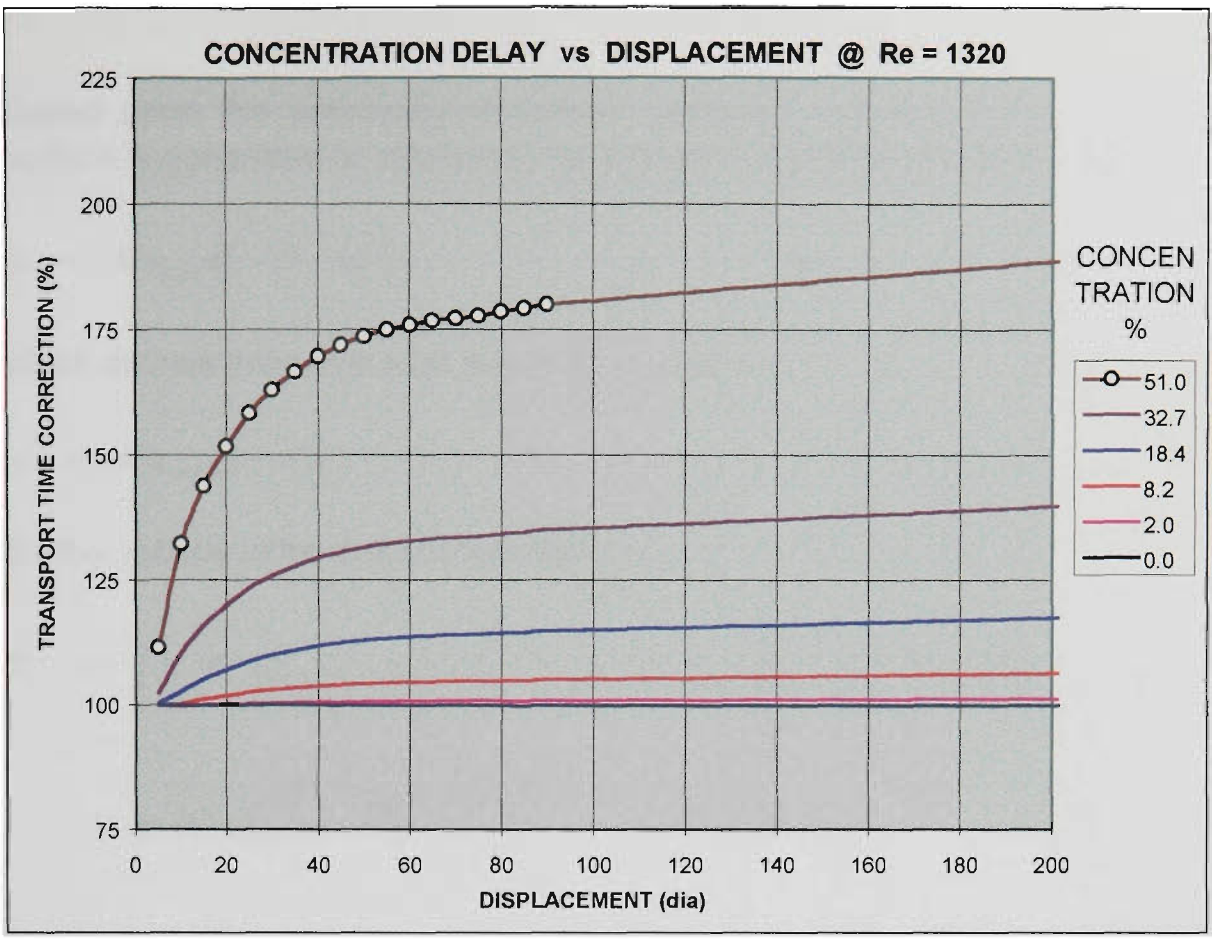

Figure 7.13 - Transport time penalty for developing laminar flow, expressed as a function of smoke detection threshold, at any displacement

Consider now the case of a turbulent flow regime. Proceeding as we did for the laminar flow case, Figure 7.14 illustrates the solid of revolution for the fully-developed velocity profile in a manner consistent with Figure 7.8.

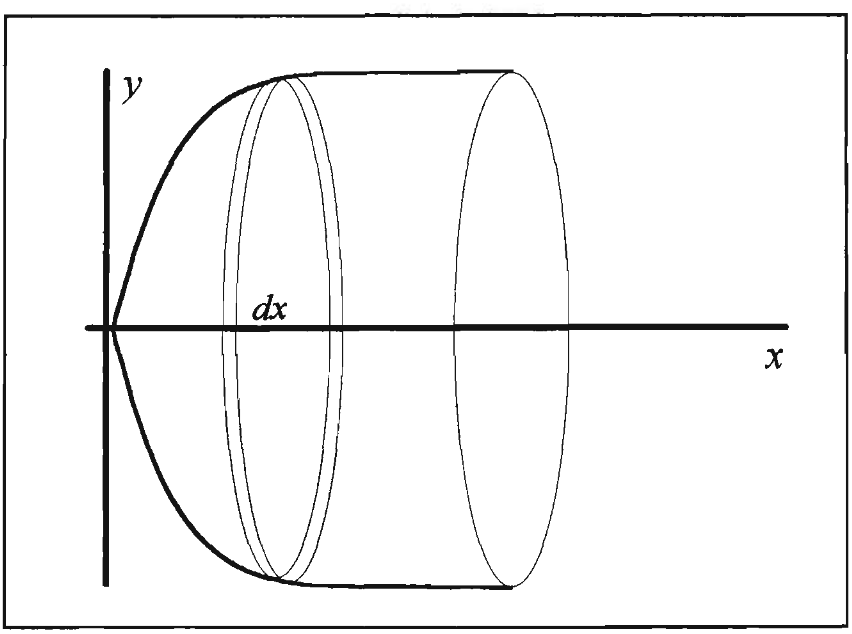

Figure 7.14 - Obtaining the solid of revolution for the turbulent flow profile

Based upon the previously-mentioned Schlicting equation for $\mathrm{Re} = 4000$, the surface is generated by rotation of the following equation about the x axis:

$$y = R\, u_{core} \left(1 - (1-x)^6\right)$$

which defines the same area above the x axis as:

$$y = R\, u_{core} \left(1 - x^6\right)$$

So the volume of the solid of revolution is:

$$V_r = \int_0^1 \pi\, R^2\, u_{core}^2\, (1-x^6)^2\, dx = \pi\, R^2\, u_{core}^2 \int_0^1 \left(1 - 2x^6 + x^{12}\right) dx$$

$$= \pi\, R^2\, u_{core}^2 \left[x - \frac{2x^7}{7} + \frac{x^{13}}{13}\right]_0^1 = 0.791\, \pi\, R^2\, u_{core}^2$$

For conservation of mass, and expressing in general terms for any value of n:

$$V_r = \pi\, R^2\, u_{core}^2 \left(1 - \frac{2}{n+1} + \frac{1}{2n+1}\right) = \pi\, R^2\, u_{avg}$$

$$\frac{u_{avg}}{u_{core}^2} = 1 - \frac{2}{n+1} + \frac{1}{2n+1} = \frac{(n+1)(2n+1) - 2(2n+1) + (n+1)}{(n+1)(2n+1)}$$

$$= \frac{2n^2 + 3n + 1 - 4n - 2 + n + 1}{(n+1)(2n+1)} = \frac{2n^2}{2n^2 + 3n + 1}$$

$$\frac{u_{core}^2}{u_{avg}} = \frac{2n^2 + 3n + 1}{2n^2}$$ so if $n = 6$ then $$u_{core}^2 = 1.264\, u_{avg}$$

Since $u_{core} = 1.29\, u_{avg}$ at $\mathrm{Re} = 4000$ (when $n = 6$) then:

$$\frac{u_{core}^2}{u_{core}} = \frac{1.264\, u_{avg}}{1.29\, u_{avg}} = 0.980 \quad (= u_{core})$$

So we obtain the velocity ratio in terms of the velocity exponent thus:

$$R_u = \frac{u_{core}}{u_{avg}} = \frac{2n^2 + 3n + 1}{0.980 * 2\, n^2} = \frac{2n^2 + 3n + 1}{1.96\, n^2}$$

Obtaining n in terms of the known core velocity ratio is implicit in the above equation which requires an iterative computation. Figure 7.15 presents the results of using the above equation to obtain a range of exponent values, enabling an equation to the curve of best fit to be developed, thereby to enable the exponent value to be obtained explicitly:

$$n \;=\; -209.23\,R_u^3 + 893.71\,R_u^2 - 1282.8\,R_u + 622.73$$

So, provided that the velocity profile can be described by an inverse-power law curve of the form proposed by Schlicting ($u_{core} = u_{avg}\,(r/R)^{1/n}$), we now have an equation that can provide the value of the velocity profile exponent, given the value of the core velocity ratio obtained from the LV results of Chapter 6. Figure 7.16 shows the form of the equation for a range of values of core velocity ratio with the associated values of exponent necessary for the conservation of mass.

However, to consider the velocity profile at intermediate displacements is rather more complex than was the case for laminar flow because of the boundary layer transition which occurs at about $16dia$ (see Figure 6.38 and Table 6.1). Up to this point, the velocity profile should be similar to the laminar flow case. The LV results (Figures A6.6 (a) to (o)) indicate a gradual change in lateral profile beyond $30dia$ until about $100dia$, where the profile is fully developed.

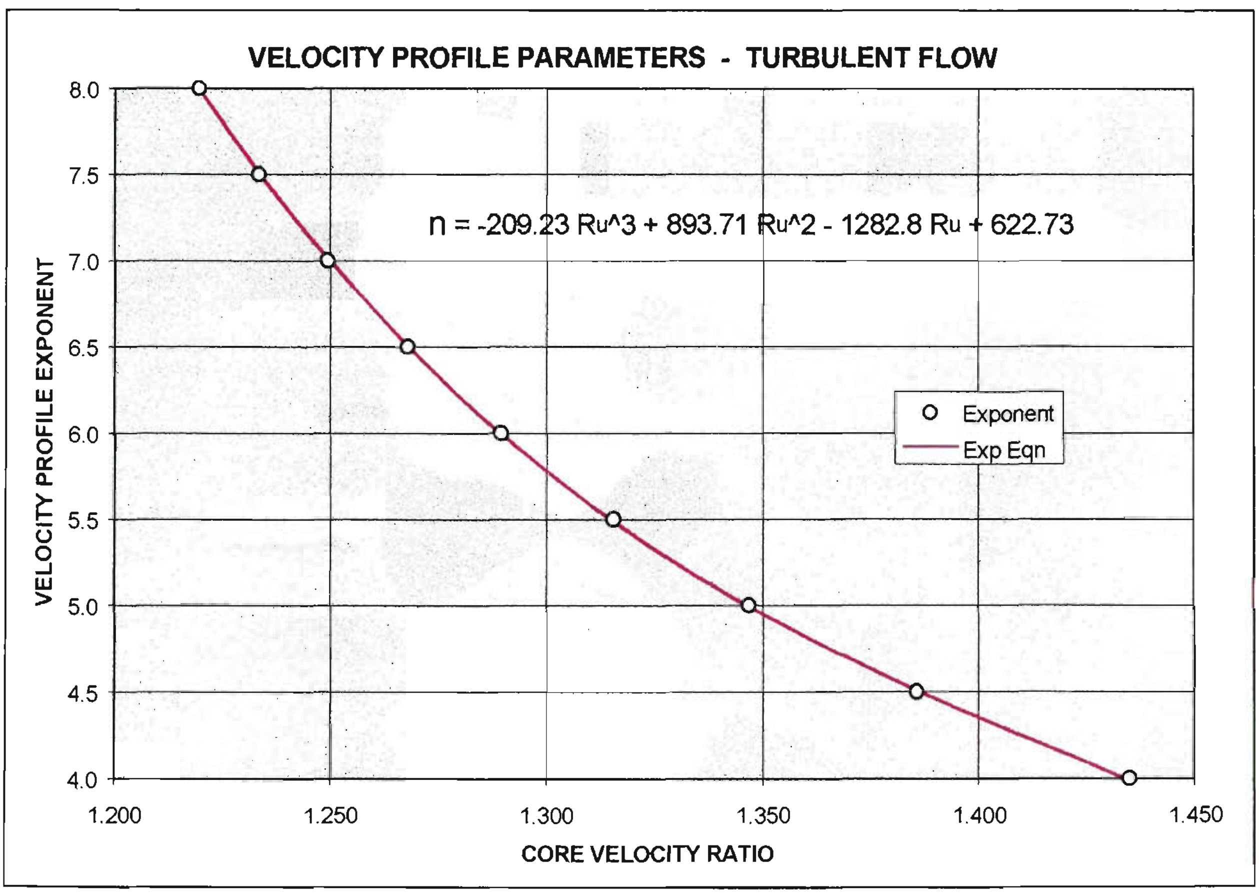

Figure 7.15 - Obtaining the lateral velocity profile exponent explicitly from the longitudinal core velocity ratio data, for turbulent flow regimes

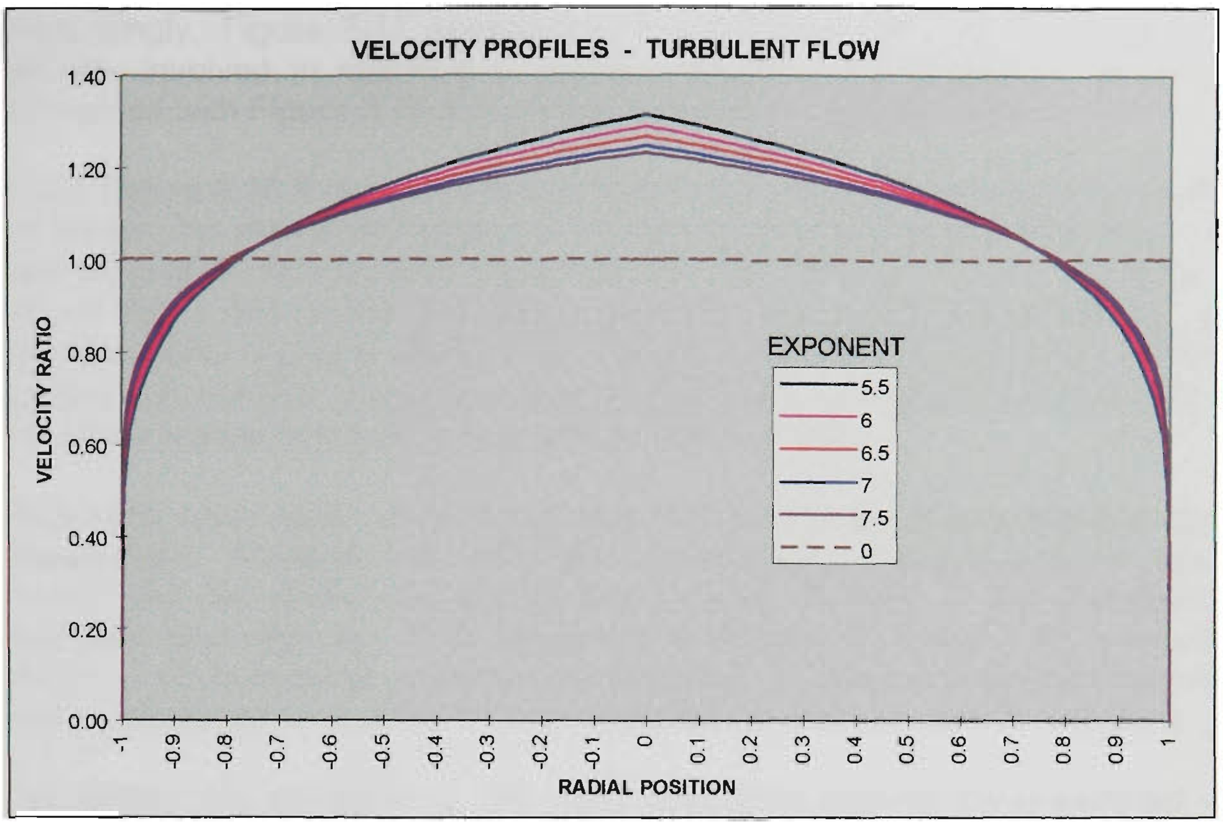

Figure 7.16 - Turbulent velocity profiles based upon an inverse power law

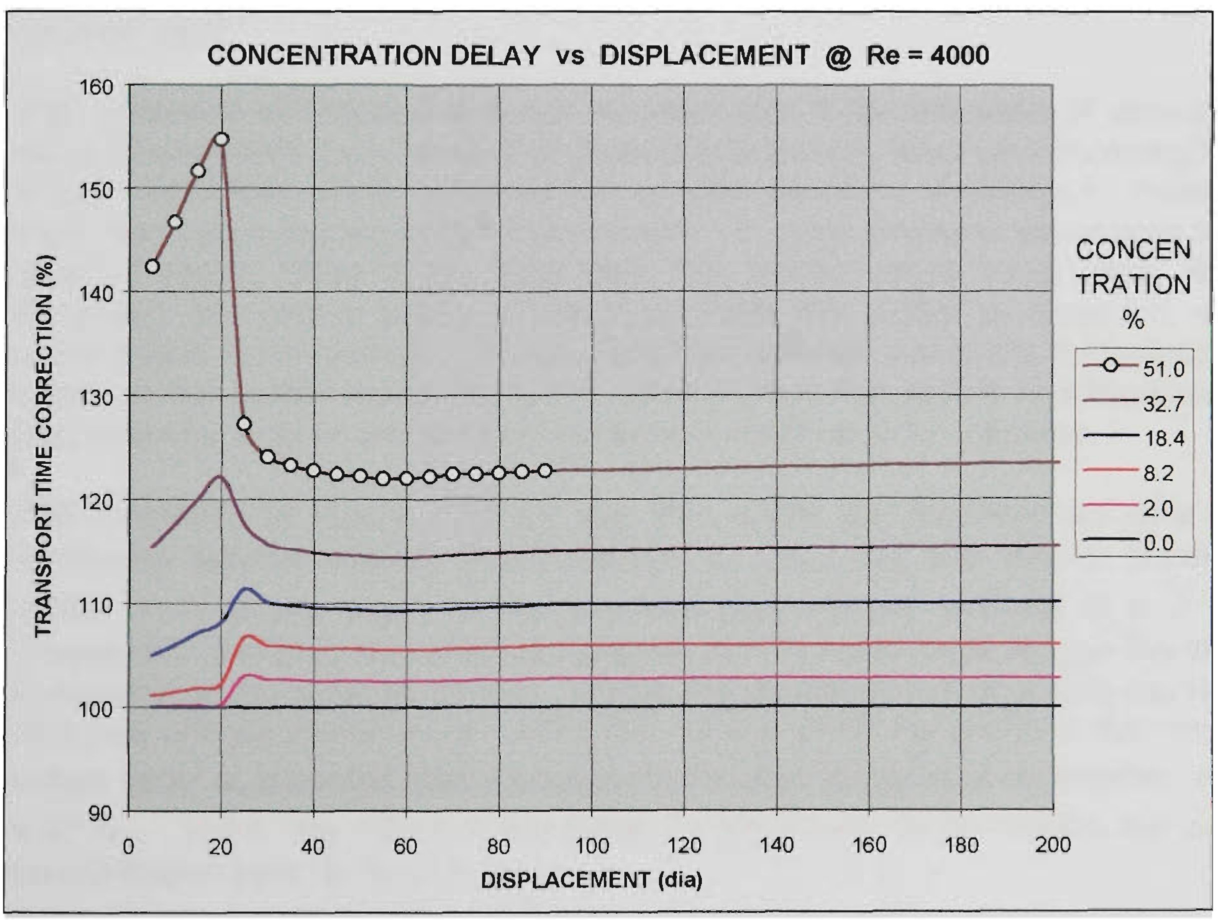

Figure 7.17 - Transport time penalty (%) for turbulent flow, expressed as a function of smoke detection threshold (%), at any displacement

Accordingly, Figure 7.17 presents an indication of the smoke transport time penalty involved in reaching a required smoke concentration. This is to be compared with Figure 7.13 and similar conclusions can be drawn.

From Figure 6.38 it can be expected that, particularly at displacements in excess of $100 dia$, the results of Figure 7.17 would apply to all Reynolds numbers within and beyond the flow transition region ($2000 < \mathrm{Re} < 4000$ *approx.*). In addition, after about $100 dia$ the curves are almost flat and linear. For these reasons, at the displacements typically used in the field (100-400 *dia*), the minimum detectable smoke concentration would be essentially constant throughout the pipe segments for which a transitional or turbulent flow regime applies.

Therefore, once again, we can conclude that the use of a fixed correction factor is appropriate. However it is not clear that the <u>same</u> correction factor (such as +25%) can be applied throughout the laminar, as well as the transition and turbulent flow regimes. With reference to Figures 7.13 and 7.17, a correction factor of +25% requires a smoke concentration of 25% in the laminar flow region but a concentration of about 53% in the transition and turbulent flow regions.

To resolve this discrepancy, the other simplifying assumption is revisited - that essentially no mixing takes place between the smoke and the clean air at the 3-D boundary of the velocity profile. Bird, Stewart and Lightfoot (1994 p630) note that turbulent eddies will hasten diffusion by promoting the rapid exchange of species in a manner analogous to convection, so mixing in disturbed and developing flows could be rapid.

With reference to Figure 7.6 it can be seen that if (for the sake of discussion) radial mixing takes place only at a given displacement, then the concentration of smoke within that whole cross-section of pipe would be unchanged. However, there may be an impact further downstream - if some smoke is transferred to the clean-air region close to the pipe wall, this smoke would travel more slowly. Moreover, this smoke would be replaced inside the profile by clean air, which would travel more quickly. These combined effects, occurring throughout the length of the profile would dilute the smoke within the profile and increase the time taken for a given smoke concentration to build up at the detector.

With reference to Figure 7.18 we see that, within the displacement of a fully-developed laminar velocity profile (where $u_{max} / u_{avg} = 2$), the volume inside the profile ($\pi R^2 u_{avg}$) is equal to half the total pipe volume involved ($2 \pi R^2 u_{avg}$). Therefore in the limit, the effect of complete mixing would be to reduce the smoke concentration by a factor of two. Within the displacement of a fully-developed turbulent velocity profile at $\mathrm{Re} = 4000$, the volume inside the profile is the same as before ($\pi R^2 u_{avg}$), but the total pipe volume involved is significantly smaller, at $1.29 \pi R^2 u_{avg}$. Here, the effect of complete mixing would be to reduce the smoke concentration by a factor of 1.29.

Therefore, recalling the above discussion with reference to Figures 7.13 and 7.17, then to achieve the smoke transport time correction of +25% in the case of laminar flow would require a smoke concentration of $2*25\% = 50\%$, while in the case of turbulent flow the required concentration would be 1.29*53% = 68%. Although these results are not identical, they are of similar magnitude.

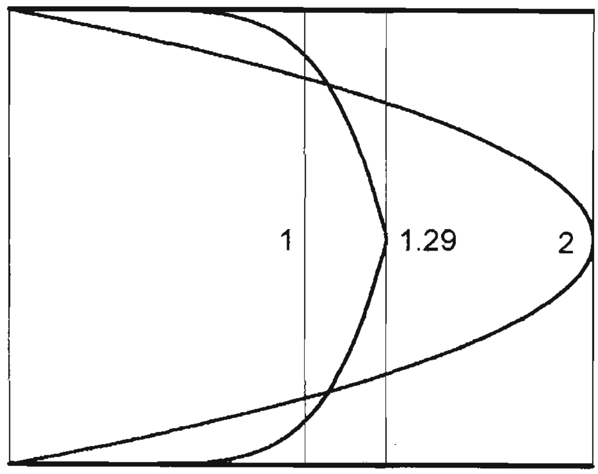

Figure 7.18 - Relative volumes within velocity profiles

Conversely, by inspection it can be seen that if a +25% time penalty is incurred as a result of smoke concentration within a laminar flow regime, then the same concentration within a turbulent flow regime should involve a +20% time penalty. So the gap is now reduced to 5% and is becoming insignificant.

Finally, this remaining gap can be seen as virtually closed, upon recognition that in most systems, the Reynolds number rarely exceeds 3200, well below the figure of 4000 for which the +20% correction could be expected to apply.

Although analysis of the effect of mixing could now proceed by considering the case of developing flow regimes, this would produce similar results to the above and it is already clear that there is a basis for adopting a fixed correction factor throughout the system. As discussed in Chapter 9, experiments have revealed that a figure of +25% is appropriate for the type of smoke test employed - using the Underwriters Laboratories (UL) approved synthetic smoke dispenser which through repeated experiments has been found to deliver smoke with a density of adequate consistency for the measurement (or classification) of smoke transport time. A large number of systems in the field are tested in this manner (accepted benchmark). However, it would be prudent to allow for manual adjustment of this figure within the system modelling software, to account for different test methods.

7.5 FRICTION FACTOR DEVELOPMENT

It is evident from an understanding of Chapters 5 and 6 that with initially-disturbed flows, the flow regime is not fully developed until a displacement of some 100 to 400 *dia* (depending upon the Reynolds number), and that the pressure drop per unit length is subject to change throughout this development region. Consequently, until the flow regime is fully developed, the pressure drop (and friction factor) along a straight pipe will vary. Because in an aspirated pipe system the flow regime is repeatedly disturbed at many positions, the dynamic nature of the friction factor could give rise to errors in calculating the pressure distribution throughout the pipe system, affecting the flow rate through sampling holes and the overall system operating point.

Sparrow, Lin and Lundgren (1964) have used momentum equations to analyse the velocity growth profile for laminar flow development and have extended this analysis to cover the incremental pressure drop throughout that region. They state that the pressure drop can be conveniently represented as a sum, the first term of which corresponds to a fully-developed flow and the second term of which is a correction for the effects of the velocity profile development. They propose the following equation (expressed in current terminology):

$$\frac{\Delta P}{\frac{1}{2}\,\rho\,u_{pipe}^{2}} \;=\; f\,\frac{x}{D_{pipe}} + K(x) \;=\; 16\,\frac{x\,/\,R_{pipe}}{u_{pipe}\,R_{pipe}\,/\,k} + K(x)$$

If the correction term $K(x)$ is ignored, this equation will be recognised as the Darcy-Weisbach equation, transposed in order to produce dimensionless terms, and with f then set to 64/Re. It should be noted that the important feature of <u>any</u> such equation, is that the transient term, in this case $K(x)$ must asymptote to zero once the steady-state condition is reached (beyond the effective development region). This should be true whether the transient term is initially negative or positive - its influence disappears upon completion of the transient condition. However, the equation for $K(x)$ proposed by Sparrow et al. is:

$$K(x) \;=\; \frac{4}{3} + \sum_{i=1}^{\infty} \frac{8}{\alpha_i^2}\left(e^{\alpha_i^2\,X} - 3\right)e^{\alpha_i^2\,X}$$

where the eigenvalues α_i are roots tabulated within their paper and derived from other equations involving a more detailed discussion than is warranted here. This pressure-drop increment has been evaluated numerically and is presented in Figure 7.19, reaching a final value of 1.24. Sparrow et al. report that this result is in good general agreement with the results of Langhaar (1942), Atkinson and Goldham (1938) when expressed in equivalent terms, although their final values are 1.41 and 1.28 respectively.

The results as presented show that the increment rises from an initial value of zero and asymptotes to a final value, which seems in contradiction to the requirement of a transient equation as noted above. Moreover, the fact that this equation rises rather than falls toward its final value, seems in contradiction to the current results which consistently indicate that the friction factor (and pressure drop) is higher during the development phase. However, upon interpretation of the equations it becomes clear that the friction factor may be determined as the sum of two parts in which f_e is the transient, entry component:

$$f \;=\; f_e + f_\infty \;=\; \frac{K(x)}{x\,/\,D_{pipe}} + \frac{64}{\mathrm{Re}}$$

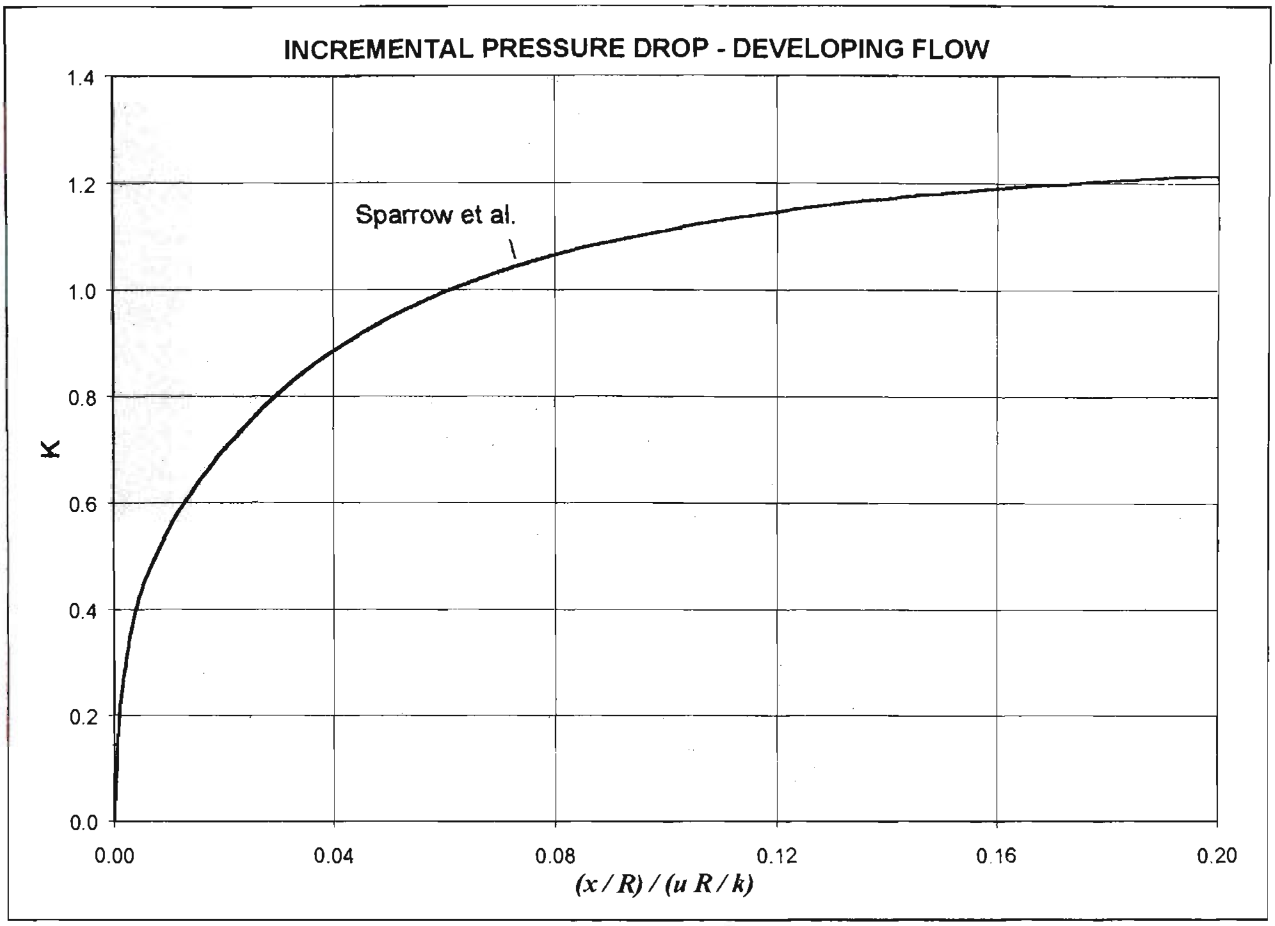

Figure 7.19 - Incremental pressure drop for developing flow (Sparrow et al. 1964)

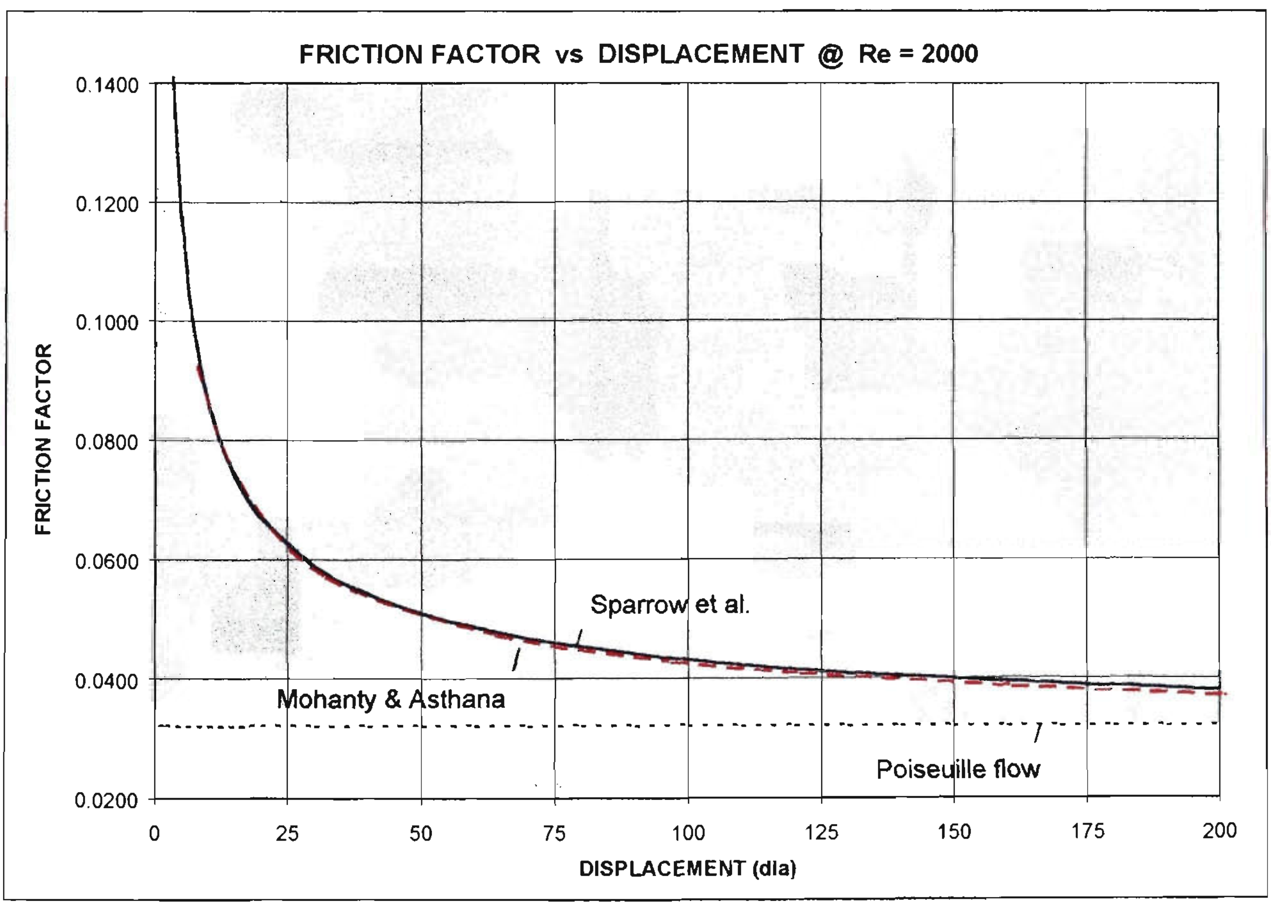

Figure 7.20 - Friction factor development at Re = 2000

Figure 7.20 presents the outcome of using this equation for $\mathrm{Re} = 2000$, where we see that the friction factor development profile is of the broadly anticipated shape. Included for reference is the final value (dotted line) indicating the friction factor applicable beyond the entry length, and to which the curve asymptotes.

Sparrow et al. express concern that experimental data on pressure drop in a developing flow appear to be surprisingly scarce, the only suitable data being available from Shapiro et al. (1954), with which the agreement is considered good. However, they report there is a wide spread of measured values for fully-developed flows by various researchers. As a consequence of the uncertainty in these data, Sparrow et al. express the view that it is difficult to make a clear appraisal of the various analytical predictions. In comparing their velocity growth results favorably with measured data, Sparrow et al. cite Pfenniger (1952) as having been able to maintain laminar flow conditions for a *pipe* Reynolds number as high as 50,000. Clearly the calculations and the measured data are applicable to idealised conditions.

More-recently, Mohanty and Asthana (1978) have published a more-detailed analysis in which the entrance region is divided into two parts - the inlet region and the filled region (or fully-viscous region, after Shingo 1966). The former is completed where the boundary layer reaches the pipe centre, but they find that Poiseuille flow (a truly parabolic velocity profile) is not reached until completion of the latter, filled region. At $\mathrm{Re} = 2000$ the length of the entrance region is $72dia$ whereas the filled region is not completed until $300dia$. These lengths are directly proportional to Reynolds number.

Mohanty and Asthana state that boundary-layer equations are valid in the inlet region, while full Navier-Stokes equations have to be applied in the filled region. Their dimensionless term used to express the displacement is: $\xi = x \,/\, \mathrm{R}\ \mathrm{Re}$ which, when compared with that of Sparrow et al., namely: $(x \,/\, \mathrm{R}) \,/\, (u\ \mathrm{R} \,/\, k)$, produces values of half the magnitude (because of substitution of radius for diameter in Re). Mohanty and Asthana's results also relate to the alternative set of values commonly used for friction factor, in which Poiseuille flow is expressed as $f = 16/\mathrm{Re}$ rather than $f = 64/\mathrm{Re}$, and their results are presented in dimensionless form. Taking these points into account, in Figure 7.20 the results obtained by Mohanty and Asthana for friction factor development are compared with those which were derived from Sparrow et al. at $\mathrm{Re} = 2000$, to confirm the current analysis.

Mohanty and Asthana verified their results experimentally at Reynolds numbers of 1875, 2500 and 3250, however, these do not describe transitional or turbulent flow regimes because the idealised flow conditions meant that laminar flow was maintained throughout.

Since all of the above results are based upon idealised (undisturbed) flow conditions, they can only be taken as a guide. For current purposes where it is required to represent completely-disturbed flows, descriptions of which have not been found in the literature, it will be necessary to rely upon current experimental resources.

To measure the change in friction factor per unit length accurately would require a pressure gauge of higher resolution, stability and accuracy than is currently available. The choice of $3000mm$ as the length for the test pipe in earlier experiments was in recognition of the need to generate sufficient pressure drop along the pipe, to produce reliable results at low flow rates. However, this length corresponds to a displacement of some $142dia$ and much of the flow regime development phase is encompassed within this distance. For this reason, instrumentation providing some 10 times greater resolution, enabling measurement steps in the order of $5dia$, would be required to produce reliable results, especially at flow rates as low as of $10 litre/min$. Since this is not practical another approach is needed.

It is likely that the core velocity growth curve, which defines the flow regime development, to some extent defines the development of the friction factor. This would provide an opportunity to estimate the dynamics of friction factor development in a manner that could possibly be verified experimentally, despite low resolution. For convenience a Reynolds number of 2000 is selected, because an equation of best fit to the core velocity growth (R_u = 2 - 0.655 e^(-d/113) if $n >$ 5) as shown on Figure 6.52 has been developed. On the initial assumption that the friction factor develops at approximately the same rate as the core velocity, then the friction factor development curve at $Re = 2000$ will be governed by:

$$f_d \approx f_0 - (f_0 - f_\infty)\left(1 - 0.655 e^{-d/113}\right)$$

where f_d is the friction factor at a displacement of d diameters, f_0 is at the seat of the disturbance (the start of the pipe segment) and f_∞ occurs where the friction factor has reached its final value (within 1%).

With reference to Figure 5.18 it was found that for a completely disturbed flow regime, the friction factor is 0.0425 (i.e. f_0) whereas in the case of fully-established steady flow it should fall to $f = 64/Re = 0.0320$ (i.e. f_∞). It is expected that the friction factor falls from its maximum value, to 0.0320 within the displacement of several hundred diameters, in accordance with the above equation as illustrated in Figure 7.21.

The experiment apparatus of Chapter 5 effectively provides the **average** friction factor within the $3000mm$ segment of pipe immediately downstream of the sampling hole. The figure of 0.0425 would be locally (instantaneously) correct, somewhere near the middle of this segment, namely at about $71dia$. Therefore the graph of Figure 7.21 has been adjusted so that the curve passes through $f =$ 0.0425 at $71dia$. It can be seen that this fixes the instantaneous value of the friction factor at the entry threshold, at 0.0619.

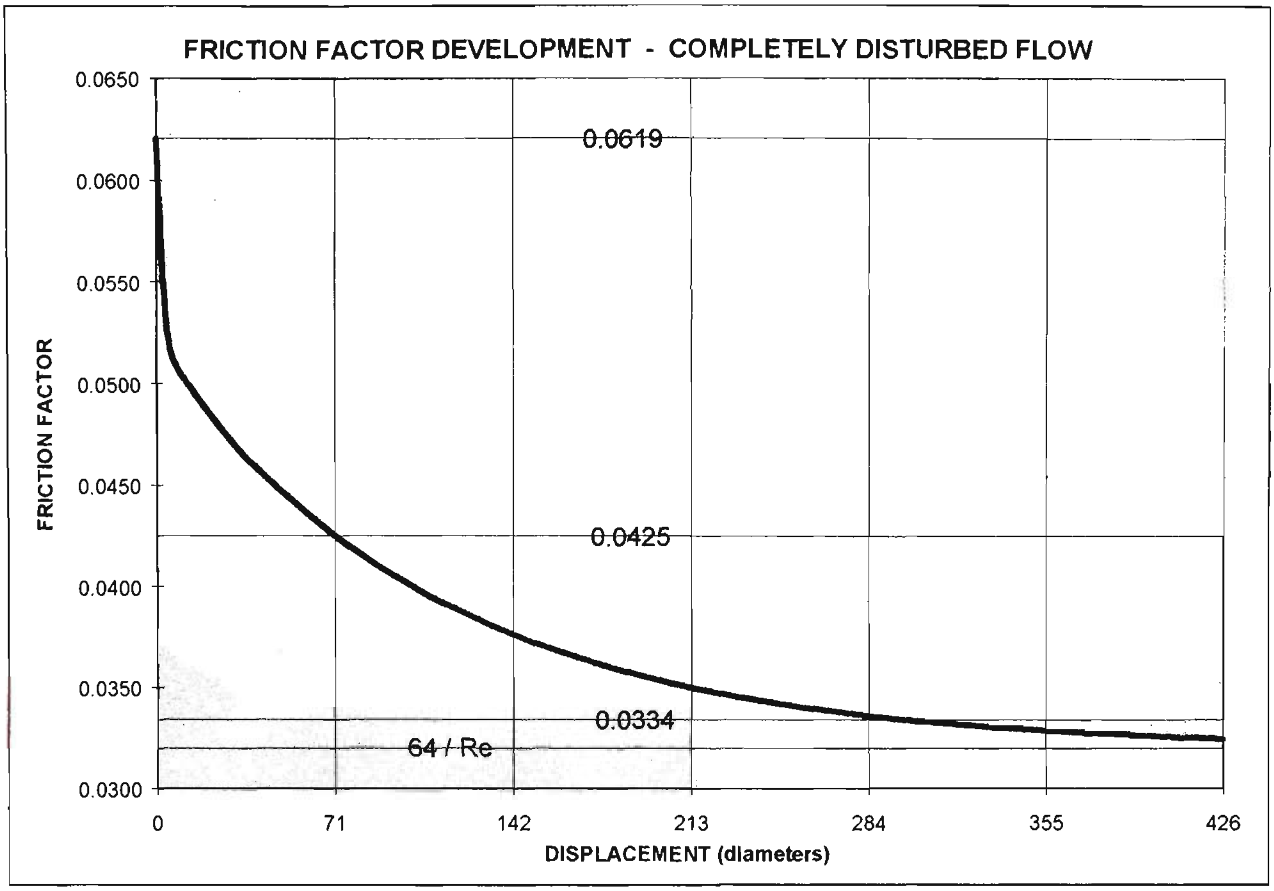

Figure 7.21 - Estimated friction factor reduction versus displacement for initially-disturbed flow at $Re = 2000$

Figure 7.21 represents the development of friction factor in the case of a flow regime that is initially disturbed completely. To consider the effect of lower levels of disturbance we refer to Figure 5.18 (at $Re = 2000$). Note that the disturbance level is defined volumetrically. That is, the flow rate of the disturbing induction jet from the sampling hole, is expressed as a percentage of the relatively undisturbed upstream flow rate. Therefore it is consistent to regard Figure 7.13 as the 100% disturbed case (100% of the air entering the segment is disturbed).

Disturbance	12-100%	6.7%	3.5%	2.5%	1.9%	1.3%	0.8%	0.0%
Friction Factor	0.0425	0.0421	0.0412	0.0401	0.0400	0.0398	0.0380	0.0334

Table 7.1 - Friction factor versus disturbance level averaged over first $142dia$ ($Re = 2000$)

The data of Figure 5.18 is presented for convenience in Table 7.1. It is expected that the disturbance level will dissipate in accordance with the curve of Figure 7.13 regardless of the level of initial disturbance (i.e. regardless of the starting-point on the curve, the remainder of the curve would be unchanged in shape). If the friction factor data of Table 7.1 is matched with the curve of Figure 7.21 for each of the disturbance levels, then we can obtain the curves for each disturbance level as shown in Figure 7.22.

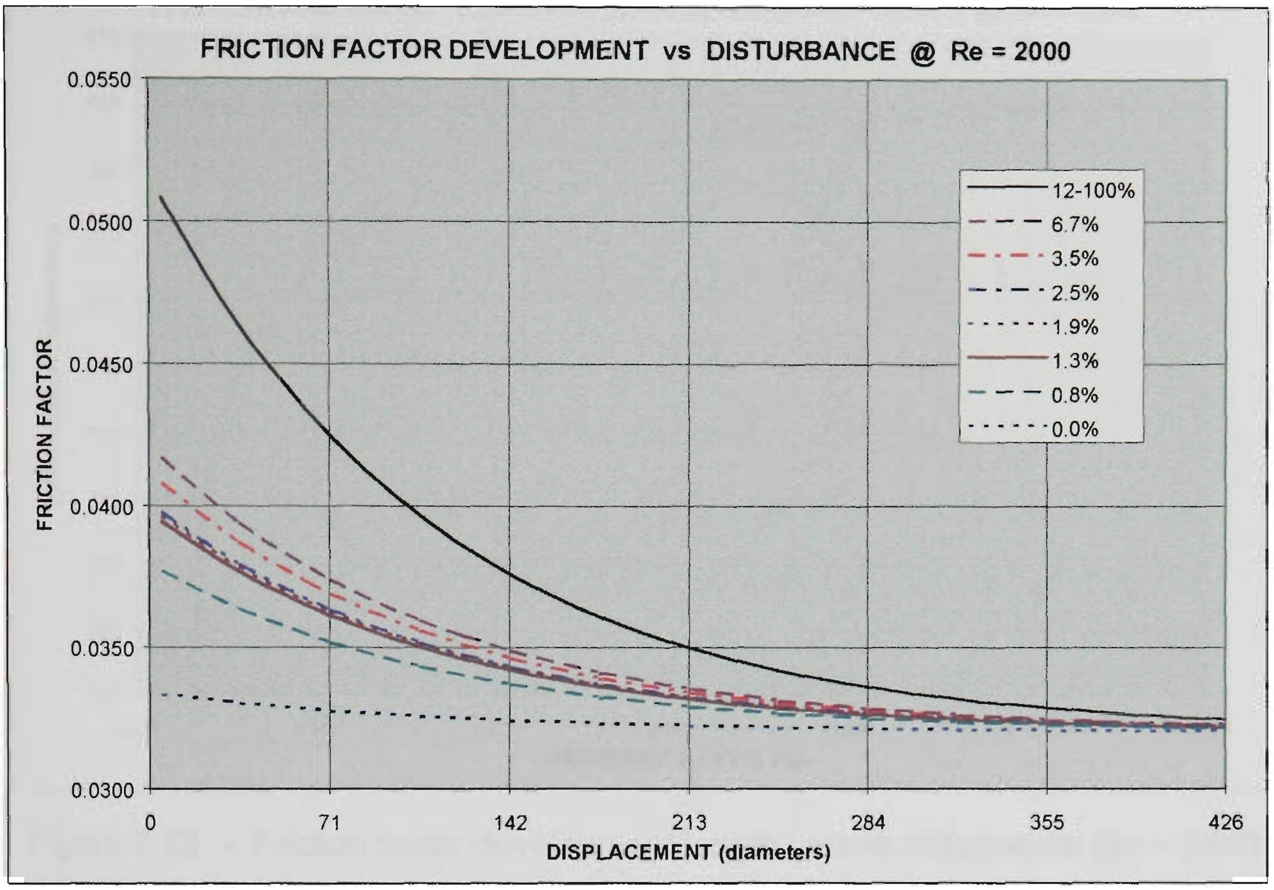

Figure 7.22 - Friction factor development with disturbance level ($Re = 2000$)

Finally in Table 7.1 the friction factor obtained for the undisturbed case is 0.0334 whereas theory (64/Re) predicts a value of 0.0320. This discrepancy must be explained and horizontal gridlines at both of these values have been included in Figure 7.21. At the time when the experiment apparatus was established, the entry length was understood to be in the vicinity of $120dia$ ($2.5m$). In the light of Figure 6.38 the entry length is now understood to be some $400dia$ ($8.5m$), in the case of laminar flows. In re-appraising the experiment conditions it now becomes apparent that the data of Table 7.1 with respect to "zero" disturbance would in fact be subject to a low level of residual disturbance from the pipe entry. This is because the experiment setup involved a $4.5m$ length of straight pipe ahead of the $3000mm$ test segment, which means that the figure of 0.0334 should be locally accurate in the vicinity of $284dia$ ($4.5+1.5$ m). Remarkably, Figure 7.21 shows that the friction factor reduces to 0.0334 at about $295dia$, representing a small error. This result increases confidence in the friction factor development model proposed.

It was then expected that this residual disturbance could cause an error in calculating the magnitude of the disturbance introduced downstream of the sampling hole, affecting the values in Table 7.1. To determine the magnitude of this error it is necessary to complete the current line of investigation and analysis.

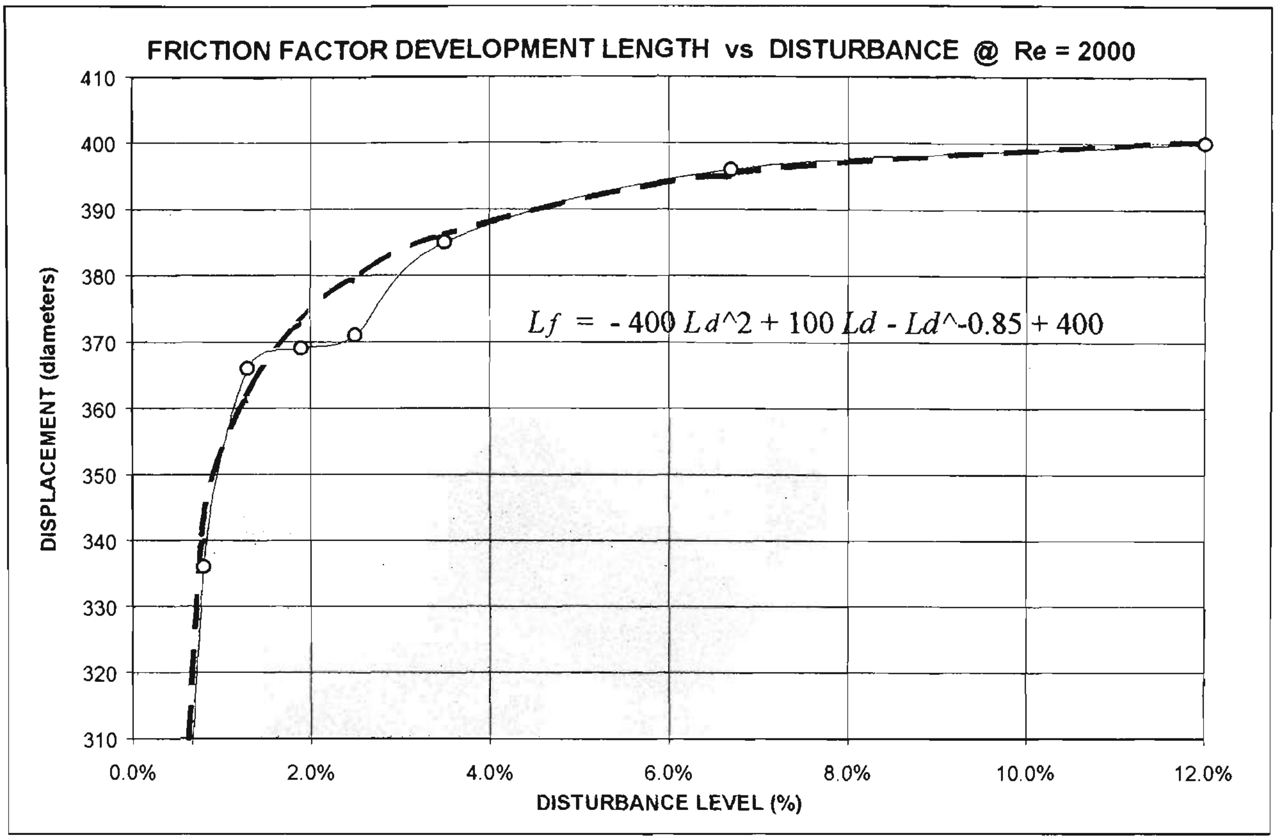

Figure 7.23 - Friction factor development length versus disturbance (Re = 2000)

Based upon Figure 7.22 it is possible to determine the "friction factor development length" as a function of the disturbance level (again, defined as the displacement at which the friction factor diminishes to within 1% of its final value). This is presented in Figure 7.23 where a high level of consistency in the data is seen. Included in Figure 7.23 as a dashed curve is the graph of an equation of good fit to these data (determined manually):

$$L_f \quad = \quad -400\,L_d^2 + 100\,L_d - L_d^{-0.85} + 400$$

where L_f (*dia*) is the friction factor development length and L_d (%) is the level of disturbance. By application of this equation it can be shown that the contribution of the residual disturbance mentioned above, is equivalent to 0.2% which is insignificant at the point where additional disturbance is introduced by a sampling hole.

Based upon the apparent success of this approach it was decided to consider an alternative Reynolds number, particularly Re = 1500, being the lowest considered in Figure 5.18. It was therefore necessary to develop a curve of best fit to the core velocity growth curve of Figure 6.38 (at the nearest Reynolds number), from which to derive an equation for the expected friction factor development profile:

$$f_d \quad \approx \quad f_0 - (f_0 - f_\infty)\left(1 - \left(1E{-}14\,d^6 + 0.01\,d + 0.3\,d^{0.6} + 1\right)^{-1}\right)$$

The resulting friction factor development curve is presented in Figure 7.24, while Figure 7.25 introduces the data of Figure 5.18 at Re = 1500.

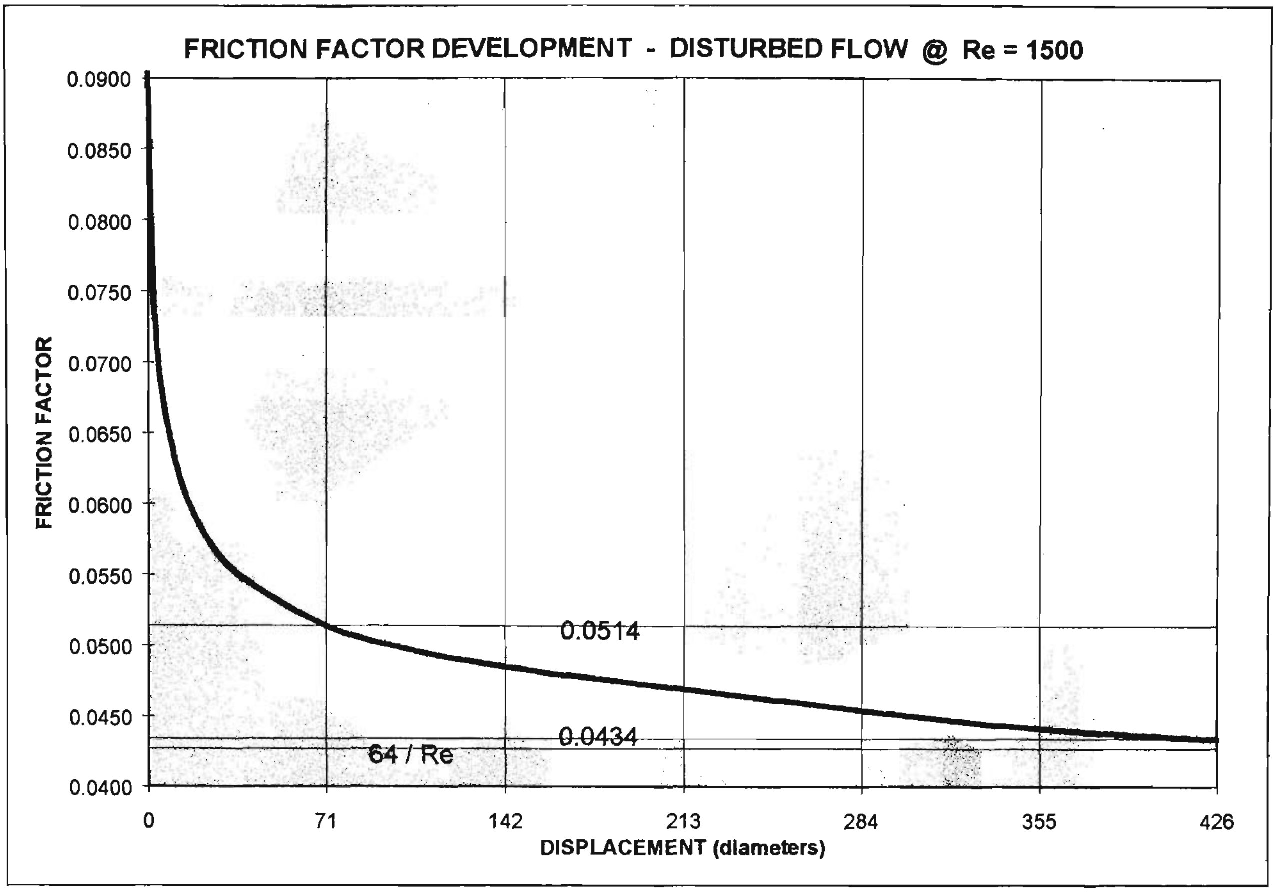

Figure 7.24 - Estimated friction factor reduction versus displacement for initially-disturbed flow at Re = 1500

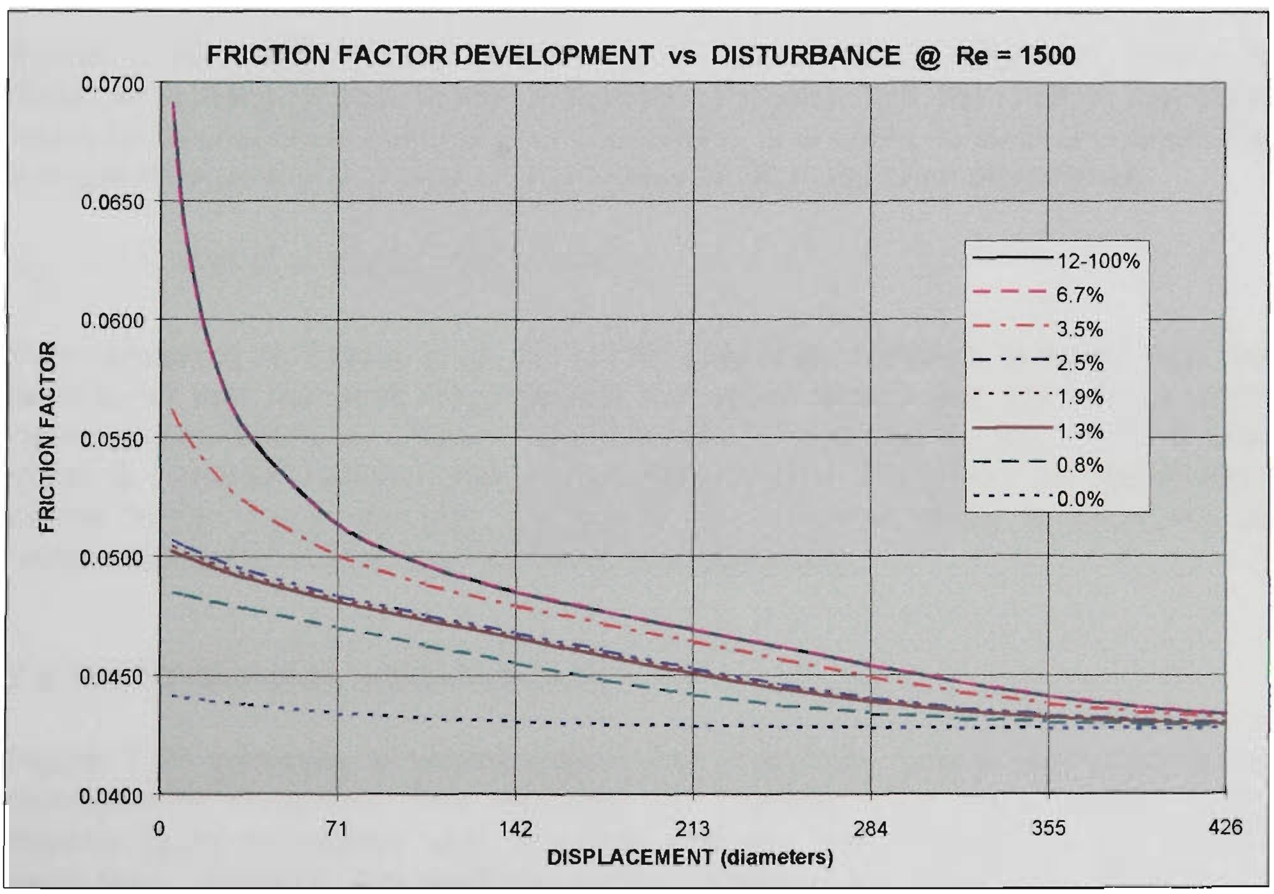

Figure 7.25 - Friction factor development with disturbance level (Re = 1500)

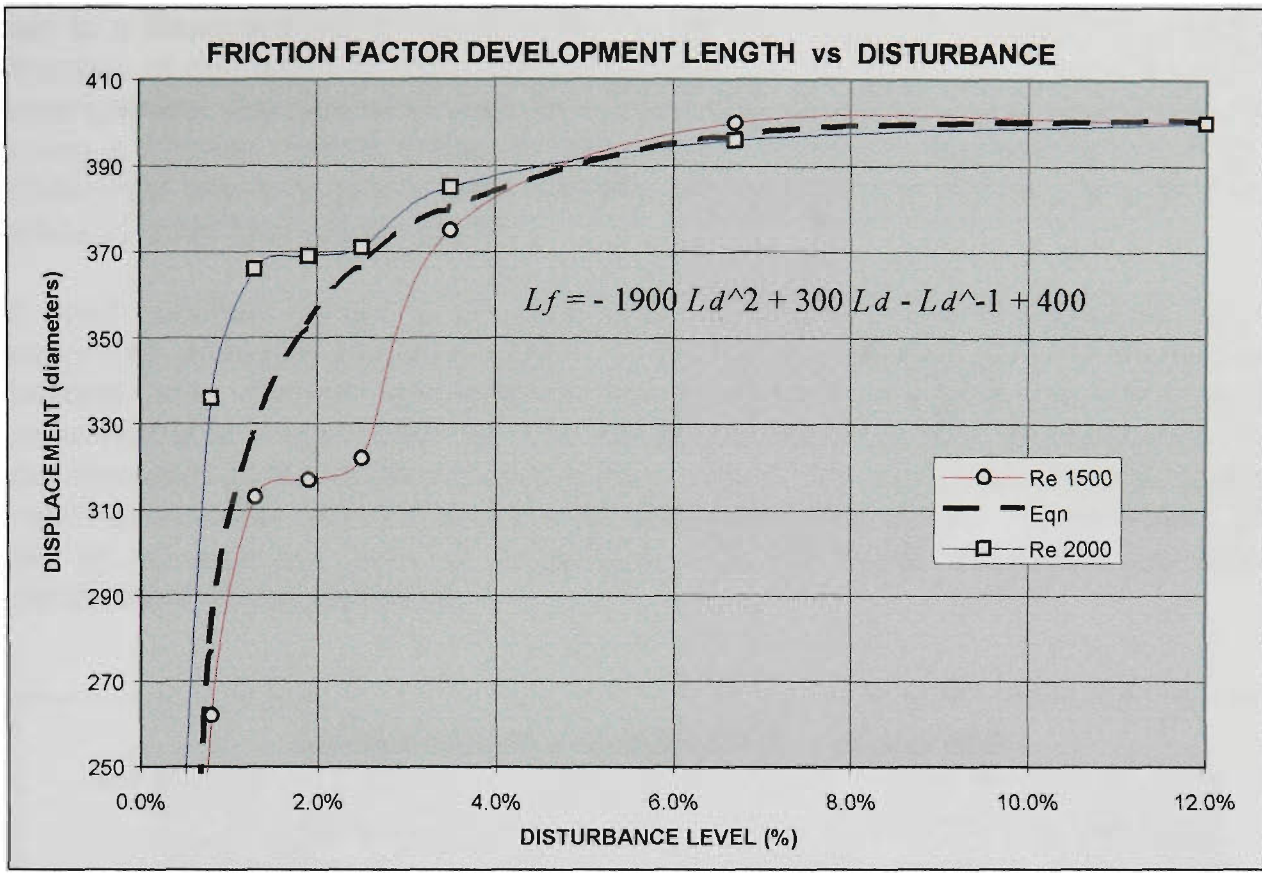

Figure 7.26 - Friction factor development length versus disturbance

Figure 7.26 presents the friction factor development length in terms of disturbance level for $\mathrm{Re} = 1500$. The data of Figure 7.23 ($\mathrm{Re} = 2000$) has been included for comparison and a good correlation is evident, to such an extent that a single new equation of best fit to both sets of data has been determined:

$$L_f \;=\; -1900\, L_d^2 + 300\, L_d - L_d^{-1} + 400$$

With reference to Figure 6.38, at higher Reynolds numbers involved with the transitional and turbulent flow regimes we would expect that the friction factor develops completely by $100dia$. Deissler (1955) finds that for $\mathrm{Re}{=}10^4$ the friction factor is developed within about $10dia$ (undisturbed). Therefore, the significance of the friction factor development profile phenomenon could be regarded as restricted to laminar flow regimes for current purposes.

7.6 EXPERIMENTAL VERIFICATION

Figure 7.26 provides a useful insight into the likely nature of friction factor development in laminar flow regimes, but confidence in these results would depend upon correlation with accurate pressure drop measurements of high resolution. Although the available instrumentation had inadequate resolution it was decided to attempt an approximate experimental verification of the friction factor development profile assumed above.

A 21.2*mm* diameter test pipe was drilled to produce pressure taps at 5*dia* intervals, out to a displacement of 100*dia* from the pipe entry (without introducing possible sources of disruption to the pipe flow regime). To replicate the LV experimental arrangement, the pipe entry was left open (although similar results were obtained using a 12.9*mm* control orifice at the entry). The two tubes connecting to the differential pressure gauge were applied successively to adjacent pressure taps, while all other taps were closed.

It was found that, except by the pipe entry, intervals of 5*dia* were too small for the expanded pressure gauge resolution of 0.25Pa, so intervals of 10*dia* were used beyond 10*dia*. Further increasing the interval would increase the pressure drop to more-readable magnitudes but would defeat the objective of measuring the development profile in the necessary detail. Also, it proved impracticable to take readings at a flow rate of 10 *litre/min* so settings of 20 to 60 *litre/min* were used (as set by an aspirator bank in conjunction with the digital flowmeter connected downstream of the test pipe).

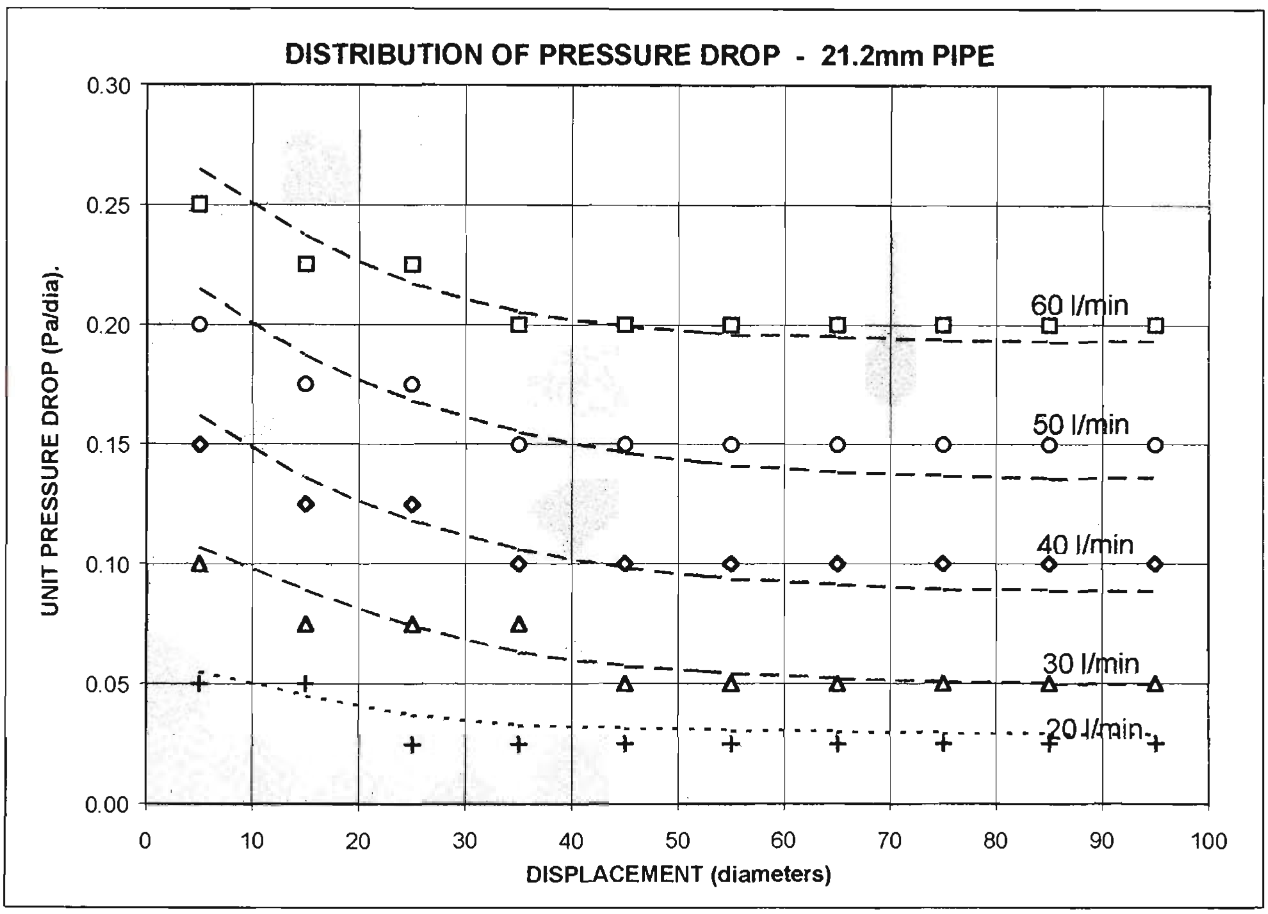

Figure 7.27 - Pressure drop per unit pipe length, versus displacement

The results are presented in Figure 7.27, together with curves of good fit to the data. The curve in the case of 20*litre/min* is shown dotted to indicate a lower level of confidence in the data. These results have been standardised by dividing the pressure drop by the pressure tap interval (*dia*), to produce results in terms of pressure drop per unit pipe length in diameters. In the circumstances, the degree of consistency among the sets of data is surprisingly high.

These curves of fit have been used to estimate the shape of the friction factor development profile applicable to each Reynolds number, as presented in Figure 7.28. The magnitude of the friction factor could not be accurately represented, given the instrument resolution and the short displacement intervals. Since the friction factor is directly proportional to the pressure drop, an error of one half of the least significant digit on the flowmeter (the best case) would represent a typical error of 10% in the friction factor results (while ranging from 5 to 50 % overall). Therefore, the curves of fit in Figure 7.27 have been adjusted to match the previously obtained results that were averaged at $71dia$ (Figure 5.17) despite which, the curves retain an acceptably good fit to the data.

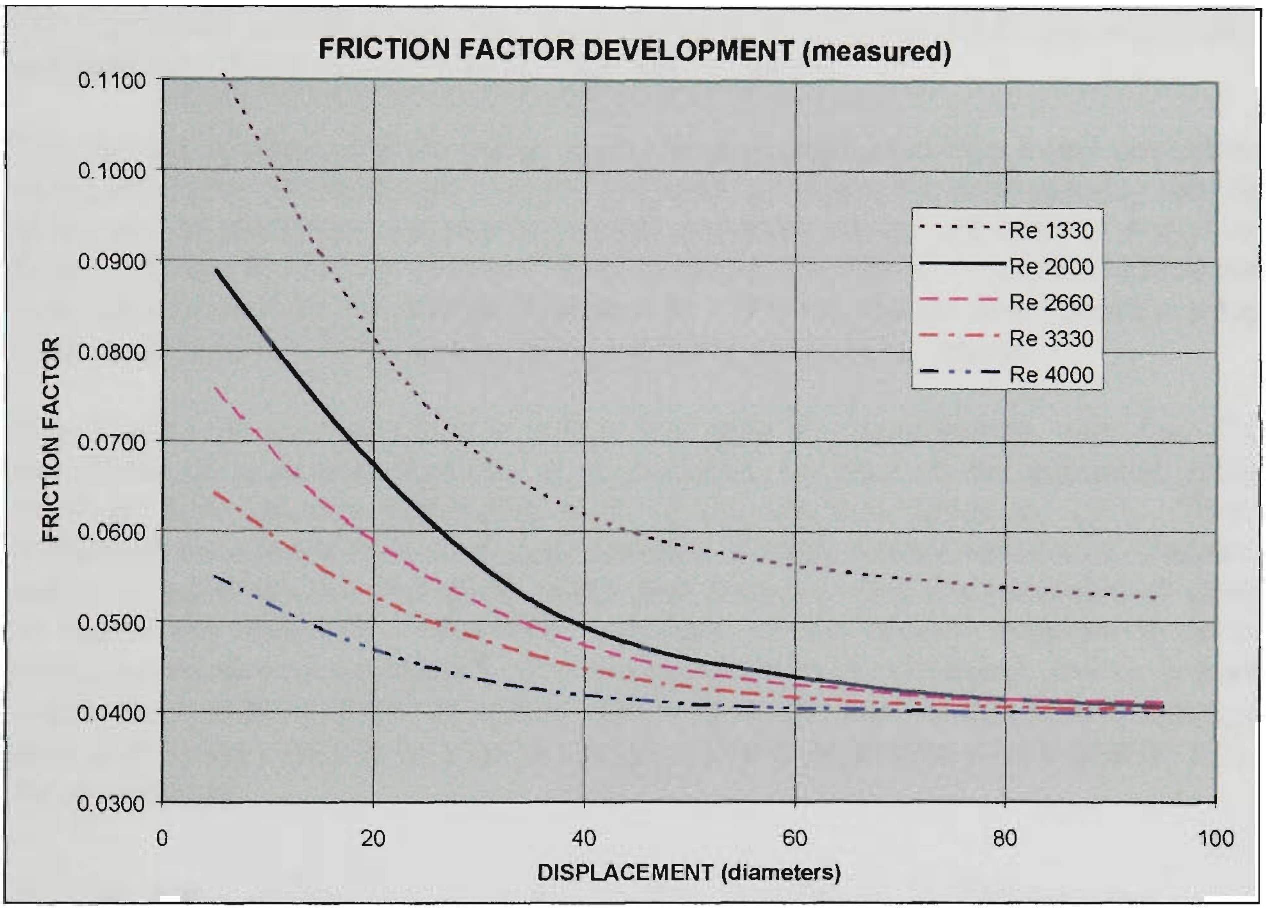

Figure 7.28 - Measured friction factor development profiles

These results indicate that in the case of transitional and turbulent flow regimes ($Re \geq 2660$), the friction factor is fully developed within $100dia$. This is consistent with the LV results as presented in Figure 6.38. At lower Reynolds numbers the friction factor is fully developed at greater displacements. The results at $Re = 2000$ are also broadly consistent with expectation based upon the LV results as presented in Figure 7.23 (although developing at a somewhat lesser rate). Put another way, the results of Figure 7.28 do not dismiss the value of Figure 7.21.

The need for a more-detailed study is regarded as an opportunity for a separate research program when suitable instrumentation becomes available. In the absence of such research it is decided to rely upon the averaging effect inherent in the experimental method using a $3000mm$ pipe segment, located immediately downstream of the disturbance. Most pipe segments used in the field are of a similar order of length.

7.7 CONCLUSIONS

A model representing a series of core velocity growth profiles in an aspirated pipe with six sampling holes has been developed (Figure 7.1) to evaluate the proposed modelling methodology. This series has a broadly similar form to that which was anticipated from an analysis of guidelines within the literature, but it has significant differences in detail. The pattern which emerges is consistent throughout, so a high level of confidence in the methodology has been gained. The individual sector errors and cumulative error (Figure 7.16) are significantly reduced over initial models based upon the literature.

The impact of using bends within such an aspirated pipe has been considered using the same methodology (Figure 7.4) and, although the core velocity reached at the end of each pipe segment is similar (whether bends are fitted or not), there is an increase in smoke transport time of about 5% due to reduced intermediate velocities caused by the bends (Figure 7.5). The results obtained provide a high level of confidence in the ability of the model to account for bends.

The impact of smoke dilution within the pipe in combination with the finite sensitivity of a smoke detector is considered, in view of an apparent smoke transport time penalty increasing each of the segment times by 25%. This is explained as a combination of phenomena. Firstly, the LV results of Chapter 6 led to an accurate determination of the time taken for the first molecule of smoke to reach the detector. However, detection of the smoke requires a certain minimum smoke concentration. On the assumption of no mixing, smoke is borne within the velocity profile "envelope" within the pipe and the increase in transport time due to the need to achieve a certain detectable smoke concentration (C_s) at the detector is:

$$T_{r\%} = 100 \frac{u_{core}}{2\, u_{avg} \left(1 - C_S\right)} \qquad or \qquad T_{r\%} = 100 \frac{u_{core}}{1.29\, u_{avg} \left(1 - \sqrt{C_S}\right)^{\frac{1}{6}}}$$

in the case of fully-developed laminar or turbulent flow regimes respectively. This effect taken in isolation would require a smoke concentration of 20% in the case of laminar flow or 54% in the case of turbulent flow ($\mathrm{Re} = 4000$), to produce the expected time penalty of 25%.

There was no evidence of a reduction in sensitivity, with increasing distance of the smoke injection point from the detector. This would have implied progressive condensation or settling-out of smoke particles on the pipe walls en-route. Such an effect would only increase the above discrepancy.

In order to consider the effect of developing flow regimes a new, universal power law was developed, to describe the lateral shape of the velocity distribution curve for laminar flow at any stage of development (i.e. at any given displacement, x):

$$u_r = R_u\, u_{avg} \left(1 - \left(\frac{r}{R}\right)^{n_x}\right) \qquad where \qquad n_x = \frac{2}{R_u - 1}$$

where u_r is the local velocity at radius r, and R_u is the core velocity ratio at the given displacement as obtained from the LV results (Chapter 6). In the case of turbulent flow, the above equations are applicable until the point of boundary-layer transition. An <u>inverse power law</u> may be applied beyond this transition region, for which a new equation has been developed to determine the value of the exponent:

$$u_r = R_u\, u_{avg} \left(1 - \frac{r}{R}\right)^{\frac{1}{n_x}} \qquad n_x = -209.23\, R_u^3 + 893.71\, R_u^2 - 1282.8\, R_u + 622.73$$

After studying the transport time penalty as a function of smoke detection threshold in accordance with the above equations (Figures 7.13 and 7.17), it was discovered that beyond about $100dia$, the penalty becomes largely independent of displacement such that a fixed correction factor is expected to apply throughout either the laminar or turbulent regions. However, based upon the assumption of no mixing, the value of the correction factor is different for the two regions.

After considering the effect of complete mixing of the smoke at all points along the pipe, it was found that the required smoke concentration is increased in direct proportion to the core velocity ratio (R_u). This brings the required smoke concentrations proportionally closer together, at 50% and 68% respectively in the case of fully-developed laminar and turbulent flow regimes.

Furthermore, after considering the highest Reynolds numbers applicable to typical systems installed in the field (3200), it was found that using a correction factor to increase the computed time (based upon the LV results) by a fixed 25%, throughout the entire length of the pipe, was indeed appropriate. However, provision has been made in the software to accommodate other values, relevant to different smoke sources (generating different particle size and shape distributions), especially where incipient fires are involved.

The friction factor changes in harmony with the development of the flow regime and this has a significant effect in laminar flow regimes. An attempt has been made to characterise the profile of this friction factor development as a function of displacement, at $\mathrm{Re} = 2000$, and also at $\mathrm{Re} = 1500$ which indicates similar results. In each case the proposed equation is of the form:

$$f_d \approx f_0 - (f_0 - f_\infty)\left(1 - 0.655 e^{-d/113}\right) \qquad for \qquad \mathrm{Re} = 2000$$

$$f_d \approx f_0 - (f_0 - f_\infty)\left(1 - \left(1E{-}14\, d^6 + 0.01\, d + 0.3\, d^{0.6} + 1\right)^{-1}\right) \qquad for \qquad \mathrm{Re} = 1500$$

This method equates the friction factor development length to the flow regime development length (the entry length). Given that this length relates to initially fully-disturbed flows, then at reduced levels of initial disturbance (as determined by the sampling hole flow rate), the friction factor development length would be reduced. An equation has been determined, to model this length (L_f) according to the flow disturbance level (L_d):

$$L_f \quad = \quad -1900\, L_d^2 + 300\, L_d - L_d^{-1} + 400$$

which matches the LV experiment data (of Chapter 6) within $\pm 15\%$ (Figure 7.13). Importantly, this length is not significantly reduced below $400dia$ (being laminar flow) unless the disturbance level is less than 2% (which would rarely be the case).

Having established a model for the expected friction factor development profile, an experiment was conducted in an attempt to verify these results. Despite the coarseness of the data (Figure 7.27), the data sets are mutually consistent and the shape of the curves of good fit to these data, are broadly consistent with the model.

Nevertheless, due to the inadequacy of available instrumentation to perform experiments at very high resolution, a sufficiently high level of confidence in the approach used has not been gained. Instead, given that the friction factor measurement experiments were conducted using a pipe segment of $3000mm$, and given that this length is of similar magnitude to most pipe segment lengths used in the field, then the data of Figure 5.19 will be relied upon. Conducting the foregoing type of experiment and analysis in greater detail using equipment of higher resolution is seen as an opportunity for further research when this equipment becomes available.

CHAPTER 8 - THE SYSTEM MODELLING PROGRAM

8.0 INTRODUCTION

The "ASPIRE" program is a software tool used to analyse and optimise the design of aspirated smoke detection systems. This software represents the culmination of the current research project. Its development has facilitated an analysis of the relative significance of all components within a system. As such it is fundamental to the thesis. Chapter 8 provides an understanding of the objectives and coding of the software.

8.1 MODEL OBJECTIVES

Referring to Figure 1.1, it is required to model existing or proposed systems to encompass:

- the smoke transport time from each sampling hole to the detector
- the air flows through each sampling hole and each pipe
- the effect of all components - aspirator, detector, dust filter, pipes, bends, holes, nozzles, capillary tubes and the end vent.

A further objective of the tool is to demonstrate to the system designer, the relative significance of the various parameters in a system, so that an optimum design can be applied to each field situation. "What-if" analyses are facilitated, so the system designer understands the value in selecting pipework of a given diameter for example. The parameters include:

- the ambient air temperature and pressure (altitude)
- the detector head model, type and sensitivity setting (fire alarm level)
- the type and composition of dust filter
- the aspirator setting (cutoff pressure at constant voltage or speed)
- the number of pipes in the system (zone)
- the length of the selected pipe (sector)
- the position of the first sampling hole (measured from the detector)

- the spacing of subsequent sampling hole positions, whether fixed or varied
- the internal diameter of the pipe
- whether the pipe diameter is stepped-down along its length
- the number of holes and the hole diameter at each position
- whether the sampling hole diameter is stepped-up along the pipe
- the end vent diameter, and whether capillary tube(s) are used there
- the size, number, length and curvature of capillary tubes at each position
- whether fixed or adjustable sampling hole sizes at each capillary tube
- the number and size of bends between each sampling position

The ASPIRE program will determine the system operating point (system pressure and flow rate) for the given aspirator setting. At each sampling point position along the pipe, and at the end vent, the program will calculate:

- the differential pressure within the pipe
- the flow rate through the sampling hole
- the percentage of total flow rate through the sampling hole
- the effective sensitivity of the sampling hole based upon dilution
- the time taken for smoke to reach the detector from that position

In addition, the program will summarise the result for the pipe (sector) so that an overall judgement of performance can be made:

- the overall (un)balance in flows amongst all the holes, as a figure of merit
- the share of total pipe flow in sampling holes (excluding the end vent)
- the worst-case, maximum smoke transport time, as a figure of merit.

The program will be capable of modelling a system comprising many pipes which may have widely differing parameters. The program will summarise the results of all such pipes (sectors) within the system (zone), facilitating comparisons between sectors. The program will provide for the inclusion of site details and comments, will provide a graphical presentation of the system layout, and will facilitate the storage of data for later retrieval and amendment.

8.2 STRUCTURE OVERVIEW

The DOS version of the ASPIRE software is written in the Visual Basic language, divided into seven modules and 109 sub-modules for ease of maintenance. This structure will be described in greater detail later. Each major module is represented by a screen page (or pair of half-pages) as illustrated in Fig 8.1, commencing with the TITLE PAGE. Each press of the "Enter" (↵) key will cause pages 1, 2&3, 5, and 6 to be displayed in sequence, returning to page 1. These pages are illustrated in Figures 8.2 to 8.5, with fields containing the data applicable to a residential site (small system).

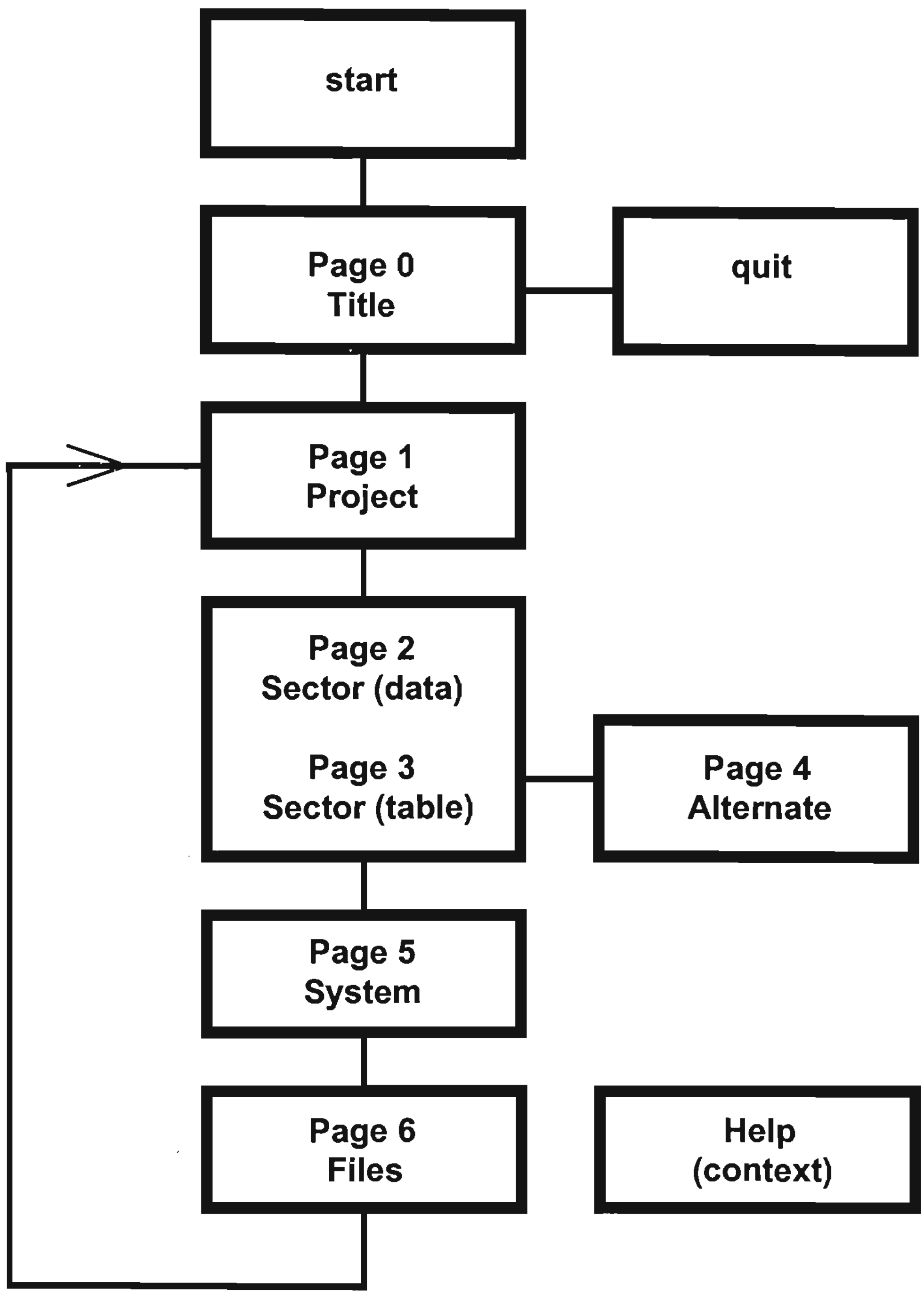

Figure 8.1 - Software paging sequence

8.3 PROJECT PAGE

Next is the PROJECT PAGE, in which the details of the particular site may be entered and filed (saved) for later reference. Space is included for the project name and address, the contact name, the system designer's name, the date, the file reference name, and there are several lines for comments.

This page also provides access to the system macro parameters including the type of smoke detector, its sensitivity, the type of dust filter, the ambient temperature and pressure (altitude), the screen colour scheme (useful with LCD displays for best contrast), the sound-effects option and the page printing option. All these options are displayed at the foot of the page.

```
     VESDA (tm) ASPIRATED PIPE SYSTEM MODELLING PROGRAM 17-AUG-1997

PROJECT: Name Family Residence_________________________________________
 STREET: 63 Name Court__________________
   CITY: Patterson Lakes________________       REGION: Vic Auatralia_
CONTACT: Christine Name________________________________________________

   ZONE: Whole house and garage_________        FLOOR: 2 levels______
DWG.REF: EL-1___________________________         DATE: 01-06-1997____
INSTALR: Dickson & Funke Pty Ltd________
CALC.BY: Peter Funke____________________         FILE: A:\NAME.ASP___

COMMENT: Sector 1: Garage-Study (level 1)______________________________
COMMENT: Sector 2: Bar-Family-Laundry-Pantry-Rumpus (level 1)__________
COMMENT: Sector 3: Bedrooms-3-2-1-4-5 (level 2)________________________
COMMENT: Sector 4: Lounge-Dining-Balconies (level 2)___________________
COMMENT: ______________________________________________________________
COMMENT: ______________________________________________________________

    Options:  Proj  Head  Dust  Temp  Snd  Col  Op  (enter)
```

Figure 8.2 - Project page layout (DOS version)

8.4 SECTOR PAGE

The SECTOR PAGE is where the details of a particular pipe are entered. These details include the number of pipes, the selected pipe, the pipe length, the position of the first sampling hole, the standard separation of the holes, the pipe internal diameter, the capillary tube internal diameter (if used), the sampling hole diameter, the endcap vent diameter, the radius of bends, and the aspirator pressure setting.

Each of these parameters is described to the user on-screen, together with an acceptable range for the parameter. A default value for each parameter is also provided. As each parameter is selected in turn, the stored value is displayed in red. This value may be accepted by pressing the Enter key, or it may be altered. The altered value is stored on pressing the Enter key. Any alteration is tested to ensure that it is consistent with other parameters, to avoid keyboard mistakes. If the alteration lies outside the acceptable range, there is a warning "beep" and the original value is displayed.

Most of the major parameters have options, displayed at the foot of the page. For example, the separation of the sampling holes may be "Fixed", which is appropriate to a neat grid pattern for the pipe and hole layout. Where such a pattern is not feasible due to physical barriers, then the individual positions of the holes may be adjusted using the "Varied" spacing option.

The pipe diameter may be "Stepped" in size along the length of the pipe, reducing in diameter in the direction away from the detector. This can be appropriate in some cases, for reduced smoke transport time, but the hole-flow balance would be reduced.

The sampling hole diameter can similarly be "Stepped" for the purpose of improving the hole-flow balance. The diameters would be increased in the direction away from the detector. Whereas this has advantages in some situations, generally it is considered difficult to supervise the correct installation of holes that vary in size at different positions. Nevertheless to illustrate a point, it is possible to calculate hole sizes automatically, such as would provide perfect (100%) balance, i.e., the flow through each hole would be identical. Using the B% option, the diameters are displayed and it becomes apparent that extremely fine adjustment is required, drilling successive holes accurately to three-significant-figure accuracy (e.g. 2.32*mm*, 2.36*mm*, etc).

```
        XenonVESDA ASPIRATED PIPE SYSTEM MODELLING PROGRAM 17-AUG-1997

       Pipe ident Nmbr (1-4)  =  2/4     Pipe Length  (4-100m) =  27.6
       1st hole posn (1-28m)  =  2.0     Hole Spacing (0.1-9m) av  3.7
       Pipe in.Dia (15-30mm)  = 12.0     Tube int.dia (4-12mm) =   5.2
       Sampling Hole (1-4mm)  av 2.1     End cap Vent (2-10mm) =   2.5
       Bend radii (12-500mm)  = 25.0     Aspir. Pressure (-Pa) = 250.9
       Pipe Flow (litre/min)  = 15.9     Aspir. Flow (lit/min) =  63.8

Hole   Posn   PPipe   Flow   Dhole   Time     Hole   Posn   Ppipe   Flow   Dhole   Time
- 1'    2.0    206    2.5    2.00     1.4
- 2     3.5    193    2.4    2.00     2.0
- 3'    7.8    161    2.2    2.00     3.9
- 4'   11.5    140    2.0    2.00     6.0
- 5    16.2    121    1.9    2.00     9.2
- 6'   20.2    109    1.5    3.00    14.6
- 7    23.2    102    1.7    2.00    17.3
- 8    27.6     98    1.7    2.00    29.1

 Pipe: 2  Bal: 65%  Share: 100%  MaxTime: 32s            Sector option? /

    Options:  N L 1 S D T H V B P F  S%  B%  Cc  Alt  Op  / \  (enter)
```

Figure 8.3 - Normal Sector page layout (DOS version)

Each row of data displayed in the table applies to a pipe segment, the first column being the segment and hole sequence number (Hole), then the position of the hole as measured away from the detector (Posn, *m*), the differential pressure at the hole within the pipe (PPipe, Pa), and the flow rate within the pipe sector (Flow, *m/sec*). The fifth column has three possibilities - the percentage of the total pipe flow represented by the hole flow (Flo%, *%*) or, if the B% option has been selected, then it is the hole diameter (DHole, *mm*) or, if the S% option has been selected, then it is the hole smoke-sensitivity required to reach the detector alarm threshold (Sen%, *%/m*). In the last column, the smoke transport time from that hole to the detector is shown (Time, *sec*).

Below the table is the summary line which shows, for the selected **Pipe** number, the **Balance** achieved for that pipe (being the flow rate through the least sensitive hole compared with the average sensitivity of all the holes excluding the end vent), the **Share** of the total pipe flow passing through sampling holes (excluding the end vent), and **MaxTime**, the maximum smoke transport time (from the least favoured hole, including any capillary tube delay and the detector processing delay). These parameters are figures of merit for the pipe, with Balance and Share preferably above 70% and MaxTime below either 60 or 90 *sec* according to the risk level and the prevailing fire codes.

The system designer is expected to adjust the various physical dimensions of the system to optimise the system performance, firstly in terms of these figures of merit and secondly in terms of the individual tabulated values.

```
          XenonVESDA ASPIRATED PIPE SYSTEM MODELLING PROGRAM 17-AUG-1997

          Pipe ident Nmbr (1-4)  =  2/4    Pipe Length  (4-100m)  =  27.6
          1st hole posn  (1-28m) =  2.0    Hole Spacing (0.1-9m)  av  3.7
          Pipe in.Dia  (15-30mm) = 12.0    Tube int.dia (4-12mm)  =   5.2
          Sampling Hole  (1-4mm) av 2.1    End cap Vent (2-10mm)  =   2.5
          Bend radii (12-500mm)  = 25.0    Aspir. Pressure (-Pa)  = 250.9
          Pipe Flow (litre/min)  = 15.9    Aspir. Flow (lit/min)  =  63.8

Posn  #.B  Pipe  Tube  #.H  Sen%  Time    Posn #.B  Pipe  Tube #.H  Sen%  Time
 2.0   1   12.0   1.0   1    .87   1.4
 3.5   0   12.0   1.0   1    .94   2.0
 7.8   1   12.0   1.0   1   1.2    3.9
11.5   1   12.0   1.0   1   1.4    6.0
16.2   0   12.0   1.0   1   1.7    9.2
20.2   1   12.0   4.0   1   5.1   14.6
23.2   0   12.0   1.0   1   2.2   17.3
27.6   0   12.0   1.0   V   1.7   29.1


  Pipe: 2  Bal: 65%  Share: 90%  MaxTime: 32s        Alt sector option? \

                       Options:  Output  \  (enter)
```

Figure 8.4 - Alternative Sector page layout (DOS version)

8.4.1 Alternative information display

Upon selection of the **Alt**ernative table layout option, the data presented is of a physical specification nature rather than the fluid dynamics results, as shown in Figure 8.4. This table is of more use to installers than system designers, and details the number of bends within a segment (#.B), the pipe internal diameter (Pipe, *mm*), the capillary tube internal diameter (Tube, *mm*), the number of holes drilled at a particular position (#.H), the hole diameter (Hole, *mm*), the smoke sensitivity at that hole sufficient to reach the detector alarm threshold (Sens%, *%/m*) and the transport time for smoke from that hole to reach the detector.

8.4.2 Sector modelling methodology

Based upon all the relevant parameters for the pipe, a system operating point is calculated. The methodology proceeds as follows:

1) All the parameters for the selected pipe (sector) are entered manually, including the aspirator setting.

1 2) A first guess at the system flow rate can be made (this first guess would be entered manually, which was originally of benefit to experienced users using slow computers but this has ceased to be a concern).

2 3) The system pressure is calculated for the given system flow rate.

4) The pressure drop through the selected detector and the selected filter is calculated at the given system flow rate. The pressure at the start of the pipe is obtained by subtracting the detector and filter losses (from the system pressure).

5) The pipe flow rate equals the given system flow rate divided by the number of pipes (because at this preliminary stage, all pipes are presumed equal).

6) The first segment length is obtained and the appropriate number of bend lengths is subtracted. This assumes a simplistic "square grid" method of pipe measurement has been used. The remaining segment length is divided by the number of bends, forming sub-segments - this assumes the worst case condition that the bends are separated to the maximum extent.

3 7) The pressure drop for the first sub-segment of pipe is calculated using the friction factor applicable to disturbed flows in rough pipes (then multiplied by the number of bends in the segment).

8) The pressure drop caused by bends within the segment is calculated at the segment flow rate, and added to the above.

9) The pressure inside the pipe at the first hole position is obtained by subtracting the pressure drop of the first segment (including bends).

10) The flow through the first hole is determined by the local differential pressure and the hole diameter, using the hole-flow equation, and the effects of ultraflow and infraflow are incorporated.

11) The flow through the first hole is subtracted from the pipe flow rate, to determine the flow in the next pipe segment.

12) The pressure drop caused by the energy of acceleration of the induction jet entering the first hole, to reach the speed of the pipe flow, is calculated.

13) The process loops back to step 6, incrementing the hole position. For each sampling hole or segment, the local pressure, the flow rate and the transport time are stored in a matrix array.

14) The process continues until the end of the pipe is reached, or until the local pressure reaches zero.

15) If the local pressure reaches zero prematurely, then the system pressure is incremented automatically and the iteration restarts at step 3.

16) If sufficient pressure remains, then the endcap vent is reached. The endcap vent is of a given size, and will produce a calculable flow rate at the available pressure. If this calculated flow rate is more than the remaining pipe segment flow, then the system flow rate is incremented and the iteration restarts at step 3. If this flow rate is less than the remaining pipe segment flow, then the system flow rate is decremented and iteration restarts at step 3. If there is a close match between the flows, then a solution has been found (dynamic equilibrium).

17) The data from the matrix array is displayed in a table for all hole positions. The overall results are calculated and displayed at the foot of the table - these are the Balance% (the flow through the most distant sampling hole compared with the average hole flow), the Share% (the total flow through sampling holes excluding the endcap vent), and the transport time.

The use of capillary tubes introduces a further subroutine, to calculate the pressure drop caused by the tube. This modifies the operation of step (10).

The incrementing or decrementing of the system flow rate as mentioned in step (15) or (16) is performed in a particularly simple and efficient manner, to ensure rapid closing on the final result, and is described as follows:

> The current trial system flow rate is defined as Q_C. If this flow proves too high, then Q_C becomes the new high-flow marker, Q_H. If instead this flow proves too low, then Q_C becomes the new low-flow marker, Q_L. The next

trial value for Q_C then becomes the average between Q_H and Q_L, so it can never lie beyond the previously tested bounds. At each iteration, Q_H or Q_L are improved (the span being always halved), bringing Q_C rapidly closer to the final value. The method ensures that the initial changes in Q_C are large, for rapid closing, then subsequent changes are decreasingly small, to refine the result.

Having obtained a set of results, the computer operator then must decide whether these results are acceptable. Any of the parameters can be adjusted and a new system operating point determined. As previously stated, the aim of the software is to encourage users to experiment with "what-if" scenarios, to gain a better understanding of the significance of particular parameters, to arrive at an optimum design.

Having become satisfied with the results for an individual pipe, it remains to repeat the process for all other pipes. Eventually the parameters and (preliminary) results for all pipes are obtained.

If the pipes and components are all different, it would be noted that each has a different operating point, i.e. a differing system pressure and flow rate. With one common aspirator, there can be only one system pressure, so this discrepancy must be resolved - a function of the SYSTEM PAGE.

8.4.3 Detailed information displays

To facilitate verification of the computations (and debugging the software), two additional formats of the SECTOR PAGE are available. In the first wide format option (FW - "Fix Wide format"), the data displayed for each sector are the hole number and position (as before), the pipe flow rate (QPipe, *litre/min*), the air velocity in the pipe (VPipe, *m/sec*), the Reynolds number (RePipe), the friction factor (fPipe), the pressure drop in the pipe (dP.P, Pa), the pressure drop of the hole induction jet (dP.J, Pa), the pressure drop in bends (dP.B, Pa), the pipe differential pressure (PPipe, Pa), the flow rate through the hole (QHole, *litre/min*), and smoke transport time (Time, *sec*). This display is illustrated in Figure 8.4.

In the second wide format option (FT - "Fix capillary Tube format"), the data displayed for each sector are once again the hole number and position, then the length of the capillary tube (L.T, *m*), the pipe differential pressure (PPipe, Pa), The hole flow rate (QHole, *litre/min*), the average velocity in the capillary tube (VTub, *m/sec*), the Reynolds number in the tube (RTube), the friction factor in the tube (fTube), the differential pressure at the hole after taking account of the pressure drop in the tube (PHole, Pa), the diameter of the hole (DHole, *mm*, which may be of a specified size, or as adjusted to provide 100% hole flow balance), the smoke transport time delay incurred by the tube (TTube, *sec*), and the total smoke transport time for that hole (Time, *sec*).

```
XenonVESDA ASPIRATED PIPE SYSTEM MODELLING PROGRAM 17-AUG-1997

Pipe ident Nmbr (1-4)  =  2/4     Pipe Length   (4-100m)  =  27.6
1st hole posn (1-28m)  =  2.0     Hole Spacing (0.1-9m)  av  3.7
Pipe in.Dia (15-30mm)  = 12.0     Tube int.dia (4-12mm)  =    5.2
Sampling Hole (1-4mm)  av 2.1     End cap Vent (2-10mm)  =    2.5
Bend radii (12-500mm)  = 25.0     Aspir. Pressure (-Pa)  = 250.9
Pipe Flow (litre/min)  = 15.9     Aspir. Flow (lit/min)  =  63.8

Hole   Posn  QPipe  VPipe  RePipe  fPipe  dP.P  dP.J  dP.B  PPipe  QHol  Time
- 1'    2.0   21.9   3.23   2568   .0407  41.5  14.6   3.1   173    5.4   4.1
- 2     3.5   17.4   2.57   2042   .0418  20.7   3.6   0.0   152    4.1   4.6
- 3'    7.8   13.3   1.96   1557   .0503  41.0   9.3   1.7   109    3.3   6.2
- 4'   11.5   10.0   1.47   1167   .0595  23.4   6.6   1.0    85    2.8   8.0
- 5    16.2    7.2   1.06    840   .0762  20.0   4.5   0.0    65    2.3  11.1
- 6'   20.2    4.8   0.71    568   .1127  11.4   0.2   0.3    53    0.8  18.1
- 7    23.2    4.1   0.60    478   .1340   7.3   2.8   0.0    46    1.8  18.5
-EV    27.6    2.3   0.34    267   .2393   6.0   0.0   0.0    40    2.3  27.3

 Pipe: 2  Bal: 65%  Share: 90%  MaxTime: 32s           Sector option? /

   Options:  N L 1 S D T H V B P F  S%  B%  Cc  Alt  Op  / \  (enter)
```

Figure 8.5 - Wide format, pipe segment data display (DOS version)

```
XenonVESDA ASPIRATED PIPE SYSTEM MODELLING PROGRAM 17-AUG-1997

Pipe ident Nmbr (1-4)  =  2/4     Pipe Length   (4-100m)  =  27.6
1st hole posn (1-28m)  =  2.0     Hole Spacing (0.1-9m)  av  3.7
Pipe in.Dia (15-30mm)  = 12.0     Tube int.dia (4-12mm)  =    5.2
Sampling Hole (1-4mm)  av 2.1     End cap Vent (2-10mm)  =    2.5
Bend radii (12-500mm)  = 25.0     Aspir. Pressure (-Pa)  = 250.9
Pipe Flow (litre/min)  = 15.9     Aspir. Flow (lit/min)  =  63.8

Hole   Posn  L.T  PPipe  QHole  VTub  Rtube  fTube  PHole  DHole  TTub  Time
- 1'    2.0  1.0   173    4.5   3.52   1215  .0527    97   2.00   0.2    4.1
- 2     3.5  1.0   152    4.1   3.24   1119  .0572    82   2.00   0.2    4.6
- 3'    7.8  1.0   109    3.3   2.61    900  .0711    53   2.00   0.2    6.2
- 4'   11.5  1.0    85    2.8   2.19    757  .0846    38   2.00   0.2    8.0
- 5    16.2  1.0    65    2.3   1.82    626  .1022    26   2.00   0.3   11.1
- 6'   20.2  1.0    53    0.8   0.60    208  .3071     1   3.00   3.4   18.1
- 7    23.2  1.0    46    1.8   1.41    487  .1351    16   2.00   0.4   18.5
-EV    27.6  1.0    40    2.3   1.79    616  .1039     2   4.00   0.3   27.3

 Pipe: 2  Bal: 65%  Share: 90%  MaxTime: 32s           Sector option? /

   Options:  N L 1 S D T H V B P F  S%  B%  Cc  Alt  Op  / \  (enter)
```

Figure 8.6 - Wide format, capillary tube data display (DOS version)

8.5 SYSTEM PAGE

The SYSTEM PAGE summarises the results for all the pipes in a table. Here the different system operating points are displayed. It remains to "**Auto-compute**" the system as a whole, taking account of the differing sets of pipe parameters. This could not be done within the previous SECTOR PAGE because all the parameters for all of the pipes had not yet been entered.

Based upon pipe system characteristic equations for each pipe as determined by calculations within the previous page, a new, common system equation is predicted. By selecting the **Auto-compute** option, a common system operating pressure is estimated, and applied to each of the pipes in turn, whereby a new pipe flow rate is calculated and the iterations are restarted.

XenonVESDA ASPIRATED PIPE SYSTEM MODELLING PROGRAM 17-AUG-1997

Head 0.10%/m full-scale, Foam dust filter, Regular aspirator x1, +20°C

SUMMARY FOR INDIVIDUAL PIPES

=== PIPE ===	==1==	==2==	==3==	==4==	==5==	==6==	==7==	==8==
PILE LENGTH	27.0	27.6	28.0	31.0				
FIRST POSITN	19.0	2.0	4.0	5.0				
HOLE SPACING	≈ 4.0	≈ 3.7	≈ 4.8	≈ 6.5				
HOLE POSITNS	3 -	8 -	6 -	5 -				
PIPE INT DIA	12.0	12.0	12.0	12.0				
TUBE INT DIA	5.2	5.2	5.2	5.2				
SAMPLNG HOLE	3.0	≈ 2.1	2.0	2.0				
END CAP VENT	3.0	2.0	2.0	2.0				
HOLE%BALANCE	87.1	65.1	70.0	76.0				
HOLE % SHARE	100.0	100.0	100.0	100.0				
MAXIMUM TIME	21.4	32.1	28.0	38.7				
PIPE PRESSRE	272.8	250.9	264.5	270.0				
AMBIENT±PRES	+0.0	+0.0	+0.0	+0.0				
PIPE FLOW RT	10.5	15.9	12.7	11.3				
PIPE % SHARE	?	?	?	?				

Options: Duplicate Prepare Auto-compute Op / \ (enter)

Figure 8.7 - System page layout (DOS version)

These results are automatically refined by computing the system again, iteratively, until the incremental change in system operating point with each iteration becomes insignificant. Until the **Auto-compute** sequence has been executed, the **PIPE%SHARE** field is filled with question marks. In the above example, the common system operating pressure proves to be 264.8Pa, with a system flow rate of 50.7*litre/min*. For each project the acceptability of the overall system results may be judged from the table. The individual pipe results - balance, share and transport time appear in red if they breach nominal boundaries (70%, 70% or 90*sec* respectively).

8.6 FILES PAGE

The FILES PAGE enables the data to be filed on disk for future reference. This page provides the file management options to Load, Save, Rename, or Erase files, and to display the names of all files on the selected directory. The directory path may be specified, but the default is C:\ASPIRE\SITE. All ASPIRE files are tagged with the ".ASP" extension. The name of the operator and the date on which the file was generated, are both saved.

To assist with locating or identifying a file, a subroutine was written to sort the file names alphabetically. The files are presented in a table of five columns width (each column field being 12 characters wide), and 90 files can be listed on one page. Files are chosen using the cursor arrow keys and the selected file is highlighted.

```
      XenonVESDA ASPIRATED PIPE SYSTEM MODELLING PROGRAM 17-AUG-1997

  ACACIA.ASP     AIRPORT1.ASP   AIRPORT2.ASP   ASTORIA.ASP    BOEING01.ASP
  BOEING02.ASP   BOEING03.ASP   BRISBANE.ASP   CANAVRAL.ASP   CONTRLRM.ASP
  FACTORYE.ASP   FACTORYW.ASP   GEORGES.ASP    HONGKONG.ASP   HONKONG1.ASP
  HUBBLE.ASP     KENNEDY.ASP    KOWLOON.ASP    LIBRARY1.ASP   LIBRARY2.ASP
  NAME.ASP       PARLIMNT.ASP   SHELL.ASP      SHELL1.ASP     TESTSITE.ASP
  UNVERSTY.ASP   VICTORIA.ASP   XANADU.ASP

       Options:  Drive  Load  Save  Rename  Erase  Op  / \  (enter)
```

Figure 8.8 - Files page layout (DOS version)

8.7 CONTEXT HELP PANELS

There are 30 panels of context-driven HELP information. At any prompt, the appropriate panel is displayed upon pressing the "F1" key or the "?" key. This is formatted as a window in the lower half of the screen so that the main data and the options prompt remain visible. Some typical examples of help panel information is presented in Figure 8.9. All panels are updated with each version of software, minimising the need for hard copy documentation and ensuring that the advice always aligns with the correct version.

HELP on ASPIRATOR PRESSURE

The ASPIRATOR PRESSURE is determined by motor speed which is controlled by software within VESDA Laser PLUS (tm). You can select the ECONOMY, REGULAR or BOOSTED position, or anywhere between. Use the cursor arrow keys to select the required position, then note its effect on transport time, etc. The ECONOMY position is used with comparatively small systems, to conserve energy. The BOOSTED position is used with large systems or where the fastest response is required. Take note of the RPM setting for programming your detector.

HELP on HOLE DIAMETER

The performance of a system can be predicted, only if all the parameters are accurately known. This applies especially to the sampling point HOLE DIAMETER which has a critical effect. It is assumed that each hole has been drilled accurately and at 90° to the pipe with square shoulders and without swarf or burrs. Location of holes close to pipe sockets would provide access to deburr inside. To improve the BALANCE in air flows through the holes, their diameters can be STEPPED. Also, the NUMBER of HOLES (or capillaries) at each position can be set.

HELP on NUMBER OF HOLES

The NUMBER of HOLES (sampling points) at each position can be set from zero to four. Generally, ONE sampling hole is used. However, the pipe may be run above a corridor, with capillary tubes (equi-length) directed toward opposite rooms, requiring TWO sampling points at each location. Or the pipe may be run above a partition wall, with one tube directed toward each of FOUR adjacent rooms (i.e. at the crosspoint). ZERO holes can be used to simulate a Heat Activated Sampling Point (HASP tm) prior to its activation.

HELP on END VENT

A cap containing a vent hole is fitted to the far end of each pipe. To predict system performance, it is critical that the END CAP VENT DIAMETER is made accurately, free from swarf or burrs. Typically the vent is larger than other holes so that a large slug of air comes from the far end. Otherwise, for a long pipe the smoke transport TIME could be very slow indeed. However, too large a vent would impair the good BALANCE and SHARE of flow among sampling holes. A capillary tube(s) may be used for a below-ceiling end vent (with pipe capped).

HELP on PIPE DIAMETER

The INTERNAL DIAMETER of the PIPE must be known so that air velocities can be calculated. The external diameter is not significant, except for strength. PVC electrical conduit is typically used, with 16, 21 or 26mm internal diameter, being 20, 25 or 32mm external diameter respectively. The diameter can be STEPPED down in size at various positions along the pipe, which may improve the transport TIME at the expense of hole flow BALANCE (enter S to select diameter Steps; enter N for Nil steps). Also see HELP on FIRST POSITION.

Figure 8.9 - Some typical HELP panels

In addition, a schematic plan of the pipe layout can be displayed on an overlying page. By pressing the “F2” key or the “!” key, this new page-sized window will appear. This interprets the file array data (from flies of any age/version) to generate a schematic diagram that indicates the quantity and relationship between all elements of the pipework. The clarity of this display tends to highlight to the operator, errors in the type and position of the various components.

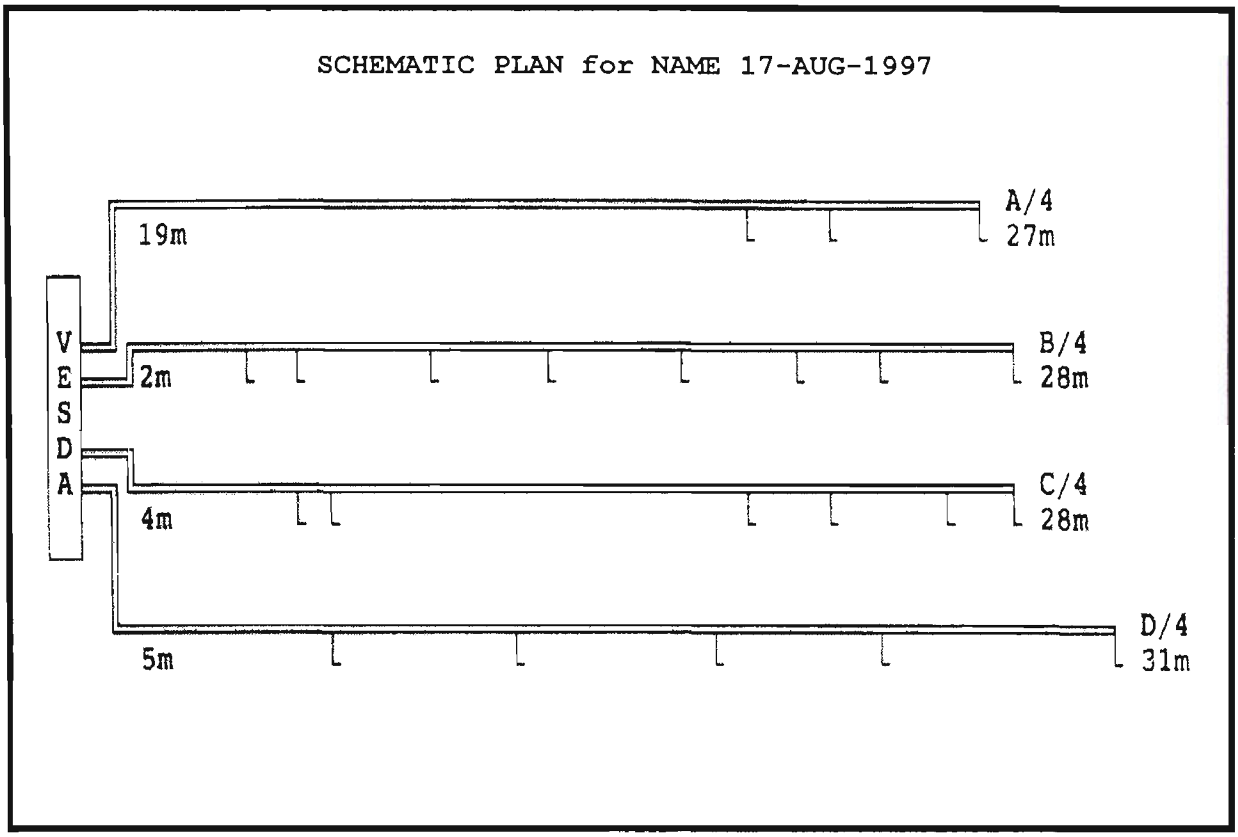

Figure 8.10 - Typical schematic plan (DOS version)

Symbols are used to indicate particular components. In Figure 8.10 each pair of parallel lines represents a pipe which connects to the aspirated smoke detector inlet manifold. A standard sampling hole drilled into the pipe wall is represented by a "o" while a "L" represents a capillary tube and nozzle (as is the case for each position in Figure 8.10). When more than one hole or nozzle is be used at any location, the number is indicated by additional tabs.

The distance to the first hole is indicated at the start of each pipe, while the total length of each pipe is indicated at the end. Up to eight pipes can be accommodated and the plan is set-out accordingly, automatically. In cases where the pipes are not installed in parallel runs, an alternative, vertical backbone type layout is available which shows the detector at the bottom, middle position. The pipes can be arranged in various ways, for example there can be two pipes branching to the left and four to the right. In all cases the schematic is automatically scaled to fit the page.

To illustrate some of the adaptability required of the "graphics package", some alternative schematic examples are shown in Figures 8.11 and 8.12.

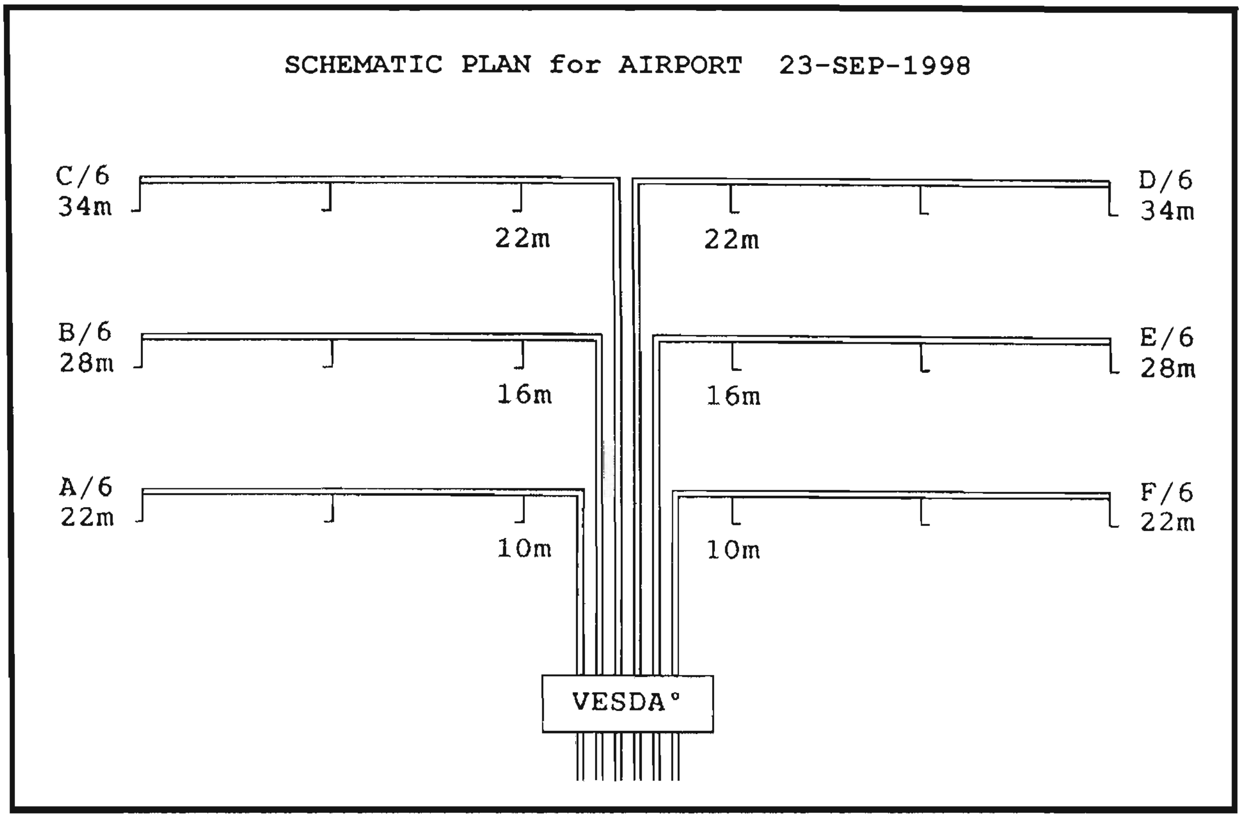

Figure 8.11 - Schematic plan for airport terminal ceiling
(mirrored system with 12 branches)

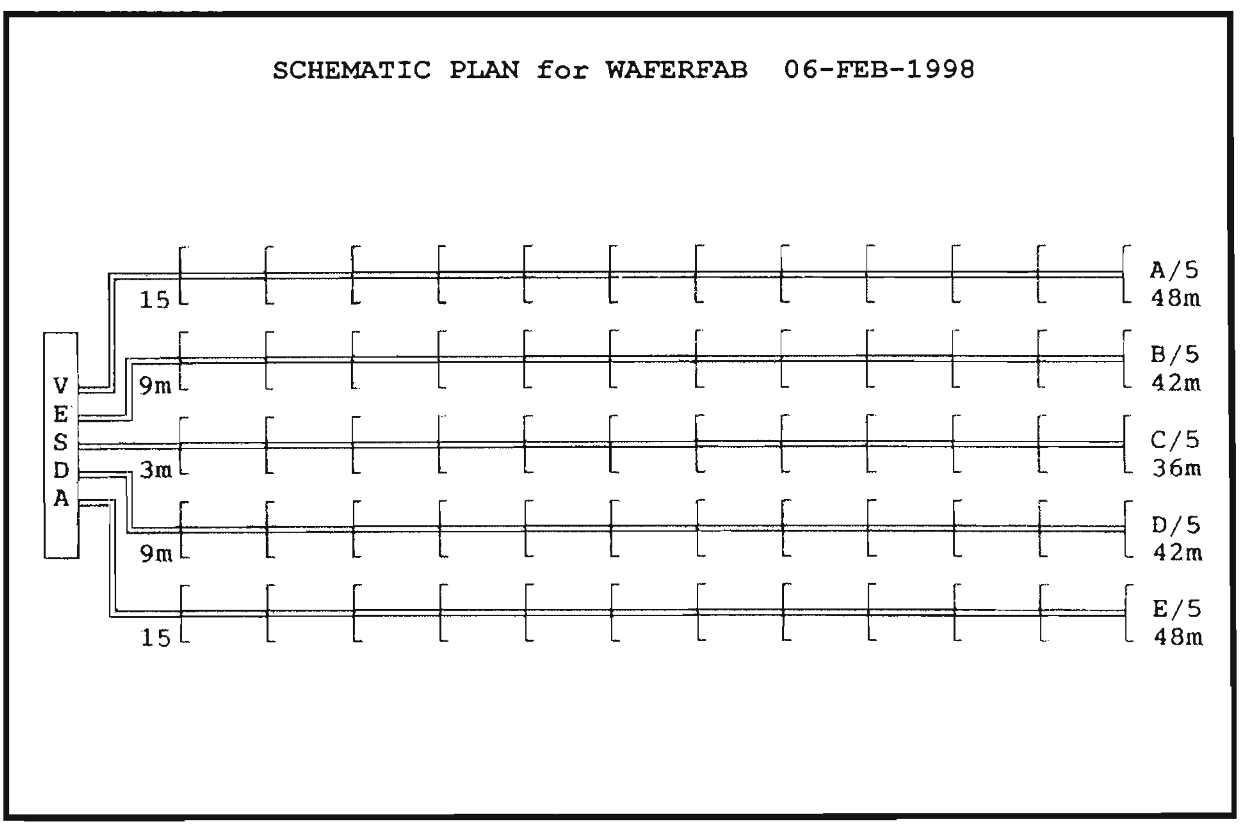

Figure 8.12 - Schematic plan for microchip wafer fabrication clean room
(square grid layout of nozzle pairs under floor grille)

8.8 SUB-MODULAR STRUCTURE

As illustrated in Figure 8.13, the software modules and sub-modules may be categorised into three levels (shown as vertical). A module comprises a collection of sub-modules, described collectively as an OPTION GROUP. Level 1 is used to select the required page (providing access within an OPTION GROUP), and to select the options or data fields displayed on that page.

OPTION GROUP 1 permits selection of site details, temperature, product type, display mode, etc. OPTION GROUP 2 permits selection of the major parameters such as pipe length, pipe diameter, general hole separation, general hole size, etc. OPTION GROUP 3 provides options affecting the computation and display of data for the individual sector (single pipe). OPTION GROUP 5 permits selection of system display and computational functions (multi-pipe). OPTION GROUP 6 is used for disk file management.

At level 2 the selected data field within a page may be altered by the user. Any new data is tested before acceptance. Options relating to minor parameters (such as individual hole sizes or positions deviating from general values) may be selected at this level. Also at level 2 is the backbone of the calculation engine (within OPTION GROUP 3). Within OPTION GROUP 6, level 2 holds the disk file management routines.

At level 3 the values of the minor parameters that were selected at level 2 may be altered. Within OPTION GROUP 2 this generally involves automatic placement of the cursor at each data field, and on each press of the Enter key, progressing through the tabulated data and providing the opportunity for alteration. Again, any new data is tested before acceptance.

Level 3 also contains the supporting subroutines that are not associated with data entry or option selection, including the calculation subroutines used in OPTION GROUP 3. Many others are used for general purposes and may be called by several different sub-modules. Arguably these utilities could be regarded as level 4 sub-modules, but this would complicate the schematic as presented in Figure 8.1.

This schematic shows the label of each sub-module in its general relationship to other sub-modules. Most sub-modules use a seven-character label to assist in presentation of the structure (avoiding boxes to conserve space). Within an OPTION GROUP module, level 2 sub-modules can only be called from level 1. Level 2 sub-modules cannot be called from outside that GROUP. Level 3 sub-modules can only be called by a level 2 sub-module within the same GROUP, except for the utility routines (marked with an apostrophe) that could be called from another GROUP at level 2. The intention of this rigid and predictable structure is to avoid software bugs and facilitate maintenance or ongoing development.

Level 1	Level 2	Level 3
OPTION.0	PAGE.00	ENTRKEY'
	DISCLAM	ENTRTXT'
	NEWUSER	DEFAULT
	QUITASP	BORDERS'
		ERRLIST'
		PRTSCRN'
OPTION.1	PAGE.01	
	PROJECT	
	HEADSEL	
	FILTERS	
	TEMPSET	SITERAZ
	COLOURS	NOCOMNT'
OPTION.2	PIPENUM	
	IDENTNO	STDLIST'
	PIPELEN	FIXDATA
	FSTPOSN	SCANMIR
	POSNGAP	BENTEST
	PIPEDIA	HOLPOSN
	TUBEDIA	STEPDIA
	HOLEDIA	TUBELEN
	ENDVENT	NUMHOLE
	BENDRAD	STPHOLE
	XEPRESS	BENDLOC
	LAPRESS	BARDISP
	AMBIENT	NO.MORE
	PIPEFLO	CROSWND
OPTION.3	ITERATE	POSITNS
	COMPSEG	PARAMET
	COMPSYS	INCFLOW
	TABDONE	DECFLOW
	RESULTS	FFACTOR
	LOGDATA	BENDROP
	PREPARE	ULTRFLO
	COMBINE	CALTUBE
	COMPUTE	CALHOLE
		INFRFLO
		PIPTIME
		TUBTIME
OPTION.5	PAGE.02	MARKERS
	PAGE.03	DISDATA
	PAGE.04	SUMMARY
	PAGE.05	SPECIAL
	COPYPIP	PASSWRD
		DISPSYS
		DELAYTM
OPTION.6	PAGE.06	FILSORT
	FILEDIR	
	FILEGET	
	FILLOAD	
	FILSAVE	
	FILNAME	
	FILERAZ	
HELP	PLAN.1	Plan.Border
	PLAN.2	Plan.Print
	30 HELP PAGE SUB-MODULES	

Figure 8.13 - Sub-module structure

8.8.1 Coding Examples

The source code in Visual Basic for DOS contains some 280,000 bytes so a discussion of the code implementation is limited to presenting a few small subroutine coding blocks, including comments, that should serve to convey the required objectives of efficiency and simplicity (for ease of maintenance and high speed processing). Some spaces required for syntax are removed in order to fit long equations onto one line. Firstly, some indication of the development of the original model that was required from time to time over a period of years, can be gained from the summary of modifications which appears (for maintenance purposes) at the start of the listing:

```
'Major modifications history:

'MC 04-JAN-94 Page.1 added for project site details & comments
'MC 10-FEB-94 Page.6 FileLoad accepts & converts old files
'MC 26-MAR-94 Page.5 summary extended with minor parameters
'MC 24-APR-94 Page.6 dedicated to disk file management, 90/page
'MC 27-APR-94 Split into 4 main modules to overcome 64k file barrier
'RK 04-MAY-94 For Everlock to go through required startup procedure
'MC 09-JUN-94 Page.2 major parameter modules broken out to subs
'MC 10-JUN-94 New formulae for head loss in several filter types
'MC 15-JUN-94 Completely restructured into 6 main modules, 78 subs
'MC 25-JUN-94 7th module added with 22 context Help windows (F1 or ?)
'MC 05-JUL-94 System schematic plan diagrams added (F2 or !)
'MC 05-SEP-94 Multiple aspirators in series/parallel (XPres, XFlow)
'MC 16-AUG-95 Absolute atmospheric pressure & temperature adjustments
'MC 20-SEP-95 Comments extended and variable names expanded
'MC 22-SEP-95 Directory path added for file subdirectories
'MC 15-OCT-95 Iteration closing speed increased with new algorithm
'MC 30-OCT-95 Stub option does not increase positions count
'MC 18-DEC-95 Files selectable using cursor arrows, more Help added
'MC 23-FEB-96 Removed Everlock; default files path C:\ASPIRE\SITE
'MC 29-APR-96 Extension to cover VESDA LaserPLUS detector
'MC 01-MAY-96 Generalization of aspirator equ'n (Term2, Term1, Pmax)
'MC 30-JUL-96 All brands of detector characterized & selectable
'MC 29-NOV-96 Stub option treated as end vent on capillary tube
'MC 02-DEC-96 Selectable timing algorithms C0-C3.  Fast autocompute
'MC 21-JAN-97 Restructured - data arrays to separate print routines
'MC 21-FEB-97 Parameters redefined to suit Delphi (Pascal) trans'n
'MC 05-MAR-97 Page.4 amended to consolidate user-oriented data
'MC 18-MAR-97 Removed option to have sampling holes beside end vent
'MC 07-MAY-97 Engine consolidated so coeff's set before iteration
'MC 27-MAY-97 Hole sensitivity det. by Fire threshold setting only
'MC 02-JUL-97 Drive can be A: to Z:, default to C: if unavailable
'MC 02-JUL-97 Files list (Page.6) sorted into alphabetical order
'MC 03-JUL-97 Old files with Stub option corrected for Posns & DVent
'MC 09-JUL-97 Auto-compute error reduction improved; auto recompute
'MC 03-AUG-97 PREPARE sub ensures correct individual operating points
'MC 29-AUG-97 BENDROP sub to accurately calculate bend pressure drops
'MC 04-SEP-97 Auto-compute based upon pipe pressure not aspirator
'MC 09-SEP-97 Divide pipe into identical branches after first posn
'MC 08-OCT-98 Incorporation of new friction factor algorithms
'MC 12-NOV-98 Incorporation of ULTRAFLOW algorithms
'MC 26-NOV-98 Incorporation of new Time Factor algorithms
'MC 18-DEC-98 Inclusion of VESDA Compact and Nohmi VESDA detectors
```

```
SUB INCFLOW () : 'Increase flow with rapid closing of iteration

  IF QPipe(Pipe%, 1) > QLowmark THEN QLowmark = QPipe(Pipe%, 1)
  'raise the low benchmark to the existing, inadequate flow

  QPipe(Pipe%, 1) = QLowmark + (QHighmark - QLowmark) / 2
  QPipe(Pipe%, 0) = QPipe(Pipe%, 1)
  'try another flow, averaged within the benchmarks

END SUB


SUB DECFLOW () : ' Decrease flow with rapid closing of iteration

  IF QPipe(Pipe%, 1) < QHighmark THEN QHighmark = QPipe(Pipe%, 1)
  'reduce the high benchmark to the existing, excessive flow

  QPipe(Pipe%, 1) = QHighmark - (QHighmark - QLowmark) / 2
  QPipe(Pipe%, 0) = QPipe(Pipe%, 1)
  'try another flow, averaged within the benchmarks

END SUB


FFACTOR(Dis%): ' Get friction factor ( ... includes algorithms such as:)

  ReI = RePipe(Pipe%, Posn%): 'shorten the equations
  .
  .
  DISTURB7: 'Friction factor for maximally disturbed flows (>7%)

  SELECT CASE ReI
    CASE IS < 997:       FfI = 64 / ReI
    CASE 997 TO 2170:    FfI = 7.1E-09*ReI^2 - .000043*ReI + .1
    CASE 2170 TO 2480:   FfI = .041
    CASE 2480 TO 2870:   FfI = - 8.07E-09*ReI^2 + 4.83E-05*ReI - .0301
    CASE IS > 2870:      FfI = .1389 / (ReI^.15)
  END SELECT
  RETURN
  .
END SUB


SUB BENDROP () : 'Calculate the pressure drop in a bend

  IF Bflag(Pipe%) = 0 OR Bends(Pipe%, Posn%) = 0 THEN
    BendLoss = 0
  ELSE
    Re = RePipe(Pipe%, Posn%): 'shorten the equations
    SELECT CASE Re
      CASE IS < 2323: Loss1 = 9.4E-11*Re^3 + 3.5E-07*Re^2
      CASE 2323 TO 2994: Loss1 = 1.766E-06*Re^2 - .0118*Re + 20.9
      CASE IS > 2994: Loss1 = 8.7E-08*Re^2 + .000055*Re + .455
    END SELECT
    'this is the bend loss for the first bend
    B = Bends(Pipe%, Posn%) - 1
    BendLoss = Loss1 + 1E-07*B*Re^2 + (.00035 + .00025*B)*Re
    'incremental effect of additional bends
  END IF
  PBend(Pipe%, Posn%) = BendLoss

END SUB
```

```
SUB CALHOLE () : 'Calculate hole size for given flow rate & pressure

  IF QHole(Pipe%, Posn%) <= 0 OR PHole(Pipe%, Posn%) <= 0 THEN
    DHole(Pipe%, Posn%) = 0
    EXIT SUB
  END IF

  IF FixBal(Pipe%) = 1 THEN
       QHoleI = QhBal(Pipe%) * 60000
  ELSE QHoleI = QHole(Pipe%, Posn%) * 60000
  END IF

  KHoleT = QHoleI / SQR(PHole(Pipe%, Posn%))
  KHole = KHoleT / SQR(1.192 / rho): 'Temperature adjust ref 23degC

  Ax = .0391
  Bx = .0075
  Cx = -KHole
  DHoleI = (SQR(Bx ^ 2 - 4 * Ax * Cx) - Bx) / (2 * Ax)
  'revised hole diameter (m)

  DHole(Pipe%, Posn%) = DHoleI * 1000
  'revised hole diameter (mm)

END SUB



SUB TUBTIME () : 'Calculate capillary tube transport time

  IF Tflag(Pipe%) = 0 OR LTube(Pipe%, Posn%) = 0 THEN
    TubeTime = 0
  ELSE
    DTubeI = DTube(Pipe%, Posn%) / 1000
    LDTube = LTube(Pipe%, Posn%) / DTubeI
    VTubeI = VTube(Pipe%, Posn%)
    TubeTime = DTubeI*(LDTube+24*LOG(2-EXP(-LDTube/24)))/(2*VTubeI)
  END IF
  TTime(Pipe%, Posn%) = TubeTime

END SUB



FILESORT: 'routine to sort files into alphanumeric order

  Sorted% = 1
  FOR X% = 1 TO (FileTotal% - 1)
    IF FileList(X%) > FileList(X% + 1) THEN
      Sorted% = 0
      Dummy$ = FileList(X%)
      FileList(X%) = FileList(X% + 1)
      FileList(X% + 1) = Dummy$
    END IF
  NEXT X%
  IF Sorted% = 0 THEN GOTO FILESORT
  RETURN

END SUB
```

```
TIMEFAC: 'LV linear approximations to Time Factor

  SELECT CASE PDlen

    CASE IS < 15:
      TimeFactor = .746 * PDlen + .3

    CASE 15 TO 100:
      SELECT CASE RePipeI
      CASE IS < 660:       Ft1 = .555 * PDlen + 3.3
                           Ft2 = Ft1
                           ReL = 0: ReS = RePipeI
      CASE 660 TO 1320:    Ft1 = .555 * PDlen + 3.3
                           Ft2 = .555 * PDlen + 3.5
                           ReL = 660: ReS = 660
      CASE 1320 TO 2000:   Ft1 = .555 * PDlen + 3.5
                           Ft2 = -.00066 * PDlen^2 + .701 * PDlen + 1.1
                           ReL = 1320: ReS = 680
      CASE 2000 TO 2660:   Ft1 = -.00066 * PDlen^2 + .701 * PDlen + 1.1
                           Ft2 = .694 * PDlen + 1.15
                           ReL = 2000: ReS = 660
      CASE 2660 TO 3330:   Ft1 = .694 * PDlen + 1.15
                           Ft2 = .746 * PDlen + .3
                           ReL = 2660: ReS = 670
      CASE 3330 TO 4000:   Ft1 = .746 * PDlen + .3
                           Ft2 = .772 * PDlen + .1
                           ReL = 3330: ReS = 670
      CASE IS > 4000:      Ft1 = .772 * PDlen + .1
                           Ft2 = Ft1
                           ReL = RePipeI: ReS = 1
      END SELECT

    CASE IS > 100:
      SELECT CASE RePipeI
      CASE IS < 660:       Ft1 = .52 * PDlen + 7.2
                           Ft2 = Ft1
                           ReL = 0: ReS = RePipeI
      CASE 660 TO 1320:    Ft1 = .52 * PDlen + 7.2
                           Ft2 = .52 * PDlen + 7.4
                           ReL = 660: ReS = 660
      CASE 1320 TO 2000:   Ft1 = .52 * PDlen + 7.4
                           Ft2 = -.00011 * PDlen^2 + .579 * PDlen + 8.3
                           ReL = 1320: ReS = 680
      CASE 2000 TO 2660:   Ft1 = -.00011 * PDlen^2 + .579 * PDlen + 8.3
                           Ft2 = .7245 * PDlen - 1.46
                           ReL = 2000: ReS = 660
      CASE 2660 TO 3330:   Ft1 = .7245 * PDlen - 1.46
                           Ft2 = .7657 * PDlen - 1.36
                           ReL = 2660: ReS = 670
      CASE 3330 TO 4000:   Ft1 = .7657 * PDlen - 1.36
                           Ft2 = .7753 * PDlen - .23
                           ReL = 3330: ReS = 670
      CASE IS > 4000:      Ft1 = .7753 * PDlen - .23
                           Ft2 = Ft1
                           ReL = RePipeI: ReS = 1
    END SELECT

  END SELECT

  TimeFactor = Ft1 + ((Ft2 - Ft1) * (RePipeI - ReL) / ReS)
  SegmentTime = 1.25 * (TimeFactor * DPipeI / VMeanI) * Segments%

RETURN
```

8.9 CONCLUSIONS

Chapter 8 has specified the input and output (user interface) requirements of the system modelling software and described the program structure. Some examples of the shorter code blocks within that structure are provided in order to demonstrate the required objectives of efficiency and simplicity (for ease of maintenance and for high speed processing).

A suitable tool has been developed for the purpose of modelling any proposed or existing aspirated smoke detection systems, in a wide variety of sizes and configurations. The tool is non-prescriptive, permitting "what-if" analyses. Accordingly, this tool facilitates an understanding of the relative significance of the size, number and position of each type of component in a system and thereby assists system designers to optimise the performance of a system.

CHAPTER 9 - VALIDATION OF THE MODEL

9.0 INTRODUCTION

Having developed a computer-based system model it is necessary to validate its results by comparison with real systems. To accomplish this in detail is difficult with installed systems because of the need for pressure tappings adjacent to each sampling hole. The temporary insertion of a pressure tap element inline with the pipework at various successive locations is not possible because invariably, the pipes are attached rigidly to their supports and this does not facilitate disconnection of the sockets. Moreover, it is a Standards requirement to glue the sockets permanently. Most sites are not accessible for experiments because of disruption to, or from, the working environment. Accordingly it is therefore necessary to replicate under controlled conditions, realistic systems that can be suitably configured for testing. A limited number of installed systems are investigated and compared with the results obtained from the initial and current computer models.

9.1 MEASUREMENT OF SYSTEM RESULTS

The objective is to measure the pressure distribution throughout a pipe system as well as the smoke transport time from each sampling hole. One simplification is that, for the purpose of validating the system model it is necessary only to test a single pipe. This is because, at any given system operating pressure at the aspirator, each pipe tends to act independently. If the measured aspirator pressure is input to an accurate system model, then the pressure distribution and transport times are predetermined.

The following test system was established as the site of reference for the initial, final and any intermediate generations of the computer model. It has been found over the years that successive versions of the model which have been adjusted empirically to produce results matching this site, have proven acceptably accurate when applied to a variety of situations in the field, provided that a similar pipe size was used, and that the system was located near sea level. An objective of the current research program has been to develop a computer model that produces results closely matching those of this reference site, without resort to empirical correction factors, thereby obtaining higher accuracy, adaptability, reliability and confidence.

The reference system was composed of a single pipe of $52m$ length and $21mm$ internal ($25mm$ external) diameter, laid out on the floor of an auditorium with the sampling holes facing upward, away from the floor. This arrangement facilitated the disconnection of sockets for the insertion and removal of a short pressure tap segment. The expedient of placing the pipework on the floor was considered unlikely to introduce any error because it was intended to introduce the smoke manually using a pressurised dispenser delivering a consistent charge. Accordingly there was no need to accommodate thermal rise of the smoke towards a downward-facing hole on a ceiling-mounted pipe. The sampling holes were $2mm$ diameter and the end vent was $6mm$.

The pipe was composed of $4m$ lengths joined by their integral sockets, and contained a total of four bends of $150mm$ radius. These bends were located at 10, 18+b, 30+2b and 38+3b m from the detector (where +b refers to the effective length of the bends that were included downstream). The sampling holes were placed at $4m$ intervals (plus a bend length where relevant), with each hole being adjacent to a pipe socket. This facilitated insertion of the pressure tap as closely as possible to the hole.

Being only $50mm$ in length with an accurately machined socket that preserved the continuity of the pipe internal surface, the pressure tap segment was designed to have negligible impact on the pressure drop and flow rate at the location it was inserted (adjacent to a hole or a bend), thereby preserving the system operating point.

The air-conditioned environment of the auditorium was 23±1°C and, being situated about $300ft$ above sea level, the long term average atmospheric pressure could be taken as 100200Pa. With the aspirator relative pressure set to -325Pa under zero-flow conditions, the operating point for the system was 173Pa (reversing the negative), corresponding to a total flow rate of about $46 litre/min$. Pressure readings were taken at all sampling holes and bends.

During this process, transport time readings were taken by introducing smoke from the Underwriters Laboratories approved "smoke detector sensitivity tester", being a pressurised aerosol spray can of synthetic smoke, and using a stop watch to time the delay prior to the first indication of smoke detection at the VESDA display. It was noted that the coincidental timing of the detector refresh cycle relative to the time of smoke arrival could cause an error between 0 and 3 sec. To reduce timing errors, the detector refresh rate was increased from 0.33 to 1 sec^{-1} and at least 20 readings were taken for each position. The shortest reliable reading was accepted - not the average reading which would introduce an unwarranted delay of $0.5sec$.

Selected results from the computer model are presented in Table 9.1, where the column labeling was limited by the size and font availability in the DOS version of the software. In this table, *Hole* is the sampling hole sequence number which corresponds with the pipe segment number (note that EV refers to the end vent position), *Posn* is the hole position in metres from the detector, *QPipe* (*litre/min*) is the pipe segment flow rate, *RePipe* is the segment Reynolds number, *ffPipe* is the segment friction factor, *dP.P* (Pa) is the pressure drop in the segment, *dP.B* (Pa) is the pressure drop in the bend (if fitted), *PHole* (Pa) is the pressure within the pipe adjacent to the hole, *QHole* (*litre/min*) is the hole flow rate, *Sens* (*%/m*) is the effective smoke-sensitivity of the hole after taking account of dilution and the detector alarm threshold setting (such as 0.05%/*m*), and *Time* is the transport time for smoke injected at the hole to reach the detector.

Hole	*Posn*	*QPipe*	*RePipe*	*ffPipe*	*dP.P*	*dP.B*	*PHole*	*QHole*	*Sens*	*Time*
1	2.0	46.1	3087	0.0416	11.7	0.0	260	2.9	0.79	0.8
2	6.0	43.2	2892	0.0420	20.8	0.0	239	2.8	0.83	2.6
3	10.3	40.4	2706	0.0415	18.0	2.8	219	2.7	0.87	4.4
4	14.3	37.7	2528	0.0404	15.3	0.0	203	2.6	0.90	6.3
5	18.6	35.2	2357	0.0410	13.5	3.7	186	2.4	0.94	8.3
6	22.6	32.7	2193	0.0410	11.7	0.0	174	2.4	0.98	10.3
7	26.6	30.4	2035	0.0419	10.3	0.0	164	2.3	1.01	12.4
8	30.9	28.1	1882	0.0442	9.3	2.5	152	2.2	1.05	14.8
9	34.9	25.9	1735	0.0468	8.3	0.0	144	2.1	1.08	17.1
10	39.2	23.8	1592	0.0495	7.4	1.8	135	2.1	1.12	19.8
11	43.2	21.7	1454	0.0525	6.6	0.0	128	2.0	1.15	22.6
12	47.2	19.7	1320	0.0556	5.7	0.0	122	2.0	1.18	25.5
EV	51.2	17.8	1190	0.0589	4.9	0.0	118	17.8	0.13	28.8

Table 9.1 - Selected computer model results

It is interesting to note that the span of Reynolds numbers is 1190 to 3087, encompassing much of the flow transition region, and the range of friction factor values which vary by a factor of 1.46 down the table.

Given that the sampling holes are of equal size, the hole flow rates are reasonably well balanced, varying from 2.9 to 2.0 *litre/min* ($2.45\pm18\%$). This is defined as achieving a pipe sector balance of 82% (i.e. 100%-18%). This results in equivalent hole smoke-sensitivities of 0.79 to 1.18 %/*m*, given a detector alarm threshold setting of 0.05% (representing half-scale on a typical detector). These hole sensitivity figures take into account the effect of smoke dilution assuming the worst case condition whereby only fresh air enters all other holes and the end vent. If smoke enters two holes then by aggregation, the effective sensitivity figure halves (i.e. twice as sensitive).

Posn.	1	2	3	4	5	6	7	8	9	10	11	12
Dia.	1.84	1.88	1.93	1.97	2.02	2.06	2.09	2.13	2.17	2.21	2.24	2.27

Table 9.2 - Hole diameters (*mm*) for perfect flow balance

On selection of the B% option in the software, it can be shown that a sector balance of 100% is achievable by adjustment of the hole diameters according to Table 9.2. This results in a flow rate of $2.4 litre/min$ at each hole. It is clear that very fine adjustment of the diameters would be required in order to achieve such perfect balance and, given the difficulty in controlling the process of drilling in the field while maintaining consistent hole inlet geometry, this is an impracticable goal (even if the required drill sizes were available). It is also an unnecessary goal because test fires are not reproducible with smoke concentrations held within (e.g.) ±18% at any given time. For this reason, the preferred minimum figure of merit for hole flow balance has been set at a span of ±30% (defined as a sector balance of 70%).

Based upon the data of Table 9.1 a comparison of the measured results with those of the new computer model is presented in Figure 9.1. Referring firstly to the pressure distributions, these are as indicated in the upper, falling solid curve which is in close agreement with the overlapping set of measured data points, especially considering the opportunity for small errors within each pipe segment to build toward a substantial cumulative error at the end. The pressure drop due to bends can be seen at the four relevant locations.

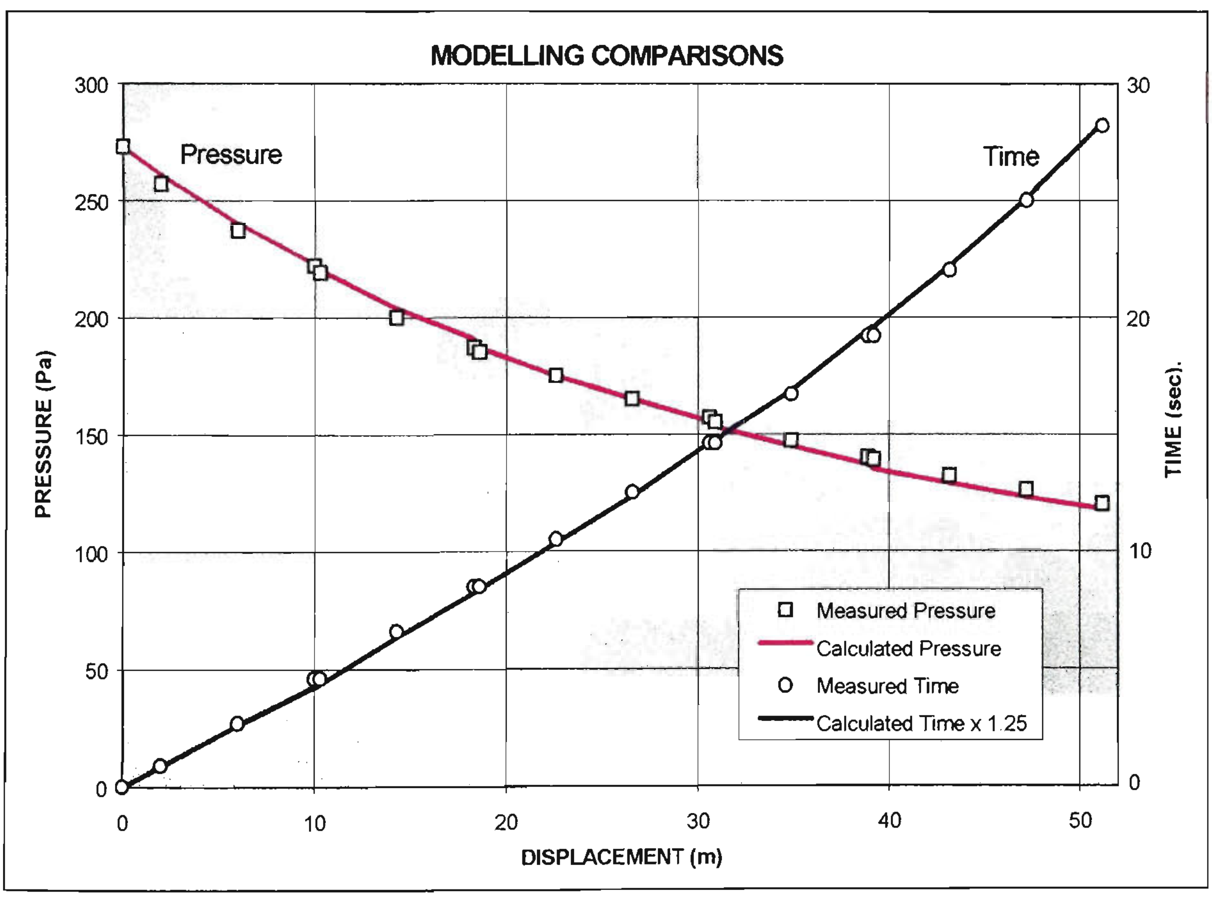

Figure 9.1 - Comparison of measured and modelled results

Unlike the initial computer model, this close agreement has been obtained without the application of any empirical correction factor in any segment (i.e. at any Reynolds number). Such an outcome was most gratifying indeed.

The magnitude of improvement in modelling accuracy gained from the new computer model can be gauged from Figure 9.2 where the measured pressure distribution is compared with the calculated results (middle graph). In addition, Figure 9.2 includes the results that would be obtained using the Nikuradse friction factors for both smooth (lower graph) and rough pipes (upper graph) which were relied upon in the initial model. So as to minimise the number of variables altered at one time, the other parameters used in the model incorporate the latest results, i.e. the hole flow equations of Chapter 4 and the detector characteristic equations of Chapter 2 are used.

It can be seen in Figure 9.2 that the modelling results using the Nikuradse data increasingly diverge from the measured results (represented by the axis), particularly at the higher displacements. The new-model results display a smaller error overall and more importantly, do not significantly diverge from the measured results. Note that errors would exist in the measured data (data scatter) which would influence the apparent errors in all graphs. Indeed this would appear to explain the consistency of errors in all three "models" within the first $15m$ - small errors in the measured data.

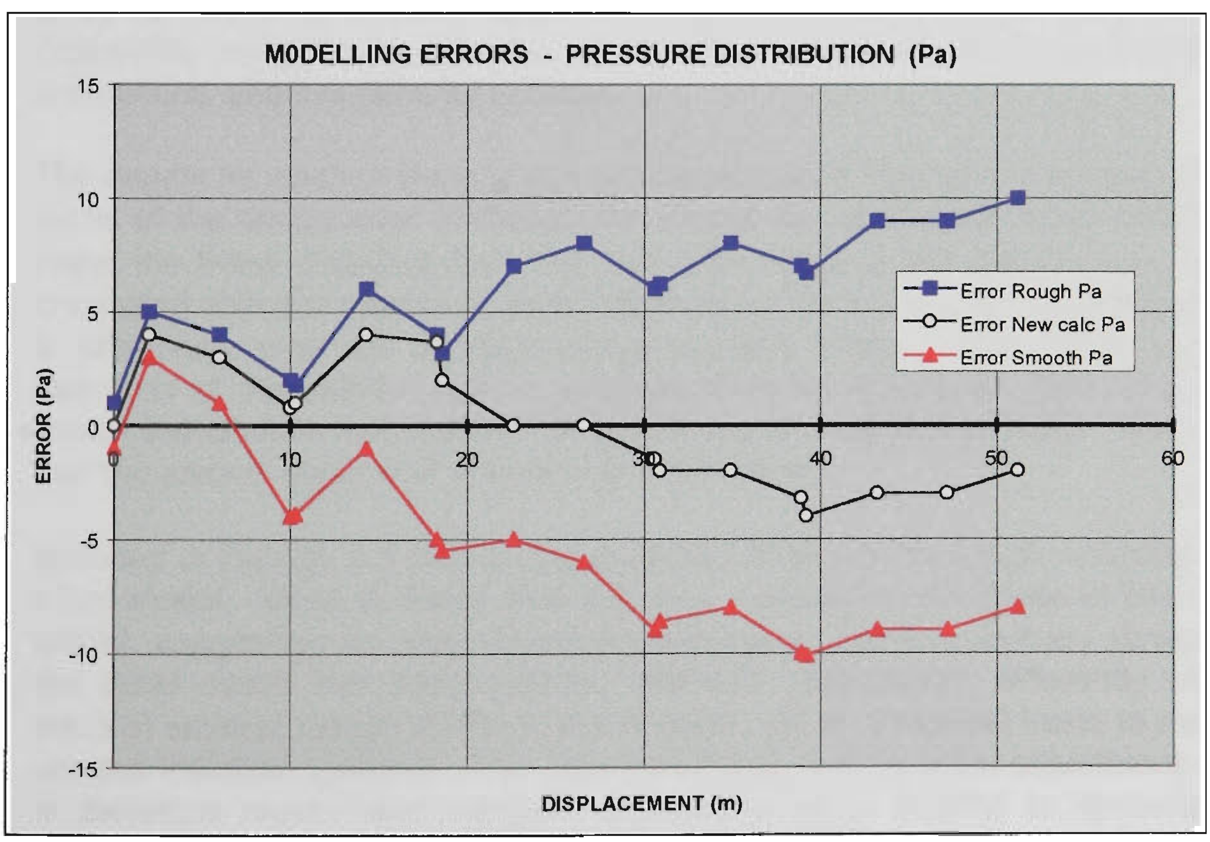

Figure 9.2 - Errors in pressure distribution using initial, and new estimates of friction factor

Figure 9.1 includes the calculated results for smoke transport time as a solid rising curve. The time axis has been placed on the right hand side, permitting both pressure and time data to be displayed on one page. As discussed in Chapter 7, to take account of the finite sensitivity of the detector coupled with smoke dilution effects within the pipe, it had proven necessary to increase the calculated transport time results by 25% across the board to achieve the close agreement shown. However, it is interesting to confirm in Figure 9.1 that the discrepancy of 25% is appropriate to all results, irrespective of the Reynolds number prevailing in the given segment.

9.2 FURTHER VALIDATION TRIALS

Having gained a high level of confidence in the ability of the model to represent the pressure and flow distributions around a system, further attention was paid to validating the smoke transport time, particularly with a view to further confirmation of the 25% time penalty discussed above. An installed system was available for testing in the factory area underneath the auditorium. This comprised a two-pipe system on the Western half of the factory, and a three-pipe system on the Eastern half. The overall pipe lengths of the Eastern system were 26.6 and 29.3 m above electronics assembly lines (each with 12 sampling holes and an end vent), and 8m in a short branch covering an amenities area (with two holes and a vent). The smoke transport times for each hole and vent in the assembly-area pipes were tested thoroughly using the usual pressurised smoke dispenser and stop watch in conjunction with the detector display.

The results for each of these pipes are presented in Figures 9.3 (a) and (b) in terms of the timing error (although the simple 8m section has been omitted). Here, the times obtained from the computer model (solid graph) have been compared with the measured times (defined as the x-axis), and expressed as a difference error on a segment-by-segment basis. This basis avoids distortion of the results due to possible error accumulation, given that the model calculations are performed on the same (segmental) basis. We see that the error is about half a second in most cases.

Included in Figures 9.3 (a) and (b) as dotted lines are the results of using the initial model. Most of these data are very consistent with those of the new model, suggesting an insignificant improvement. On the contrary however, the initial model had been heavily "adjusted" (calibrated), differently within each of several ranges of Reynolds number, on an empirical basis to match several installed systems. The new model has had no such adjustment and is therefore much more reliable, particularly when applied to systems of different configuration from those previously tested.

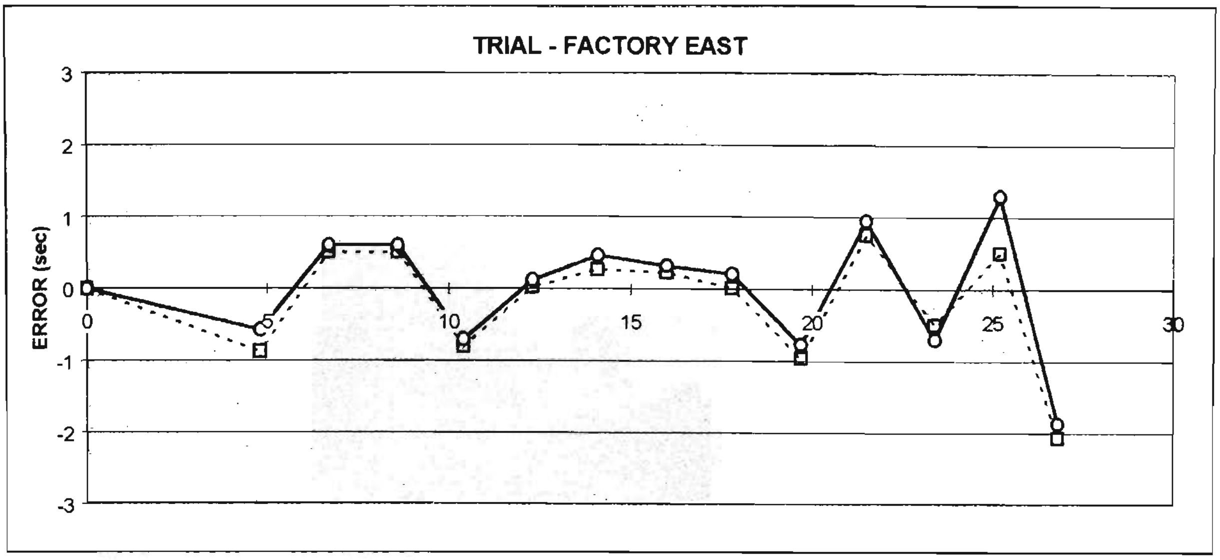

Figure 9.3 (a) - Inferred transport time errors for East factory system
(26.6 m branch)

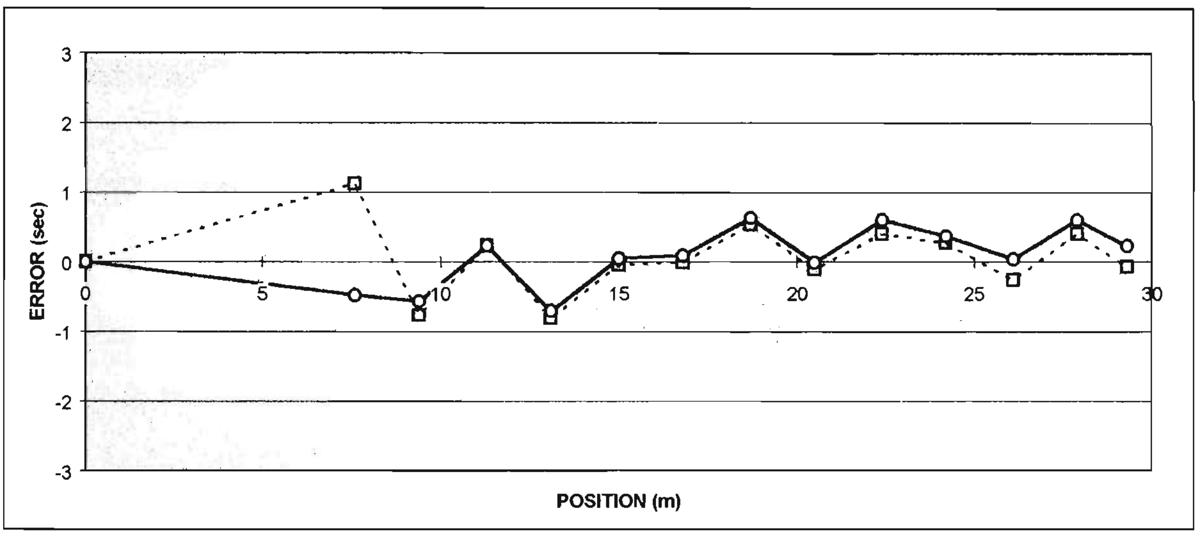

Figure 9.3 (b) - Inferred transport time errors for East factory system
(29.3 m branch)

Given the different approaches taken in the development of the initial and new models for transport time, the similarity in the trends of the pairs of graphs is remarkable, and most unlikely to be coincidental. This suggests a small but common element to the graphs - measurement error. Accordingly it is possible to conclude that the new model is a suitable, and more credible, replacement for the initial model.

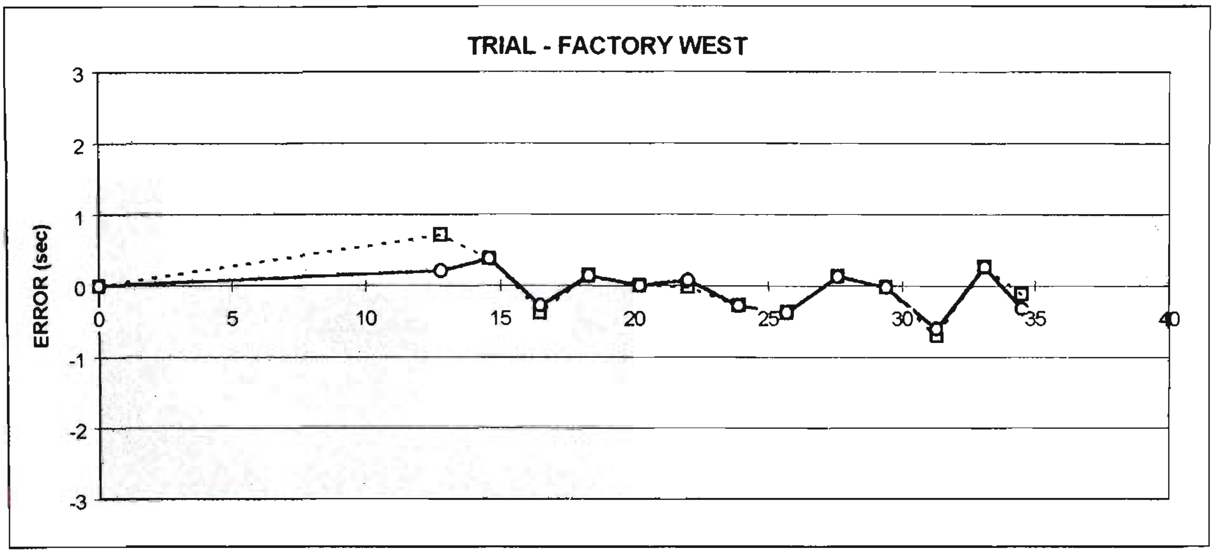

Figure 9.4 (a) - Inferred transport time errors for West factory system ($34.5m$ branch)

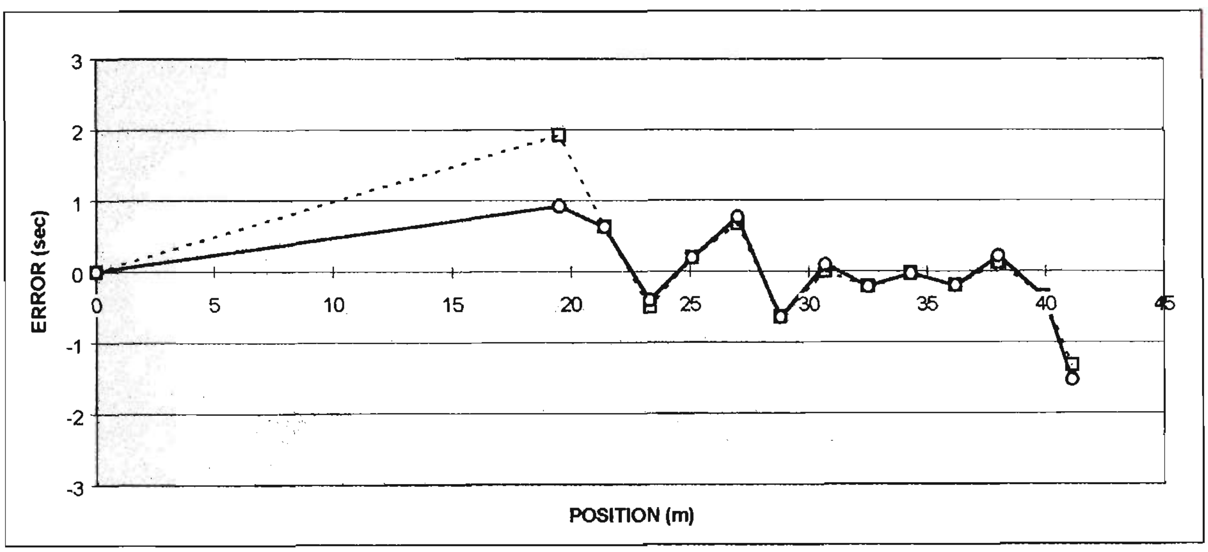

Figure 9.4 (b) - Inferred transport time errors for West factory system ($41.1\ m$ branch)

Turning now to the results of testing the Western factory area system, this has pipe lengths of 34.5 and 41.1 m (each again having 12 sampling holes and an end vent). The results as presented in Figures 9.4 (a) and (b) have been treated in the same manner as the Eastern system and the same conclusions can be drawn, except to add that the initial model appears consistently to incorporate an unusually large error in the nearest pipe segment (which is also the longest segment and therefore the one most likely to reveal errors).

9.3 AMBIENT CONDITIONS

In view of the findings in Section 2.6, a typical large system was modelled to quantify the overall influence of ambient air temperature and pressure. Firstly, Figure 9.5 (a) presents the air density ("Rho") and kinematic viscosity ("Kin" scaled x10^4) for a temperature range of -20 to +60 °C, at the highest (1050*millibar*) and lowest (265*millibar*) ambient pressures ever expected to be encountered in the field (the latter typically applies at an elevation of 10,000*ft*).

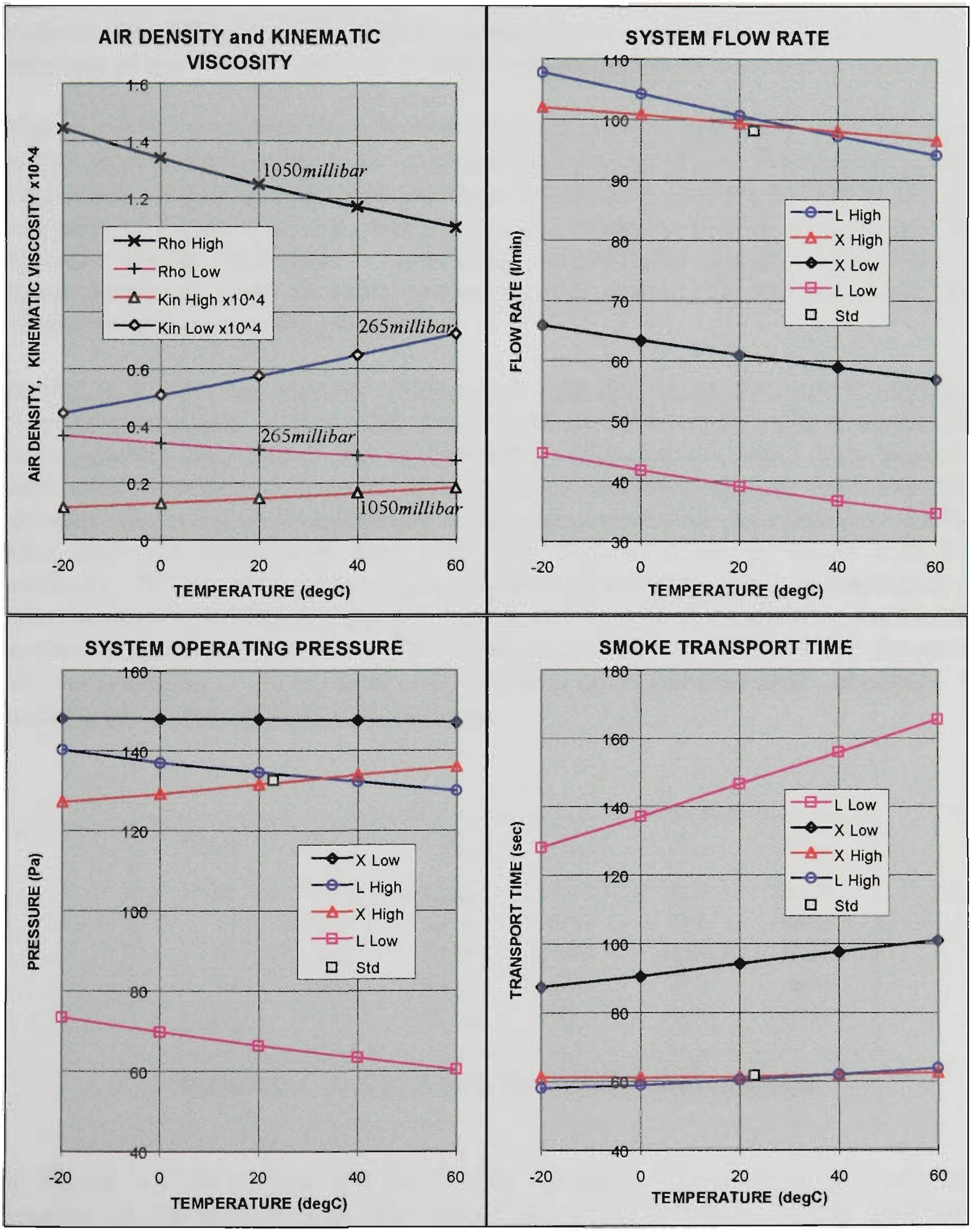

Figure 9.5 (a to d) - The influence of ambient temperature and pressure on air density, and system operating flow rate, pressure, and transport time

The most typical of large systems comprises four pipes (two at $52m$ and two at $48m$) using twelve $2mm$ holes at $4m$ spacing, with pipe of $21mm$ internal diameter and a $4mm$ end vent. The above range of ambient temperatures and pressures was applied to the model of such a system, selecting either a Xenon VESDA Mk3 ("X") or a VESDA LaserPLUS ("L") package - i.e. a constant-voltage or a constant-speed aspirator.

To obtain identical results at 23°C and $1002 millibar$ (adopted as the standard) it proved necessary to set the former aspirator to 315Pa (at cutoff) with the latter set to 3600RPM. Note that because of the complex dynamics of the total system, for different pipe system configurations a different setting could be required of the former aspirator to align with the latter.

Figure 9.5 (b) presents the effect on the system operating flow rate (with the white square representing the standard system operating flow rate for both detectors). It can be seen that the large deviation in air density and kinematic viscosity of Figure 9.18 (a), has a more pronounced effect in the case of the constant-speed aspirator - exhibiting significantly greater temperature dependence at high ambient pressure, and some 50% greater flow rate reduction at low ambient pressure.

In Figure 9.5 (c) we see the influence of ambient pressure upon the system operating pressure, which in the case of the VESDA LaserPLUS, is some four times greater than that of the VESDA Mk3, with opposite sign. This opposite sign was unexpected because the aspirator pressure reduces with reducing density. Upon closer investigation it was discovered that, because the VESDA Mk3 package contains a dust filter and detector head in series with the aspirator, the pressure drop across these components reduces (because of the reduced flow rate) at a greater rate than the aspirator pressure, so the net system operating pressure actually rises, as indicated in Table 9.3 (calculated at $1002 millibar$). This does not occur if a constant-speed aspirator is substituted in the VESDA Mk3 package.

Temp	Q_{system}	P_{asp}	P_{filter}	P_{head}	P_{system}
-20	101.4	220.8	60.7	32.6	127.8
0	100.1	215.9	56.7	29.1	130.2
20	98.6	211.9	53.4	25.9	132.6
40	97.1	208.5	50.4	23.3	134.8
60	95.5	205.6	47.8	20.9	137.0

Table 9.3 - Model results for VESDA Mk3 package

In Figure 9.5 (d) we see that the smoke transport time is consistent with the inverse of the system flow rate shown in Figure 9.5 (b). This is obviously because the transport time is predominantly determined by the average air velocity throughout the pipe (which is proportional to flow rate if the pipe diameter is held constant).

It is important to emphasise that the full span of influences shown in Figures 9.5 (a to d) represent extreme cases which are most unlikely to be encountered by any one system, even if installed on board a modern aircraft (commonly pressurised to $8000ft$ or lower, including the cargo hold which is a good application for aspirated smoke detection). However, these influences must be taken into account in the design of products and systems.

It is also important to distinguish between smoke detectors that are calibrated with absolute sensitivity, and less-accurate smoke detectors that resort to self-adjusting sensitivity to compensate for temperature drift, soiling (dust buildup on detector internal surfaces) and the environmental background (air pollution and airborne dust). The degree of early-warning, or indeed the level of immunity to unwanted alarms, provided by this latter type of detector, cannot be reliably predicted over time.

We may conclude that for most fixed installations using aspirated smoke detectors calibrated with absolute sensitivity, the influence of ambient conditions which change over time would not significantly affect the smoke detection performance, as compared with the results obtained during commissioning and acceptance of the system.

However, the influence of changing ambient conditions does place a demanding requirement on the accuracy and stability of the anemometer (which is commonly installed within a detector), to compensate for those changes, in monitoring for possible leakages or blockages within the system. Only in this situation is the constant-speed aspirator to be preferred, because the constant-voltage aspirator tends to compensate for changes and thereby partially to mask the effects of leakage or blockage.

9.4 SYSTEM PARAMETER OPTIMISATION

Having validated the model, it can now be applied to the design of aspirated smoke detection systems. In particular the model can be used to undertake a sensitivity analysis of the numerous parameters affecting the performance of an aspirated pipe system. This is useful in gaining a "feel" for the most appropriate range of parameter values to use, particularly for the pipe length, pipe internal diameter, separation of sampling holes (which also determines the number of positions), sampling hole diameter, and the end vent diameter. Other parameters include the number and size of bends, the number, size, length and curvature of capillary tubes, and the size of nozzles. Such an analysis could be further extended to cover a range of aspirator settings and a selection of dust filters, as well as ambient temperature, pressure, and crosswind.

To recapitulate, the “figures of merit” for a system are:

⇒ the smoke transport ***time*** (which is the worst-case delay for smoke to arrive at the detector from the least-favorable position),

⇒ the ***balance*** (describing the variation in smoke-sensitivity throughout the system due to the inequality of hole flow rates, and is again the worst-case figure representing the least-favorable position), and

⇒ the ***share*** (being the proportion of the total air flow in the pipe contributed by all the sampling holes, excluding the end vent). This last figure of merit is used to avoid excessive smoke-sensitivity at the end vent compared with a typical hole.

In various jurisdictions the *time* is required to be no more than $90sec$ for general applications, although $60sec$ is often specified for high-risk areas. In the interest of achieving reasonably uniform smoke-sensitivity throughout the zone, the *balance* and *share* are each required to be at least 70% (preferably 80%). It should be noted that for simplicity, all sampling holes in a given pipe are usually specified at the same size, but as an option, the *balance* can be set to 100% so that the required diameter of each hole is computed and displayed. This often requires fine increments in drill sizes which are not generally available. Therefore as a compromise, it is also possible to set preferred steps in hole diameter (according to available drill sizes) and to judge the suitability of the *balance* obtained.

In the following examples presented, a VESDA Mk3 detector has been selected with the aspirator set to 300Pa (at cutoff). A single pipe is also assumed. However, the results would translate to multiple pipes or to other detectors (only the available pressure is different, which does not significantly alter the optimum value of pipework parameters).

The ambient temperature and pressure are set to 23°C and $1.013millibar$ respectively. For simplicity, the separations between adjacent hole positions have been made equal throughout the pipe length, including the first position (if the separation does not divide into the length precisely, the shortfall is taken-up at the end vent position).

In each case, the *time*, *balance* and *share* are presented in response to a variation in the hole or vent diameter, pipe length or internal diameter, and are repeated for a family of three sets of curves to reveal the trends. The salient features are discussed and the optimum configuration is stated.

Six different scenarios are presented as one-per-page as follows:

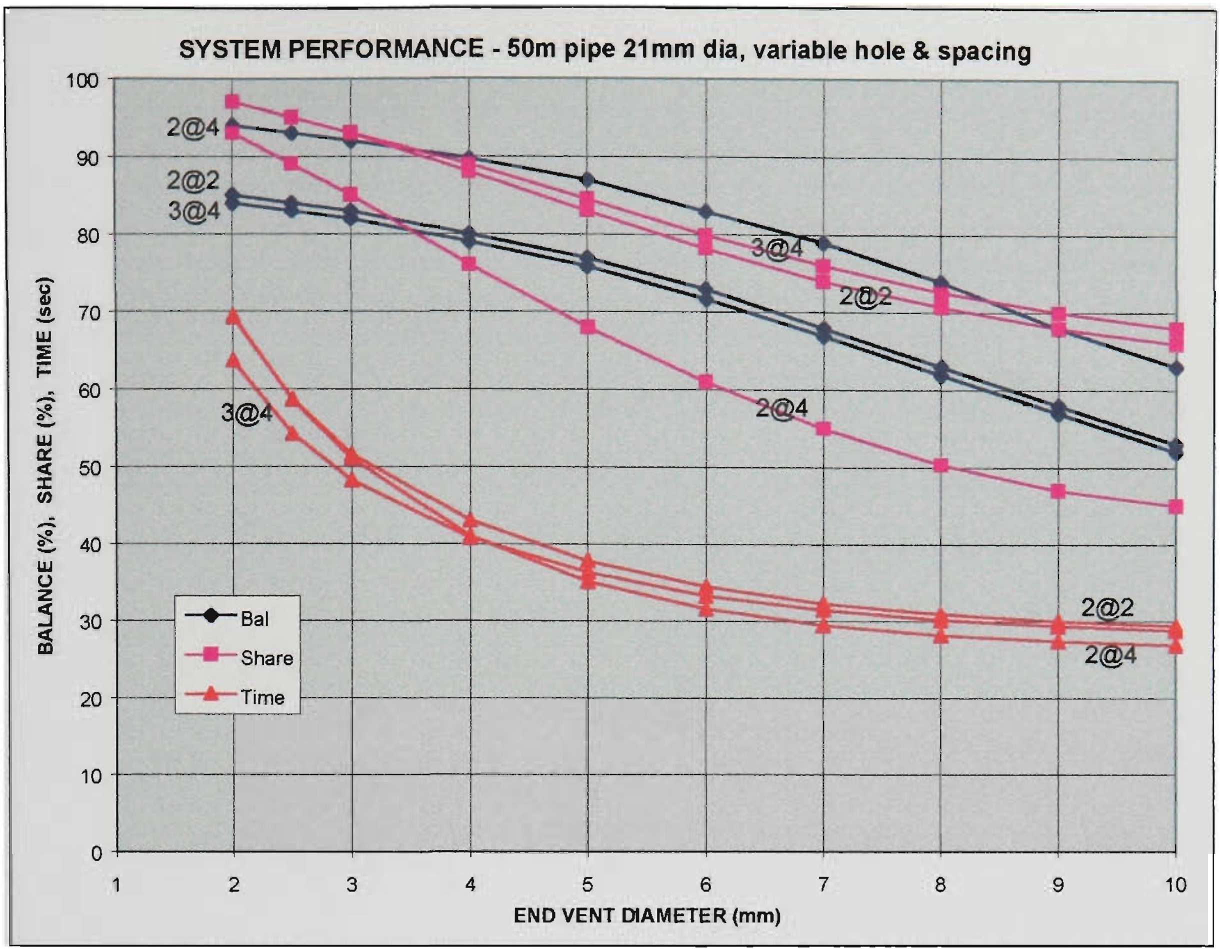

Figure 9.6 - Optimising the end vent diameter ($50m$ pipe)

Figure 9.6 simulates a pipe fixed at $50m$ length and $21mm$ internal diameter, with a variable end vent size. The sampling holes are either 2 or 3 mm with hole separations of 2 or 4 m. The three configurations shown, have $2mm$ holes at $4m$ separation (2@4), $2mm$ holes at $2m$ spacing (2@2), and $3mm$ holes at $2m$ spacing (3@2). The 2@2 and 3@4 configurations have a similar system flow rate because the latter has half as many holes of approximately twice the cross-sectional area.

The *times* for all configurations are similar, and indicate that an end vent greater than $6mm$ would produce little advantage, while a vent smaller than $4mm$ would produce excessive *times* (this indicates the merit of allowing the end vent to have a size that is different from the sampling holes). The 2@2 and 3@4 configurations produce similar *balance* and *share* across the range, becoming unacceptable for end vents larger than about $6mm$. The 2@4 configuration produces an acceptable *balance* for end vents less than $9mm$, but the *share* is unacceptable unless the vent is about $4mm$ or less.

The optimum configuration is either 2@2 or 3@4, depending upon whether the smaller area resolution is beneficial at the site (e.g. a highly divided space), or whether the larger hole size is preferable from a soiling-resistance viewpoint.

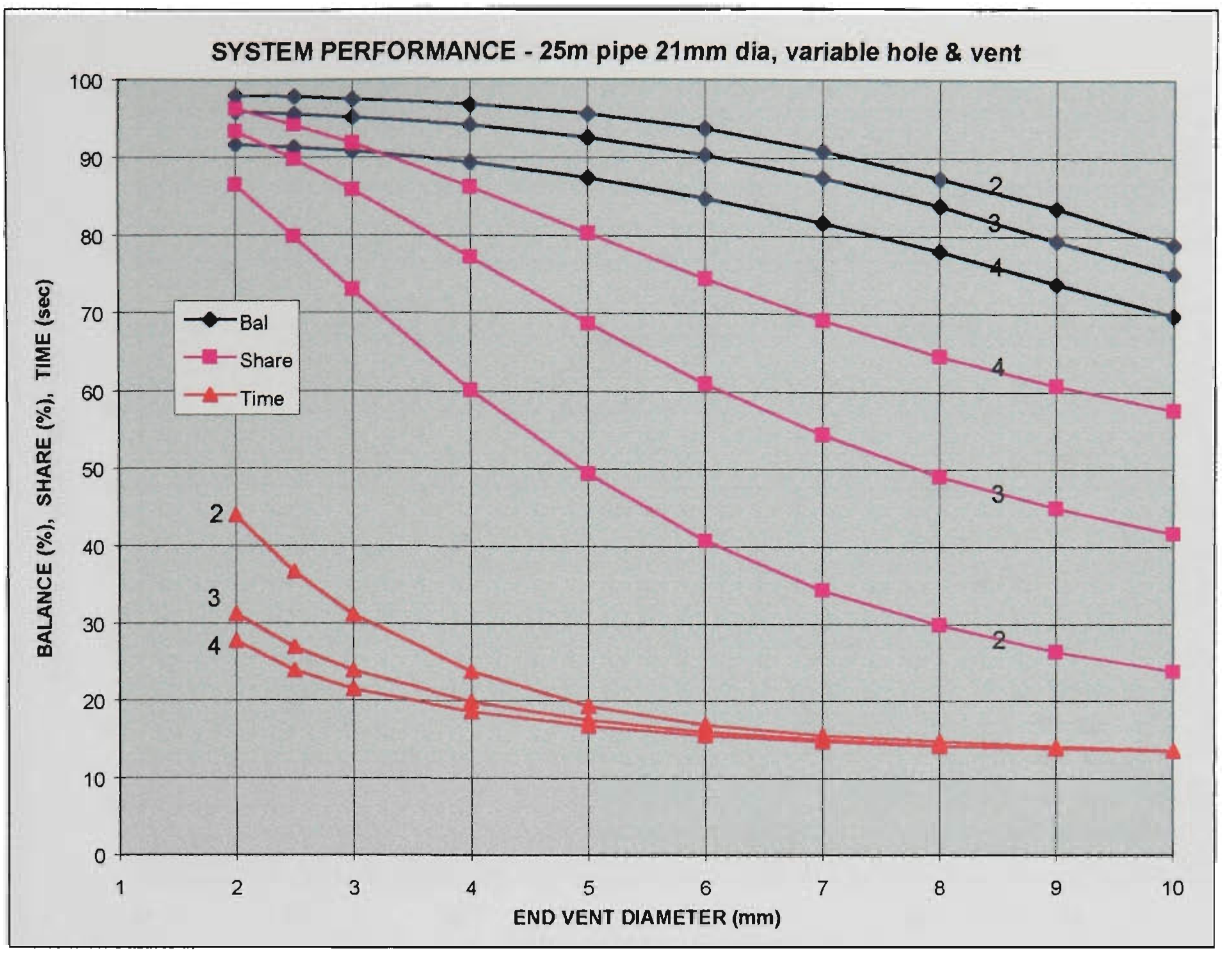

Figure 9.7 - Optimising the end vent diameter ($25m$ pipe)

Figure 9.7 simulates a pipe fixed at $25m$ length and $21mm$ internal diameter, with a variable end vent size. The sampling hole separation is set at $4m$. The three configurations shown, have 2, 3 or 4 mm hole diameters.

The *times* for all configurations are similar if the end vent is larger than about $5mm$, and there is little advantage in using a vent greater than $6mm$. An acceptable *balance* is achieved for all configurations although it becomes marginal in the case of a $4mm$ hole and $10mm$ vent. The *share* is strongly affected by the combination of hole and vent sizes.

Since there are only 6 positions, the optimum configuration for this relatively short pipe has a hole diameter of $4mm$ because this has the most acceptable *share*. Best performance is obtained for an end vent of 4 to 6 mm.

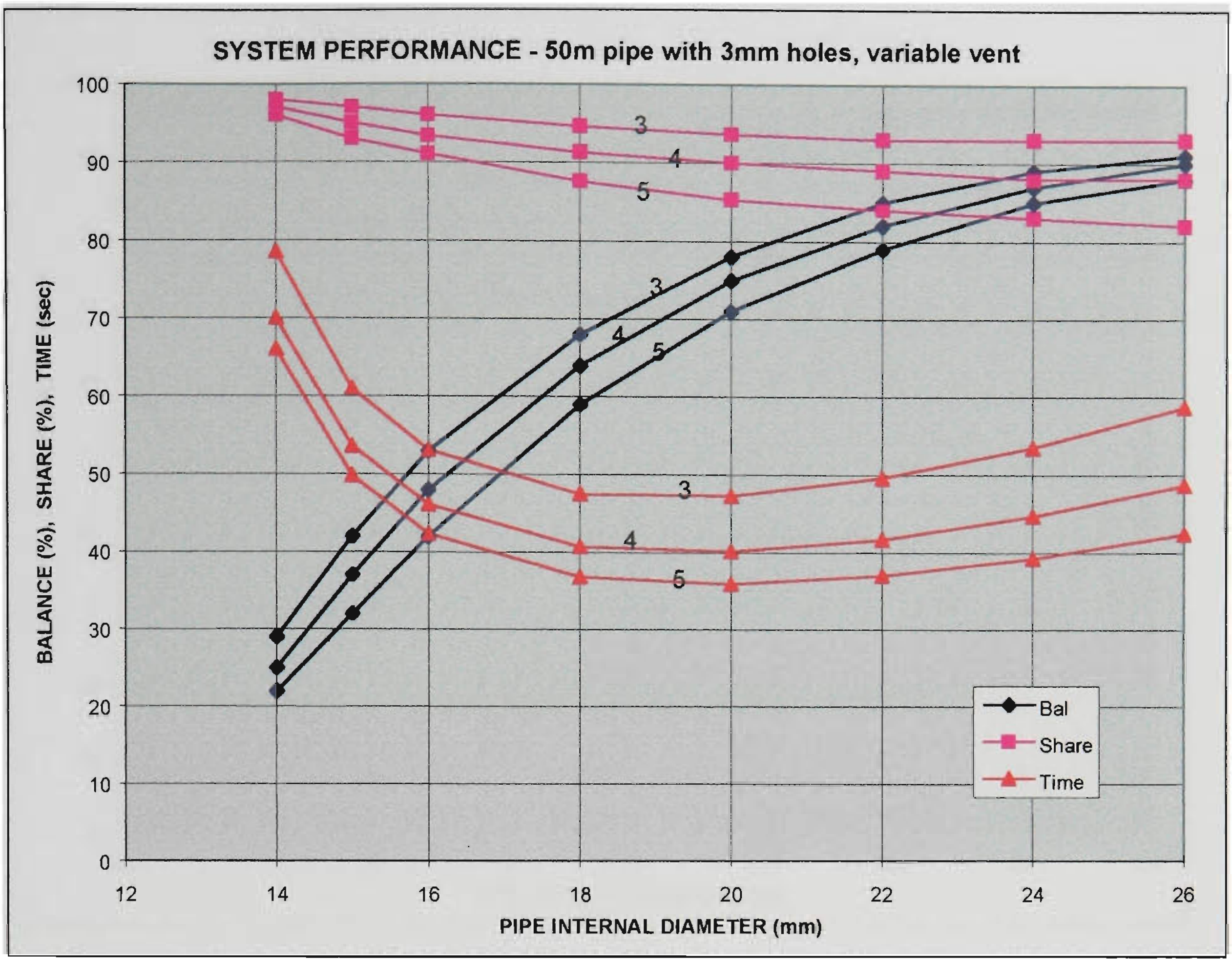

Figure 9.8 - Optimising the pipe diameter (50*m* pipe)

Figure 9.8 simulates a pipe fixed at 50*m* length, with a variable internal diameter. Sampling holes of 3*mm* are used throughout, with a separation of 4*m*. The three configurations shown, have end vents of 3, 4, or 5 *mm*.

A 5*mm* end vent produces the shortest *times*, and for each vent, the minimum *time* is obtained for a pipe diameter between 17 and 22 *mm*. However, the *balance* improves significantly with increasing pipe diameter, becoming acceptable above about 20*mm*. The *share* is acceptable in each case, reducing with increased pipe diameter.

Taking account of all the above, the optimum configuration has a 20 to 21 *mm* diameter pipe with a 4*mm* end vent.

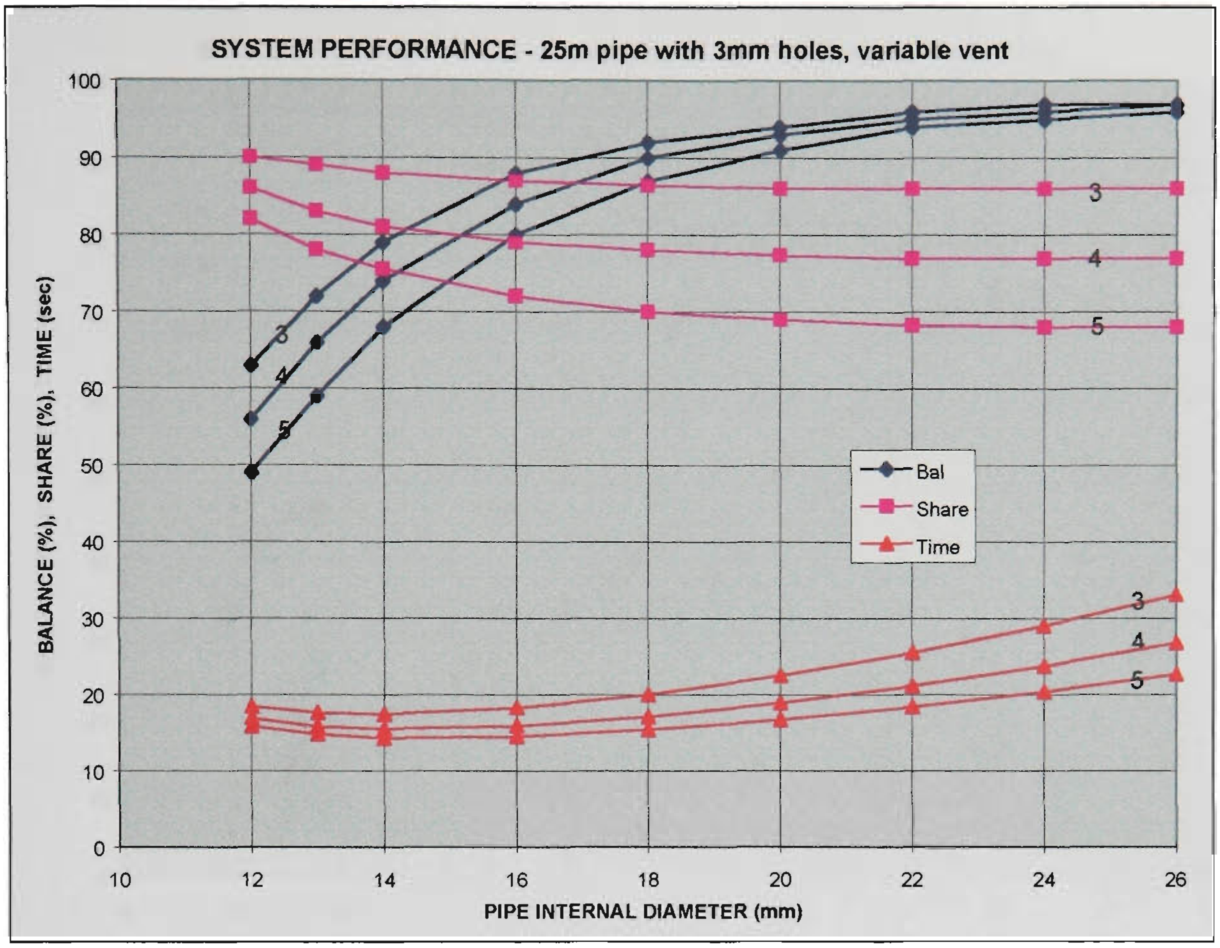

Figure 9.9 - Optimising the pipe diameter ($25m$ pipe)

Figure 9.9 simulates a pipe fixed at $25m$ length, with a variable internal diameter. Sampling holes of $3mm$ are used throughout, with a separation of $4m$. The three configurations shown, have end vents of 3, 4, or 5 mm.

A $5mm$ end vent produces the shortest *times*, and for each vent, the minimum *time* is obtained for a pipe diameter between 12 and 16 mm. However, the *balance* improves significantly with increasing pipe diameter, becoming acceptable above about $14mm$. In the case of 3 and 4 mm end vents, the *share* is acceptable at all pipe diameters, although reducing as pipe diameter is increased. The *share* is unacceptable for pipe diameters above $18mm$ in the case of a $5mm$ vent.

Taking all these factors into account, the optimum configuration would have a $16mm$ pipe diameter with a $4mm$ end vent.

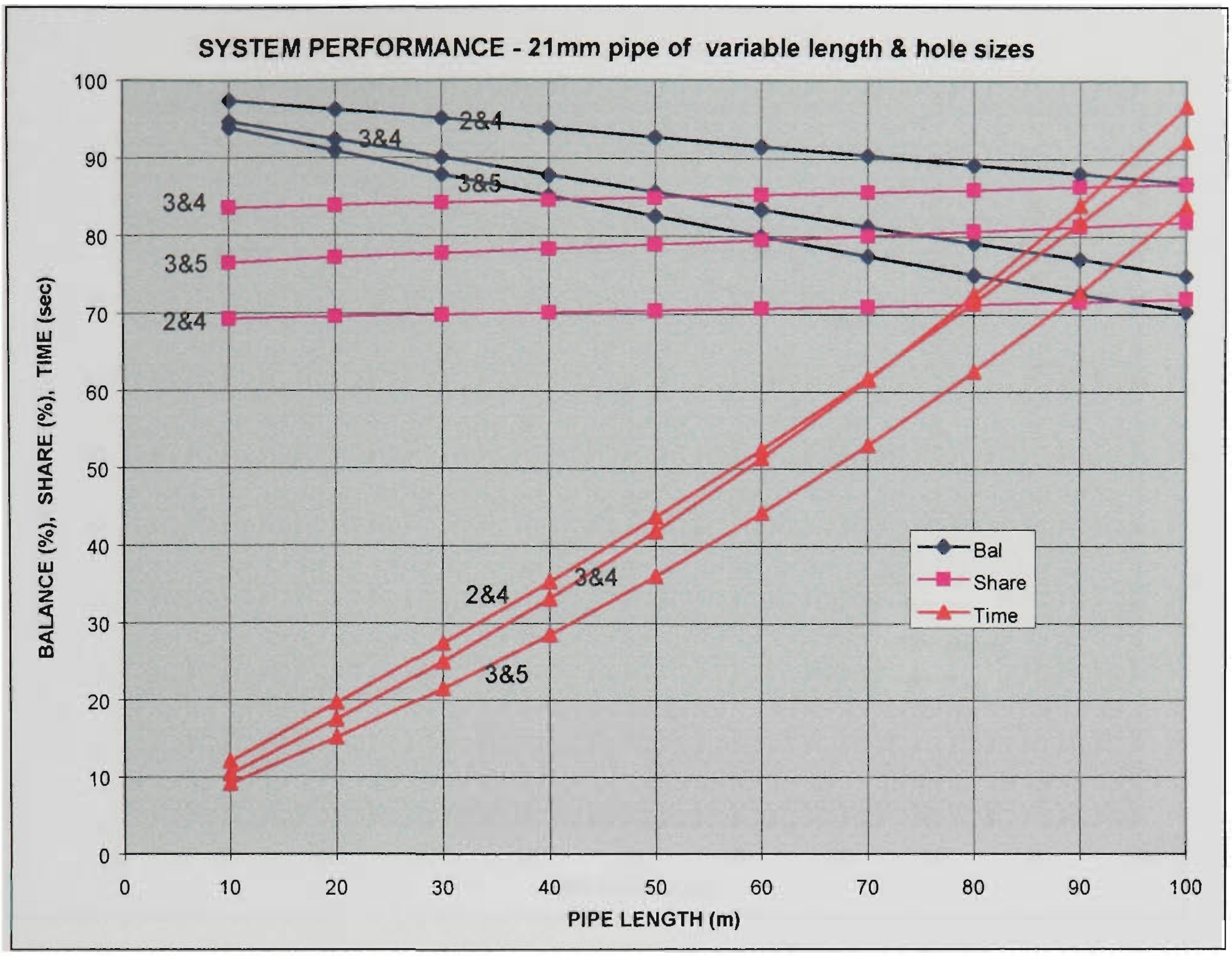

Figure 9.10 - Optimising a hole size suitable for all pipe lengths

Figure 9.10 simulates a pipe of $21mm$ internal diameter for which the pipe length is increased from 10 to 100 m. The pipe always contains 10 positions so the hole separations range from 1 to 10 m respectively. The three configurations shown, use sampling holes of $2mm$ with an end vent of $4mm$ (2&4), $3mm$ holes with a vent of $4mm$ (3&4), and $3mm$ holes with a vent of $5mm$ (3&5).

We see that the 3&5 configuration consistently provides the shortest *times*, but also provides the least favorable *balance*, falling to about 70% at $100m$. It achieves an acceptable *share*, especially at long lengths. The 2&4 configuration achieves the best overall *balance* and reasonably good *times* at long pipe lengths, but its *share* is only marginally acceptable. The 3&4 configuration provides the best *share* and an acceptable *balance* at all lengths, but provides the poorest *times* at long lengths.

The optimum configuration across the range would be 3&5 - a $3mm$ hole with $5mm$ end vent.

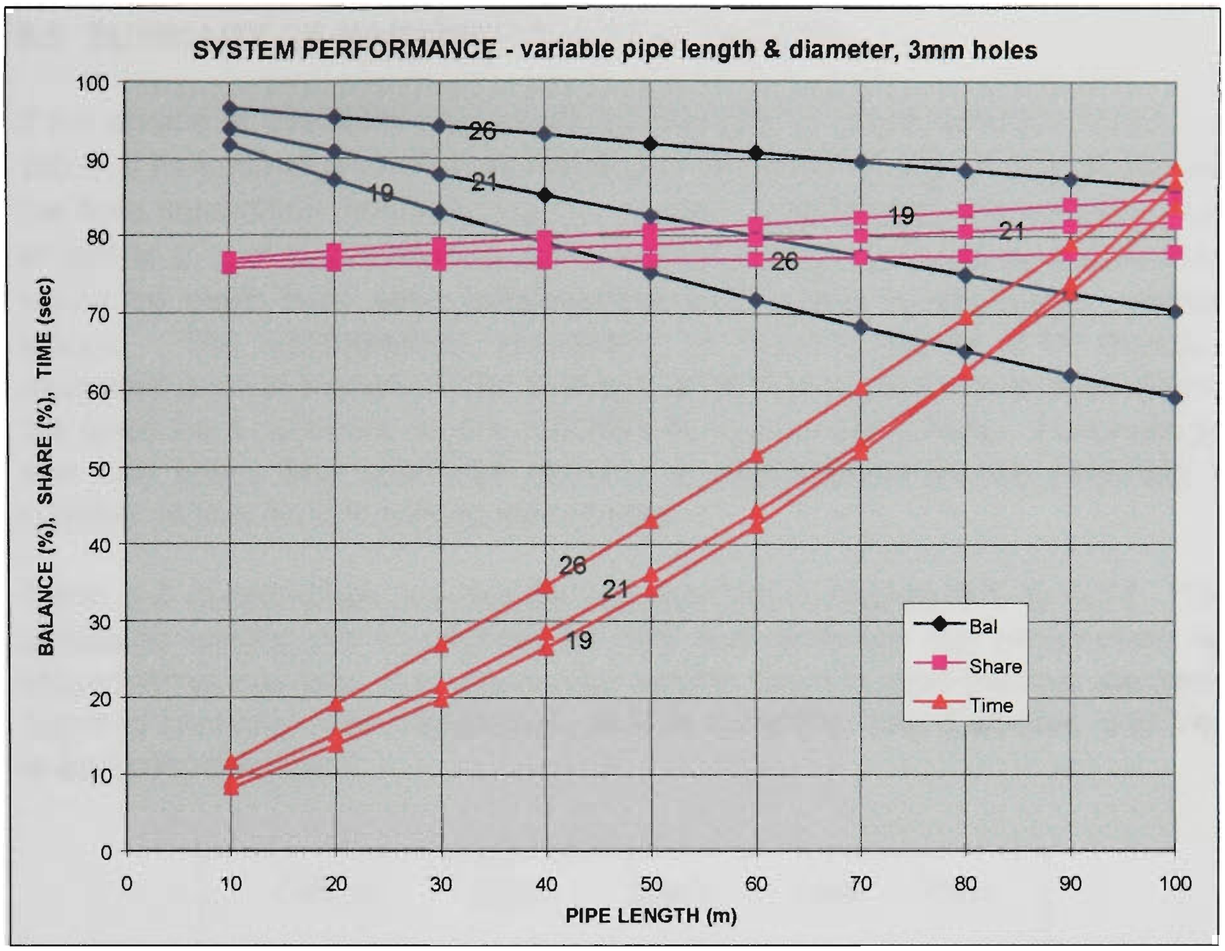

Figure 9.11 - Optimising the pipe diameter with length

Figure 9.11 simulates a pipe of various internal diameters for which the pipe length is increased from 10 to 100 m. The pipe always contains 10 positions so the hole separations range from 1 to 10 m respectively. The sampling holes are $3mm$ and, to ensure a maximum *time* of less than $90sec$, the end vent is set to $5mm$. The three configurations shown, use pipe internal diameters of 19, 21 and 26 mm. These represent the three sizes commonly available within that range.

The shortest *time* is obtained for the $19mm$ pipe (producing the highest velocity at a given flow rate) until the pipe length exceeds $80m$, beyond which the $21mm$ pipe is superior (due to its reduced pressure drop at a given flow rate). However, the best overall *balance* is achieved with the $26mm$ pipe. An acceptable *share* is achieved for all pipe diameters and lengths.

The optimum choice across the range would be $21mm$ although the *balance* falls close to 70% at $100m$. For the $100m$ case, $26mm$ could be used, with a relatively small *time* penalty. A pipe of $19mm$ would be unsatisfactory for use in excess of about $60m$.

9.5 SUMMARY OF PARAMETER OPTIMISATIONS

If the choice of available pipe length was limited to $10m$ increments from 10 to 100 m, if its internal diameter was limited to the three most common sizes, and the hole separation limited to $2m$, $4m$ or 10% of the length, the sampling hole limited to 2, 3 or 4 mm, and the end vent limited to 3, 4, 5 or 6 mm, then there would be more than 1000 combinations from which to determine optimum values. The optimisations presented in Figures 9.5 to 9.11 therefore represent a small sample of the arrangements that could be examined (hence the need for a software model available to system designers). However, we see that these few examples provide a useful guide to the selection of suitable values for the various parameters.

Table 9.4 summarises the results obtained from Figures 9.5 to 9.11. The optimised results are highlighted in bold text while the set parameters are shown in normal text. *Length* is pipe length, *Diam* is pipe internal diameter, *Sep'n* is sampling hole separation, *Hole* is sampling hole diameter, and *Vent* is end vent diameter.

Length	*Diam*	*Sep'n*	*Hole*	*Vent*
50*m*	21*mm*	4*m*	**3mm**	**4mm**
25*m*	21*mm*	4*m*	**4mm**	**5mm**
50*m*	**21mm**	4*m*	3*mm*	4*mm*
25*m*	**16mm**	4*m*	3*mm*	4*mm*
10-100*m*	21*mm*	1-10*m*	**3mm**	**5mm**
10-100*m*	**19-26mm**	1-10*m*	3*mm*	5*mm*

Table 9.4 - Results of parameter optimisations

The pipe length is determined by the size of the zone and the required coverage density of sampling holes (typically positioned in the same manner as conventional smoke detector points, on a square grid pattern, although there are numerous possible arrangements).

Within that area, there is a tradeoff between the number of pipes versus the length of each pipe. To illustrate this point, consider a square room that requires a single pipe length of $96m$ (this continuous pipe would normally include three parallel runs, in an "S" pattern). For convenience let the hole separations be $8m$ and the sampling hole as well as the end vent be $3mm$. Selecting a Xenon VESDA Mk3 detector with the aspirator set to 315Pa at cutoff, the *time* would be $115.9sec$, the *balance* 73.9% and the *share* 93.5%. In this case the *time* exceeds the required $90sec$ limit.

Now consider the same area covered by two pipes of $48m$ with the other parameters unaltered. The aggregate pipe length is of course the same as before. The *time* reduces to 59.1*sec*, the *balance* increases to 94.2% and the *share* reduces to 83.7%. So the simple expedient of placing the detector at the midpoint of the same pipework, reduces the time by 56.8*sec* (nearly half), not only meeting the Standard 90*sec* requirement but also meeting the alternative, high-risk environment specification of 60*sec.*

If the length of each pipe is halved again so that four pipes of 24*m* are used to cover the same area, the *time* reduces to 40.1*sec*, the *balance* increases to 99.1% and the *share* reduces to 66.1%. In this case the *share* is a little outside the design criterion of 70% (which could be met by altering the end vent but that is not the point of this analysis). Whereas this arrangement provides the shortest time, it may require the detector to be mounted centrally in the protected zone, which may be impractical.

The final option considered is to use three pipes of 32*m* (which generally would allow the detector to be conveniently located midway along a side wall). Here, the time is 46.1*sec*, the balance is 97.8% and the share is 74.8%. All of these results are satisfactory and represent a considerable improvement over the first arrangement, while employing the same aggregate length of pipework and involving the same cost. All of the outcomes are summarised in Figure 9.12.

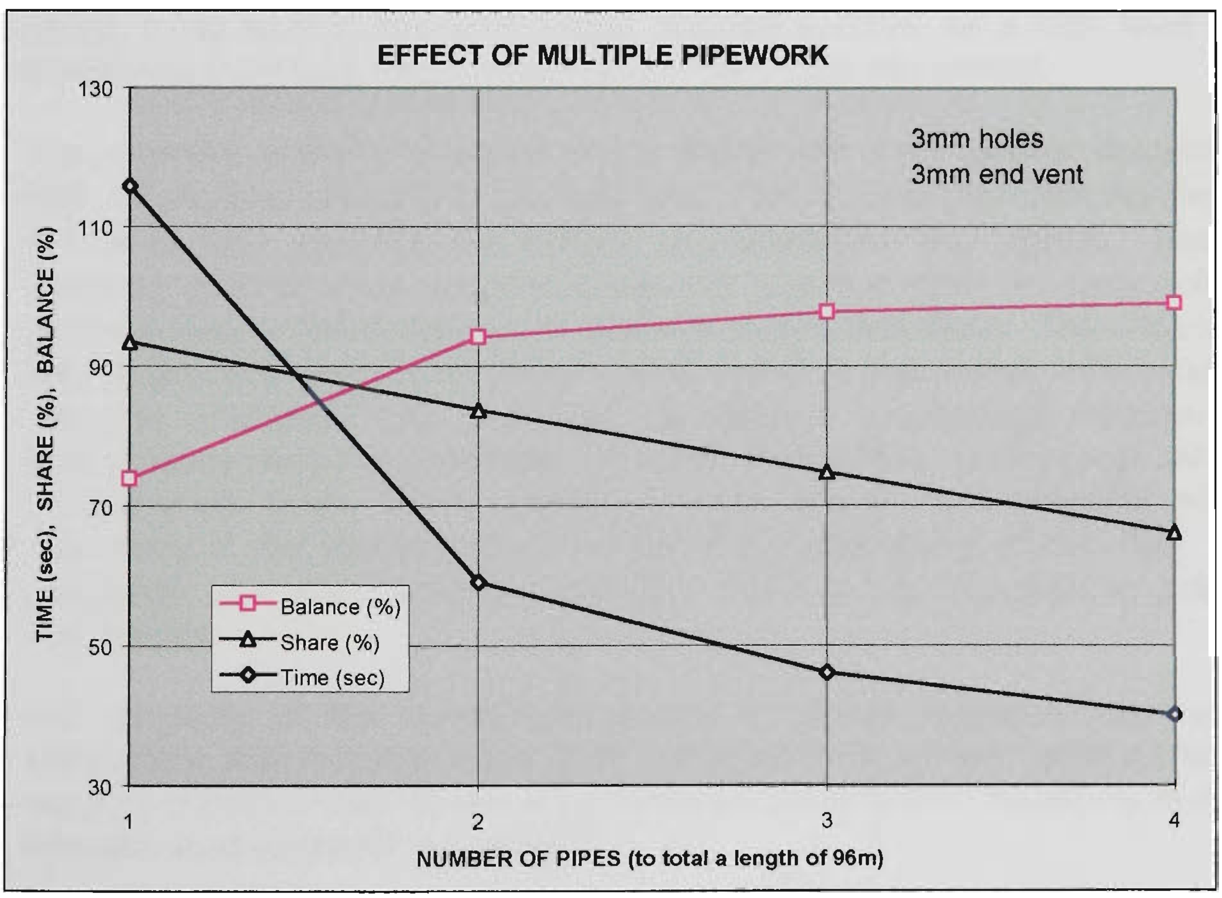

Figure 9.12 - Selecting the optimum pipe arrangement for a given total pipe length (a given zone size)

In summary, it has been shown that having multiple short pipes is generally more efficient than having one long pipe. No pipe should exceed $100m$ in length and with multiple pipes, the aggregate length should not exceed $200m$.

On this basis, for a given pipe the optimum parameters are in the vicinity of the following: pipe diameter $21mm$, hole separation $4m$, hole diameter $3mm$, end vent $4mm$. This is a useful starting point but all designs should be optimised using the software tool that was developed as part of this project.

9.6 CONCLUSIONS

The new version of the computer-based model utilising all of the findings from the current research program has been applied to the reference aspirated pipe system for which comprehensive measurement data is available. Close agreement between the model and the measured results was found in terms of pressure distribution throughout the system (Figure 9.1). When comparing the pressure distribution errors obtained from the new model, with those of the initial model which relies on the Nikuradse friction factors for either smooth or completely rough pipes, the improvement in accuracy is a factor of three at the full length of the pipe (Figure 9.2). This reference system is known to be representative of typical installed systems so a high level of confidence in the wider applicability of the new model was gained.

The reference system has a pipe of $52m$ length and $21mm$ internal diameter, with 12 sampling holes and a $6mm$ end vent. The range of Reynolds numbers is 1190 to 3087, spanning the laminar and transitional flow regions. Using sampling holes of a set diameter ($2mm$), the hole flow rates are reasonably well balanced at $2.45 litre/min$ $\pm 18\%$ (defined as 82% balanced). The effective hole sensitivities range from 0.79 to 1.18 $\%/m$ which is satisfactory for the early detection of incipient fires given that the system is increasingly sensitive if smoke enters more than one hole. To achieve equal flow rates through all of the sampling holes (100% balance), would require hole diameter size increments in the vicinity of $0.035mm$ which is impracticable (Table 9.2). If practicable size increments are available, these can be modelled to judge their benefit.

The accuracy of the model with respect to smoke transport time was satisfactory after inclusion of a fixed, universal time penalty factor to take account of both smoke dilution within the pipe and the finite sensitivity of the detector, as determined in Chapter 7.

Further validation trials have focused upon the accuracy of the smoke transport time algorithm, corrected for smoke concentration threshold. These trials provide a highly satisfactory correlation with measured data, the error averaging about half of one second for any given pipe segment, and being within about two seconds in aggregate for the total pipe. This is quite a satisfactory outcome, however, it can be inferred that the standard measurement process is the dominant source of these errors, so the accuracy of the model is even greater than that indicated.

Having established the validity of the model, the effects of change in ambient pressure and temperature on the total system were studied. The Xenon VESDA Mk3 (constant-voltage aspirator) provides significantly more stable performance than the VESDA LaserPLUS (constant-speed aspirator), with the former tending to compensate for changes in air density. For a typical large pipe system, subject to the extremes of possible ambient conditions (-20 to +60 °C, 1050 to 265 *millibar*), the smoke transport time increases by some 65% in the former case, and 175% in the latter. However, in a fixed location, the likely variations in ambient conditions are unlikely to alter the transport time by more than a few percent in either case. Moreover, the compensatory effect of the former renders it more difficult for the inbuilt anemometer to detect small changes in system flow rate that may be caused by minor pipe leakage or minor hole blockage.

The pipe length is determined by the size of the zone and the required coverage density of sampling holes (typically positioned in the same manner as conventional smoke detector points, on a square grid pattern, although there are numerous possible arrangements).

Within that area, there is a tradeoff between the number of pipes versus the length of each pipe. It has been shown that having multiple short pipes is generally more efficient than having one long pipe. No pipe should exceed $100m$ in length and with multiple pipes, the aggregate length should not exceed $200m$.

By application of the model it has been found that as a general rule, the optimum key parameters for pipework are in the vicinity of the following: pipe diameter $21mm$, hole separation $4m$, hole diameter $3mm$, end vent $4mm$. This is a useful starting point but all designs should be optimised using the software tool that was developed as part of this project.

CHAPTER 10 - SUMMARY OF CONCLUSIONS

10.1 - OUTCOME OF LITERATURE REVIEW

After studying some 1200 synopses and papers, a limited coverage of undisturbed, developing laminar and turbulent pipe flow regimes has been found. Much of this work applies to idealised laminar flows or to Reynolds numbers well above the range applicable to aspirated pipe systems.

There is no coverage of initially disturbed, developing laminar or turbulent pipe flow, nor of developing transitional pipe flow, nor is there any reference to the impact of jet induction on developing or developed flow regimes.

In the literature there is a significant uncertainty in determining the friction factor, in the region of transitional flow (approximately $2200<Re<3500$). This region is important, because it is relevant to a large proportion of the pipework in typical aspirated smoke detection systems. Furthermore, the literature does not establish the effect upon friction factor caused by disturbances to the flow regime (whether that regime is nominally laminar, transitional or turbulent). Therefore, any assumption that flow regimes can be regarded everywhere as fully-developed, is likely to introduce significant error.

No comprehensive and reliable theoretical study exists in the literature with experimentally verified results, that can model the real flow of smoke in aspirated pipes normally containing fresh air. Other authors interested in modelling aspirated smoke detection systems have made common assumptions about the friction factor and the effect of air velocity on smoke transport time, that are based upon fully-developed flow regimes within round pipes. Moreover, one author claiming to achieve balanced flow (equality of sampling hole flow rates i.e. equality of smoke-sensitivity throughout the system) uses a methodology that can introduce errors exceeding a binary order of magnitude in the flow rate through an individual sampling hole.

10.2 - SAMPLING HOLE CHARACTERISATION

The flow characteristics applicable to a range of typical sampling hole sizes (2 to 4 *mm* diameter), capillary tube nozzle sizes (2 to 4 *mm* diameter), and end vent sizes (2 to 8 *mm* diameter) have been determined. It was discovered that the accuracy of "square-law" equations are inadequate. Quadratic equations have been developed to model the static flow rates at room temperature (23°C) near sea level, with further equations to take account of differing ambient temperature and atmospheric pressure (see Chapter 2).

10.3 - SAMPLING HOLE GEOMETRY

The effect of altering the geometry of a sampling hole by rounding the inlet shoulder was investigated with a view to minimising the possibility of dust buildup and clogging, or whistle noise. This rounding was found to cause a 2, 3 or 4 *mm* diameter hole to behave as a 2.16, 3.38 or 5.09 *mm* non-rounded hole respectively. The expectation based upon the literature, was that the change in flow coefficient would be much greater, requiring the use of much smaller holes in order to retain appropriate hole flow rates. Significant size reduction would have defeated the purpose of minimising dust clogging. As matters stand, rounding of the inlet is a suitable option.

10.4 - CAPILLARY TUBE AND NOZZLE

The combination of a capillary tube and a sampling nozzle has been modelled with a 4th-order equation of 19 terms. It was found that within the typical range of tube sizes (0.5 to 2 *m* length and 5*mm* internal diameter), the hole diameter has the dominant effect over the tube length in determining the flow rate. However, with longer tubes the flow rate gradually and linearly falls toward zero as the tube length increases toward infinity (see Figure 4.54).

Subsequently the equation has been improved to take into account the fact that capillary tubes are rarely straight. The effect of coiling the tubes can be to increase the pressure drop significantly. The dimensionless Coil Friction Correction Factor (F_c) has been developed to describe this increase in terms of coil radius (R_c which is expressed as a ratio of tube radii). The equation is:

$$F_C = 1 + C_C \,\mathrm{Re} \qquad \text{where:}$$

$$C_C = -1.07E{-}10\, R_C^3 + 4.1E{-}08\, R_C^2 - 6.95\,E-06\, R_C + 7.4E{-}04 \geq 1.3E{-}04$$

This also describes the increase in friction factor above that of undisturbed flow in straight pipes, while the range of differential pressures, nozzle and tube dimensions are such that the flow regime is likely to be laminar. The equation for modelling the capillary tube and nozzle combination then becomes:

$$Q_{nozzle} = \pi\, D_{nozzle}^2 \left(\left(t_1^2 + 4\, t_2\, \Delta P_{pipe} \right)^{\frac{1}{2}} - t_1 \right) \Big/ 8\, t_2$$

where:

$$t_2 = \left(\frac{15000\, \pi\, D_{nozzle}^2}{K_{nozzle}} \right)^2 \qquad \text{and:} \qquad t_1 = \frac{32\, F_C\, \rho\, k\, L_{tube}\, D_{nozzle}^2}{D_{tube}^4}$$

Overall the effect of a typical degree of tube coiling (radius of $60dia$ e.g. $300mm$) can be approximately to reduce the flow rate in the tube at a given differential pressure by as much as 14% (see Figure 5.41).

10.5 - ULTRAFLOW

The phenomenon of **Ultraflow** has been discovered whereby the expected hole flow rate caused by static pressure, is exceeded because of the upstream flow rate in the pipe. At any given pressure, this Ultraflow (as a component of the total hole flow) initially increases in small measure as the upstream flow rate increases. Then an upstream flow rate threshold is reached, above which the hole flow rate increases more strongly, and linearly with upstream flow rate, having become largely independent of pressure.

Take for example, the case of a typical sampling hole ($2mm$ diameter) in a typical pipe ($21mm$ diameter) operating at a pressure differential of 100Pa (see Figure 4.8). At a pipe upstream flow rate of up to 40litre/min the hole flow rate is maintained at about 1.8litre/min. Experimental results reveal that at the same operating pressure, if the pipe upstream flow rate is increased by 50% to 60litre/min (which is beyond the ultraflow threshold) then the hole flow rate increases to about 2.5litre/min. This is an increase of almost 40% (the expected increase would have been zero because the static pressure differential has not been altered).

An explanation for the cause of this phenomenon of Ultraflow is proposed in terms of the entrainment of hole flow by the main pipe flow (see Figure 4.42). A combination of the ambient pressure differential and entrainment by the pipe upstream flow causes a jet of air to be induced into the main pipe flow, causing disturbance to the flow regime.

Each quantum of air comprising the induction jet must be accelerated to reach the velocity of the main pipe flow. This acceleration force causes an additional pressure drop in the vicinity of the hole, for which an equation has been derived theoretically. The effect of the pipe velocity profile has also been considered by reference to a momentum correction factor, so the resulting equation provides a satisfactory match to experimental data:

$$\delta P_{jet} \;=\; \rho \left(\frac{\left(Q_{up} + Q_{jet}\right)^2 - \beta\, Q_{up}^2}{A_{pipe}^2} \right)$$

where Q_{up} is the upstream flow rate, Q_{jet} is the jet (or hole) flow rate and β is the momentum correction factor applicable to the upstream velocity profile. This factor can have a value as large as 1.33 or 1.02 in the case of fully-developed laminar or turbulent flow regimes respectively.

Based upon the above calculation for the jet acceleration pressure drop, the entrainment phenomenon has been investigated theoretically with reference to a partly analogous jet ejector pump. Consistent results have been obtained, including the asymptotic nature of the phenomenon. The ratio of operating head to discharge head (R_H) has been derived theoretically as:

$$R_H = \frac{P_{up}/\rho + u_{up}^2 / C_{jet}}{\left(P_{up} + \delta P_{jet}\right)/\rho + \left(Q_{up} + Q_{jet}\right)^2 / 2A_{pipe}^2}$$

where:

$$C_{jet} = \left(D_{hole} + 1\right)\left(D_{pipe}/21.2\right)^{0.8}$$

and where C_{jet} is an empirical coefficient of entrainment which is introduced to correct for the deflection of the pipe upstream flow path by the impinging jet. After extensive consideration of all the experimental results (Figures 4.8, 4.10, 4.12, 4.22 and 4.25), very close agreement is obtained. The equation for R_H is implicit because:

$$Q_{jet} = Q_{stat} + Q_{ultra} = Q_{stat} + Q_{up}\left(1 - \sqrt{R_H}\right)$$

which takes into account the superposition of hole flows due to static pressure and Ultraflow (entrainment). Therefore it is necessary to provide an iterative solution. Nested iteration is required because the hole flow rate is incremented by entrainment which in turn increments the jet acceleration pressure drop, which in turn affects the value of R_H.

10.6 - INFRAFLOW

The phenomenon of **Infraflow** has been quantified whereby the expected hole flow rate caused by static pressure, can be reduced as a result of external flows. This reduction is greatest for external flows oriented mutually at right angles to the pipe axis and to the hole meridian radial. The magnitude of the hole flow reduction can be represented by a cubic equation which includes the crosswind velocity. It is noted that essentially no further reduction in hole flow occurs, at any crosswind velocity (up to $12 m/sec$), as the pressure differential rises above about 400Pa. At a crosswind velocity of $10 m/sec$ the maximum hole flow reduction is $0.73 litre/sec$ which is quite significant, representing 21%.

It has been further discovered that pipe upstream flow does not affect the magnitude of Infraflow, so that the two phenomena of Ultraflow and Infraflow can be applied by superposition.

10.7 - SAMPLING HOLE ANGLE

The effect of drilling the sampling hole at an angle (other than a right angle) to the pipe, was discovered to have negligible effect on the hole flow coefficient. Apparently because the pipe wall thickness is too small to impart a significant change in the induction jet trajectory, control of this angle does not provide a means for controlling the magnitude of Ultraflow.

10.8 - PIPE FRICTION FACTOR

It has been discovered that the friction factor data published in the literature are not appropriate for use in aspirated pipe systems because of frequent disturbances to the flow regime induced by pipe bends or sampling holes. New data have been obtained experimentally, which provide the friction factor applicable to straight pipe within a range of Reynolds numbers ($400<Re<4000$) and levels of disturbance appropriate to aspirated smoke detection systems. These data were broadly confirmed as a result of experiments conducted with pipe of much smaller diameter.

The level of disturbance (L_D) is calculated as a ratio of the air flow rate induced by a sampling hole (Q_{hole}), to the upstream flow rate in the pipe (Q_{pipe}). The friction factor increases as the disturbance level increases, until about 7% disturbance, beyond which there is no significant further increase in friction factor. For example, an algorithm for determining the friction factor applicable to maximally-disturbed flows ($L_D > 7\%$) is:

$\mathrm{Re} < 2170$: $\quad f = 7.1E\text{-}09\ \mathrm{Re}^2 - 4.3E\text{-}05\ \mathrm{Re} + 0.1$

$2170 < \mathrm{Re} < 2480$: $\quad f = 0.0401$

$2480 < \mathrm{Re} < 2875$: $\quad f = -8.07E\text{-}09\ \mathrm{Re}^2 + 4.83E\text{-}05\ \mathrm{Re} - 0.0301$

$\mathrm{Re} > 2875$: $\quad f = 0.1389 / \mathrm{Re}^{0.15}$

The friction factor at intermediate levels of disturbance is obtained by interpolation of Figures 5.17 and 5.18. The errors involved in using published data to determine the friction factor (Moody chart), which assume undisturbed, fully-developed flow regimes, can be as large as -30 to +53 % within the range of Reynolds numbers from 1000 to 10,000.

10.9 - THE IMPACT OF BENDS

The impact on friction factor has also been determined in the particular case of pipes containing 90° bends. It was discovered that one bend is sufficient completely to disturb the flow regime whereby additional bends in the immediate vicinity do not further disturb the flow regime. An algorithm for the pressure drop due to one bend, and equations for each additional bend, have been determined in terms of Reynolds number. For example, at a Reynolds number of 2300 (35*litre/min*) the loss for the first bend is 3Pa, while the incremental loss for each additional bend is only 2Pa (see Figure 5.34).

It was also discovered that the pressure drop caused by a bend is independent of the bend radius (within the experimental accuracy). This is because the pressure drop is dominated by the pair of sockets necessarily provided at each end, and to a lesser extent because the smaller radius bends have a shorter length (less friction loss) which tends to compensate for their sharper change in flow direction.

10.10 - THE IMPACT OF SOCKETS

Within a straight pipe segment, the effect of sockets (without bends) is to increase the friction factor so that the pipe becomes effectively rough. However, the flow regime is not significantly disturbed so the precise location of sockets would not need to be known when modelling the smoke transport time of an aspirated system (refer Chapter 6). This provides a very important simplification to the model in terms of the requirements for data entry.

Whereas the flow regime disturbance induced by pipe bends or sampling holes is expected to dissipate over some distance along a pipe (the disturbance dissipation length), the typical separation of pipe bends and sampling holes is of similar magnitude to the scale of the experimental apparatus, so it is proposed to apply the algorithm and equations mentioned in Section 10.10 throughout an aspirated pipe system.

10.11 - OTHER SYSTEM COMPONENTS

The various other system components have all been characterised for inclusion in the model. These include a range of commercially-available smoke detectors and aspirators with their various available settings.

A comprehensive range of dust filter types has also been characterised for selection within the model. A new dust filtration technology was developed and has been evaluated for its tendency to arrest smoke particles with increasing dust loading. This tendency has a significant impact on the effective sensitivity of the detection system, initially and over time. A multi-layer reticulated foam design proved superior to other technologies and was independently tested in London Underground where it provided a service life in excess of eight times that of the previously used technology.

10.12 - DETERMINATION OF CORE VELOCITY

After extensive experimental work using Laser Velocimetry and analysis of some two million readings, a model has emerged (see Figure 6.52) that describes the core velocity growth profile throughout the laminar, transitional and early turbulent flow regimes, where such flows are initially disturbed. This model indicates that for laminar flows, the core velocity does not reach 99% of its final value until a displacement of some $400dia$. This compares with a figure of $120dia$ quoted in the literature, applicable to undisturbed laminar flows. This disturbance dissipation length is not significantly reduced below $400dia$ unless the disturbance level is less than 2% (which is rarely the case).

For example at $\mathrm{Re} = 2000$, beyond $5dia$ the developing core velocity ratio rises in accordance with the following equation, which reaches the value 1.98 at $400dia$:

$$R_u = 2 - 0.655\, e^{(d/113)}$$

In the case of transitional and turbulent flow regimes, the core velocity initially rises to a peak value (at a displacement corresponding to the boundary layer transition) and then falls, reaching 101% of its final value within some $100dia$. This compares with a figure of $60dia$ quoted in the literature, applicable to undisturbed flows.

10.13 - BOUNDARY LAYER TRANSITION

As an unexpected consequence of the investigation, the point of boundary layer transition (for initially-disturbed flows) as a function of *pipe* Reynolds number (Re) has been discovered (see Figure 6.53 and Table 6.1). This reveals that the critical *entry* Reynolds (Re_e) number is not fixed in value but has a range obtainable from:

$$\mathrm{Re}_e = 8.9\,\mathrm{Re}^2 / (\mathrm{Re} - 2150) \qquad \textit{where} \qquad \mathrm{Re} > 2350$$

This *entry* Reynolds number ranges in value from approximately 250,000 at $\mathrm{Re} = 2400$, to a surprisingly low (in view of the literature) 64,000 at $\mathrm{Re} = 4000$.

10.14 - TIME FACTOR

A simplified method of approximation to the smoke transport time (T_T) within a pipe segment has been derived and the new term, Time Factor (F_T), has been defined for use in the following equation:

$$T_T = F_T \frac{D_{pipe}}{u_{avg}}$$

which can be applied with significantly greater accuracy than previous methods. Linear approximations to the Time Factor curves at each Reynolds number have been developed (see Figures 6.39 and 6.54) and these show a significant improvement in the cumulative error involved in determining the smoke transport time. For all *pipe* Reynolds numbers up to 4000 and at displacements (d) less than $15dia$, an equation has been determined. Beyond $15dia$, the Time Factor may be obtained from the linear approximation:

$$F_T = t_1\, d + t_0$$

where the gradient and offset terms t_1 and t_0 depend on the Reynolds number (see Table 6.2), requiring different sets of values within the range 15 to 100 *dia*, and above $100dia$. However, at $\mathrm{Re} = 2000$, a closer approximation to the Time Factor may be obtained from the following quadratic equations:

$$15 < d < 100 \qquad F_{2000} = -6.6E\text{-}04\, d^2 + 0.701\, d + 1.1$$

$$d > 100 \qquad F_{2000} = -1.1E\text{-}04\, d^2 + 0.579\, d + 8.3$$

The errors incurred by using the approximations are well within $\pm 1\%$ beyond $25dia$, and within $\pm 5\%$ at lower displacements. The Time Factors applicable to intermediate values of Reynolds number are obtained by interpolation. This does not involve large errors because of the relatively small divergence among the equations.

10.15 - FRICTION FACTOR DEVELOPMENT

The friction factor changes in harmony with the development of the flow regime and this has a significant effect in laminar flow regimes. An attempt has been made to characterise the profile of this friction factor development as a function of displacement. For example at $\mathrm{Re} = 1500$ the proposed equation is of the form:

$$f_d \approx f_0 - (f_0 - f_\infty)\left(1 - \left(1E{-}14\, d^6 + 0.01\, d + 0.3\, d^{0.6} + 1\right)^{-1}\right)$$

This method equates the friction factor development length to the flow regime development length (the disturbance dissipation length). Given that this length relates to initially fully-disturbed flows, then at reduced levels of initial disturbance (as determined by the sampling hole flow rate), the friction factor development length would be reduced. An equation has been determined, to model this length (L_f) according to the flow disturbance level (L_d):

$$L_f = -1900\, L_d^2 + 300\, L_d - L_d^{-1} + 400$$

which matches the LV experiment data (of Chapter 6) within $\pm 15\%$ (see Figure 7.13). Again, this disturbance dissipation length is not significantly reduced below $400dia$ (being laminar flow) unless the disturbance level is less than 2%.

An experiment was conducted in an attempt to verify the friction factor development model, with broadly consistent results. Nevertheless, due to the inadequacy of instrument resolution, a sufficiently high level of confidence in the approach used has not been gained. Instead, given that the friction factor measurement experiments were conducted using a pipe segment length of similar magnitude to most pipe segment lengths used in the field, then the data of Figure 5.19 will be relied upon. Conducting the foregoing type of experiment and analysis in greater detail using equipment of higher resolution is seen as an opportunity for further research.

10.16 - DEVELOPMENT OF A SYSTEM MODEL

A model representing a series of core velocity growth profiles in an aspirated pipe with six sampling holes has been developed (see Figure 7.1) to evaluate the proposed modelling methodology. This series has a broadly similar form to that which was anticipated from an analysis of guidelines within the literature, but it has significant differences in detail. The pattern which emerges is consistent throughout, so a high level of confidence in the methodology has been gained. The individual sector errors and cumulative error (see Figure 7.3) are significantly reduced over previous models used.

The impact of using bends within such an aspirated pipe has been considered using the same methodology (see Figure 7.4) and, although the core velocity reached at the end of each pipe segment is similar (whether bends are fitted or not), there is an increase in smoke transport time of about 5% due to reduced intermediate velocities caused by the bends (see Figure 7.5). The results obtained provide a high level of confidence in the ability of the model to account for bends.

10.17 - VALIDATION OF THE MODEL

A computer-based model utilising all of the findings from the current research program has been applied to a reference aspirated pipe system for which comprehensive measurement data is available. Close agreement between the model and the measured results was found in terms of pressure distribution throughout the system (see Figure 9.1). When comparing the pressure distribution errors obtained from the new model, with those of the previous model which relies on the Nikuradse friction factors for either smooth or completely rough pipes, the improvement in accuracy is a factor of three at the full length of the pipe (see Figure 9.2). This reference system is known to be representative of typical installed systems so a high level of confidence in the wider applicability of the new model was gained.

10.18 - THE IMPACT OF SMOKE DILUTION

The accuracy of the model with respect to smoke transport time was less than satisfactory. However, upon increasing each of the segment times by 25%, close agreement with the measured results was obtained. This apparent discrepancy is explained by smoke dilution. Firstly, the LV results of Chapter 6 led to an accurate determination of the time taken for the first molecule of smoke to reach the detector. However, the reliable detection of smoke requires a certain minimum smoke concentration.

An extensive theoretical analysis to characterise the rate of buildup of smoke concentration at the detector was undertaken, involving laminar and turbulent velocity profiles. In order to consider the effect of <u>initially-disturbed, developing</u> flow regimes a universal power law was developed, to describe the shape of the velocity distribution curve for laminar flow at any stage of development (i.e. at any given displacement). In the case of turbulent flow, this equation is applicable until the point of boundary-layer transition. An inverse power law may be applied beyond this transition region

After studying the transport time penalty as a function of smoke detection threshold in accordance with these equations (see Figures 9.10 and 9.14), it was discovered that beyond about $100dia$, the penalty becomes largely independent of displacement such that a fixed correction factor is expected to apply throughout either the laminar or turbulent regions. However, based upon the assumption of no mixing, the value of this correction factor is different for the two regions. After considering the effect of complete mixing of the smoke at all points along the pipe, it was found that the required smoke concentration (to reach the detection threshold) is increased in direct proportion to the core velocity ratio (R_u).

Furthermore, after considering the highest Reynolds number applicable to typical pipe systems (3200), it was found that using a correction factor to increase the computed time (based upon the LV results) by a fixed 25%, throughout the entire length of the pipe, was indeed appropriate (this could drop to 20% at higher Reynolds numbers). Provision should be made in the software to accommodate other values, relevant to different smoke sources (optical densities), especially where incipient fires are involved.

Further validation trials have focused upon the accuracy of the smoke transport time algorithm, corrected for smoke concentration threshold. These trials provide a highly satisfactory correlation with measured data, the error averaging about half of one second for any given pipe segment, and being within about two seconds in aggregate for the total pipe. This is quite a satisfactory outcome, however, it can be inferred that the measurement process is the dominant source of these errors, so the accuracy of the model is even greater than that indicated.

10.19 - THE IMPACT OF TEMPERATURE AND PRESSURE

Having established the validity of the model, the effects of change in ambient pressure and temperature on the total system were studied. The constant-voltage aspirator (Xenon VESDA Mk3) provides significantly more stable performance than the constant-speed aspirator (VESDA LaserPLUS), with the former tending to compensate for changes in air density. For a typical large pipe system, subject to the combined extremes of possible ambient conditions (-20 to +60 °C, 1050 to 265 *millibar*), the smoke transport time increases by some 65% in the former case, and 175% in the latter. However, in a fixed location, the likely variations in ambient conditions are unlikely to alter the transport time by more than a few percent in either case. Moreover, the compensatory effect of the former renders it more difficult for the inbuilt anemometer to detect small changes in system flow rate that may be caused by minor pipe leakage.

10.20 - FINAL CONCLUSION

In many instances the findings of this project are surprising and are at odds with generally accepted knowledge in the literature. The data gathered and the results of their analysis could not have been anticipated on the basis of conventional wisdom.

The impact of initially disturbed, developing flow regimes upon pressure drop (and friction factor) as determined in this project, has application to the general study of fluid dynamics, particularly in laminar, transitional and early turbulent flow regimes ($400<Re<4000$) in round pipes. This is particularly applicable to the design of practical systems where idealised conditions do not apply, such as pipelines within $400dia$ of valves, bends, orifices, pumps, filters or other disturbing devices, or in heat exchanger pipes (where the straight sections of pipe would rarely be long enough to render $400dia$ as insignificant). Importantly, for pipe lengths up to $400dia$ (the disturbance dissipation length, dependent on Re), the pressure drop is always greater than that predictable from the literature, typically on the order of +30% (averaged over the first 142dia). Any disturbance level greater than 7% is sufficient to cause such an increase in pressure drop.

Also of general interest to the study of fluid dynamics is characterisation of the core velocity development for laminar, transitional and early turbulent flow regimes, the lateral velocity profile development in these regimes and the position of boundary layer transition in developing turbulent regimes, as well as the principles of efficient dust filter design. Of further general interest is the use of quadratic equations, more-accurately to characterise system components such as orifices, bends, multiple bends, filters, sockets and pumps, including the impact of ambient temperature and pressure (altitude).

For the particular case of aspirated systems typically used for early detection of small concentrations of smoke and other airborne pollutants, several additional discoveries were made in relation to sampling hole geometry and angle, acceleration of the induction jet, the phenomena of Ultraflow and Infraflow, the effect of sampling nozzles and the coiling of capillary tubes, the pressure drop of bends which is independent of bend radius, the impact of sockets, estimation of the Time Factor based upon the core velocity growth profile, and the impact of smoke dilution due to the developing lateral velocity profile. All of the information has been applied to the development of a software model of aspirated smoke detection systems which gives reliable predictions of the balance in sensitivity of all sampling holes in a system as well as the smoke transport time from each hole to the detector, enabling the optimisation of system design with unprecedented accuracy.

Elements of this project specifically concerned with aspirated pipework, such as Ultraflow, may find wider application in the modelling of induction manifolds or leakage into low-pressure pipelines.

LIST OF REFERENCES

AHLQUIST, N.C. & CHARLSON, R.J. 1967 "*A New Instrument for Evaluating the Visual Quality of Air*", Journal of the Air Pollution Association, v17, no7

AL-ALI, H.H. & SELIM, M.S. 1993 "*Momentum and Heat Transfer in the Entrance Region of a Parallel Plate Channel*", Applied Scientific Research 51, pp663-675

AS 1603.8 1996 "*Automatic Fire Detection and Alarm Systems - Part 8: Multi Point Aspirated Smoke Detectors*", Standards Association of Australia

AS 2936 1987 "*SAA Fan Test Code*", Standards Association of Australia, p15

BARBIN, A.J. & JONES, J.B. 1963 "*Turbulent Flow in the Inlet Region of a Smooth Pipe*" ASME Journal of Basic Engineering v29 p29

BERNERO, S. & MUNKUTLA, S. 1995 (June 19-22) "*Turbulent Pipe Flow Development at Moderate Reynolds Numbers*" Proceedings of 26th AIAA Fluid Dynamics Conference at San Diego, California

BIRD, B.R., STEWART, W.E. & LIGHTFOOT, E.N. 1994 "*Transport Phenomena*", John Wiley & Sons

BREMHORST, K. 1995 "*Accuracy of Laser Doppler Anemometry*" occasional paper, Dept. of Mechanical Engineering, University of Queensland

CAMPOS-SILVA, J.B., COTTA, R.M. & APARECIDO, J.B. 1992 "*Analytical Solutions to Simultaneously Developing Laminar Flow Inside Parallel Plate Channels*" International Journal of Heat & Mass Transfer v35 n4

CHARLSON, R.J. 1968 (May) "*Integrating Nephelometer*", United States Patent 3,563,661

CHARLSON, R.J., AHLQUIST, N.C., SELVIDGE, H. & MacCREADY, P.B.Jr. 1969 "*Monitoring of Atmospheric Aerosol Parameters with the Integrating Nephelometer*", Journal of the Air Pollution Association, v19, no12

CHEREMISINOFF, N.P. *1990 "Practical Fluid Mechanics for Engineers and Scientists*", Technomic Publishing Co, p219

LIST OF REFERENCES

CONTINUED

CHURCHILL, S.W. & CHAN, C. 1994 (July 1) "*Improved Correlating Equations for the Friction Factor for Fully Turbulent Flow in Round Pipes and Between Parallel Plates, both Smooth and Naturally Rough*", Industrial & Engineering Chemistry Research Journal, p2016

COLE, M.T. 1983 a (March) *"Improvements relating to Light Absorbers",* Australian Patent 575845

COLE, M.T. 1983 b (May) *"Optical Smoke Detectors",* Australian Patent 3184384

COLE, M.T. 1983 c (May) *"Improvements relating to Solid-State Anemometers and Temperature Gauges",* Australian Patent 4229885

COLE, M.T. 1983 d (July) *"Heat Activated Sampling Point for Smoke Detection Systems",* Australian Patent 3023684

COLE, M.T. 1983 e (August) *"Improvements relating to Smoke Detection Apparatus (Solid-State Scattered-Light Detection)",* Australian Patent 3184184

COLE, M.T. 1983 f (October) *"Improvements relating to Smoke Detection Apparatus (Signal Processing Block & Controls)",* Australian Patent 3453784

COLE, M.T. 1983 g (November) "*E700 Mk2 Air Sampling Techniques*", IEI Pty Ltd

COLE, M.T. 1988 (March) *"Improvements to Fluid Pollution Monitoring Apparatus (Laser Monitor)",* Australian Patent 3400593

COLE, M.T. 1990 (June) *"Improvements relating to Gaseous Fluid Aspirator or Pump",* Australian Patent 8070891

COLE, M.T. 1991 a, "*Optimisation of Aspiration Techniques for Air Pollution Monitoring*", Master of Engineering Thesis, Monash University, pp19-34

COLE, M.T. 1991 b (October) *"Improvements relating to a Sampling Chamber for a Pollution Monitor",* Australian Patent 2774692

LIST OF REFERENCES

CONTINUED

COLE, M.T. 1992 a (May) *"Improvements relating to Smoke Detector Scanning Apparatus",* Australian Patent 4050493

COLE, M.T. 1992 b (May) *"Gas Sampling Point for Smoke or Pollution Detection Systems",* Australian Patent 4050393

COLE, M.T. 1995 a (April) *"Improved Communications Architecture for Pollution Detection System",* Australian Patent Application PN2185

COLE, M.T. 1995 b (May) *"Exponential Display for Pollution Detection Apparatus",* Australian Patent Application PN3092

DIESSLER, R.G, 1955 (Nov) National Advisory Committee Technical Note 3016, ASME Journal, 77:7

DOUGLAS, J.F, GASIOREK, J.M. & SWAFFIELD, J.A. 1979 *"Fluid Mechanics*", Pitman, p285

ECCLESTON, A.J, KING, N.K. & PACKHAM, D.R. 1974 "*The Scattering Coefficient and Mass Concentration of Smoke from some Australian Forest Fires*", APCA Journal, v24, no11

EINSTEIN, A. 1905/1926 "*Investigations on the Theory of the Brownian Movement*", translated by Methuan & Co

GARLAND, J.A. & RAE, J.B. 1969 "An Integrating Nephelometer for Atmospheric Studies and Visibility Warning Devices", Journal of Physics E (Scientific Instruments), v3, no4

GOLDSTEIN, S. 1938 "*Modern Developments in Fluid Dynamics*" Clarendon Press, Oxford UK, v1, p39

IEI Pty Ltd 1991 "*VESDA™ System Manual*", company publication

JOHNSON, P.F. 1986 "*Fire Detection in Computer Facilities*" Fire Technology, v22, no1, pp14-31

JORGENSEN, R. 1962 "*Fan Engineering*", Buffalo Forge Company, 6th Ed.

LIST OF REFERENCES

CONTINUED

JUMPETER, A.M. 1976, "Jet Pumps", Chapter 4 in KARASSIK, I.J. "Pump Handbook", McGraw Hill

LANGHAAR, H.L. 1942, Transactions of the American Society of Mechanical Engineers, Journal of Applied Mechanics A 64, p55

MARR, J.J. 1928 (July) *"Smoke Detector",* United States Patent 1,775,834

MARTINUZZI, R. & POLLARD, A. 1989 *"Comparative Study of Turbulence Models in Predicting Turbulent Pipe Flow"*, AAII Journal, v 27, no 1

MOHANTY, A.K. & ASTHANA, S.B.L. 1978 "Laminar Flow in The Entrance Region of a Smooth Pipe", Journal of Fluid Mechanics pp433-447

NIKURADSE, J. 1932 *"Gesetzmassigkeit der Turbulenten Strömung in Glatten Röhren" (trans: "Laws of Turbulent Flow in Smooth Pipes"),* Verein Deutscher Ingenieure-Forshungsheft, no 356

NOTARIANNI, K.A. 1988 (August) "*Modeling and Design of Equal Sampling-Rate Multi-Orifice Dynamic Smoke Detection Sampling Tube Networks*", Master of Science Thesis, Worcester Polytechnic, Ma

NOTARIANNI, K.A. 1992 (April) *"Balanced Fluid Flow Delivery System",* United States Patent 5,103,212

PACKHAM, D.R. & GIBSON, L. 1973 (June) *"Smoke Detector",* Australian Patent 56513/73

PACKHAM, D.R, 1974 "*Relationships between Scattering Coefficient, Visual Range, Particulate Concentration and Percent Obscuration*", CSIRO internal report

PACKHAM, D.R, GIBSON, L & LINTON, M. 1975 "*Detection of Smoke in Air-conditioned and Ventilated Buildings*", Telecommunications Journal of Australia, v 25, no 3

PETERSEN, J. 1980 *E700 - VESDA installation guide,* IEI Pty Ltd company publication

LIST OF REFERENCES

CONTINUED

PFENNIGER, W. 1952 "*Experiments with Laminar Flow in the Inlet of a Tube at High Reynolds Numbers*", Northrop Aircraft Inc Rowthorne California

ROBERSON, J.A. & CROWE, C.T. 1975 "*Engineering Fluid Mechanics*", Houghton Mifflin Company, p298

ROTTA, J. 1956 "*Experiments in factors contributing to the formation of turbulent flow in pipes*" (trans), Ing. Arch, 24, pp258-281

SCHLICHTING, H. 1951 "*Boundary Layer Theory*", McGraw-Hill, 7th edition 1987, pp598-600, pp640-643

SPARROW, E.M., LAN, H.S. & LUNDGREN, T.S. 1964 "*Flow Development in the Hydrodynamic Entrance Region of Tubes and Ducts*", The Physics of Fluids v7, p338

STEPANOFF, A.J. 1957 "*Centrifugal and Axial Flow Pumps*" 2nd Ed, John Wiley & Sons Inc.

TAYLOR, N.A. 1984 (October) "*Modelling of Air Flows Through the Sample Pipe of a Smoke Detection System*", Internal report, Safety & Reliability Directorate, United Kingdom Atomic Energy Authority

TELECOM AUSTRALIA 1995 "*Installation, Commissioning and Maintenance of Multi-point Aspirated Smoke Detection Systems*" Telstra Corporation Limited, Network Operations, Standards Procedure TPH1525

VARDY, A. 1990 "Fluid Principles", McGraw-Hill, p88

VISION PRODUCTS Pty Ltd, 1997 "*VESDA® System Design Manual, version 2.0*", company publication

YAKHOT, A. & ORSZAG, S.A. 1993 "*Numerical Simulation of Turbulent Flow in the Inlet Region of a Smooth Pipe*", Journal of Scientific Computing, v8 no2 pp111-121

APPENDICES

A1.1 Xenon VESDA Mk3

The VESDA Mk3 contains a true integrating nephelometer utilising a Xenon lamp to produce a continuous incident light spectrum from $1400nm$ (infra-red) to $200nm$ (ultra-violet). The incident light illuminates a large volume of smoke (about $3000mm^3$) and the light scattered at almost all angles is detected by a wide-bandwidth PIN photodiode receiver to produce an analog smoke concentration level. By simultaneously integrating over volume, wavelength and angles, the detector is sensitive to a complete range of particle sizes and its analog output signal is proportional to the smoke mass. Smoke mass ($\mu g/m^3$) has the most direct correlation with fire intensity (rate of fuel consumption). Because of the short wavelength components of the spectrum, it can be calibrated with pure gases. It is available with a range of smoke sensitivity spans from 0.01 to 0.1 $\%/m$, through to 0.1 to 1.0 $\%/m$, each offering three selectable alarm thresholds. The Xenon lamp is a consumable part, typically replaced at 4-year intervals. Formerly manufactured by IEI Pty Ltd (Australia), which in 1995 merged with the current manufacturer, Vision Systems Limited (Australia).

A1.2 VESDA LaserPLUS

The VESDA LaserPLUS detector uses a near infra-red, semiconductor laser diode with a beam that is collimated to pass through a cylindrical detection chamber. Some light that is scattered by smoke particles passing through the beam, is detected by a receiver positioned at a specific angle to the beam axis. There is provision for a second separate receiver positioned at a different angle, with the intention to provide information about the particle size. This provision of two channels may assist toward overcoming the disadvantage inherent with all such lasers, of having a narrow bandwidth of incident infra-red light, which tends to favour the detection of large particles at the expense of small ones. Soiling of the optics within the chamber is minimised by a curtain of cleaned air. The detector has a very wide dynamic range of sensitivity and can cover the equivalent 0.005 to 32 *%/m* obscuration. Therefore it is provided with four selectable alarm thresholds, the last being suitable for initiation of fire suppression systems. A digital display of smoke concentration is also available. Manufactured by Vision Systems Limited (Australia).

A1.3 HART, HSSD, UniLASER or AnaLASER

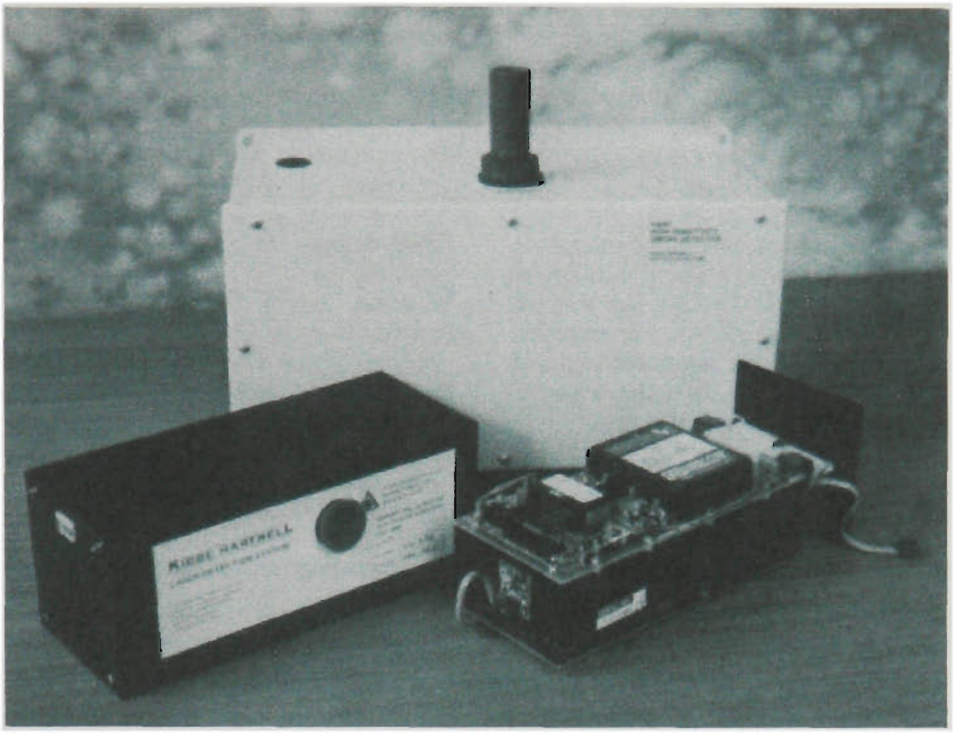

The HART (or HSSD, Sensa, UniLaser or AnaLaser) detector utilises particle-counting technology previously developed for dust monitoring in clean rooms. It employs a near infra-red, semiconductor laser diode focused to a 100μ diameter target area, positioned in the centre of a pipe. Particles (including smoke) passing through this target cause some light to be scattered at a right-angle towards a highly sensitive SPAD receiver which is stabilised by using a Peltier device. This light produces a pulse in response to each particle so the rate of pulses indicates the smoke concentration (assuming a given, constant air flow rate). It is available with a range of smoke sensitivity spans from 0.01 to 0.1 *%/m*, through to 0.05 to 0.5 *%/m*, each offering three selectable alarm thresholds (early models actually relied upon using the control and display card of the Xenon VESDA, with which it competed). Unlike other brands, the use of a dust filter is not advocated so to minimise soiling of the optics, the operation manual has specified maintenance cleaning after six months of service. Manufactured by Kidde Hartnell (UK) with some control and display equipment produced by Kidde Fenwal (USA).

A1.4 STRATOS

The STRATOS detector is neither a nephelometer nor a particle counter. It uses a near infra-red, semiconductor laser diode to produce a beam that is focused to a point at the centre of a hole within a coaxial concave “mirror”. Smoke passes through this hole and, as the smoke approaches a region approximately half way between the mirror and the laser source, some light from the beam is scattered by the smoke toward the mirror within a narrow range of angles. Some of this scattered light is reflected back towards a PIN photodiode receiver, to produce an analog signal in proportion to the smoke concentration. Unlike the previously-described detector technologies, this device does not produce absolute smoke concentration readings. It is claimed to be continuously self-adjusting in sensitivity (within a factor span of 40 times) to overcome soiling or temperature drift, so its sensitivity to smoke at any given moment is unknown. It is responsive to the short-term change in conditions rather than the absolute level of smoke. This presents a difficulty for Fire Safety Engineers in designing for alarms or other responses to be generated at particular smoke levels (i.e. danger levels). It is available with a master-slave (1 master zone to 3 slave zones) signalling protocol but this option does not comply with various fire codes because, if the master fails, all four zones are lost. Manufactured by Air Sense Technologies Limited (UK).

A1.5 IFD CIRRUS

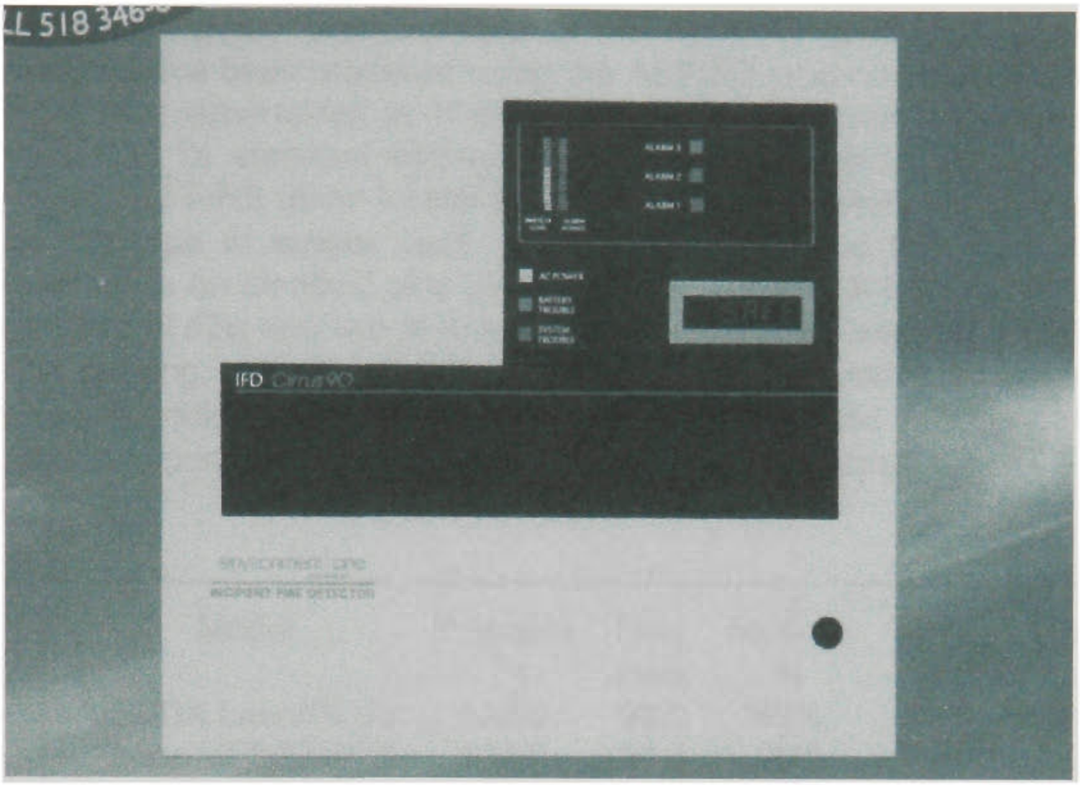

The IFD CIRRUS detector uses the principle of the Wilson Cloud Chamber previously developed to view nuclear particle radiations. Smoky air is drawn into a chamber and humidified. A low pressure is then rapidly drawn so that moisture condenses around airborne smoke and dust particles (condensation nuclei). This forms a coating of water around the particles, producing droplets of much greater size than the original particles (as fog), rendering them visible to a light obscuration beam detector of modest sensitivity. Because it is claimed that the droplets tend to form a similar size regardless of the size of the original particle, the analog signal is proportional to the number of particles (i.e. a particle counting technology). Like all particle-counters, it is susceptible to having its sensitivity biased toward small particles which tend to be much larger in number, at the expense of large particles. To overcome this, some models have been fitted with a "pyroliser" - a small furnace that completes the combustion of the large particles to produce many more, small particles ready for detection. However, this furnace requires significant energy. The detector requires regular replenishment of its reservoir of distilled water. Previously manufactured by Environment/One Corporation (USA), and now Protec Fire Detection (UK).

This product was not available for characterisation within the computer model.

A1.6 COMPARATIVE PERFORMANCE

The fluid dynamics characteristics of the available aspirated smoke detector packages have been modelled using the ASPIRE program, including the Xenon VESDA Mk2 superseded in 1990. For comparative purposes each detector is modelled at its standard setting, with the smoke-sensitivities assumed to be equivalent (a FIRE alarm threshold of $0.05\%/m$), which would in practice depend upon the type of smoke used. It is further assumed that each detector is connected to an identical pipe system, being the default layout comprising four pipes (two at $52m$ and two at $48m$), each using twelve $2mm$ holes (of equal size) at $4m$ spacing, with pipe of $21mm$ internal diameter and a $4mm$ end vent, at ambient conditions of 23°C and $1002 millibar$. The results in order of increasing smoke transport time (worst case) were obtained as follows:

Model	Pressure Pa	Flow *l/min*	Balance %	Time *sec*	ΔT *sec*
VESDA LaserPLUS	132.0	98.0	89%	61.6	0.0
Xenon VESDA Mk3	132.9	98.4	89%	61.7	0.1
Stratos	83.7	75.5	87%	79.8	18.2
Xenon VESDA Mk2	66.1	65.7	86%	92.6	31.0
HART	63.4	64.1	86%	94.5	32.9

APPENDIX 2 - CHARACTERISATION OF SYSTEM COMPONENTS

A2.1 LABORATORY INSTRUMENTATION

It has been determined experimentally that to characterise any aspect within the wide range of aspirated system designs encountered or envisaged, the maximum required pressure differential is 1000Pa (being negative with respect to atmosphere), with a resolution of 1Pa or better. The maximum required flow rate is 200*litre/min* with a resolution of 0.1*litre/min*. (Note: in the text, flow rate is expressed as *litre/min* instead of *l/min* for visual clarity).

Obtaining a sufficiently accurate set of data has proven difficult, with many different methods providing inconsistent readings. Especially so with regard to flow rate, where anemometers (both thermal and propeller), gasmeters and rotameters have proven unreliable across the flow range, or cause excessive restriction of the air flow and excessive pressure drop. For example a $2000 Fischer & Porter rotameter (20-290 *litre/min*) relied upon for quite some time, was ultimately found to have an error of +53% at 20*litre/min*, reducing to +11% at 110*litre/min* which was the maximum attainable flow due to its high restriction. The instrument had been calibrated by the supplier only at full-scale, and its inaccuracy at lower flow rates was eventually found to invalidate thousands of readings taken over several months, together with their analysis and the conclusions drawn.

The pressure gauge was a Yokogawa UMO4 which proved quite stable and reliable except for the accuracy with which its zero-point could be set.

It was because of intractable discrepancies with theoretical calculations that the rotameter had lost credibility and eventually a more reliable device was located overseas. This was a Furness FC096G-200L, laminar plate flowmeter complete with FC016 digital manometer calibrated in *litre/min*.

Even so, there were further minor inconsistencies in readings. The manuacturer's calibration certificate was consulted and it was noted that spot-check correction data was available separately for the laminar plate flowmeter and the digital manometer, throughout the flow range. These data had to be combined appropriately to produce an overall correction. The following calibration equation was derived from these data, as presented in Figure A2.1:

$$Q = -\ 0.000002\ R^3 + 0.0004\ R^2 + 0.993\ R - 0.0537$$

where Q is the true flow rate and R is the manometer reading. Even when the laboratory was maintained at a temperature held constant within less than 1°C throughout a test run, there was a significant drift evident in readings at zero flow and it proved necessary to verify the zero setting (by blocking the flow) before taking each reading. This blocking of the flow also provided an opportunity to check for leakage. Because of the time taken for the aspirator pressure and the instrument readings to stabilise, this zero check increased the time required to take any set of readings by a factor of four (based on three minutes per reading).

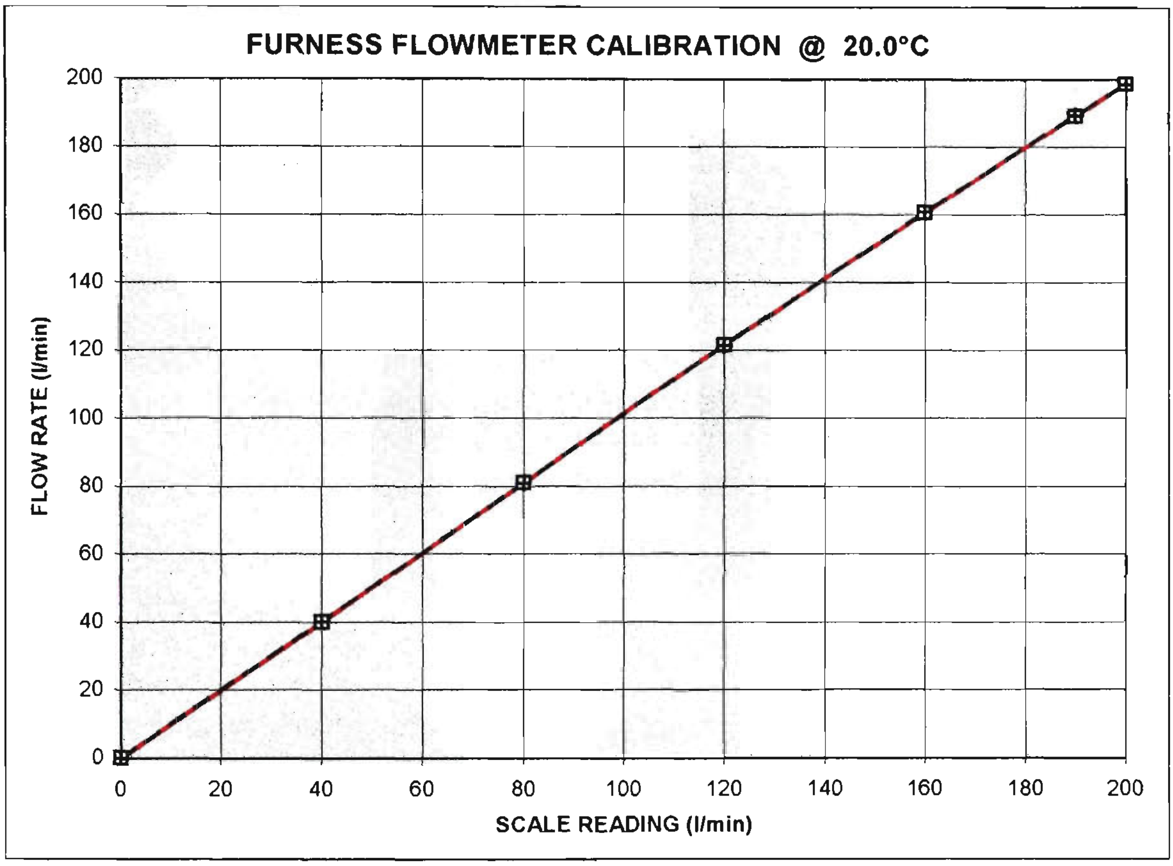

Figure A2.1 - Calibration curve of the flowmeter

A2.2 GRAPH PLOTTING AND CURVE FITTING

Microsoft Excel version 5.0 for Windows 3.11 or Windows 95 has been used extensively for spreadsheet analysis of data, for graph plotting, and to assist with determining the curves of best fit to the data. This has provided a very significant improvement in productivity as well as presentation. However, it should be noted that in all attempts to determine a curve of best fit, it has been found necessary to verify the equations generated and displayed by Excel. Despite Excel's promising least-squares verification of its curve fitting routine, often there were significant errors detected when the presented equation was incorporated within the spreadsheet and graphed.

It was deduced that these errors were caused by rounding in the terms as presented. For example, the coefficient 0.00000166 could be displayed as 0.000002, producing an error of +20%. In this example, the displayed coefficient has 6 decimal places but only one significant figure, whereas three or four significant figures are often required for good curve-fitting. Therefore it became necessary to test every equation and in most cases, each coefficient had to be improved manually, and exhaustively so, to ensure a good match with data.

Another limitation with Excel (and Corel Quatro) lies with scaling of the horizontal axis. Although most graphical formats require equal increments in this axis, one format ("scatter") permits variable steps. However, even with a scatter format, the package is designed for only one set of values on this axis. This can create a problem for presenting multiple graphs on one page (in differing colours or styles) if the axis values are not identical for each graph.

For example, the characteristic of a pipe system component is measured in terms of pressure drop versus flow rate. In the case of (say) a small orifice, the flow range may be 0 to 20 *litre/min* with data increments of 2*litre/min*. At the other extreme, for a large orifice the flow range may be 0 to 200 *litre/min* with data increments of 10*litre/min*. The two graphs of this data could not readily be presented on the same page because the increments are different.

Whereas in the latter example above, it is possible to take all readings at 2*litre/min*, this would require 100 readings which is not justifiable in terms of improved accuracy. It is also impractical because, as indicated in Section 2.1, adjustment of the system and the instrumentation readings are generally required to settle for three minutes between readings, so 100 readings would take 5 hours. In that time, the laboratory conditions (particularly temperature) would usually change sufficiently to upset the validity of earlier readings. In fact it has been found highly desirable to complete a set of readings within one hour, to ensure repeatability.

Moreover, with certain types of data, it is not possible to have predefined increments of the axis because the data is derived by calculation rather than read directly from an instrument. One such example is Reynolds number.
Therefore some graphs are presented individually. This is done to indicate the quality of the curve of best fit. Thereafter, several of these curves of best fit can be combined on one Figure for comparison. Alternatively, the data can be by interpolated to achieve a common set of increments at the axis.

Subsequently, by experimentation a method was developed for permitting multiple sets of values on the horizontal axis. This involves placing all sets of data into one pair of columns, while separating each set with a clear row (to avoid a "re-trace" line). However, the resulting family of curves can not be differentiated in terms of legend, or line and data point colours or styles, so this method is used only where confusion between curves would not arise.

A2.3 FLOW RATE DISCONTINUITIES

Despite the precautions detailed in Sections 2.1 and 2.2, further apparent inconsistencies persisted. When testing the flow rate through small holes, and by applying a square-law curve of best fit to the data, there appeared to be a step change (discontinuity) in the flow rate. An example of this relating to the typical, $2mm$ diameter sampling hole is illustrated in Figure A2.2.

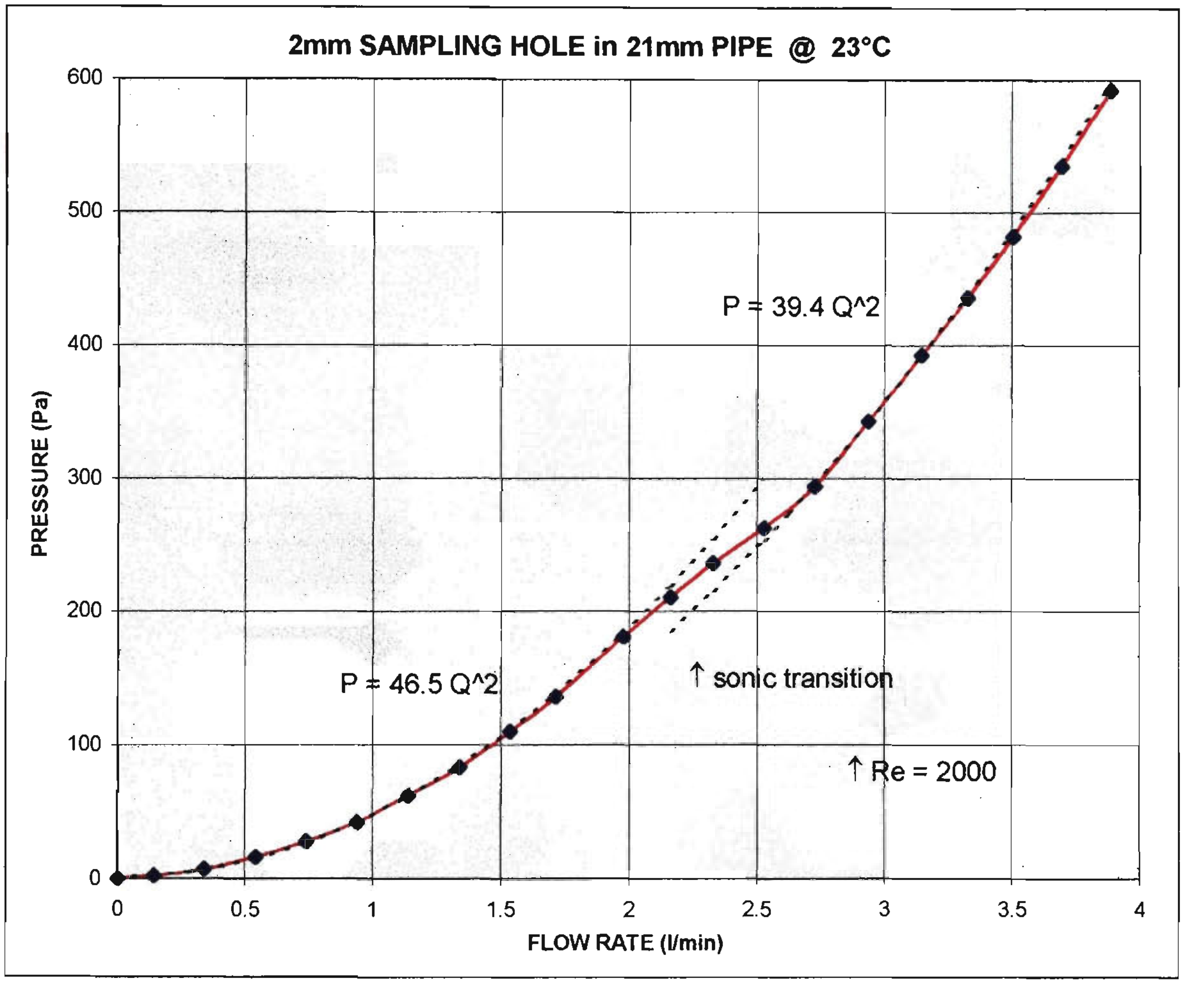

Figure A2.2 - Flow rate discontinuity in $2mm$ orifice

Based upon the average velocity through the hole of given size, this step change occurred at a Reynolds number in the general vicinity of 2000, accompanied by a significant change in the sound level (whistle) produced. It was postulated that there was an unknown flow regime transition taking place within the hole, causing a significant alteration to the loss coefficient.

Given that no prior evidence of such a discontinuity had been seen in the literature, this intriguing discovery was treated with caution. It was noted that in order to obtain a greater total flow rate to suit the span of the flowmeter, a number of pipes and holes had been tested in parallel.

Three configurations of the experiment are illustrated schematically in Figure A2.3. The second configuration involved four, one metre branch pipes connected symmetrically with "Y" joining pieces forming a manifold. Thus, four identical branches were fed into the flowmeter, with an aspirator connected to the flowmeter outlet. Each branch had a sealed end cap and a side-wall hole (orifice) close to the end. A pressure tapping was fixed in the still-air region upstream of each side-wall hole so that the pipe internal pressure at the hole could be monitored (there would be no upstream flow and hence no upstream pressure drop to upset the pressure reading).

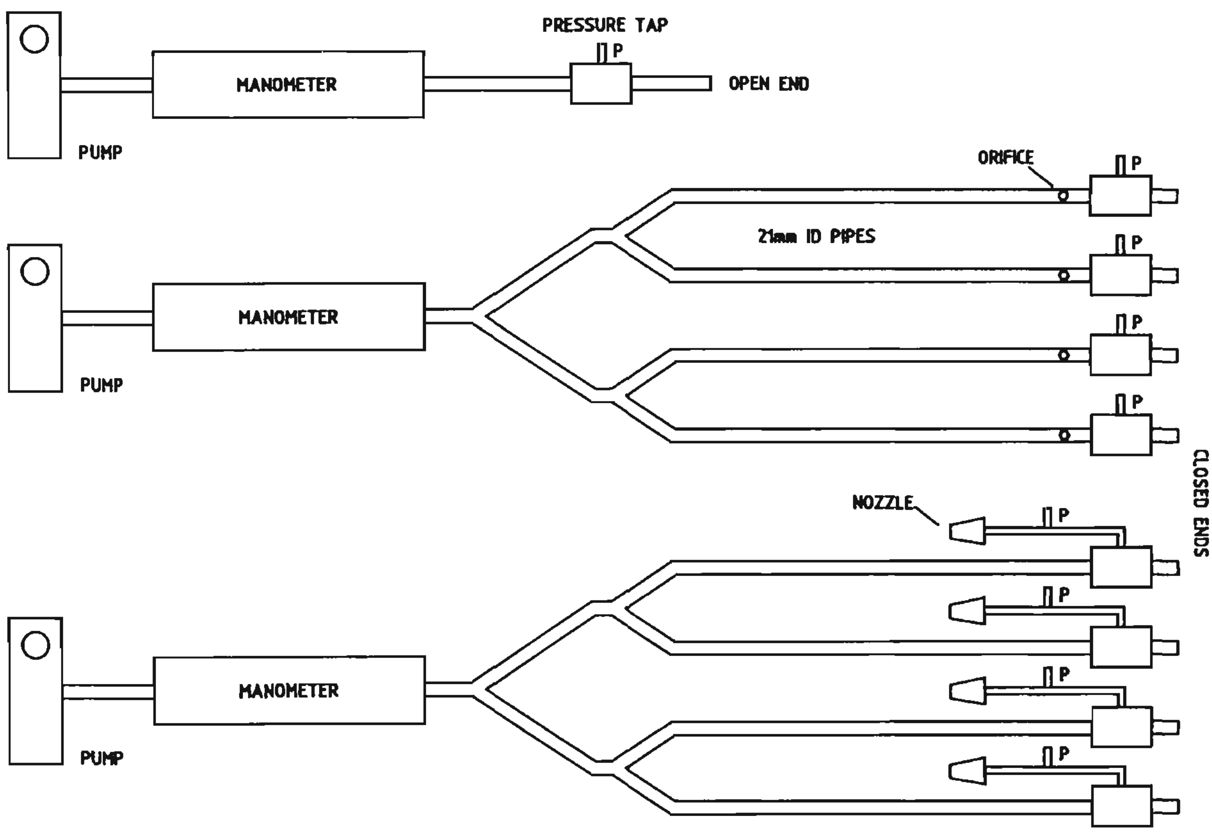

Figure A2.3 - Experiment configurations for holes and nozzles

Initially, each side-wall hole was drilled at $1.0mm$ diameter. Over the range of flow rates, the pressure developed behind each hole was recorded. For each flow rate setting, it was regarded as essential that all four pressure readings be the same, thereby indicating that the holes were practically identical. Then the total flow rate could be divided by four to obtain the average individual hole flow rate. This experiment was completed for the four sets of holes at diameters of $1.0, 1.5, 2.0, 2.5$ and $3.0\ mm$.

A similar configuration was tried using nozzles instead of side-wall holes, as included in Figure A2.3. These nozzles were designed for penetration of a ceiling with the pipework concealed above, connected to the pipe via a short length of flexible "capillary" tube. In this case the pressure tapping was a "T" connector inline with each capillary tube. The experiments were conducted with nozzle hole sizes of $2.0, 2.5$ and $3.0\ mm$ diameter.

Discontinuities in the data persisted for all hole sizes to varying degrees. The position of each discontinuity bore a broadly consistent relationship to Reynolds number and the sound level transition. In fact, in the region of the discontinuity, the sound level appeared to "surge", breaking between the higher and lower sound levels in a staccato manner. Curves of best fit to the data could be obtained using a square law characteristic, interrupted at the discontinuity, whereby at higher flow rates the square law characteristic was resumed with a smaller coefficient. The transitional flow phenomenon seemed to be confirmed.

Then a level of doubt was introduced by noting that at significantly higher flow rates, a further discontinuity could be observed in some cases. These higher-level discontinuities corresponded to Reynolds numbers of 4000 or more (analogous to one octave higher, suggesting an acoustic resonance effect). No explanation for this in terms of flow regime could be offered.

The linearity of the flowmeter remained in question and, because of the importance of the potential discovery, it was decided to repeat the tests rigorously involving the blockage of one or more of the four holes to produce a different total flow rate (i.e. operating the flowmeter at a different point in its span). This had previously been avoided because in many cases the flow rates would be quite low and possibly outside the linear calibration range of the instrument (the first certified calibration point being at $40 litre/min$).

Experiments were first undertaken with one of the four holes blocked. To achieve this, each of the four holes was blocked in turn, one at a time, to verify complete symmetry. In this manner, readings were taken throughout the pressure and flow range. Then two holes were blocked, in each of the four possible combinations (i.e. block holes AB, CD, AC or CD), and readings were taken throughout the pressure and flow range. Then three holes were blocked in each of the four possible combinations, and readings were again taken throughout the pressure and flow range. This whole procedure was repeated for several hole sizes.

It was confirmed that the discontinuities changed position with respect to Reynolds number, according to the number of holes in operation. In the case of four operating holes, the discontinuity corresponded to a flowmeter reading in the vicinity of 10*litre/min* (2.5*litre/min* per pipe). In the case of three holes, the discontinuity again corresponded to about 10*litre/min* (3.3*litre/min* per pipe). For two hole and one hole operation, the discontinuity at about 10*litre/min* persisted. All of the data were broadly consistent with a quantisation error within the flowmeter at about 10*litre/min*. The broad correlations with Reynolds number or acoustic noise that were apparent in earlier experiments were dismissed as coincidental.

For confirmation, the manufacturer was consulted via fax and although they were initially very responsive in seeking further details, they could offer no explanation for the discontinuity. It was concluded that they privately accepted the likelihood of a quantisation error but were embarrassed and were not prepared to confirm such a possibility. Accordingly it was decided that obvious discontinuities in the data should be carefully inspected and "smoothed out" by interpolation. All the data should be analysed by curves of best fit, and preferably, readings near the bottom of the scale (being 0-200 *litre/min* overall) should be avoided where possible.

Nevertheless in the broad span of its operation, the flowmeter was regarded as the most accurate instrument available. It should be noted that in a small number of instances, some of the instrument readings presented, have been adjusted by 0.1 or 0.2 *litre/min* (by inspection) to remove obvious small inconsistencies with neighboring readings. It was considered that such interpolation would be most unlikely to skew the results, especially when a large number of readings are taken.

APPENDIX 4 - HOLE FLOW CHARACTERISATION

A4.1 EXPERIMENTAL TECHNIQUE AND SETUP

Experimental techniques were needed that would detect the effect of upstream flow rate upon hole flow rate. This proved to be a difficult challenge using the available equipment. Firstly, the hole flow rate could not be measured directly. This is because the range of hole flow rates was low, in the vicinity of $1 litre/min$ ($1.7 \times 10^{-5} m^3/sec$). Flowmeters having negligible insertion loss are not generally available at this flow rate, and any interruption to the natural streamlines had to be avoided.

Some conceivably non-disruptive techniques (with questionable accuracy for this task) such as Laser Velocimetry or Ultrasonic Anemometry were not available for these experiments. Accordingly it was resolved to measure both the upstream and downstream flow rates simultaneously. Subtraction of the former would yield the hole flow rate. However, only one accurate flowmeter was available, and in any case, its insertion loss was very high and the experimental system would not easily support two such losses.

The flowmeter (a Furness Controls, FC-096G laminar flow element with its FC-016 digital manometer) was used to monitor downstream flow rates in all experiments. It was also used to calibrate a set of stainless-steel "control orifices" in association with a digital pressure gauge (a Yokogawa UMO4). These calibrated orifices (end vents) were fixed and sealed to the far end of the test pipe, adjacent to a 4-port pressure tap placed $150mm$ downstream. Initially, the rigid PVC test pipe was of $25mm$ outside, $21mm$ inside diameter.

A distance of $3000 \pm 0.5\ mm$ separated the pressure tap from the sampling hole location, with the flowmeter attached by a flexible straight coupling some $1m$ further downstream. The outlet of the flowmeter was similarly attached to a bank of four aspirators (centrifugal air pumps) connected in series-parallel to obtain sufficient pumping capacity (principally to overcome the pressure drop caused by the flowmeter). Being a long parallel-plate laminar-flow device, the flowmeter was expected to dampen any significant aspirator flow pre-rotation or induction pressure pulsation from transmitting upstream, and influencing the sampling hole flow. The aspiration pressure (being negative relative to atmosphere) was adjusted by means of a 10-30V DC power supply.

The pressure gauge was already in use with the standard orifices measuring upstream flow rate, so to obtain the differential pressure reading at the hole, the pipe pressure drop was first calibrated. This involved another, temporary pressure tap at the proposed location of the sampling hole. Using a $10.36mm$ diameter control orifice at the far end of the pipe, the pipe pressure drop versus flow rate was obtained as shown in Figure A4.1.

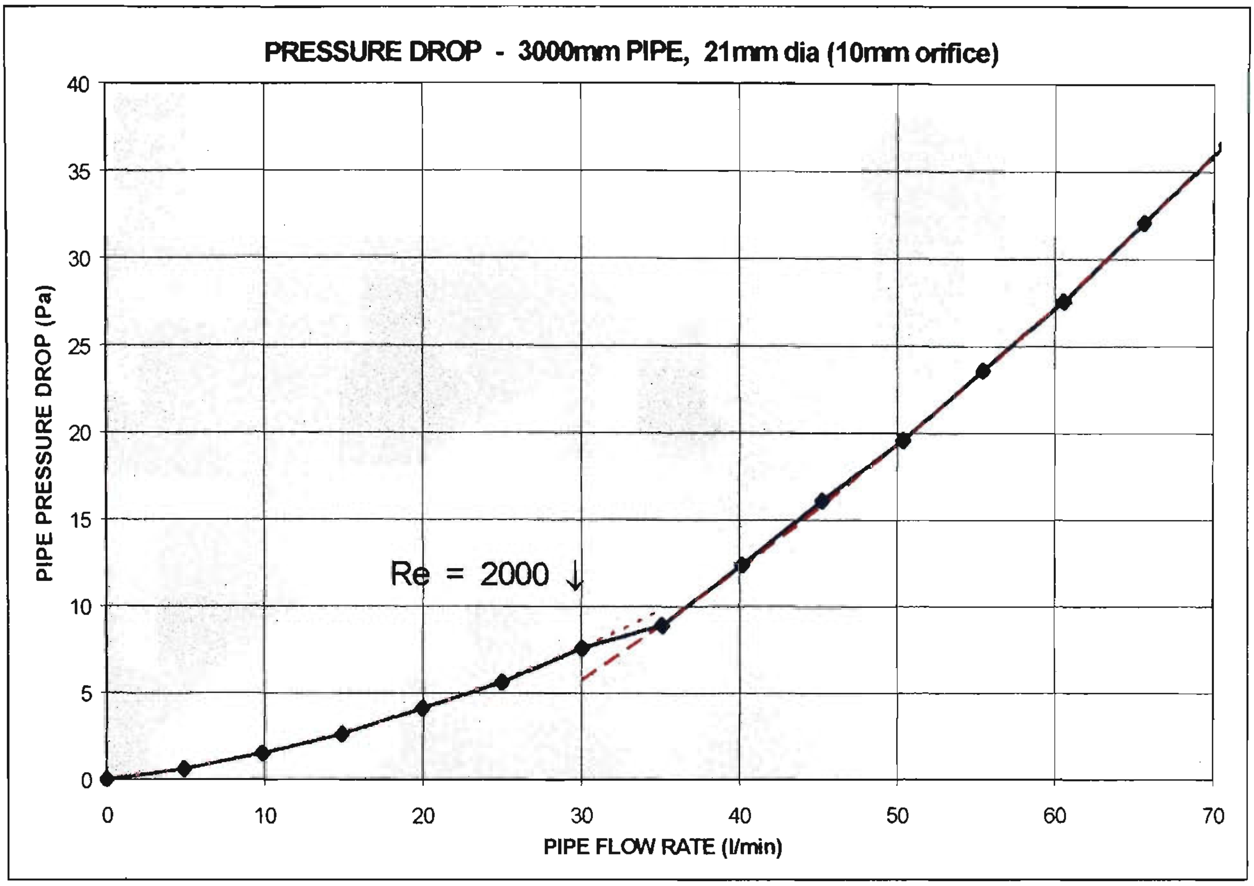

Figure A4.1 - Pipe pressure drop calibration

The transition from laminar to turbulent flow is clearly visible in Figure A4.1, and the point where the Reynolds number, Re = 2000, is indicated for reference. Repeating the experiment with other orifice diameters did not alter the data values. Two curves of best fit to the data, representing the laminar and turbulent flow regimes, were determined as:

$$Q_{pipe} < 30: \quad \Delta P_{pipe} = 0.0050\, Q_{pipe}^2 + 0.1033\, Q_{pipe}$$

$$Q_{pipe} > 35: \quad \Delta P_{pipe} = 0.00317\, Q_{pipe}^2 + 0.0425\, Q_{pipe} - 9.85$$

where Q_{pipe} (*litre/min*) is the pipe flow rate and ΔP_{pipe} (*Pascal*) is the static pressure drop along the pipe. Thus, in subsequent experiments with a sampling hole, the pressure at the hole would be obtained from the first pressure tap measurement (which also provides the pipe flow rate), plus the calculated pipe pressure drop obtained from the above equations.

There was conjecture as to whether the pipe pressure drop would be affected by the existence of a sampling hole, with its disturbance reflecting back upstream. A subsequent series of experiments used a *2mm* hole opposite a single-port pressure tap, together with the full range of control orifices. These orifices determined the relative magnitude of the upstream flow rate compared with the hole flow rate.

The results obtained for all of the orifices are overlaid in Figure A4.2. These experiments revealed that the pressure drop was increased by only as much as 3Pa and this increase was principally restricted to the turbulent flow region. With typical hole pressures in the order of hundreds of Pascal, this was not considered to introduce a significant error in the estimation of hole pressures.

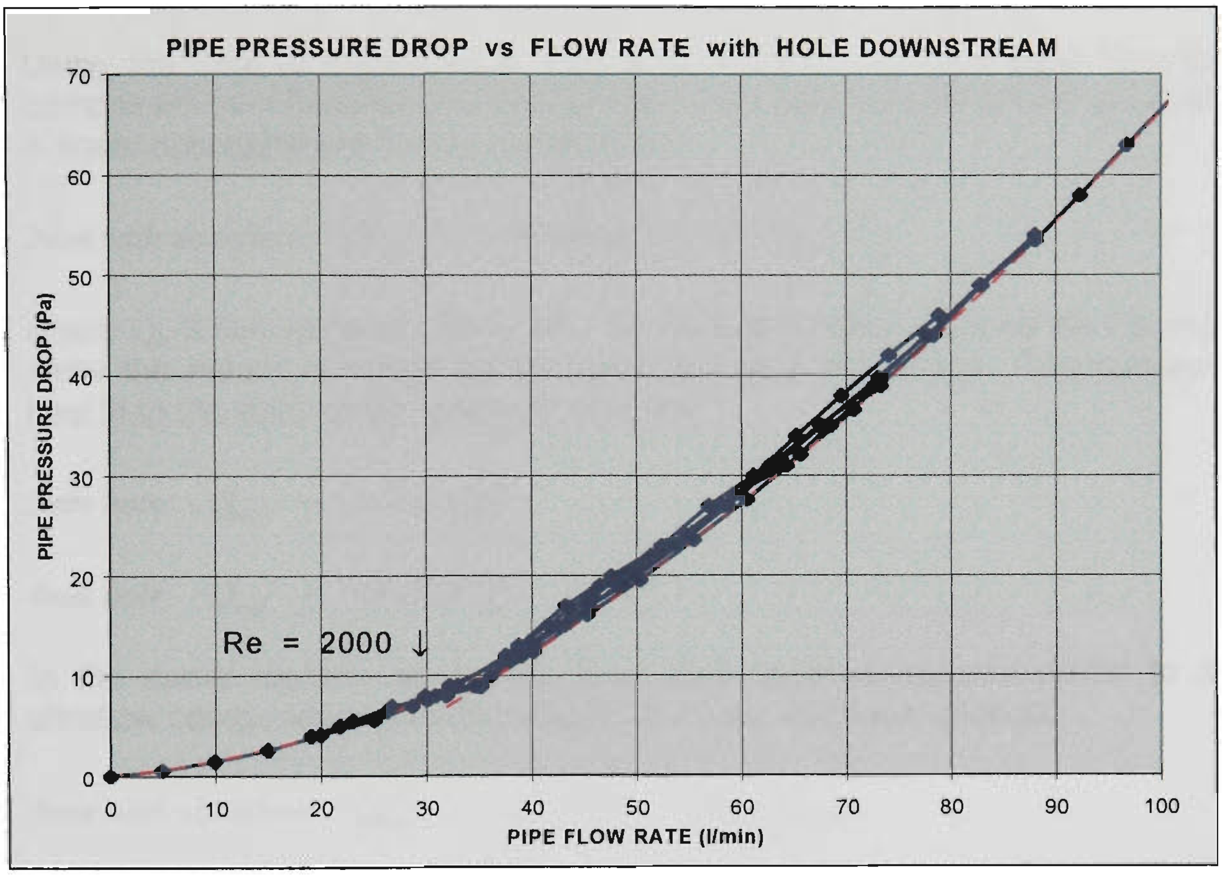

Figure A4.2 - Effect of a downstream hole on pipe pressure drop (found by overlaying the results for the various upstream control orifices)

Having established a technique for determining the hole flow rate and pressure, results were obtained for holes of 2, 3 and 4 *mm* diameter using control orifices of 0, 4.00, 5.31, 7.37, 10.36 and 12.9 *mm* diameter. The 0*mm* orifice corresponded to a blocked pipe (zero upstream flow) which provided the reference data for comparison with conditions of upstream flow.

Figure A4.3 contains graphs of the data obtained with a 2*mm* hole, using the full range of control orifices as indicated (with notation simplified by rounding to the nearest integer, and with "0*mm*" representing nil upstream flow). A curve of best fit to the data for nil upstream flow is:

$$2mm\ hole: \quad Q_{stat} = 0.137\,\Delta P_{stat}^{0.54}$$

where Q_{stat} is the hole flow due to the static pressure, ΔP_{stat}. Set against this reference curve, it can be clearly seen that at a given hole pressure, when in the presence of upstream flow, the hole flow rate is increased significantly. This was a surprising phenomenon not anticipated in the literature.

Note that in Figure A4.3 the data obtained for non-zero upstream flow rates have been connected with straight lines, and curves of best fit have not been included, to avoid clutter and to clarify the data set groupings.

Using the data of Figure A4.3, Figure A4.4 shows the increased hole flow component as a function of upstream flow rate, here referred-to as "ultraflow". A linear approximation to this ultraflow is:

$$\text{2mm with ultraflow:} \quad Q_{hole} = 0.060\left(Q_{up} - 32\right) + Q_{stat}$$

where Q_{up} is the upstream flow rate. To verify this effect, Figures A4.5 to A4.8 show the results obtained for the $3mm$ and $4mm$ hole sizes. The curves of best fit to the data for nil upstream flow are:

$$\text{3mm hole:} \quad Q_{stat} = 0.323\,\Delta P_{stat}^{0.52}$$

$$\text{4mm hole:} \quad Q_{stat} = 0.667\,\Delta P_{stat}^{0.50}$$

In the same manner as for the $2mm$ hole, a linear approximation to the ultraflow component was estimated for the $3mm$ and $4mm$ holes as:

$$\text{3mm with ultraflow:} \quad Q_{hole} = 0.055\left(Q_{up} - 32\right) + Q_{stat}$$

$$\text{4mm with ultraflow:} \quad Q_{hole} = 0.055\left(Q_{up} - 24\right) + Q_{stat}$$

The magnitude of experimental error is evident in the lack of smoothness in the graphs of hole flow versus pressure. Nevertheless, it was possible to plot an average of 13 points for each of the six graphs, on each Figure. This is regarded as a sufficient number, for curves of best fit to be drawn with confidence. For example in the case of Figure A4.3 with a $12.9mm$ orifice:

$$Q_{hole2/13} = -7E-05\,\Delta P_{stat}^2 + 0.0465\,\Delta P_{stat} - 0.204; \qquad R^2 = 0.9857$$

where R^2 is the least-squares value, indicating a confidence level of 98.6%. In the case of the ultraflow graphs, the error is particularly evident because it is magnified by the process of subtracting a smooth set of data (the static flow equation), rendering the variations relatively larger. The linear data trend is therefore difficult to place with confidence. Despite this difficulty there is a broadly consistent pattern arising from these sets of data.

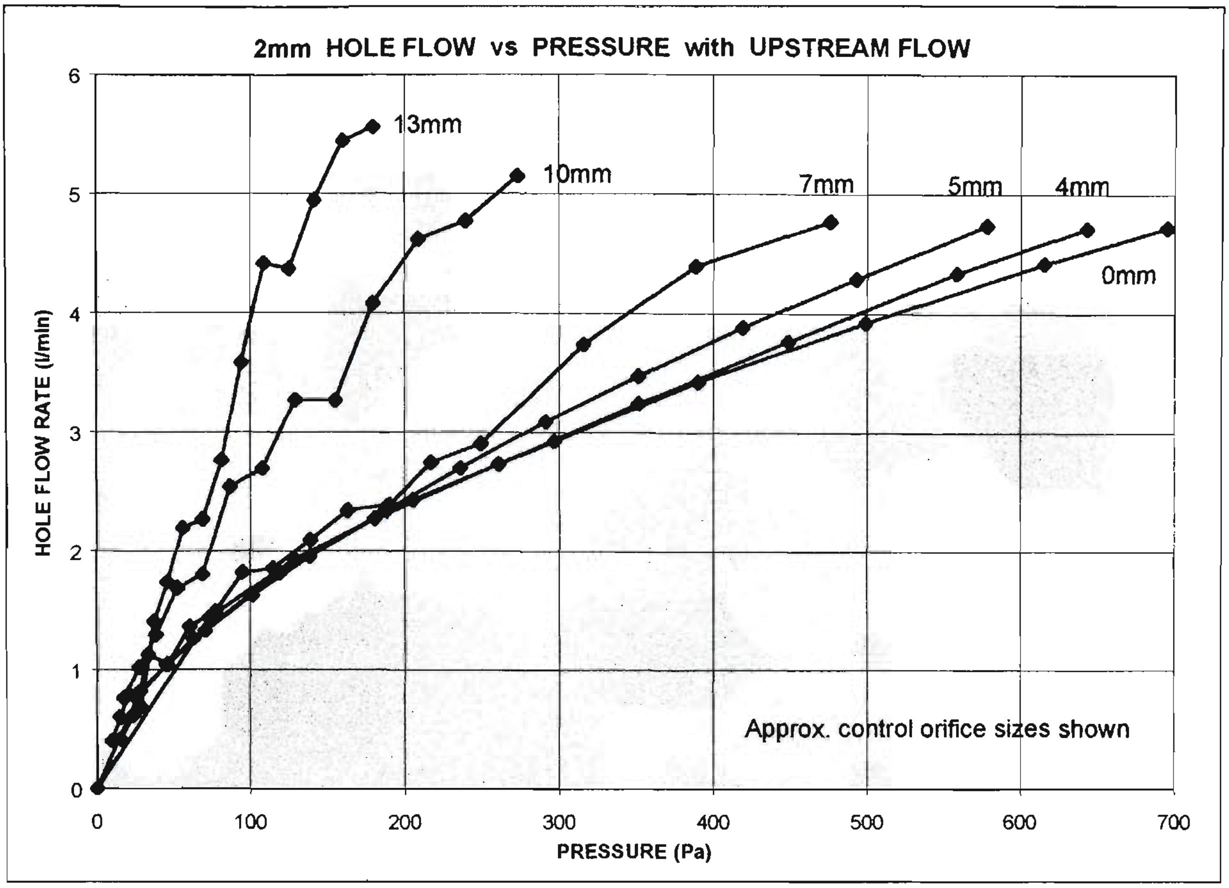

Figure A4.3 - *2mm* hole flow with upstream flows

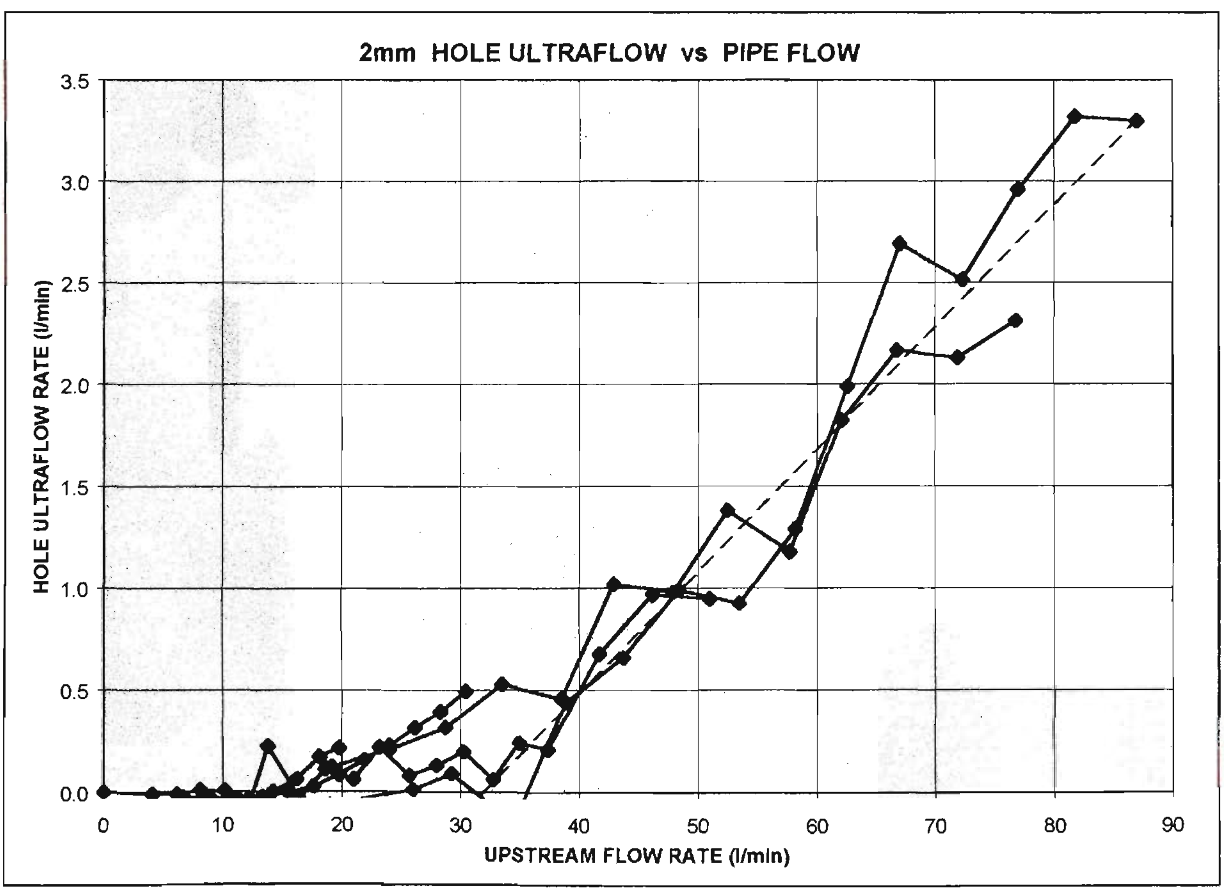

Figure A4.4 - *2mm* hole ultraflow component

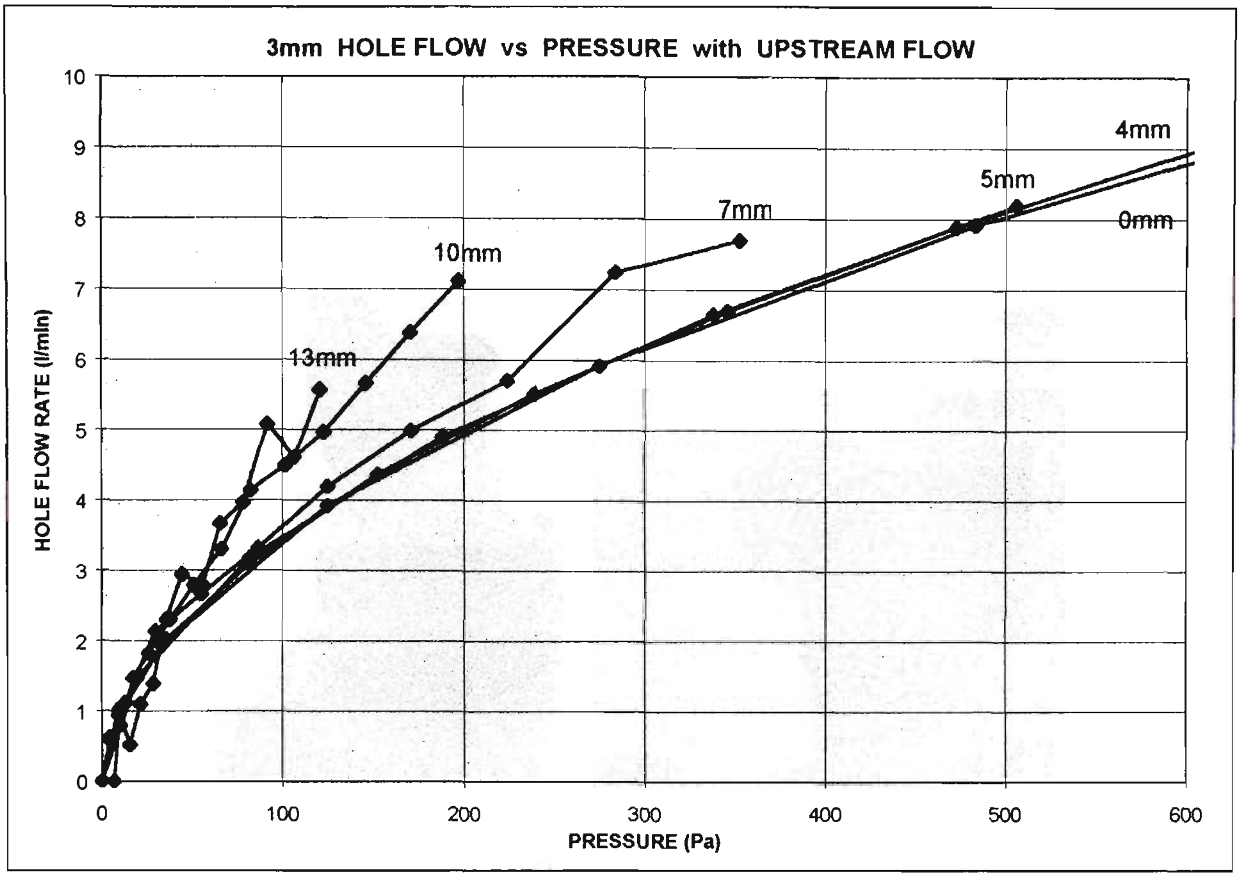

Figure A4.5 - $3mm$ hole flow with upstream flows

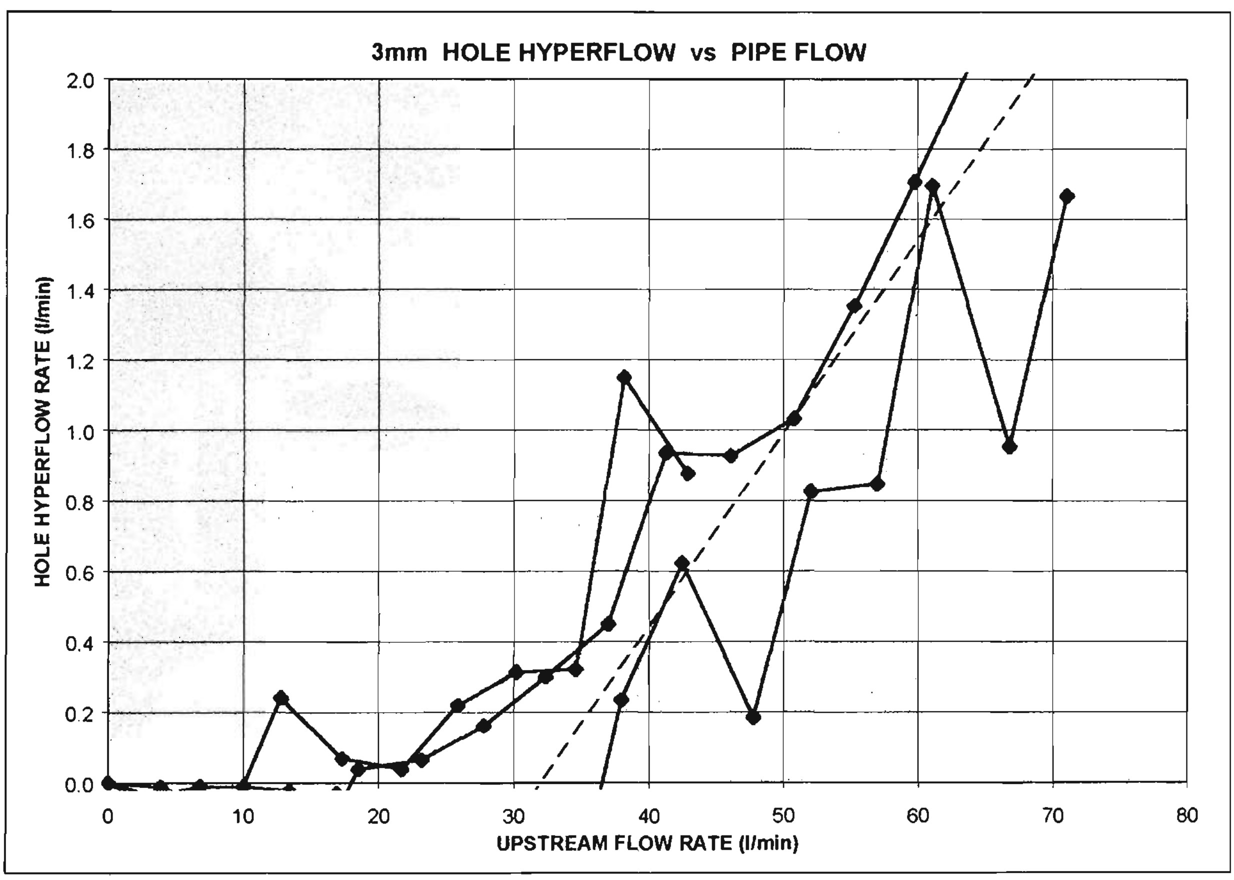

Figure A4.6 - $3mm$ hole ultraflow component

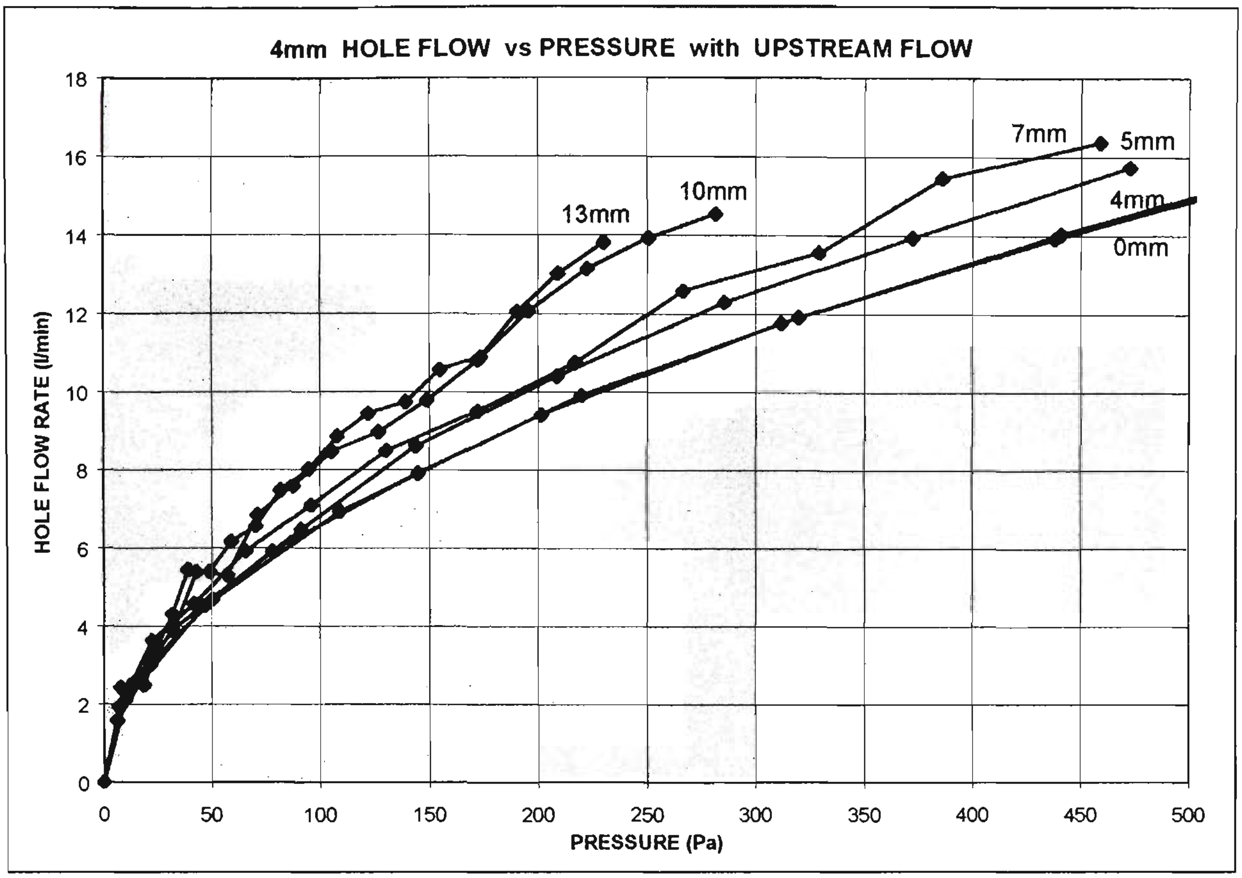

Figure A4.7 - $4mm$ hole flow with upstream flows

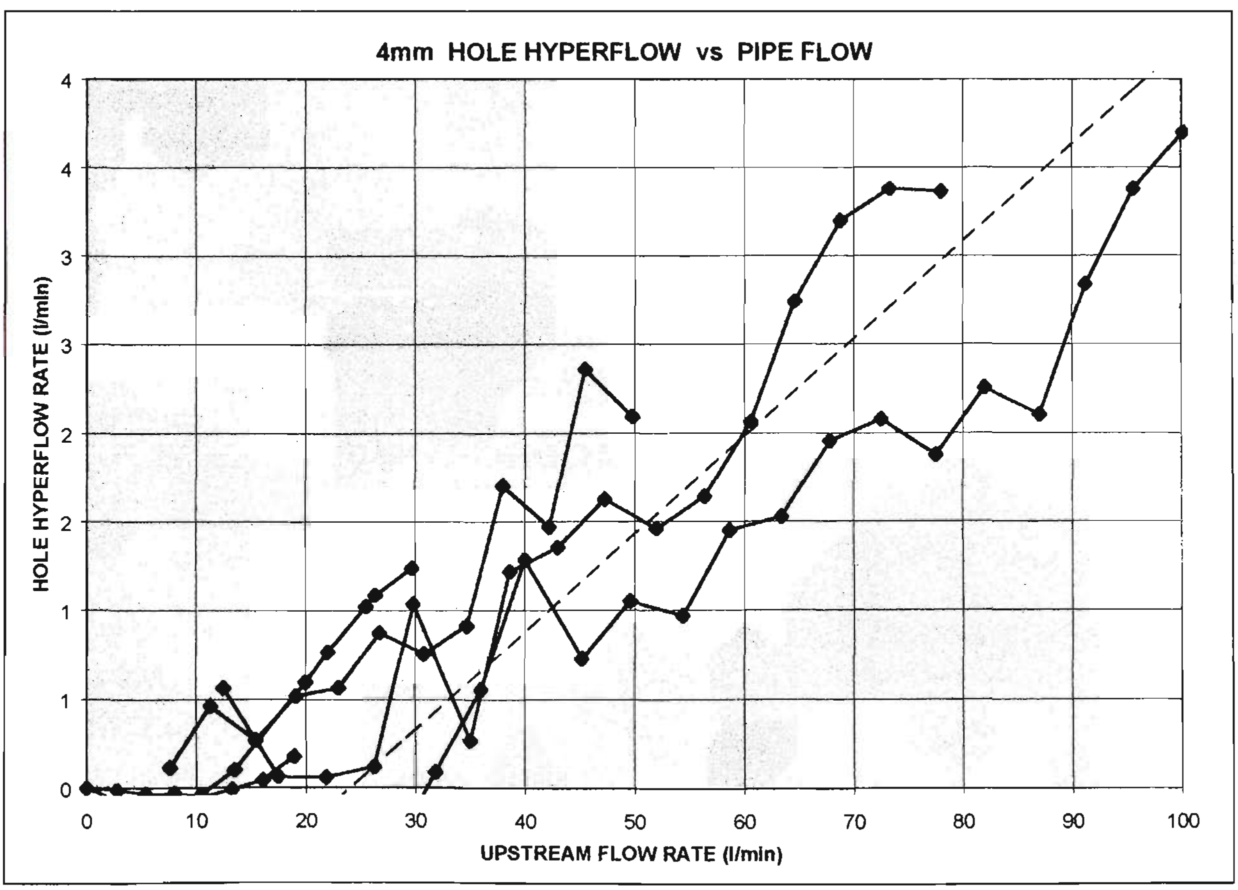

Figure A4.8 - $4mm$ hole ultraflow component

It is noted that in a more detailed view, the data relating to the $3mm$ hole is a little inconsistent inasmuch as the gradient should be higher (say 0.0058) and the offset lower (say 28), for consistency with the $2mm$ and $4mm$ holes.

The conclusion to be drawn at this stage is that at low upstream flow rates, the hole flow rate is governed only by the static pressure differential. At a given pressure, beyond a threshold upstream flow rate, the hole flow rate increases linearly with upstream flow rate. This threshold and rate of increase depend on the hole diameter and possibly the pipe diameter.

The experimental error arises from the lack of resolution in the instruments as well as temperature drift. In particular, the upstream flow rate is derived from the control orifice calibration which has its own error. The pressure gauge, which is used for orifice calibration as well as for pressure and flow readings has a resolution of 1Pa, which represents a significant variation at low flow rates. For example, at a pressure reading of 10Pa with a $10.36mm$ orifice, the flow rate is $20 litre/min$. Since the orifice flow rate varies as the square root of pressure, an error of $\pm 1\text{Pa}$ (10%) represents a flow error of 3.2% $(\pm 0.6 litre/min)$. The resolution of the flowmeter is six times higher, at $0.1 litre/min$. Viewed conversely therefore, a flow variation of six times the flowmeter resolution is required before it becomes evident in the control orifice reading, so further consideration of the pressure gauge resolution is necessary. This is addressed in Chapter 4.

A4.2 INITIAL ANALYSIS

In an attempt to characterise the effect of upstream flow rate on hole flow rate, the original data generating Figure 4.7 (Chapter 4) were re-presented in such terms, in Figure A4.9. This shows the data aligning into three groups, corresponding to the three hole sizes. Each of these groups produces a pair of essentially linear graphs, corresponding with the two control orifices used. The data relating to the $2mm$ hole are essentially converged upon one line (dashed) which passes through the origin. The data relating to the other holes converge less perfectly upon lines (also dashed) which similarly pass through the origin. The three lines were found to be highly consistent, each conforming to the linear equation:

$$Q_{hole} \quad = \quad \left(0.155 D_{hole} + 0.108\right) Q_{up}$$

where Q_{up} is the upstream flow rate. Although this simplicity was an encouraging result, the fact that the data was not entirely convergent (within the error span), was a matter of concern.

Presentation of the hole Reynolds number in terms of pipe upstream Reynolds number, provided no improvement in the convergence of each pair of graphs, save that the lines of best fit came a little closer to each other. Presenting the hole flow rate in terms of dynamic pressure (by converting the upstream flow rate to average velocity and using $P_{dynamic} = \rho u^2 / 2$) did not improve the convergence either, and the lines of best fit became curved (as square root functions).

Then it was decided to graph the normalised Reynolds number for each hole, versus the pipe upstream Reynolds number. This was normalised by dividing each hole Reynolds number by the equation to the lines of best fit (above). The result is shown in Figure A4.10. This Figure in effect represents the spread of data, indicating the error range, which is broadly within $\pm 10\%$ above $Re = 2000$, with an increasing error at lower Reynolds numbers. This degree of error was regarded as unsatisfactory and a new approach was used in an attempt to improve the convergence of the data.

It was noted that at a given upstream flow rate for a given hole size, the separation of a pair of graphs represented a different hole pressure. In an attempt to converge the graphs, an interpolation procedure was used. A convenient set of upstream flow rates in steps of $10 litre/min$ was selected. At each upstream flow rate, the data was interpolated to determine the hole pressure differential and the hole flow rate, for each of the three hole sizes and for the two control orifices. The work was simplified because the pipe characteristic determined that, for a given orifice and a given upstream flow rate, the pressure at the hole was always the same, regardless of the hole size. Thus, for each sampling hole size, at a given upstream flow rate it was possible to present the incremental hole flow due to an increment in pressure as shown in Figure A4.11. Linear relationships are evident.

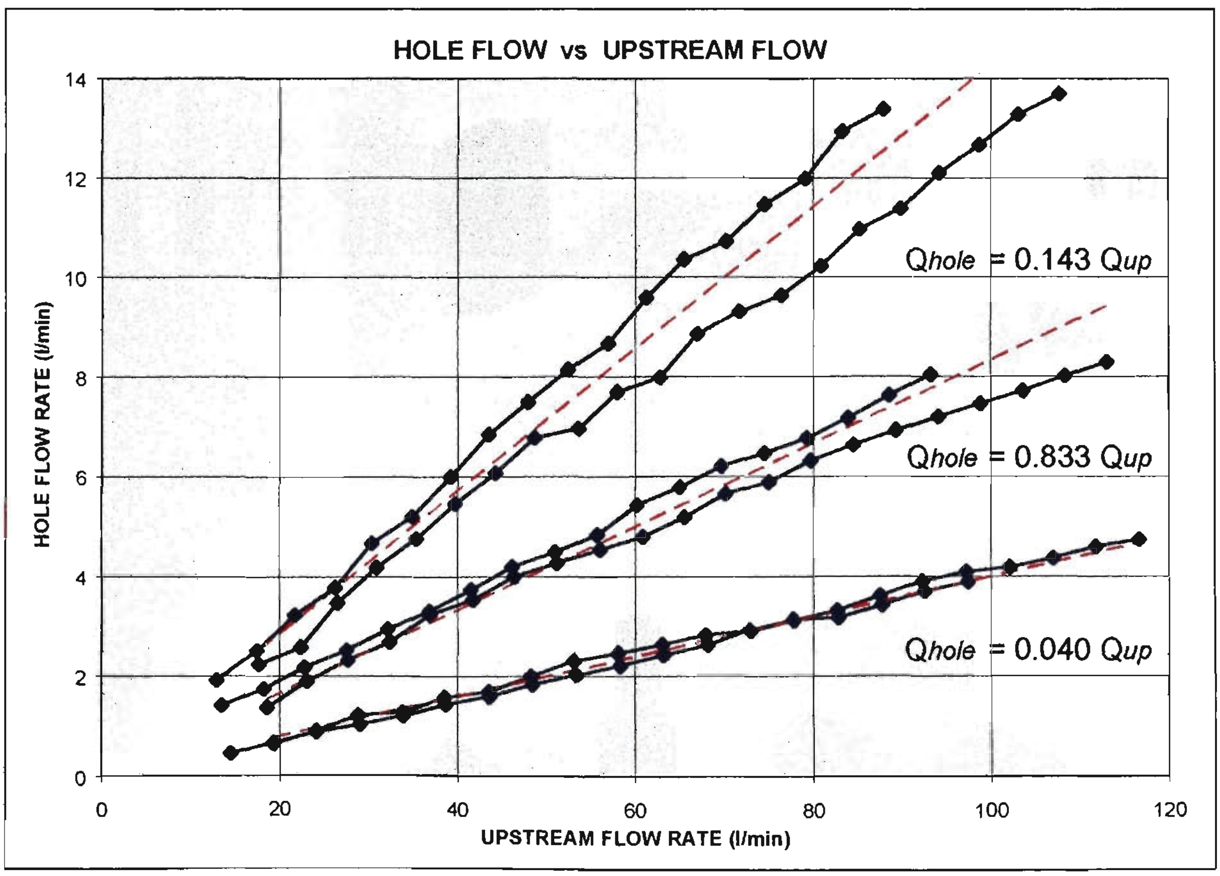

Figure A4.9 - Hole flow versus pipe upstream flow

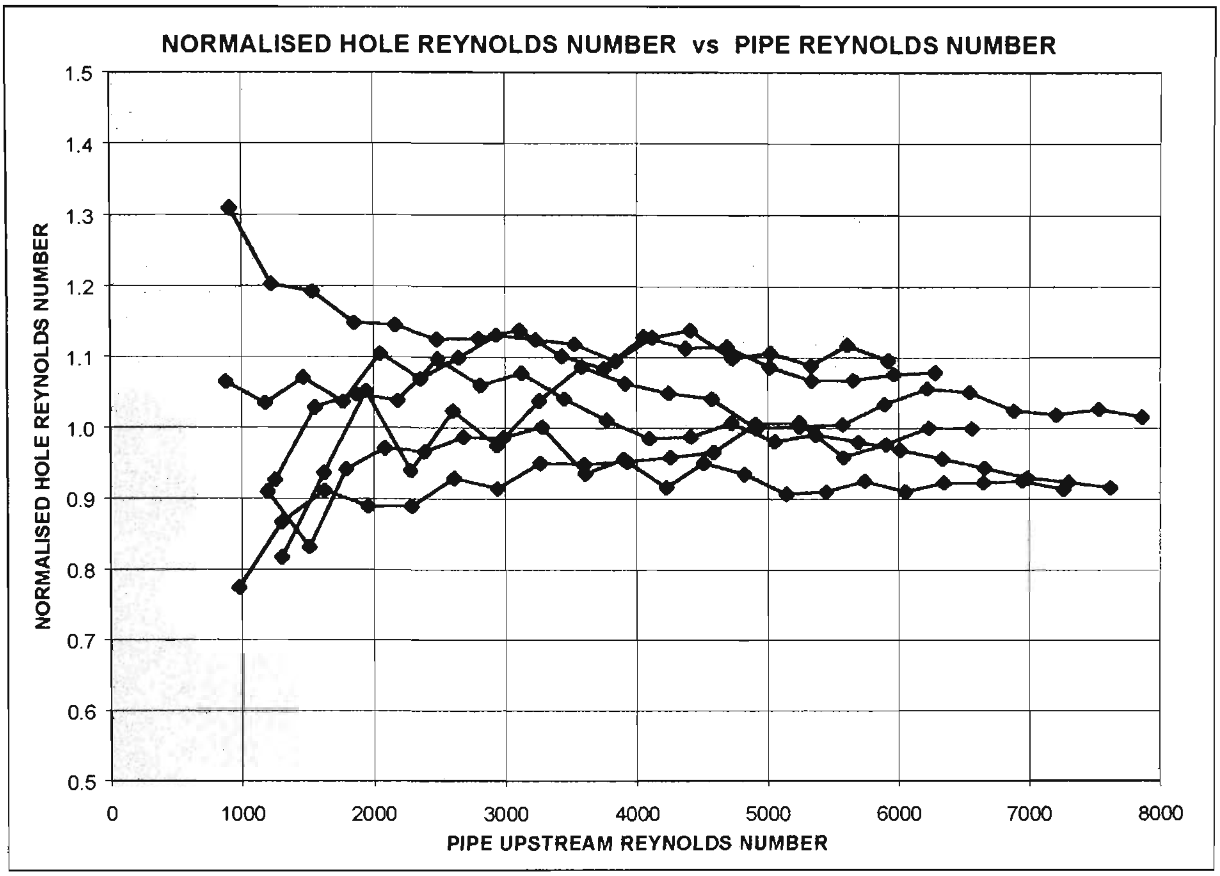

Figure A4.10 - Normalisation of hole and pipe Reynolds numbers

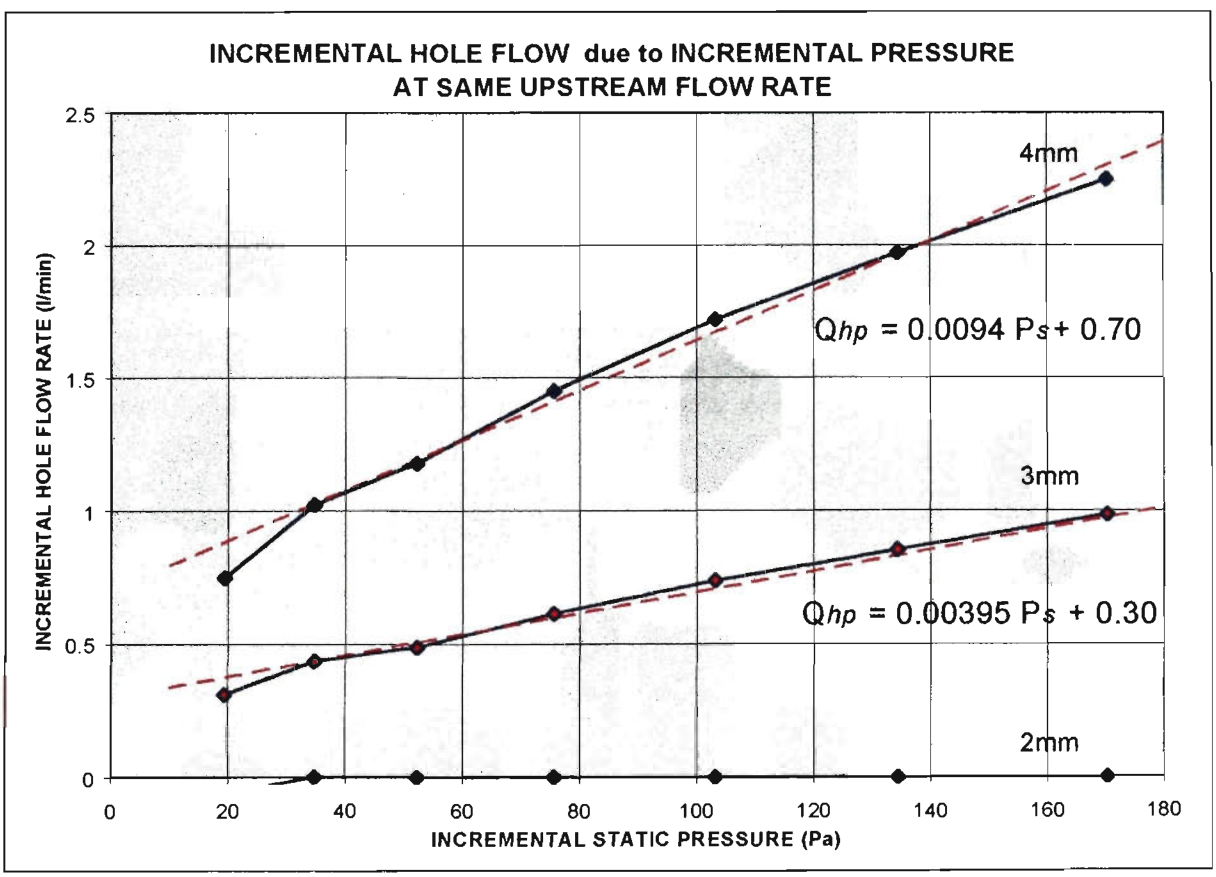

Figure A4.11 - Incremental hole flow and pressure

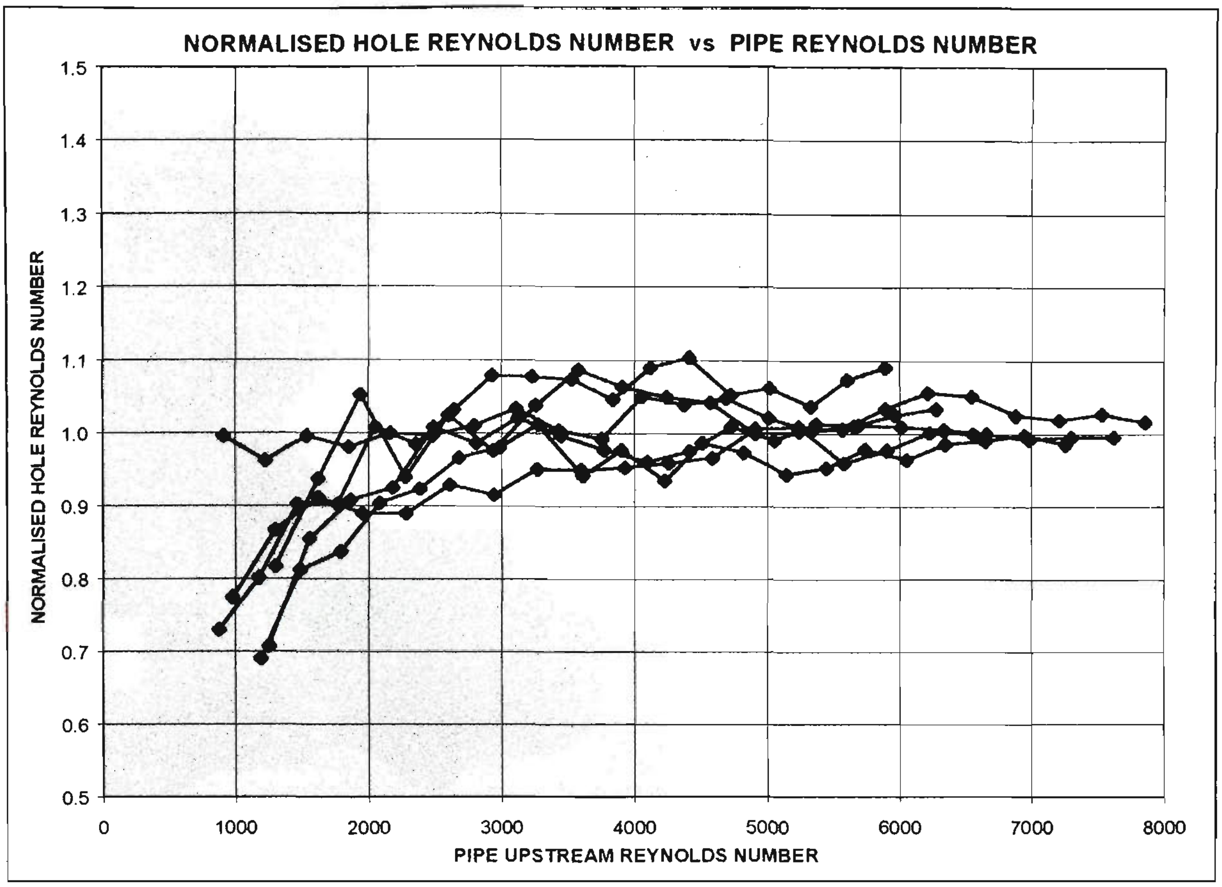

Figure A4.12 - Revised normalisation of hole and pipe Reynolds numbers

By including the equations of best fit to the graphs in Figure A4.11 within the analysis of the original data, it was possible to improve the convergence of the graphs, resulting in the improved error range as indicated by comparing Figure A4.12 with Figure A4.10.

It was felt that the equations of Figure 4.11 could be used within an algorithm to characterise hole flow generally. However, for verification it was decided to visualise the model that would be constructed from the approach taken hitherto. Figure A4.13 presents a three-dimensional view used to combine the effects of static pressure, pipe upstream flow and hole flow, with flow rates expressed as Reynolds numbers.

The foreground curve of Figure A4.13 represents the hole flow caused by static pressure whereas the background sloping plane represents the effect of upstream flow rate. The discontinuity between these effects was regarded as highly unlikely and a new approach to the analysis was commenced, as discussed in Chapter 4.

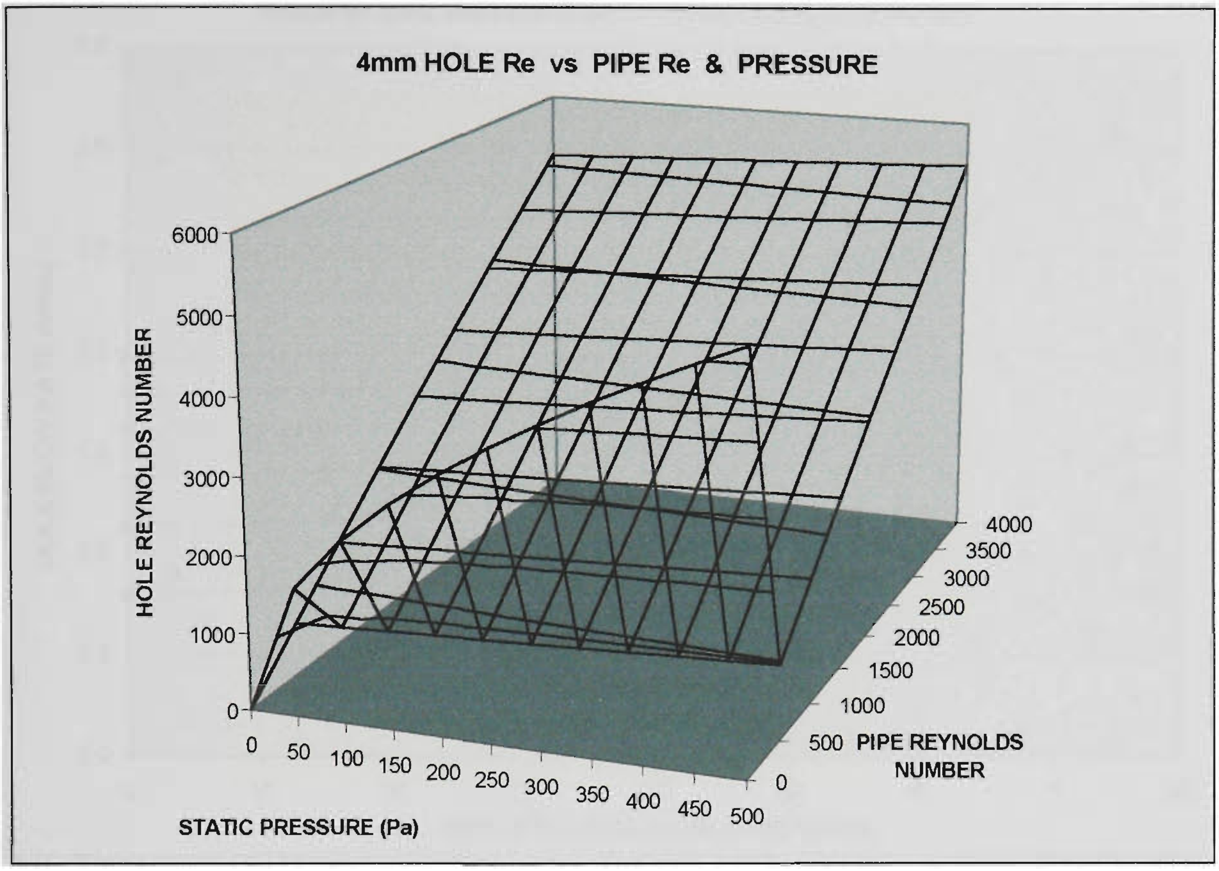

Figure A4.13 - Three-dimensional representation of hole flow which fails continuity examination

A4.3 ULTRAFLOW MODELLING RESULTS

In Section 4.14 a method was derived for modelling the form and magnitude of the Ultraflow phenomenon using the following equations by iteration:

$$Q_{jet} = Q_{stat} + Q_{ultra} = Q_{stat} + Q_{up}\left(1 - \sqrt{R_H}\right)$$

$$R_H = \frac{P_{up}/\rho + C_{jet}\, u_{up}^2/2}{\left(P_{up} + \delta P_{jet}\right)/\rho + \left(Q_{up} + Q_{jet}\right)^2 / 2A_{pipe}^2}$$

$$\delta P_{jet} = \rho\left(\frac{\left(Q_{up} + Q_{jet}\right)^2 - \beta Q_{up}^2}{A_{pipe}^2}\right)$$

$$C_{jet} = \frac{2}{\left(D_{hole} + 1\right)\left(D_{pipe}/21.2\right)^{0.8}}$$

Results obtained for several combinations of hole and pipe diameters are shown in Figures A14 – A17, where the closeness of fit to the experimental data can be seen from the asymptote (shown dotted).

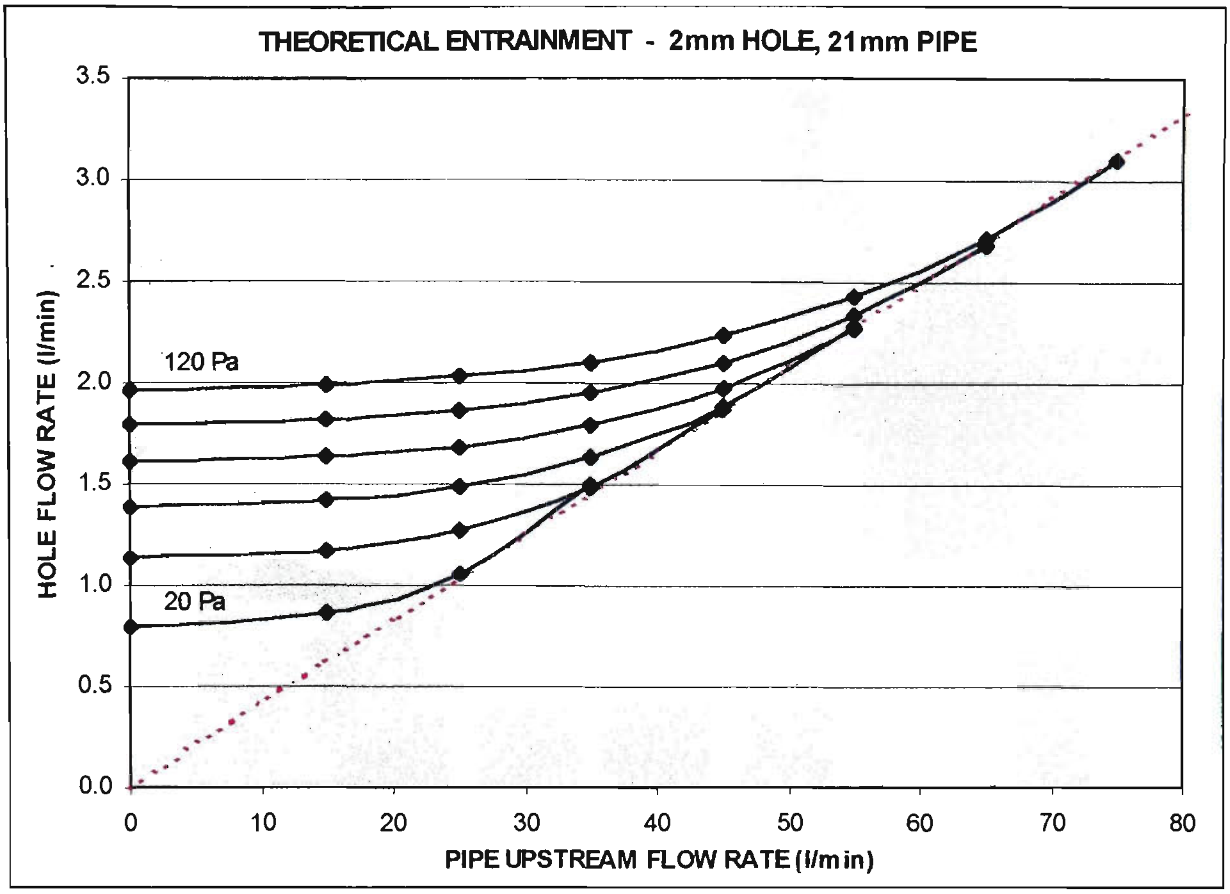

Figure A4.14 - Theoretical results for $2mm$ hole in $21mm$ pipe

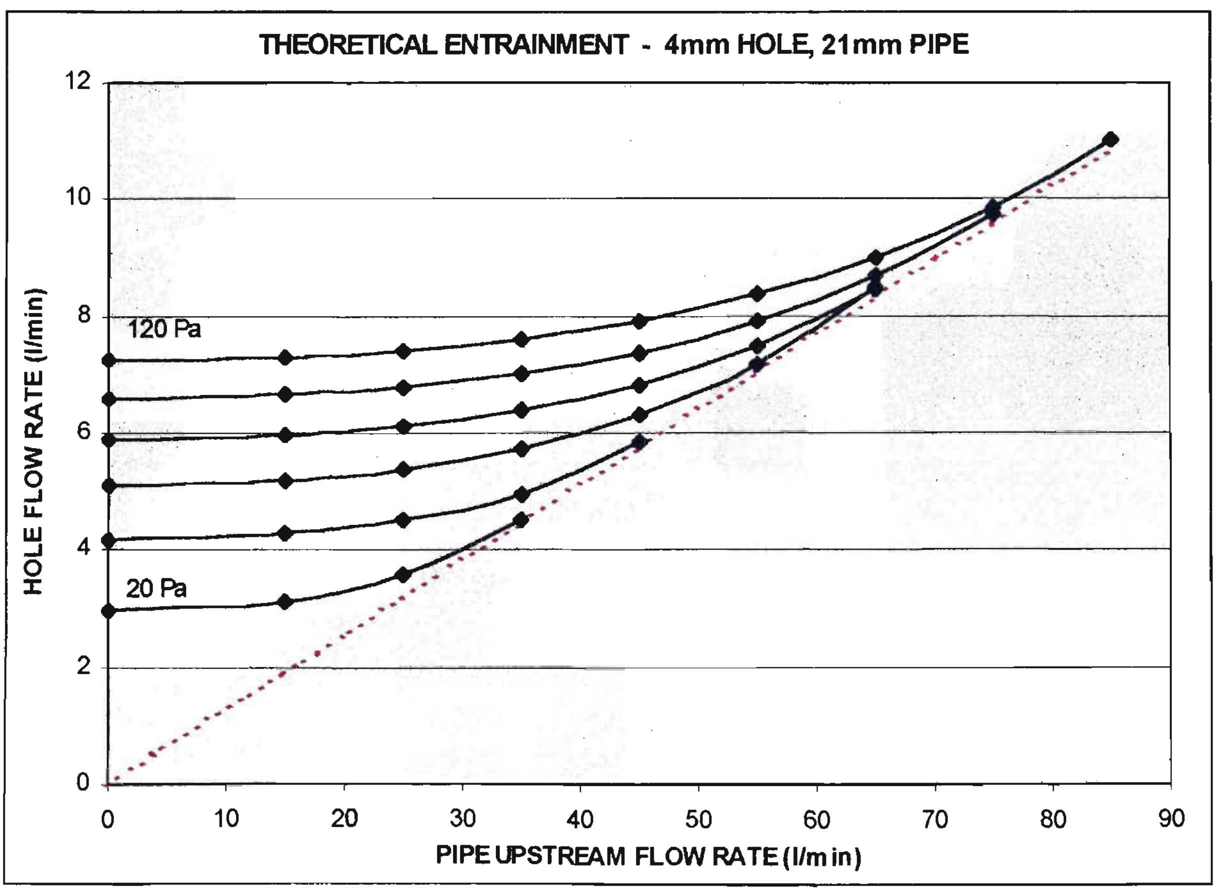

Figure A4.15 - Theoretical results for $4mm$ hole in $21mm$ pipe

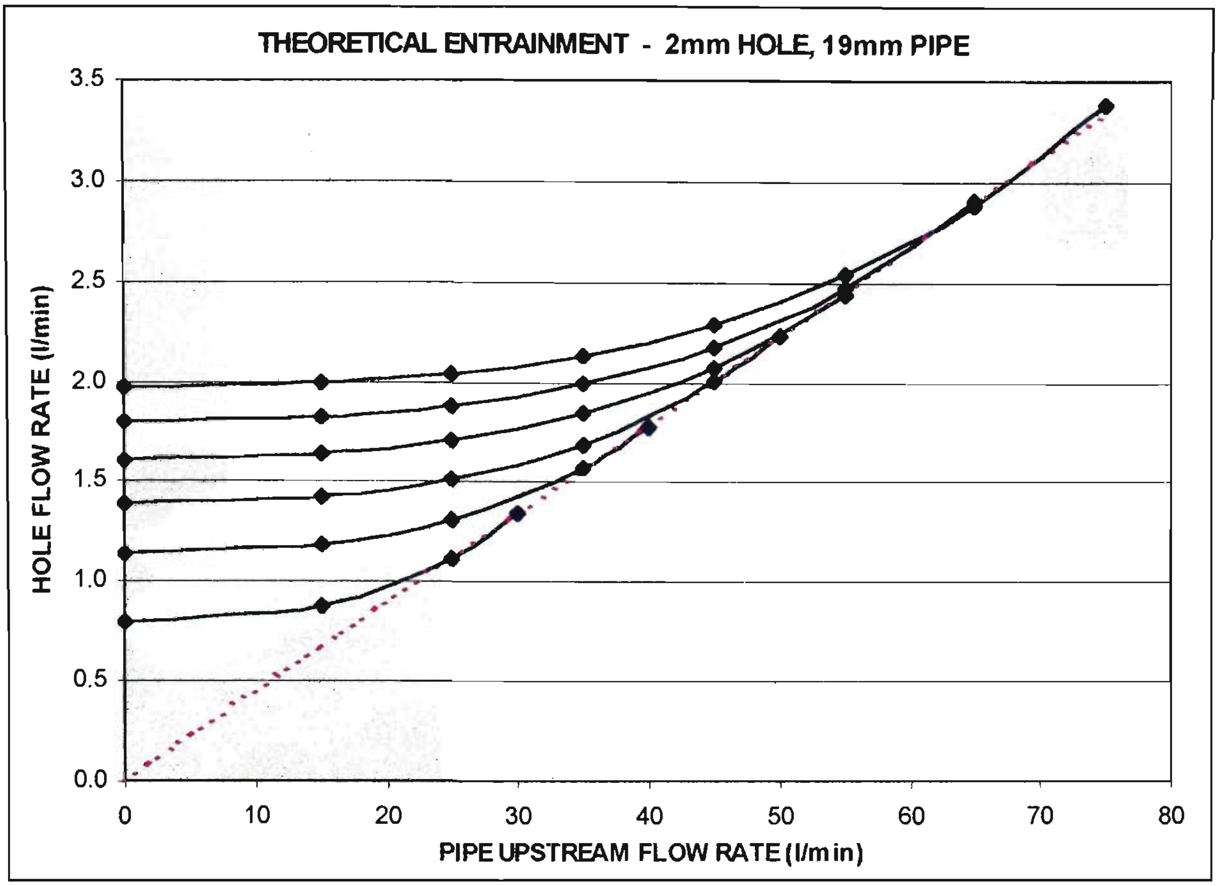

Figure A4.16 - Theoretical results for 2mm hole in 19mm pipe

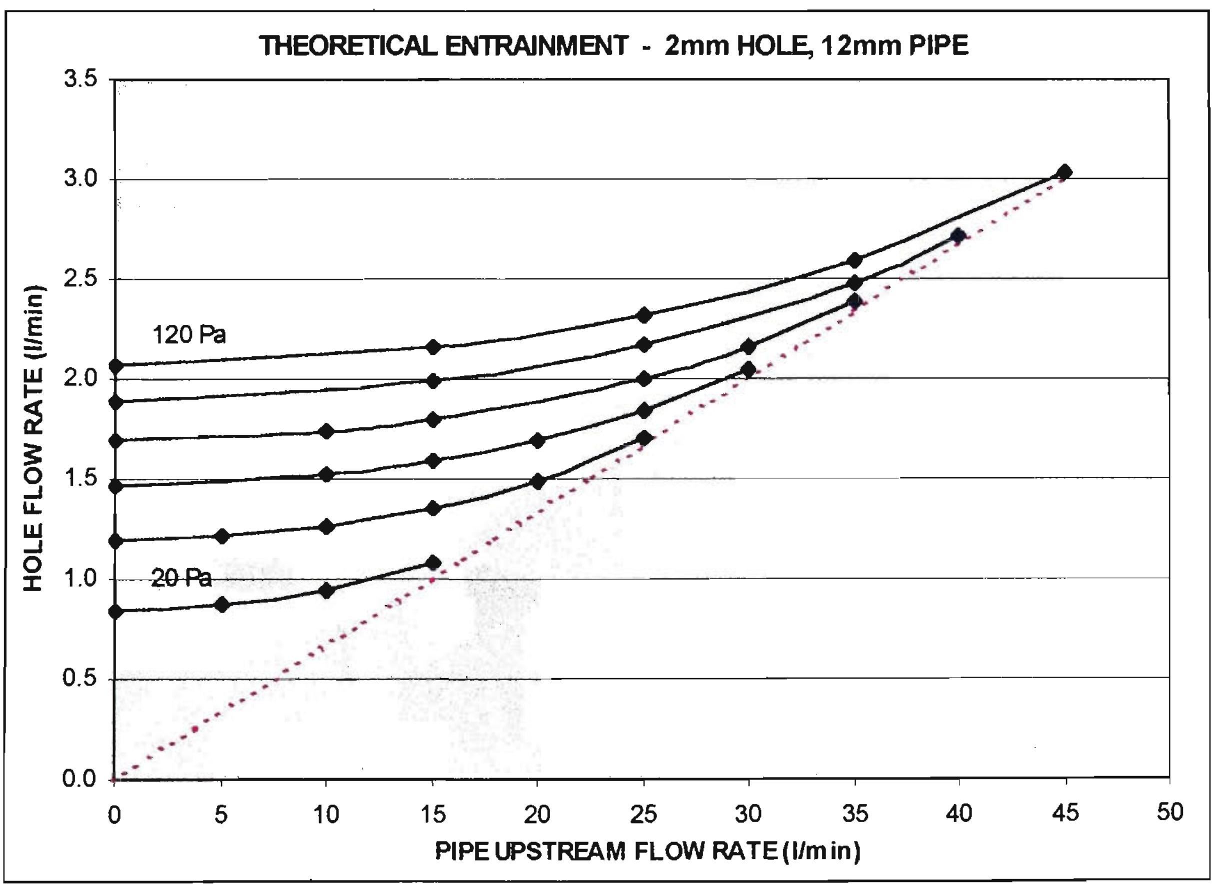

Figure A4.17 - Theoretical results for 2mm hole in 12mm pipe

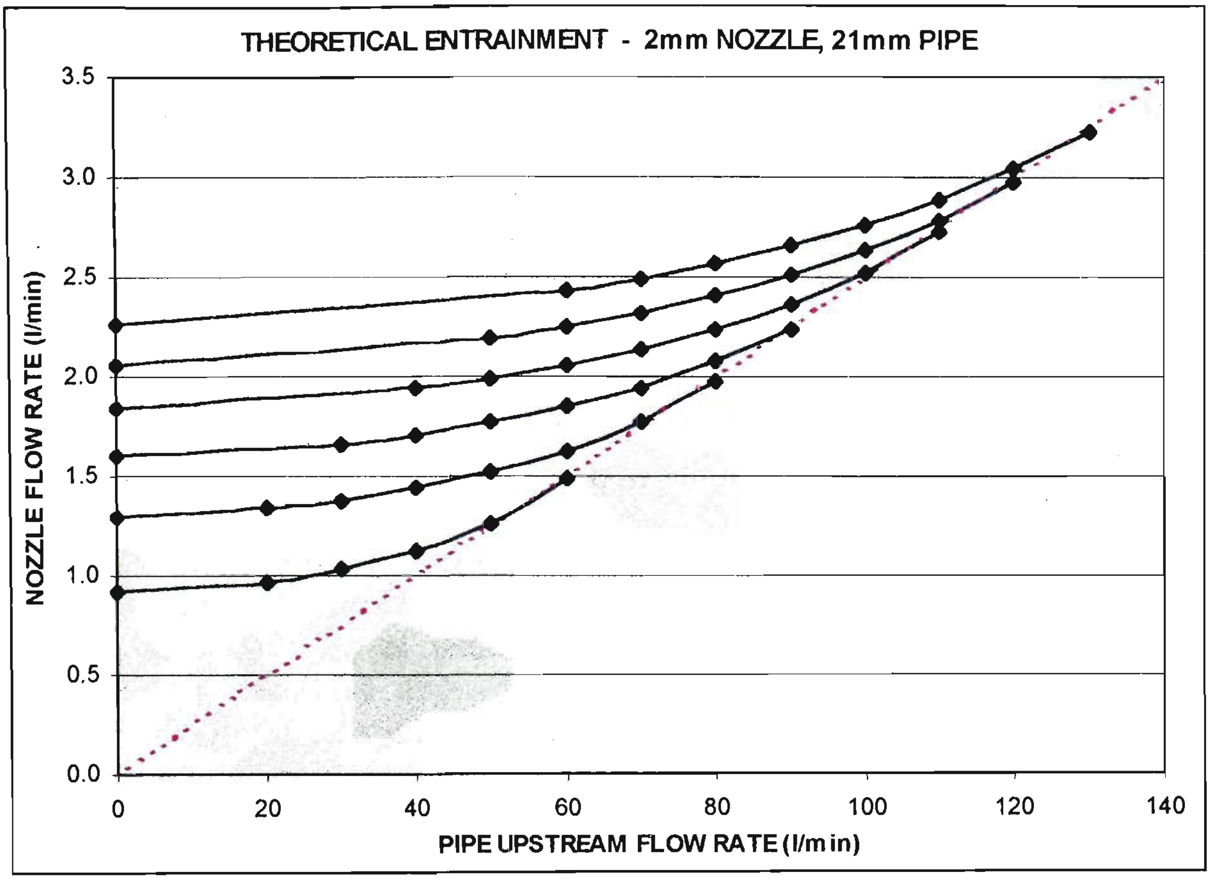

Figure A4.18 - Theoretical results for $2mm$ nozzle with $21mm$ pipe

In the special case of a capillary nozzle which has a capillary tube and pipe adapter, the entrainment geometry is significantly different from a sampling hole and the velocity of the induction jet and its impact upon the upstream flow will be significantly reduced. With reference to Figure A.18 it has been found that a good match of the theoretical data to the asymptote obtained from the experimental data, can be achieved if the value adopted for the entrainment coefficient, C_{jet} is unity. Given the diffuse nature of the induction jet in the case of the capillary tube adapter, unity is probably the minimum attainable value for C_{jet}.

APPENDIX 6 - DETERMINATION OF CORE VELOCITY

A6.0 LASER VELOCIMETRY RESULTS

The six sets of LV results are presented and discussed as follows.

A6.1 LV results for Re = 660

Figures A6.1 (a) to (n) present an analysis of the data collected in relation to a pipe flow rate of 10*litre/sec*, corresponding to Re = 660. The upper graph is the mean velocity (v_{core}) at each position along the pipe radius, starting from position -1 which is approximately 1*mm* before the pipe centreline, and progressing in 1.5*mm* steps to position +5, which is 8*mm* after the centre. A dotted line is graphed over the data points, indicating a smoothed curve of best fit to the data.

The lower set of data graphed in each of Figures A6.1 (a) to (i) is the RMS turbulence (v_{turb}). The turbulence data typically reach a minimum value at the pipe centre, rising as the wall is approached. This results from the combined effects of optical interference from the glass wall, as well as an expected increase in the fluctuation of velocity encountered within the target due to the wall proximity. In fact the turbulence data may be regarded as an indication of the magnitude of uncertainty, i.e. the total error band. Based on these figures, the accuracy of the results obtained at the pipe centre is considered good, while the results close to the pipe wall are less reliable.

Figures A6.1 (j) to (n) covering the displacements from 50 to 70 *dia*, lack the turbulence data because these, together with the velocity and turbulence data for a displacement of 75 to 90 *dia* (at Re = 660) were lost during the process of having the files transferred to CDROM. The data that remain have a further difficulty in that the separate setup of the LV for the second segment of pipe proved not to be centred in the same manner, so the first position was not past the centreline. Nevertheless, the results are encouraging in that the development of a parabolic velocity profile becomes evident as a trend throughout the Figures, and the loss of data at higher displacements has not proven critical because of the low Reynolds number.

Curves representing the smoothed data used in Figure 6.13 have been included as dotted lines in Figures A6.6 (a) to (n). It is because the smoothing is three-dimensional (rather than two-dimensional), that some of these curves do not perfectly fit the data on some Figures (particularly at small displacements).

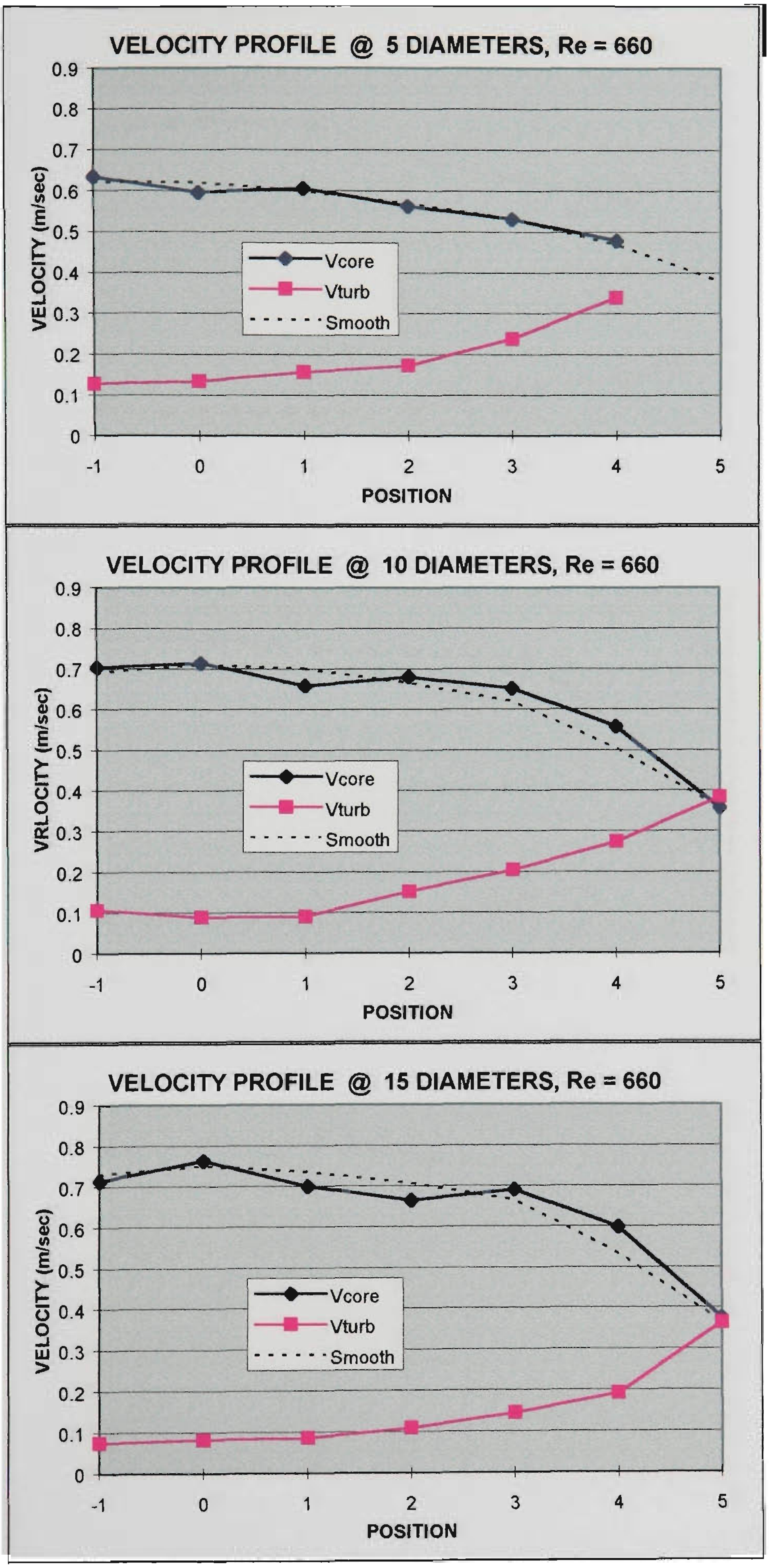

Figures A6.1 (a), (b), (c) - Velocity profiles at Re = 660

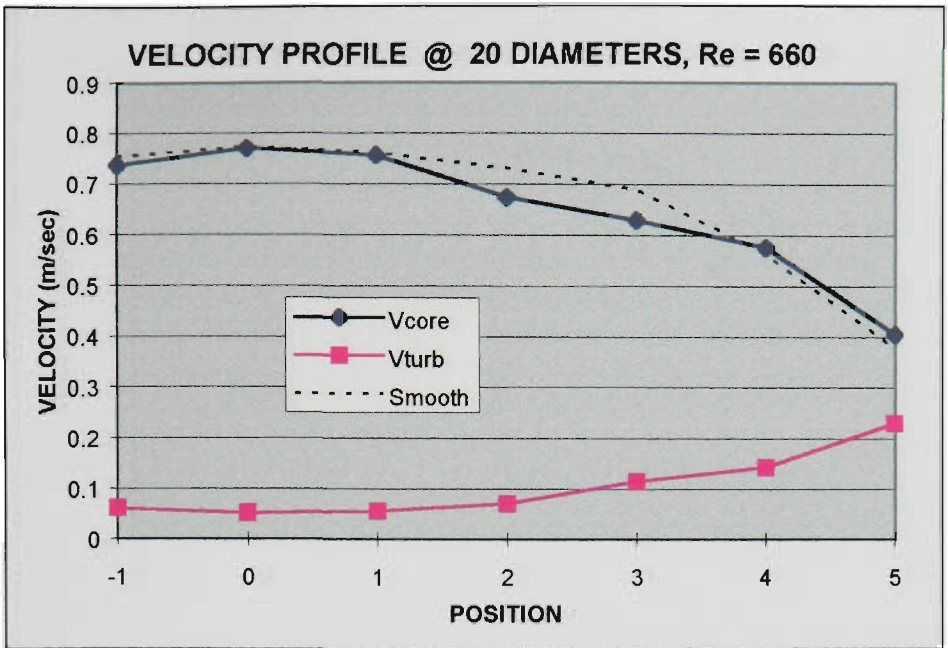

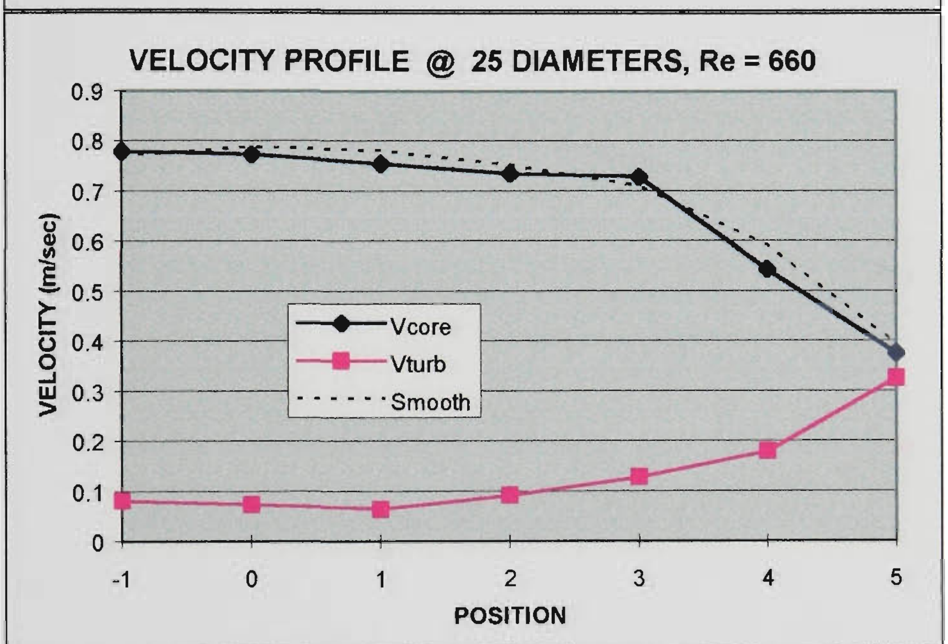

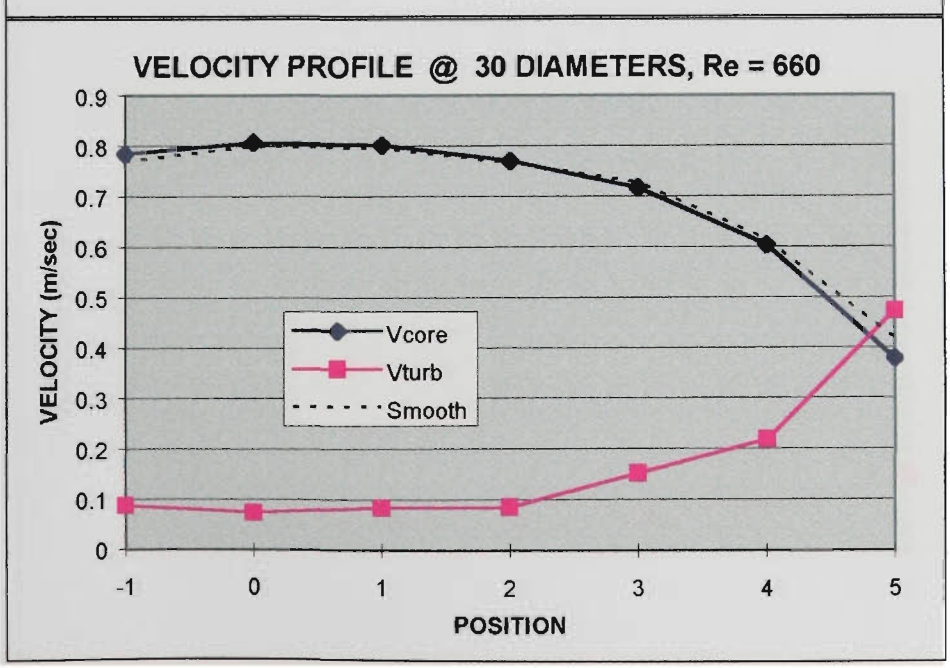

Figures A6.1 (d), (e), (f) - Velocity profiles at $\mathrm{Re} = 660$

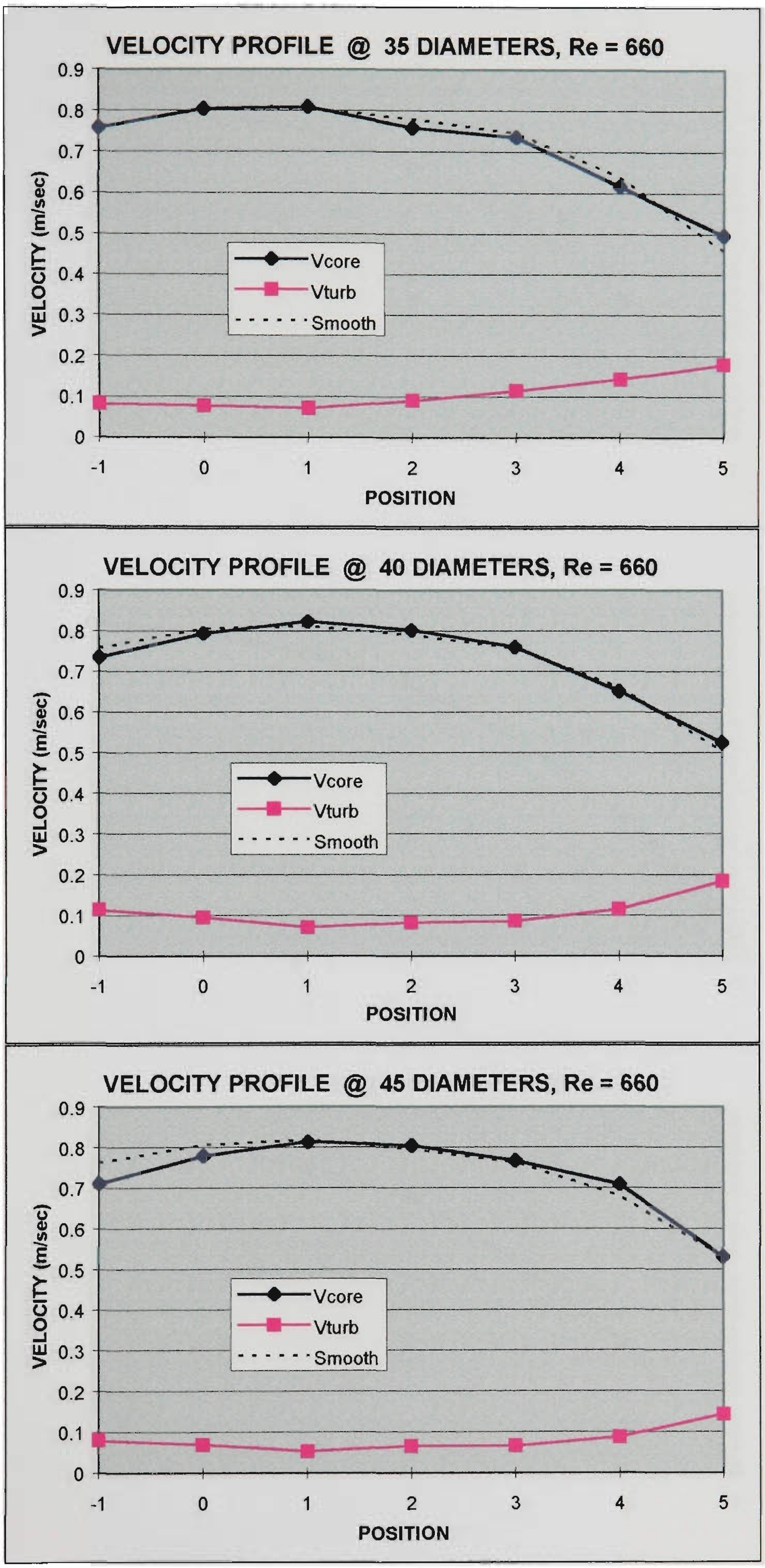

Figures A6.1 (g), (h), (i) - Velocity profiles at Re = 660

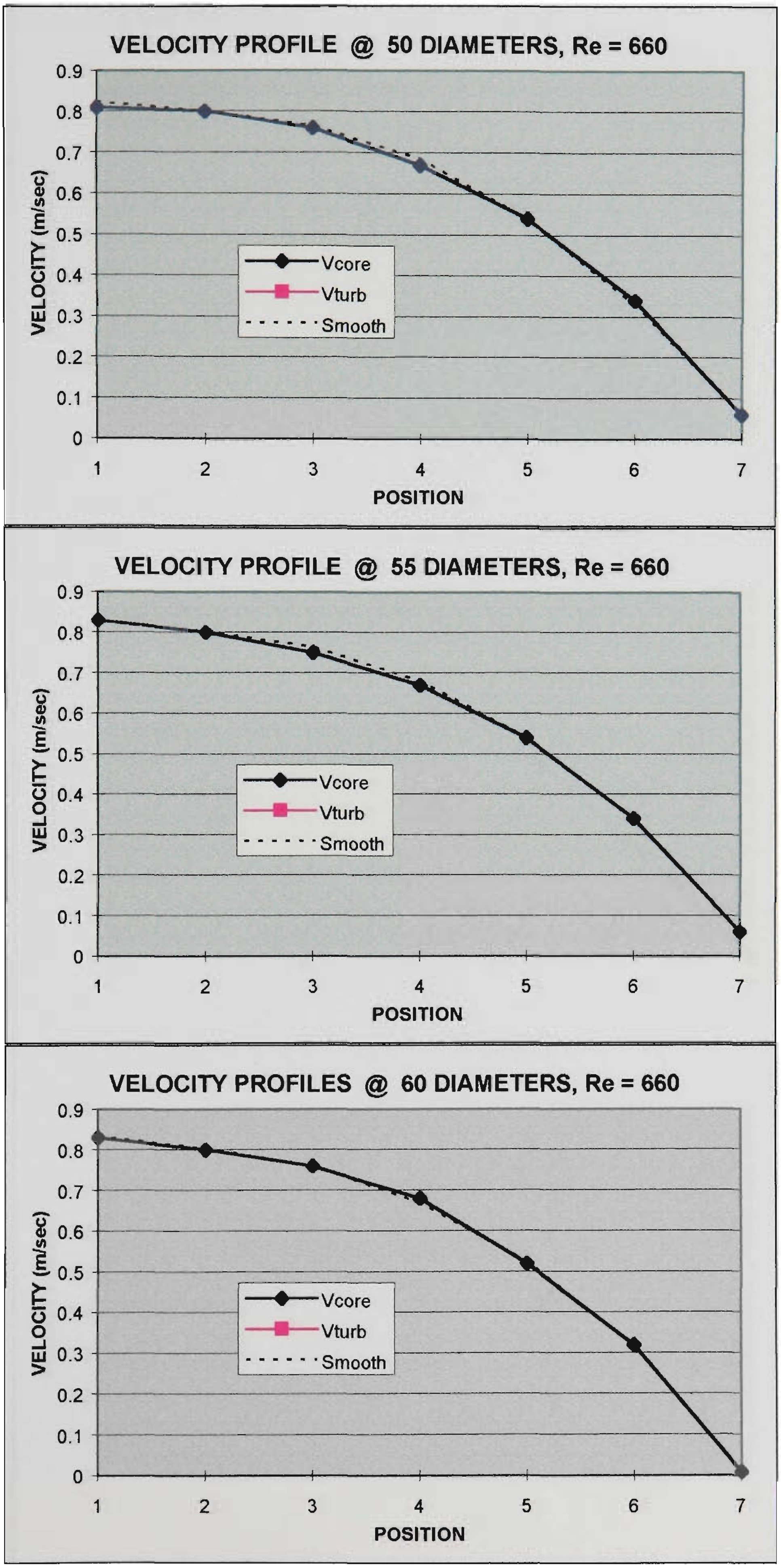

Figures A6.1 (j), (k), (l) - Velocity profiles at Re = 660

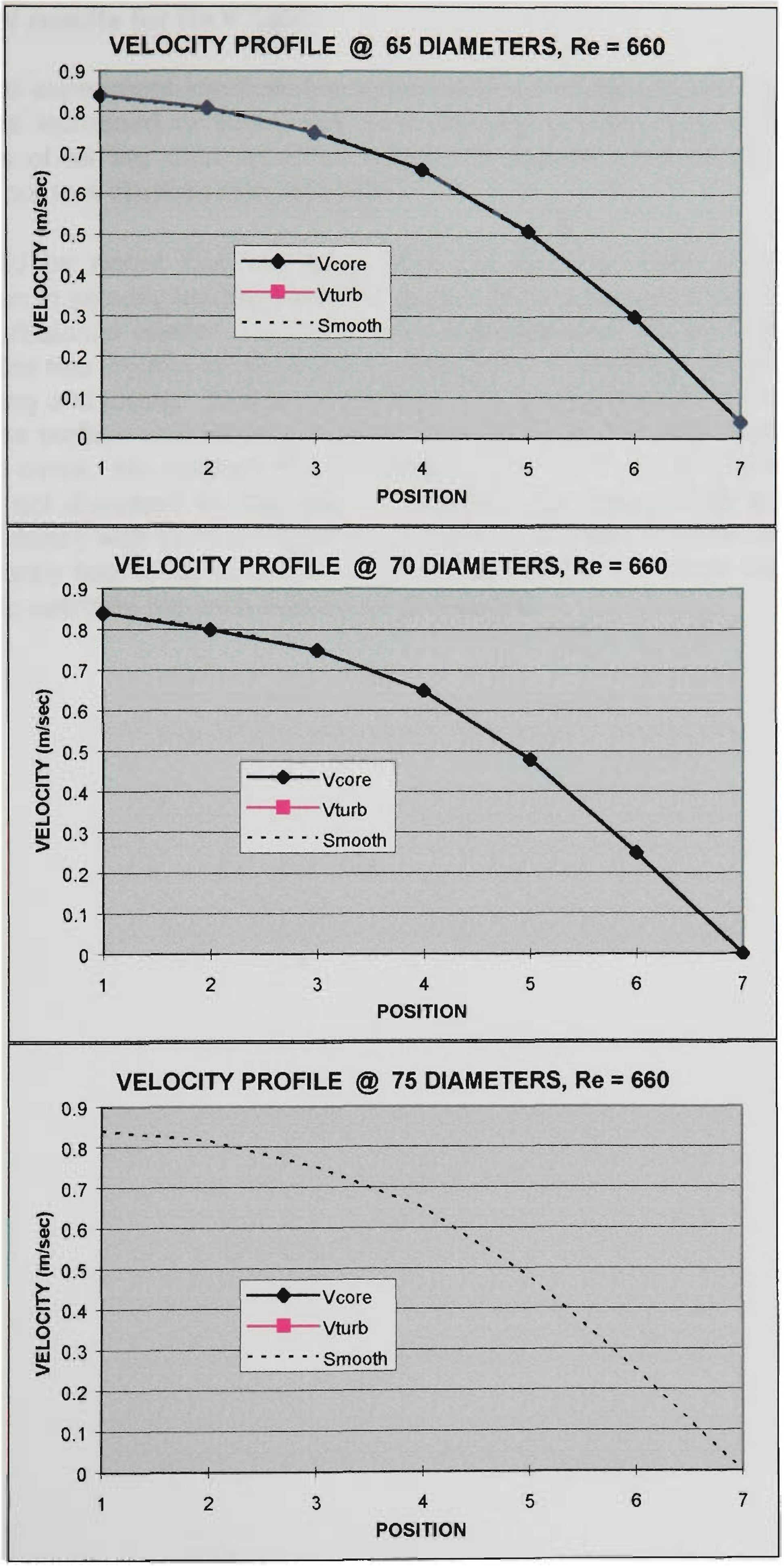

Figures A6.1 (m), (n), (o) - Velocity profiles at Re = 660

A6.2 LV results for Re = 1320

The next experiment involved the same setup as before except that the flow rate was increased to $20 litre/min$, such that $Re = 1320$. The results of the analysis of all the data recorded appear in Figures A6.2 (a) to (r), which extend out to a displacement of $90 dia$.

It should be noted that in Figure A6.2 (p), at $80 dia$ there is an unusual reduction in velocity reading near the centre of the pipe, accompanied by high RMS turbulence levels. However, this displacement is in the vicinity of the join in the two lengths of glass pipe, where there is distortion of the glass due to melting and fusing. This problem highlights the importance of the quality of the glass surface and helps to explain the fact that not all data points lie on a smooth curve. No residual effect is evident at 85 or 90 dia, indicating that the flow is not disrupted by the join. Figure A6.2 (j) also exhibits a degree of inconsistency with surrounding displacements, but these imperfections do not significantly take away from the overall consistency of the whole data and the ability to estimate the core velocity growth curve.

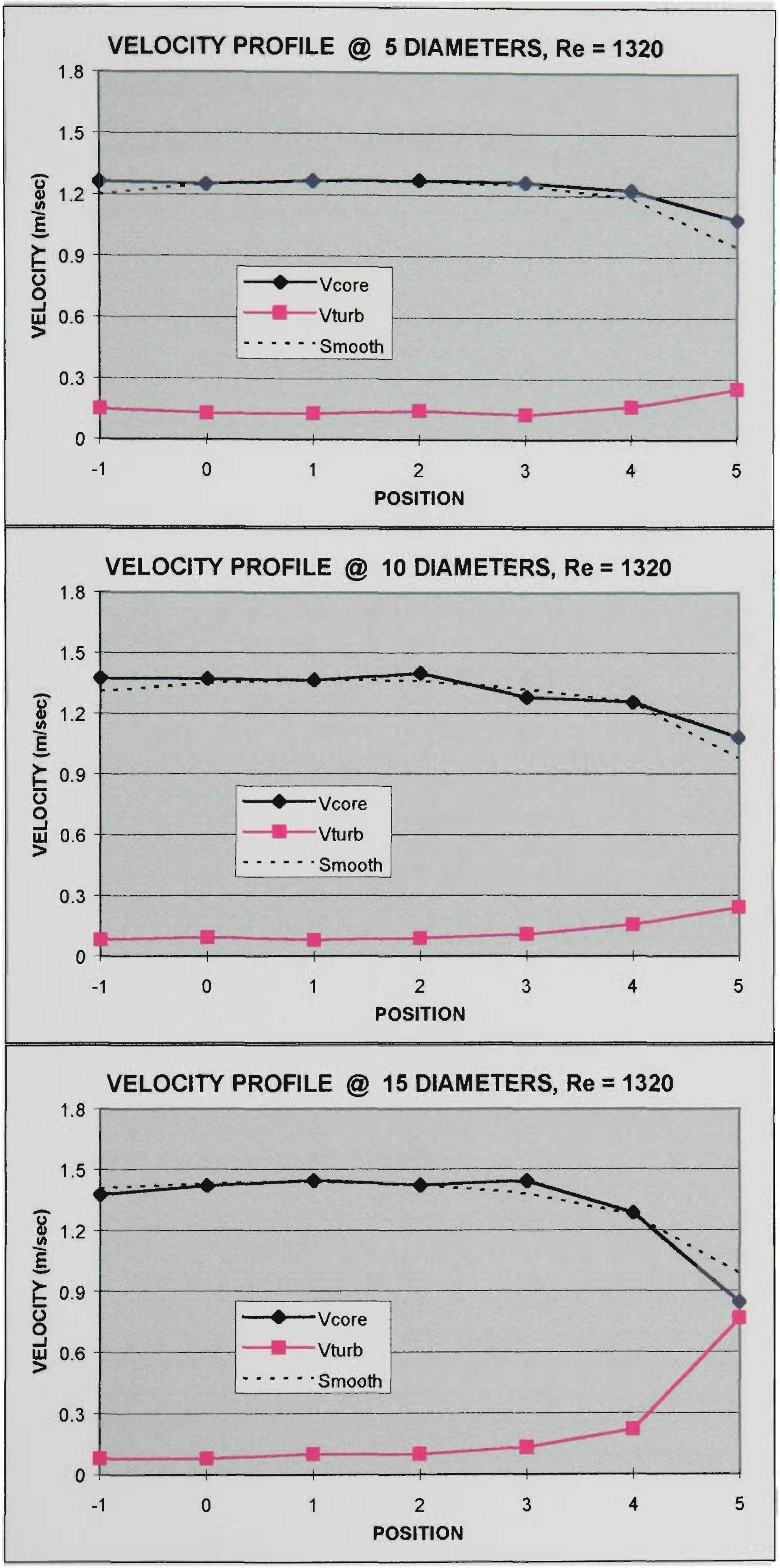

Figures A6.2 (a), (b), (c) - Velocity profiles at Re = 1320

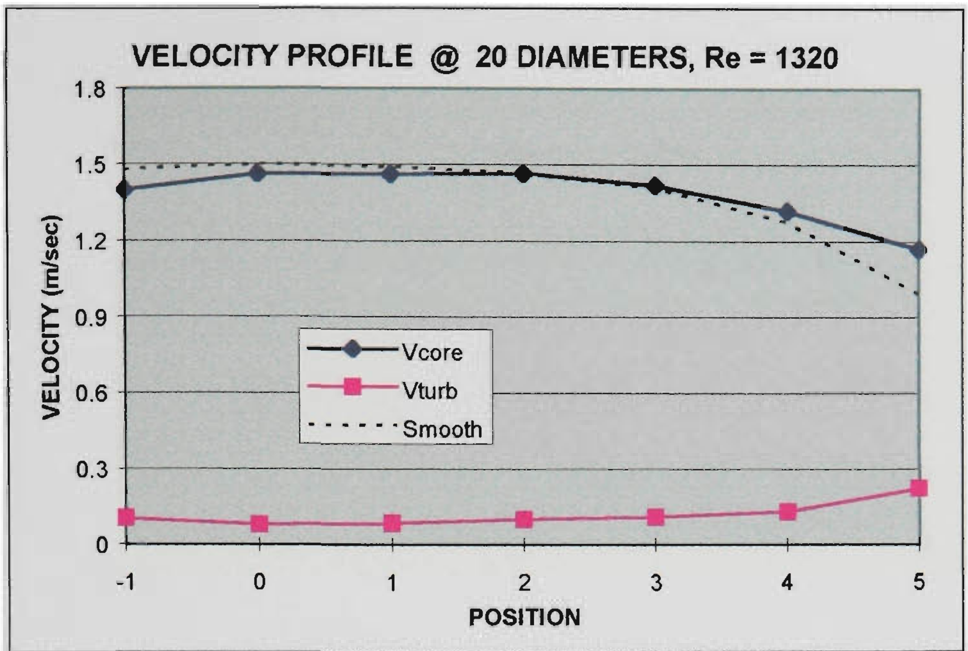

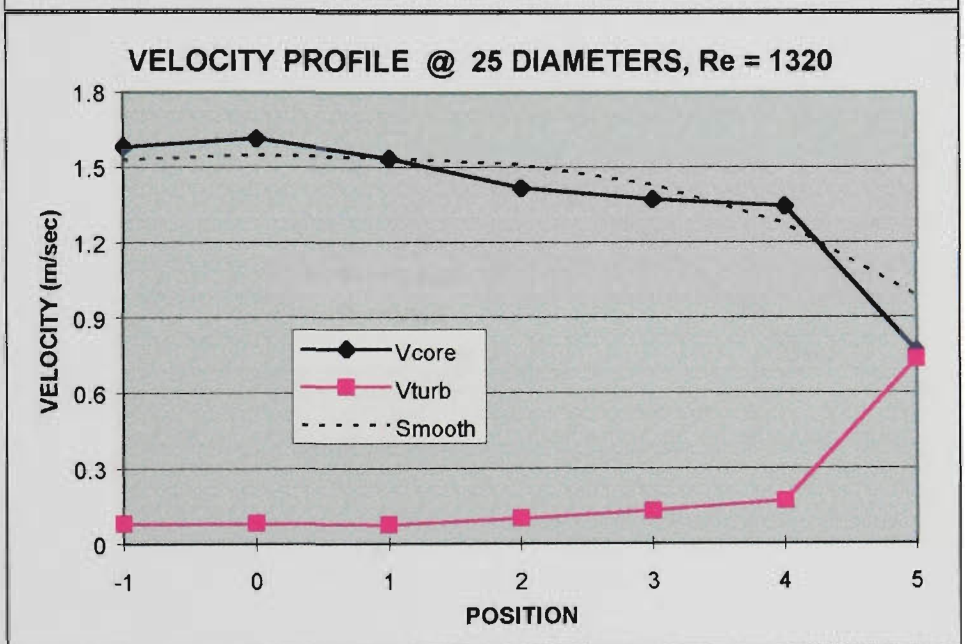

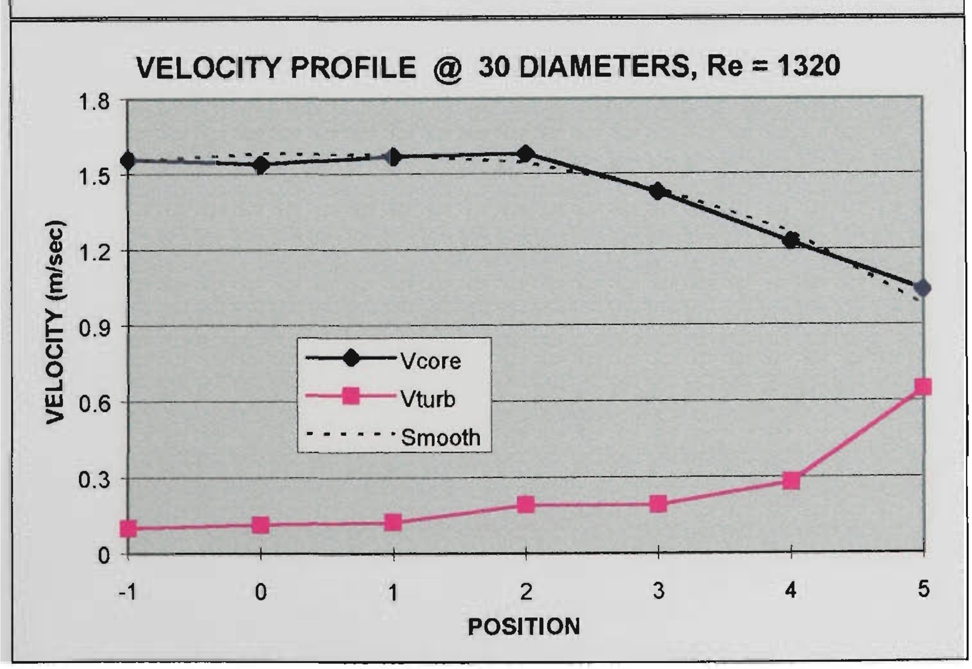

Figures A6.2 (d), (e), (f) - Velocity profiles at Re = 1320

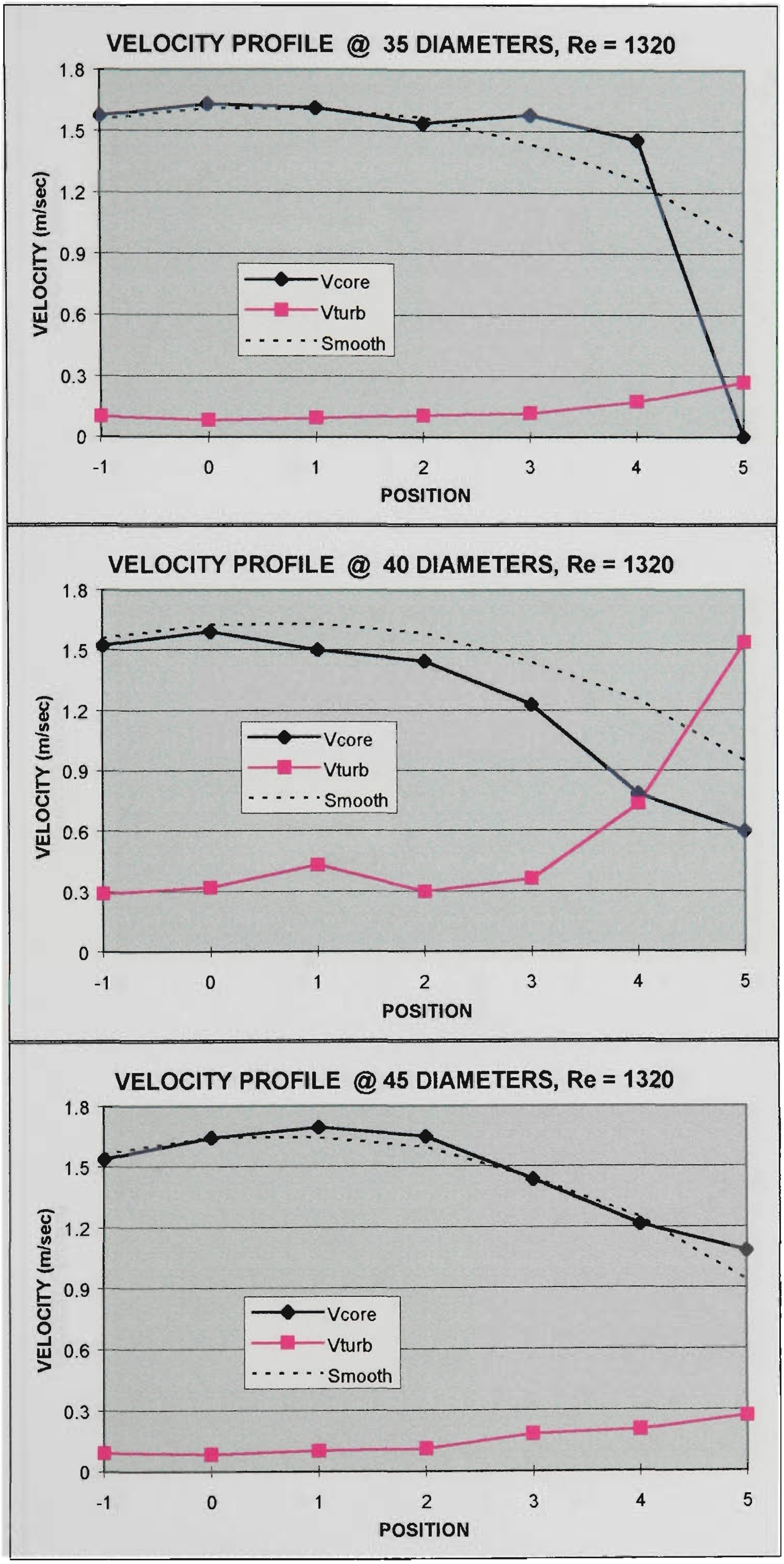

Figures A6.2 (g), (h), (i) - Velocity profiles at Re = 1320

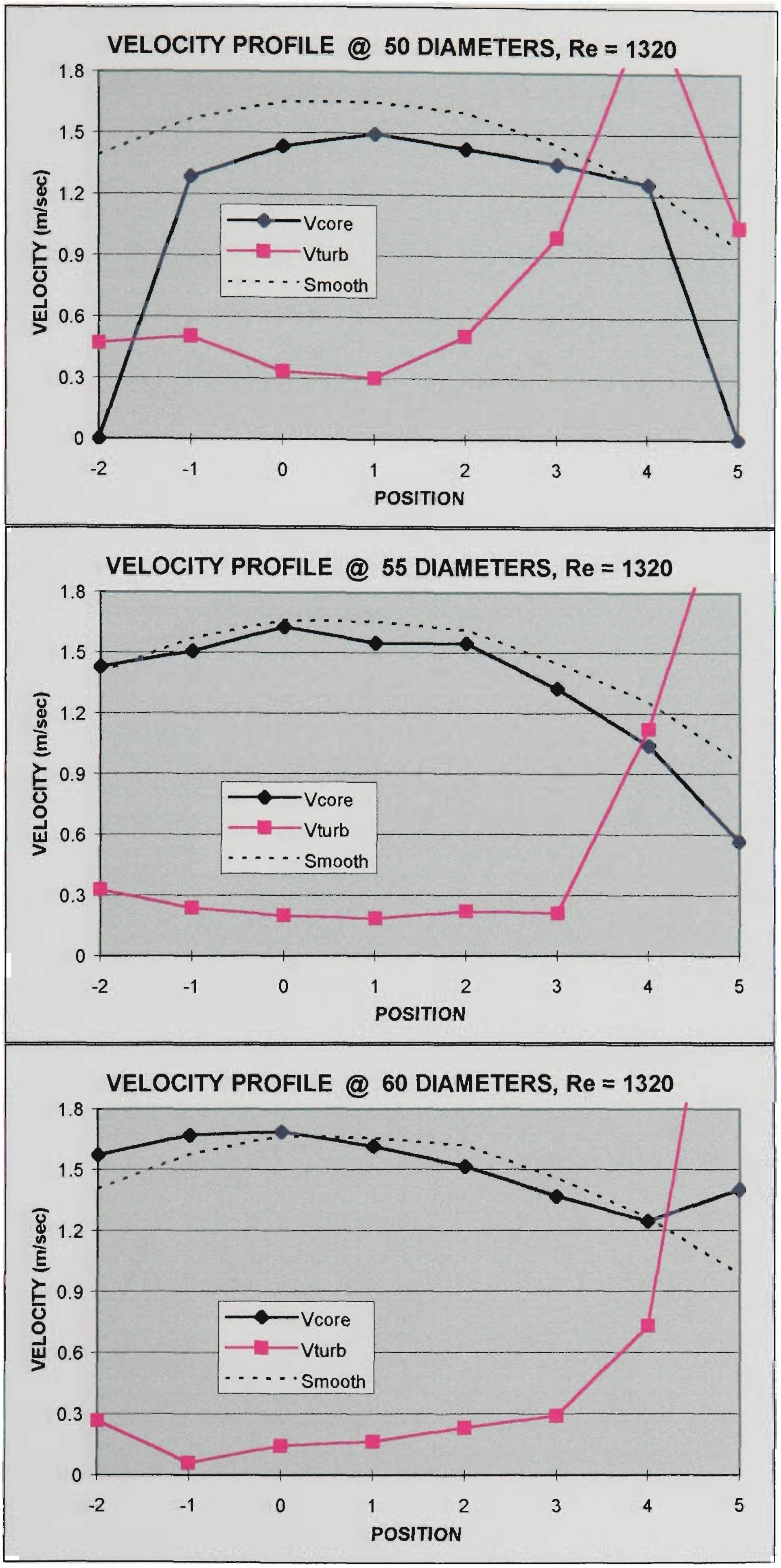

Figures A6.2 (j), (k), (l) - Velocity profiles at Re = 1320

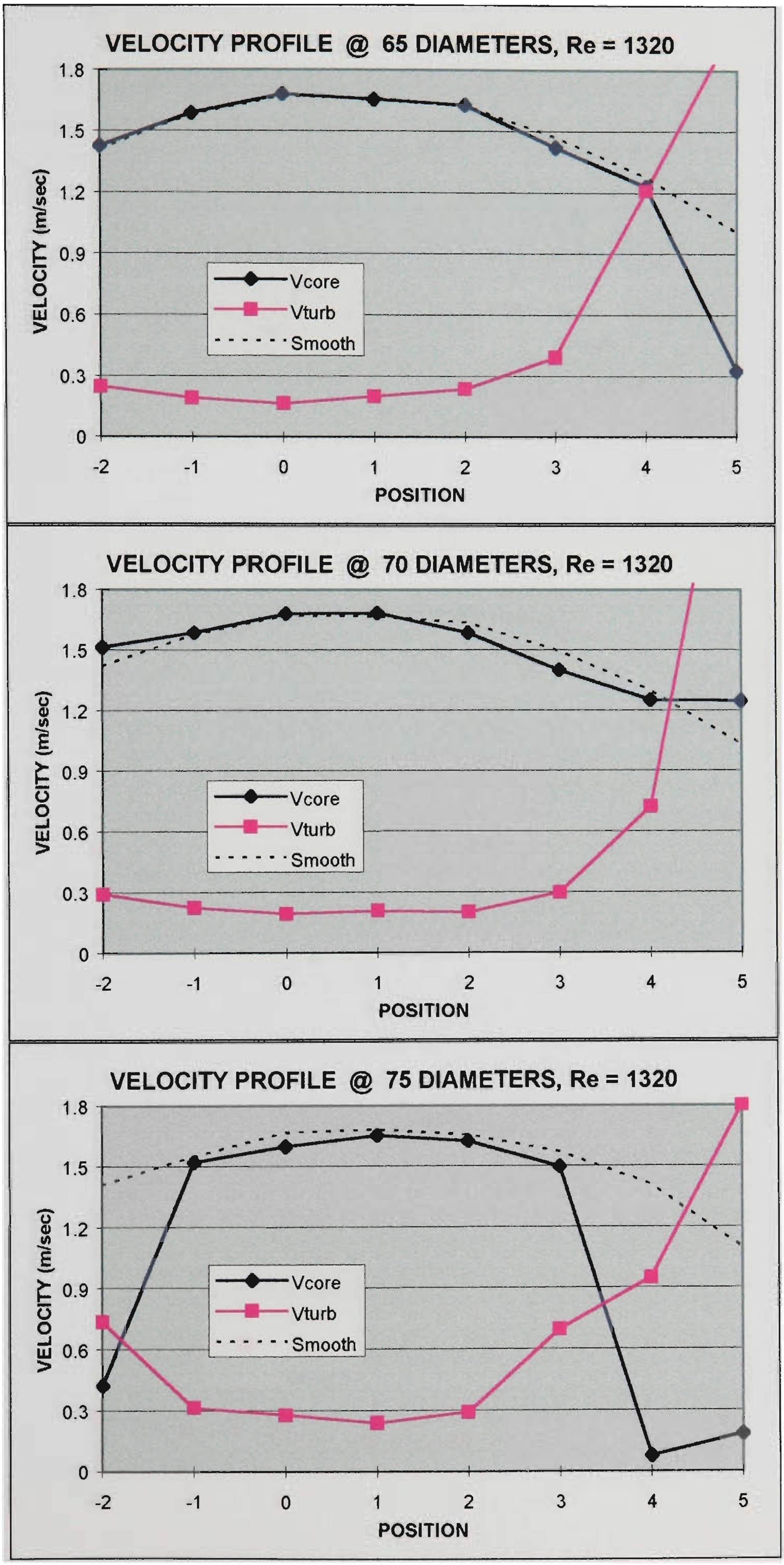

Figures A6.2 (m), (n), (o) - Velocity profiles at Re = 1320

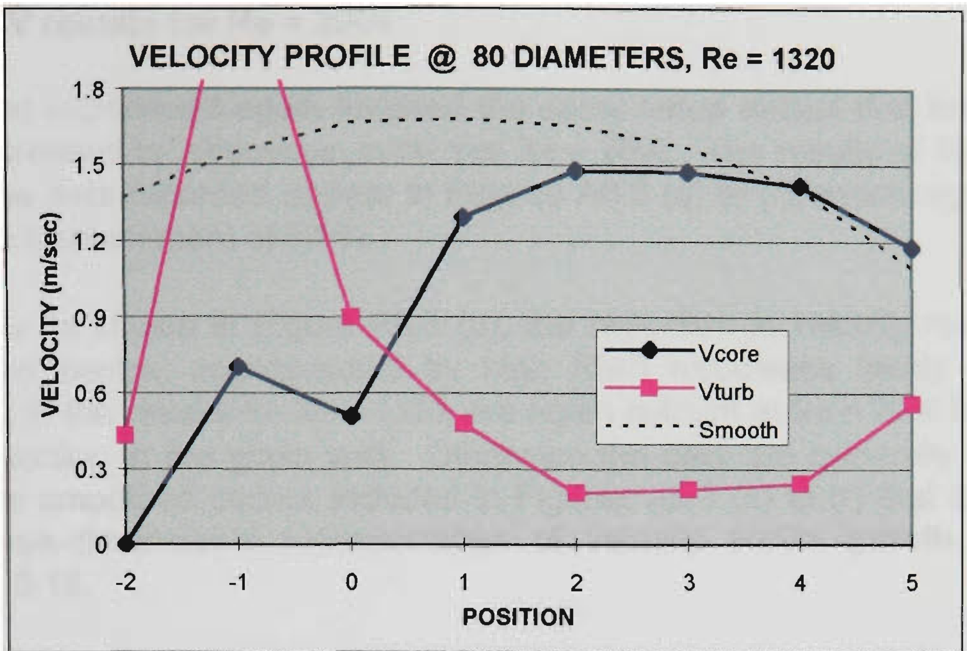

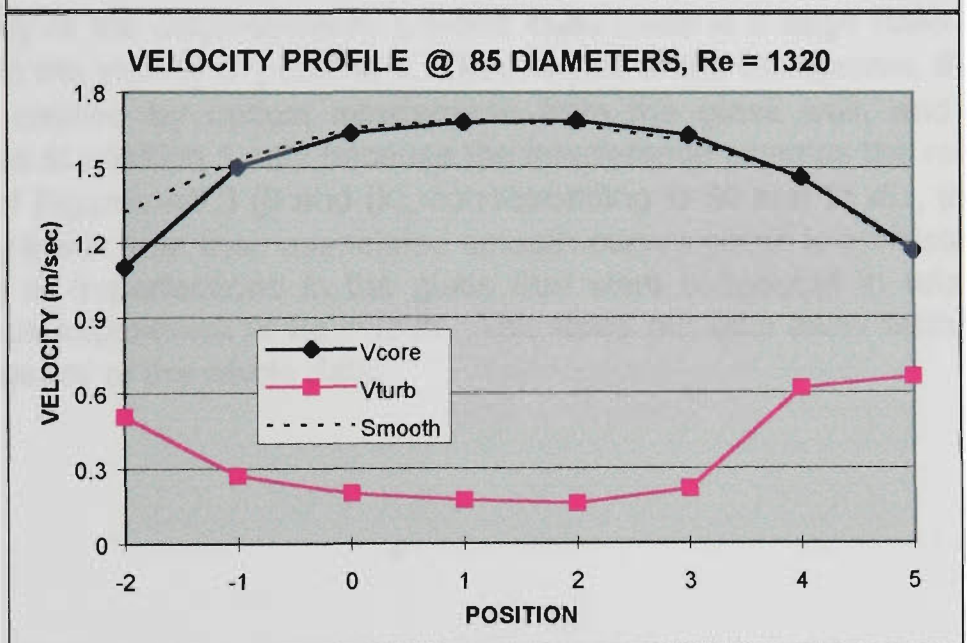

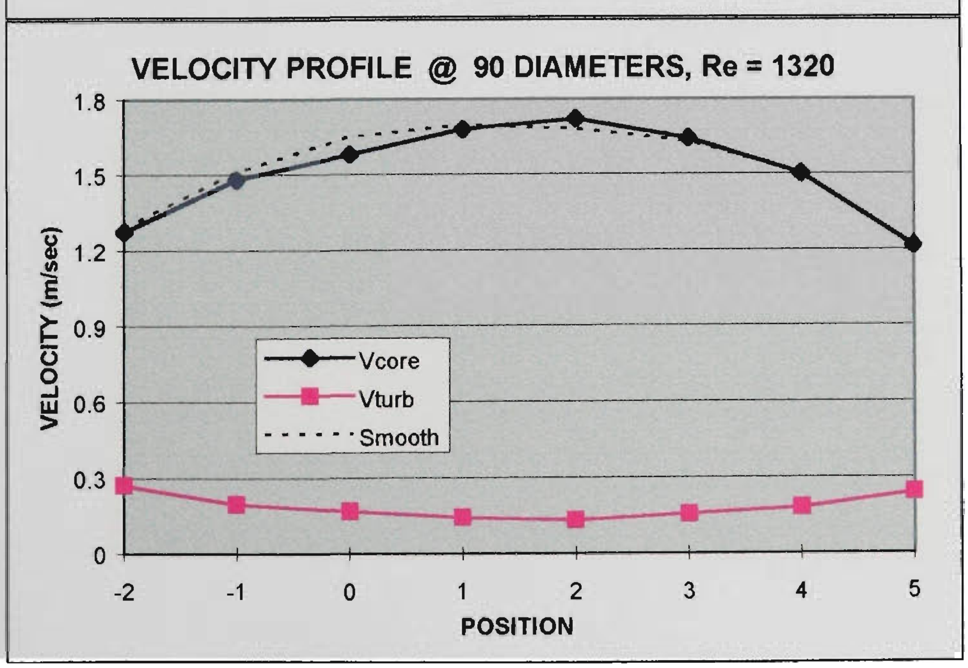

Figures A6.2 (p), (q), (r) - Velocity profiles at Re = 1320

A6.3 LV results for Re = 2000

The next experiment again involved the same setup except that the flow rate was increased to 30*litre/min*, such that $\mathrm{Re} = 2000$. The results of the analysis of all the data recorded appear in Figures A6.3 (a) to (r), which again extend out to a displacement of 90*dia*.

At 80*dia* as shown in Figure A6.3 (p), the reduction in velocity reading near the pipe centre, accompanied by high RMS turbulence levels that were evident in the results for $\mathrm{Re} = 1320$, are again evident at $\mathrm{Re} = 2000$ because of the distortion in the glass wall. Otherwise the data are generally consistent with the smoothed curves included in Figures A6.3 (a) to (r) that derive from the three-dimensional representation of velocity profile growth shown in Figure 6.16.

At many of the displacements beyond 45*dia* there is a large RMS turbulence value in the vicinity of position 4. On analysis of the histograms, this appears to be caused by optical interference from the glass wall, and the figure reduces at position 5 only because the interference swamps the result. In the case of Figures A6.3 (j) and (k), corresponding to 50 and 55 *dia*, the data are slightly lower than their associated smooth curves which is consistent with the soiling or imperfections in the glass that were suspected in relation to the previous experiment at $\mathrm{Re} = 1320$. This does not take away from the overall consistency of the whole data.

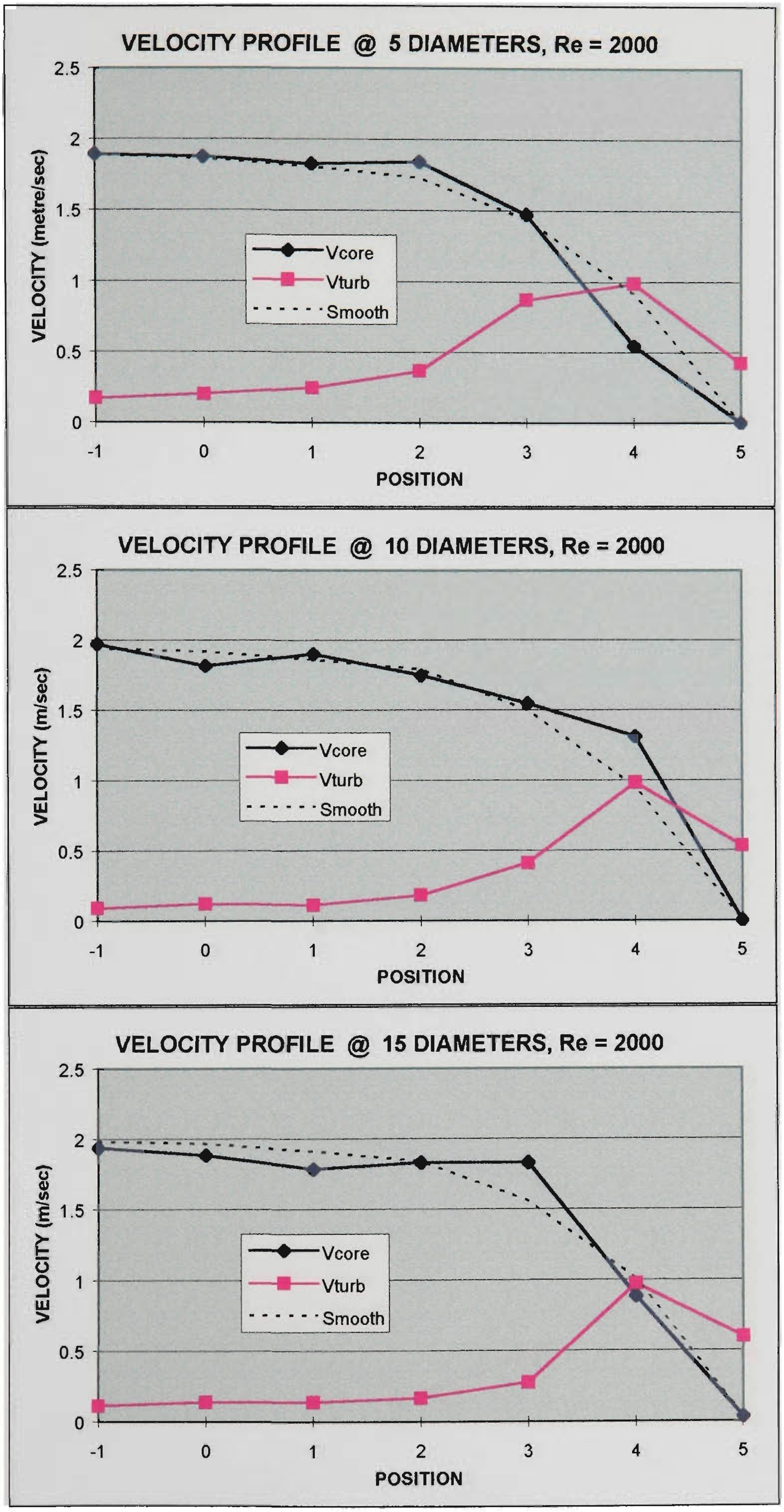

Figures A6.3 (a), (b), (c) - Velocity profiles at Re = 2000

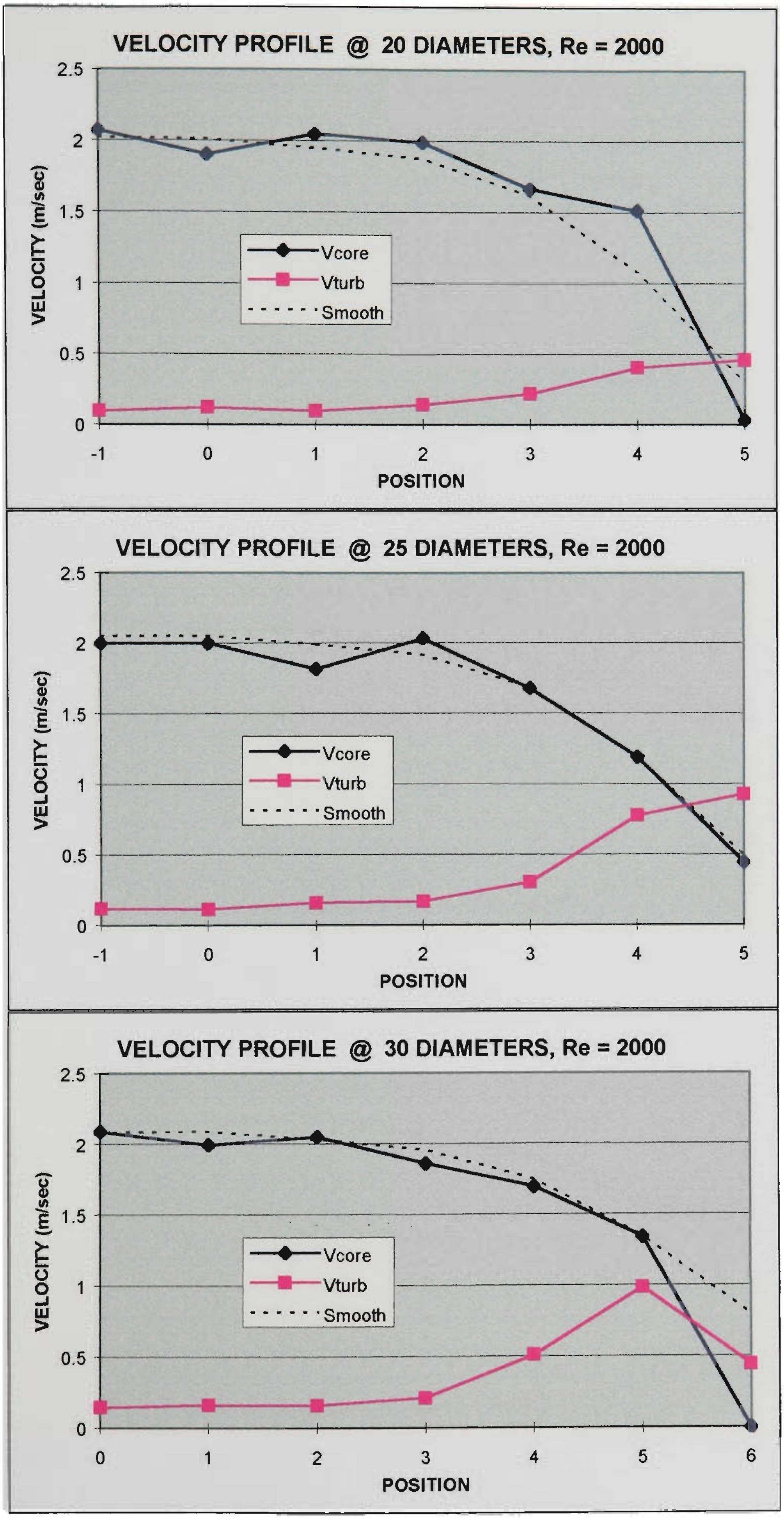

Figures A6.3 (d), (e), (f) - Velocity profiles at Re = 2000

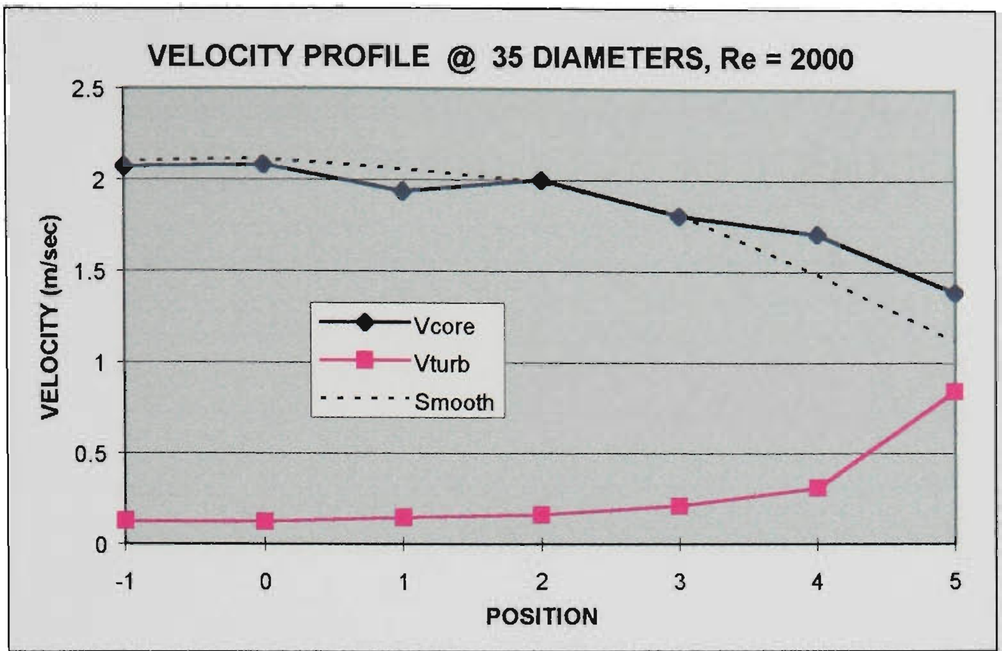

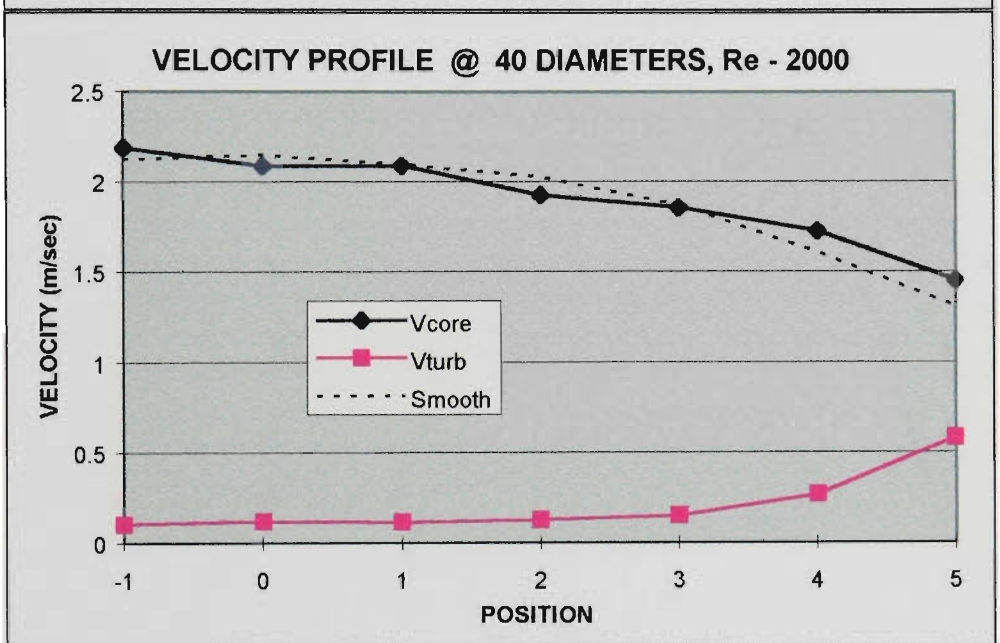

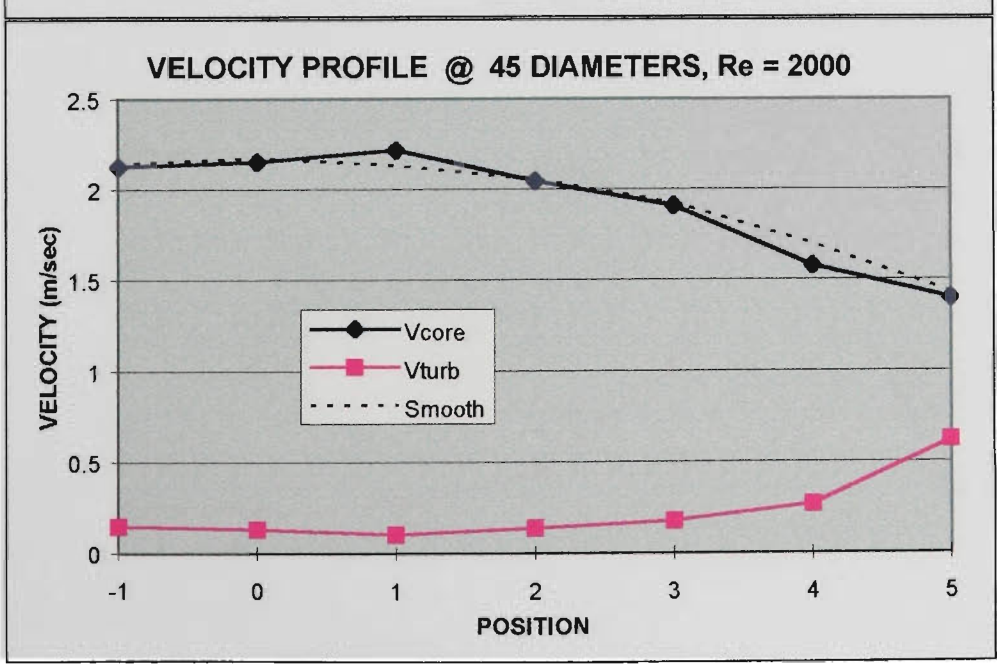

Figures A6.3 (g), (h), (i) - Velocity profiles at Re = 2000

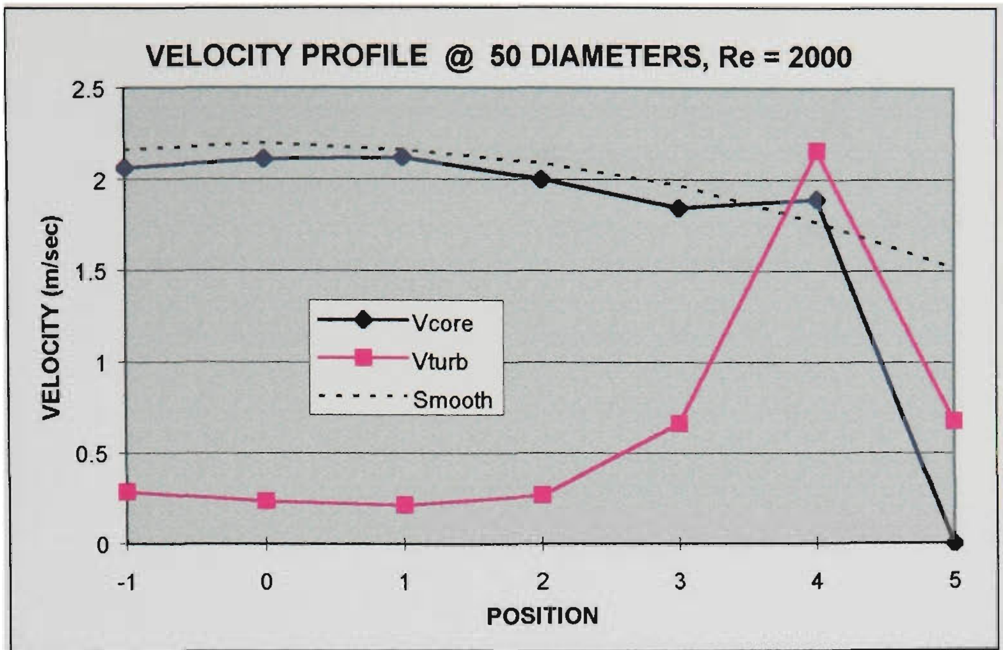

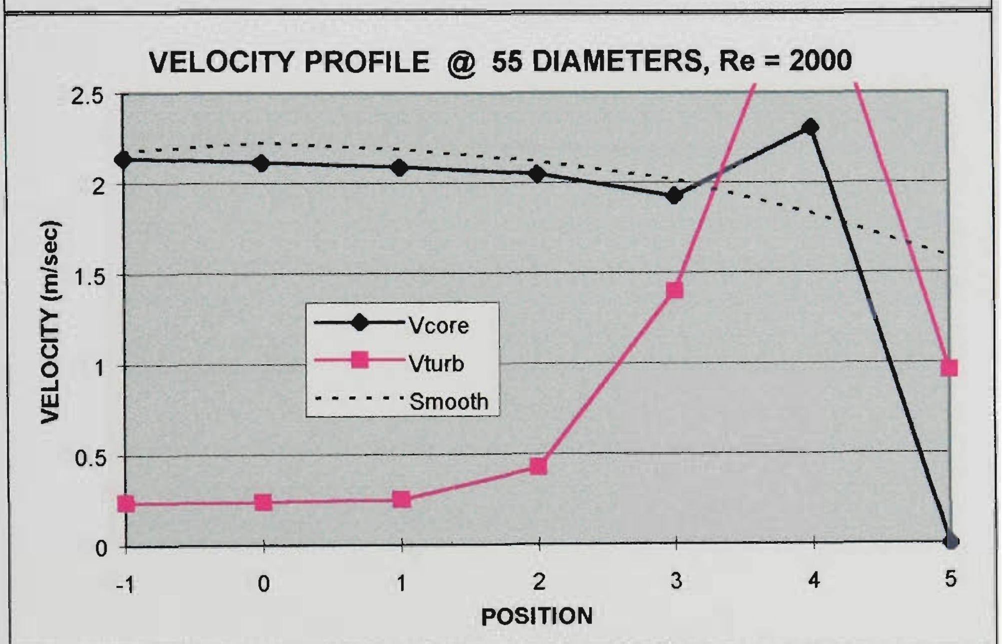

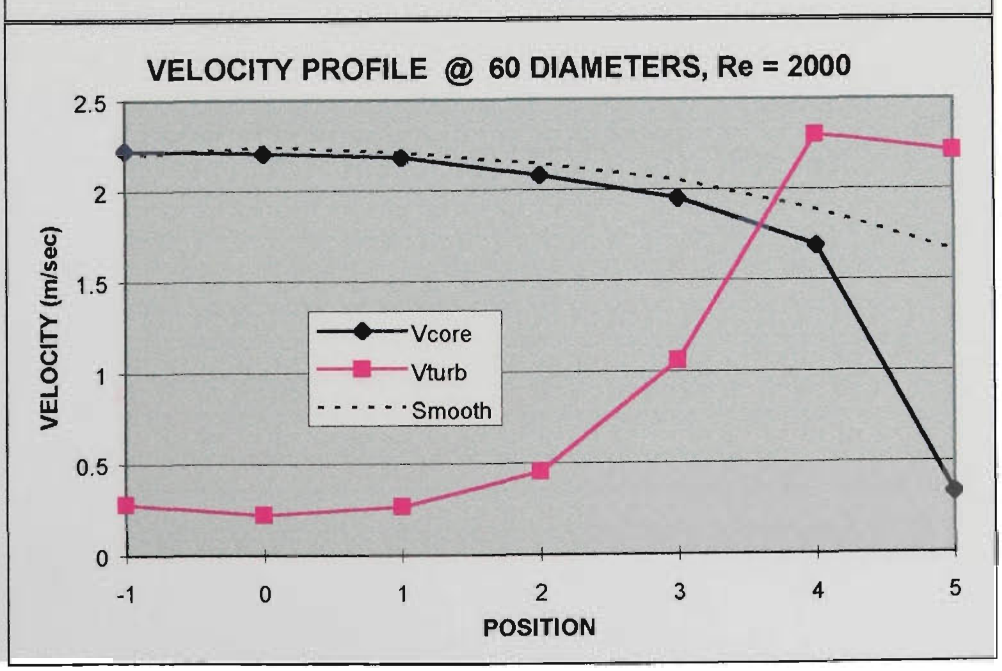

Figures A6.3 (j), (k), (l) - Velocity profiles at Re = 2000

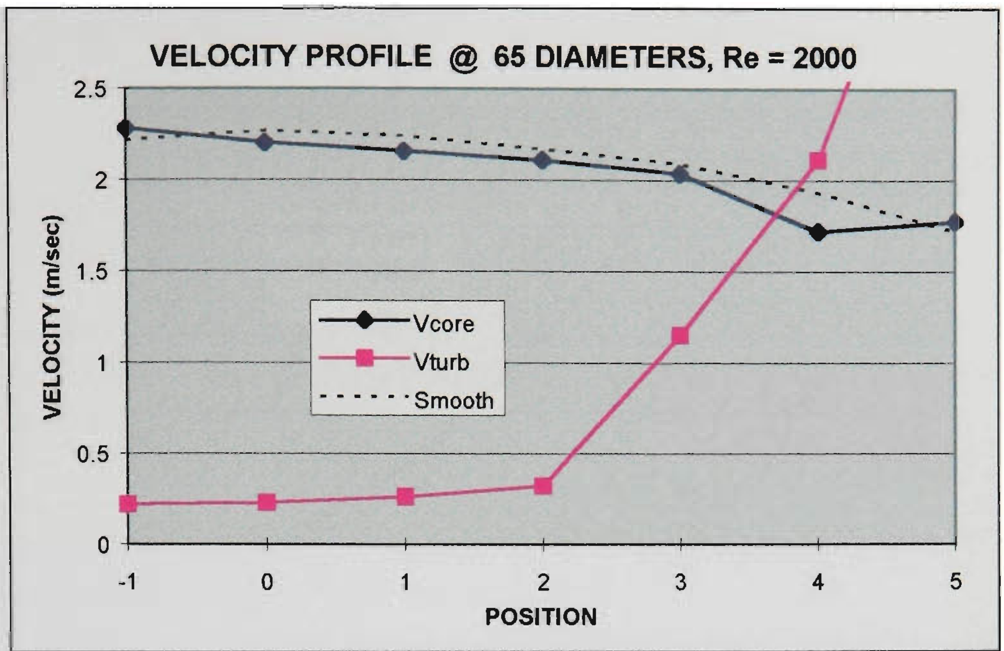

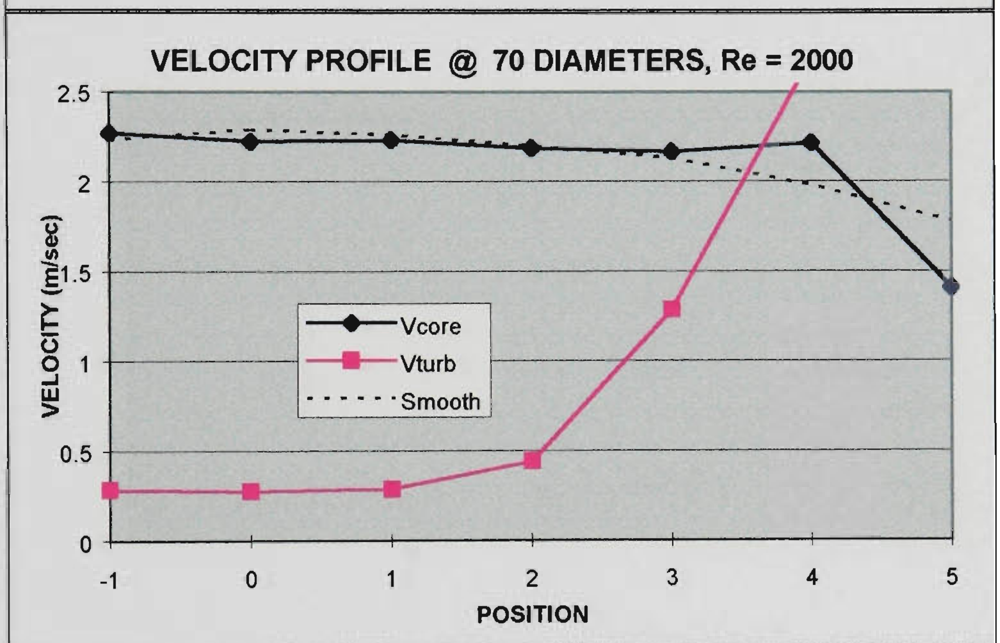

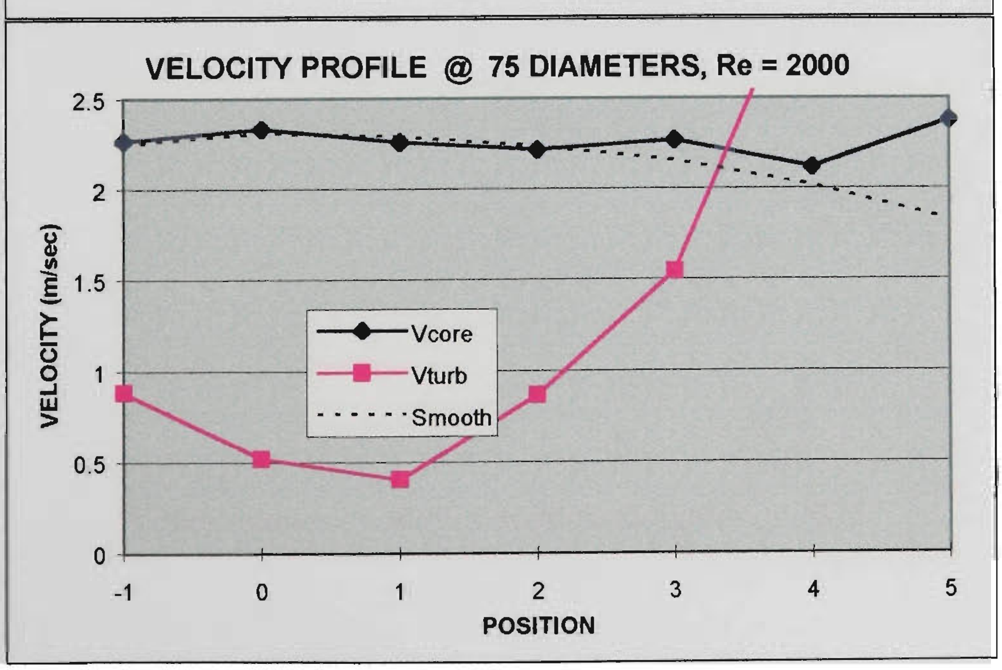

Figures A6.3 (m), (n), (o) - Velocity profiles at $Re = 2000$

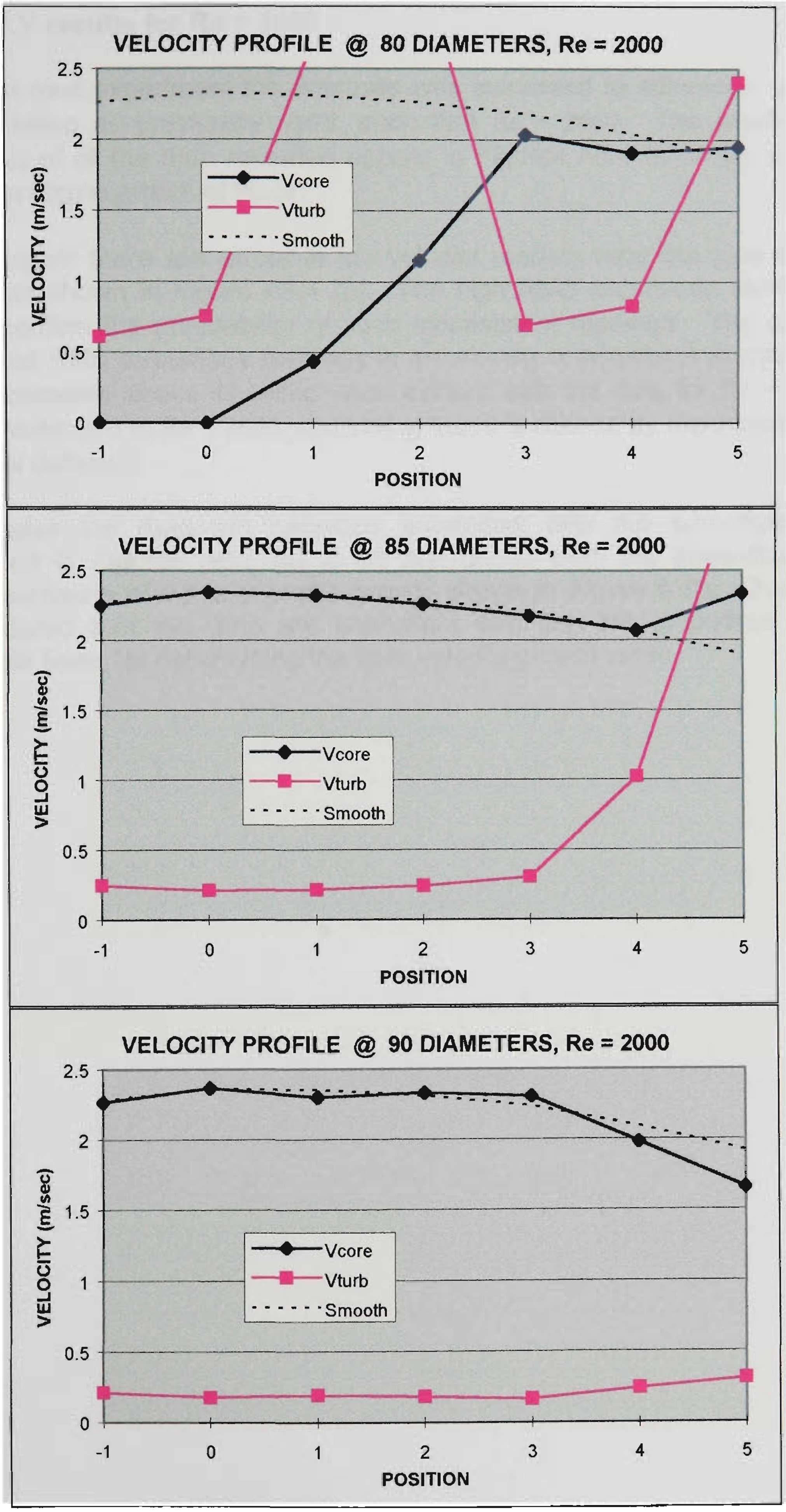

Figures A6.3 (p), (q), (r) - Velocity profiles at Re = 2000

A6.4 LV results for Re = 2660

For the next experiment the flow rate was increased to $40 litre/min$ using the same setup as previously used, such that $\mathrm{Re} = 2660$. The results of the analysis of all the data recorded appear in Figures A6.4 (a) to (r), extending out to a displacement of $90dia$.

Once again there are errors in the velocity reading near the pipe centre at $80dia$ as shown in Figure A6.4 (p). The high RMS turbulence levels in this area confirm the unreliability of such inconsistent readings. The pattern of elevated RMS turbulence readings in the vicinity of position 4 at many of the displacements above 45 (which was evident with the data for $\mathrm{Re} = 2000$), is again exhibited at $\mathrm{Re} = 2660$, confirming that it is caused by experimental error (optical defects).

Otherwise the data are generally consistent with the smoothed curves included in Figures A6.4 (a) to (r) that derive from the three-dimensional representation of velocity profile growth shown in Figure 6.16. Overall, it is considered that the data are consistent and that the smoothed result is suitable basis for determining the core velocity growth curve.

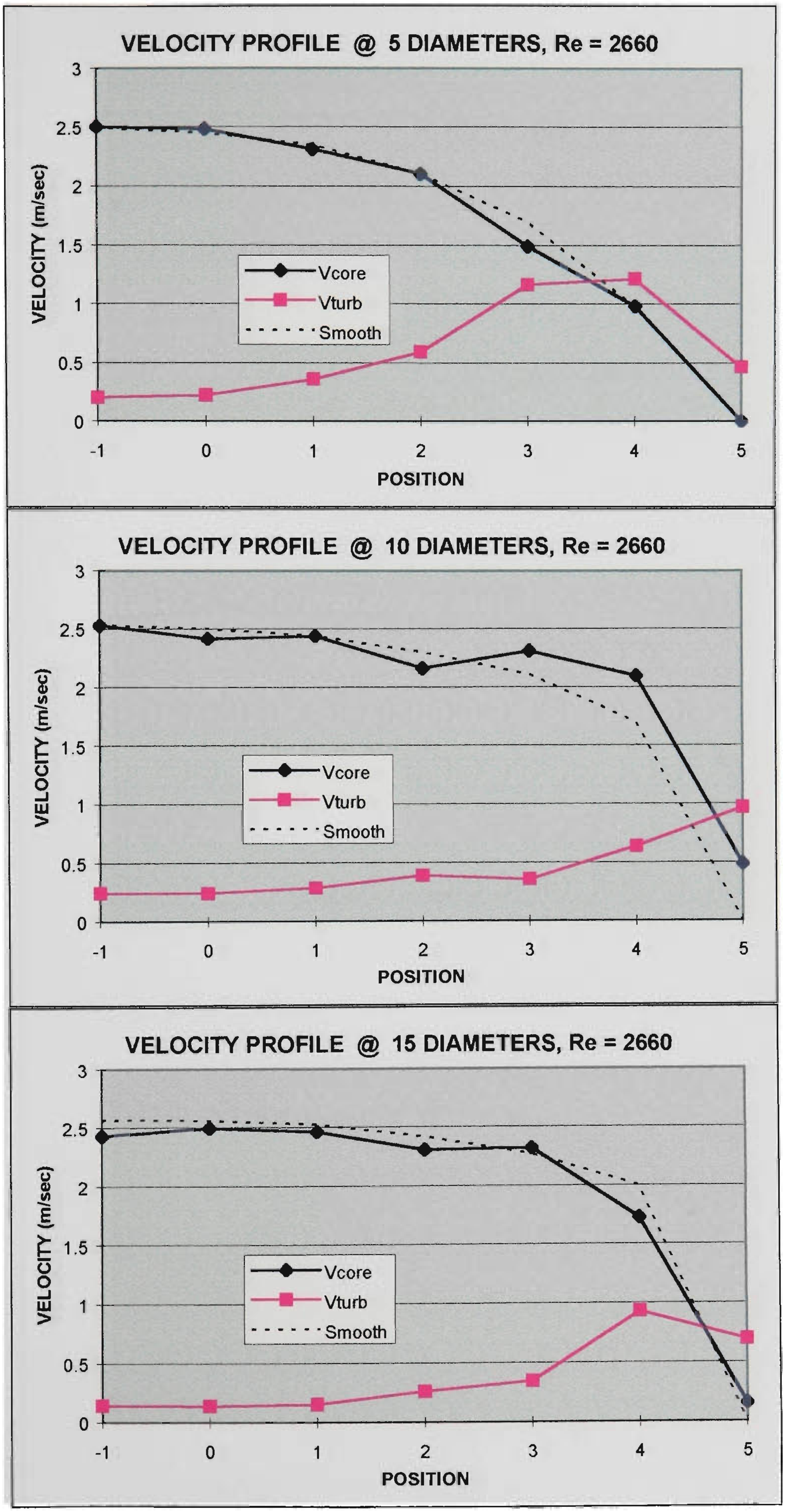

Figures A6.4 (a), (b), (c) - Velocity profiles at Re = 2660

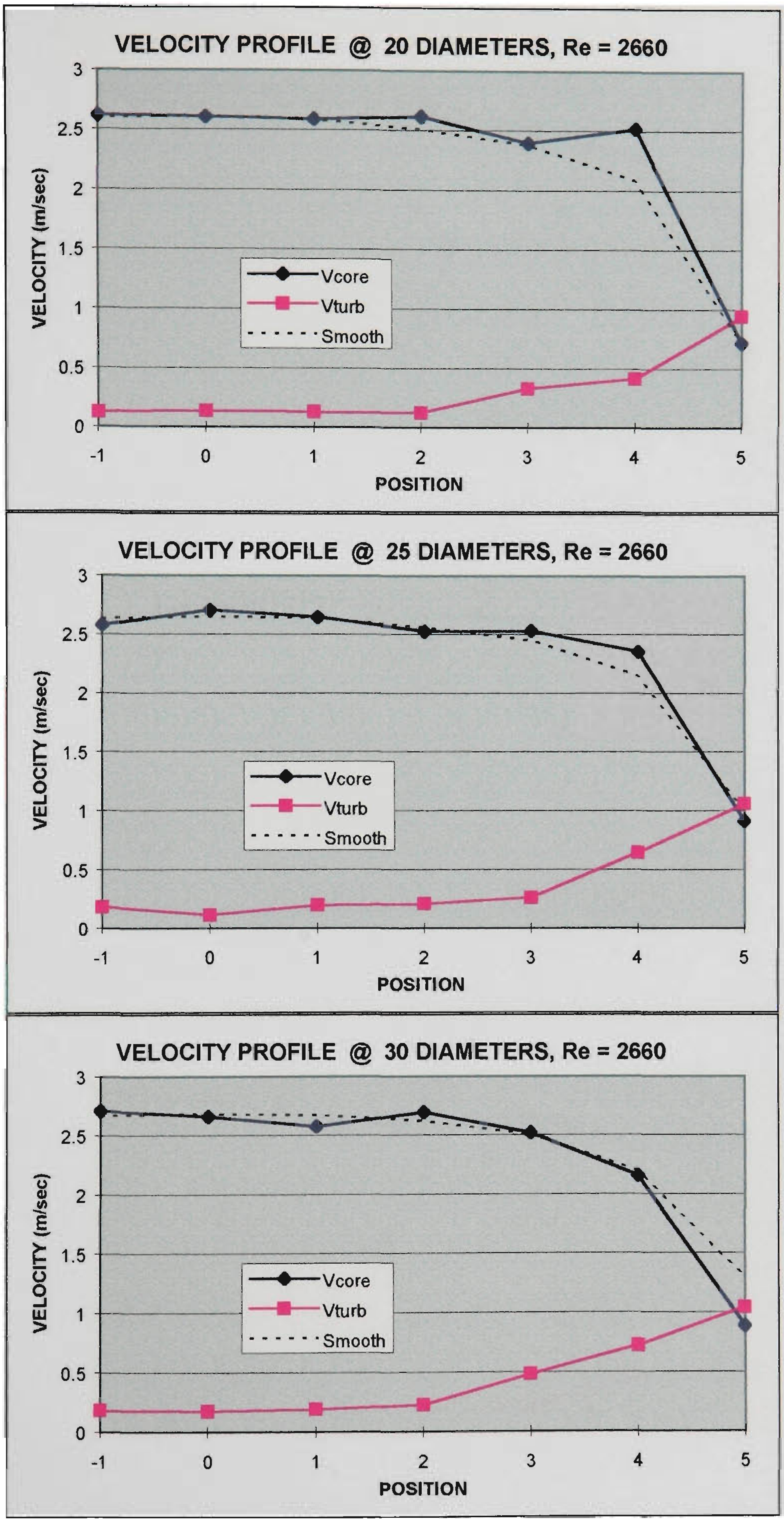

Figures A6.4 (d), (e), (f) - Velocity profiles at Re = 2660

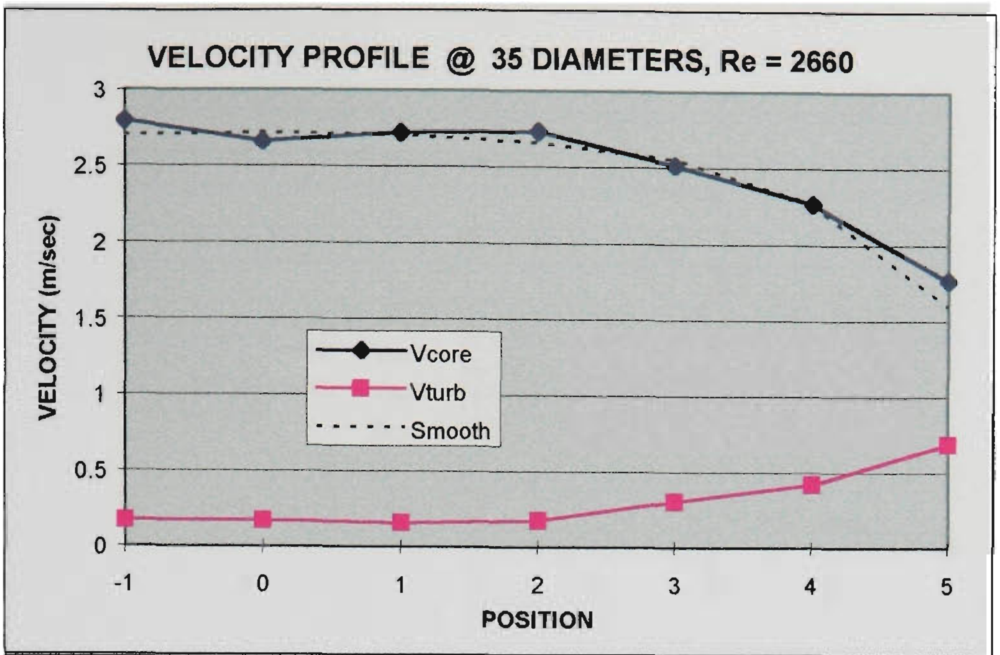

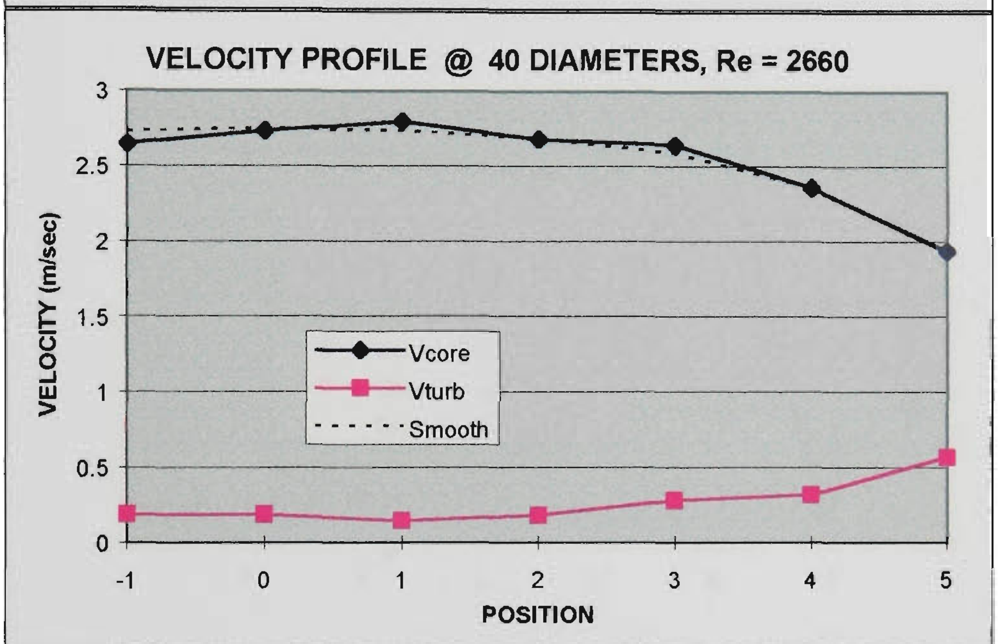

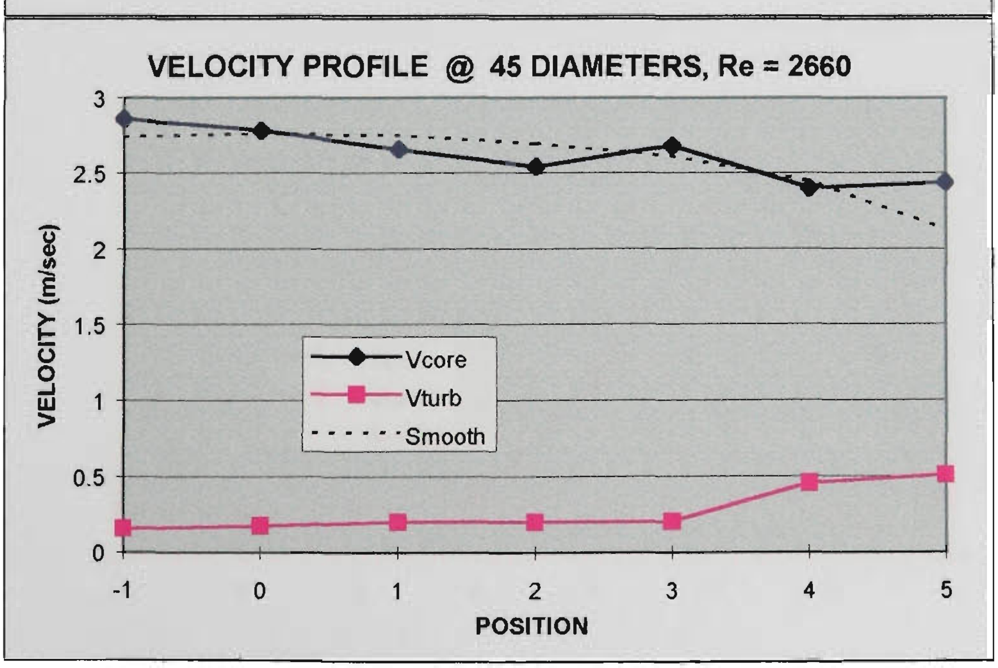

Figures A6.4 (g), (h), (i) - Velocity profiles at Re = 2660

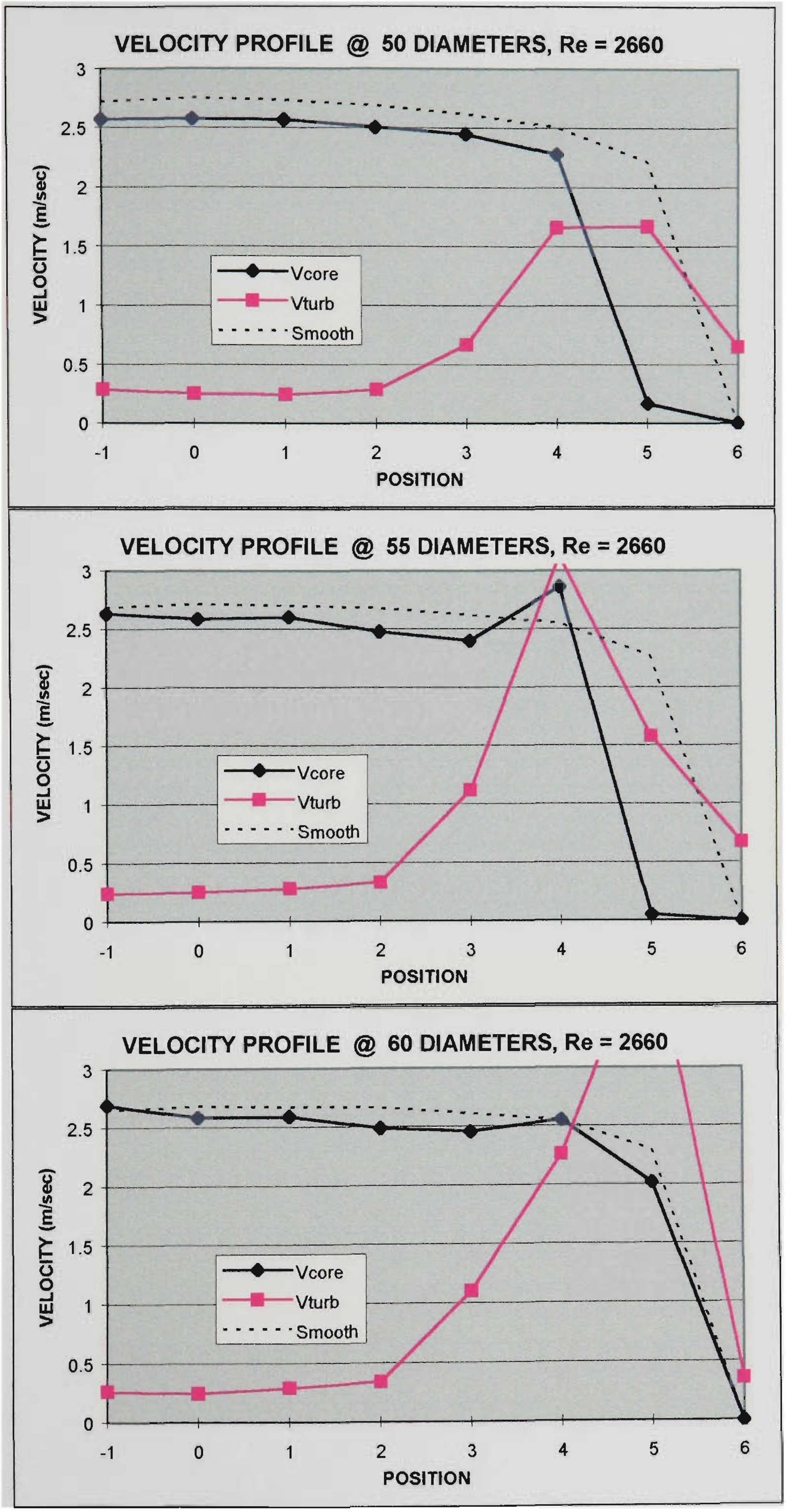

Figures A6.4 (j), (k), (l) - Velocity profiles at Re = 2660

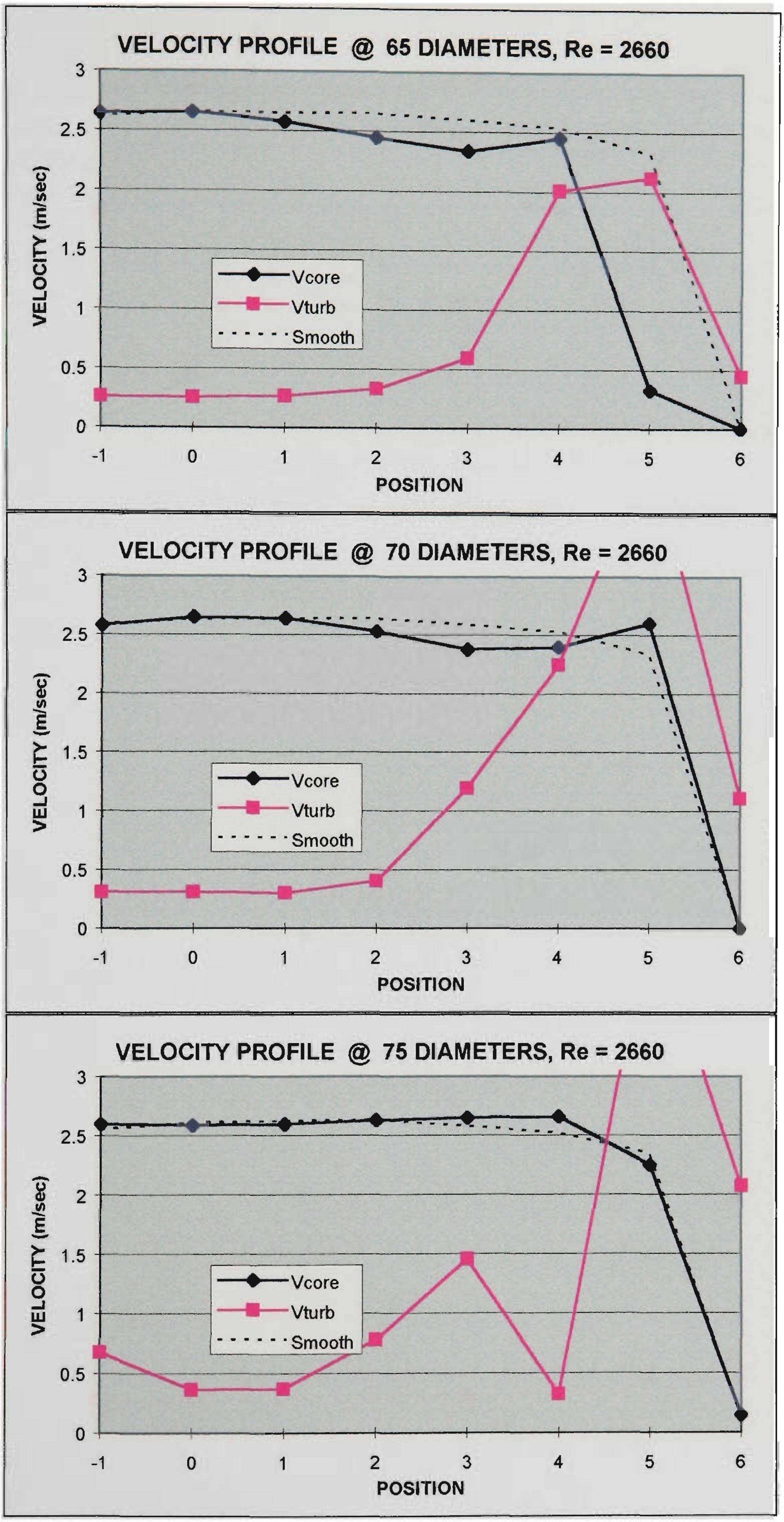

Figures A6.4 (m), (n), (o) - Velocity profiles at $Re = 2660$

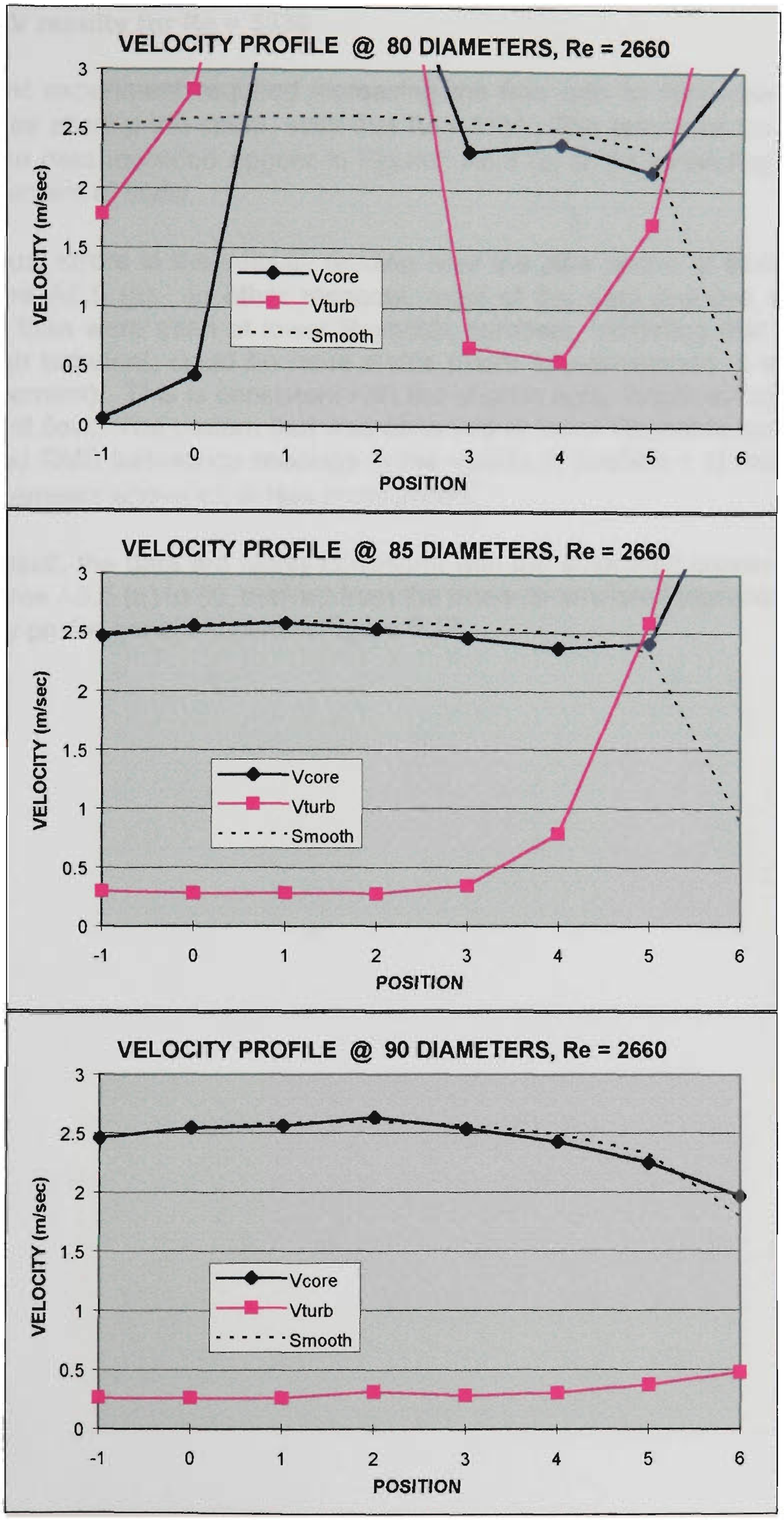

Figures A6.4 (p), (q), (r) - Velocity profiles at Re = 2660

A6.5 LV results for Re = 3330

The next experiment required increasing the flow rate to $50 litre/min$ without otherwise altering the setup, such that $Re = 3330$. The results of the analysis of all the data recorded appear in Figures A6.5 (a) to (r), extending out to a displacement of $90 dia$.

The usual errors in the velocity reading near the pipe centre at $80 dia$ appear in Figure A6.5 (p). In other respects, most of the data produce smoother graphs than were seen at lower Reynolds numbers, indicating that the flow, although turbulent, could be more stable (more fully-developed at any given displacement). This is consistent with the shorter entry length anticipated for turbulent flow. The pattern that was observed at lower Reynolds numbers, of elevated RMS turbulence readings in the vicinity of position 4 at many of the displacements above 45, is less pronounced.

As a result, the data are highly consistent with the smoothed curves included in Figures A6.5 (a) to (r), derived from the three-dimensional representation of velocity profile growth shown in Figure 6.17.

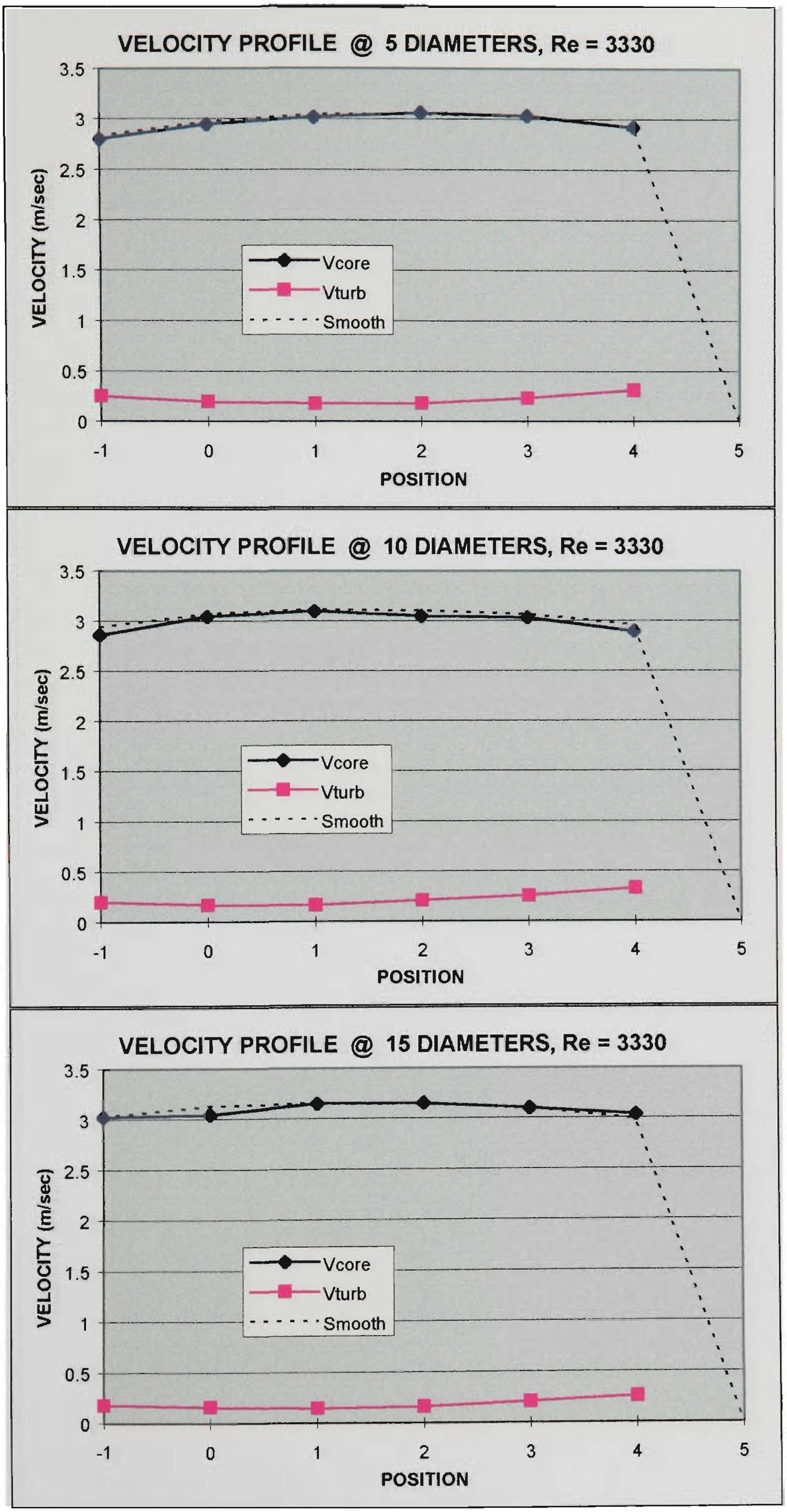

Figures A6.5 (a), (b), (c) - Velocity profiles at Re = 3330

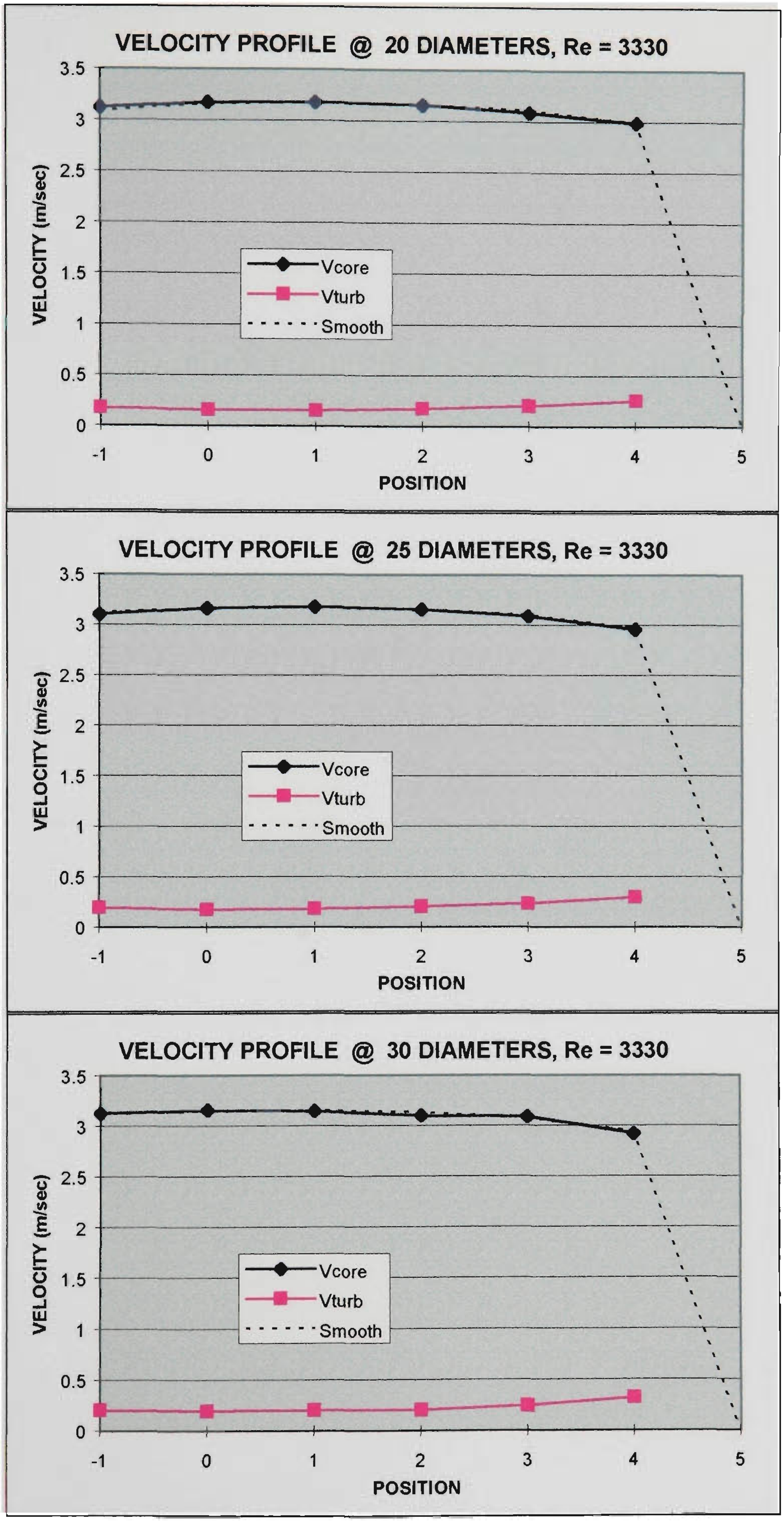

Figures A6.5 (d), (e), (f) - Velocity profiles at Re = 3330

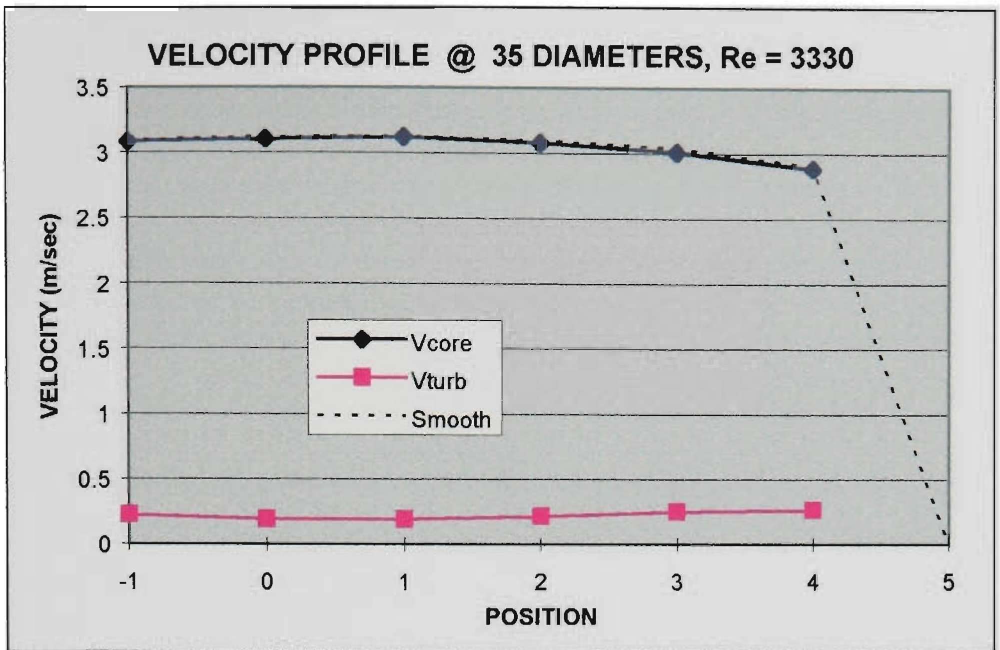

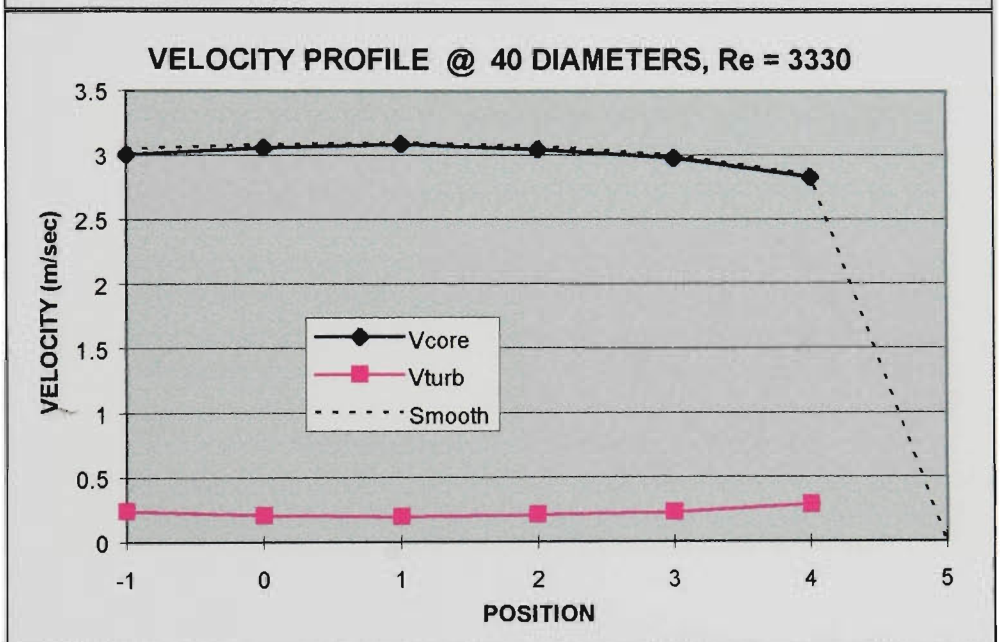

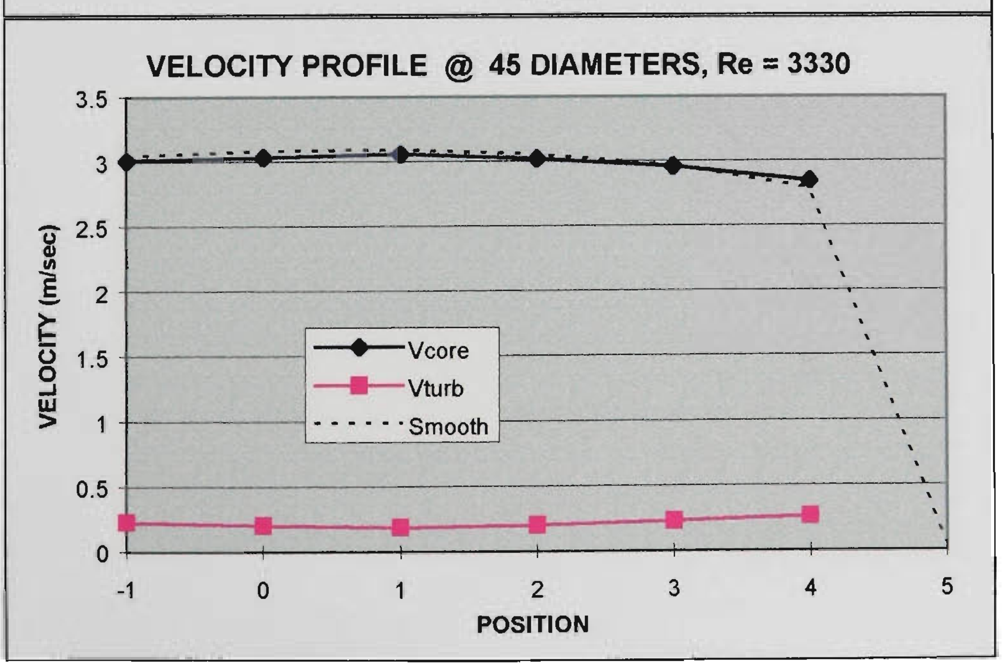

Figures A6.5 (g), (h), (i) - Velocity profiles at Re = 3330

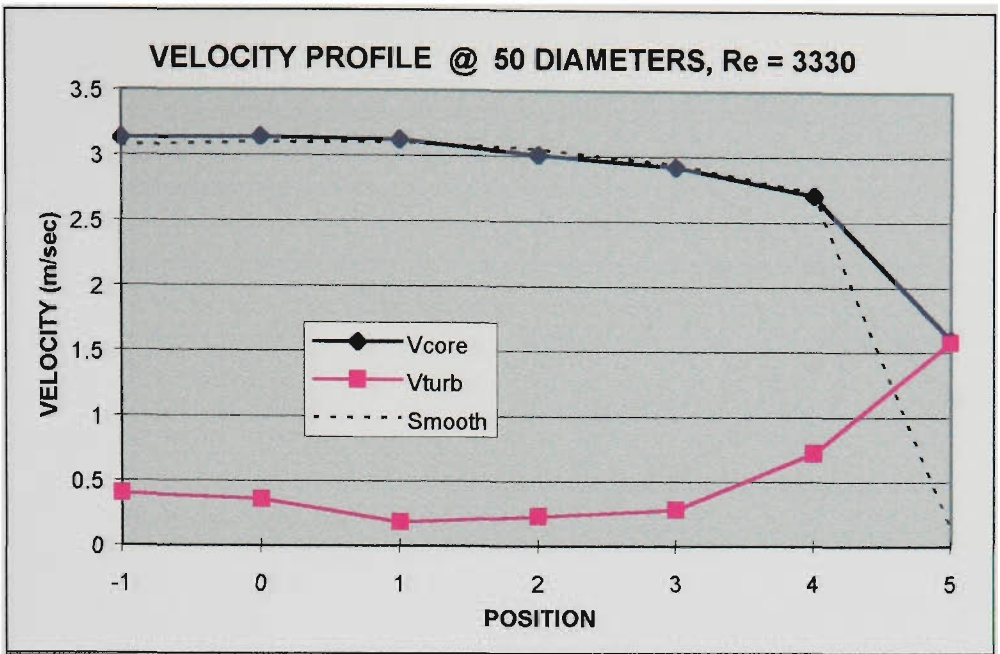

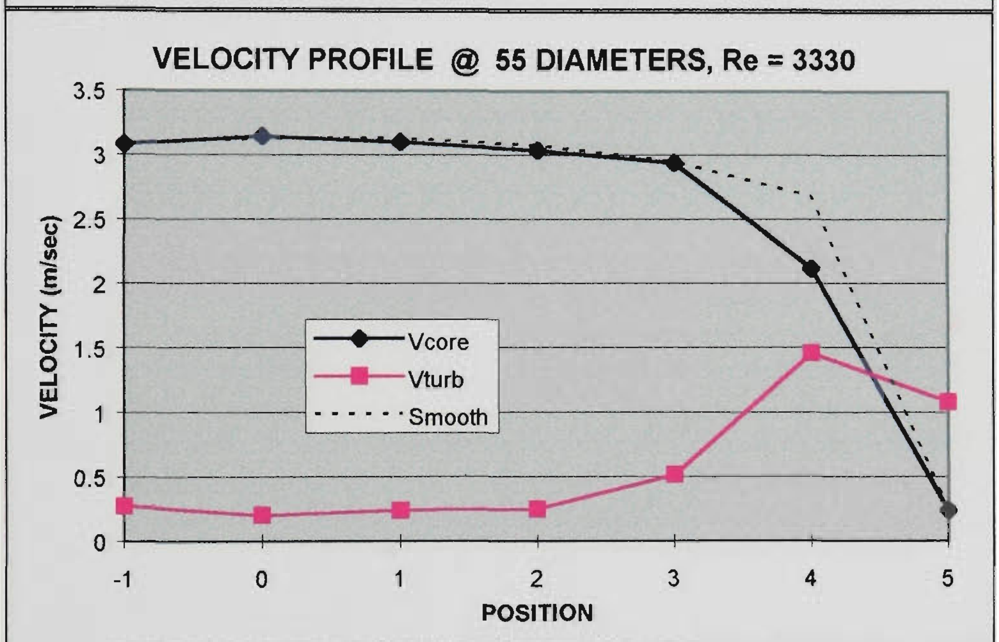

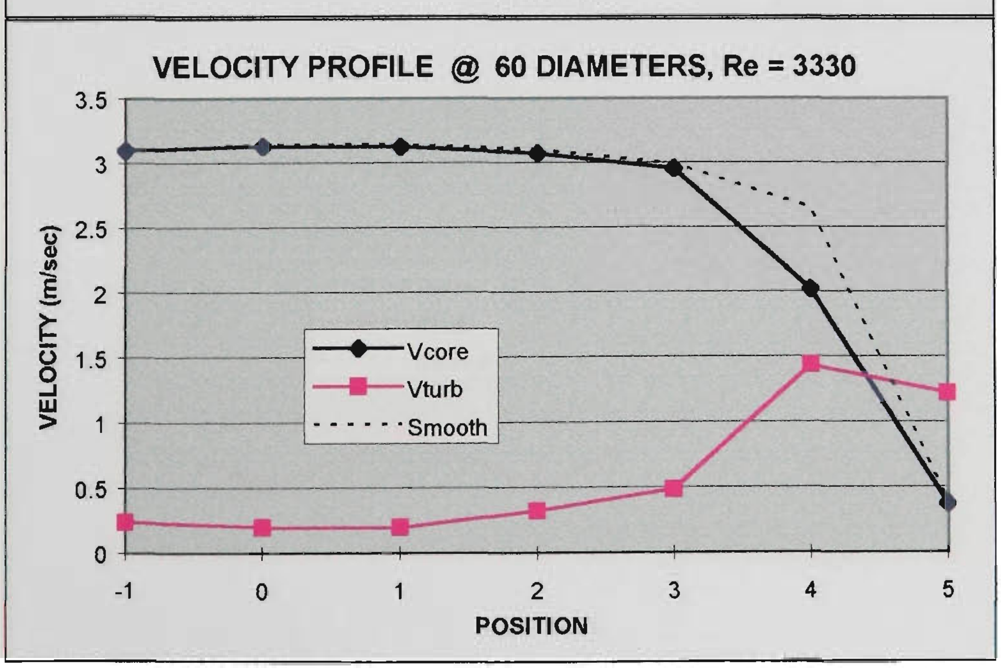

Figures A6.5 (j), (k), (l) - Velocity profiles at Re = 3330

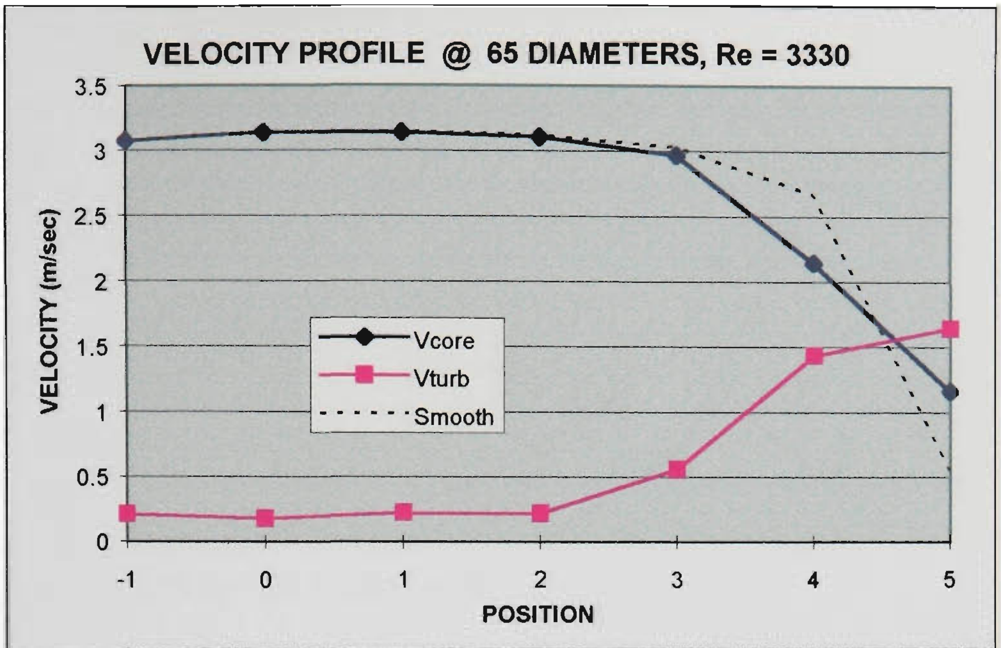

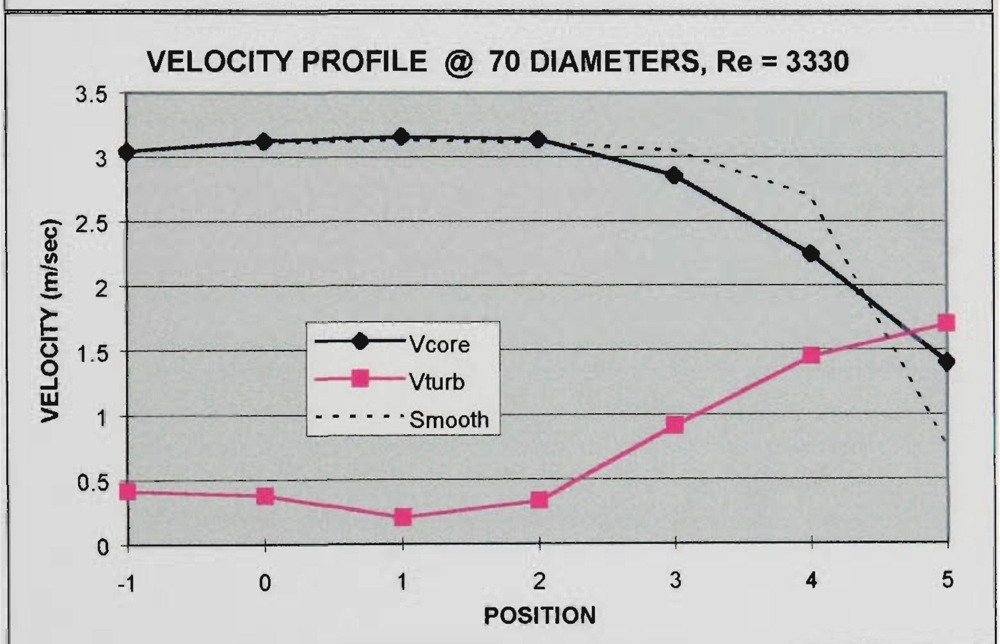

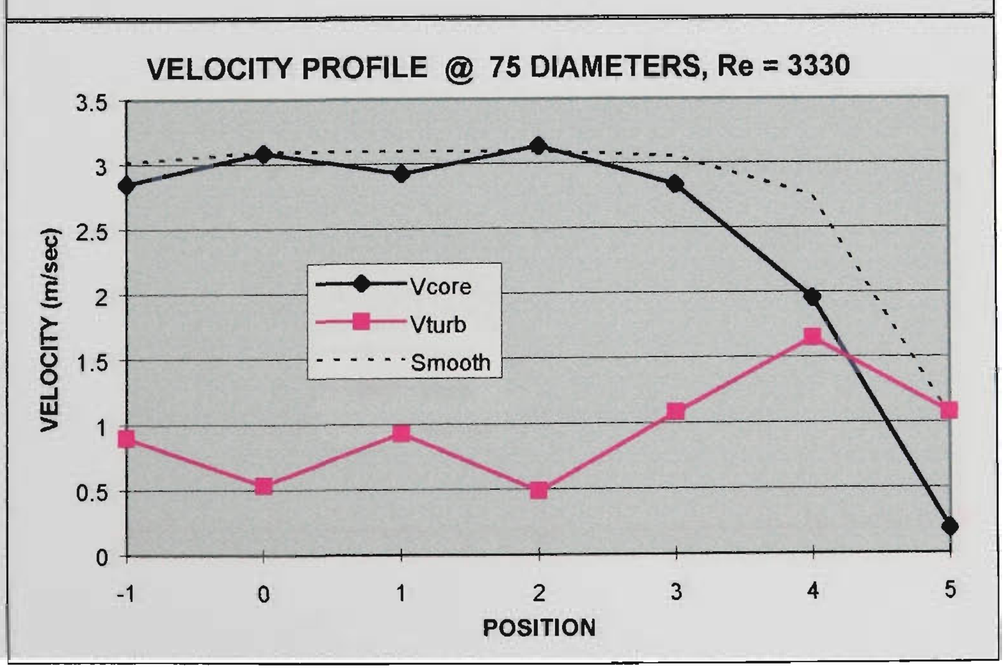

Figures A6.5 (m), (n), (o) - Velocity profiles at Re = 3330

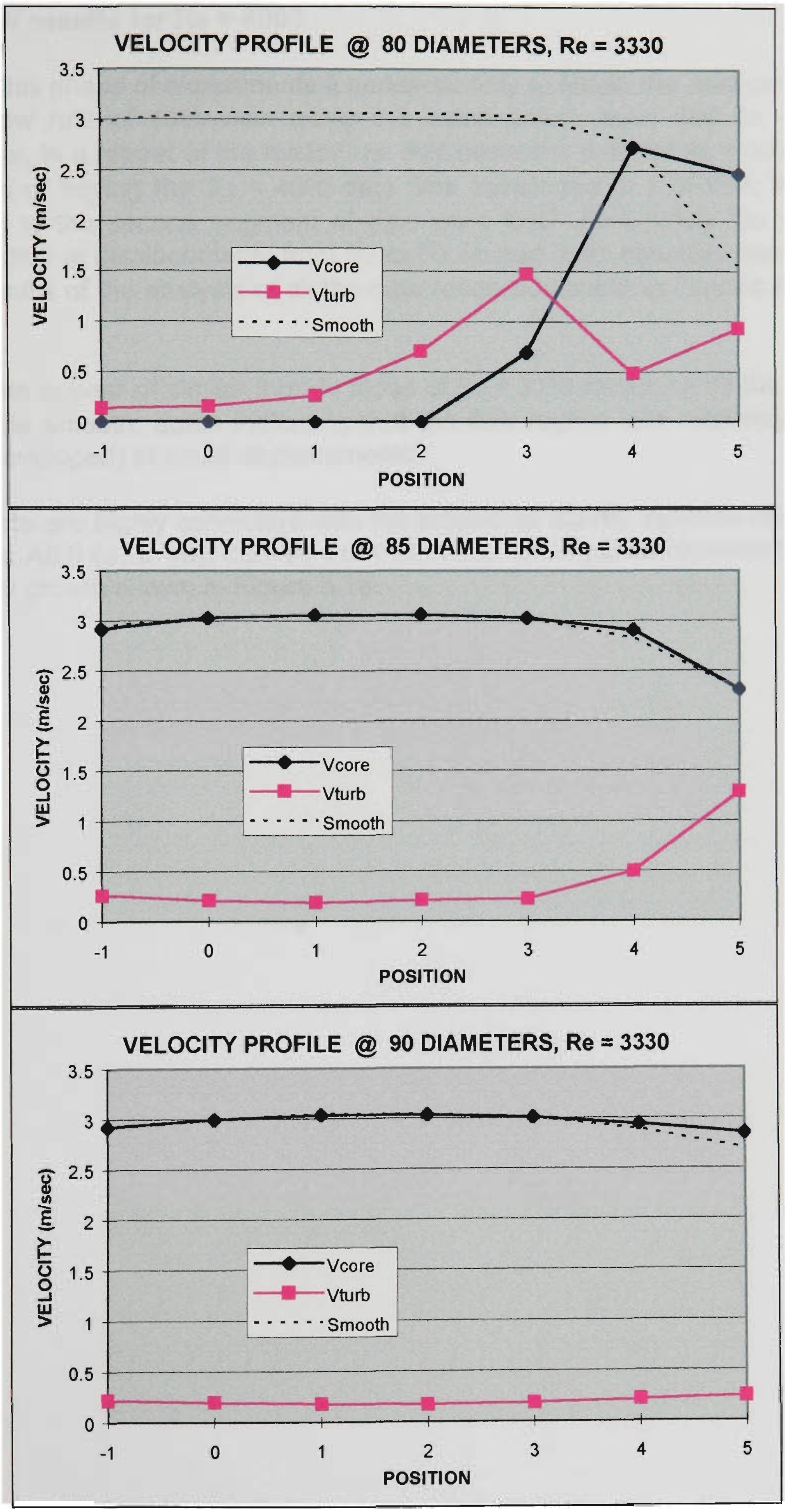

Figures A6.5 (p), (q), (r) - Velocity profiles at Re = 3330

A6.6 LV results for Re = 4000

Within this phase of experiments it remained only to obtain the data pertaining to a flow rate of *60litre/min* using the same setup, such that Re = 4000. However, in a repeat of the misfortune that beset the data for Re = 660, in the process of having the Re = 4000 data files transferred to CDROM, the files relating to the second segment of pipe were lost. Fortunately the velocity information at displacements from 50 to 70 *dia* had been recorded separately. The results of the analysis of all the data recorded appear in Figures A6.6 (a) to (o).

The data appear of similar form to those of Re = 3030 inasmuch as the graphs are quite smooth, again indicating that the flow regime was relatively stable (well-developed) at small displacements.

The data are highly consistent with the smoothed curves included in each of Figures A6.6 (a) to (n), derived from the three-dimensional representation of velocity growth shown in Figure 6.18.

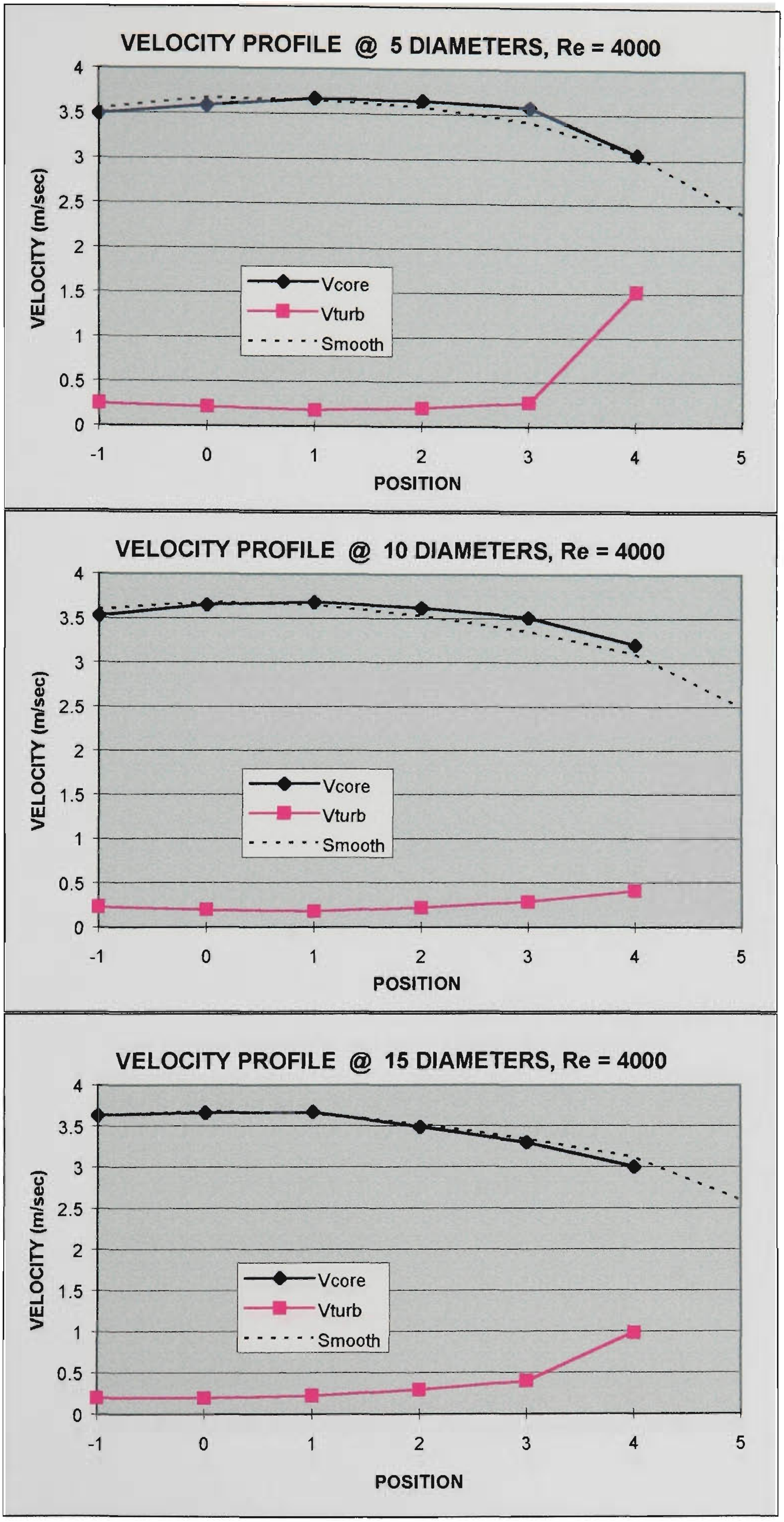

Figures A6.6 (a), (b), (c) - Velocity profiles at Re = 4000

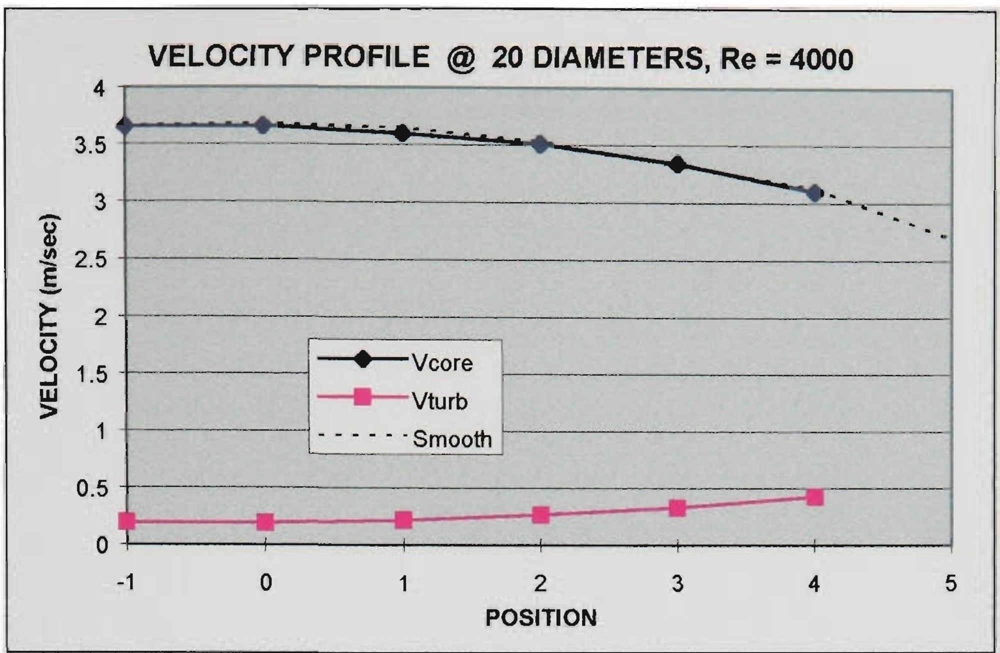

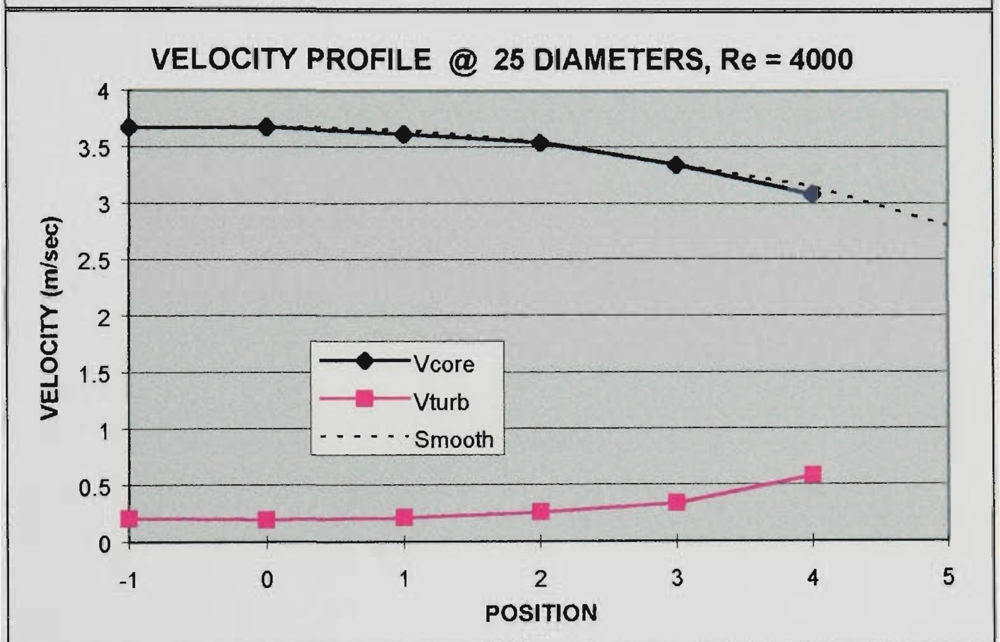

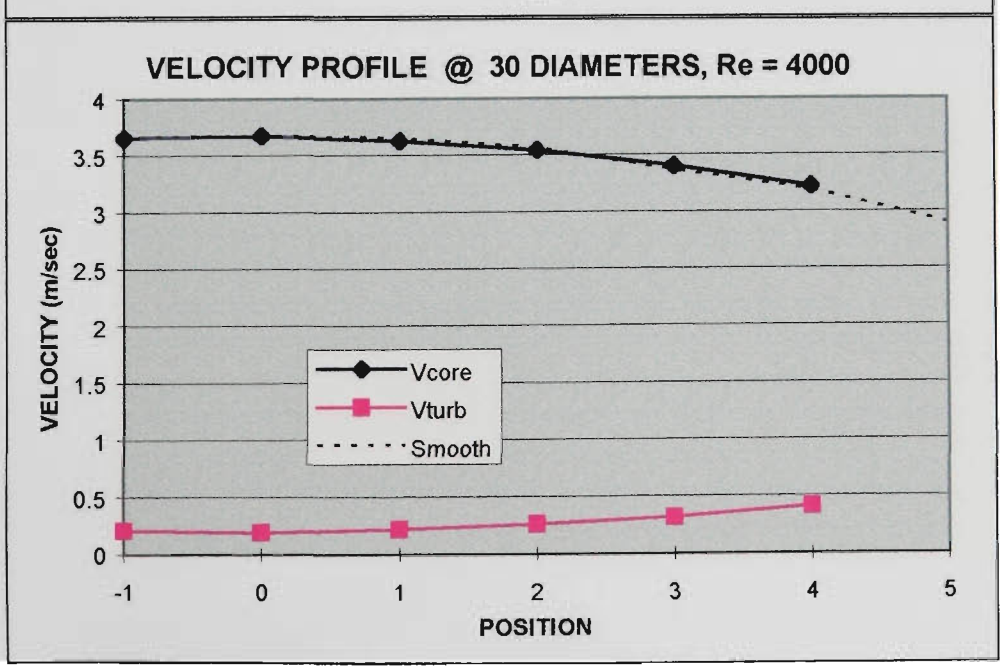

Figures A6.6 (d), (e), (f) - Velocity profiles at Re = 4000

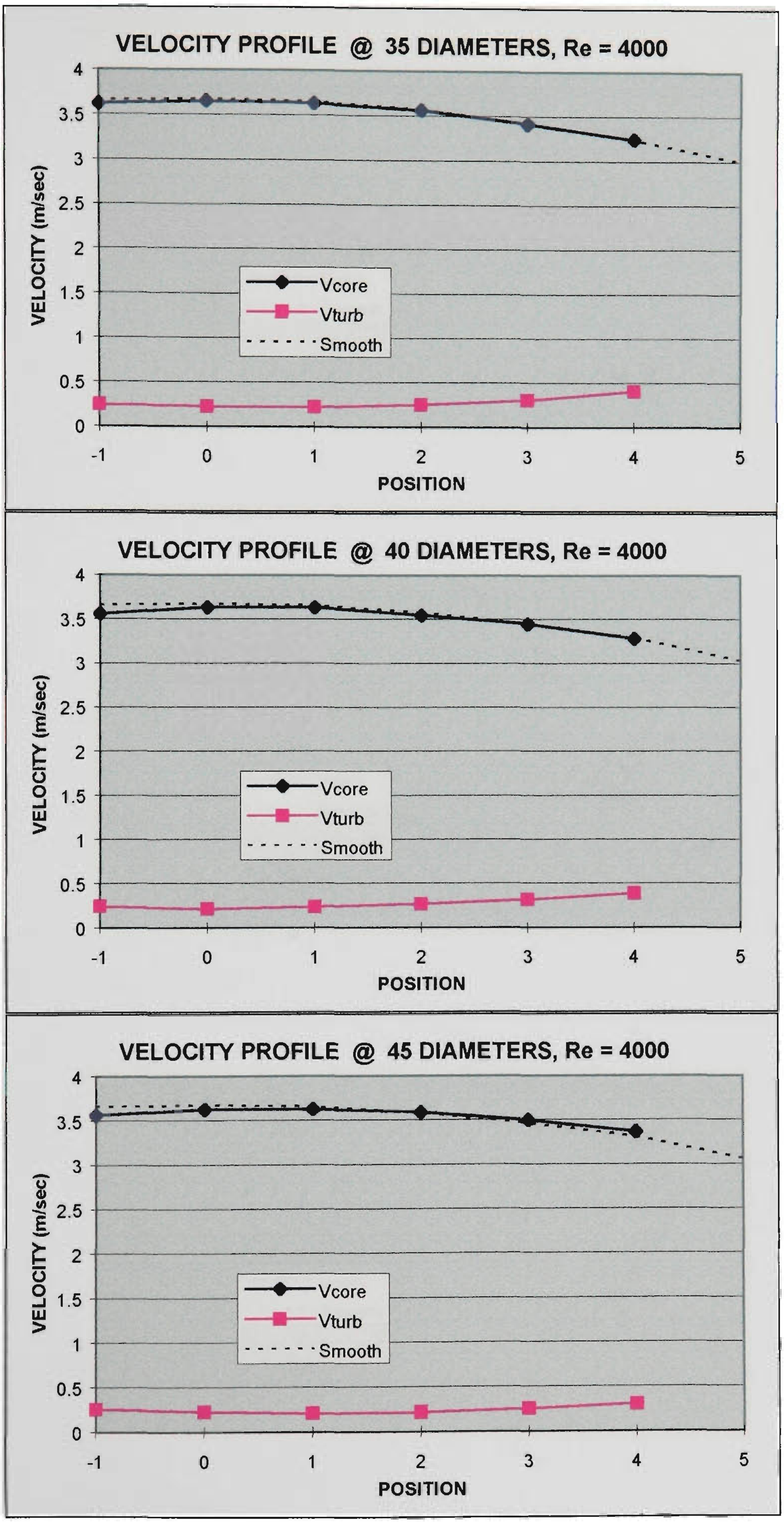

Figures A6.6 (g), (h), (i) - Velocity profiles at Re = 4000

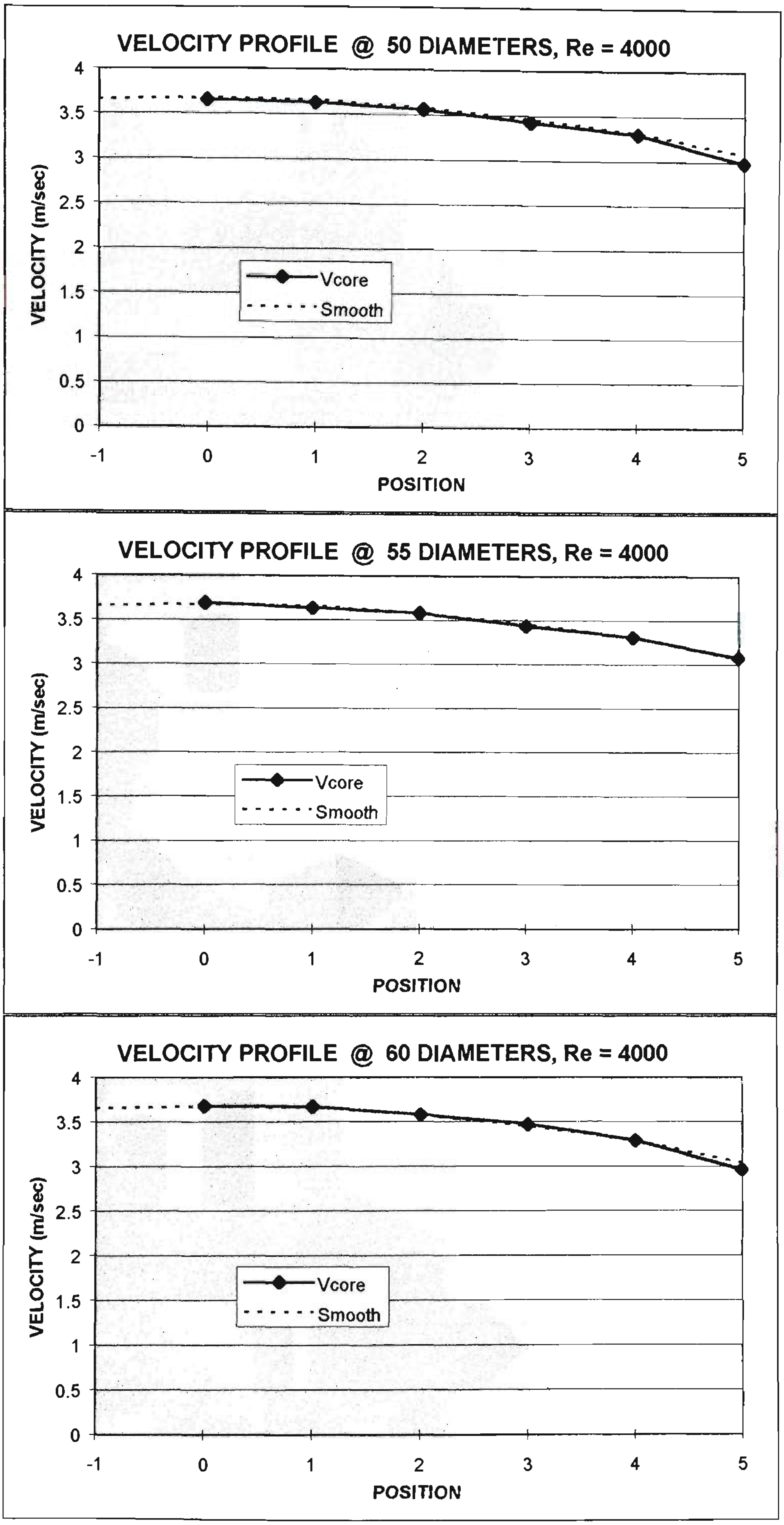

Figures A6.6 (j), (k), (l) - Velocity profiles at Re = 4000

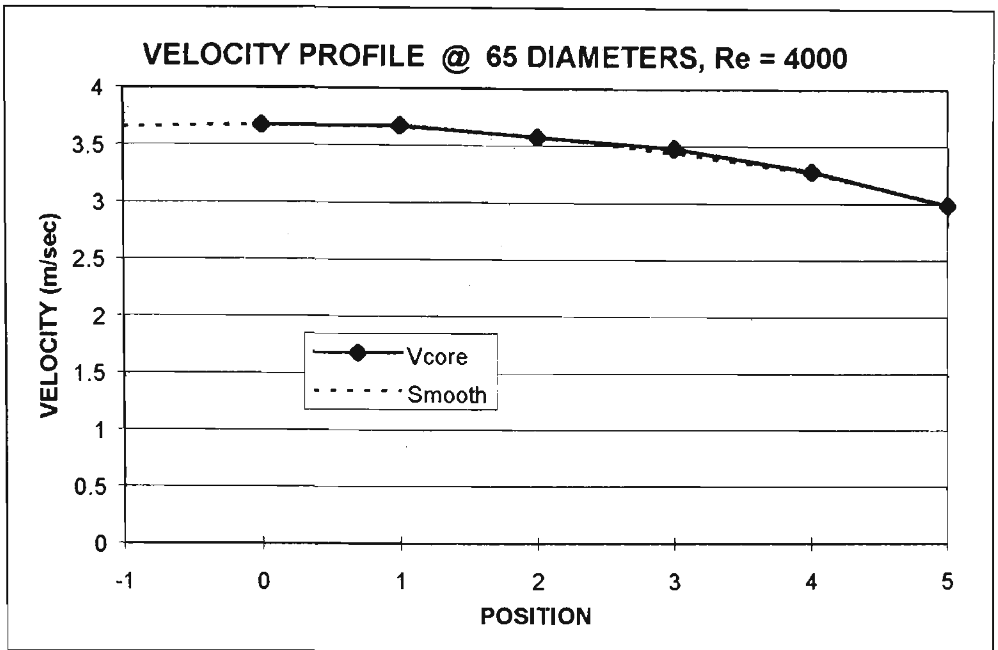

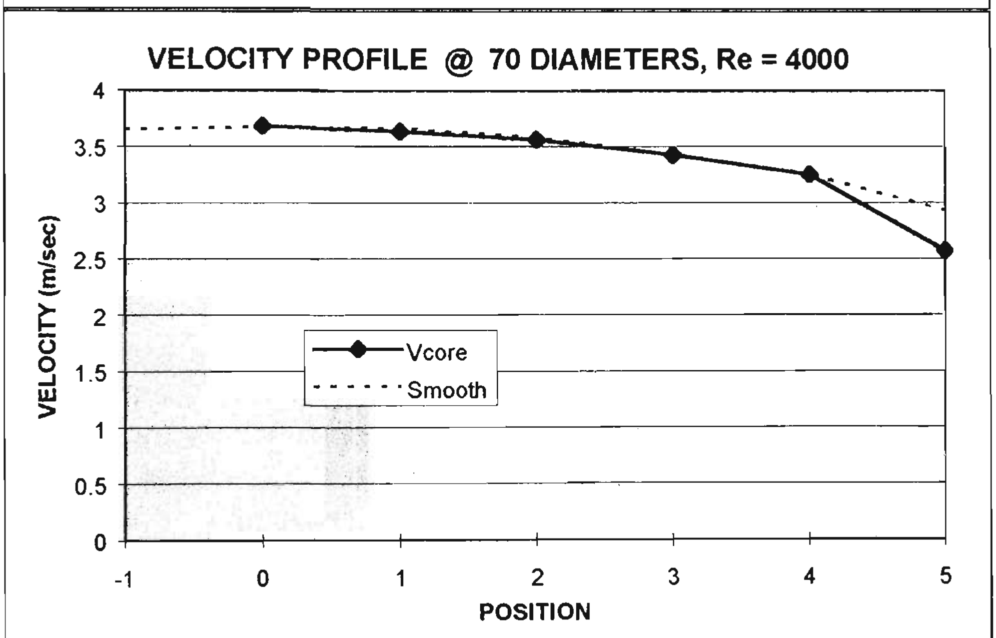

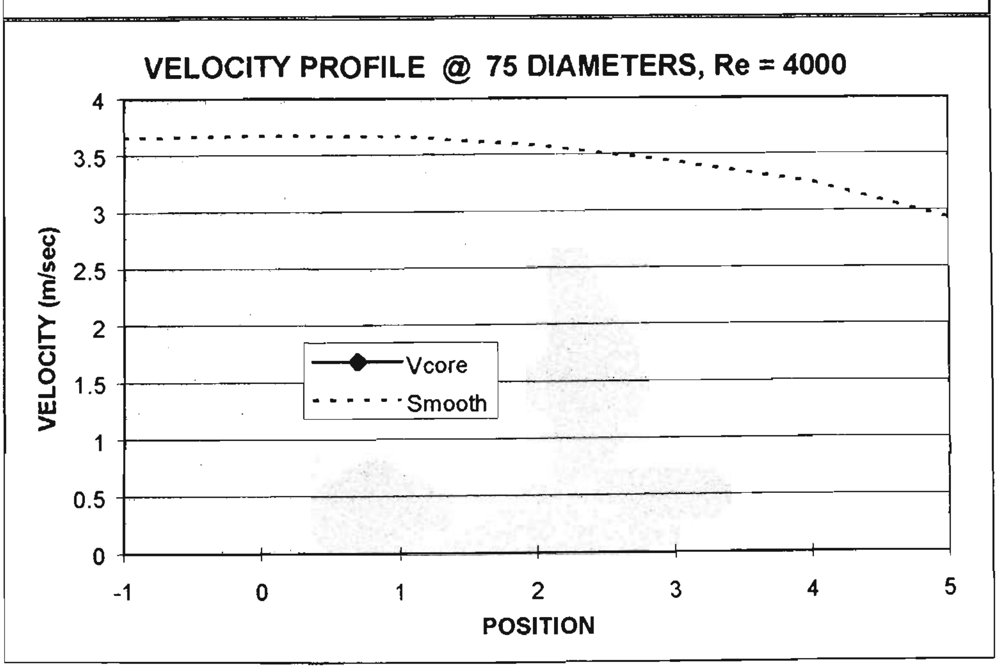

Figures A6.6 (m), (n), (o) - Velocity profiles at Re = 4000

A6.7 ALTERNATIVE TIME FACTOR'

It was noted that in applying the equation for Time Factor there was some duplication inasmuch as both the average velocity and the Reynolds number had to be specified. These two parameters are directly related at a given temperature and pipe diameter ($\mathrm{Re} = D_{pipe}\, u_{avg} / k$) so arguably, only one of them need be specified. Thus we can obtain:

$$T_x = F_T \frac{D_{pipe}}{u_{avg}} = \frac{F_T\, D^2_{pipe}}{k\,\mathrm{Re}}$$

This equation gives rise to an alternative dimensionless Time Factor' and results in the new graphs presented in Figure A6.7. Again, dotted curves have been included to indicate the graphs that would result from using the original exponential equations (refer Figure 6.9) and these retain a close association with the LV-based graphs. Overall it is noted that Figure A6.7 shows a wider divergence of the graphs than was evident in Figure 6.30, which does not suggest an improvement.

However, a better indication of the usefulness of this alternative Time Factor' is obtained from the 3-D representation in Figure A6.7, which has been sliced to produce Figure A6.8. In both Figures A6.7 and A6.8 we can see trends developing at the extremes of Reynolds numbers used. In the case of higher Reynolds numbers it would be possible to extrapolate to moderately higher values with some confidence. The same confidence cannot be held for extrapolations below $\mathrm{Re} = 660$, where the graphs appear to trend toward infinity at $\mathrm{Re} = 0$. For reliable extrapolation, it is necessary that the curves show a linear trend, and are preferably horizontal or of low gradient as was the case in Figure 6.32.

Although this alternative Time Factor' is not convenient for extrapolation, linear approximations were developed in the same manner as Figure 6.33 and presented in Figure A6.10. Once again the data points lie in close proximity to the linear approximations.

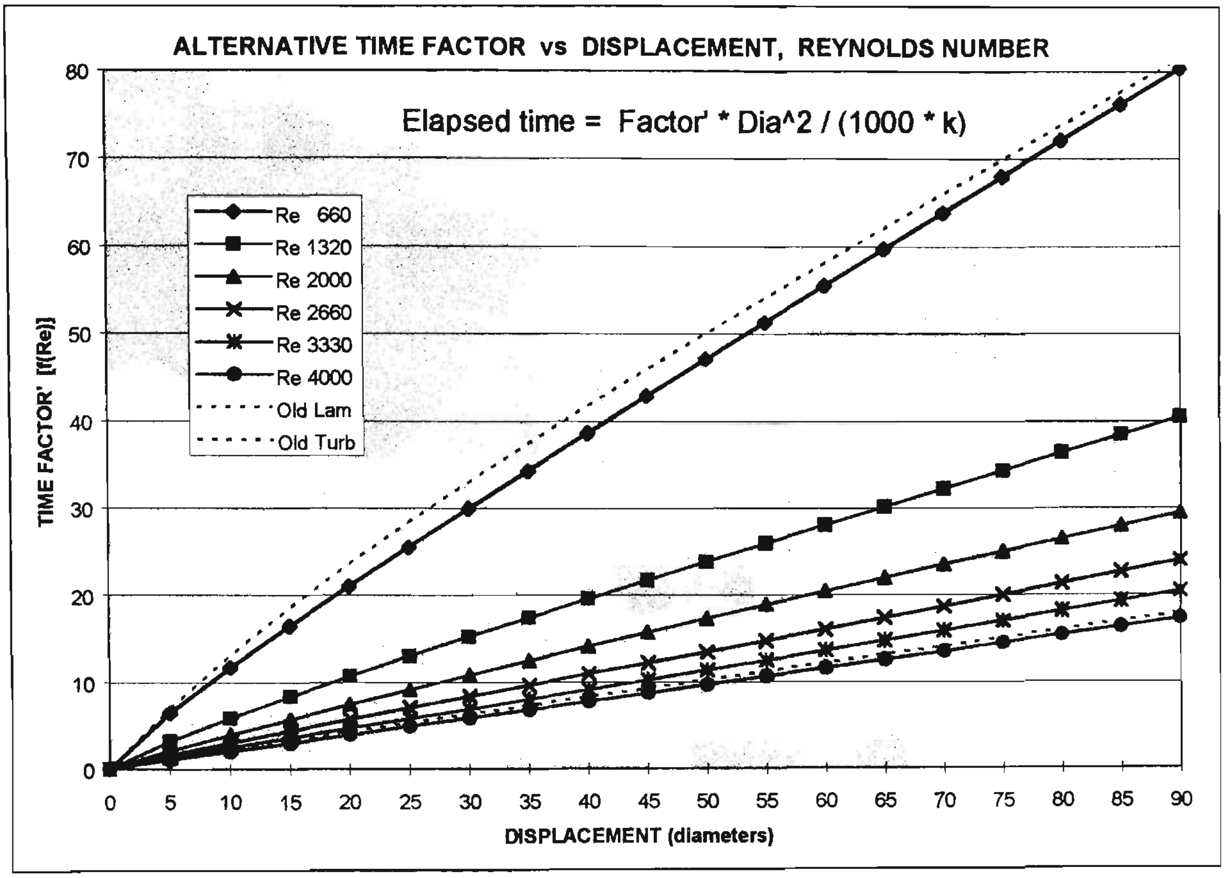

Figure A6.7 - Alternative Time Factor' versus displacement

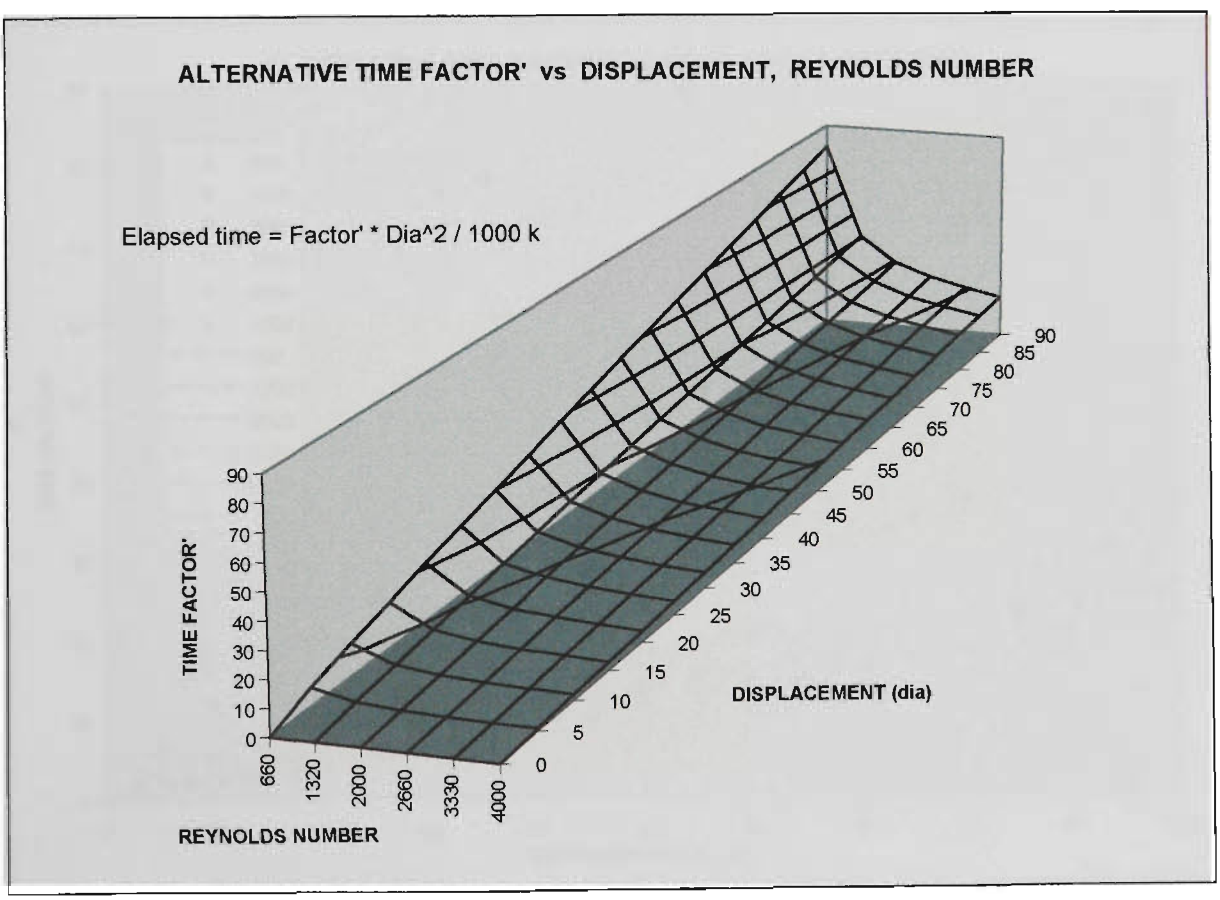

Figure A6.8 - 3D representation of alternative Time Factor'

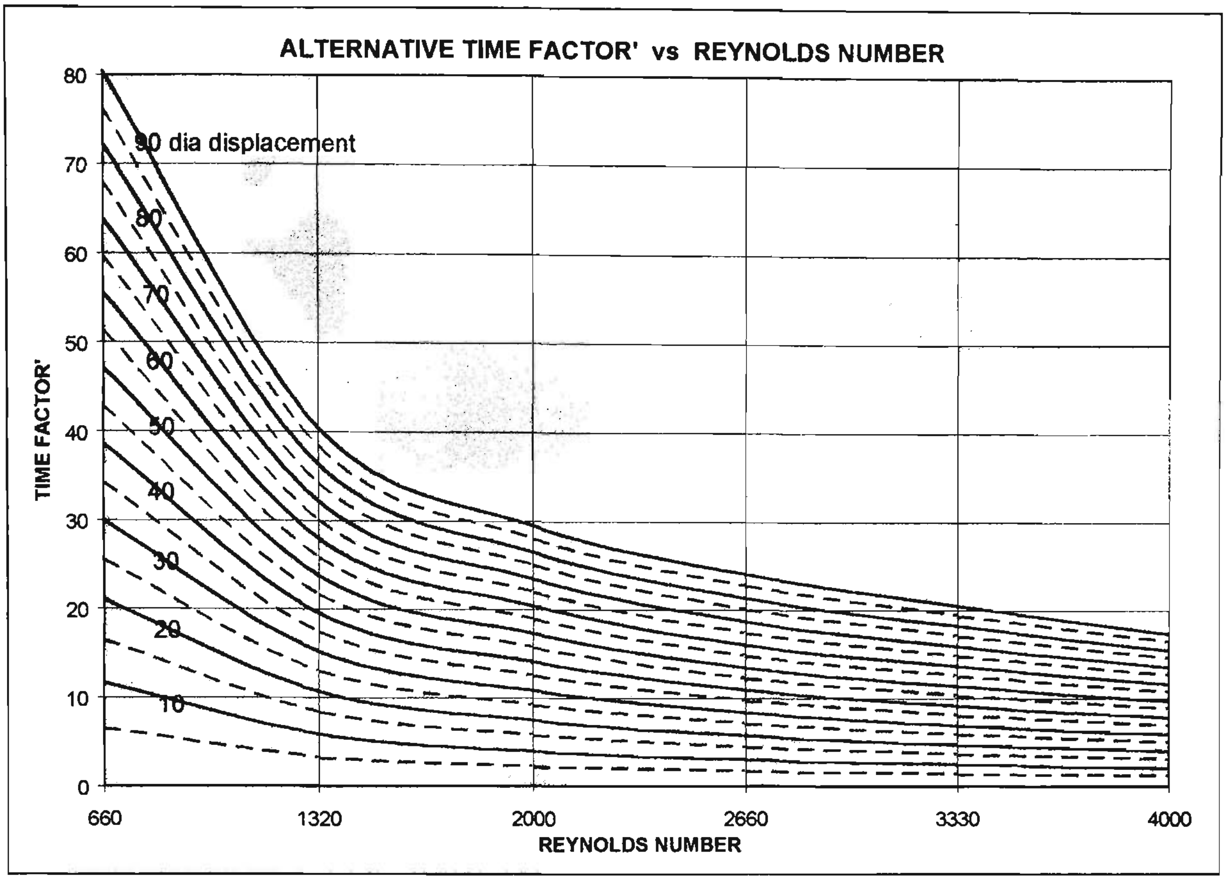

Figure A6.9 - Alternative Time Factor versus Reynolds number, displacement

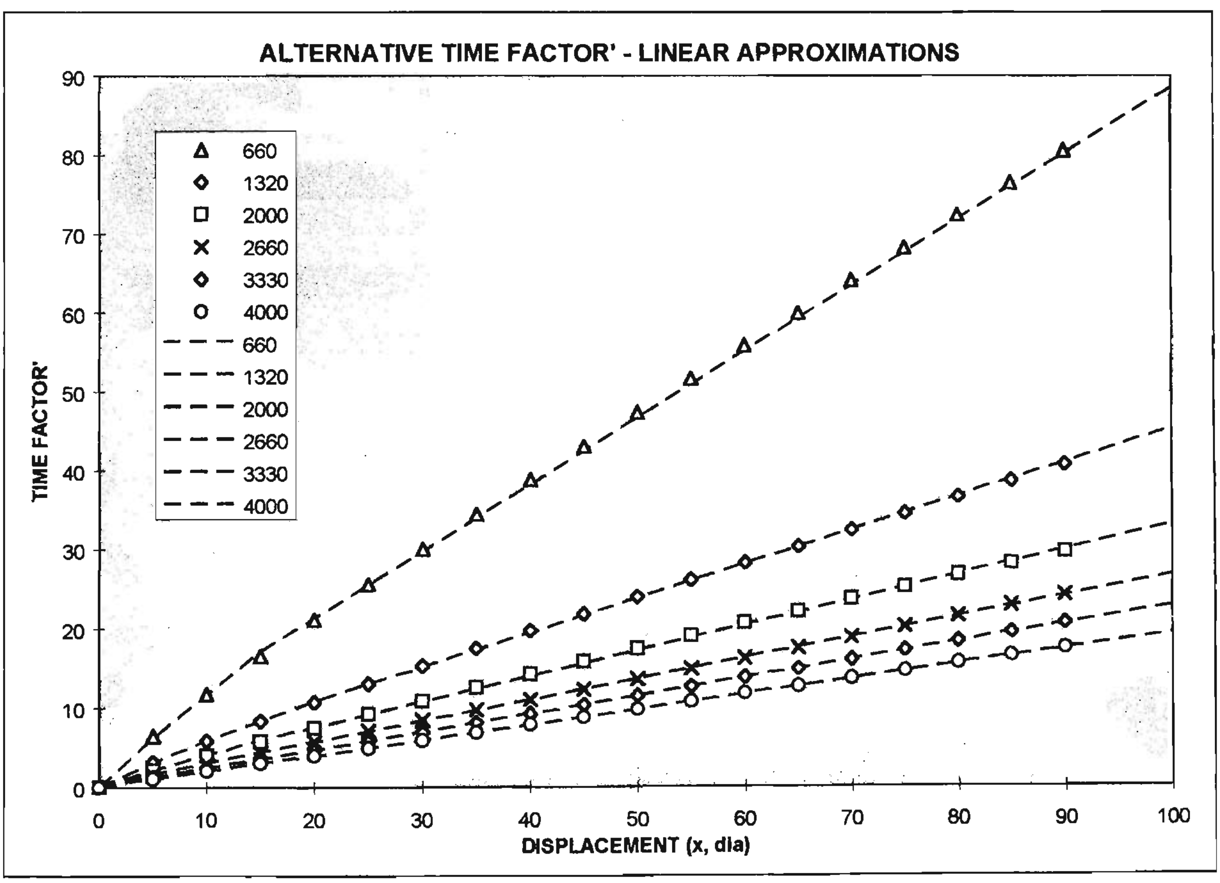

Figure A6.10 - Linear approximations to alternative Time Factor'

With reference to Figure A6.10 it was found that for displacements more than $15dia$, the following equations provided the linear approximations to the alternative Time Factor':

$$F_{0660} = 0.8400\,d + 4.500$$

$$F_{1320} = 0.4280\,d + 2.300$$

$$F_{2000} = 0.3180\,d + 1.200$$

$$F_{2660} = 0.2610\,d + 0.500$$

$$F_{3330} = 0.2250\,d + 0.188$$

$$F_{4000} = 0.1912\,d + 0.129$$

Figure A6.11 presents the magnitude of the errors of fit between the data points and the linear approximations thereto, in terms of percentage divergence. In this case we see that the errors are generally smaller than was the case in Figure 6.34, but not greatly so. Given the difficulty of extrapolation, overall this alternative Time Factor' does not present significant advantages over the original.

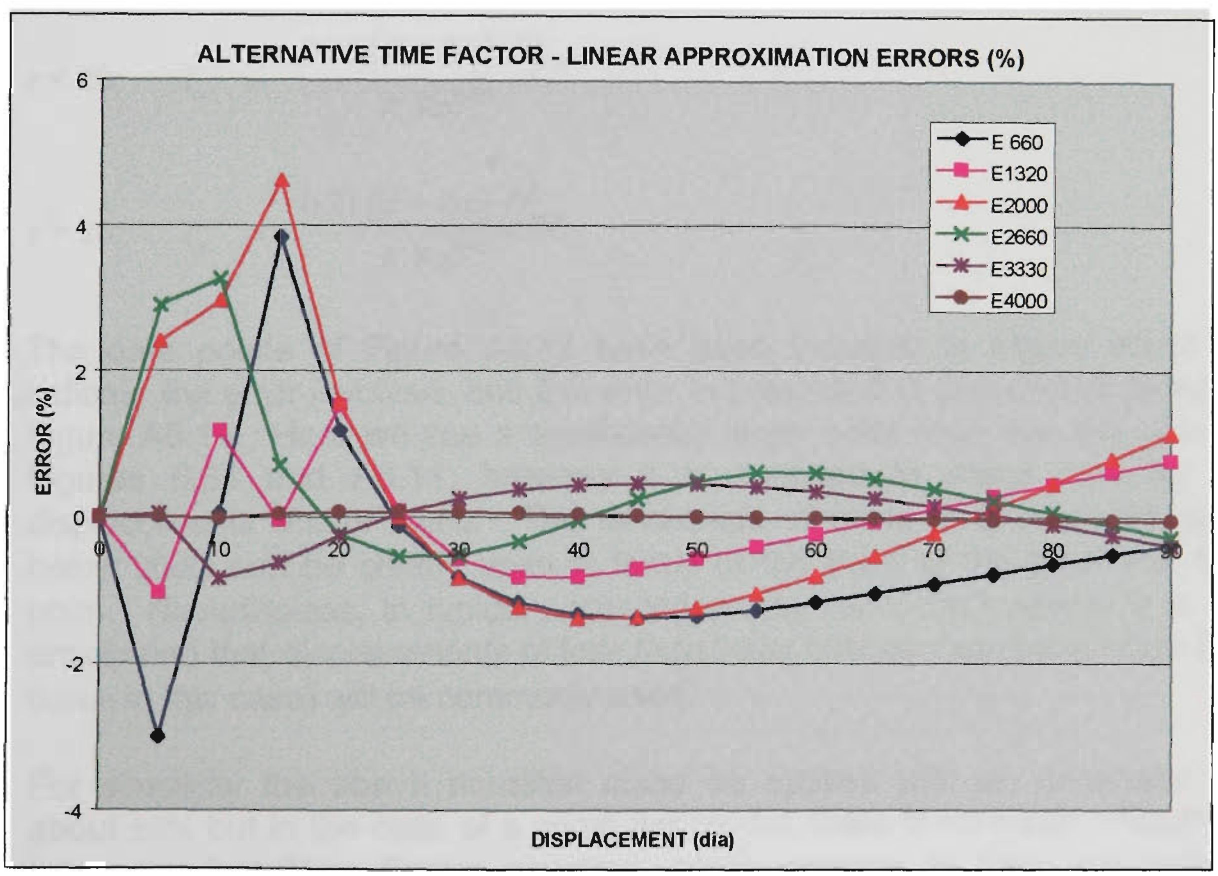

Figure A6.11 - Errors from linear approximations to alternative Time Factor'

A6.8 FURTHER ALTERNATIVE TIME FACTOR"

In a further attempt to obtain convergence of the graphs it was noted that manipulation of the Reynolds number within the alternative Time Factor' equation could be fruitful. After exploring various approaches aimed at minimising the errors, the following equation was determined:

$$T_x = F_T \frac{D_{pipe}^2}{k \mathrm{Re}^{0.85}}$$

Figure A6.12 is the result of applying this equation and we see that this result produces the highest degree of convergence yet achieved. It should be noted that the highest-placed graph in the group occurs for $\mathrm{Re} = 660$ and the lowest-placed graph occurs for $\mathrm{Re} = 1320$ (rather than, say $\mathrm{Re} = 4000$), which demonstrates that the exponent of Re, namely 0.85, represents the optimum value in order to achieve best convergence.

With this degree of convergence it is possible to develop a curve of best fit to represent all of the graphs, as presented in AFigure 6.13. To produce a relatively simple equation to this curve it has been broken into two parts, above and below a displacement of $20dia$:

$$x < 20: \quad T_x = \frac{0.26\left(d + 0.2\right) D_{pipe}^2}{k \mathrm{Re}^{0.85}}$$

$$x > 20: \quad T_x = \frac{0.21\left(d + 0.6\right) D_{pipe}^2}{k \mathrm{Re}^{0.85}}$$

The data points of Figure A6.12 have been included in Figure A6.13 to indicate the error involved, and this error is presented in percentage terms in Figure A6.14. Here we see a significantly larger error than was the case in Figures 6.34 and A6.11, however it is confined to about ±5% for all displacements above $30dia$. The advantage of using a different equation below $20dia$ can be clearly seen in terms of the trend of the graphs at that point. Nevertheless, in typical aspirated smoke detection systems it is not anticipated that displacements of less than $30dia$ between sampling holes (i.e. $0.64m$ in this case) will be commonly used.

For simplicity the above equation could be applied with an uncertainty of about ±5% but in the case of a computer model, there is no major difficulty in using the first Time Factor equation, which appears to have the highest accuracy combined with the ability to extrapolate beyond the current range of Reynolds numbers. This is expected to be particularly important at the low end ($\mathrm{Re} < 660$).

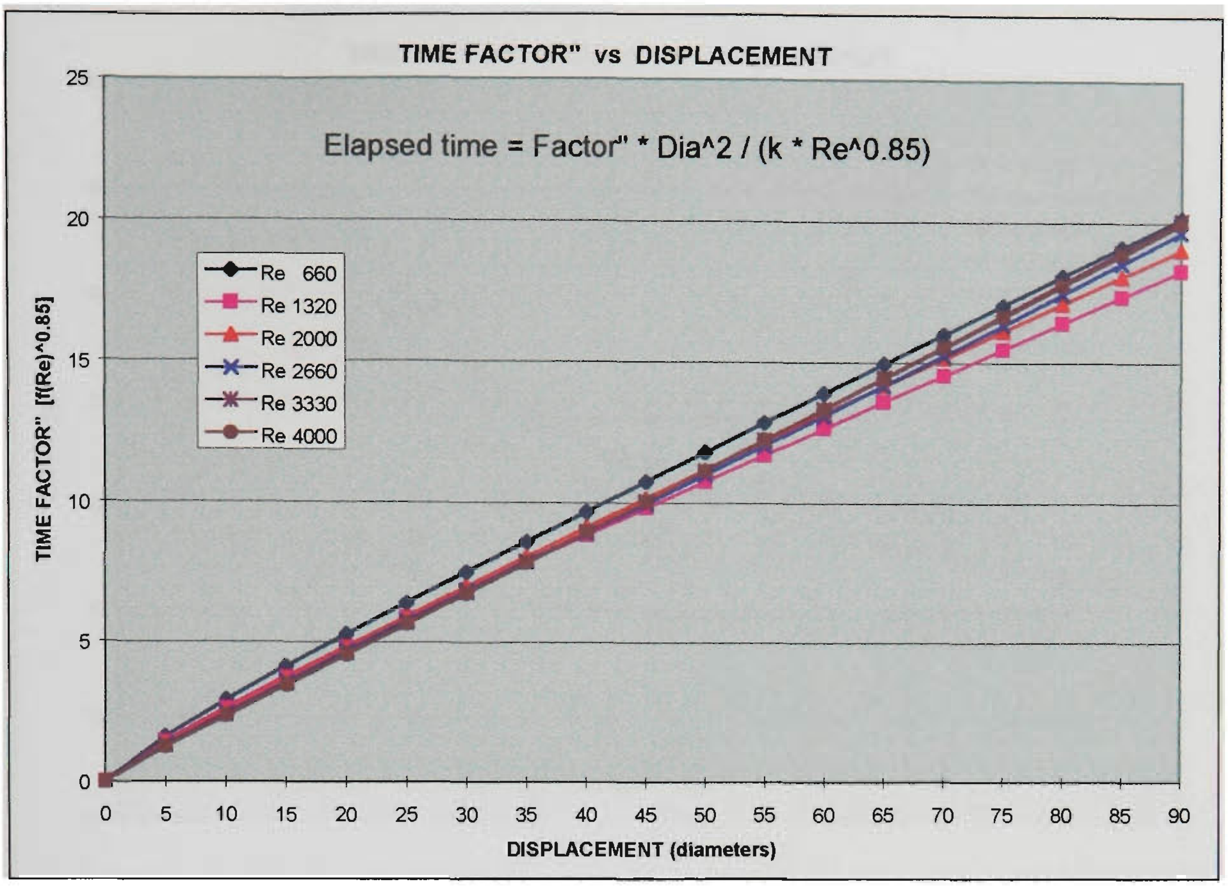

Figure A6.12 - Time Factor" based on $Re^{0.85}$

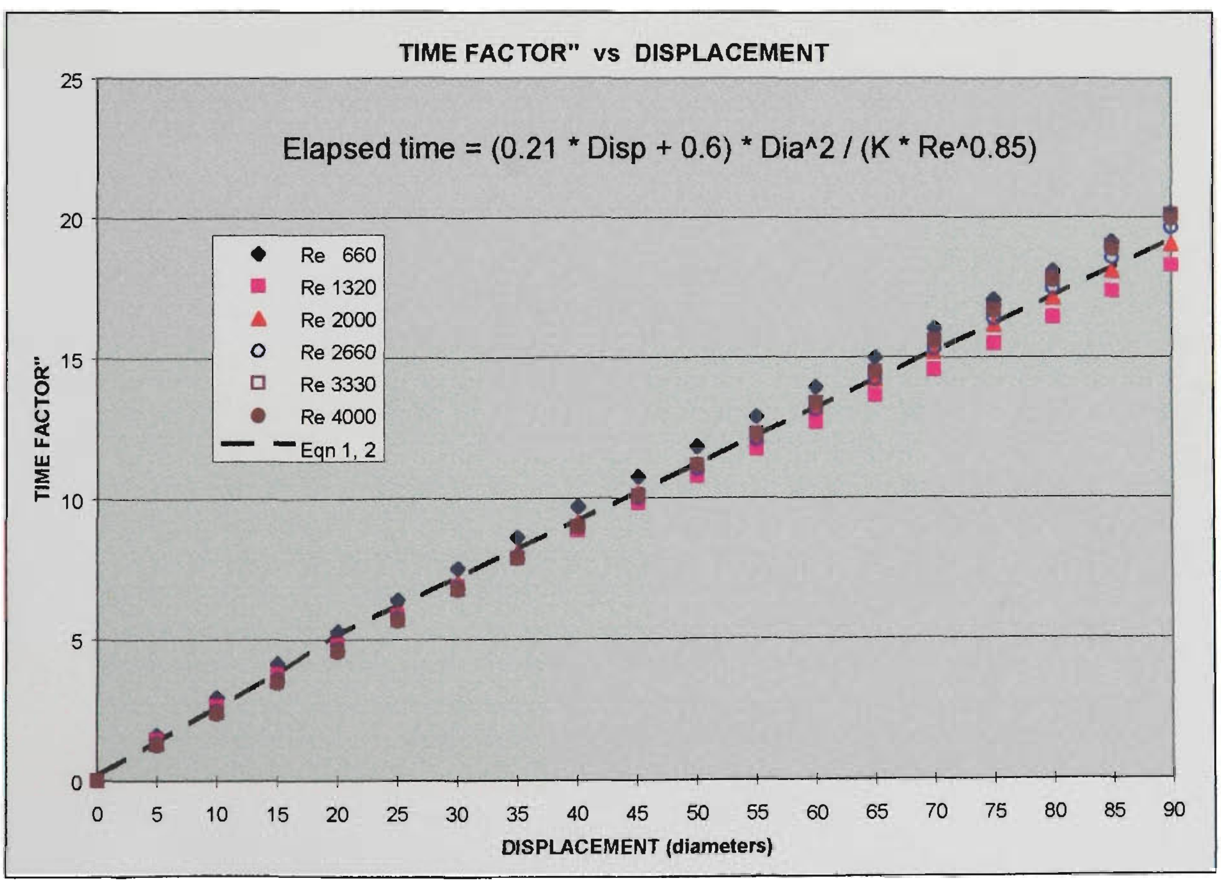

Figure A6.13 - Curve of best fit to Time Factor"

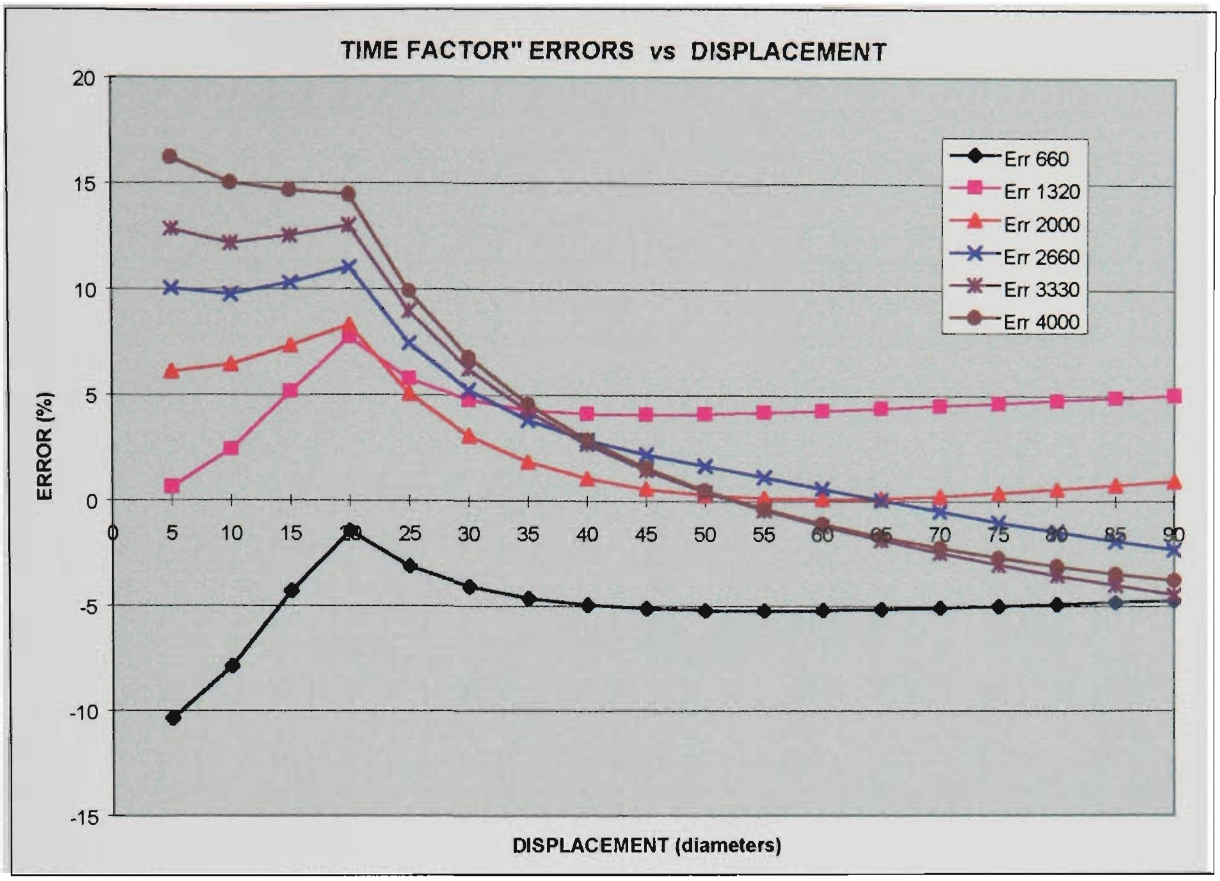

Figure A6.14 - Errors from curve of best fit to Time Factor"